BJR

THE BRITISH JOURNAL OF RADIOLOGY

Volume 65 Number 771 March 1992

39

203–211 = 25

CUK-H06083-28-P25862

28

39

X-ray Diagnosis • Ultrasound • Interventional Radiology
Radiotherapy • Oncology • Hyperthermia
Nuclear Medicine • Nuclear Magnetic Resonance
Radiation Physics • Radiobiology • Radiation Protection

BJR is published by The British Institute of Radiology BIR

NEW!

Self-Developing Radiation Sensitive Film for Quality Control Measurements and Routine Dosimetry in Radiation Therapy

GAFCHROMIC™ Dosimetry Media

Easy To Use...

NO Dark Rooms,

NO Film Cassettes,

NO Processing Required!

- Sensitive to Gamma, Electron, and X-Ray Radiations.
- Self-Developing – No Chemical Processing Required.
- Insensitive to Ambient Room Light.
- Dose Rate and Energy Independent Response.

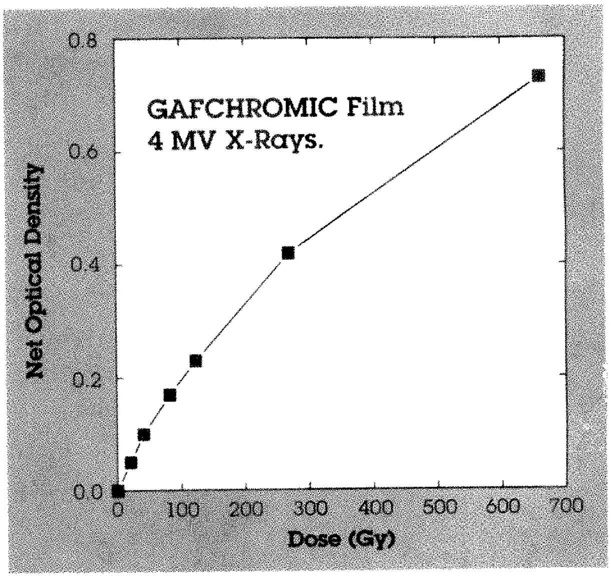

GAFCHROMIC™ dose response curve for 4 Mv X-rays.

FREE SAMPLE!

GAFCHROMIC is a colorless, grainless film that registers a deep blue color when irradiated.

For detailed information and a FREE SAMPLE of GAFCHROMIC, phone 516-741-6360, FAX 516-741-5414, or write and request Bulletin 5021-14.

TM, GAF Chemicals Corporation

NUCLEAR ASSOCIATES

VICTOREEN

Division of VICTOREEN, INC.
100 VOICE ROAD • P.O. BOX 349
CARLE PLACE, NY 11514-0349 U.S.A.
(516) 741-6360
FAX (516) 741-5414

P25862

BJR THE BRITISH JOURNAL OF RADIOLOGY

Established 1896

The Editorial Board

Honorary Editors
D. G. Shaw, FRCP, FRCR
F. A. Duck, BSc, MSc, PhD

Deputy Editors
C. K. Bomford, BSc, MPhil, FInstP
D. M. King, MB, BS, FRCR, DMRD
D. M. Tait, MB, ChB, MRCP, FRCR
J. W. Hopewell, BSc, PhD

Associate Editors
H. Baddeley, MB, BS, DMRD, FRCR, MRACR
R. Beaney, BSc, MB, ChB, MD, MRCP, FRCR
J. B. Bingham, MA, MRCP, MSc, FRCR
P. R. Blake, MD, MB, BS, BSc, FRCR
D. J. Cole, MB, BS, MRCP, FRCR
D. R. Dance, MA, PhD, FIPSM
A. M. Davies, MB, ChB, DMRD, FRCR
P. Dawson, BSc, PhD, MB, BS, MRCP, MInstP, FRCR
A. H. Freeman, MB, BS, FRCR
J. Glaholm, BSc, MRCP, FRCR
R. M. Harrison, BSc, MSc, PhD, FInstP
D. Hirst, BSc, PhD
H. C. Irving, MB, BS, DMRD, FRCR
P. C. Jackson, BSc, PhD, FInstP, CPhys, FIPSM
J. B. Karani, FRCR
A. M. Peters, BSc, MSc, MB, ChB, MD, MRCPath
D. W. Pilling, MB, ChB, DCH, DMRD, FRCR
J. F. Reidy, MB, BS, FRCP, FRCR
M. B. Rubens, MB, BS, LRCP, MRCS, DMR, FRCR
R. A. Shields, PhD
P. J. Shorvon, MB, BS, MRCP, FRCR
J. Tudor, MB, BS, FRCR
A. R. Valentine, MB, BS, MRCS, LRCP, FRCR, DMRD
J. Virjee, MB, ChB, FRCR
T. E. Wheldon, BSc, PhD, FInstP
G. H. Whitehouse, MB, BS, FRCP, FRCR, DMRD

Associate Editors Overseas
S. G. A. Chenery, PhD, FCCPM (North America)
B. J. Cremin, MD, FRCR, FRACR (South Africa)
R. Fox, DPhil (Australia)
M. Takahashi, MD (Japan)

Managing Editor: T. R. Hogan, BSc, PhD

The British Journal of Radiology is published monthly by the British Institute of Radiology, 36 Portland Place, London W1N 4AT. Telephone 071-580 4189 (editorial); Facsimile 071-255 3209. Editorial communications should be addressed to the Honorary Editors in accordance with the Instructions to Authors published in the January issue each year, copies of which may be obtained from the Managing Editor upon request.

Advertisements. Communications should be addressed to the Advertising Manager at the above address. Tel. 071-631 1168.

Subscriptions. The monthly fulfilment is carried out by BJR Subscriptions, PO Box 500, Leicester LE99 0AA, UK. Telephone 0858 410510; Facsimile 0858 434190.

The 1992 annual subscription to *The British Journal of Radiology* is £152 for EEC (incl. UK) readers and £167 for readers in the rest of the world.

These prices include delivery by sea mail; airmail rates are £10 extra for Europe and £30 extra for the rest of the world, effective from March 1992. Copies of this journal sent to subscribers in Bangladesh, Canada, India, Japan, Pakistan, Sri Lanka and USA are air-speeded for quicker delivery at no extra cost. Subscriptions are on a calendar year basis only.

Back issues prior to the current volume can be ordered from the British Institute of Radiology at the address above.

US mailing agents: Mercury Airfreight International Ltd Inc. Second class postage paid at Rahway, NJ, USA. Postmaster: send address corrections to The British Journal of Radiology, c/o Mercury Airfreight International Ltd Inc., 2323 Randolph Avenue, Avenel, NJ 07001, USA.

THE BRITISH INSTITUTE OF RADIOLOGY

BIR

Founded 1897
Incorporated by Royal Charter
Patron: Her Majesty The Queen

The British Institute of Radiology is an association of persons interested in radiology and allied subjects. Meetings are held monthly from October until May. Particulars of membership and other information may be obtained on application to the General Secretary at the Institute, 36 Portland Place, London W1N 4AT. The British Institute of Radiology is a registered charity, no. 215869.
Telephone: 071-580 4085 and 071-580 4189
Fax: 071-255 3209.

President
S. C. Lillicrap, DSc, PhD, FInstP, FIPSM
Honorary Secretaries:
N. W. Garvie, MAMB, BChir, MRCP, DMRD, FRCR, MSc
M. P. Law, BSc, PhD
Honorary Treasurer
D. S. McIntosh, BSc, PhD, MRPharmS, MRSC, MIMC
General Secretary
Mary-Anne Piggott, BSc, MBA, MBIM

Analyze

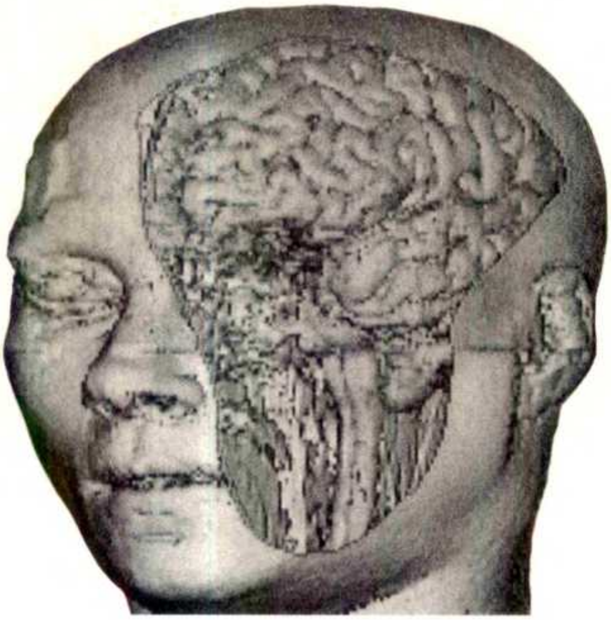

- Image visualization software for standard UNIX workstations.
- Multimodal data compatibility with extensive format import utilities.
- Interactive 2-D image display.
- Advanced 3-D image manipulation.
- Image analysis and quantification in 2-D and 3-D.
- Developed by the MAYO Foundation Biomedical Computer Resource.
- Available with annual software upgrade.

Available in Europe from:

CNSoftware Ltd

"The Old Post Office"
Worthing Road
Southwater
W. Sussex
RH13 7DT

Phone +44 (0)403 733607
FAX +44 (0)403 733609

sun microsystems

VOL 65 NO 771 MARCH 1992

The British Journal of Radiology
Contents

Papers

Page

The incidence and significance of fluid–fluid levels on computed tomography of osseous lesions 193
A. M. Davies, V. N. Cassar-Pullicino and R. J. Grimer

CT evaluation of lymph node status at presentation of prostatic carcinoma 199
J. Spencer and S. Golding

Duplex pulsed Doppler sonography in the differential diagnosis of hepatocellular carcinoma and other common hepatic tumours 202
Z.-Y. Lin, W.-Y. Chang, L.-Y. Wang, S.-C. Chen, W.-L. Chuang, M.-Y. Hsieh and J.-F. Tsai

Intrarenal Doppler ultrasound studies in normal and acutely obstructed kidneys 207
P. M. Rodgers, J. A. Bates and H. C. Irving

Bone mineral density in healthy normal women and reproducibility of measurements in spine and hip using dual-energy X-ray absorptiometry 213
M. J. Haddaway, M. W. J. Davie and I. W. McCall

Echo pattern of lymph nodes in colorectal cancer: an *in vitro* study 218
S. R. Rafaelsen, O. Kronborg and C. Fenger

Computed tomography in agenesis of the lung in infants 221
A. C. Argent and B. J. Cremin

Results of a survey of doses to paediatric patients undergoing common radiological examinations 225
C.-L. Chapple, K. Faulkner, R. E. J. Lee and E. W. Hunter

Dose reduction by the use of erbium filtration in a general radiographic room 232
R. W. Cranage, C. J. Howard and A. D. Welsh

Measurement of extrafocal radiation by computed radiography 238
R. H. Miettunen

The dose-rate effect in interstitial brachytherapy: a controversy resolved 242
E. J. Hall and D. J. Brenner

Neoadjuvant intra-arterial chemotherapy in inflammatory carcinoma of the breast 248
J. I. Bilbao, J. Rebollo, J. M. Longo, F. Mansilla, L. Muñoz-Galindo and J. M. Vieitez

The potential of ytterbium 169 in brachytherapy: a brief physical and radiobiological assessment 252
S. M. Loft, I. P. Coles and R. G. Dale

Technical notes

The application of microdosimetry to the metrology of low-energy X rays used in mammography 258
A. J. Waker and M. Marco

Accuracy of pelvimetry measurements on CT scanners 261
J. P. Wade

A fine needle aspiration technique using high negative pressure 264
J. C. Rhymer, D. W. McRobbie and J. E. Boultbee

Case reports

Linear scleroderma and melorheostosis 266
A. Siegel and H. Williams

Sonographic detection of neonatal hydrometrocolpos 268
A. K. Banerjee, O. Clarke and L. M. MacDonald

An unusual osteochondral body in association with calcium pyrophosphate dihydrate crystal deposition disease 271
A. C. Jones, B. J. Preston and M. Doherty

Three-dimensional imaging of dual isotope data-sets in a case of acute myocardial infarction 273
H. P. Dilhuydy, D. McNamara, R. J. Lemieux, Y. Martel and J. A. de Guise

Case of the month

Dysphagia paediatrica 279
B. M. Stephenson

Short communication

Percutaneous sclerotherapy for simple renal cysts in children 281
I. Reiner, S. Donnell, M. Jones, H. L. M. Carty and A. M. K. Richwood

Correspondence

Anatomy of percutaneous femoral artery puncture 283
F. Stubbs and D. C. Cumberland
Authors' reply 283
G. G. Hartnell and D. Grier

Proceedings

Proceedings of the British Institute of Radiology
International particle therapy meeting. 7 June 1991 284

Book reviews

Interventional Computed Tomography. *R. M. M. Seibel and D. H. W. Gronemeyer* 287
Treatment of Radiation Injuries. *D. Browne, J. F. Weiss, T. J. MacVittie and M. V. Pillai* (Eds) 287
Digital Imaging In Diagnostic Radiology. *J. D. Newell and C. A. Kelsey* (Eds) 287
The Radiologic Clinics of North America. *H. J. Burhenne* (Ed) 288
BIR Bulletin *facing page* 288

© 1992 The British Institute of Radiology. This publication is copyright under the Berne Convention and the Universal Copyright Convention. All rights reserved, apart from any relaxations permitted under national copyright laws, no part of this publication may be reproduced, stored in a retrieval system or transmitted in any form or by any means without the prior permission of the copyright owners. Permission is not, however, required to copy abstracts of papers or of articles on condition that a full reference to the source is shown. Multiple copying of the contents of the publication without permission is always illegal. Published by The British Institute of Radiology, 36 Portland Place, London W1N 4AT. Origination by BPCC Whitefriars Ltd, Tunbridge Wells, and printed and bound in Great Britain by BPCC Wheatons Ltd, Exeter.
ISSN 0007 1285

VOL 65 NO 772 APRIL 1992

The British Journal of Radiology
Contents

Papers

Page

Diagnosis of brain death: superiority of perfusion studies with $^{99}\text{Tc}^{\text{m}}$-HMPAO over conventional radionuclide cerebral angiography 289
A. de la Riva, F. M. González, J. M. Llamas-Elvira, J. M. Latre, A. Jimenez-Heffernan, E. Vidal, Mª Martinez, M. Torres, R. Guerrero, F. Alvarez and A. Mateo

Computed tomographic assessment of intraperitoneal fluid distribution prior to intraperitoneal chemotherapy for ovarian cancer 295
P. M. Hughes, I. Zammit-Maempel and D. Murphy

How good is ultrasound in the detection and evaluation of anterior abdominal wall defects? 298
S. A. Walkinshaw, M. Renwick, G. Hebisch and E. N. Hey

Detection and evaluation of fetal goitre by ultrasound 302
E. F. Avni, F. Rodesch, C. Vandemerckt and D. Vermeylen

Impedance plethysmography and thrombo-embolic disease 306
D. Glew, T. Cooper, A. E. Mitchelmore, D. Parsons, P. R. Goddard and M. Hartog

The role of $^{99}\text{Tc}^{\text{m}}$-HMPAO white cell imaging in suspected orthopaedic infection 309
C. Copping, S. M. Dalgliesh, N. J. Dudley, P. A. Griffiths, M. Harrington, R. Potter and B. D. Smith

Benign non-infected urachal cyst in an adult: review of the literature and a case report 313
M. K. Al-Hindawi and S. Aman

Cranial stereotactic multiple arc radiotherapy; treatment planning using angiographic images 317
E. S. Thomson and P. Clegg

Computer-assisted generation of multi-leaf collimator settings for conformation therapy 321
A. R. Hounsell, P. J. Sharrock, C. J. Moore, A. J. Shaw, J. M. Wilkinson and P. C. Williams

An investigation of the dose equivalent to radiographers from a high-energy neutron therapy facility 327
J. Finch and D. E. Bonnett

The determination of total filtration on mammographic X-ray sets 334
K. J. Robson, C. J. Kotre and K. Faulkner

Technical note

A comparison of four mammographic image quality test objects 339
M. Payne and C. P. Lawinski

Case reports

Sonographic features in a case of Fitz-Hugh-Curtis syndrome masquerading as malignancy 342
B. Banerjee, A. Rennison and B. E. Boyes

Peripheral neuropathy simulating lymphoma 344
R. J. Swingler, R. E. Cull, D. Kean and L. Turnbull

Dystrophic umbilical artery calcifications in an infant 348
G. Beluffi, P. Fiori and A. T. Pandiscia

Small bowel fistula secondary to endarteritis obliterans, complicating chemotherapy for small bowel lymphoma 349
S. Knowles, H. E. Smart, A. Al-Dawoud and D. J. Kerr

Case of the month

A case of malignant hypertension 351
P. H. Williams and A. P. Hemingway

Erratum 353
J. Law

Correspondence

Ultrasonic findings in visceral *Pneumocystis carinii* infection in AIDS 354
P. Grech

Relapsing polychondritis 355
B. S. Mantell

Chest radiograph scoring system for use in pre-term infants 355
I. Hyde

Authors' reply 355
A. Greenough, B. Yuksel, J. Karani and A. Page

Proceedings

Proceedings of the British Institute of Radiology
Hypoxic cell sensitizers: back in fashion? 15 November 1991 356

Book reviews

MRI of the extremities: an anatomic atlas. *H. S. Kang and D. Resnick* 360
Atlas of diagnostic radiology of the horse part 3: diseases of the head, neck and thorax. *K. Dik and I. Gunsser* 360

BIR Bulletin *facing page* 360

© 1992 The British Institute of Radiology. This publication is copyright under the Berne Convention and the Universal Copyright Convention. All rights reserved, apart from any relaxations permitted under national copyright laws, no part of this publication may be reproduced, stored in a retrieval system or transmitted in any form or by any means without the prior permission of the copyright owners. Permission is not, however, required to copy abstracts of papers or of articles on condition that a full reference to the source is shown. Multiple copying of the contents of the publication without permission is always illegal. Published by The British Institute of Radiology, 36 Portland Place, London W1N 4AT. Origination by BPCC Whitefriars Ltd, Tunbridge Wells, and printed and bound in Great Britain by BPCC Wheatons Ltd, Exeter.

ISSN 0007 1285

VOL 65 NO 773 MAY 1992

The British Journal of Radiology

Contents

Papers

Page

High-intensity zone: a diagnostic sign of painful lumbar disc on magnetic resonance imaging 361
C. Aprill and N. Bogduk

The basal turn of the cochlea 370
P. D. Phelps

Magnetic resonance imaging of extracranial head and neck tumours 375
J. Kabala, P. Goddard and P. Cook

The role of 3D CT in the assessment of acetabular fractures 384
R. L. Guy, P. A. Butler-Manuel, P. Holder and R. N. Brueton

Hydatid disease of the liver: evaluation of ultrasound and computed tomography 390
M. I. El-Tahir, M. F. Omojola, T. Malatani, A. H. Al-Saigh and O. A. Ogunbiyi

The spine deformity index in osteoporosis is not related to bone mineral and ultrasound measurements 393
P. Bernecker, P. Pietschmann, F. Winkelbauer, E. Krexner, H. Resch and R. Willvonseder

Computed tomography in abdominal trauma: an audit of usage and image quality 397
A. R. Padhani, C. J. E. Watson, L. Clements, R. Y. Calne and A. K. Dixon

The incidence and severity of hypoxia associated with ^{99}Tc^{m} Technegas ventilation scintigraphy and ^{99}Tc^{m} MAA perfusion scintigraphy 403
J. M. James, J. J. Lloyd, B. C. Leahy, R. A. Shields, M. C. Prescott and H. J. Testa

Quality assurance of computer controlled radiotherapy treatments 409
H. M. Morgan

New evidence that tamoxifen does not induce osteoporosis: a nuclear activation analysis and absorptiometry study 417
J. Kalef-Ezra, D. Glaros, G. Klouvas, J. Hatzikonstantinou, A. Karantanas, K. C. Siamopoulos and N. Pavlidis

Radical treatment of angiosarcoma of the scalp using megavoltage electron beam therapy 421
S. M. Sagar and C. M. Pujara

Quantitative analysis of CT brain images: a statistical model incorporating partial volume and beam hardening effects 425
R. F. McLoughlin, M. V. Ryan, P. M. Heuston, C. T. McCoy and J. B. Masterson

The Reference Man in diagnostic radiology dosimetry 431
B. A. Lindskoug

Technical notes

Calibration of a 0.08 Tesla magnetic resonance imager for *in vivo* T_1 and T_2 measurement 438
S. F. Keevil, G. Dolke, P. Armstrong and M. A. Smith

The disappearing bladder—modifying imaging techniques after rectal excision 442
W. C. G. Peh, N. C. Chokshi and C. H. Young

Case reports

Magnetic resonance imaging and treatment of an unusual seminoma metastasis occurring in the parasellar region 445
R. L. Guy, M. Mason and L. Janse Van Rensburg

^{99}Tc^{m} HMPAO SPECT in progressive multifocal leucoencephalopathy 447
J. V. Bowler, P. T. G. Davies and G. D. Perkin

Increased attenuation value of a colloid cyst of the third ventricle following ventricular decompression 449
N. G. Warnock and T. Powell

Diagnosis and treatment of an oesophageal stricture due to lichen planus 451
P. D. Holder, W. L. Wong, J. Pemberton, R. P. H. Thompson and S. C. Parker

Case of the month

An underdiagnosed abdominal mass? 453
R. D. Edwards and W. Kincaid

Short communication

The value of transvaginal scanning in the assessment of second trimester oligohydramnios 455
P. Twining

Correspondence

Biliary dilatation and pseudo-tumour of the liver 458
P. Gresch

The use of theophylline, an adenosine antagonist in the prevention of contrast media induced nephrotoxicity 459
M. R. Gandhi, P. Brown, C. A. J. Romanowski, S. K. Morcos, S. Campbell, A. M. El Nahas and T. A. Gray

A sense of déjà vu 459
J. Ratcliffe

Altered radiotherapy fractionation in medulloblastoma 460
N. P. Bates and M. V. Williams

Authors' reply 461
P. N. Plowman, D. Doughty and D. Sebag-Montefiore

Proceedings

Proceedings of the British Institute of Radiology
Cerebral blood flow—practical measurement and clinical relevance, a multimodality approach, 12 February 1991 463

Book reviews

Textbook of Radiopharmacy: Theory and Practice. *C. B. Sampson* (Ed) 467
Renal Cystic Disease AFIP Atlas of Radiologic-Pathologic Correlation Fascicle I. *D. S. Hartman* 467
Textbook of Uroradiology. *N. Reed, R. W. McCallum and C. M. Sandler* 467
Essentials of Neuroimaging. *J. R. Kirkwood* 468

BIR Bulletin *facing page* 468

© 1992 The British Institute of Radiology. This publication is copyright under the Berne Convention and the Universal Copyright Convention. All rights reserved, apart from any relaxations permitted under national copyright laws, no part of this publication may be reproduced, stored in a retrieval system or transmitted in any form or by any means without the prior permission of the copyright owners. Permission is not, however, required to copy abstracts of papers or of articles on condition that a full reference to the source is shown. Multiple copying of the contents of the publication without permission is always illegal. Published by The British Institute of Radiology, 36 Portland Place, London W1N 4AT. Origination by BPCC Whitefriars Ltd, Tunbridge Wells, and printed and bound in Great Britain by BPCC Wheatons Ltd, Exeter.
ISSN 0007 1285

1992, *The British Journal of Radiology*, *65*, 193–198

VOLUME 65 NUMBER 771 MARCH 1992

The British Journal of Radiology

The incidence and significance of fluid–fluid levels on computed tomography of osseous lesions

By A. M. Davies, FRCR, *V. N. Cassar-Pullicino, FRCR and †R. J. Grimer, FRCS

Departments of Radiology, Royal Orthopaedic Hospital, Birmingham, *Robert Jones & Agnes Hunt Orthopaedic Hospital, Oswestry, and †The Bone Tumour Treatment Service, Royal Orthopaedic Hospital, Birmingham, UK

(*Received March 1991 and in revised form June 1991*)

Keywords: Aneurysmal bone cyst, Computed tomography, Bone tumours

Abstract. The demonstration of a fluid–fluid level (FFL) within an osseous lesion on computed tomography (CT) has been reported as suggestive of an aneurysmal bone cyst (ABC) although FFLS have also been rarely found in association with other lesions. This study was conducted to determine the frequency of FFLS on CT in a group of ABCs and a series of patients presenting to a major tertiary referral centre for the treatment of bone tumours. An FFL was present on CT in 21 (84%) of the 25 ABCs and in 17 was multiple. FFLs are typical of the mid ("blow-out") or late phase of development of an ABC and not the incipient ("permeative") stage or where the internal architecture of the tumour has been disrupted by biopsy or previous surgery. In a 3-year period, 16 ABCs were found in 491 bone lesions referred to a bone tumour treatment centre. CT of the ABCs revealed FFLs in 14 (87.5%) cases. Within the same period, 728 CTs of these and other bone lesions were performed and FFLs were identified in two further cases: a massive telangiectatic osteosarcoma and a conventional osteosarcoma following chemotherapy. The diagnostic significance of an FFL on CT for ABC is: sensitivity = 87.5%, specificity = 99.7%, positive predictive value = 87.5%, negative predictive value = 99.7%, accuracy = 99.4%. An FFL within a bone lesion on CT remains strongly suggestive of an ABC although the radiologist should be wary of a rare telangiectatic osteosarcoma.

The demonstration of a fluid–fluid level (FFL) within an osseous lesion on computed tomography (CT) has been reported as suggestive of an aneurysmal bone cyst (ABC) (Hudson, 1984; Hertzanu et al, 1984; Cory et al, 1989; Davies & Evans, 1989) and has been shown with magnetic resonance (MR) (Hudson et al, 1985; Beltran et al, 1986; Cory et al, 1989). This CT feature is now considered sufficiently characteristic to be included in radiological textbooks (Resnick & Niwayama, 1988; Murphy et al, 1989). One of the original reports did, however, note that FFLs could also occur in a telangiectatic osteosarcoma (Hudson, 1984). FFLs have been further associated, albeit rarely, with a number of other lesions, so a recent study concluded that "the presence of FFLs in bone or soft tissue tumours (on CT) cannot be considered diagnostic of any particular tumour" (Tsai et al, 1990). The purpose of this paper is to review the CT examinations of a series of ABCs for FFLs and to determine the incidence and diagnostic significance of this feature in a large consecutive series of CT examinations of osseous lesions.

Patients and methods

The radiographs and CT examinations of a series of 25 ABCs were reviewed for the presence of FFLs.

A retrospective review was conducted of the reports of all skeletal CT examinations performed by two radiologists serving a busy tertiary referral centre for the diagnosis and treatment of bone tumours. Both radiologists were aware of the potential significance of an FFL on CT before the start of the 36-month study period. The CT examinations themselves were reviewed in all cases in which the subsequent histology was shown to be a condition previously described in association with an FFL. Details of patient referrals to the Birmingham Bone Tumour Treatment Service within this period were obtained.

Results

Of the 25 ABCs there were 15 female and 10 male patients with an age range of 10–60 years and a mean age of 23 years. The commonest sites, with four cases each, were the proximal fibula (Fig. 1) and pelvis. There were three cases each in the spine, proximal humerus and tibia and two cases each in the forearm bones (Fig. 2), proximal and distal femora. Single cases were found in the scapula (Fig. 3) and calcaneum. An FFL

Address correspondence to Dr A. M. Davies, Consultant Radiologist, Royal Orthopaedic Hospital, Woodlands, Northfield, Birmingham B31 2AP, UK.

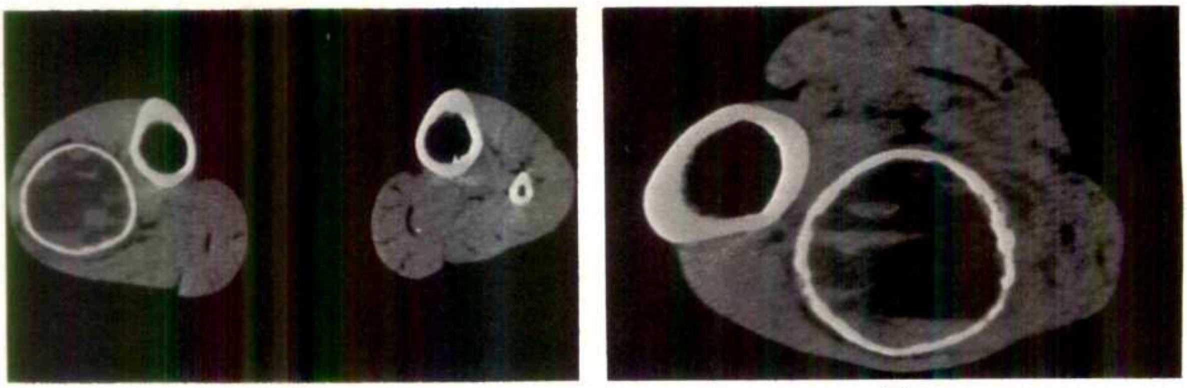

(a) (b)

Figure 1. Central ABC of the proximal fibula in a 13-year-old male showing multiple FFLs when supine (a) with reversal when rescanned prone (b).

on CT was present in 21 (84%) cases and was shown to be multiple in 17 (Figs 3, 4). The FFLs were best demonstrated when the images were viewed on a narrow window width with a low window level of less than 100 Hounsfield units (HU). The supernatant density was always of lower density (range 10–55 HU) than the precipitant or dependent fluid (range 48–85 HU).

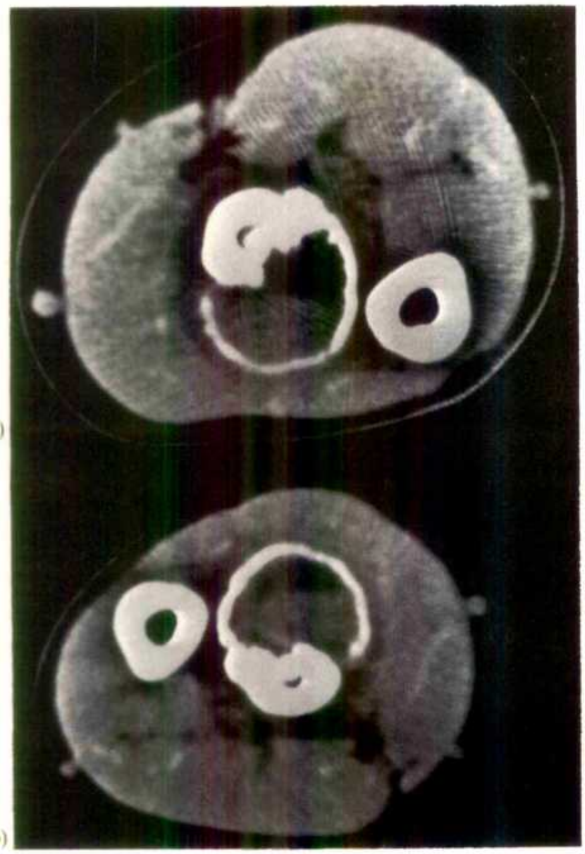

(a)

(b)

Figure 2. Eccentric ABC arising in the radial diaphysis of a 25-year-old female on supination (a) and pronation (b) showing reversal of the FFLs on repositioning.

The orientation of the FFLs altered to remain horizontal in all four cases in which the patients were rescanned after repositioning (Figs 1, 2). A period of immobilization after repositioning the patient, to allow the fluid contents to settle and create the FFL, was not found necessary as in all four cases the FFLs were clearly visible on the repeat examination in the time required to obtain a further digital scout and subsequent axial images (Figs 1, 2).

Coronal and sagittal T_1-weighted magnetic resonance (MR) images were available in one pubic ABC and confirmed the FFL detected by CT (Fig. 5). The dependent layer exhibited a homogeneous lower signal than the heterogeneous supernatant layer (Fig. 5b).

Relative "expansion" of bone was evident from the plain radiographs in all but one of the 21 cases with an FFL on CT. In only one of the negative cases was there any significant bony expansion. Two further FFL negative cases were recurrent ABCs that had been curretted

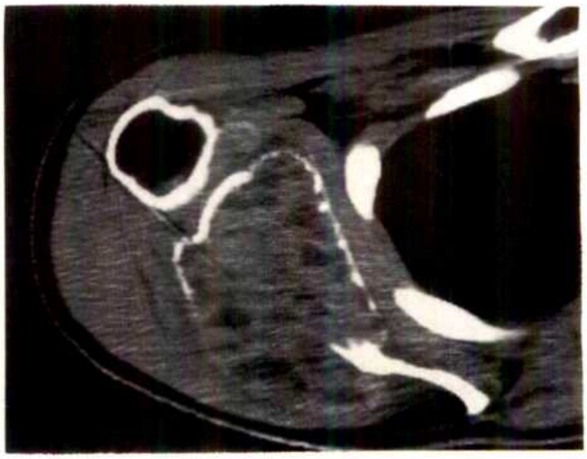

Figure 3. ABC in the scapula of a 25-year-old male showing multiple FFLs.

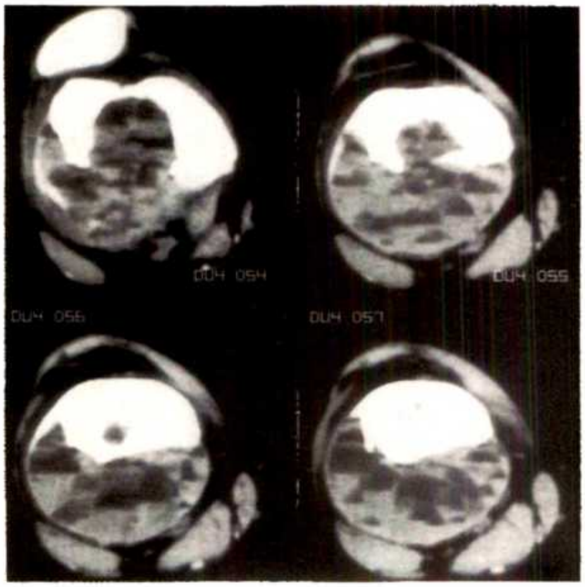

Figure 4. ABC in the distal femur of a 16-year-old male showing multiple FFLs.

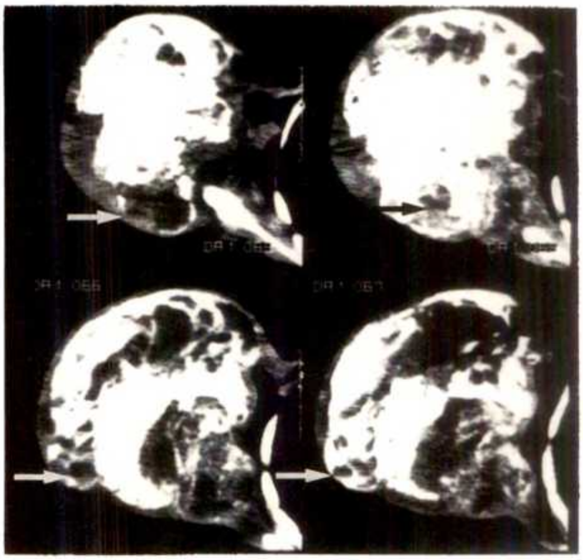

Figure 6. Telangiectatic osteosarcoma of the proximal humerus in a 12-year-old female showing multiple small FFLs (arrowed).

and bone grafted 7 and 10 years before. Multiple FFLs identified in the scapular ABC (Fig. 3) were no longer present on a repeat CT performed shortly after biopsy.

Within a 36-month period, 491 new bone lesions were consecutively referred to the Birmingham Bone Tumour Treatment Service. The final diagnosis of these cases is summarized in Table I and compared with the published incidence (Dahlin & Unni, 1986). 16 ABCs were histologically proven and account for 3.2% of the total. 728 skeletal CT examinations were performed in this period. The excess number, over and above the 491 referrals, consist of follow-up examinations and restaging examinations on cases referred during and before the study period. CT of the 16 ABCs revealed FFLs in 14 (87.5%) cases (Figs 3, 4). FFLs were identified in two further cases: a massive telangiectatic osteosarcoma (Fig. 6) and a conventional osteosarcoma following chemotherapy (Fig. 7). The significance in quantitative terms of an FFL on CT being diagnostic of an ABC is shown in Table II. The FFLs present in the osteosarcoma post-chemotherapy altered to remain horizontal when the tumour was rescanned after repositioning. The behaviour of an FFL with postural change was, therefore, independent of the histological diagnosis.

Discussion

ABC is a benign, typically solitary lesion of bone usually seen in a patient less than 20 years of age. It is neither a true cyst nor a neoplasm and although the precise aetiology remains obscure, current theories favour a periosteal or intraosseous malformation secondary to trauma or a pre-existing bone lesion (Biesecker et al, 1970). Pathologically, ABCs consist of varying amounts of fibrous vascular tissue surrounding

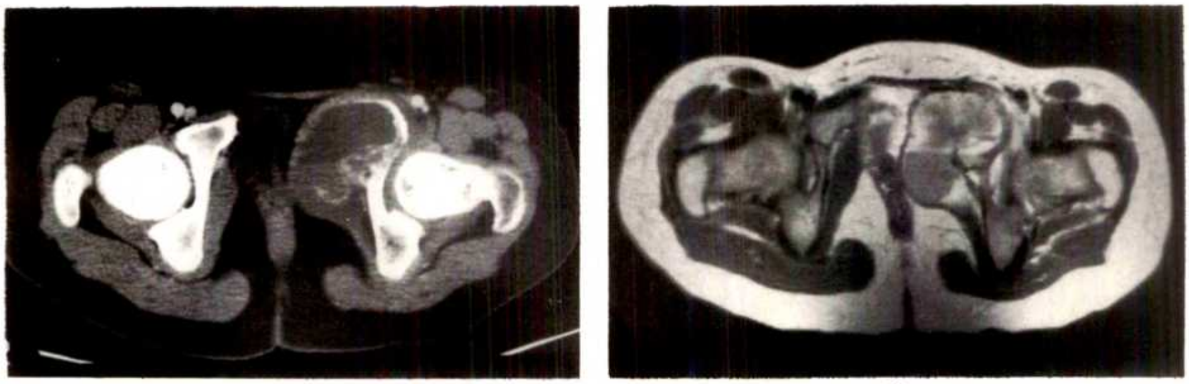

(a) (b)

Figure 5. ABC of the pubis of a 12-year-old female showing an FFL on CT (a) and T_1-weighted MR (b).

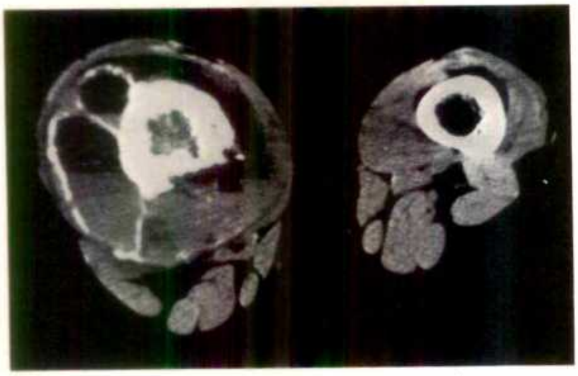

Figure 7. Necrotic osteosarcoma of the distal femur post-chemotherapy in a 12-year-old male showing multiple FFLs that were not present on the pre-chemotherapy CT scan.

Table II. Confidence of an FFL on CT being diagnostic of an ABC

Sensitivity	87.5%
Specificity	99.7%
Positive predictive value	87.5%
Negative predictive value	99.7%
Accuracy	99.4%

cavities filled with blood or serosanguinous fluid (Jaffe, 1950; Lichtenstein, 1950). Initial optimism that the demonstration of an FFL on CT was characteristic of an ABC (Hertzanu et al, 1984; Hudson, 1984) was expressed with caution as one of the original reports also showed a similar appearance in a telangiectatic osteosarcoma (Hudson, 1984) and it was concluded that "... in the future other lesions may be found to contain fluid levels as well" (Hudson et al, 1985).

Excluding air–fluid levels, which may be present if CT is performed after biopsy or unusually in a simple bone cyst (Hahn et al, 1984), and fat–fluid levels, rarely associated with haematogenous osteomyelitis (Rafii et al, 1984), FFLs have also been described in isolated cases of chondroblastoma (Kahmann et al, 1985; Murphy et al, 1989), giant cell tumour (Kaplan et al, 1987), fibrous dysplasia (Simpson et al, 1989; Tsai et al,

Table I. Incidence by diagnosis in this study compared with published data

Diagnosis	Overall study incidence (%)	Study incidence of "primary tumours of bone" (%)	Published incidence of "primary tumours of bone"[a] (%)
Chondroma/osteochondroma	1.8	2.6	11.1
Chondroblastoma	0.8	1.1	0.9
Chondromyxoid fibroma	0.2	0.3	0.4
Chondrosarcoma	8.1	11.5	8.4
Osteoid osteoma	2.2	3.2	2.8
Osteoblastoma	0.4	0.6	0.7
Osteosarcoma	22.0	31.0	14.6
Parosteal osteosarcoma	1.0	1.4	0.6
Paget's sarcoma	1.4		
Radiation sarcoma	0.6		
Giant cell tumour	8.5	12.0	4.8
Ewing's tumour	12.0	16.9	4.6
Lymphoma of bone	1.6	2.3	5.4
Myeloma	1.8	2.6	33.5
Adamantinoma	0.2	0.3	0.3
Non-ossifying fibroma	0.6	0.9	1.1
Fibrosarcoma/MFH	4.0	5.5	3.0
Chordoma	0.6	0.9	3.0
Other primary sarcomas	1.8	2.6	1.1
Simple bone cyst	1.4	2.0	
Aneurysmal bone cyst	3.2	4.6	2.4
Fibrous dysplasia	3.8		
Eosinophilic granuloma	1.0		
Infection	4.9		
Post-traumatic lesions	3.5		
Non-neoplastic[b]	3.7		
Metastases	8.3		
	(*n* = 491)	(*n* = 348)	(*n* = 8750)

[a] From Dahlin & Unni, 1986 (including ABC as a "primary bone tumour").

[b] Includes normal variants, Paget's, avascular necrosis, etc.

1990), simple bone cyst and recurrent malignant fibrous histiocytoma of bone (Tsai et al, 1990).

ABCs can arise in association with a recognized primary benign or malignant bone lesion, including non-ossifying fibroma, chondroblastoma, giant cell tumour, osteoblastoma, osteosarcoma, simple bone cyst, chondromyxoid fibroma and fibrous dysplasia (Biesecker et al, 1970; Bonakdarpour et al, 1978; Dahlin & McLeod, 1982). FFLs might be expected to occur in both primary and secondary ABCs; for example, Diercks and co-workers (1986) have shown a clear FFL on CT in a case of a secondary ABC developing in a patient with fibrous dysplasia. None of the 25 ABCs in our series, however, was shown histologically to arise in a pre-existing bone lesion although other diagnoses might have been tenable from the plain radiographs at presentation in several cases. In one series of 105 ABCs, there was no definite primary tumour, although microscopic areas resembling non-ossifying fibroma, osteoblastoma and fibrous dysplasia were found (Ruiter et al, 1977).

To demonstrate an FFL with either CT or MR, it is obviously necessary for the imaging to be perpendicular to the plane of the FFL. The true fluid nature of the cysts was revealed by the persistence of the horizontal orientation of the FFLs following repositioning of the patients (Figs 1, 2) but this feature was not specific to the ABCs. Unlike Hudson, no significant period of immobilization was found necessary following repositioning for the cyst contents to settle out and the FFL to reconstitute (Hudson, 1984). This may be due to the improved technology of CT scanners since that study, which may also explain, in part, the higher incidence of FFLs in ABCs in our study (84%) as compared with the cases collected over a period of 11 years by Cory and co-workers (70%) (Cory et al, 1989) or Hudson's original paper (35.3%) (Hudson, 1984).

ABCs of long bones have been classified according to site of origin within the bone: central, eccentric-cortical or parosteal (Sherman & Soong, 1957). The site of origin within bone was not a factor in determining the presence or absence of an FFL on CT in this series whereas the degree of bony "expansion" was. Plain radiographs of the cases with FFLs showed the lesions to be midphase ("blow-out") or late phase lesions (Mirra, 1989) in which expansion is a prominent feature. Only one of the FFL-negative cases showed bony expansion and a further case showed a diffusely permeative pattern typical of the incipient phase (Mirra, 1989). The predominance of mid- and late-phase ABCs can be explained by the tertiary referral pattern of the unit and may also be a further contributory factor to the high incidence of FFLs in this series. Obviously the rare "solid" ABC (Buirski & Watt, 1984; Sanerkin et al, 1983) cannot be expected to exhibit an FFL irrespective of the stage of evolution of the lesion.

The large number of cases (almost 500) and the similar proportions of the various histologies to the published literature (Table I) (Dahlin & Unni, 1986) would indicate that the data on which this study is based could be considered representative of primary osseous lesions in the general population. On this assumption the diagnostic significance of an FFL on CT for ABC remains remarkably high (Table II) despite suggestions to the contrary (Tsai et al, 1990). Indeed, the accuracy (Table II; 99.4%) would have been even higher if the cases in which the histology was already known (the osteosarcoma post-chemotherapy and two recurrent ABCs) had not been included as a false positive and false negative results, respectively.

FFLs were not found in this study when the internal architecture of the ABC had been disrupted by previous surgery or biopsy. The presence of an FFL in an osseous lesion before biopsy/surgery or chemotherapy suggests a benign pathology, most probably an ABC. To the authors' knowledge, an FFL on CT has not been described in association with an osseous metastasis.

It is important to remain aware of the telangiectatic osteosarcoma, which may have a prominent vascular component that radiologically and pathologically can be mistaken for an ABC or vice versa (Fig. 6). This rare tumour, accounting for 1.8% of the osteosarcomas in this study (two cases) and 1.9–2.5% in the published literature (Farr et al, 1974; Matsuno et al, 1976), carries a considerably poorer prognosis than conventional osteosarcoma. The one telangiectatic osteosarcoma that did not exhibit FFLs also arose at one of the commonest sites for an ABC in this study, the proximal fibula. The plain radiographs showed an expansile lesion with the "finger-in-the-balloon" sign often seen in mid- and late-phase ABCs (Mirra, 1989) and the CT revealed low-density areas consistent with vascular spaces. Thorough radiological–pathological correlation is therefore necessary to distinguish an ABC from a telangiectatic osteosarcoma.

The visibility of an FFL requires the presence of different densities within the fluid medium promoting a layering phenomenon. The fluid consistency within ABCs varies from blood to serous or serosanguinous fluid (Jaffe, 1950). A simplistic explanation for an FFL on CT of an ABC is that it represents layering of blood: red cells below, plasma above (Lindbom et al, 1961) in the presence of local fibrinolytic activity preventing clot formation (Ruiter et al, 1975). However, the detection of an FFL does not correlate with the type of fluid found within ABCs. Despite similar fluid characteristics, on analysis only half of 12 ABCs showed an FFL on CT (Hudson, 1984).

The pathological characteristics of FFL components demonstrated by MRI in benign and malignant tumours were different, with serous fluid and old haemorrhage found in ABCs compared with recent haemorrhage and liquefaction necrosis in malignancy (Tsai et al, 1990). When ABCs were imaged by both CT and MRI the FFLs were equally well seen (Hudson et al, 1985; Beltran et al, 1986; Cory et al, 1989; Tsai et al, 1990). In the Tsai and co-workers series, two of the three lesions in which an FFL was seen only on MRI were not ABCs (Tsai et al, 1990). It would appear that in ABCs, CT is just as sensitive as MRI in detecting an FFL.

A consistent temporal relationship in the MRI appearances of a haematoma does not exist (Ehman et al, 1988). The contents of ABCs show a wide range of signal intensities on both T_1- and T_2-weighted sequences (Hudson et al, 1985; Beltran et al, 1986; Cory et al, 1989; Tsai et al, 1990). The different relaxation parameters are a feature of intracystic haemorrhage of different ages, the amount of serous fluid and the byproducts of haemoglobin degradation, especially extracellular methaemoglobin. The MRI pulse sequences emphasizing T_1 contrast show the FFLs most clearly in both ABC and anticoagulated human blood, while T_2 contrast sequences render the FFLs invisible when the echo time (TE) is increased beyond 60 ms (Hudson et al, 1985) and 120 ms (Cory et al, 1989). As the T_2 values of plasma and red blood cell layers are similar (Hudson et al, 1985), the signal intensity difference that creates the visible FFL is due chiefly to the difference in T_1 values (Fig. 5b). However, the T_1 images shown in the published literature are inconsistent in the density appearances to the two layers, with the inferior layer appearing either hypointense (Tsai et al, 1990) or hyperintense (Cory et al, 1989). This suggests that minor variations in the chosen TE and repetition time (TR) or the fluid level components, despite a T_1 weighting, can have a profound effect on the overall appearances of the FFL. Irrespective of the pulse sequences the inferior layer always appears of uniform intensity while the superior layer in ABCs often has mixed areas of increased and isointense signals within it (Fig. 5b) (Beltran et al, 1986; Tsai et al, 1990).

Acknowledgments

We are grateful to Dr S. Chapman for one of the cases included in this series.

References

Beltran, J., Simpson, D. C., Levy, M., Herman, L., Weis, L. & Meuller, C. F., 1986. Aneurysmal bone cysts: MR imaging at 1.5T. *Radiology*, *158*, 689–690.

Biesecker, J. L., Marcove, R. C., Huvos, A. J. & Mike, V., 1970. Aneurysmal bone cyst: a clinicopathologic study of 66 cases. *Cancer*, *26*, 615–625.

Bonakdarpour, A., Levy, W. M. & Aegerter, E., 1978. Primary and secondary aneurysmal bone cyst: a radiological study of 75 cases. *Radiology*, *126*, 75–83.

Buirski, G. & Watt, I., 1984. The radiological features of "solid" aneurysmal bone cysts. *British Journal of Radiology*, *57*, 1057–1065.

Cory, D. A., Fritsch, S. A., Cohen, M. D., Mail, J. T., Holden, R. W., Scott, J. A. & Derosa, G. P., 1989. Aneurysmal bone cysts: imaging findings and embolotherapy. *American Journal of Roentgenology*, *153*, 369–373.

Dahlin, D. C. & McLeod, R. A., 1982. Aneurysmal bone cyst and other non-neoplastic conditions. *Skeletal Radiology*, *8*, 243–250.

Dahlin, D. C. & Unni, K. K., 1986. *Bone Tumors: General Aspects and Data on 8542 Cases*, 4th edn (Charles C Thomas, Springfield).

Davies, A. M. & Evans, N., 1989. Case of the month: a painful knee. *British Journal of Radiology*, *62*, 1103–1104.

Diercks, R. L., Sauter, A. J. M. & Mallens, W. M. C., 1986. Aneurysmal bone cyst in association with fibrous dysplasia: Case report. *Journal of Bone & Joint Surgery*, *68B*, 144–146.

Ehman, R. L., Berquist, T. H. & McLeod, R. A., 1988. MR imaging of the musculoskeletal system: a 5 year appraisal. *Radiology*, *166*, 313–320.

Farr, G. H., Huvos, A. G., Marcove, R. C., Higinbotham, N. L. & Foote, F. W. Jr., 1974. Telangiectatic osteosarcoma: a review of 28 cases. *Cancer*, *34*, 1150–1158.

Hahn, P. F., Rosenthal, D. I. & Erhlich, M. G., 1984. Case report 286. *Skeletal Radiology*, *12*, 214–217.

Hertzanu, Y., Mendelsohn, D. B. & Gottschalk, F., 1984. Aneurysmal bone cyst of the calcaneus. *Radiology 151*, 51–52.

Hudson, T. M., 1984. Fluid levels in aneurysmal bone cysts: a CT feature. *American Journal of Roentgenology*, *141*, 1001–1004.

Hudson, T. M., Hamlin, D. J. & Fitzsimmons, J. R., 1985. Magnetic resonance imaging of fluid levels in an aneurysmal bone cyst and anticoagulated human blood. *Skeletal Radiology*, *13*, 267–270.

Jaffe, H. L., 1950. Aneurysmal bone cyst. *Bulletin of the Hospital for Joint Diseases*, *11*, 3–13.

Kahmann, R., Gold, R. H., Eckardt, J. J. & Mirra, J. M., 1985. Case report 337: chondroblastoma of the calcaneum. *Skeletal Radiology*, *14*, 301–304.

Kaplan, P. A., Murphy, M., Greenway, G., Resnick, D., Sartoris, D. J. & Harms, S., 1987. Fluid–fluid levels in giant cell tumours of bone: report of two cases. *Journal of Computer Assisted Tomography*, *11*, 151–155.

Lichtenstein, L., 1950. Aneurysmal bone cyst. *Cancer*, *3*, 279–289.

Lindbom, A., Soderberg, G., Spjut, H. S. & Sunnqvist, O., 1961. Angiography of aneurysmal bone cysts. *Acta Radiologica*, *55*, 12–16.

Matsuno, T., Unni, K. K., McLeod, R. A. & Dahlin, D. C., 1976. Telangiectatic osteogenic sarcoma. *Cancer*, *38*, 2538–2547.

Mirra, J. M., 1989. Aneurysmal bone cyst. In *Bone Tumors: Clinical, Radiologic and Pathologic Correlations* (Lea & Febiger, Philadelphia), pp. 1267–1298.

Murphy, W. A., Totty, W. G., Destouet, J. M., Hardy, D. C., Monsees, B. S., Reines, W. R. & Gilula, L. A., 1989. In *Computed Body Tomography with MRI Correlation*, 2nd edn, ed. by J. K. T. Lee, S. S. Sagel & R. T. Stanley (Raven Press, New York), pp. 926, 927, 930.

Rafii, M., Firooznia, M., Golimbu, C. & McCauley, D. I., 1984. Hematogenous osteomyelitis with fat–fluid level shown by CT. *Radiology*, *153*, 493–494.

Resnick, D. & Niwayama, G., 1988. *Diagnosis of Bone and Joint Disorders*, 2nd edn (W. B. Saunders, Philadelphia), p. 3838.

Ruiter, D. J., Lindeman, J., Haverkate, F. & Noordhoek, V., 1975. Fibrinolytic activity in aneurysmal bone cysts. *American Journal of Clinical Pathology*, *64*, 810–816.

Ruiter, D. J., Van Rijssel, T. G. & Van der Velde, E. A., 1977. Aneurysmal bone cysts. *Cancer*, 39, 2231–2239.

Sanerkin, N. G., Mott, M. G. & Roylance, J., 1983. An unusual intraosseous lesion with fibroblastic, osteoblastic, aneurysmal and fibromyxoid elements. "Solid" variant of aneurysmal bone cyst. *Cancer*, *51*, 2278–2286.

Sherman, R. S. & Soong, K. Y., 1957. Aneurysmal bone cyst: its roentgen diagnosis. *Radiology*, *68*, 54–64.

Simpson, A. H. R. W., Creasy, T. S., Williamson, D. M., Wilson, D. J. & Spivey, J. S., 1989. Cystic degeneration of fibrous dysplasia masquerading as sarcoma. *Journal of Bone & Joint Surgery*, *71B*, 434–436.

Tsai, J. C., Dalinka, M. K., Fallow, M. D., Zlatkin, M. B. & Kressel, H. Y., 1990. Fluid–fluid level: a nonspecific finding in tumors of bone and soft tissues. *Radiology*, *175*, 779–782.

1992, *The British Journal of Radiology*, *65*, 199–201

CT evaluation of lymph node status at presentation of prostatic carcinoma

By John Spencer, MRCP, FRCR and Stephen Golding, DMRD, FRCR
Regional CT Unit, Churchill Hospital, Oxford OX3 7LJ, UK

(*Received 7 June 1991 and in revised form 12 August 1991, accepted 20 September 1991*)

Keywords: Computed tomography, Prostate cancer, Lymph nodes

Abstract. Computed tomographic (CT) studies performed within a general oncology service in 104 consecutive patients with prostatic carcinoma were reviewed retrospectively to assess the incidence and distribution of lymphadenopathy. All patients were staged with CT at initial presentation, had normal skeletal scintigrams and were candidates for radical radiotherapy. The likelihood of lymphadenopathy was associated with increasing T-stage. 57 of the 92 (62%) patients without lymph node enlargement had local disease confined to the prostate (T2 or less) compared with only two of the 12 (17%) patients with enlarged nodes. Lymph node enlargement was more likely with a primary tumour of poorly differentiated histology. 12 patients (11.5%) had lymphadenopathy by established CT criteria; six with pelvic nodal enlargement alone and six with enlargement of pelvic and retroperitoneal nodes. In all patients pelvic nodal enlargement predominated and no patient had isolated retroperitoneal lymphadenopathy. Our findings indicate that CT staging studies of prostatic cancer do not need to include the retroperitoneum if there is no lymphadenopathy at or below the aortic bifurcation.

Carcinoma of the prostate is the commonest malignancy of the male genitourinary tract and the second most common fatal neoplasm in males after cancer of the bronchus (Office of Population Censuses and Surveys, 1988). Over half of patients present with advanced disease and about 40% have positive skeletal scintigrams at presentation (Hayward et al, 1987). Before the introduction of computed tomography (CT) assessment of lymphatic spread was made by lymphography (LG). By the mid 1980s CT had replaced LG as the initial method of lymphatic imaging in patients with prostate cancer (Dixon, 1985). We do not now perform LG in these patients; this is in keeping with other oncology centres (Moskovic et al, 1991).

We have retrospectively examined the CT staging studies of 104 consecutive patients with no evidence of skeletal metastases and have assessed the incidence and pattern of lymph node enlargement. We report the influence of T-stage as assessed by CT and histological grade as predictors of lymphatic involvement.

Patients and methods

A total of 104 consecutive patients with histologically proven prostatic carcinoma were referred for staging by CT at presentation of disease in a general oncology service. All patients were candidates for treatment by radical radiotherapy and had no evidence of metastatic disease or advanced local disease as judged by clinical examination by a urologist and radiotherapist, chest radiograph and skeletal scintigraphy.

All CT examinations were supervised by the same radiologist using a standardized technique. Examinations were performed using either an IGE 8800 or IGE PACE machine. Sections were taken with 10 mm collimation at 15 mm intervals from the level of T12 to L5 and then contiguous 10 mm sections were obtained to the level of the symphysis pubis. Oral contrast medium was routinely administered; 600 ml of 2% Gastrograffin at a minimum of 30 min before the examination and a further 200 ml immediately before scanning. Intravenous contrast was administered and additional CT sections were obtained at the discretion of the supervising radiologist. Rectal contrast was not used unless specifically indicated. These CT studies were reviewed retrospectively to assess the T-stage and the incidence and pattern of lymphadenopathy.

CT T-staging of the prostate used standard criteria: disease was staged as T2 or less if there was no evidence of local extension beyond the capsule of the prostate, and included prostates with smooth nodular deformity; staged as T3 when there was evidence of local periprostatic extension of disease beyond the capsule or into the seminal vesicles but not to other adjacent organs or to the pelvic sidewall; a CT staging of T4 indicated extension of disease either to the pelvic sidewall or into adjacent organs other than the seminal vesicles (Husband, 1989).

CT N-staging employed standard CT criteria: retroperitoneal nodes of greater than 10 mm in diameter and pelvic nodes of greater than 15 mm in diameter were regarded as involved with metastases (Lee & Marx, 1989). The liver, the adrenal glands and the lung bases were also assessed for evidence of metastatic disease. The histological grading of primary prostate cancer obtained from surgical specimens or needle biopsy was ascertained from a review of the case notes.

Results

104 men of average age 66.5 years (range 43–84 years) were studied. 92 had no evidence of lymph node

enlargement on CT review, six had pelvic node enlargement alone and six had evidence of pelvic and retroperitoneal node enlargement. No patient studied had retroperitoneal nodal enlargement in the absence of pelvic node enlargement. One patient had isolated unilateral adrenal enlargement; aspiration biopsy revealed a tuberculous abscess, an unusual finding which was reported separately (Hughes & Golding, 1990). No distant metastases other than lymphatic metastases were evident on review of the CT studies.

There was no clinically significant difference in age between the groups of patients with or without evidence of lymph node enlargement (Table I). The higher the CT T-stage the greater the likelihood of CT evidence of lymph node enlargement (Table II). 57 of the 92 (62%) patients without lymph node enlargement showed no evidence of local spread beyond the prostate (T2 or less) compared with only two of the 12 (17%) patients with enlarged nodes. The maximum size of the enlarged lymph nodes varied from 1.5 to 7 cm. 10 of the 12 patients had discrete lymphadenopathy and two had large pelvic lymph node masses (Table III). Lymph node enlargement was more likely with poorly differentiated histology of the primary tumour. Histological grading was available in 10 of the 12 patients with lymphadenopathy of whom seven had poorly differentiated and three had moderately differentiated tumours.

The 92 patients with no evidence of lymphatic involvement at CT proceeded either to radical external beam radiotherapy planned by CT or to radioactive iodine seed implantation. Two of the six patients with pelvic lymphadenopathy had external beam radiotherapy with their radiation fields modified by the presence of local pelvic lymphadenopathy. The remaining 10 patients with lymphadenopathy proceeded to hormonal treatment. Only two of these 10 cases had follow-up CT studies and in both there has been regression of lymphatic disease.

Table I. Comparison of patients with or without CT nodal enlargement

Age (years)	Node negative (92 patients)	Node positive (12 patients)
59 or less	11	3
60–69	35	6
70–79	43	3
80 or more	3	0
Total	92	12
Average age	66.8 years	64.5 years

Table II. Comparison of CT T-stage and CT N-stage (104 patients)

CT T-stage	Node negative (number of patients)	Node positive (number of patients)
T2 or less	57	2
T3	28	6
T4	7	4

Table III. Maximum size of enlarged lymph nodes (12 patients)

Maximum node size	Number of patients
1–2 cm	7 (P and R)
2–4 cm	3 (P)
4 cm or more	2 (P)

Site of maximum sized node: P = pelvic; R = retroperitoneal.

Discussion

CT is used widely in the United Kingdom for the evaluation of T- and N-stage in patients with cancer of the prostate. CT is considerably more accurate than clinical examination in the assessment of the local or T-stage of the prostate (Dobbs & Husband, 1985). It alters the T-stage as assessed clinically in about 40% of cases. Transrectal ultrasound (TRUS) is superior to CT in assessing the tumour confined within the prostate, early capsular breach and invasion of the seminal vesicle (Salo et al, 1987). TRUS cannot reliably assess more advanced pelvic disease, for example, spread to the sidewall. TRUS gives no information about nodal status. Magnetic resonance imaging (MRI) has also been assessed for the T-staging of prostate cancer with accuracies of 83–89% reported (Biondetti et al, 1987; Hricak et al, 1987). To achieve improved accuracy over CT the MRI study must include multiplanar and multisequence protocols lasting approximately 1 hour (Hricak et al, 1987). Thus there are significant time penalties when using MRI. For centres performing radical prostatectomy the superior pre-operative early T-stage assessments possible with TRUS and MRI appear advantageous. Expertise in and availability of these techniques are limited. For most UK centres CT will provide the staging information required to guide management decisions when considering treatment with radical radiotherapy (RT).

In our unit patients with no evidence of skeletal or lymphatic metastases are offered radical RT. If CT shows evidence of retroperitoneal nodal enlargement RT is not offered. In some patients with small volume pelvic lymphadenopathy RT may be modified in terms of field and dose to accommodate the abnormal findings of CT, but in cases of bulky pelvic lymphadenopathy again radical RT is not appropriate. Thus, the N-stage as assessed by CT has an important bearing on patient management.

The accuracy of CT for N-stage evaluation in cancer of the prostate has been estimated between 70 and 93% as compared with histological assessment of lymphadenectomy specimens (Golimbu et al, 1981; Levine et al, 1981; Morgan et al, 1981). Both CT and LG have been used to assess N-stage pre-treatment. LG is unable to show consistently the obturator and hypogastric node groups which harbour the earliest lymphatic metastases of prostate cancer (Levine et al, 1981). CT is able to demonstrate both these nodal groups but relies on nodal enlargement as its sole criterion of metastatic involvement. Unenhanced CT may be unable to differentiate between tortuous or dilated vessels and enlarged nodes. MRI relies upon the same size criteria as CT for the assessment of lymphatic metastases, but is able to distinguish nodes from vessels without the need for intravenous contrast. Overall, the accuracy of CT is similar to that of LG in the assessment of N-stage in prostate cancer. There are no large series comparing CT with MRI in N-stage assessment of prostate cancer.

The incidence of lymphatic disease in our group of patients is broadly similar to other series using either CT or LG as methods of staging assessment, once allowance is made for patients with skeletal metastases in other series (Zingg et al, 1974; Hayward et al, 1987). Only patients who had normal skeletal scintigrams and who were candidates for radical radiotherapy were included in our series.

The CT pattern of lymph node enlargement revealed in our series has not been emphasized previously. Lymph node enlargement appeared to be a vertical process and no patient had evidence of isolated retroperitoneal lymph node enlargement. This finding is also of importance for those using MRI to assess N-stage in prostate cancer patients. There has been reference to isolated retroperitoneal lymphatic involvement at LG (Zingg et al, 1974), but the unreliable demonstration of pelvic nodes by LG casts doubt on these findings. Further, it is not stated whether patients with abnormal retroperitoneal nodes at LG in their series had normal skeletal scintigrams; some 29% of those with abnormal LG studies had skeletal metastases. Operative dissection and analysis of nodal groups confirms our finding that spread to periaortic nodes occurs only with associated involvement of pelvic nodes (Flocks et al, 1959). The CT appearances of the lymphadenopathy in our series were of single or multiple discretely enlarged nodes in 10 patients, with only two of our 104 patients showing massive lymphadenopathy (confluent nodal enlargement), both at pelvic sites. No patient showed direct extranodal spread of disease.

We have found CT to be a valuable method of staging candidates for radical radiotherapy of prostate cancer. In our experience an absence of pelvic lymph node enlargement indicates that CT will not reveal retroperitoneal node enlargement. CT staging assessment at presentation of prostate cancer may be confined to examination of the pelvis in those patients with no lymph node enlargement at or below the aortic bifurcation.

Acknowledgments

We are grateful to our colleagues in the Departments of Radiotherapy and Urology for permission to report details of their patients.

References

Biondetti, P. R., Lee, J. K. T., Ling, D. & Catalona, W. J., 1987. Clinical stage B prostate carcinoma: staging with MR imaging. *Radiology, 162*, 325–329.

Dixon, A. K., 1985. The current practice of lymphography: a survey in the age of computed tomography. *Clinical Radiology, 36*, 287–290.

Dobbs, H. J. & Husband, J. E., 1985. The role of CT in the staging and radiotherapy planning of prostatic tumours. *British Journal of Radiology, 58*, 429–436.

Flocks, R. H., Culp, D. & Porto, R., 1959. Lymphatic spread from prostate cancer. *Journal of Urology, 81*, 194–196.

Golimbu, M., Morales, P., Al-Askari, S. & Shulman, Y., 1981. CAT scanning in staging of prostatic cancer. *Urology, 18*, 305–308.

Hayward, S. J., McIvor, J., Burdge, A. H., Jewkes, R. F. & Williams, G., 1987. Staging of prostatic carcinoma with radionuclide bone scintigraphy and lymphography. *British Journal of Radiology, 60*, 79–81.

Hricak, H., Dooms, G. C., Jeffrey, R. B. et al, 1987. Prostatic carcinoma: staging by clinical assessment, CT, and MR imaging. *Radiology, 162*, 331–336.

Hughes, D. & Golding, S., 1990. Unusual appearances of an adrenal mass on computed tomography. *British Journal of Radiology, 63*, 137–138.

Husband, J. E. S., 1989. Staging of bladder and prostate cancer. In *CT Review*, ed. by J. Husband (Churchill Livingstone, Edinburgh), pp. 203–215.

Lee, J. K. T. & Marx, M. V., 1989. Pelvis. In *Computed Body Tomography with MRI Correlation*, ed. by J. K. T. Lee, S. S. Sagel and R. J. Stanley (Raven Press, New York), pp. 851–898.

Levine, M. S., Arger, P. H., Coleman, B. G., Mulhern, C. B., Jr, Pollack, H. M. & Wein, A. J., 1981. Detecting lymphatic metastases from prostatic carcinoma: superiority of CT. *American Journal of Roentgenology, 137*, 207–211.

Morgan, C. L., Calkins, R. F. & Cavaicanti, E. J., 1981. Computed tomography in the evaluation, staging, and therapy of carcinoma of the bladder and prostate. *Radiology, 140*, 751–761.

Moskovic, E., Fernando, I., Blake, P. & Parsons, C., 1991. Lymphography—current role in oncology. *British Journal of Radiology, 64*, 422–427.

Office of Population Censuses and Surveys, 1988. *Cases of Diagnosed Cancer Registered in England and Wales in 1984*. Series MBI No 16 (HMSO, London).

Salo, J. O., Kisivaari, L., Rannikko, S. & Lehtonen, T., 1987. Computerised tomography and transrectal ultrasound in the assessment of local extension of prostatic cancer before radical retropubic prostatectomy. *Journal of Urology, 137*, 435–438.

Zingg, E. J., Fuchs, W. A., Heritier, P. & Gothlin, J., 1974. Lymphography in carcinoma of the prostate. *British Journal of Urology, 46*, 549–554.

1992, *The British Journal of Radiology*, *65*, 202–206

Duplex pulsed Doppler sonography in the differential diagnosis of hepatocellular carcinoma and other common hepatic tumours

By Zu-Yau Lin, MD, MS, Wen-Yu Chang, MD, Liang-Yen Wang, MD, Shinn-Cherng Chen, MD, MS, Wan-Long Chuang, MD, MS, Ming-Yuh Hsieh, MD and Jung-Fa Tsai, MD, DrMedSci

Department of Internal Medicine, Kaohsiung Medical College Hospital, 100 Shih-Chuan 1st Road, Kaohsiung City 807, Republic of China

(*Received 8 April 1991 and in revised form 11 July 1991, accepted 16 August 1991*)

Keywords: Hepatocellular carcinoma, Metastatic liver cancers, Hepatic haemangioma, Ultrasound, Doppler studies

Abstract. 180 previously untreated consecutive patients with liver tumours (308 lesions), including 104 hepatocellular carcinomas (148 lesions), 43 metastases (116 lesions) and 33 haemangiomas (44 lesions), were studied to determine the value of duplex sonography in the differentiation of hepatocellular carcinoma from other tumours. For lesions measuring $\leqslant 5$ cm in diameter, hepatocellular carcinoma demonstrated the highest rate and haemangioma demonstrated the lowest rate of Doppler signals from within the lesions. To differentiate malignancy from haemangioma, the presence or absence of Doppler signals from these lesions were used as criteria. The specificity and positive predictive value were very high (100%, 100%), but the sensitivity, negative predictive value and accuracy were low (61.5%, 48.3%, 71.7%, respectively). With one exception, all lesions measuring < 3 cm in diameter with detectable Doppler signals were hepatocellular carcinoma. Using these results it is possible to differentiate hepatocellular carcinoma from metastases and haemangioma with high sensitivity, specificity, positive and negative predictive value, and accuracy (80.8%, 96.4%, 95.5%, 84.4%, 88.9%, respectively, for metastases; 80.8%, 100%, 100%, 81.5%, 89.6%, respectively, for haemangioma). We conclude that Doppler signals from within a lesion in combination with its size can aid differentiation of hepatocellular carcinoma from two other kinds of common hepatic tumour.

The liver can be affected by both benign and malignant neoplasms. The benign ones are usually of no clinical importance. Haemangioma is the commonest benign tumour of the liver, found in about 5% of autopsies (Sherlock, 1989). Malignant disease of the liver, however, needs immediate and intensive management. As the liver is second only to regional lymph nodes as a site for metastatic disease, secondary deposits in the liver are much more common than primary ones (Sherlock, 1989). On the other hand, hepatocellular carcinoma (HCC) is the most frequent primary malignancy of the liver (Munoz & Bosch, 1987). Accurate diagnosis of hepatic tumours is of clinical importance because of the different management of these conditions.

Duplex pulsed Doppler ultrasound (US), which combines real-time B-mode imaging with pulsed wave Doppler, has made it possible to detect blood flow from small lesions in the liver. Recently, Taylor et al (1987) reported that duplex US could aid in the differential diagnosis of focal liver lesions. Subsequently, Yasuhara et al (1988) also stated that duplex US might aid the differential diagnosis of small liver tumours. However, Ohnishi and Nomura (1989) disagreed, concluding that duplex US was of limited value in the diagnosis of small hepatic focal lesions including HCC. Therefore, as an extension of their work, we investigated the incidence of Doppler signals from three kinds of common hepatic tumour (HCC, metastases, haemangioma) to assess the potential role of duplex US in differential diagnosis.

Materials and methods

180 previously untreated consecutive patients with liver tumours were studied by duplex pulsed Doppler US between August 1989 and May 1990. 140 patients were male and 40 were female, with an age range of 24–80 years. 104 patients had HCC, 43 patients had metastases and 33 patients had haemangiomas. The diagnosis of HCC was made by US-guided percutaneous aspiration cytology or biopsy. In addition, all patients with HCC had at least one positive result with computed tomography (CT), angiography or serum alpha-fetoprotein (AFP) measurement (> 400 ng/ml). Of the 43 patients with metastases, 38 patients were diagnosed by US-guided percutaneous aspiration cytology or biopsy of the liver lesions with the combination of biopsy (or aspiration biopsy) of their primary cancers. Although the primary site of the other five patients could not be identified, the possibility of HCC was excluded by histology, serum AFP determination and imaging studies. Haemangioma was diagnosed by hepatic arteriography (Friedman et al, 1987a) in 16

Address correspondence and reprint requests to Zu-Yau Lin.

patients, by contrast-enhanced dynamic CT (Friedman et al, 1987a) and US follow-up of at least 6 months without any change in the lesions of five patients without known neoplasm, and by US-guided percutaneous biopsy in one patient. The diagnosis of haemangioma in the other 11 patients without known neoplasm was made by US-guided percutaneous aspiration and the characteristic US findings of spherical, uniformly hyperechoic nodules (Onodera et al, 1983). They were also followed-up by US for at least 6 months without any change in the lesions.

When a clearly separated tumour was defined as one lesion, there were 148 lesions in patients with HCC, 116 lesions in patients with metastases and 44 lesions in patients with haemangioma. The size of the lesions was assessed by B-mode real-time US.

75 patients with HCC and 16 patients with haemangioma had angiographic data for comparison with the Doppler results. Angiography was performed for transcatheter arterial embolization in patients with HCC and for diagnosis in patients with haemangioma.

Doppler examination was performed with a 3.75 MHz sector scanner combined with a duplex pulsed-wave Doppler system (SSA 100A, Toshiba). The wall filter was set at 100 Hz, and the pulse repetition frequency was set at 4 KHz. The Doppler gain (set at 2–4) and the echo level (set at 6–8), which were used to alter the strength of the Doppler signals from the display of the spectral profile, were set at their optimum conditions to obtain a clear outline of flow waves with a minimum of background noise. The depth of the measured area was limited to less than 10 cm to prevent interference of signals from adjacent vessels because of far-field divergence of the ultrasound beam (Kisslo et al, 1986). The real-time image and the Doppler mode were displayed simultaneously, so the exact area from which Doppler signals were originating could be identified.

All patients were examined in the supine or left decubitus position, and Doppler signals were detected during suspended respiration. To investigate Doppler signals from a lesion, the Doppler cursor was manipulated under B-mode real-time US within the lesion, with a sample width of 2, 3 or 5 mm depending on the size of the lesion. If Doppler signals were detected from an area within a lesion, the probe direction and the Doppler cursor were manipulated to exclude Doppler signals transmitted from adjacent unrelated vessels. Also the Doppler cursor did not extend beyond the margin of the lesion to prevent sampling adjacent vessels. The whole lesion was studied meticulously from every possible direction to prevent a false negative result. Before we concluded that there were no detectable Doppler signals from a lesion, the examination was carried out for at least 20 min for lesions measuring < 3 cm in diameter, 30 min for lesions between 3 and 5 cm, and 45 min for lesions measuring > 5 cm in diameter. Sampling of Doppler signals was also attempted in the hepatic parenchyma in all patients.

Results

The rates of detection of Doppler signals from the three kinds of liver tumour were analysed with respect to lesion size (Table I). For lesions measuring ⩽ 5 cm in diameter, HCC demonstrated a significantly higher rate of Doppler signals than the others ($p < 0.005$). Moreover, almost all lesions measuring > 5 cm in diameter in patients with HCC had detectable Doppler signals (98.9%). With one exception, all lesions measuring < 3 cm in diameter with detectable Doppler signals were HCC (Fig. 1). The exception was meta-

Table I. Relationship between Doppler signals and lesion sizes in hepatocellular carcinoma, metastases and haemangioma

Lesion size (mean ± SD)	Total	Doppler signals				Percentage of detectable signals	p value
		P	C	P+C	N		
< 3 cm*							
HCC (1.80 ± 0.56)	32	20	3	0	9	71.9%	$< 0.005^a$
Meta (1.72 ± 0.57)	60	1	0	0	59	1.7%	$< 0.005^a$
Haema (1.60 ± 0.56)	29	0	0	0	29	0%	
3–5 cm*							
HCC (3.57 ± 0.41)	28	14	4	7	3	89.3%	$< 0.005^a$
Meta (3.53 ± 0.47)	31	14	3	0	14	54.8%	$< 0.005^b$
Haema (3.54 ± 0.61)	10	0	0	0	10	0%	
> 5 cm							
HCC	88	31	8	48	1	98.9%	
Meta	25	13	3	3	6	76%	
Haema	5	0	1	0	4	20%	

* The difference in lesion size is not significant between the three kinds of tumour ($p > 0.05$, t-test).
[a] χ^2-test; [b] Fisher's exact test.
HCC: hepatocellular carcinoma, Meta: metastatic liver cancer, Haema: haemangioma, P: pulsatile waves, C: continuous waves, N: without detectable Doppler signals.

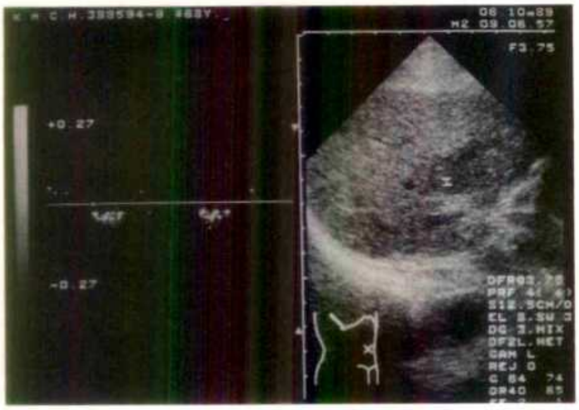

(a)

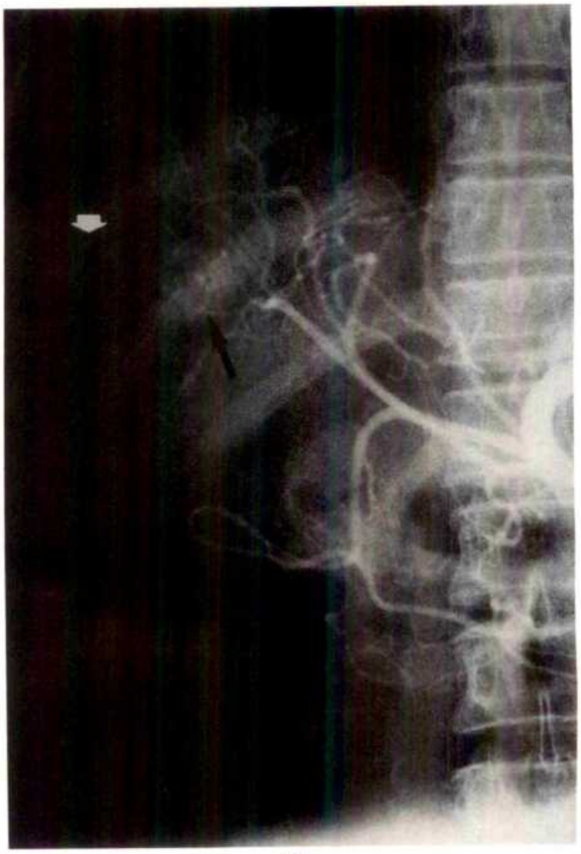

(b)

Figure 1. Small hepatocellular carcinoma measuring 1.7 cm in diameter. (a) Right oblique intercostal scan demonstrates small pulsatile waves from within the lesion. (b) Angiography shows tumour vessels and stain (black arrow). Another smaller lesion which was missed by B-mode real-time ultrasound was discovered by angiography (white arrow).

stasis from a transitional cell carcinoma of the urinary system (Fig. 2). Hepatic parenchyma showed no Doppler signals other than small areas corresponding to the hepatic artery, portal vein and hepatic vein.

To differentiate malignant tumours from haemangioma, or HCC from metastases and haemangioma, lesion sizes and Doppler results were considered together. Patients with at least one lesion measuring $\leqslant 5$ cm in diameter that demonstrated Doppler signals were classified as malignancy. Use of this definition to differentiate malignancy from haemangioma carried high specificity and positive predictive value, but low sensitivity, negative predictive value and accuracy (Table II). On the other hand, patients with at least one

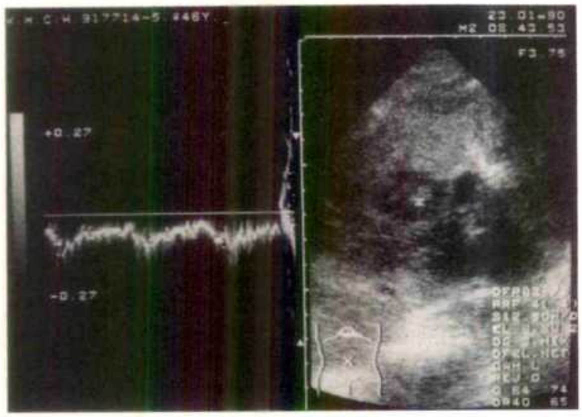

Figure 2. Metastatic liver cancer from transitional cell carcinoma of the urinary system showing pulsatile waves from within one of the lesions (2.8 cm × 2.0 cm).

Table II. Differential diagnosis of malignant tumours and haemangioma in 106 patients with at least one lesion measuring $\leqslant 5$ cm in diameter

	Malignant tumours	Haemangioma	Total
Doppler results[a]			
(+)	48	0	48
(−)	30	28	58
Total	78	28	106

Sensitivity = 61.5%, specificity = 100%, accuracy = 71.7%, positive predictive value = 100%, negative predictive value = 48.3%.

[a] A patient with at least one lesion measuring $\leqslant 5$ cm in diameter that demonstrated Doppler signals was defined as Doppler result (+).

Table III. Differential diagnosis of hepatocellular carcinoma and metastases in 54 patients with at least one lesion measuring $\leqslant 3$ cm in diameter

	Hepatocellular carcinoma	Metastases	Total
Doppler results[a]			
(+)	21	1	22
(−)	5	27	32
Total	26	28	54

Sensitivity = 80.8%, specificity = 96.4%, accuracy = 88.9%, positive predictive value = 95.5%, negative predictive value = 84.4%.

[a] A patient with at least one lesion measuring < 3 cm in diameter that demonstrated Doppler signals was defined as Doppler result (+).

Table IV. Differential diagnosis of hepatocellular carcinoma and haemangioma in 48 patients with at least one lesion measuring < 3 cm in diameter

	Hepatocellular carcinoma	Haemangioma	Total
Doppler results[a]			
(+)	21	0	21
(−)	5	22	27
Total	26	22	48

Sensitivity = 80.8%, specificity = 100%, accuracy = 89.6%, positive predictive value = 100%, negative predictive value = 81.5%.

[a] A patient with at least one lesion measuring < 3 cm in diameter that demonstrated Doppler signals was defined as Doppler result (+).

lesion measuring < 3 cm in diameter that demonstrated detectable Doppler signals were classified as patients with HCC. Use of this definition could differentiate HCC from metastases and haemangioma with high sensitivity, specificity, positive predictive value, negative predictive value, and accuracy (Tables III, IV). We preferred to use patient numbers rather than lesion numbers as units for statistical calculation because some patients had more than one lesion measuring $\leqslant 5$ cm in diameter. Statistical results would be misleading if each lesion was considered separately.

The Doppler signals were compared with the angiographic findings in 99 lesions from 75 patients with HCC and 21 lesions from 16 patients with haemangioma. 87 out of 91 HCC lesions (95.6%) with detectable Doppler signals demonstrated tumour vessels on angiography. The other four HCC lesions (4.4%) showed tumour stain only. All HCC lesions without detectable Doppler signals demonstrated tumour staining only on angiography. All 21 lesions with typical findings of haemangioma on angiography showed no detectable Doppler signal from the lesions.

Discussion

Taylor et al (1987) reported the results of Doppler examination in 68 consecutive patients with focal liver lesions, including 12 HCC that were all > 4 cm in diameter. The Doppler signals in HCC were significantly different from those in metastases and haemangioma. When high-velocity signals (> 5 kHz) were seen from the periphery of the focal liver lesions, HCC was highly likely. Furthermore, from the results of correlation with angiographic findings, the authors suggested that the high-velocity Doppler signals were associated with large pressure gradients resulting from arterioportal shunting. Therefore, they concluded that duplex Doppler US could aid in the differential diagnosis of focal liver lesions. Subsequently, Yasuhara et al (1988) reported that Doppler examination might offer the possibility of a differential diagnosis of small liver tumours. Eight out of 10 HCC less than 2 cm in diameter demonstrated detectable Doppler signals from within the tumours while nine regenerative nodules did not. However, Ohnishi and Nomura (1989) sampling Doppler signals from within the body of the tumour and its periphery reported somewhat different results. Although high-velocity signals (> 3 kHz) were obtained only in HCC measuring > 4 cm in diameter with arterioportal shunting, peak frequencies less than 2.6 kHz could be demonstrated in smaller carcinomas and in other hepatic focal lesions. They concluded that measurement of the peak frequency shifts was of little value in the differentiation of small HCC from other lesions encountered clinically.

However, absolute values of peak frequency shift are of limited use in the clinical situation of interrogating hepatic tumours with Doppler because of variation of the angle the Doppler beam makes with the direction of flow. When the US beam is directed parallel to flow, the angle is 0° and the Doppler signals obtained will be the maximum possible. In contrast, when the angle is 90° no Doppler signals will be obtained (Mark et al, 1986). Although this limitation probably does not interfere significantly with our interpretation of the results from very high-velocity blood flow related to arterioportal shunting (because of its easy detection and high frequency shifts), it interferes significantly with the results from tumours without arterioportal shunting, which show smaller Doppler shifts. Furthermore, without colour Doppler imaging as a guide, vessels in the periphery of the tumour may actually be hepatic vessels stretched by the mass rather than its supplying artery. The signal characteristics of these vessels should not be analysed together with those of tumour vessels for obvious reasons. Therefore, the present study was designed to detect Doppler signals from within the tumour and attempted to differentiate three kinds of common hepatic tumour by the presence or absence of Doppler signals, but not by the difference in their peak frequency shifts.

The present study demonstrated that Doppler signals were more frequently detected in HCC than in the other

P25862

tumours. This result is in accordance with angiographic findings in these tumours. Classically, HCC shows a hypervascular mass with tumour angioneogenesis; only a small percentage (5–10%) of HCC are hypovascular-to-avascular compared with the liver parenchyma (Friedman et al, 1987b). From our comparative study between Doppler signals and angiographic findings of HCC, all lesions with tumour vessels showed Doppler signals. Although four HCC lesions with detectable Doppler signals demonstrated tumour stain only on angiography, a lower sensitivity of hepatic angiography for small vessels may be the explanation (Takayasu & Okuda, 1987). Thus, a high rate of detectable Doppler signals from HCC lesions could be expected. On the other hand, angiography of haemangioma shows prolonged filling of the dilated vascular lake from the arterial phase to the late hepatogram phase and delayed washout of contrast medium (Chuang, 1987). This suggests that flow velocity within the haemangioma is very low. Low flow velocity gives rise to very low Doppler shifts, which may be filtered out by the 100 Hz wall filter. Therefore, in the present study all haemangiomas except one, which was > 5 cm in diameter with continuous waves from the lesion, were without detectable Doppler signals. This result was similar to the previous reports (Taylor et al, 1987; Yasuhara et al, 1988; Ohnishi & Nomura, 1989). A lesion with detectable Doppler signals, especially a pulsatile waveform, is unlikely to be an haemangioma. Because the angiographic features of metastic liver cancers range from hypervascular and isovascular to hypovascular on coeliac arteriography (Chuang, 1987), the rate of detectable Doppler signals from these lesions was not surprisingly between those for HCC and haemangioma.

In hepatic parenchyma, no Doppler signals were obtained except from the focal lesions or from the small areas that corresponded with the hepatic artery, portal vein and hepatic vein. This is similar to previous reports (Yasuhara et al, 1988; Ohnishi & Nomura, 1989). Therefore, Doppler signals from within a lesion are of clinical significance and can be used to characterize liver tumours. In the present study, almost all lesions < 3 cm in diameter with detectable Doppler signals were due to HCC. This could differentiate HCC from metastases and haemangioma with high sensitivity, specificity, positive predictive value, negative predictive value, and accuracy. A patient with at least one lesion measuring < 3 cm in diameter with detectable Doppler signals is likely to have HCC. Although we needed sufficient time to exclude no detectable Doppler signals from within a lesion, it took only about 15–20 min for all lesions with detectable Doppler signals to be identified.

From the present study we conclude that the presence or absence of Doppler signals from within a lesion in combination with its size can aid the differentiation of HCC from metastases and haemangioma.

References

Chuang, V. P., 1987. Hepatic angiography. In *Neoplasms of the Liver*, ed. by K. Okuda & K. G. Ishak (Springer-Verlag, Tokyo), pp. 259–277.

Friedman, A. C., Fishman, E. K., Radecki, P. D., Scatarige, J. C., Sherman, J. L., Farmlett, E. J., Markle, B. M., Dachman, A. H. & Pakter, R., L., 1987. Focal diseases. In *Radiology of the Liver, Biliary Tract, Pancreas and Spleen*, ed. by A. C. Friedman (Williams & Wilkins, Baltimore), pp. 173–183(a); pp. 220–246(b).

Kisslo, J., Mark, D. B. & Adams, D., 1986. Pulsed and continuous wave Doppler. In *Basic Doppler Echocardiography* ed. by J. Kisslo, D. Adams & D. B. Mark (Churchill Livingstone, New York), pp. 25–46.

Mark, D. B., Adams, D. & Kisslo, J., 1986. The Doppler principle and the study of cardiac flow. In *Basic Doppler Echocardiography*, ed. by J. Kisslo, D. Adams & D. B. Mark (Churchill Livingstone, New York), pp. 7–23.

Munoz, N. & Bosch, X., 1987. Epidemiology of hepatocellular carcinoma. In *Neoplasms of the Liver*, ed. by K. Okuda & K. G. Ishak (Springer-Verlag, Tokyo), pp. 3–19.

Ohnishi, K. & Nomura, F., 1989. Ultrasonic Doppler studies of hepatocellular carcinoma and comparison with other hepatic focal lesions. *Gastroenterology*, *97*, 1489–1497.

Onodera, H., Ohta, K., Oikawa, M., Abe, M., Kanno, T., Yoda, B. & Goto, Y., 1983. Correlation of the real-time ultrasonographic appearance of hepatic hemangiomas with angiography. *Journal of Clinical Ultrasound*, *11*, 421–425.

Sherlock, S., 1989. Hepatic tumours. In *Diseases of the Liver and Biliary System*, ed. by S. Sherlock (Blackwell Scientific Publications, Oxford), pp. 584–617.

Takayasu, K. & Okuda, K., 1987. Celiac angiography in the diagnosis of small hepatocellular carcinoma. In *Neoplasms of the Liver*, ed. by K. Okuda & K. G. Ishak (Springer-Verlag, Tokyo), pp. 279–287.

Taylor, K. J. W., Ramos, I., Morse, S. S., Fortune, K. L., Hammers, L. & Taylor, C. R., 1987. Focal liver masses: differential diagnosis with pulsed Doppler US. *Radiology*, *164*, 643–647.

Yasuhara, K., Kimura, K., Ohto, M., Matsutani, S., Ebara, M., Tsuchiya, Y. & Saisho, H., 1988. Pulsed Doppler in the diagnosis of small liver tumours. *British Journal of Radiology*, *61*, 898–902.

1992, *The British Journal of Radiology*, *65*, 207–212

Intrarenal Doppler ultrasound studies in normal and acutely obstructed kidneys

By P. M. Rodgers, FRCR, J. A. Bates, DCR, DMU and H. C. Irving, FRCR

Department of Radiology, St James' University Hospital, Beckett Street, Leeds LS9 7TF, UK

(*Received 4 April 1991 and in final form 19 August 1991, accepted 4 September 1991*)

Keywords: Doppler, Resistance index (RI), Obstructed kidney

Abstract. Renal ultrasound examinations and intrarenal arterial Doppler studies were performed on 48 patients with normal renal tracts and 20 patients presenting with acute renal colic resulting from ureteric calculus, 14 of whom had urographic evidence of renal obstruction. The mean resistance index (RI) of the Doppler waveforms obtained on the 14 obstructed kidneys (70.4 ± 6.22) was significantly higher than the mean RI of the 96 normal kidneys (62.4 ± 6.43). The mean difference between the RIs of the obstructed kidneys and their contralateral non-obstructed kidneys (8.37 ± 4.43) was also significantly higher than the differences in RI seen between pairs of normal kidneys (2.70 ± 1.71). Five out of 14 obstructed kidneys showed no pelvicalyceal dilatation and could not have been shown to be obstructed on conventional sonography. Four of these five had RI changes suggestive of obstruction and thus 13 of 14 obstructed kidneys would have been identified as obstructed by a combination of Doppler and conventional sonographic findings. 10 of the 14 obstructed kidneys were re-examined after passage of a urinary calculus and nine showed a reduction in the RI of the previously obstructed kidneys. The 10th subsequently required ureterolithotomy.

Sonography is a sensitive method of detecting dilatation of the renal collecting system (Ellenbogen et al, 1978), and therefore has been recommended for investigating renal colic (Erwin et al, 1984; Hill et al, 1985), but its use in the diagnosis of acute renal obstruction is limited when dilatation has not developed.

Recent work has suggested that duplex Doppler sonography may be used to distinguish obstructed and non-obstructed dilated collecting systems by measuring changes in arterial Doppler waveforms (Platt et al, 1989a, b).

This study aimed to examine the intrarenal arterial Doppler characteristics of normal kidneys and to document the sonographic and Doppler changes in a group of patients with acute ureteric obstruction.

Methods and materials

Two groups were examined:

1. A control group (48) consisting of patients routinely attending the ultrasound department for non-renal abdominal ultrasound examination (33), plus 15 healthy volunteers.
2. A group of patients (20) attending the hospital with renal colic, subsequently confirmed to be due to ureteric calculi by intravenous urography (IVU).

Plain radiographs and IVUs were obtained on the colic group during admission and these patients were subsequently divided, by the presence or absence of a persistent dense nephrogram, into obstructed (14) and indeterminate (6) cases. The indeterminate cases all had ureteric calculi. Most had distended collecting systems and ureters proximal to the calculus but contrast medium was seen to pass beyond the obstruction. None showed a persistent dense nephrogram.

Ultrasound examinations were performed, either before, during or after the IVU, on an Acuson 128 with colour flow Doppler facility, using a 3.5 Hz sector probe. Routine longitudinal and transverse images of both kidneys were obtained for assessment of pelvicalyceal dilatation, the presence of calculi or other morphological abnormality. These were recorded in the symptomatic group and were exclusion criteria for the normal group.

The intrarenal vessels were then identified using colour flow Doppler, and waveforms were recorded from arteries at the cortico-medullary junction (*i.e.* interlobar or arcuate arteries). Recordings were obtained from at least three separate vessels in each kidney in all of the obstructed kidneys and in 78 kidneys from the normal group. (Where fewer than three readings per kidney were obtained, these were included in the general group data but excluded from the subsequent comparisons of differences between pairs of kidneys.)

From each recording the resistance index (RI), the difference between the systolic peak and diastolic trough as a percentage of the systolic peak, was measured using the Acuson on-screen measurement system. From this, a mean RI value for each kidney was calculated.

In accordance with local practice, once a diagnosis had been made, if the symptoms settled without complication, patients were discharged to be reviewed as outpatients. Follow-up examinations were performed on 10

Address correspondence to Dr H. C. Irving.

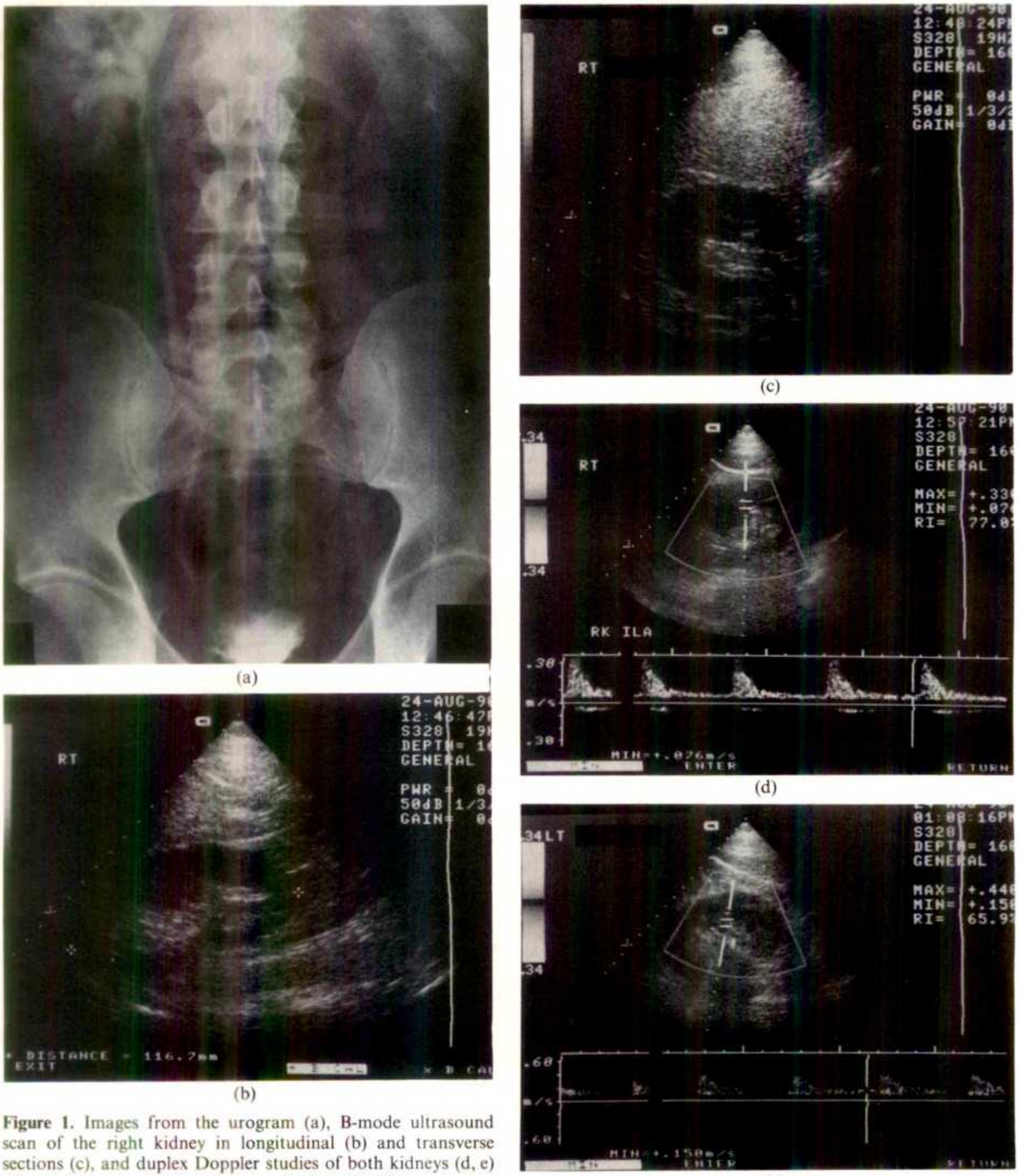

Figure 1. Images from the urogram (a), B-mode ultrasound scan of the right kidney in longitudinal (b) and transverse sections (c), and duplex Doppler studies of both kidneys (d, e) of a patient presenting with acute right renal colic.

patients from the obstructed group at between 2 weeks and 3 months after presentation.

Results

Between May and November 1990 a total of 405 intrarenal arterial Doppler recordings were made on 136 kidneys. Each examination took 15–30 min to perform, depending on the co-operation of the patient, and no patient had to be excluded because it was not possible to obtain adequate Doppler waveforms.

Figure 1 shows images from the urogram, B-mode ultrasound scan and duplex Doppler studies performed

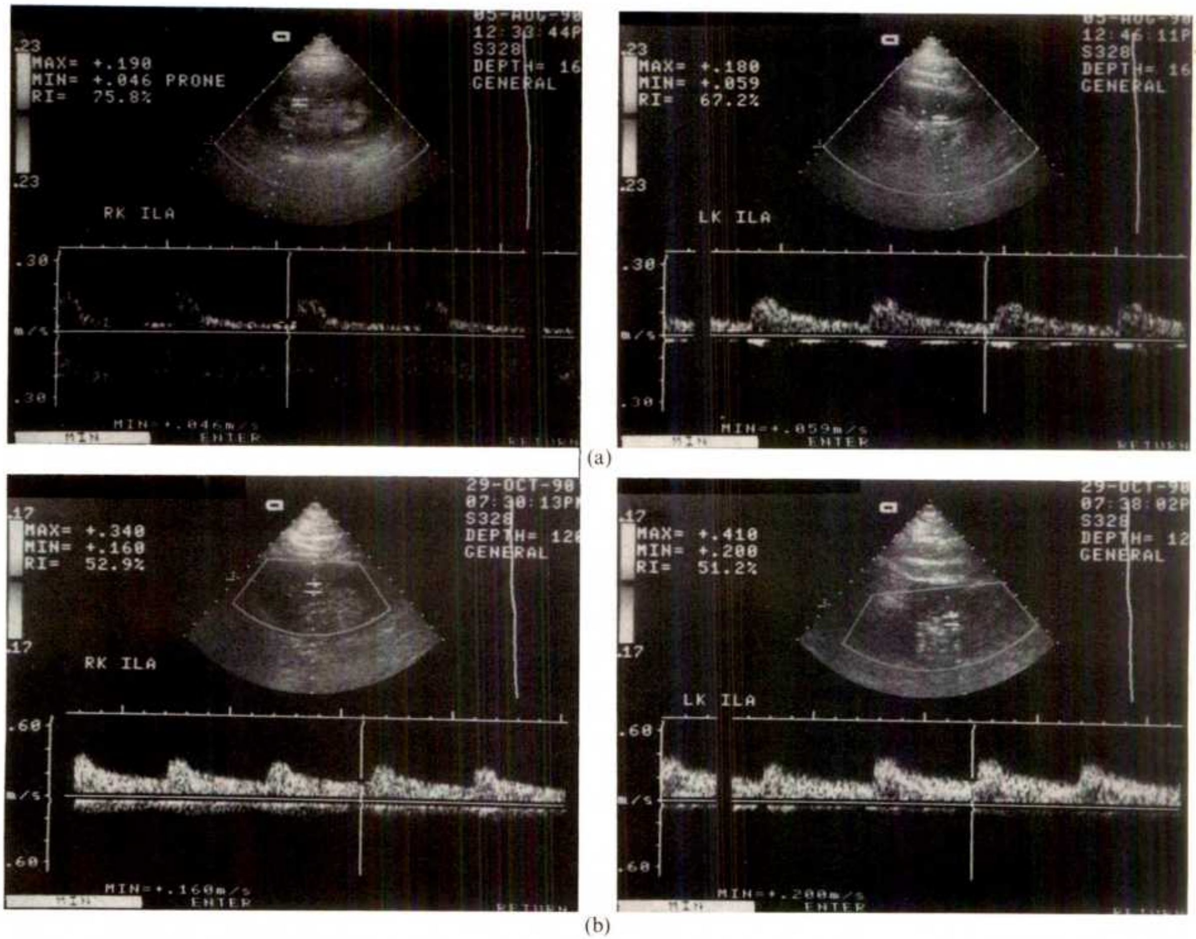

Figure 2. Doppler studies of both kidneys of a patient with acute right renal colic (a) and following relief of obstruction (b).

on one of the patients in acute ureteric obstruction. Figure 2 shows duplex Doppler studies from another patient before and after relief of obstruction.

The group mean RI values and standard deviations (SD) for the normal, obstructed and indeterminate kidneys are given in Table I, together with the statistical significance of the separation of the normal and obstructed groups obtained using the Mann-Whitney *U*-test. This analysis of the group data showed the separation of the normal and obstructed groups to be highly significant ($p < 0.001$). The indeterminate group could not be statistically distinguished from the normals.

Table I. Mean RIs of all kidneys studied

	Mean RI ($\pm$SD)
Normal kidneys (96)	62.3 (± 6.43)
Obstructed kidneys (14)	70.4 (± 6.22)
Indeterminate kidneys (6)	64.6 (± 6.74)

Statistical significance (MWU Test), Normal vs Obstructed $p = < 0.0002$.

Figure 3 contains graphic representations of the RI distributions of the normal group (3a), normals and obstructed cases (3b), and normals and indeterminate cases (3c).

The ultrasound images of the colic group were independently scored for pelvicalyceal dilatation on a scale of 0 to 3, reflecting nil, mild, moderate and severe dilatation, respectively. These results, together with the mean RI values, for each of the kidneys in the colic group are given in Table II. The final column gives the RI difference values for each pair of kidneys.

Although the range of RIs in obstructed kidneys was significantly higher than in normals, there was marked overlap of data, with RIs in four obstructed kidneys under 65. However, the "RI differences" of the obstructed and respective normal kidneys in these overlap cases is marked (see Table II). When the mean RI differences of the three groups are calculated and statistically compared (Table III), the results are much

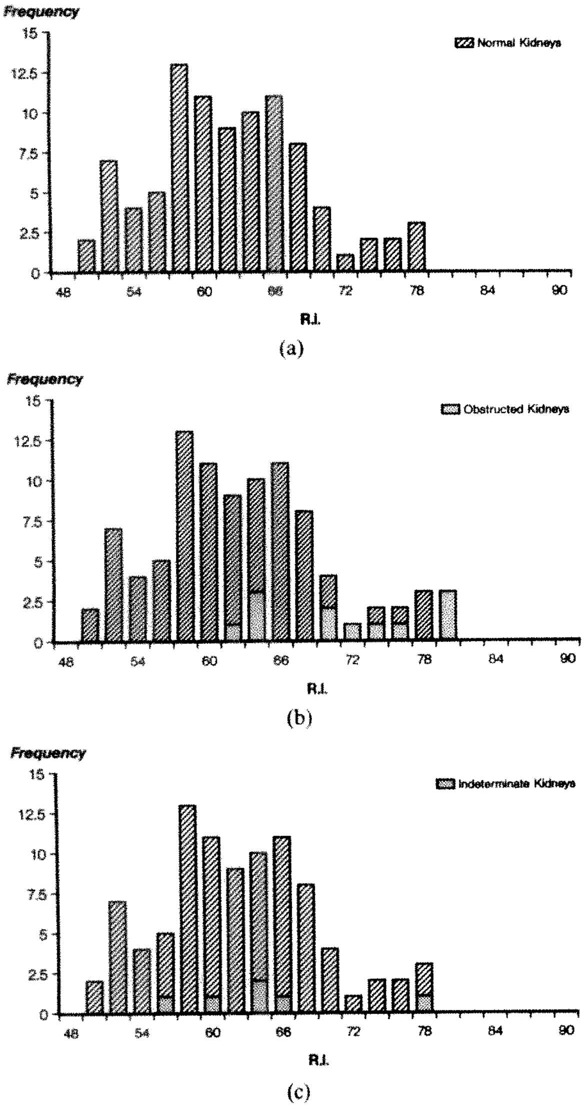

(a)

(b)

(c)

Figure 3. Graphs of the ranges of RI values in the three groups studied. (a) The normal kidneys; (b) the obstructed and (c) the indeterminate kidneys, which are shown against the normal range.

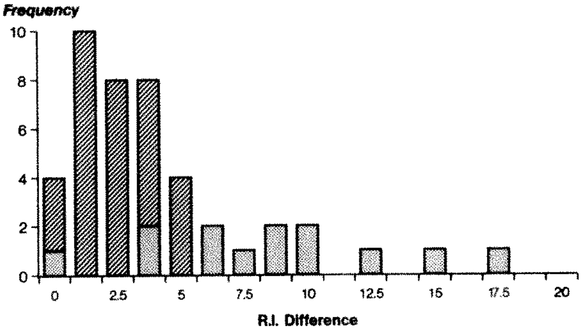

Figure 4. The ranges of interrenal "RI difference" values in the normal (lined) and obstructed (speckled) groups.

more discriminating for normal and obstructed kidneys. Again, the indeterminate and normal kidneys could not be statistically separated.

Figure 4 shows graphically the distribution of the "RI difference" values of the normal and obstructed groups.

In the four cases referred to above, the obstructed kidneys all had mean RIs > 6.5 higher than their respective non-obstructed kidneys, *i.e.* beyond two standard deviations (SD) from the mean for interrenal RI differences in our normal group.

The follow-up Doppler examinations, performed on 10 of the 14 obstructed cases, showed a fall in the RI of the previously obstructed kidney in nine cases. The exception was a more complicated case with an acute-on-chronic obstruction requiring surgical intervention.

Discussion

Animal studies have demonstrated that a complex series of events follows acute ureteric obstruction (Murphy & Scott, 1966; Ryan et al, 1987). Initially a rise in the intraluminal pelvi-ureteric pressure occurs without dilatation. This is followed by a haemodynamic response of altered perfusion as a result of increased vascular resistance. If the obstruction is not relieved, hydronephrosis develops.

Although sonography is widely used for demonstrating collecting system dilatation resulting from obstruction, several papers have documented the limitations of sonography (a) in the period between obstruction and onset of dilatation, (b) in the failure to recognize obstruction when dilatation cannot occur owing to the nature of the pathological process affecting the kidney, and (c) in the separation of dilated non-obstructed and dilated obstructed kidneys (Amis et al, 1982; Maillet et al, 1986; Naidich et al, 1986; Lalli, 1977; Lyons et al, 1988).

Thus, except when direct pressure measurements have been obtained during invasive interventional procedures (percutaneous nephrostomy, etc.), the diagnosis of acute renal obstruction has rested on the IVU and the manifestation of these haemo- and urodynamic responses as a dense persistent nephrogram with delayed excretion of contrast medium into the affected pelvicalyceal system.

The availability of duplex Doppler systems now raises the possibility of expanding the role of sonography in acute renal obstruction by allowing direct assessment of these haemodynamic responses. As the renal vascular resistance rises in response to obstruction, the predominant change in the Doppler waveform is a drop in the diastolic flow. This is most simply measured and expressed as the RI. This development may allow ultrasonographic recognition of acute ureteric obstruction in the absence of dilatation.

Recent work has documented significant elevation in the intrarenal resistance index in established renal

Table II. Mean RIs and degree of pelvicalyceal dilatation in both kidneys of 20 patients with renal colic

Obstructed kidneys		Non-obstructed kidneys		RI difference
PCS	Mean RI	PCS	Mean RI	
0	79.2	0	61.1	18.1
1	72.1	0	56.7	15.4
1	75.2	0	63.2	12.0
3	62.3	0	52.7	9.7
0	64.8	0	55.2	9.6
1	70.7	0	62.5	8.3
1	70.1	0	61.7	8.3
0	79.7	0	71.6	8.2
0	63.6	0	56.4	7.2
1	63.4	0	57.0	6.5
1	73.8	0	68.0	5.8
0	79.4	0	75.4	3.6
1	69.4	0	70.2	0.8
1	62.3	0	62.8	−0.5
Indeterminate		Non-obstructed		
2	63.7	0	61.2	2.5
0	77.4	1	75.7	1.7
2	60.3	0	59.4	0.9
0	66.8	0	67.8	−1.0
1	55.4	0	59.2	−3.8
1	64.3	0	70.3	−6.0

PCS = Collecting system dilatation: 0 = no dilatation; 1 = mild dilatation; 2 = moderate dilatation; 3 = severe dilatation.

obstruction, distinguishing between dilated obstructed and dilated non-obstructed kidneys and suggesting a discriminatory RI of 70 (0.70) between the obstructed and normal kidneys studied (Platt et al, 1989a, b).

Our study aimed first to examine a group of normal patients to establish a range of normal RI values and, secondly, to see if the RI changes could be demonstrated in renal colic at presentation, especially before the development of demonstrable dilatation.

The normal range based on 96 kidneys (average 62.3±6.43) was wide with eight normals showing RIs greater than 70. The data suggested a trend to increasing RI values with age (Fig. 5) but the numbers at the extremes of the age range were too small to be analysed statistically.

In the assessment of collecting system dilatation of the obstructed kidneys (Table II), five of 14 showed no dilatation and eight of 14 showed only mild dilatation. Several of the highest RI values and RI differences were seen in the non-dilated group, *i.e.* in the group that would appear sonographically normal without Doppler examination, whereas the indeterminate group, which could not be distinguished from normals by Doppler results, contained two of six moderately dilated systems and only one non-dilated system.

As a group, the acutely obstructed kidneys (14) showed a significant elevation in RIs (70.4±6.22) compared with the normals but six had RIs below 70

Table III. Mean interrenal RI differences of all kidney pairs studied

	Mean RI difference (±SD)
Normal kidneys	2.70 (±1.71)
Obstructed kidneys	8.37 (±4.43)
Indeterminate kidneys	2.53 (±1.90)

Statistical significance (MWU Test), Normal vs Obstructed $p = < 0.0001$.

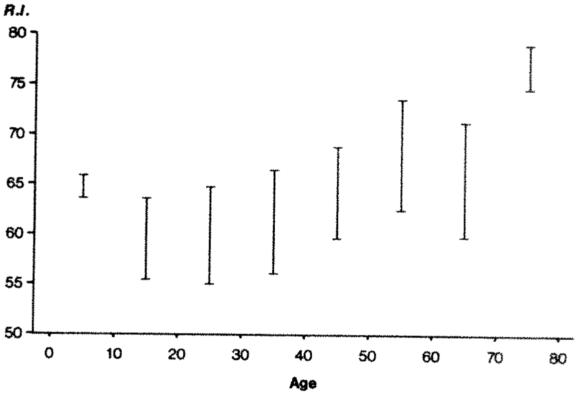

Figure 5. The range of RI values in normal cases according to age (years).

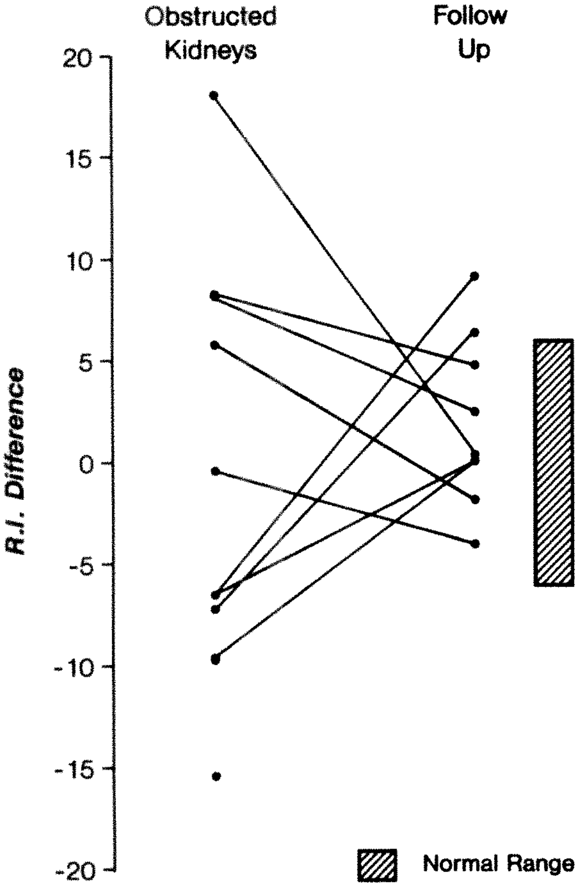

Figure 6. Changes in interrenal "RI differences" of kidneys at presentation in acute obstruction and at follow-up. (Positive RI difference indicates the right renal RI value is greater than the left and vice versa.)

showing considerable overlap with the upper normal range. However, the comparison of the mean RI of the obstructed kidney with its contralateral non-obstructed kidney proved much more discriminating.

Taking the difference in RI between the obstructed and normal kidney greatly reduces the overlap with normal. Only two of the 14 had RI differences within two standard deviations of the normal range. Taking an RI difference of 6 as a discriminator for obstruction would have resulted in one out of 38 false positives and four out of 14 false negatives.

Follow-up examinations were performed in 10 of the obstructed cases, generally following a clear history of passage of a urinary calculus. In nine cases there had been a reduction in the interrenal "RI differerence" values either into or towards the normal range (Fig. 6).

It was notable on the follow-up examinations that the mean RI of the contralateral non-obstructed kidney had also fallen in several cases (see Fig. 2). This is perhaps not surprising as the renal arterial blood flow is dependent on systemic as well as local factors, *e.g.* heart rate, cardiac output, blood pressure, etc., and will be susceptible to the effects of pain and of analgesics and other medications. However, most of these factors will affect both kidneys equally, giving further advantage to measuring the RI difference between kidneys rather than relying on the absolute RI value of the affected kidney.

Conclusion

This study supplements the existing evidence that renal Doppler recordings can distinguish between dilated acutely obstructed and dilated non-obstructed kidneys by demonstrating changes in renal blood flow.

It has also been shown that, in acutely obstructed kidneys, renal Doppler recording can demonstrate altered renal perfusion before pelvicalyceal system dilatation so increasing the accuracy of ultrasound in the investigation of renal disease.

Acknowledgment

We wish to thank the staff of the Medical Illustration Department of St James' University Hospital, Leeds, for their work with the graphics and illustrations.

References

AMIS, E. S., CRONAN, J. J., PFISTER, R. C. & YODER, I. C., 1982. Ultrasonic inaccuracies in diagnosing renal obstruction. *Urology, XIX,* 101–105.

ELLENBOGEN, P. H., SCHEIBLE, F. W., TALNER, L. B. & LEOPOLD, G. R., 1978. Sensitivity of gray scale ultrasound in detecting urinary tract obstruction. *American Journal of Roentgenology, 130,* 731–733.

ERWIN, B. C., CARROLL, B. A. & SOMMER, F. G., 1984. Renal colic: the role of ultrasound in initial evaluation. *Radiology, 152,* 147–150.

HILL, M. C., RICH, J. I., MARDIAT, J. G. & FINDER, C. A., 1985. Sonography *vs.* excretory urography in acute flank pain. *American Journal of Roentgenology, 144,* 1235–1238.

LALLI, A. F., 1977. Retroperitoneal fibrosis and inapparent obstructive uropathy. *Radiology, 122,* 339–342.

LYONS, K., MATTHEWS, P. & EVANS, C., 1988. Obstructive uropathy wihout dilatation: a potential diagnostic pitfall. *British Medical Journal, 296,* 1517–1518.

MAILLET, P. J., PELLE-FRANCOZ, D., LAVILLE, M., GAY, F. & PINET, A., 1986. Nondilated obstructive acute renal failure: diagnostic procedures and therapeutic management. *Radiology, 160,* 659–662.

MURPHY, G. P. & SCOTT, W. W., 1966. The renal haemodynamic response to acute and chronic ureteral occlusions. *Journal of Urology, 95,* 636–657.

NAIDICH, J. B., RACKSON, M. E., MOSSEY, R. T. & STEIN, H. L., 1986. Nondilated obstructive uropathy: percutaneous nephrostomy performed to reverse renal failure. *Radiology, 160,* 653–657.

PLATT, J. F., RUBIN, J. M., ELLIS, J. H. & DIPIETRO, M. A., 1989a. Duplex Doppler US of the kidney: differentiation of obstructive from nonobstructive dilatation. *Radiology, 171,* 515–517.

PLATT, J. F., RUBIN, J. M. & ELLIS, J. H., 1989b. Distinction between obstructive and nonobstructive pyelocaliectasis with duplex Doppler sonography. *American Journal of Roentgenology, 153,* 997–1000.

RYAN, P. C., MAHER, K. P., MURPHY, B., HURLEY, G. D. & FITZPATRICK, J. M., 1987. Experimental partial ureteric obstruction: pathophysiological changes in upper tract pressures and renal blood flow. *Journal of Urology, 138,* 674–678.

1992, *The British Journal of Radiology*, *65*, 213–217

Bone mineral density in healthy normal women and reproducibility of measurements in spine and hip using dual-energy X-ray absorptiometry

By *M. J. Haddaway, BTech, M. W. J. Davie, MD, FRCP and *I. W. McCall, FRCR

Charles Salt Research Centre and *Department of Diagnostic Imaging, Robert Jones and Agnes Hunt Orthopaedic and District Hospital, Oswestry, Shropshire SY10 7AG, UK

(*Received 6 December 1990 and in revised form 16 July 1991, accepted 12 September 1991*)

Keywords: Bone mineral density, Reference values, Spine, Hip, DEXA

Abstract. Bone mineral density (BMD) using dual-energy X-ray absorptiometry (DEXA) has been measured in 394 healthy normal women. BMD is highest at the end of the 3rd decade and declines from 45 to 75 years by 0.0095 g/cm^2/year in the lumbar spine and by 0.0052–0.0078 g/cm^2/year in the upper femur depending on the site. BMD appears to increase in the 8th decade. Reproducibility (coefficient of variation (CV) of repeated measurements) was lowest in the lumbar spine (1.45%) and highest in Ward's triangle (4.29%). CV was not influenced by age at any site and by osteoporosis only in the femoral neck. BMD increased from L2 to L4 but the increase could not wholly be accounted for by the size of the vertebra, suggesting that the posterior elements were contributing to the observed increase of bone density.

Osteoporosis is a common disorder in the community, especially amongst elderly women. The occurrence of a fracture in osteoporosis depends on several factors, an important one of which is the mechanical strength of bone, a property closely related to the density of bone (Carter & Hayes, 1976). Bone density measurement using dual-energy X-ray absorptiometry (DEXA) has been reported to have better precision than earlier techniques (Hansen et al, 1990). The technique is increasingly being used in establishing risk of fracture and as a means of following the effect of treatment. It is therefore important to establish a reference range for bone density at different ages. It is also important to establish, in the healthy normal population and in patients with osteoporosis, the reproducibility of repeated measurements within subjects. Data for a normal range are available from the manufacturers of the Hologic QDR 1000 and from a study in London (Hall et al, 1990). It is not clear whether the patients used to generate the manufacturer's data were carefully screened. The data from London refer to the lumbar spine only and were relatively deficient in older subjects, with only 17 out of 169 subjects over 60 years of age. To amplify the data relating to the normal range at all sites, bone mineral density (BMD) has been measured in a large number of women who are part of the Shropshire osteoporosis programme. Reproducibility has also been investigated and the results applied to long-term studies of change of bone mass.

It has also been reported, using quantitative computed tomography (QCT), that the cancellous bone in the vertebral body declines with caudal progression from L1 to L3 (Steiger et al, 1990). Since DEXA measures the bone mineral in the whole vertebra it is possible that this finding might not apply using DEXA. We have analysed the BMD in L2–L4 using DEXA and compared the results with those reported using QCT (Steiger et al, 1990) and have investigated possible reasons for the discrepant findings.

Subjects and methods

Normal subjects

394 healthy Caucasian women were recruited. Those under 40 years of age were recruited from hospital staff and women's organizations, and those over 40 years exclusively from women's organizations. The age ranged from 18 to 82 years. All subjects over 40 years were screened with a questionnaire, serum calcium, creatinine, phosphorus and liver function tests, serum osteocalcin, and 24 h urine calcium, phosphorus, creatinine and hydroxyproline, and had a lateral radiograph of the dorsal and lumbar spine to ensure absence of vertebral fracture. The presence of osteoarthritis was not investigated and was not therefore an exclusion criterion. Subjects were excluded if they had ever taken corticosteroids, had had thyrotoxicosis or undergone bilateral ovariectomy, had received thyroxine or oestrogen replacement therapy, or were taking high-dose calcium supplements. Hysterectomy and the taking of the contraceptive pill did not exclude, nor did smoking and drinking habits although these were recorded.

Measurements

DEXA measurements were performed using an Hologic QDR 1000 densitometer. Total bone mineral was measured at each site and "density" (BMD)

---

*Address correspondence to: Mr M. J. Haddaway, Principal Medical Physicist, Robert Jones and Agnes Hunt Orthopaedic and District Hospital, Oswestry, Shropshire SY10 7AG, UK.

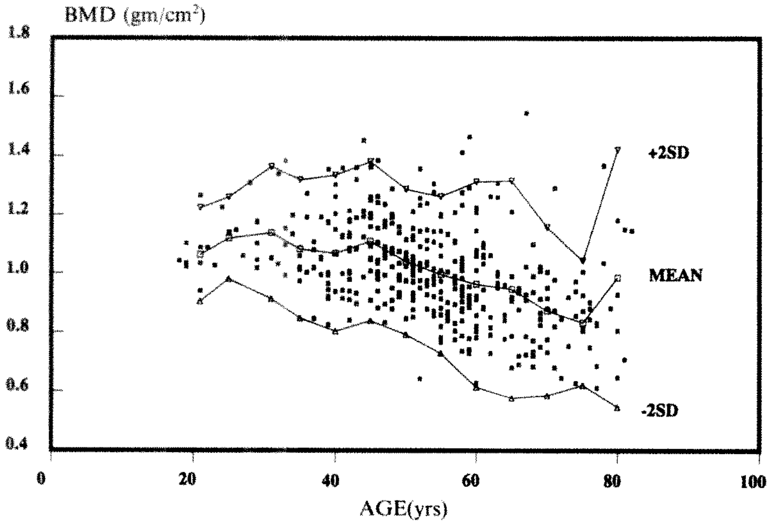

Figure 1. BMD in the lumbar spine of 394 normal women.

measured as (bone mineral/area). The QDR 1000 measures attenuation by the patient's body compared with an internal machine standard. These data are presented as values of bone mineral content (BMC), projected area (in the coronal plane) and BMD (BMD = BMC/area) which is expressed in g/cm^2, a density related to area. These are given for each vertebra, together with an "average" value for all three vertebrae together. Mean BMD was calculated in 5-year age bands (whereby 43–47 years was designated as 45 years, for example). The area measured is referred to here as "coronal area". A facility (called "Compare") is incorporated in the software and allows precise reproduction of analysis on repeat scans. DEXA measurements of L2–L4 and of the right upper femur were recorded over a period between December 1988 and June 1990.

Reproducibility

The precision of measurement was assessed in a further group of 55 subjects (12 men, 43 women). 24 subjects had vertebral osteoporosis (indicated by crush or wedge fractures) not affecting L2–L4. 31 subjects had BMDs appropriate to their age and did not have any vertebral fractures. They were selected by their ability to attend twice on the same day. All 55 had scans of the spine and 51 had scans of the upper femur. Each subject left the scanning table for a significant period between scans. The two images were analysed and two separate readings obtained (using the "Compare" facility for the second study). From these two sets of readings the coefficients of variation (CV) were calculated for each site (Slosman et al, 1990).

Other statistical tests

Student's *t*-test was used to compare differences between readings and to compare osteoporotic with non-osteoporotic subjects at different measurement sites. Rank tests were used to test for bias of repeat measurements, Fisher's variance test was used for the spread of BMD (Table I) and linear and exponential regression were used to calculate rates of bone loss with age.

Vertebral dimensions

Vertebral dimensions for L2–L4 were measured from the lateral spine radiographs of 52 subjects selected at random from the main body of 394 subjects. An interactive image analysis system was used to determine the co-ordinates of the vertebrae, and the superior and inferior antero-posterior dimensions were calculated from these co-ordinates and averaged. The locations of the points used to determine the co-ordinates were similar to those described by the group at the Henry Ford Hospital (Nelson et al, 1990). An estimate of vertebral body volume was made from the product of the coronal area calculated by the QDR 1000 and the average of the

Table I. Variance of BMD in 10-year age groups[a]

Age group:	30	40	50	60	70	80
Site *n*	22	75	121	95	50	19
Lumbar spine	0.012	0.019	0.017	0.026	0.025	0.039
F ratio	1	1.58	1.42	2.17*	2.08*	3.25*
Femur						
Neck	0.008	0.011	0.010	0.010	0.011	0.004
Troch	0.004	0.012	0.008	0.011	0.010	0.006
Inter	0.010	0.020	0.015	0.017	0.028	0.011
Total	0.006	0.016	0.019	0.015	0.019	0.007
Ward's	0.008	0.014	0.011	0.010	0.013	0.007
F ratio (Total)	1	2.67*	3.17*	2.5*	3.17*	1.17

*$p < 0.05$ (variance ratio test).

[a] 30 is equivalent to ages 25–35 years, for example.

Note: The 80-year age group includes one additional subject aged 85 years. Omission of this subject does not alter the statistical results.

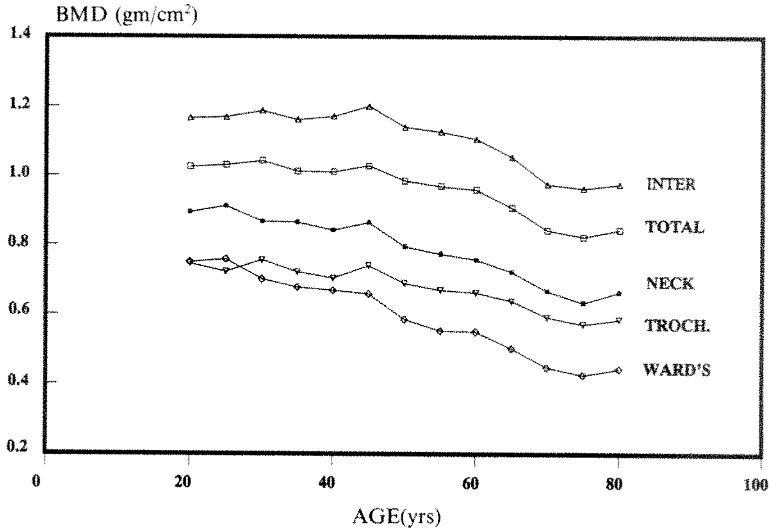

Figure 2. Mean values of BMD at different sites in the upper femur (Inter = intertrochanteric area; Total = total area; Neck = femoral neck; Troch. = trochanteric area; Ward's = Ward's triangle).

superior and inferior antero-posterior dimensions on the radiograph. Magnification effects, inherent in the radiographic technique, were not corrected for in this study, since they were the same at each vertebral level, within individual subjects.

This research programme has been passed by the Robert Jones and Agnes Hunt Orthopaedic Hospital Ethical Committee.

Results

Mean BMD at all sites declined after 45 years until the 8th decade. Results for the lumbar spine appear in Fig. 1. The rate of loss of mean bone density (g/cm^2/year) from age 45–75 years was 0.009 (= linear) and 0.0095 (exponential) in the lumbar spine. At the upper end of the femur (Fig. 2) the rates of decline varied with the site, being 0.0072 (exp = 0.0097) in the femoral neck, 0.0052 (exp = 0.0082) in the trochanteric area, 0.0078 (exp = 0.0075) in the intertrochanteric area, 0.0071 (exp = 0.0063) in total area and 0.0074 (exp = 0.0143) in Ward's triangle. Advancing age was associated with an increase of variance around the mean. Compared with the 30-year age group this reached significance at the 5% level in the lumbar spine of subjects aged 55–85 years (10-year bands) and in the upper femur (total area) in subjects aged 35–75 years (Table I). The highest mean peak bone mass occurred in the 30-year group in the lumbar spine (Fig. 1) and, in the femur, at the total and trochanteric sites. In the neck of femur and Ward's triangle the highest values occurred earlier in the 25-year group (Fig. 2).

Percentage difference between readings within indivi-

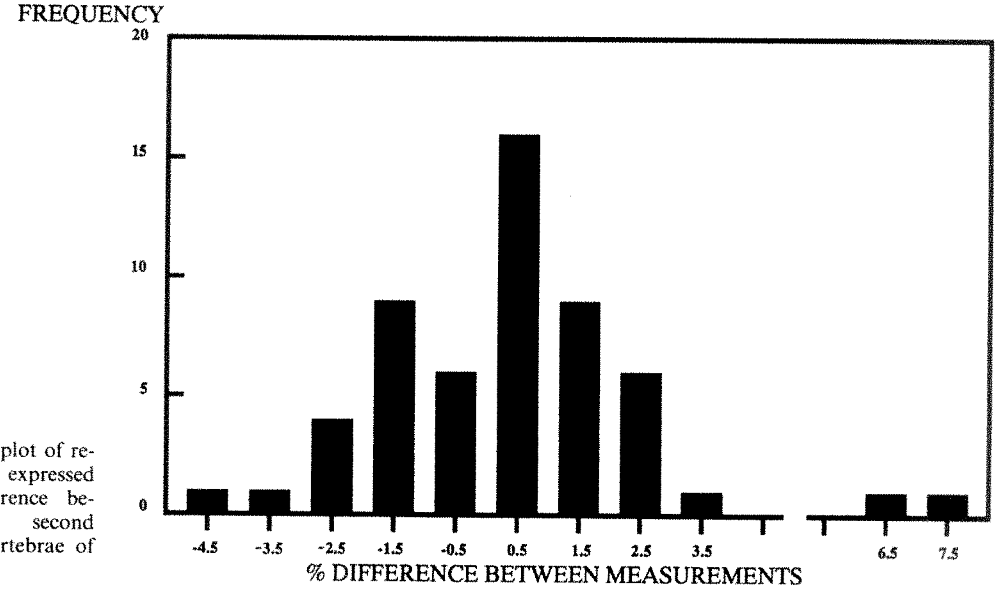

Figure 3. Frequency plot of repeatability of BMD, expressed as percentage difference between first and second measurements, in vertebrae of 55 subjects.

Table II. Coefficient of variation (%) of spine and femur sites using QDR 1000

	L2	L3	L4	Aver.	Neck	Troch.	Inter	Total	Ward's
Osteoporotic	3.11	3.24	2.15	1.71	2.51	2.77	1.98	2.01	7.41
Non-osteoporotic	2.33	1.73	1.60	1.30	1.83	1.61	2.43	2.21	2.50
All	2.60	2.27	1.80	1.45	2.07	2.02	2.34	2.17	4.29

dual subjects was examined and is presented for the lumbar spine in Fig. 3. This did not correlate with age or BMD at any site and there was no significant difference in the repeat measurements between osteoporotic and non-osteoporotic subjects except in the femoral neck ($p = 0.02$). No systematic trend was found between the first and the second readings. CV calculated for all sites is shown in Table II. The lowest CV was found in the lumbar spine reading and the highest in Ward's triangle.

In the lumbar spine BMD ($n = 394$) increased from L2 to L3 and again from L3 to L4 (Table III). The area measured by the Hologic QDR 1000 also increased from L2 to L4 (Table III). The differences in area between each vertebra were highly significant ($p < 0.0001$). There was no correlation between vertebral area and age.

The antero-posterior dimension of L2–L4 was calculated as described in 52 subjects. This dimension increased between L2 and L3 and between L3 and L4. No relationship was found between the change of BMD in any two vertebral levels and the change either in the antero-posterior dimension (X-ray) or in the volume of the vertebral body (calculated from Hologic coronal area × X-ray antero-posterior dimension) between the same two vertebral levels.

Discussion

The average BMD in the lumbar spine and the rate of decline (cross-sectional) recording a 25% loss of bone mass between 45 and 75 years accord with previous studies using dual-photon absorptiometry (DPA) or DEXA methods (Riggs et al, 1986; Ribot et al, 1988; Hall et al, 1990). In contrast with studies using DPA in the USA, the present study suggests that mineral is no longer being lost from the spine and the upper femur from the 8th decade onwards. Other series in which sufficient elderly subjects are included also show the same phenomenon (Ribot et al, 1988). The cessation of bone loss in old age may be a real phenomenon, and may be associated with hyperostosis around spondylolytic motion segments, or result from the population studied being biased, since the necessity to attend for scanning may have meant that only the fittest of elderly subjects were able to attend for studies. It will be important to confirm this finding with longitudinal studies. If bone loss is limited to the 45–75 year age group, this may indicate that there is an age after which hormone replacement therapy becomes less relevant. Alternatively, there may be a time limit to the effect of oestrogen withdrawal.

There is a trend for the variance of BMD in the population to increase significantly after the age of 50 years at all sites, and a similar trend is discernible in previously published DEXA data that refer only to the lumbar spine BMD (Hall et al, 1990). Such variance is by no means a universal finding in population studies of bone density that have employed DPA. Some reports show very similar variances or standard deviations at different ages (Riggs et al, 1982; Ribot et al, 1988). This difference may be related more to the degree of selection of the patients than to the different technology. A population sample in which all the subjects have been carefully selected may not reflect the biological heterogeneity of the underlying population. In one study, selection was so rigorous that only about 25% of an otherwise healthy population were eventually included (Ribot et al, 1988).

The reproducibility of the measurements (CV) in the lumbar spine (1.45) is similar to the values in an earlier report, which showed a trend for the mean CV in the lumbar spine to increase from 0.9 in the pre-menopausal period to 1.5 in the late post-menopausal age group (Hansen et al, 1990). We did not find a significant deterioration of CV with age at any site either in the

Table III. Change in BMD and vertebral dimensions with vertebral level

	L2		p (L2 vs. L3)	L3		p (L3 vs. L4)	L4	
	Mean	SD		Mean	SD		Mean	SD
BMD (g/cm^2)	0.95	0.17	**	1.01	0.17	*	1.05	0.12
QDR area (cm^2)	13.6	1.3	**	15.3	1.45	**	17.0	1.68
AP X-ray dim. (mm)	38.9	2.6	*	40.0	2.6	*	40.6	2.1

*$p < 0.001$, **$p < 0.0001$ (one-tailed t-test). AP X-ray dim. = antero-posterior X-ray dimension.

normal population or in the whole group. The osteoporotic subjects had a similar CV to the non-osteoporotic subjects at all sites except Ward's triangle.

Using these data for CV and multiplying by $2 \times \sqrt{2}$ gives the 95% confidence limit for the difference between sequential readings on the same patient. This would give, in the case of the lumbar spine, a value of 4.07%. Reference to Table II shows that the lumbar spine has the lowest CV of any site. Since it also exhibits the most rapid cross-sectional decline of bone mass with age of any site, changes in BMD are likely to be detected early at this site. Longer periods of observation in individual subjects will be required before sites in the femur, with higher CV and lower rates of loss, show significant changes.

In these studies BMD increased progressively from L2 to L4 as distinct from the decrease of density in the central core of vertebral body cancellous bone between L2 and L3 found by QCT (Steiger et al, 1990). There are several possible explanations for this. Because the QDR 1000 measures the whole vertebra without regard to the depth (antero-posterior dimension of the vertebral body), it could be accounted for by the antero-posterior dimension increasing progressively from L2 to L4. Undoubtedly the antero-posterior dimension measured from radiographs increases from L2 to L4, but the increment is small and no relationship is found between changes in bone density and changes in antero-posterior dimension or volume. The cortical envelope of L4 might be greater than at L2. There is, however, no evidence that the proportion of cortical bone changes in the body of the vertebrae between L2 and L4 (Nottestad et al, 1987; Haddaway et al, 1989). The increase in density found with caudal progression from L2 to L4 could also arise from an increase in the mass of the posterior elements of the vertebrae, but this requires experimental verification.

The loss of apparent bone density (measured by physical methods) in the lumbar spine obtained from cadavers aged 25–75 years is between 25 and 45% (Britton & Davie, 1990). The loss of bone density over the same age group measured by DEXA approximates the lower end of this range. However bone mechanical strength declines 2–2.5 times faster than does apparent density (Mosekilde et al, 1987; Britton & Davie, 1990). Thus considerable loss of bone strength can arise from small changes of density thereby stressing the importance of the precision of bone densitometry measurements. With the estimated 95% confidence limit of BMD measurement in the lumbar spine being about 4%, it is likely that differences of about 8% in strength are occurring before detection is possible.

In conclusion, using DEXA we have established a range for BMD in the lumbar spine and femur for normal women living in the UK and have shown that BMD falls in all sites from about 45 to 75 years. The precision is best at the lumbar spine and worst at Ward's triangle. Bone density increases from L2 to L4 in the lumbar spine and this cannot be accounted for by an increase in vertebral depth.

References

Britton, J. M. & Davie, M. W. J., 1990. Mechanical properties of bone from iliac crest and relationship to L5 vertebral bone. *Bone, 11*, 21–28.

Carter, D. R. & Hayes, W. C., 1976. Bone compressive strength: the influence of density and strain rate. *Science, 194*, 1174–1176.

Haddaway, M., Grantham, S. & Davie, M. W. J., 1989. Contribution of cortical and trabecular bone to density in lumbar vertebrae and relationship of trabecular density to mechanical strength. In *Osteoporosis and Bone Mineral Measurement*, ed. by E. F. J. Ring, W. D. Evans & A. S. Dixon (IPSM, York), pp. 186–191.

Hall, M. L., Heavens, J., Cullum, I. D. & Ell, P. J., 1990. The range of bone density in normal British women. *British Journal of Radiology, 63*, 266–299.

Hansen, M. A., Hassage, C., Overgaard, K., Marslaw, U., Riis B. J. & Christiansen, C., 1990. Dual energy X-ray absorptiometry. A precise method of measuring bone mineral density in the lumbar spine. *Journal of Nuclear Medicine, 31*, 1156–1162.

Mosekilde, L., Mosekilde, L. & Danielson, C. C., 1987. Biomechanical competence of vertebral trabecular bone in relation to ash density and age in normal individuals. *Bone, 8*, 79–85.

Nelson, D., Peterson, E., Tilley, B., O'Fallon, W. M., Chao, E., Riggs, B. L. & Kleerekopper, M., 1990. Measurement of vertebral area on spine X-rays in osteoporosis: reliability of digitising techniques. *Journal of Bone and Mineral Research, 5*, 707–716.

Nottestad, S. Y., Baumel, J. J., Kimmel, D. B., Recker, R. R. & Heaney, R. P., 1987. The proportion of trabecular bone in human vertebrae. *Journal of Bone and Mineral Research, 2*, 221–229.

Ribot, C., Tremollieres, F., Pouilles, J. M., Louvet, J. P. & Guiraud, R., 1988. Influence of the menopause and aging on spinal density in French women. *Bone and Mineral, 5*, 89–97.

Riggs, B. L., Wahner, H. W., Melton, L. J., III, Richelson, L. S., Judd, H. L. & Offord, K. P., 1986. Rates of bone loss in the appendicular and axial skeletons of women. *Journal of Clinical Investigation, 77*, 1487–1491.

Riggs, B. L., Wahner, H. W., Seeman, E., Offord, K. P., Dunn, W. L., Mazess, R. B., Johnson, K. A. & Melton, L. J., III, 1982. Changes in bone mineral density of the proximal femur and spine with aging. *Journal of Clinical Investigation, 70*, 716–723.

Slosman, D. O., Rizzoli, R., Donath, A. & Bonjour, J.-Ph., 1990. Vertebral bone mineral density measured laterally by dual energy X-ray absorptiometry. *Osteoporosis International, 1*, 23–29.

Steiger, P., Block, J. E., Steiger, S., Heuck, A. F., Friedlander, A., Ettinger, B., Harris S. T., Gluer, C. G. & Genant, H., 1990. Spinal bone mineral density measured with quantitative CT: effect of region of interest, vertebral level and technique. *Radiology, 175*, 537–543.

1992, *The British Journal of Radiology*, *65*, 218–220

Echo pattern of lymph nodes in colorectal cancer: an *in vitro* study

By S. R. Rafaelsen, MD, O. Kronborg, MD, PhD and *C. Fenger, MD, PhD

Departments of Surgical Gastroenterology and *Pathology, Odense University Hospital, DK-5000 Odense, Denmark

(*Received 12 July 1991 and accepted 12 September 1991*)

Keywords: Colorectal carcinoma, Lymph nodes, Ultrasonography

Abstract. Surgical specimens from 75 patients with colorectal cancer were examined within 15 min of removal with a 7.5 MHz linear-array transducer. The echo pattern of 139 lymph nodes was analysed to evaluate previous criteria of malignancy and to establish other possible criteria, which could be tested *in vivo*. The pathologist examined each node without knowledge of the sonographic finding. Malignant nodes were larger than benign nodes. Of 21 nodes less than 5 mm in diameter, 20 were benign. Round nodes were malignant more often (45/78) than ovoid nodes (6/61). A homogeneous echo pattern was associated with malignancy in 39 of 82 nodes in contrast to 12 of 57 with a heterogeneous pattern. Thirty-one nodes were ovoid as well as heterogeneous and all of these were benign. A hyperechoic centre was found in 14 nodes of which two were malignant. The highest predictive value for malignancy (59%) was obtained by combining the discriminative properties of shape, homogeneity and echogenicity.

Evaluation of tumour invasion depth in the rectum by transrectal ultrasonography is accurate in a high percentage of cases according to histopathological findings (Wang et al, 1987; Jochem et al, 1990), but evaluation of lymph node involvement seems to be less reliable, resulting in a large number of false predictions of cancer (Beynon et al, 1989; Rifkin et al, 1989; Hildebrandt & Feifel, 1990).

A few *in vitro* studies of the echo pattern of the lymph nodes have been reported, evaluating only a small number of nodes in colorectal specimens. Involved lymph nodes were stated to be hypoechoic and display a sharp demarcation (Tio & Tytgat, 1986; Hildebrandt et al, 1990). However, there are no generally accepted criteria for classification of benign or malignant lymphadenopathy (Feifel et al, 1990). It is impossible to be confident that lymph nodes identified by ultrasonography *in vivo* are the same as those being examined by the pathologist. We therefore analysed the echo pattern of a large number of lymph nodes *in vitro* in order to evaluate previously reported criteria of malignancy and also to identify other possible criteria, which might subsequently be tested *in vivo* at transrectal ultrasonography.

Materials and methods

Lymph nodes in surgical specimens removed from 75 patients with primary colorectal cancer were examined. The intestine was opened along the anti-mesenteric border and the fresh specimen was examined within 15 min of surgical resection, in a degassed water bath at approximately 37°C. The ultrasound examination was performed by the first author using a Picker CS 9500 scanner with a 7.5 MHz linear-array transducer.

139 lymph nodes were obtained from 40 female and 35 male patients (Table I). They were described by localization, size, shape, homogeneity and demarcation. Lymph nodes with echogenicity equal to or more hypoechoic than that of the tumour itself were classified as malignant and those being less hypoechoic as benign.

The examinations were documented using video printer and video tape. After sonographic description of the individual lymph nodes, they were removed from the specimen and fixed with 4% formaldehyde in phosphate

Table I. Specimens and lymph nodes

Type of resection	Number of patients	Number of nodes	Number of malignant nodes
Abdominoperineal resection	7	19	7
Low anterior resection	28	55	26
Sigmoid resection	14	24	8
Left hemicolectomy	6	11	3
Transverse colectomy	5	8	2
Right hemicolectomy	15	22	5
Total	75	139	51

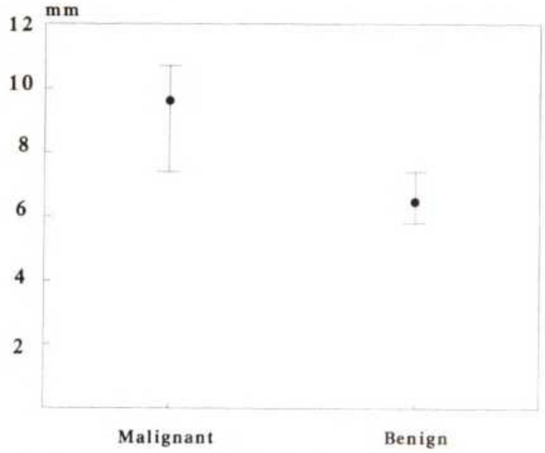

Figure 1. Median size of malignant and benign lymph nodes (9.3 mm against 6.3 mm) with 95% confidence limits ($p < 0.0001$).

buffer (pH = 7.0). The pathologist examined each node without knowledge of the prediction of ultrasonography.

The statistical evaluation included the unpaired Mann-Whitney test to compare medians; proportions were compared by χ^2 test or, when appropriate, Fischer's exact test. Significance was stated for $p < 0.05$.

Results

The pathologist described 51 nodes as malignant and 88 as benign. The ultrasonologist described 87 nodes as malignant and 52 as benign using previously mentioned criteria. Prediction of malignancy was correct in 48 of the 87 nodes ($PV_{pos} = 55\%$) and of benignity in 49 of the 52 nodes.

The median size of malignant nodes was significantly larger than that of benign nodes (9.3 mm against 6.3 mm) with no overlap of 95% confidence limits (Fig. 1). Lymph nodes less than 5 mm were benign in 20 of 21 cases. 23 of the 31 nodes greater than 10 mm were malignant.

Table II. Results of studies *in vitro*

Descriptive measurements	Malignant nodes	Benign nodes	Significance
0– < 5 mm	1	20	
5– < 10 mm	27	60	$p < 0.0001$
10+ mm	23	8	
Round	45	33	$p < 0.00005$
Ovoid	6	55	
Homogeneous	39	43	$p < 0.005$
Heterogeneous	12	45	
Sharp	29	54	NS
Non-sharp	22	34	
Tumour near	47	77	NS
Tumour far	4	11	

Size: greatest diameter; Round: width is more than three-quarters of the length; Tumour near: less than 5 mm from tumour margin.

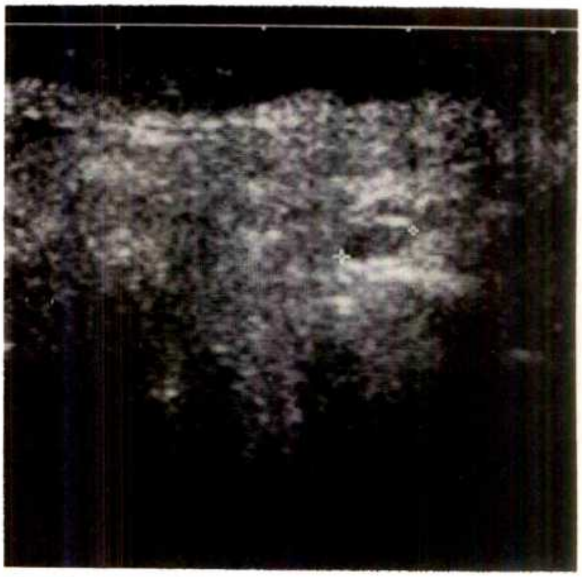

Figure 2. *In vitro* ultrasound scan showing a primary tumour with an adjacent 5 mm ovoid and heterogeneous lymph node. Benign histopathology.

Round nodes were malignant more often than ovoid nodes. This was also true for homogeneous compared with heterogeneous nodes (Table II). 52 nodes were round as well as homogeneous and 32 of these were malignant. 31 lymph nodes were both ovoid and heterogeneous (Fig. 2) and all 31 were benign (95% confidence limits: 89–100%). Demarcation and localization did not discriminate between malignant and benign nodes (Table II).

All lymph nodes were more or less hypoechoic. No completely hyperechoic nodes were imaged. A hyperechoic centre was found in 14 nodes, two of which were metastatic nodes with central necrosis, the rest being benign. Three lymph nodes displayed a central hyperechoic line; they were all benign.

Accepting that nodes being ovoid as well as heterogeneous would never be malignant and using this criterion in combination with that of echogenicity, would increase the predictive value for malignancy from 55% to 59%. No other ultrasonographic criteria were found to reduce the number of false positive results.

Discussion

The present results confirm that an ultrasonographic characterization of lymph node metastases from colorectal cancer may be wrong in 45% of cases. This means that the examination cannot be recommended for selection of patients with rectal cancer for pre-operative radiotherapy unless it is accepted that patients with a less advanced stage than Dukes' C will be treated in a substantial number. Biopsy will be necessary to increase the diagnostic accuracy. So far ultrasound-guided biopsy of perirectal lymph nodes has only been reported in single cases (Quam et al, 1989).

The size of the nodes had some discriminative significance confirming previous results (Beynon et al, 1989), but more than 25% of the nodes less than 10 mm in diameter were malignant and 28 out of the 51 malignant nodes were less than 10 mm. This distribution is in accordance with previous clinicopathological findings (Herrera-Ornelas et al, 1987), making large size a poor criterion for identifying most of the node metastases, but still a criterion with a high positive predictive value.

The shape alone also had some discriminative ability, most of the malignant nodes being round but more than 40% of the round nodes were benign. Similar results have been found by others (Marchal et al, 1985; Aibe et al, 1986).

Finally, homogeneity offered significant discrimination, but again whilst most of the malignant nodes were homogeneous, 52% of the homogeneous nodes were benign. This finding seems not to have been reported before.

Sharp demarcation of the borders of the lymph nodes has suggested malignancy in a previous study (Tio & Tytgat, 1986), but our results did not confirm this. Most of the examined nodes were within a distance of 5 mm of the tumour, which is similar to that in *in vivo* studies; apical lymph nodes are seldom visualized (Tio et al, 1991).

The presence of a hyperechoic centre has been suggested as a sign of benignity (Marchal et al, 1985), which was to some degree confirmed (12 out of 14).

Description of echogenicity is controversial. Hyperechoic lymph nodes may actually mean less hypoechoic than the tumour itself (Tio & Tytgat, 1986). It may be more important to compare the relative echogenicity between the tumour and the nodes, since echogenicity also depends on structure of the overlying tissue, transducer frequency and gain setting of the equipment (Smeets et al, 1990). Like Beynon et al (1989), we did not identify any hyperechoic lymph nodes.

Malignant lymph nodes have no reflectors according to Hildebrandt et al (1990), and therefore reflect less sound than benign lymph nodes, explaining a more hypoechoic and homogeneous pattern in the former. However, the present results could only give partial confirmative evidence to this statement.

The combination of ovoid shape and heterogeneity demonstrated a very high probability of a benign lymph node in our study. The possible value of this finding will have to be tested in a clinical setting, ideally in patients selected for colorectal surgery having pre-operative endoluminal ultrasonography. At the same time, it will be possible to evaluate the benefit from combining previous ultrasonographic criteria of benignity with those presented, provided that it is done blindly. It is hoped that ultrasound-guided biopsy of the nodes will be easier to perform; until then, the discriminative features of different echo patterns are important.

References

AIBE, T., ITO, T., YOSHIDA, T., NOGUCHI, T., OHTANI, T., FUJI, T. & TAKEMOTO, T., 1986. Endoscopic ultrasonography of lymph nodes surrounding the upper GI tract. *Scandinavian Journal of Gastroenterology, 123* (Suppl.), 164–169.

BEYNON, J., McC MORTENSEN, N. J., FOY, D. M. A., CHANNER, D. L., RIGBY, H. & VIRJEE, J., 1989. Preoperative assessment of mesorectal lymph node involvement in rectal cancer. *British Journal of Surgery, 76*, 276–279.

FEIFEL, G., HILDEBRANDT, U. & McC MORTENSEN, N. J., 1990. *Endosonography in Gastroenterology, Gynecology and Urology* (Springer-Verlag, Berlin, Heidelberg), p. VII.

HERRERA-ORNELAS, L., JUSTIANO, J., CASTILLO, N., STULC, J. P. & MITTELMAN, A., 1987. Metastases in small lymph nodes from colon cancer. *Archives of Surgery, 122*, 1253–1256.

HILDEBRANDT, U. & FEIFEL, G., 1990. Endorectal sonography. *Surgery Annual, 22* 169–183.

HILDEBRANDT, U., KLIEN, T., FEIFEL, G., SCHWARTZ, H., KOCH, B. & SCHMITT, R. M., 1990. Endosonography of pararectal lymph nodes: *in vitro* and *in vivo* evaluation. *Diseases of the Colon and Rectum, 33*, 863–868.

JOCHEM, R. J., READING, C. C., DOZOIS, R. R., CARPENTER, H. A., WOLFF, B. & CHARBONEAU, J. W., 1990. Endorectal ultrasonography staging of rectal carcinoma. *Mayo Clinic Proceedings, 65*, 1571–1577.

MARCHAL, G., OYEN, R., VERSCHAKELEN, J., GERLIN, J., BAERT, A. L. & STESSENS, R. C., 1985. Sonographic appearence of normal lymph nodes. *Journal of Ultrasound in Medicine, 4*, 417–419.

QUAM, J. P., READING, C. C. & CHARBONEAU, J. W., 1989. Transrectal sonographically guided biopsy of a perirectal lymph node in recurrent rectal carcinoma. *American Journal of Roentgenology 153*, 1101.

RIFKIN, M., SAUNDRA, M. & MARTS, G., 1989. Staging of rectal carcinoma: prospective comparison of endorectal US and CT. *Radiology, 170*, 319–322.

SMEETS, A. J., ZONERLAND, H. M., VOORDE, F. & LAMERIS, J. S., 1990. Evaluation of abdominal lymph nodes by ultrasound. *Journal of Ultrasound in Medicine, 9*, 325–331.

TIO, T. L. & TYTGAT, G. N. J., 1986. Endoscopic ultrasonography in analysing peri-intestinal lymph node abnormality. *Scandinavian Journal of Gastroenterology, 123* (Suppl.), 158–163.

TIO, T. L., COENE, P. P. L. O., VAN DELDEN, O. M. & TYTGAT, G. N. J., 1991. Colorectal carcinoma: preoperative TNM classification with endosonography. *Radiology, 179*, 165–170.

WANG, K. Y., KIMMEY, M. B., NYBERG, D. A., MACK, L. A., HAGGITT, R. C., SHUMAN, W. P., FRANKLIN, D. W. & SILVERSTIEN, F. E., 1987. Colorectal neoplasms: accuracy of US in demonstrating the depth of invasion. *Radiology, 165*, 827–829.

1992, *The British Journal of Radiology*, 65, 221–224

Computed tomography in agenesis of the lung in infants

By A. C. Argent, MMed, FCP and *B. J. Cremin, MD, FRCR, FRCAR

Paediatric Pulmonology Service and *Department of Radiology, Red Cross War Memorial Children's Hospital, University of Cape Town, Cape Town, South Africa

(*Received 28 March 1991 and in revised form 19 July 1991, accepted 4 September 1991*)

Keywords: Lung agenesis, Computed tomography

Abstract. This paper describes the clinical and radiological findings in three infants with agenesis of a single lung. In the two cases of right lung agenesis, severe gastro-oesophageal reflux was present. In these two cases, contrast-medium-enhanced computed tomography (CT) excluded vascular compression of major airways in one patient but demonstrated mild compression in the other. Conventional CT in the case of left lung agenesis demonstrated posterior herniation of the contralateral right lung.

Computed tomography (CT) of the chest is an effective method for elucidating the anatomy of suspected agenesis of the lung. When performed dynamically with a bolus injection of contrast medium it is a relatively simple method for excluding tracheal compression by abnormal or displaced major vessels. We have seen three cases of agenesis of the lung in the last year and performed dynamic CT on two of them and conventional CT on the other.

Materials and methods

The CT scans were performed on an Elscint 2400 with 4 mm increments over the intrathoracic trachea. The dynamic scans were performed at 6 s intervals during which a 2 ml/kg bolus of Conray 180 was injected into an upper limb vein.

Case 1

L.H., a girl from a normal delivery, presented to the hospital at 5 months of age. Her history was of marked shortness of breath for 2 weeks. She weighed 6.18 kg and was hyperventilating with subcostal recession at the rate of 80 breaths per min. Chest radiographs showed an overexpanded left lung with mediastinal shift to the right. The right side was underinflated and no right lung was visible (Fig. 1). A high-kV radiograph of the thorax showed absence of the right main bronchus apart from a small 1 cm stump (Fig. 2). At fluoroscopy the terminal trachea appeared to narrow abnormally during expiration. A barium swallow showed no abnormal extrinsic compression. Marked gastro-oesophageal reflux was present. Echocardiography showed dextrocardia and situs solitus with an otherwise normal heart. A dynamic CT scan was performed to exclude any pseudovascular ring and this showed a normal trachea (Fig. 3).

Over 2 weeks therapy with oxygen and bronchodilators the child made an uneventful recovery. At the time of discharge on pro-kinetic agents her respiratory rate was 40 breaths per min. The final diagnosis was agenesis of the right lung with a respiratory infection of the single left lung secondary to aspiration.

Case 2

A.R. was born by normal vaginal delivery. She presented at the age of 1 month with a history of wheezy breathing since birth. She was mildly tachypnoeic. The chest radiograph showed agenesis of the right lung and hyperinflation of the left lung. Echocardiography showed a normal heart displaced to the right side. Barium swallow demonstrated no extrinsic vascular compression but mild gastro-oesophageal reflux was present. A dynamic CT scan confirmed the absence of the right lung, and also showed some indentation of the left lateral border of the trachea by the descending aorta (Fig. 4). There was no overt compression to suggest the presence of either a vascular or pseudovascular ring.

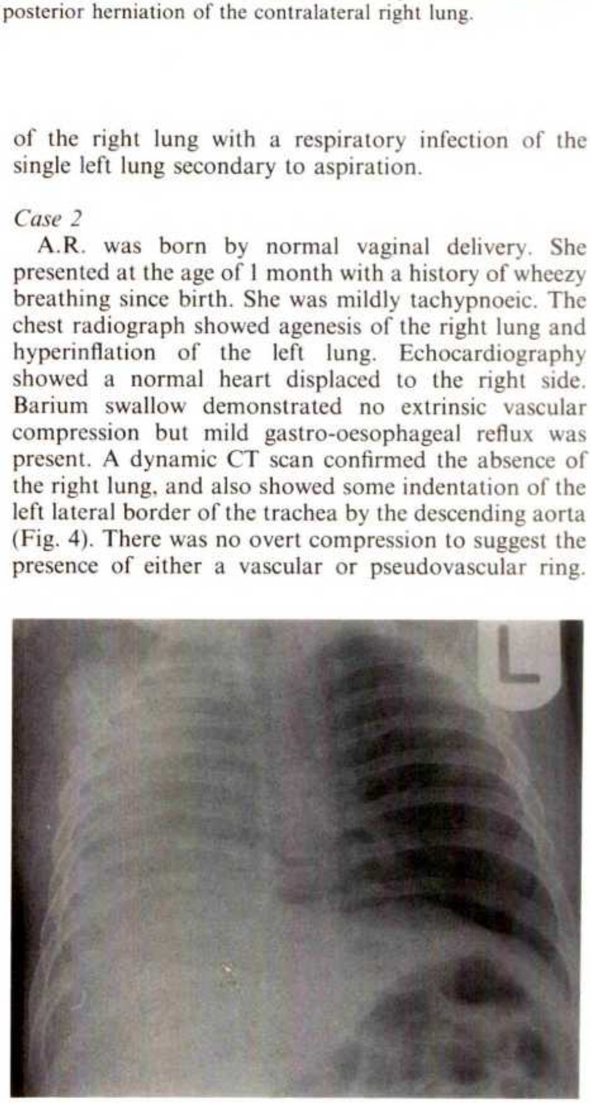

Figure 1. Chest radiograph demonstrating mediastinal displacement and agenesis of the right lung.

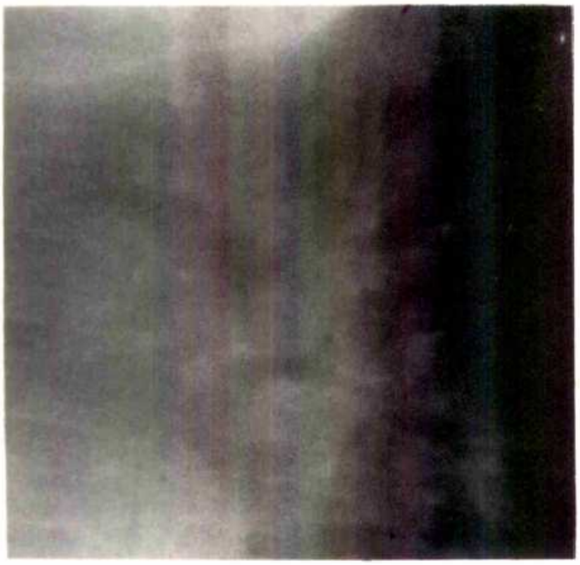

Figure 2. High-kV radiograph showing narrowing of terminal trachea and a small stump of right main bronchus.

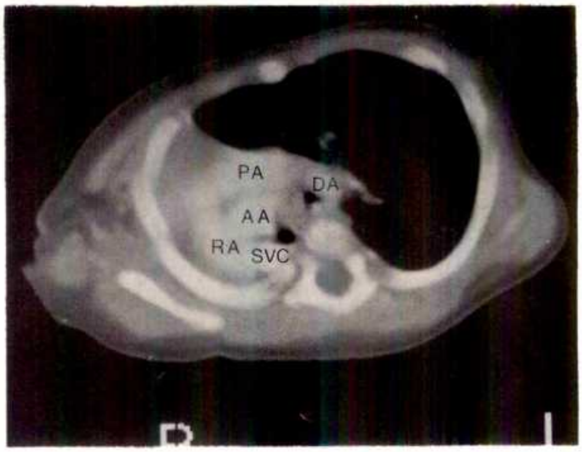

Figure 3. Dynamic CT scan showing opacification of the superior vena cava (SVC) and major vessels. The right atrium (RA) is posteriorly placed and the pulmonary artery (PA) is directed to the left. The ascending aorta (AA) is to the right of the air-filled oesophagus and the descending aorta (DA) is antero-lateral to the trachea. There is no abnormal compression.

Bronchoscopy showed no vascular compression of the trachea or left main bronchus, but the left main bronchus was unusually narrow.

She required assisted ventilation on three separate occasions for obstructive airways disease. Regular treatment consisted of anti-reflux therapy and oral steroids. Subsequently her condition has gradually improved despite intermittent admissions for exacerbations of respiratory symptoms.

Case 3

V.B. presented at 2½ months of age with a history of cough and difficult breathing since birth. There was no family history of congenital abnormalities and she had no siblings. On examination, her weight was 4.12 kg and the child had respiratory distress with a respiratory rate of 60 breaths per min. There was no cyanosis but she had severe subcostal recession. The trachea was deviated to the left and the heart was palpable in the left chest. No breath sounds were heard on the left side and the right lung was overinflated. A systolic murmur was present over the precordium. A chest radiograph showed an overexpanded plethoric right lung and a lucency in the left posterior hemithorax.

A CT scan of the chest showed agenesis of the left lung together with posterior herniation of the right lung

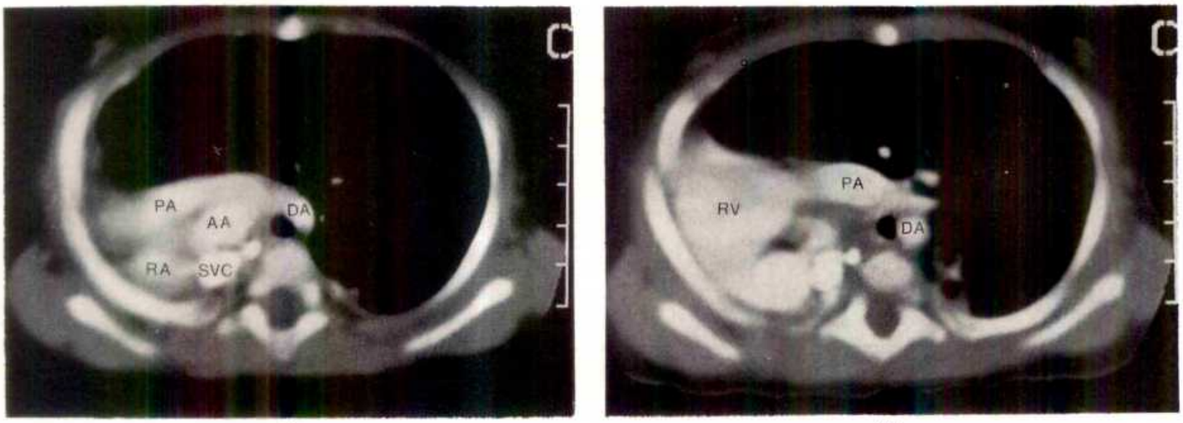

(a) (b)

Figure 4. (a) Dynamic CT scan showing posteriorly placed right atrium (RA) with anterior left pulmonary artery (PA). The oesophagus has been opacified and the superior vena cava (SVC) is postero-lateral and the ascending aorta (AA) antero-lateral. The descending aorta (DA) is antero-lateral to the trachea. (b) Dynamic CT scan at 4 mm increment caudal to (a). The descending aorta (DA) is now lateral to the trachea and causing mild compression of the trachea.

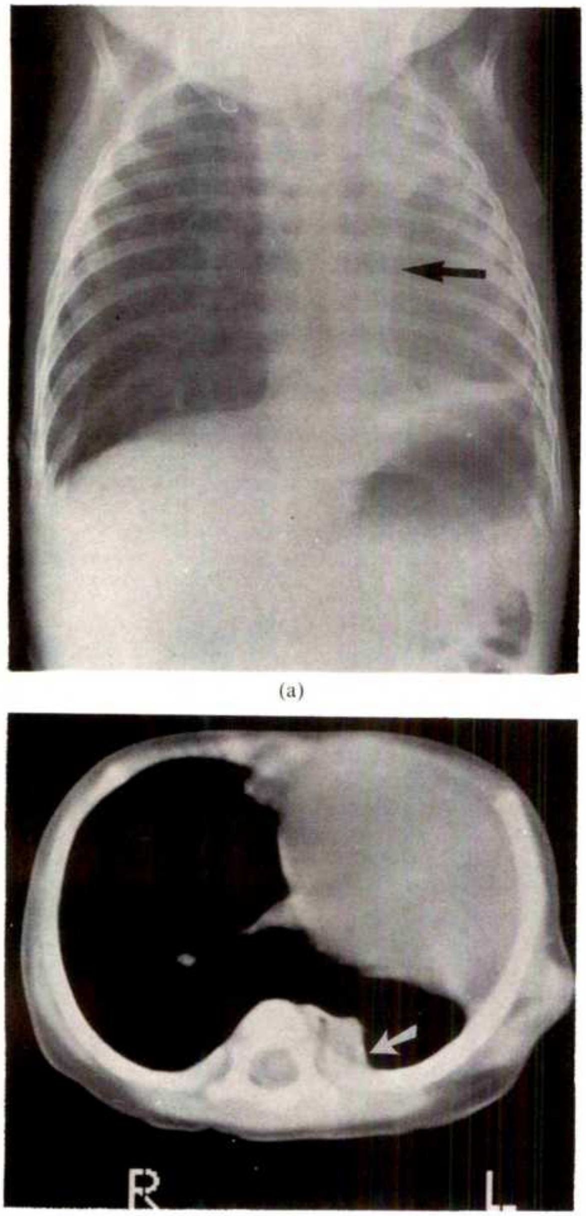

(a)

(b)

Figure 5. (a) Chest radiograph of left lung agenesis. The right lung shows plethoric vascular markings. The left thorax shows a lucency with a well defined medial border (arrow). (b) CT scan showing posterior herniation of the right lung, explaining the mediastinal border (arrow) noted in Fig. 5(a).

into the left hemithorax (Fig. 5). Echocardiography and cardiac catheterization showed a large perimembranous outlet ventricular septal defect (VSD) with pulmonary hypertension. A single pulmonary artery was present. A ventilation perfusion scan showed ventilation perfusion and washout to be within normal limits on the right. A small area of the left mid-zone just below the level of the hilum, corresponding to the herniated portion of the right lung, was ventilated and perfused. The small amount of gas that entered this region washed out slowly.

The child failed to thrive owing to the size of the left to right cardiac shunt and she was operated on for closure of the VSD. Agenesis of the left lung was confirmed at surgery. Twelve hours after surgery a sudden cardiac arrest caused her death.

Discussion

Agenesis is defined as complete absence of the lung and its bronchus (Felson, 1972). It is a comparatively rare condition with an incidence of one in every 10 000–15 000 autopsies (Olcott & Dooley, 1943; Fergusson & Neuhauser, 1944). It has an equal distribution on both sides (Oyomada et al, 1953). Our Case 2 had a bronchial stump, which closely fits into the category of aplasia (Oyomada et al, 1953). However, the bronchial stump was so small that the overall appearance and effect were the same as agenesis.

Agenesis of the lung may be asymptomatic and be discovered accidentally during routine examination. About 50% of cases have other congenital anomalies, of which 25% are vascular (Marioni, 1962). Other anomalies include oesophageal atresia (Brereton & Rickwood, 1983) and maldevelopment of diaphragm, lip and palate, genitourinary tract, vertebrae and radius (Wexels, 1951). Agenesis of the right lung carries a poorer prognosis and it is suggested that the greater shift of the heart and mediastinum with corresponding distortion of blood vessels and bronchi may be the cause (Schaffer & Rider, 1957). Compression of the trachea by a normal, stretched aorta with right lung agenesis has been reported (McCormick & Kuhns, 1979; Dohlemann et al, 1990). Excessive kinking of the trachea and the functioning bronchus may be exacerbated by the displaced aorta (Harrison & Hendren, 1975).

Our reason for performing dynamic chest CT in our first two cases was to exclude these possibilities. Case 1 had showed transient narrowing of the terminal trachea on fluoroscopy but CT revealed no compression. Case 2 showed only mild compression and surgery was not indicated. Both patients subsequently improved without any surgical intervention.

Oesophageal anomalies have been associated with agenesis of the lung in several reports (Novak, 1981; Brereton & Rickwood, 1983; Benson et al, 1985; Dohlemann et al, 1990). It is noted that in the two infants with right agenesis there was severe gastro-oesphageal reflux on barium swallow, and both patients improved symptomatically on anti-reflux therapy.

Case 3 was of interest because of the posterior herniation of the non-affected lung. The classical radiographic features of agenesis of the lung are a unilateral non-aerated hemithorax with raised hemidiaphragm and narrowed intercostal spaces. The heart shadow is shifted to the side of the missing lung and is close to the lateral chest wall. When there is marked lung herniation this appears as a vague translucency on the affected side.

Herniation usually occurs through the anterior mediastinum. Posterior herniation has never been reported in right lung agenesis, and has been documented only twice in association with agenesis of the left lung (Booth & Berry, 1967; Nelson et al, 1967).

Agenesis of a single lung is not usually a lethal condition; however, associated abnormalities may severely compromise respiratory function and impair the prognosis. In infants, diagnostic imaging must be directed at identifying correctable anatomical or functional anomalies. We have shown that contrast-enhanced CT scans of the chest demonstrate the anatomy well enough to exclude significant vascular compression of the major airways. A barium study is also indicated to exclude oesophageal anomalies or associated gastro-oesophageal reflux.

References

Benson, J. E., Olsen, M. M. & Fletcher, B. D., 1985. A spectrum of bronchopulmonary anomalies associated with tracheoesophageal malformations. *Pediatric Radiology, 15,* 377–380.

Booth, J. B. & Berry, C. L., 1967. Unilateral pulmonary agenesis. *Archives of Disease in Childhood, 442,* 361–374.

Brereton, R. J. & Rickwood, A. M. K., 1983. Esophageal atresia with pulmonary agenesis. *Journal of Pediatric Surgery, 18,* 618–620.

Dohlemann, C., Mantel, K., Schneider, K., Guntner, M., Kreuzer, E. & Hecker, W. C., 1990. Deviated trachea in hypoplasia and aplasia of the right lung: airway obstruction and its release by aortopexy. *Journal of Pediatric Surgery, 25,* 290–293.

Felson, B., 1972. Pulmonary agenesis and related anomalies. *Seminars in Roentgenology, 7,* 17–30.

Ferguson, C. F. & Neuhauser, E. B. D., 1944. Congenital absence of the lung (agenesis) and other anomalies of the tracheobronchial tree. *American Journal of Roentgenology, 52,* 459–471.

Harrison, M. R. & Hendren, W. H., 1975. Agenesis of the lung complicated by vascular compression and bronchomalacia. *Journal of Pediatric Surgery, 10,* 813–817.

Marioni, P., 1962. Agenesis of the lung. *Diseases of the Chest, 41,* 232–236.

McCormick, T. L. & Kuhns, L. R., 1979. Tracheal compression by a normal aorta associated with right lung agenesis. *Pediatric Radiology, 130,* 659–660.

Nelson, C. S., McMillan, I. K. R. & Bharucha, P. K., 1967. Tracheal stenosis, pulmonary agenesis, and patent ductus arteriosus. *Thorax, 22,* 7–12.

Novak, R. W., 1981. Laryngotracheoesophageal cleft and unilateral pulmonary hypoplasia in twins. *Pediatrics, 67,* 732–734.

Olcott, C. T. & Dooley, S. W., 1943. Agenesis of lung in an infant. *American Journal of Diseases of Childhood, 65,* 776–789.

Oyomada, A., Gasul, B. M. & Holinger, P. H., 1953. Agenesis of the lung. Report of a case, with a review of all previously reported cases. *American Journal of Diseases of Children, 85,* 182–201.

Schaffer, A. J. & Rider, R. V., 1957. A note on the prognosis of pulmonary agenesis and hypoplasia according to the side affected. *Journal of Thoracic Surgery, 33,* 379–382.

Wexels, P., 1951. Agenesis of the lung. *Thorax, 6,* 171–192.

1992, *The British Journal of Radiology*, *65*, 225–231

Results of a survey of doses to paediatric patients undergoing common radiological examinations

By C.-L. Chapple, BA, MSc, K. Faulkner, MSc, PhD, *R. E. J. Lee, MB, BS, FRCR and
*E. W. Hunter, DCR

Regional Medical Physics Department, Newcastle General Hospital, Westgate Road, Newcastle-upon-Tyne
NE4 6BE and *Department of Radiology, Royal Victoria Infirmary, Queen Victoria Road,
Newcastle-upon-Tyne NE1 4LP, UK

(*Received 9 July 1991 and in revised form 12 September 1991, accepted 20 September 1991*)

Keywords: Paediatric radiology, Radiation protection

Abstract. A survey has been performed to investigate typical radiation dose levels for children undergoing a number of common radiological examinations. Doses have been assessed using a Diamentor ionization chamber to measure dose–area product, and by attaching thermoluminescent dosemeters to the patient's skin to determine entrance and organ doses. The survey has been automated by using a personal computer for data collection and storage. Doses have been monitored for a large number of children, primarily in a dedicated paediatric X-ray room, and the results presented can be used as a baseline for making comparative measurements elsewhere. Entrance skin doses were found to range from 0.3 mGy to 5.7 mGy for radiographic examinations, and values of dose–area product from 3 to 225 cGy cm^2. The corresponding dose ranges for fluoroscopic examinations are 7.4–26.2 mGy and 130–1241 cGy cm^2.

The contribution of diagnostic radiology towards the annual radiation dose to the population has been well documented (Shrimpton et al, 1986). Paediatric patients are considered to be at particular risk for a number of reasons, including their higher risk factors for certain types of cancer (Stather et al, 1988), the increased opportunity for expression of induced cancers, their likely non-cooperation, and the high frequency of some examinations during childhood (Wall et al, 1986). Many surveys of doses to adult patients have been carried out, but to date very few data have been published on the level of radiation dose to paediatric patients from diagnostic radiology. The recent National Survey (Shrimpton et al, 1986) included only very small numbers of children, and the results of Fendel et al (1989) and Zankl et al (1989) are derived for specific ages, and hence are not generally applicable.

In view of the limited published data, a survey has been initiated to determine typical dose levels for children of different age groups undergoing a number of common radiological examinations. The majority of the data have been collected from a dedicated paediatric X-ray room, in order to determine baseline dose values, and the survey has been extended to other rooms and departments. Doses have been assessed using both thermoluminescent dosemeters attached to the patient's skin and a Diamentor ionization chamber to measure dose–area product. Data collection and analysis has been automated to increase efficiency and acceptability to staff.

The objectives of the survey were (1) to obtain typical dose values for each age group and each examination, and (2) to compare the doses received from different examinations.

Methods

Patients were divided into three age groups: (1) infants (below 1 year), (2) 1–5 years, and (3) 6–18 years. For statistical purposes, it was intended to monitor 10–20 patients in each age group for each type of examination.

Simple radiographic and screening procedures were included in the survey. The selected examinations were chest, abdomen, pelvis, skull and intravenous urography (IVU) for simple radiography; and barium meal, barium enema and micturating cystourethrography (MCUG) for fluoroscopic procedures.

A combination of direct measurements using thermoluminescent dosemeters, and indirect measurements using a dose–area product meter was used. Dose–area product was measured for all examinations using a Diamentor control box and associated large-area transmission ionization chambers. It is possible to derive patient dose, in the form of energy imparted, from the Diamentor reading, but this requires appropriate conversion factors that are not currently available for paediatrics. However, the measurement of dose–area product is useful in itself for comparative purposes. Each ionization chamber was calibrated *in situ*, and the calibration of the dose–area product meters was traceable to National Standards (Faulkner et al, 1991). The uncertainty in each measurement, as specified by the manufacturers, is ±3%.

Lithium fluoride thermoluminescent dosemeters (TLDs) were used to determine the entrance dose and appropriate organ doses for each examination. The TLDS were calibrated at diagnostic energies, using a method traceable back to the primary standard. The intrinsic uncertainty associated with each TLD measure-

Table I. Data entered by operator

Room/tube specification	
Examination	
Patient:	Name ID number Sex Age group Height Weight

Radiographic exposures	*Fluoroscopic exposures*
Radiographer	Radiologist
Projections	Number of radiographic films
kVp	Number of 100 mm films
mA	
Exposure time	
mAs	
Whether gonad protection used	
Whether automatic exposure control used	

ment is ±4%, with an additional uncertainty arising from the variation in background. This is estimated, from the standard deviation of background measurements, to be ±0.1 mSv within 95% confidence limits. This gives an additional uncertainty of ±33% for a dose of 0.3 mSv, falling to below ±10% for doses greater than 1 mSv.

Entrance doses were measured by TLDs placed on the skin surface, one at the centre of each field of view used (kidney and bladder regions for IVU). The dose to the thyroid, breasts, testes and eyes was measured by TLDs placed on the skin surface at a position corresponding to the organ of interest: front of the neck, centre-front of chest, top of inside leg, and between the eyes, respectively. The ovary dose was estimated from the mean of anterior and posterior skin dose measurements on the lower trunk region.

The collection of data has been automated by using a personal computer (CAS 286), using an amended version of an automated quality-assurance and dosimetry instrument (Faulkner et al, 1990). The radiographer is prompted to enter patient and examination details (Table I), and the Diamentor ionization chambers, attached to both the overcouch and undercouch tubes, are automatically read and re-set via a RS232 interface. These ionization chambers measure both dose–area product and screening time for each examination. The TLD identification numbers and placement positions are also entered by the radiographer after the examination has finished. For simple radiographic examinations, the exposure parameters for each exposure taken are typed in, and for fluoroscopic examinations the number of radiographic exposures or 100 mm films that were used. The use of automatic exposure control and gonad shielding is also recorded.

Results

The initial results of the survey are given in Tables II–VII. For each age group and examination type the

Table II. Doses to infants from radiographic examinations

	Chest		Pelvis		Abdomen		Skull		IVU	
	No.	Mean value	No.	Mean value	No.	Mean value	No.	Mean value	No.	Mean value
Dose–area product (cGy cm^2)	26	3.2 (1–8)	4	3.2 (2–6)	6	3.7 (1–13)	3	11.5 (9–17)	32	10.6 (4–47)
No. of films	26	1.4 (1–3)	4	2.3 (2–3)	6	1.7 (1–4)	3	2.7 (1–5)	32	3.7 (1–8)
Entrance dose (mGy)	10	0.30 (0.05–0.64)	4	0.51 (0.48–0.57)	6	0.48 (0.08–1.10)	2	0.51 (0.26–0.75)	12	0.60 (0.15–1.03)
Breast dose (mGy)	13	0.18 (0–0.60)	3	0.24 (0.06–0.38)	6	0.12 (0–0.28)	—	—	11	0.08 (0–0.2)
Thyroid dose (mGy)	14	0.14 (0–0.64)	—	—	1	0.20	2	0.20 (0.15–0.24)	12	0.08 (0–0.24)
Ovary dose (mGy)	—	—	3	0.37 (0.29–0.45)	3	0.28 (0.08–0.61)	—	—	5	0.27 (0.09–0.4)
Testes dose (mGy)	—	—	—	—	3	0.12 (0–0.20)	—	—	7	0.11 (0–0.19)
Eye dose (mGy)	—	—	—	—	—	—	2	0.51 (0.26–0.75)	—	—

Table III. Doses to 1–5 year olds from radiographic exposures

	Chest		Pelvis		Abdomen		Skull		IVU	
	No.	Mean value	No.	Mean value	No.	Mean value	No.	Mean value	No.	Mean value
Dose–area product (cGy cm^2)	30	4.7 (2–18)	12	9.9 (2–30)	11	21.4 (15–28)	6	74.0 (30–122)	37	61.9 (11–235)
No. of films	30	1.4 (1–2)	12	1.6 (1–2)	12	1	6	2.8 (1–4)	38	3.7 (3–6)
Entrance dose (mGy)	11	0.28 (0.08–0.51)	9	1.06 (0.22–3.21)	8	0.75 (0.27–1.11)	—	—	13	2.39 (0.76–4.31)
Breast dose (mGy)	12	0.16 (0–0.51)	1	0.17	7	0.12 (0–0.37)	—	—	13	0.14 (0–0.44)
Thyroid dose (mGy)	12	0.18 (0–0.47)	—	—	—	—	—	—	—	—
Ovary dose (mGy)	—	—	2	0.27 (0.23–0.30)	3	0.34 (0.14–0.43)	—	—	4	1.19 (0.61–1.61)
Testes dose (mGy)	—	—	5	0.20 (0–0.33)	4	0.10 (0–0.2)	—	—	10	0.09 (0–0.19)

Table IV. Doses to 6–18 year olds from radiographic examinations

	Chest		Pelvis		Abdomen		Skull		IVU	
	No.	Mean value	No.	Mean value	No.	Mean value	No.	Mean value	No.	Mean value
Dose–area product (cGy cm^2)	7	6.9 (2–15)	10	106 (23–302)	12	84 (29–228)	4	110 (68–146)	55	225 (33–796)
No. of films	5	1.2 (1–2)	10	1.9 (1–2)	13	1.1 (1–2)	4	2.5 (2–3)	55	3.9 (1–8)
Entrance dose (mGy)	3	0.56 (0.21–1.13)	10	3.07 (0.71–6.69)	7	1.19 (0.26–1.82)	3	2.98 (0.9–5.1)	26	5.67 (1.03–13.6)
Breast dose (mGy)	—	—	—	—	3	0.06 (0–0.18)	—	—	25	0.62 (0–8.44)
Ovary dose (mGy)	—	—	2	1.75 (1.51–1.99)	1	1.00	—	—	13	2.19 (0.59–5.31)
Testes dose (mGy)	—	—	6	0.83 (0–3.25)	—	—	—	—	11	0.18 (0–0.52)
Eye dose (mGy)	—	—	—	—	—	—	3	3.21 (1.52–5.10)	—	—

Table V. Doses to infants from screening examinations

	Barium meal		Barium enema		MCUG	
	No.	Mean value	No.	Mean value	No.	Mean value
Dose–area product (cGy cm^2)	38	130 (40–408)	10	140 (58–381)	58	168 (20–4926)
Screening time (s)	38	181 (51–383)	10	200 (106–436)	58	123 (18–1222)
No. of films	38	7.5 (2–13)	10	7.4 (2–12)	58	7.8 (3–24)
Entrance dose (mGy)	22	11.60 (2.28–32.5)	3	16.78 (9.54–27.39)	22	7.36 (0.30–22.98)
Breast dose (mGy)	22	1.18 (0–8.55)	3	0.16 (0.01–0.4)	22	0.11 (0–0.43)
Thyroid dose (mGy)	22	2.36 (0–32.5)	3	0.18 (0–0.4)	20	0.09 (0–0.51)
Ovary dose (mGy)	12	0.88 (0.03–2.17)	1	8.01	7	4.99 (0.2–9.58)
Testes dose (mGy)	7	0.25 (0.08–0.47)	2	2.85 (0.42–5.27)	12	1.96 (0.12–8.69)

mean values of dose–area product and organ doses are presented, together with the maximum and minimum values. For fluoroscopic procedures the screening time and number of radiographs taken are also given. TLDs were not used on all patients as some children were too frightened and/or uncooperative.

Discussion

A comparison of the mean dose–area product and entrance doses for these examinations is shown graphically in Figs 1–5. The measured entrance dose includes the contribution from all radiographs taken and any fluoroscopic time. The same trends between different examinations are generally reflected in each age group. The large differences in dose and dose–area product between age groups, which are a broad indication of patient size, highlight the importance of dividing the data in this way. There is a factor of up to 100 between the dose–area products for the different age groups in radiographic examinations, and a factor of 4 between the corresponding entrance dose values. For fluoroscopic investigations the factors are 10 and 4, respectively. Screening times are broadly similar for each age group. Even within one age category there is a significant range in dose values, due both to a spread in patient size and differing clinical conditions.

The results presented here have been compared with those found in the National Survey (Shrimpton et al, 1986), using the 6–18 years category as this corresponds most closely to the mean age of paediatric patients in the National Survey. Values for entrance dose per film and dose–area product per examination are listed in

Table VI. Doses to 1–5 year olds from screening examinations

	Barium meal		Barium enema		MCUG	
	No.	Mean value	No.	Mean value	No.	Mean value
Dose–area product (cGy cm^2)	22	223 (67–415)	2	947 (670–1225)	55	262 (20–5878)
Screening time (s)	22	196 (84–352)	2	439 (279–599)	55	146 (13–1010)
No. of films	22	7.9 (3–12)	2	8.0 (7–9)	56	6.3 (0–18)
Entrance dose (mGy)	7	11.07 (3–20.59)	—	—	20	11.56 (2.91–24.82)
Breast dose (mGy)	7	0.90 (0.33–1.19)	—	—	18	0.39 (0–5.08)
Thyroid dose (mGy)	7	0.86 (0–1.8)	—	—	—	—
Ovary dose (mGy)	2	0.58 (0.12–1.04)	—	—	11	6.54 (2.51–10.81)
Testes dose (mGy)	4	0.21 (0–0.19)	—	—	9	1.15 (0.20–2.38)

Table VII. Doses to 6–18 year olds from screening examinations

	Barium meal		Barium enema		MCUG	
	No.	Mean value	No.	Mean value	No.	Mean value
Dose–area product (cGy cm^2)	23	546 (101–1531)	5	1241 (407–2052)	39	433 (13–2240)
Screening time (s)	23	219 (79–426)	5	255 (66–341)	38	139 (18–533)
No. of films	23	10.4 (4–23)	5	6.6 (4–9)	39	6.5 (0–24)
Entrance dose (mGy)	13	26.19 (4.99–74.49)	—	—	21	19.96 (1.85–63.3)
Breast dose (mGy)	13	0.86 (0.28–2.3)	—	—	20	0.15 (0–0.45)
Thyroid dose (mGy)	13	0.48 (0–1.61)	—	—	—	—
Ovary dose (mGy)	6	0.43 (0.06–0.83)	—	—	12	13.46 (5.2–31.79)
Testes dose (mGy)	7	0.07 (0–0.27)	—	—	9	1.77 (0.19–1.77)

Table VIII. Comparison with National Survey

	Entrance dose/film (mGy)		Total dose–area produce (cGy cm^2)	
Examination	6–18 years	National Survey	6–18 years	National Survey
Chest	0.47	0.18 (PA)	6.9	14
Pelvis	1.62	2.94 (AP)	106	226
Abdomen	1.10	1.79 (AP)	84	149
Skull	1.19	2.47 (AP)	110	228
IVU	—	—	225	1464
	Thyroid dose			
Barium meal	0.48	0.76	546	799

PA = postero-anterior; AP = antero-posterior.

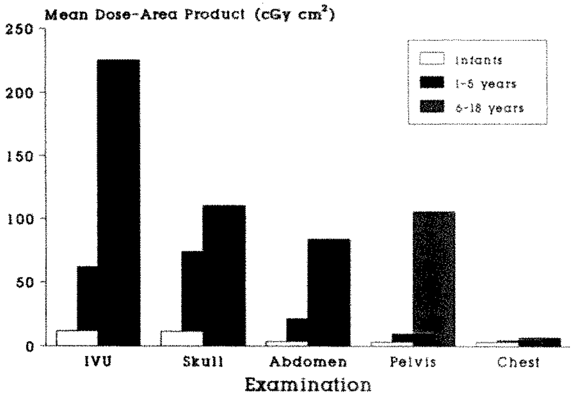

Figure 1. Variation in dose–area product: radiographic examinations.

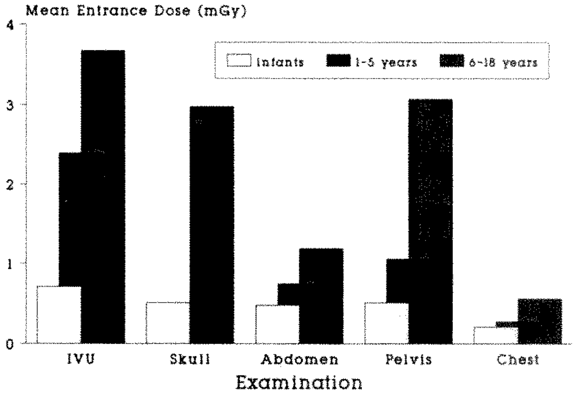

Figure 2. Variation in entrance dose: radiographic examinations.

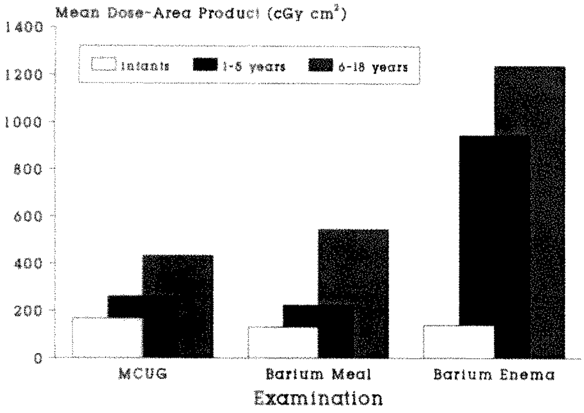

Figure 3. Variation in dose-area product: fluoroscopic procedures.

Table VIII, for each set of data. The National Survey data given are for the projection most appropriate for the comparison. Values for dose-area product are much less than those found in the National Survey. This is probably due to the fact that all measurements were made in dedicated paediatric rooms, where there already exists an emphasis on radiation protective measures such as coning down to small field sizes. The difference in the doses for the two sets of IVU measurements is also related to the differing number of radiographs taken (typically four for this data, six in the National Survey). Values of entrance dose per film are more comparable, though are still generally lower than those in the National Survey. This reflects the use of rare-earth film/screen combinations in the rooms surveyed here. The entrance dose given here for chest examinations appears greater than in the National Survey, as the latter includes a significant number of infants.

The most important factor in making comparisons of this kind is the extent of the similarity between the irradiated populations. Here the similarity is quite poor, owing to different age classifications and small numbers of patients in some groups. As children of different ages are inherently of different size and build, this will affect the radiation doses. When any difference in age range is taken into account, the agreement between the data is quite good.

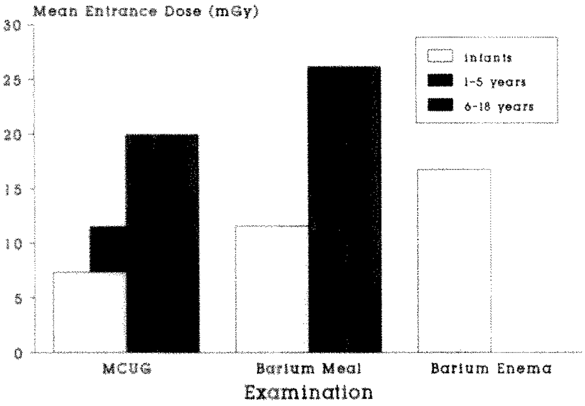

Figure 4. Variation in entrance dose: fluoroscopic procedures.

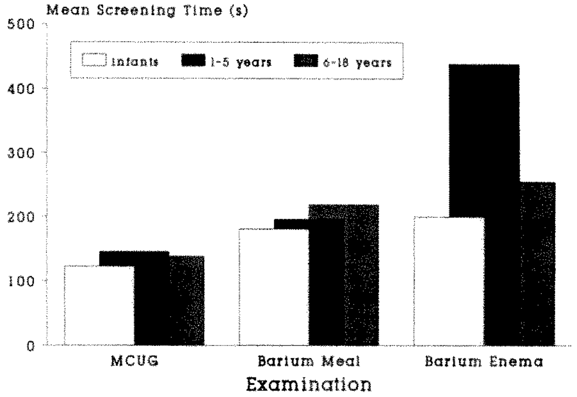

Figure 5. Variation in screening time: fluoroscopic procedures.

Conclusions

Results have been presented of doses to children in three different age groups, for three fluorographic and five simple radiographic procedures. The values given represent typical values of dose for each examination, and can be used as a baseline for making comparative measurements at other hospitals.

Acknowledgments

This study was funded by the National Health Service Locally Organized Research Schemes–Regional Research Committee of the National Regional Health Authority, and District Research Committee of Newcastle Health Authority. We wish to thank Professor K. Boddy and Dr R. Harrison for their continued support and encouragement, and also Miss E. Forster for her assistance with the TLD.

References

Faulkner, K., Busch, H. P., Cooney, P., Malone, J. F., Marshall, N. W. & Rawlings, D. J., 1991. An international intercomparison of dose–area product meters. Presented at a Seminar on Dosimetry in Diagnostic Radiology, Luxembourg, 19–21 March 1991. (Submitted for publication in *Radiation Protection Dosimetry*.)

Faulkner, K., Chapple, C.-L., Hedley, P., Kotre, C. J. & Harrison, R. M., 1990. Automated quality assurance and patient dosimetry in diagnostic radiology. *Journal of Biomedical Engineering*, *12*, 228–232.

Fendel, H., Schneider, K., Kohn, M. M. & Bakowski, C., 1989. Specific principles for optimization of image quality and patient exposure in paediatric diagnostic imaging. In *Optimization of Image Quality and Patient Exposure in Diagnostic Radiology*, BIR Report 20, ed. by B. M. Moores, B. F. Wall, H. Eriskat and H. Schibilla (British Institute of Radiology, London).

Shrimpton, P. C., Wall, B F., Jones, D. G., Fisher, E. S., Hillier, M. C., Kendall, G. M. & Harrison, R. M., 1986. *A National Survey of Doses to Patients Undergoing a Selection of Routine X-ray Examinations in English Hospitals*, National Radiological Protection Board Report NRPB-R200 (HMSO, London).

STATHER, J. W., MUIRHEAD, C. R., EDWARDS, A. A., HARRISON, J. D., LLOYD, D. C. & WOOD, N. R., 1988. *Health Effects Deeveloped from the 1988 UNSCEAR Report*, National Radiological Protection Board Report NRPB-R226 (HMSO, London).

WALL, B. F., HILLIER, M. C. & KENDALL, G. M., 1986. *National Radiological Protection Board Report NRPB-R201* (HMSO, London).

ZANKL, M., PETOUSSI, N., VEIT, R., DREXLER, G. & FENDEL, H., 1989. Organ doses for a child in diagnostic radiology: comparison of a realistic and a MIRD-type phantom. In *Optimization of Image Quality and Patient Exposure in Diagnostic Radiology*, BIR Report 20, ed. by B. M. Moores, B. F. Wall, H. Eriskat and H. Schibilla (British Institute of Radiology, London).

1992, *The British Journal of Radiology*, *65*, 232–237

Dose reduction by the use of erbium filtration in a general radiographic room

By *R. W. Cranage, MA, DPhil, †C. J. Howard, HDCR, SR and ‡A. D. Welsh, BA, MSc

Departments of †Radiology and ‡Medical Physics, Cheltenham General Hospital, Sandford Road, Cheltenham GL53 7AN, and *Department of Medical Physics, Musgrove Park Hospital, Taunton, Somerset TA1 5DA, UK

(Received 22 April 1991 and in revised form 6 September 1991, accepted 3 October 1991)

Keywords: Radiation dose, Filtration, Dose reduction, Diagnostic radiology

Abstract. The conventional aluminium filtration of a general purpose X-ray tube in a district general hospital was replaced by an erbium filter for a 2-month period. The resulting reduction in skin dose was measured for a number of examinations using thermoluminescent dosimetry. The change in effective dose equivalent was calculated from these measurements and compared with previous theoretical estimates. The use of the erbium filter had no effect on radiograph quality. It was concluded that the use of an erbium filter resulted in a worthwhile reduction in radiation dose, and was a cost-effective method of dose reduction.

Over the years there have been a number of papers published on the effect of rare-earth filters such as gadolinium, holmium, yttrium, niobium and erbium on diagnostic X-ray beams (Atkins et al, 1975; Burgess, 1985; Fleay, 1980; Thierens et al, 1991; Villagran et al, 1978). The purpose of using these filters was to reduce the radiation dose received by a patient without producing a detrimental effect on image contrast.

The filters may be divided into two groups: the heavy rare-earth materials such as gadolinium (K-edge 50 keV) and erbium (K-edge 57.5 keV) act as bandpass filters by filtering out low-energy photons and also photons above their K-shell absorption edges, which results in the mean energy of the X-ray spectra remaining unchanged. The lighter materials such as yttrium (K-edge 17 keV) and niobium (K-edge 19 keV) have K-edges that are too low to act as bandpass filters in diagnostic radiology and operate in a similar manner to conventional aluminium filters.

There has been little work undertaken to compare the image quality produced by the two groups of filters and the use of any one filter seems to have depended on its commercial availability in a convenient form, with the erbium filter having been used in most clinical studies to date.

Fleay (1980) determined that an erbium filter (K-edge, 57.5 keV) gave a satisfactory X-ray spectrum without too much attenuation and was also stable under normal atmospheric conditions. Chakera et al (1982), Fleay et al (1984) and Wesenberg et al (1983) have published papers on the use of erbium filters in diagnostic radiology and Horner et al (1988) have looked at their use in dental radiology. Wesenberg et al (1983) and Fleay et al (1984) concentrated on paediatric radiology and Chakera et al (1982) only obtained clinical results for bilateral carotid angiograms and intravenous urograms. All these papers demonstrate a substantial (approximately 50%) reduction in skin dose when an erbium filter is used in addition to an aluminium filter, but make no estimate of the reduction in effective dose equivalent. Recently, Shrimpton et al (1988) have published theoretical calculations on the effect of erbium filtration on skin dose and effective dose equivalent, which indicated that the reduction in effective dose equivalent is only slight.

The present study was designed to see if the fitting of an erbium filter leads to worthwhile reductions in effective dose equivalents for a range of examinations. An erbium filter was fitted into one of two identical X-ray rooms for a period of 2 months, and, during this period, the radiographic reject rate and the clinical acceptability of radiographs from the two rooms were compared. Skin doses were measured for similar examinations in the two rooms and the effective dose equivalent calculated for selected examinations. From these measurements a cost/benefit analysis was undertaken for the use of an erbium filter in a general purpose X-ray room.

Materials and methods

Cheltenham General Hospital had two new identical sets installed in adjacent rooms (5 and 6) for general radiography work. The X-ray tubes were Philips Super Rotalix, SR033 100 with anode angles of 13°, and the generators Philips Super 80 CP type.

The two sets were surveyed to confirm their similarity before the erbium filter was fitted. The kVps were within 1 kVp over the range 50–100 kVp as measured with a Keithley 35080 kVp divider. The output/mAs for broad and fine focus were in good agreement for both units and the automatic exposure controls were in acceptable agreement as defined by the British Institute of Radiology (BIR) document, *Assurance of Quality in the Diagnostic X-ray Department* (BIR, 1988). Details are given in Table I.

The erbium filter was a 0.1 mm thick foil mounted in a 3 mm composite sheet (Reactor Experiments Inc,

---

Address correspondence to Dr R. W. Cranage, Department of Medical Physics, Royal Cornwall Hospital, Truro TR1 3LJ.

Table I. Summary of comparison of X-ray equipment

kVp comparison

kVp set	Room 5 Aluminium filter in use kVp measured	Room 6 Erbium filter in use kVp measured
50	50	50
60	59	59
70	70	71
80	79	79
100	100	101

Comparison of outputs

mAs	mA	Output/mAs (arbitrary units)	
		Room 5 Aluminium filter in use	Room 6 Erbium filter in use
5 mAs fine focus	100	0.51	0.50
20 mAs fine focus	100	0.50	0.48
20 mAs broad focus	400	0.52	0.50

Automatic exposure control

	Output as percentage of mean for Room 5 and 6	
	Room 5 Aluminium filter in use	Room 6 Erbium filter in use
Vertical Bucky		
Side detector	101	99
Centre detectors	98	102
Horizontal Bucky		
Side detector	95	105
Centre detector	102	98

supplied by John Caunt Scientific, Eynsham). This filter was fitted to the X-ray tube in room 6 in place of the 1 mm of added aluminium filtration present. The inherent filtration of the tube and its housing was approximately 2.5 mm Al.

The two X-ray rooms shared a film processor and Kodak Lanex Regular screens with T-Mat L film was used for general work, with Kodak Lanex Detail screens with T-Mat G film for extremities. The rooms were staffed by one group of radiographers who worked for approximately equal times in each room.

The radiographers found that acceptable results were obtained by approximately doubling the mAs and leaving the kVp unchanged for exposures in the erbium filter room. Typical exposure factors for the two rooms are given in Table II. These were determined with phantoms and trial exposures and then verified over the period of the study.

Patient skin doses were measured with thermoluminescent dosemeters (TLD). Lithium fluoride chips of dimensions 3 mm × 3 mm × 1 mm enclosed in plastic sachets were positioned on the patient's skin near the centre of the field to measure entry doses. Patient doses were measured for radiographs taken with the aluminium filtered X-ray tube and the erbium filtered tube for six common examinations.

Table II. Typical exposure factors for the rooms with erbium and aluminium tube filters

Examination	kVp	Erbium filter (mAs)	Aluminium filter (mAs)
Pelvis	70	70	35
AP lumbar spine	70	60	28
Lateral lumbar spine	80	85	40
Male PA chest	70	6	4
Knees	65	9	4
Extremity	55	8	4
Pelvic phantom	70	63	29
Skull phantom	70	46	17

Table III. Analysis of patient heights and weights

Mean heights and weights for individual examinations

	Room 5 Aluminium filter		Room 6 Erbium filter	
	Weight (kg)	Height (cm)	Weight (kg)	Height (cm)
Male chest	82	178	85	180
Lumbar spine AP	74	169	72	168
Lumbar spine lateral	66	166	66	166
Pelvis	68	167	65	162

Mean (±SD) for the total sample of patients measured

	Height (cm)	Weight (kg)
Room 5 Aluminium filter	167±9	67±12
Room 6 Erbium filter	169±9	70±14

Adult patients were allocated randomly to either X-ray room for their examination. Since the doses being measured were very low the same TLD packet was placed on six patients for each examination/filter combination to allow dose to accumulate to improve the accuracy of the reading. This increased the co-ordination problems in making the measurements, but the benefits were thought to be worthwhile. The TLDs were always positioned by one of two radiographers to minimize any variation resulting from positioning. Very large and very small patients were excluded from the measurements, and the height and weight of the patients that did take part were recorded. There was no significant difference in the weight and height of the groups of patients examined using the erbium or aluminium filters (see Table III). Therefore, no significant difference would be expected in skin dose measurements in the two groups solely as a result of differences in average patient separation.

The TLDs were calibrated by exposing some of the batch to a known dose, which was measured with a calibrated 35 cm^3 chamber.

Measurements of entrance skin doses and exit doses were also made on phantoms for the pelvis and head. Exposures for these phantom measurements were determined using the amplimat automatic exposure device and then repeated exposures were made to accumulate sufficient dose for reasonably accurate TLD measurement.

It had been expected that the radiographs taken with the erbium filter might be "grey" in appearance, *i.e.* lacking in radiographic contrast. To assess the acceptability of the radiographs, the radiologists were asked to score radiographs taken with aluminium and erbium filters using a scale between 1 and 5. There were no markings on the radiographs or forms to indicate which X-ray room had been used. The radiographs were assessed for contrast, resolution and detail (*e.g.* blurring). The rating 1 indicated an unacceptable radiographic quality and 5 indicated an excellent radiograph. The results of the assessment were analysed using Student's *t*-test.

The reject rates were analysed for the two general radiography rooms prior to the fitting of the erbium filter, and the measurements were repeated after the erbium filter had been in place for a week. The radiographs were assessed by one observer at the end of each week and divided into rejects resulting from wrong exposure and rejects due to other reasons.

Permission for the study was obtained from the Health Authority Ethical Committee, and a patient information sheet was produced.

Results

There was no significant change in kVp, measured over the range 50–100 kVp by the Keithley divider, after the fitting of the erbium filter.

The half-value layer for the aluminium filtered tube was measured as 3.3 mm Al at 80 kV. This is equivalent to a tube filtration of 3.5 mm Al. The half-value layer of the erbium filtered tube was measured as 5.05 mm Al, equivalent to a filtration of 8.0 mm Al.

Table IV shows the entrance skin doses as measured by thermoluminescent dosemeters for the two filtered tubes. Each figure represents the mean dose accumulated by the six patients undergoing a given examination in one of the rooms. The accuracy of the TLD measurements was ±10% for doses above 0.01 mGy. It will be seen that the skin dose for the erbium room is approximately half that given by the "normal" room in the case of chest and spine examinations and less than one-third for knee, extremity and pelvic examinations. It will be

Table IV. Entrance skin doses (in mGy) measured by TLDs for the aluminium and erbium filtered tubes. Figures are the mean dose for six patients for each examination and filter combination

Examination	Aluminium filter	Erbium filter	Erbium filter dose as % of aluminium filter dose
Pelvis	3.80	1.10	29
Knee	0.14	0.04	29
Male chest	0.12	0.07	58
AP lumbar spine	7.70	3.30	42
Lateral lumbar spine	6.10	3.40	56
Extremity	0.15	0.04	27
Pelvic phantom	3.21	1.60	50
Skull phantom	0.18	0.10	56

Table V. Effective dose equivalents (in mSv) for the aluminium and erbium filtered tubes

Examination	Aluminium filter	Erbium filter	Percentage dose reduction due to erbium filter
Pelvis	0.90	0.32	64.0
Male PA chest	0.013	0.010	17.5
AP lumbar spine	0.58	0.41	29.0
Lateral lumbar spine	0.20	0.17	17.0

seen that the antero-posterior (AP) lumbar spine doses are similar to the lateral lumbar spine doses. Analysis of patient heights and weights (Table III) reveal that, while the patients allocated to the aluminium or erbium rooms were well matched, the patients on whom AP projection dose measurements were made were significantly larger than those undergoing lateral examinations. This was the case for both rooms and explains the unexpectedly low lateral projection doses. As the mean heights and weights of the patients were well matched for all examinations in both rooms, no corrections were made for these parameters.

The exit doses measured on the skull and pelvic phantoms were near the limit of detection for the TLD system, and although the dose for the pelvic phantom was lower in the erbium room (0.004 mGy erbium, 0.007 mGy aluminium), this was not considered to be significant as the errors in these measurements were of the order ±0.002 mGy.

The reduction in effective dose equivalent for the postero-anterior (PA) chest, AP and lateral lumbar spine and pelvic examinations was calculated as described in National Radiological Protection Board Report R186 (NRPB, 1985). The absorbed dose per unit entrance dose for the most significant organs was obtained for the erbium-filtered X-ray beam by extrapolating the results for different thicknesses of aluminium filter in NRPB (1985) to the 8.0 mm Al equivalent of the erbium beam. The effective dose equivalent was then obtained by applying the appropriate weighting factors for the organ concerned and the measured entrance skin doses. Table V shows the calculated effective dose equivalents for the erbium and aluminium rooms and the percentage by which the dose is reduced by the erbium filter.

Analysis of the reject rates in the two X-ray rooms gave a value of 14.6% for room 6 with the aluminium filter in place and 16.8% in the same room after the erbium filter had been fitted. This difference in reject rates is not significant at the $p = 0.05$ level. The reject rate resulting from poor exposure only for this room was 6.3% with the aluminium filter and 6.9% with erbium, the difference not being statistically significant. The reject rates for the erbium-filtered room showed a non-significant downward trend with time, as might be expected as the radiographers become used to the new exposure factors. The average reject rate in the room fitted with the aluminium filter throughout (room 5)

Table VI. Reject radiograph analysis

Before fitting erbium filter (aluminium filter in both rooms)		
	Room 5	Room 6
Radiographs analysed	993	1173
Exposure reject rate	8.7%	6.9%
After fitting erbium filter in Room 6		
	Room 5 (aluminium)	Room 6 (erbium)
Radiographs analysed	888	1013
Exposure reject rate	6.9%	8.4%
Total reject rate	15.0%	16.8%
Radiologists' assessment		
	Room 5	Room 6
Radiographs analysed	43	53

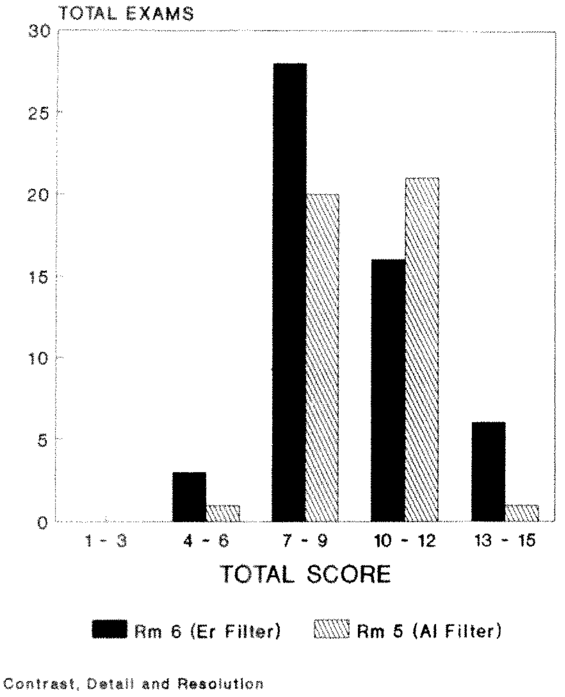

Figure 1. Radiologists' assessment of detail, contrast and resolution for radiographs produced by erbium and aluminium filtered tubes.

was 15.0% over the entire period of the measurements. Details of the analysis are given in Table VI.

Radiographs from the two rooms were scored by five radiologists for detail, contrast and resolution. Figure 1 shows the distribution of the total scores obtained by adding the detail, contrast and resolution scores together, for the two sets of radiographs. There was no significant difference at the $p = 0.05$ level between the radiographs from the aluminium and the erbium rooms. This remained the case when the contrast, resolution and detail scores were considered separately. The mean score for the aluminium filter room was 9.92 and the erbium room 9.47. This difference is not significant at the $p = 0.05$ level. Patient numbers were sufficient to detect a total mean difference of 0.22 in the radiologist's scores of contract, detail and resolution.

Discussion

Fitting an erbium filter into an X-ray tube in a busy general radiography room caused no major problems to the staff involved. The radiographers soon adjusted to the increased exposure factors made necessary by the erbium filter, and there was no significant difference between the reject rates from the two rooms.

The fitting of the filter did not appear to alter the radiographic quality or reduce the contrast of the radiographs. The erbium filter removes both high- and low-energy photons from the X-ray beam leaving the overall radiographic contrast unchanged. This is unlike the situation where copper or thick aluminium filtration is used, when a loss of contrast has been observed at the low values of kVp used for extremity radiographs (Kohn et al, 1988). The radiologists concerned were unable to tell the difference between the radiographs produced by the two rooms, and this is reflected in the lack of difference between the quality scores.

The reduction in skin dose obtained when the erbium filter was used varied from 40% for chest radiographs to over 70% for pelvic and extremity radiographs. The dose saving is especially worthwhile in the high-dose lumbar spine radiographs and similar dose reductions could be expected for intravenous urograms (IVU) and barium contrast examinations of the abdomen.

The calculated reductions in effective dose equivalent are considerably less than the reductions in skin dose. This is because the highly filtered erbium beam will result in a relatively higher dose to organs situated at depth in the body, leading to a higher effective dose equivalent for a given entrance surface dose. The effect of tube filtration on effective dose equivalent is explored in the theoretical paper by Shrimpton et al (1988). They calculate a reduction in entrance surface dose of 36% for a 70 kV PA chest radiograph when a 0.1 mm erbium plus 2 mm aluminium filter is used in place of 2.5 mm aluminium. In the present study the reduction in surface dose was measured as 42%. The difference between the reduction in effective dose equivalent of 8.5% at 70 kV calculated by Shrimpton et al and the 18% reduction of the present study is accounted for by this difference in calculated and observed entrance surface doses.

The correctness of the present paper's effective dose equivalent calculations may be shown by substituting Shrimpton's calculated surface dose for the measured surface dose in the effective dose equivalent calculations. For a surface dose reduction of only 36% the reduction in effective dose equivalent is 9%, which is almost identical to the 8.5% reduction in Shrimpton's paper. It appears, therefore, that the theoretical paper underestimates the reduction in entrance surface dose produced by the erbium filter and hence underestimates the reduction in effective dose equivalent.

The reduction in effective dose equivalent is particularly worthwhile in the case of the male pelvis where the dose for the erbium beam is only 36% of the aluminium beam dose. This is due to the large contribution of the testicular dose to the effective dose equivalent and the ratio of effective dose to entrance dose for the testes is very similar for the aluminium and erbium beams.

In general it is necessary to increase the exposure factor by 2 when using the erbium filter. This has the effect of taking the tube factors back to those used before the introduction of rare-earth intensifying screens. In theory the increased tube loading should reduce the tube life in inverse proportion; that is, the tube life should be halved. In practice, however, most tubes wear out because of factors other than anode or cathode wear, such as wear in the rotor bearings or anode crazing resulting from inefficient tube warm-up. Although there appears to be no hard evidence on this matter, it is the opinion of the author, after discussions with X-ray tube manufacturers and engineers, that the increased tube loadings produced by the use of erbium filters will have little overall effect on the tube life if used with rare-earth intensifying screens. An exception to this would be where the tube is very heavily loaded, such as in some specialist angiographic procedures.

The comparatively low cost of the erbium filter means that the fitting of such a filter is a cost-effective method of dose reduction. Russell and Webb (1987) have proposed a method of estimating the cost per life saved by various radiation protection measures.

If each X-ray tube is responsible for a 4 man-Sv of exposure per annum (Wall & Russell, 1988), a reduction in dose equivalent of 30% will lead to a reduction in exposure of 1.2 man-Sv/year. If the erbium filter has a life of 20 years the total reduction in exposure over the lifetime of the filter is $20 \times 1.2 = 24$ man-Sv. If the risk of death from radiation is 0.03 per man-Sv (NRPB, 1987) and the cost of the filter is £400, the cost of saving one life is £400 $(24 \times 0.03) =$ £560. To this figure must be added the cost of increased tube wear, but this should not be great if the filter is used in combination with rare-earth intensifying screens. The total cost of, say, £700 per life saved is much less than the cost of fitting carbon fibre table tops.

The use of erbium filtration is, therefore, a practical and cost-effective method of dose reduction when used in combination with rare-earth film/screen combinations.

Acknowledgments

The authors would like to acknowledge the help and encouragement of Miss A. Ridell, District Superintendent Radiographer, and of the radiographers and radiologists of the Cheltenham Department of Radiology.

References

ATKINS, H. L., FAIRCHILD, R. G., ROBERTSON, J. S. & GREENBERG, D., 1975. Effect of absorption edge filters on diagnostic x-ray spectra. *Radiology*, *115*, 431–437.

BIR, 1988. *Assurance of Quality in the Diagnostic X-ray Department* (British Institute of Radiology, London).

BURGESS, A. E., 1985. Physical measurements of heavy metal filter performance. *Medical Physics*, *12* (2), 225–228.

CHAKERA, T. M. H., FLEAY, R. F., HENSON, P. W. & COLE, S. M., 1982. Dose reduction in radiology using heavy metal filters. *British Journal of Radiology*, *55*, 853–858.

FLEAY, R. F., 1980. Energy band selection in radiology by K-absorption edge filtration. *Australasian Radiology*, *24*, 323–327.

FLEAY, R. F., FOX, R. A., SPRAUGE, P. L. & ADAMS, J. P., 1984. Dose reduction in radiology using rare earth filtration. *Pediatric Radiology*, *14*, 332–334.

HORNER, K., LAWINSKI, C. P. & SMITH, N. J. D., 1988. Erbium filtration for dose reduction in dental radiography. *British Journal of Radiology*, *61*, 609–612.

KOHN, M. L., GOOCH, A. W. & KELLER, W. S., 1988. Filters for radiation reduction: a comparison. *Radiology*, *167*, 255–257.

NRPB, 1985. *Organ Doses from Medical X-ray Examinations Calculated using Monte Carlo Techniques*, NRPB Report R186, by D. G. Jones and B. F. Wall (HMSO, London).

NRPB, 1987. *Interim Guidance on the Implications of Recent Revisions of Risk Estimates and the ICRP 1987 Como Statement*, NRPB Report G59 (HMSO, London).

RUSSELL, J. G. B. & WEBB, G. A. M., 1987. Valuing the man-Sievert in X-ray diagnosis. *British Journal of Radiology*, *60*, 681–684.

SHRIMPTON, P. C., JONES, D. G. & WALL, B. F., 1988. The influence of tube filtration and potential on patient dose during X-ray examinations. *Physics in Medicine and Biology*, *33*, 1205–1212.

THIERENS, H., KUNNEN, M., VAN DER PLAESTEN, A. & SEGAERT, O., 1991. Evaluation of the use of a niobium filter for patient dose reduction in chest radiography. *British Journal of Radiology*, *64*, 334–340.

VILLAGRAN, G. E., HOBBS, B. B. & TAYLOR, K. W., 1978. Reduction of patient exposure by use of heavy elements as radiation filters in diagnostic radiology. *Radiology*, *127*, 249–254.

WALL, B. F. & RUSSELL, J. G. B., 1988. The application of cost utility analysis to radiological protection in diagnostic radiology. *Journal of Radiological Protection*, *8*, 221–229.

WESENBERG, R. L., AMUNDSON, G. M. & FLEAY, R. F., 1983. Ultra low dose routine radiography utilising a rare-earth filter. *Radiology*, *149*(P) 38.

1992, *The British Journal of Radiology*, 65, 238–241

Measurement of extrafocal radiation by computed radiography

By Risto H. Miettunen, MD

Department of Diagnostic Radiology, Helsinki University Central Hospital, Meilahti Clinics, 00290 Helsinki, Finland

(*Received 28 November 1990 and in revised form 15 May 1991, accepted 3 October 1991*)

Keywords: Radiography, Digital, Technique, Instrumentation

Abstract. Measurement of radiation differences from image data is made possible by computed radiography (CR) based on storage phosphor imaging plates. The photostimulable luminescence (PSL) response is linear in a range greater than four orders of magnitude. Pinhole radiographs of focal and extrafocal radiation obtained by CR were quantitatively analysed using the technique originally introduced in recent scatter studies. No films or hard copies were used in the analysis. The material consisted of 54 images for measurement of the focal peak intensity, and a corresponding set of 54 images obtained at a 250 times greater operating sensitivity for the imaging of the extrafocal emission. The extrafocal-to-focal emission ratio was in the range of 0.001–0.006 depending on the off-focus distance. Because of the relatively large area of origin, exposure resulting from extrafocal radiation is estimated to reach up to 20% of the total radiation dosage. The results are in agreement with previous reports using other techniques and show that CR can also be used in a quantitative manner in this kind of comparative measurement.

Extrafocal radiation arising from structures of the X-ray tube around the focal spot is diagnostically useless, resulting only in poorer image quality and greater patient dosage. The phenomenon has been recognized for a long time, and most modern tubes have specific collimators to cut off part of the unwanted radiation. However, image size sets limits on the use of collimators, and the problem still exists even with modern equipment (Mattson, 1955; Shiga & Yoshida, 1963; Kuhn & Gajewski, 1971; Rao, 1974; Birch, 1976; Thomas et al, 1983).

Pinhole radiography clearly shows the distribution of extrafocal emission around the focal spot, the main source being unfocused or scattered radiation from the anode plate. Pinhole computed radiographs of extrafocal radiation from the two X-ray tubes tested in this study are shown in Figs 1a and 1b.

The storage phosphor plates of computed radiography (CR) have a linear photostimulable luminescence (PSL) response to radiation in a range greater than four orders of magnitude (Sonoda et al, 1983; Hillen et al, 1987). The sensitivity and latitude of PSL detection are adjustable, the range of diagnostic information being displayed with optimal density in a 10-bit gray scale. Only part of the total dynamic range is used in a single image.

This provides a possibility to use CR in a quantitative manner in measurement of radiation exposure under controlled conditions. Previous work has concentrated on scattered radiation (Chotas et al, 1990; Floyd et al, 1990; Miettunen et al, 1991). The aim of this study was to assess the applicability of the quantitative CR technique to calculations of the extrafocal-to-focal emission ratio, where great differences in radiation intensity are being measured.

Methods

Equipment

The CR system was a Siemens Digiscan unit with an interactive image processing work station, a μVAX host computer providing 32 Mbytes of memory, a 2 GByte optical disk memory for data storage, and two high-resolution 1023-line monitors (Siemens AG, Erlangen, Germany). Reversible data compression by Huffmann coding and simultaneous pyramid transformation are used for archiving images.

The X-ray tubes were chosen to represent a modern construction with inner collimation (Tube 1; Shimadzu RSN 742 with MPG 50 generator, Japan), and an older one without extrafocal shielding (Tube 2; Siemens B 1 150/30/50 with Gigantos 3/12 generator, Germany). It should be emphasized that the latter tube construction does not represent current technology, and was chosen only as a model for the measurements.

A pinhole diameter of 1 mm and a large-scale measurement geometry were chosen for two reasons. First, the detection of all extrafocal radiation from a relatively large area of origin was desired and second, the digital modality made it possible to use a long pinhole-to-detector distance for magnified images. A precision instrument for focal spot imaging was also tested. Because of the small viewing angle and image size this was, however, omitted and the large pinhole was found more practical for this purpose despite the lower resolution. The pinhole was drilled in a lead plate with a thickness of 3 mm. The distance from the focal

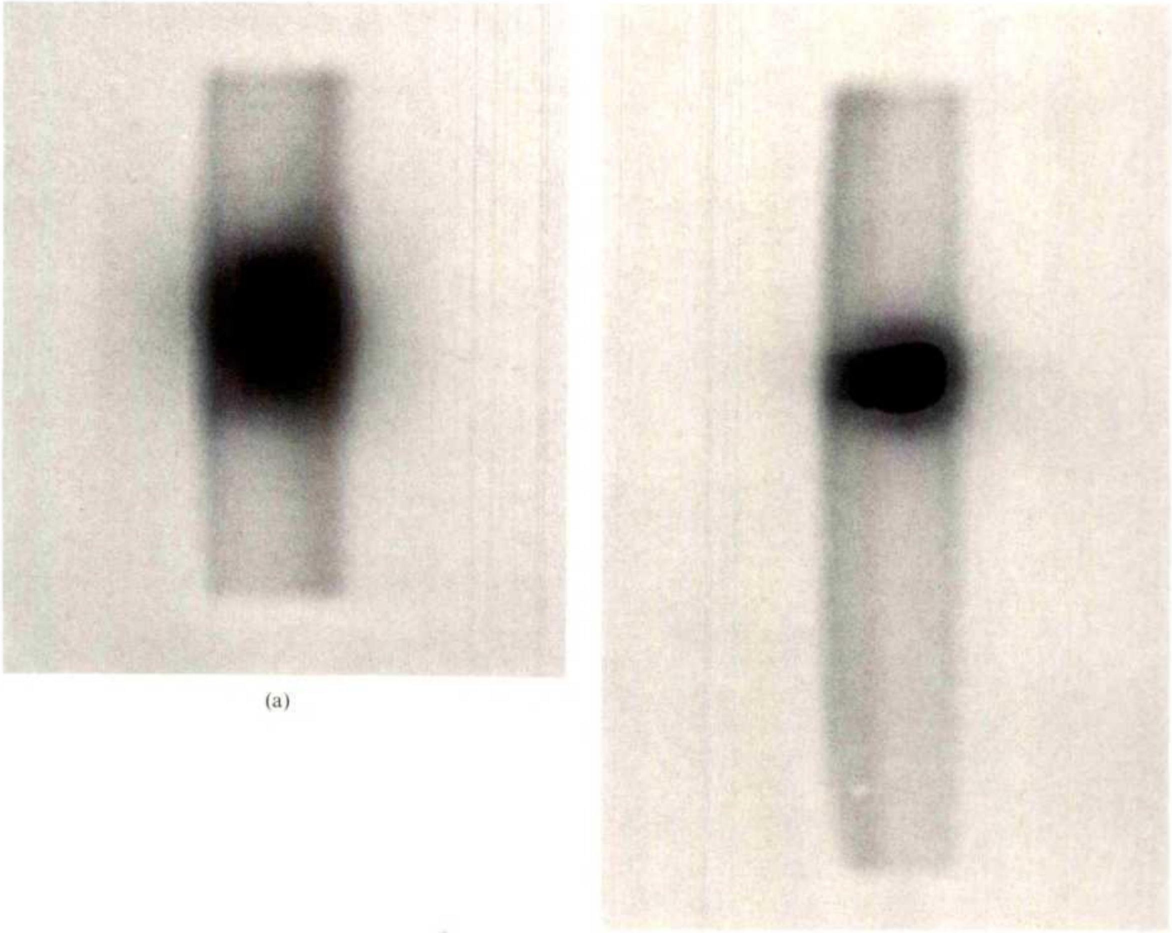

(a)

(b)

Figure 1. Pinhole radiographs of (a) tube 1 and (b) tube 2.

spot to the pinhole was 27 cm and 30 cm for the two tubes, and the detector plate was placed at 114 cm from the pinhole in all images.

Pinhole exposures

All combinations of 60, 90 and 120 kV and 40, 80 and 160 mAs were used for both tubes. In addition, all exposures were made twice for tube 1. Both large and small focal spots were examined. The material thus consisted of 108 pinhole radiographs. All images were obtained with collimators open.

Quantitative analysis

The use of CR with a fixed sensitivity and latitude for PSL detection gives the opportunity to relate differences of pixel densities to those of radiation exposure. This has been confirmed by previous studies (Chotas et al, 1990; Floyd et al, 1990; Miettunen et al, 1991).

The system sensitivity (S) and latitude (L) were manually controlled using fixed S and L values. The routine clinical programs are automatic, but for measurement tasks the manually controlled mode is essential. The images for measurement of the focal peak were obtained at a 250 times lower operating sensitivity ($S = 1$) than those for the extrafocal radiation ($S = 250$). No films were included in the analysis.

The pixel density difference between the focal and extrafocal values described above is a logarithmic measure of radiation differences. A latitude of 2.2 was used in all images, which means a $10^{2.2}$-fold dynamic range within the gray scale consisting of 1024 levels. An increase of 465 units ($= 1024/2.2$) thus means a 10-fold difference in radiation.

To relate the information obtained at $S = 250$ and $S = 1$ to each other, a value of 1115 units (465 units × log 250) was added to the focal peak values. The extrafocal-to-focal (EF/F) emission ratio was then

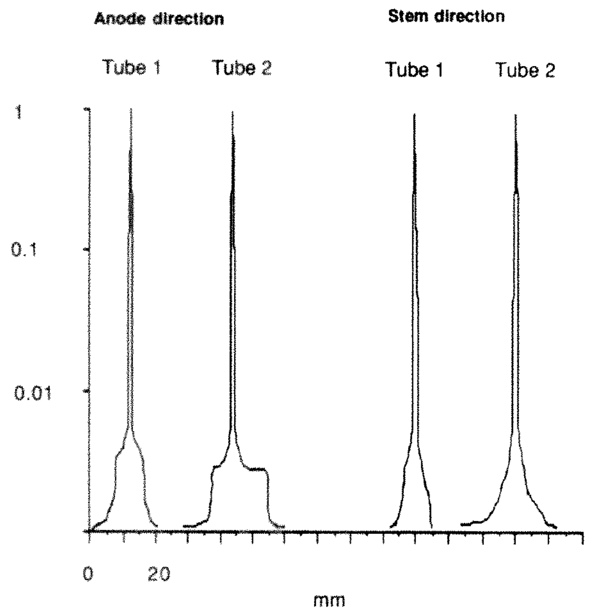

Figure 2. A schematic representation of the intensity profiles in two directions. Note that extrafocal shielding in tube 1 limits the width of the curve shoulders.

calculated from the pixel values according to the following formula:

$$\frac{\mathrm{EF}}{\mathrm{F}} = \frac{1}{\{[(\text{focal value}+1115)-\text{extrafocal value}]/465\}}$$

The pixel value profiles were obtained by the lineplot function of the system. Pixel values from the $S = 250$ radiographs were measured in two directions referring to the anode plate and stem. Points of measurement were at 2, 4 and 6 mm from the centre of the focus, as calculated from the geometry of the experiment. The peak intensity of the focal spot was measured from the

Table 1. The observed mean extrafocal-to-focal emission ratios (1/1000)

	Off-focus distance		
	2 mm	4 mm	6 mm
Anode plate direction			
Tube 1 large focus	5.9	2.3	1.7
Tube 1 small focus	3.1	1.3	1.0
Tube 2 large focus	3.8	1.9	1.6
Tube 2 small focus	2.9	1.6	1.3
Stem direction			
Tube 1 large focus	4.6	1.5	0.9
Tube 1 small focus	2.5	0.8	0.5
Tube 2 large focus	4.0	1.3	0.8
Tube 2 small focus	2.9	1.1	0.4

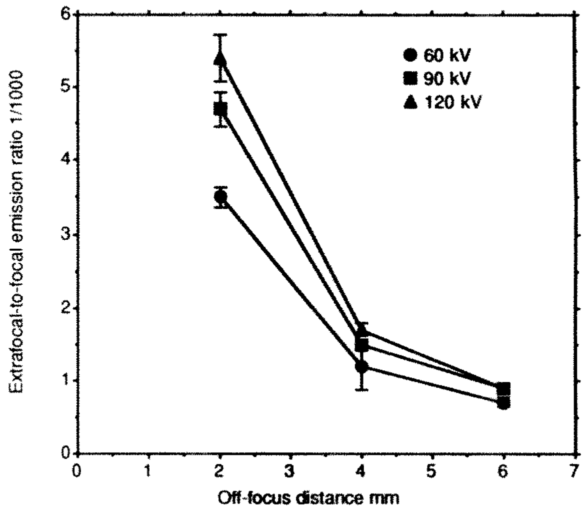

Figure 3. The effect of tube voltage on the extrafocal-to-focal emission ratio. The values are slightly greater at higher voltages.

$S = 1$ images. The same windowing showing all the information obtained (width 1026, centre 513) was used throughout the data analysis. As the system uses a reversed scale, all values were first subtracted from 1023.

Results

The intensity profiles of the two tubes are presented in Fig. 2. The extrafocal shielding limits the area of emission to a square of 18 mm × 18 mm in tube 1, whereas in tube 2 the area reaches up to 30 mm × 30 mm. No clear distinction of the actual focal spot margins could be made owing to the relatively large pinhole size. However, it could be seen that there is a boundary zone close to the focus, where the extrafocal radiation intensity rapidly increases.

The EF/F emission ratios are shown in Table 1. The calculated ratios were in the range of 0.001–0.006 depending on the distance from the centre of the focus and the axis of measurement. The latter difference results from the fact that extrafocal radiation arises mainly from the anode plate. Using an estimation of a mean EF/F emission ratio of 0.002 and an emissive area of about 100 times that of the focal spot, the exposure resulting from extrafocal radiation can be approximated as 20% of total exposure. Because the focal spot margins were not distinct in the images, a more detailed analysis of this relationship could not be made.

The EF/F emission ratio increased slightly with tube voltage. An example of this phenomenon is presented in Fig. 3. The tube mAs settings had no effect. The energy spectrum of extrafocal radiation could not be determined from the data.

Discussion

An analysis has been performed by Birch in 1976, in which an EF/F emission ratio of 0.0016–0.0024 was determined using a focused Ge(Li) detector and spectral analysis. These measurements were performed at the stem direction and at off-focus distances of 4, 6 and 8 mm. The results are in accordance with those of this study.

In a study by Rao in 1974, the EF/F emission ratio was determined by using non-screen film radiographs of a narrow slit. The ratio was 0.005–0.018, which is somewhat higher than that determined in this study. However, the use of a slit instead of a pinhole as well as the limitations of film as detector material might explain the difference at least in part.

Despite the low intensity of extrafocal radiation, its contribution to the total radiation dose is significant because of the large area of emission. Exposure dose ratios in the range of 8–30% have been reported by many authors, and there has been a significant variation between experiments (Mattson, 1955; Shiga & Yoshida, 1963; Kuhn & Gajewski, 1971; Rao, 1974; Weaver et al, 1975; Birch, 1976; Thomas et al, 1983), probably reflecting the differences between X-ray tubes.

The results show that, in addition to scatter measurement as shown by previous work, data from CR images can also be used in relative measurement of extrafocal radiation when the sensitivity and latitude of PSL detection are controlled. Compared with film detector techniques, the serious limitations caused by the narrow latitude, the non-linear density response and the required optical densitometric measurements of film can be avoided by CR. Quantitative CR can also be expected to be of use in other measurement tasks.

Acknowledgment

This study has been supported by the Finnish Radiological Society and Siemens Oy, Finland.

References

BIRCH, R., 1976. The spectrum and intensity of extra-focal (off-focus) radiation. *British Journal of Radiology*, *49*, 951–955.

CHOTAS, H. G., FLOYD, C. E., DOBBINS, J. T., III, LO, J. Y. & RAVIN, C. E., 1990. Scatter fractions in AMBER imaging. *Radiology*, *177*, 879–880.

FLOYD, C. E., CHOTAS, H. G., DOBBINS, J. T. & RAVIN, C. E., 1990. Quantitative radiographic imaging using a photostimulable phosphor system. *Medical Physics*, *17*, 454–459.

HILLEN, W., SCHIEBEL, U. & ZAENGEL, T., 1987. Imaging performance of a digital storage phosphor system. *Medical Physics*, *14*, 744–751.

KUHN, H. & GAJEWSKI, H., 1971. Die extrafokale Strahlung von Röntgendrehanodenröhren und ihr Einfluss auf die Bildqualität. *Electromedica*, *4*, 125–131.

MATTSON, O., 1955. Practical photographic problems in radiography. Thesis, University of Stockholm, Sweden.

MIETTUNEN, R. H., KORHOLA, O. A. & SAVIKURKI, S., 1991. The scatter-to-primary ratio as a function of varying X-ray absorption measured by computed radiography. *European Journal of Radiology 13*, 156–159.

RAO, G. U. V., 1974. Influence of off-focal radiation on radiographic resolution and patient exposure. *Applied Radiology*, *3*, 45–49.

SHIGA, K. & YOSHIDA, M., 1963. Methods of eliminating off-focus X-rays in rotating anode X-ray tubes. *Toshiba Review, International Edition*, *16*, 41–48.

SONODA, M., TAKANO, M., MIYAHARA, J. & KATO, H., 1983. Computed radiography utilizing scanning laser stimulated luminescence. *Radiology*, *148*, 833–838.

THOMAS, S. R., FRESHCORN, J. E., KRUGH, K. B., HENRY, G. C., KEREIAKES, J. G. & KAUFMAN, R. A., 1983. Characteristics of extrafocal radiation and its potential significance in pediatric radiology. *Radiology*, *146*, 793–799.

WEAVER, K. E., WAGNER, R. F. & GOODENOUGH, D. J., 1975. Performance considerations of X-ray tube focal spots. In: Medical X-ray photo-optical systems evaluation. *Proceedings of SPIE*, *56*, 150–158.

1992, *The British Journal of Radiology*, *65*, 242–247

The dose-rate effect in interstitial brachytherapy: a controversy resolved

By Eric J. Hall, DSc and David J. Brenner, PhD

Center for Radiological Research, College of Physicians & Surgeons of Columbia University, 630 West 168th Street, New York, NY 10032, USA

(*Received 21 May 1991 and in revised form 6 September 1991, accepted 20 September 1991*)

Keywords: Brachytherapy, Dose rate, Interstitial

Abstract. Low-dose-rate interstitial implants generally involve a range of dose rates varying from about 0.3 to 1.5 Gy/h. It has been a matter of some debate as to whether such a variation in dose rate has any impact on clinical results, *i.e.* whether implant treatment time needs to be taken into account when prescribing the treatment dose. In particular, Paterson and Ellis both published data based on clinical experience suggesting that the prescribed dose should vary with overall treatment time, whereas the Paris school suggested that isoeffect dose should not be varied for treatment times between 3 and 8 days. Experimental radiobiological data obtained *in vitro* and *in vivo* imply a significant change in biological effectiveness over this range of dose rates with a greater variation for normal-tissue late effects than for tumour control. We show, based on radiobiological considerations and model calculations, that the disagreement between the two schools in their recommendations for generating isoeffect doses for different treatment times was a result of two factors. First, the Paterson recommendation was unequivocally based on matching limiting late effects, whereas the Paris system recommendations were based on an analysis of a combination of late and early effects. Second, the Paterson recommendations were based on a dosimetry system in which the dose rate does not change greatly with tumour volume, whereas the Paris recommendations were based on a dosimetric system in which dose rate is correlated with tumour volume, which in turn is correlated with changes in both tumour control and, especially, necrosis.

Implanting radioactive sources directly into a tumour was a strategy first suggested by Alexander Graham Bell soon after the turn of the century (Bell, 1903). Over the years, various groups in different countries coined various names for this type of therapy, using the prefix *brachy* from the Greek for short range, or *endo* from the Greek for within.

Interstitial and intracavitary techniques were developed to an advanced stage at an early date because the technology was readily available. Radium in sufficient quantities was extracted and purified in the early 1900s, whereas radioactive sources of sufficient activity for teletherapy sources of adequate dose rate only came as a spin-off of World War II nuclear technology.

Radium needles

The early radioactive sources were of radium, which, because it is an element in a radioactive decay series emitting α, β and γ rays, must be encapsulated and filtered. This in turn meant that needles for interstitial use were relatively large and rigid, while tubes containing sufficient activity for intracavitary use were bulky.

Rules to distribute radium needles in planar or volume implants were devised by Parker and Paterson, aimed at producing uniform irradiation in a plane parallel to the implanted sources or at a distance outside an implanted volume (Meredith, 1967). These rules demanded a variety of needles of different linear activity. The rules were simplified and adapted by Quimby for use in the United States where needles of varying linear activity were less widely available (Quimby & Castro, 1953).

Interstitial implants generally involve the range of dose rates where the variation of biological effect with dose rate is substantial and important, at least for cells in culture where precise measurements are possible. In the case of interstitial implants in a clinical setting it was pointed out by Paterson (1963) that the limiting factor is the normal-tissue tolerance, which should be used fully to maximize the possibility of tumour control. The maximum dose that can be delivered without unacceptable damage to surrounding normal tissue depends critically on the dose rate but also on the volume of tissue irradiated. In the 1960s, Paterson deduced from clinical experience a curve of biological equivalence, based on limiting late effects, for treatments given at different dose rates. Regarding 60 Gy in 7 days as the standard tolerance dose, he proposed that an implant of shorter duration should have slightly less dose, and an implant of longer duration an augmented dose. Ellis proposed a very similar scheme for use in clinical practice; the data on which this curve was drawn were obtained from clinical experience and are attributed to T. A. Green (unpublished data, Ellis, 1968).

Iridium-192 wires

The availability of man-made radionuclides of high specific activity, notably iridium 192, allowed interstitial implants to be performed with thin flexible "wires". This constituted a revolution in brachytherapy starting in the 1950s with an improvement in comfort for the patient as well as greater flexibility and diversity of implant design.

The relatively short half-life of iridium 192 (74 days) means that, during the period of several months that the material is clinically useful, there will be a range of linear activities. The "Paris" system of dosimetry, using the same linear activity for all sources and varying the separation of the radioactive wires for different lengths (*i.e.* greater separation for longer wires and therefore larger treatment volumes) also results in dose-rate variations (Pierquin, 1971). These two factors combined, the short half-life of the iridium 192 and the dosimetry system used, result in practice in a potential three-fold variation in the total irradiation time for delivery of a given tumour dose (Pierquin et al, 1973).

In an analysis of clinical observations involving interstitial radiotherapy using iridium 192 in several hundred patients, Pierquin et al (1973) concluded that the time factor was less important than suggested by other workers. Consequently they recommended the same prescribed dose irrespective of overall time within the range 3–8 days. They were careful to point out that their conclusions were preliminary but nevertheless concluded (Pierquin et al, 1973):

> We can however say with certainty that the variation in overall treatment time for the same tumour dose from 3 days to 8 days does not appear to influence the frequency of recurrence or necrosis.

This advice, repeated many times over the years, is at variance with the clinical experience of Paterson (1963) and Ellis (1968), and in conflict with experimental radiobiological data over the dose-rate range in question, that indicates a substantial dose-rate effect and also a differing dose-rate effect for early and late effects (Withers et al, 1982).

A complication and confounding variable in the interpretation of clinical data relating dose to produce an equivalent effect to implant time (and therefore to dose rate) is the fact that, for interstitial implants, the dose rate tends to increase as the size of the implant increases. This correlation is particularly true for implants using iridium-192 wires, which are all of the same linear activity, as used in the Paris system, but less so when there is a variation in linear activity, as in the Parker and Paterson system (Meredith, 1967). The bias of larger tumours and larger treatment volumes associated with higher dose rates, while smaller tumours and smaller treatment volumes are associated with lower dose rates, was pointed out by Pierquin and his colleagues (Pierquin et al, 1973). Larger tumours, of course, require a larger dose for a given level of local control, while the maximum dose that can be tolerated by normal tissues decreases as the volume implanted increases.

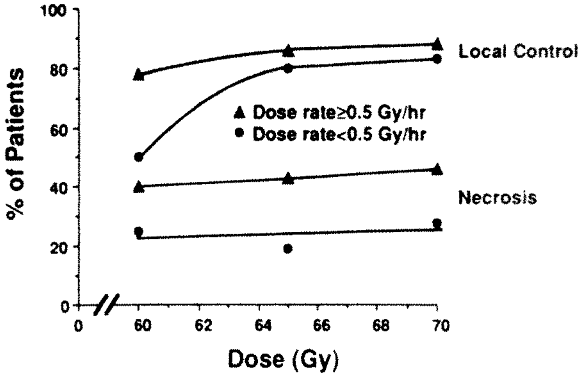

Figure 1. Incidence of local tumour control and necrosis for T1–2 squamous cell carcinoma of the mobile tongue and floor of mouth, treated with interstitial radiotherapy using iridium 192. Based on the published results of Mazeron et al (1991).

New data from the Paris group have altered their previous conclusion that the same dose could be used for treatment times of 3–8 days. Figure 1, based on the results of Mazeron et al (1991), shows the incidence of local tumour control and necrosis for T1–2 squamous cell carcinoma of the mobile tongue and floor of mouth, treated with interstitial iridium 192. This is one of the largest cohorts of patients that has been analysed who were treated by the same implantation technique, but the numbers still preclude a detailed analysis of dose rate and can distinguish only between dose rates above and below 0.5 Gy/h. The principal features of their results, as illustrated in Fig. 1, are:

1. A higher incidence of necrosis at the higher dose rate.
2. Little or no difference in local control between the two dose-rate ranges at high doses (65–70 Gy) but a clear separation at lower doses (60 Gy), with the lower dose rate being less effective.

Radiobiological data

Figure 2 shows a collection of linear-quadratic curve fits to survival data for cells of human origin *in vitro* irradiated with acute exposures at high dose rate (HDR) or in protracted exposures at low dose rate (LDR). There is a wide range of radiosensitivities at high dose rate as evidenced by the frequency distribution of α/β values, the constants in the linear-quadratic dose response relationship. At low dose rate the curves "fan out", showing an even greater range of radiosensitizers because of the extra variable between cell lines of $T_{\frac{1}{2}}$, the half-time of sublethal radiation damage repair. The details of the analysis of this set of *in vitro* data have been published previously (Brenner & Hall, 1991).

Figure 3 shows (solid lines) iso-effect curves normalized to 60 Gy in 7 days based on:

1. the α/β values and $T_{\frac{1}{2}}$ values for *in vitro* data of Fig. 2,

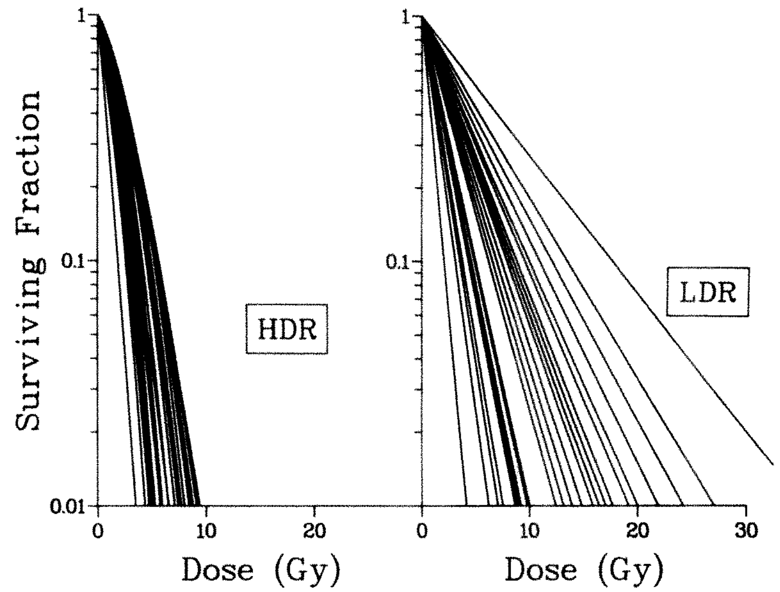

Figure 2. Survival curves for 40 cell lines of human origin cultured *in vitro* and irradiated at high dose rate (HDR), shown in the left hand panel, or at low dose rate (LDR) shown in the right hand panel. The data analysis is described in detail in Brenner and Hall (1991).

which relate to tumour control, or early responding tissue, or

2. *in vivo* late-responding tissues, using parameters from the literature and summarized in Table I.

Consider first the solid curves in Fig. 3. The iso-effect curve based on late effects is steeper than that for early effects and tumour control, *i.e.* shows a greater time (or dose-rate) dependence. This is to be expected, based on the differences between early- and late-responding tissues described by Withers et al (1982). The iso-effect curve based on late effects is also in good agreement with the clinically based recommendation of Paterson (1963) for the variation of iso-effect dose with overall treatment time, which is as it should be since Paterson's recommendation was based on limiting late effects. The dotted lines in Fig. 3 illustrate, in a qualitative way only, the effect of the complicating factor of dose rate varying with tumour size. At the one extreme, higher dose rates are associated with large tumours and large implanted volumes. This will increase the dose required to result in a given level of tumour control and decrease the dose that can be tolerated to produce a given level of necrosis, *i.e.* the tumour control iso-effect curve is made shallower, and the normal-tissue iso-effect curve is made steeper by the bias of high dose rate being associated with larger tumours and vice-versa. It should be emphasized that the dotted lines are qualitative only and illustrate the trend resulting from the fact that dose rate varies with tumour size and treatment volume, since quantitative data relating curative dose to tumour volume and tolerance dose to treatment volume are simply not available.

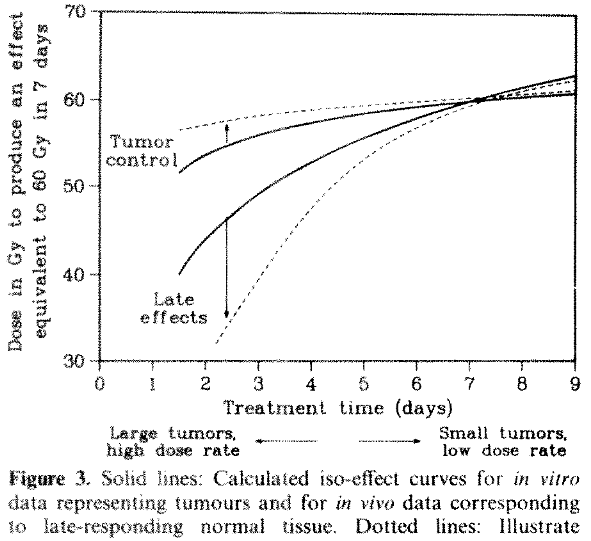

Figure 3. Solid lines: Calculated iso-effect curves for *in vitro* data representing tumours and for *in vivo* data corresponding to late-responding normal tissue. Dotted lines: Illustrate qualitatively the way in which the iso-effect curves change owing to the bias of higher dose rates being associated with larger tumours. Larger tumours require a larger dose for a given level of local control; this tends to flatten the iso-effect curve for tumour control. By contrast, the iso-effect curve for late effects in normal tissues is steeper since larger implanted volumes can tolerate smaller doses.

The radiobiological data can be used to interpret the new results of Mazeron et al (1991). In order to facilitate a direct comparison with the clinical data, which is presented in terms of probability of effect (tumour control or necrosis), we use the "double log" model, suggested by Gilbert (1974). This assumes that both tumour control and late effects result from the elimination of a given fraction ($1/K$) of cells in a given site. Thus we assume there are K groups of cells whose

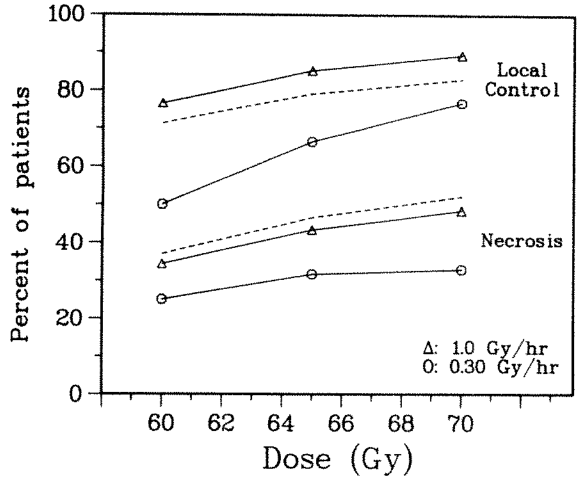

Figure 4. Solid lines: Calculated doses for local tumour control and necrosis based on the radiobiological parameters and $T_{1/2}$ from Fig. 2. The calculations are for dose rates of 1 and 0.3 Gy/h. Dotted lines: Illustrate qualitatively the direction that the 1.0 Gy/h curves for local tumour control and necrosis would be expected to move because of the bias of larger tumours associated with higher dose rates. A lower level of local control for a given dose would be expected for larger tumours, while at the same time the maximum dose that can be tolerated by normal tissues decreases for larger implanted volumes.

destruction would produce the effect, with a probability given by the first term of the Poisson distribution

$$P = \exp(-\exp(\ln K - \alpha D - G\beta D^2))$$

where α and β are the linear-quadratic parameters, and G is the term (see Brenner & Hall, 1991) which results in increased survival at the dose rate decreases. K is, of course, unknown, and we varied it to agree with the clinical data of Mazeron et al at 60 Gy at < 0.5 Gy/h. (The K values were 4.2×10^7 for tumour control and 3.9×10^8 for necrosis.)

The solid lines in Fig. 4 show calculated doses for local tumour control and necrosis based on the radiobiological parameters discussed earlier, *i.e.* values of α/β, the coefficients of the linear-quadratic model and of $T_{1/2}$, the half-time of repair of sublethal radiation damage. The calculations were made for dose rates of 1 and 0.3 Gy/h to represent the greater and less than 0.5 Gy/h clinical data in Fig. 1.

The calculation shown by the full curves assumes no relation or bias between dose rate and tumour size. As discussed above, we know that there is such a bias. Although empirical models do exist describing volume effects in tumours, they are currently not reliable enough to make quantitative predictions. The trends, however, are clear. The dotted lines show the direction in which the curves would move owing to the fact that the higher dose rates tend to be associated with larger implants and larger tumours. The shift is in the right direction, *i.e.* lower tumour control and more necrosis for the higher dose rates.

It is clear that both the new clinical results from Mazeron et al (1991) as well as the older predictions of Paterson (1963) and Ellis (1968) are both in agreement with expectations based on radiobiological theory. There is no longer any conflict between the conclusions of the Paris School and the older published work of Paterson and of Ellis. Neither is there any conflict between the clinical experience and the results of experimental radiation biology, *in vivo* and *in vitro*. Indeed the clinical results are adequately accounted for by simple models based on the experimental data.

Pulsed brachytherapy

The problems created by the variation of dose rate, which is, in practice, an inevitable consequence of using iridium-192, can be completely eliminated by the new technique of pulsed brachytherapy. In this strategy, described in detail by Brenner and Hall (1991), the individual wires or ribbons in a conventional implant are replaced by a single iridium-192 source which, under computer control from a remote afterloader, steps through the implanted catheters with dwell times designed to reflect the relative linear activity required. The source would move through the implant for about 10 min out of each hour, delivering a "pulse" of, say, 60 cGy in this time. As the source decays over a period of weeks or months, the pulse length would be gradually increased to offset the radioactive decay of the source and maintain the dose per pulse at precisely 60 cGy.

Table I. Values of α, β, α/β and $T_{1/2}$ for late-responding tissues evaluated *in vivo*

End-point	Reference	α (Gy^{-1})	β (Gy^{-2})	α/β (Gy)	$T_{1/2}$ (min)
Human skin (telangiectasia)					
(fast repair*)	Turesson & Thames (1989)	0.10	0.024	4.1	24
(slow repair*)		0.10	0.024	4.1	210
Mouse lung					
(late damage)	Travis et al (1987)	0.31	0.072	4.3	39
Rat spinal chord					
(paralysis)	Ang et al (1987)	0.066	0.019	3.4	93

* The slow and fast components of the repair were roughly equally important.

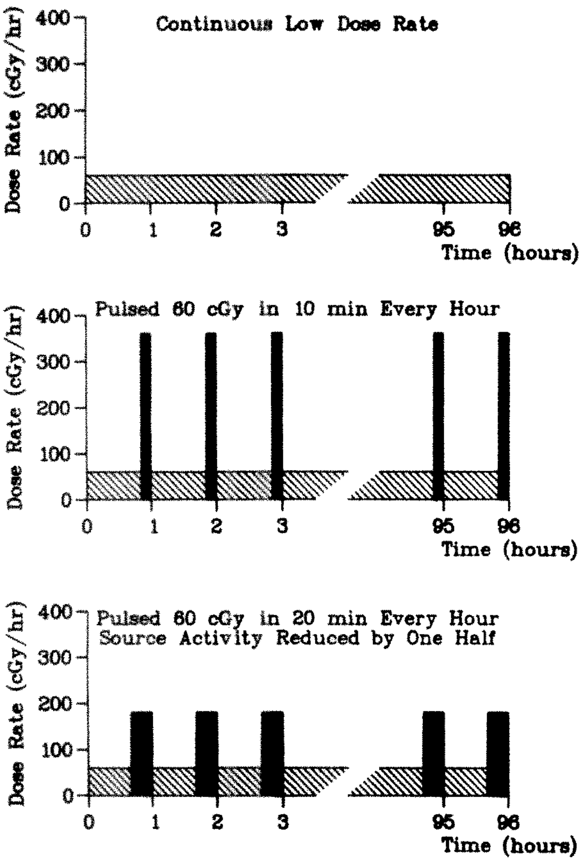

Figure 5. Illustrates the principle of pulsed brachytherapy. A continuous low dose rate of (say) 60 cGy/h is replaced by a pulse of 60 cGy delivered in 10 min. As the single iridium-192 source decays with a half-life of 74 days, the pulse length is adjusted to maintain the dose per pulse to precisely 60 cGy. Thus, the average dose rate is maintained and the overall treatment time for a given total dose remains fixed.

This is illustrated in Fig. 5. In this way the average dose rate would be maintained at 60 cGy/h, or whatever dose rate is chosen. The problems of trying to compensate for a variable dose rate to maintain local tumour control and minimize the late damage to normal tissues would then be completely eliminated. This is an additional advantage of pulsed brachytherapy to be added to those already listed by Brenner and Hall (1991).

Conclusion

In hindsight it can be seen that the disagreement between the two schools in their recommendations for generating iso-effect doses for different treatment times was a result of two factors.

1. The Paterson recommendation was unequivocally based on matching limiting late effects, whereas the Paris system recommendations were based on an analysis of a combination of late and early effects; from radiobiological theory, such a combination now appears to be unwarranted in that different iso-effects would be expected for late and early effects.
2. The Paterson recommendations were based on a dosimetry system in which the dose rate does not change greatly with tumour volume, whereas the Paris recommendations were based on a dosimetric system in which dose rate is correlated with tumour volume, which in turn is correlated with changes in both tumour control and necrosis.

Finally, it is pointed out that advances in radiotherapy technology hold the promise of making obselete such debates about correction factors for enforced changes in dose rate. The technique of pulsed brachytherapy has the potential to simulate any desired dose rate, even as the radioactive source undergoes decay.

Acknowledgments

This work was based on research supported by grant numbers CA12536 and CA24232 from the National Cancer Institute. We are grateful to Dr J. J. Mazeron for kindly providing his results prior to publication.

References

ANG, K. K., THAMES, H. D., VAN DER KOGEL, A. J. & VAN DER SCHUEREN, E., 1987. Is the rate of repair of radiation-induced sub-lethal damage in rat spinal cord dependent on the size of dose per fraction? *International Journal of Radiation Oncology, Biology, Physics*, *13*, 557–562.

BELL, A. G., 1903. The uses of radium. *American Medicine 6*, p. 261.

BRENNER, D. J. & HALL, E. J., 1991. Conditions for the equivalence of continuous to pulsed low dose-rate brachytherapy. *International Journal of Radiation Oncology, Biology, Physics*, *20*, 181–190.

ELLIS, F., 1968. Dose time and fractionation in radiotherapy. In *Current Topics in Radiation Research*, ed. by M. Ebert and A. Howard (North Holland Publishing Company, Amsterdam), pp. 359–397.

GILBERT, C. W., 1974. A double minus log transformation of mortality probabilities. *International Journal of Radiation Biology*, *25*, 633–634.

MAZERON, J. J., SIMON, J. M., LE PECHOUX, C., PIEDBOIS, P., LE BOURGEOIS, J. P. & PIERQUIN, B., 1991. Effect of dose-rate on local control and complications in definitive irradiation of T1–2 squamous cell carcinomas of mobile tongue and floor of mouth with iridium-192. *Radiotherapy and Oncology*, *21*, 39–47.

MEREDITH, W. S. (Ed.), 1967. *Radium Dosage; The Manchester System*, 2nd edn (Williams and Wilkins, Baltimore), p. 42.

PATERSON, R., 1963. *The Treatment of Malignant Disease by Radiotherapy*, 2nd edn (Edward Arnold, London).

PIERQUIN, B., 1971. Dosimetry: the relational system. In *Proceedings of Conference on Afterloading in Radiotherapy*, US Dept. of Health, Education and Welfare, publication number (FDA) 72-8024 (Rockville, New York) pp. 204–227.

PIERQUIN, B., CHASSAGNE, D., BAILLET, F. & PAINE, C. H., 1973. Clinical observations on the time factor in interstitial radiotherapy using iridium 192. *Clinical Radiology*, *24*, 506–509.

QUIMBY, E. H. & CASTRO, V., 1953. The calculation of dosage in interstitial radium therapy. *American Journal of Roentgenology*, *70*, 739–749.

TRAVIS, E. L., THAMES, H. D., WATKINS, T. L. & KISS, I., 1987. The kinetics of repair in mouse lung after fractionated irradiation. *International Journal of Radiation Biology*, *52*, 903–919.

TURESSON, I. & THAMES, H. D., 1989. Repair capacity and kinetics of human skin during fractionated radiotherapy: erythema, desquamation, and telangiectasia after 3 and 5 year's follow-up. *Radiotherapy and Oncology*, *15*, 169–188.

WITHERS, H. R., THAMES, H. D. & PETERS, L. J., 1982. Differences in the fractionation response of acutely and late responding tissues. In *Progress in Radio-Oncology*, Vol II, ed. by K. H. Karcher, H. D. Kogelnik and G. Remartz (Raven Press, New York), pp. 287–296.

1992, *The British Journal of Radiology*, *65*, 248–251

Neoadjuvant intra-arterial chemotherapy in inflammatory carcinoma of the breast

By J. I. Bilbao, MD, *J. Rebollo, MD, J. M. Longo, MD, F. Mansilla, MD, *L. Muñoz-Galindo, MD and *J. M. Vieitez, MD

Departments of Radiology and *Oncology, Clínica Universitaria, Facultad de Medicina, Universidad de Navarra, Pamplona, Spain

(*Received 4 February 1991 and in revised form 18 July 1991, accepted 3 October 1991*)

Keywords: Breast cancer, Neo-adjuvant chemotherapy, Intra-arterial chemotherapy

Abstract. From 1982 to 1989, 18 eligible patients (median age 50.5 years, range 30–72 years) with inflammatory breast carcinoma have been treated with neoadjuvant intra-arterial (IA) chemotherapy. The treatment regimen includes IA cisplatin, adriamycin, mytomycin C and thiotepa on Day 1 and intravenous 5-fluorouracil on Days 1 and 2. An objective clinical response rate of 100% (eight complete and 10 partial) has been observed. The median disease-free and overall survivals are 27 months (range 5–85+ months) and 33 months (range 8–85+ months), respectively. With a median follow-up of 21.5 months, six (33.3%) patients remain alive and free of disease and 12 patients have died because of distant metastases. No local recurrences have been observed. Intra-arterial chemotherapy is an attractive technique for the treatment of locally advanced breast carcinoma with mild toxicity and high local control rate.

Inflammatory carcinoma is the most aggresive type of breast cancer. With local methods of treatment (surgery and/or radiotherapy) high local tumour control rates can be achieved, ranging from 50% to 80% (Barker et al, 1976; Ellis & Teistelbaum, 1974; Sicher & Waterhouse, 1973). However, long-term survival is poor (5% 5-year survival rate), because most of the patients have micrometastases at the moment of diagnosis.

In patients with locally advanced (Stage III) breast cancer, the use of neoadjuvant systemic chemotherapy has shown a 70–80% response rate and a 5-year survival rate of 30% (Hortobagyi & Buzdar, 1986). This long-term survival compares favourably with that achieved with the use of local therapies. Hence, neoadjuvant chemotherapy was included in the protocols designed for the treatment of locally advanced breast carcinoma.

Intra-arterial (IA) chemotherapy is an attractive technique that allows one to achieve high drug concentrations at the tumour site using catheters placed in the regional vessels (internal mammary and distal axillary arteries) (Koyama et al, 1975). The most encouraging results with IA therapy have been observed in some localized tumours of the limbs, head and neck, and stomach (Stephens, 1983).

Results with neoadjuvant IA chemotherapy in a series of patients with inflammatory breast carcinoma are presented.

Materials and methods

Selection criteria were (1) inflammatory carcinoma and (2) absence of distant metastases at diagnosis. The presence of axillary lymph node metastases was not a criterion for exclusion. Previous staging work-up included physical examination, complete blood count, liver profile, serum creatinine, echogram or computed tomographic (CT) scan of the liver, bone scintigraphy, chest radiographs and biopsy of the tumour.

Treatment protocol

An angiographic catheter is placed intra-arterially, using the Seldinger technique, through the common femoral artery and occasionally through the left or right axillary arteries. Catheters used were: Judkins right coronary 7F (USCI), Judkins right coronary 5F (CORDIS) and selective mammary 7F (CORDIS). The tip of the catheter is placed in the internal mammary (internal thoracic) artery; approximately 40–60% of the chemotherapeutic dose is administered selectively in this artery and the other 40–60% in the subclavian artery with a distal compressive cuff in the arm to include the axilla and related areas or, in some cases, selectively in the lateral thoracic artery. The infusion time ranges from 5 to 15 min.

Treatment regimen

IA therapy. Before the procedure, adequate hydration with normal saline at 150 ml/h infusion rate for 3–4 h, 125 mg of methylprednisolone and 10 mg of deschlorpheniramine are administered. IA treatment consists of adriamycin (ADR) 40 mg/m^2, cisplatin (CDDP) 60 mg/m^2, thiotepa (TSPA) 5 mg/m^2 and mytomycin C (MMC) 6 mg/m^2 on Day 1 and intravenous 5-fluorouracil (5-FU) 500 mg/m^2 as a continuous infusion on Days 1 and 2. Immediately after the IA procedure, 50 g mannitol is administered to prevent nephrotoxicity of cisplatin. The regimen is repeated every 4 weeks. The

---

*Address correspondence to: J. I. Bilbao, Department of Radiology, Clínica Universitaria de Navarra, Avda. Pío XII s/n, 31080 Pamplona, Spain.

Table I. Characteristics of the patients

No. of patients	18
Age (years)	
Median	50.5
Range	30–72
Menopausal status	
Pre-menopausal	8
Post-menopausal	10
Histology	
Ductal infiltrating	11
Lobular infiltrating	6
Undifferentiated	1
Nodal stage	
N0	3
N1	1
N2	11
N3	3

number of cycles administered changes according to the clinical tumour response and tolerance.

Surgery. One month after the last course of chemotherapy, modified radical mastectomy is performed.

Adjuvant therapy. A total dose of 50 Gy to the chest wall and axillary nodes, 30 Gy to the supraclavicular area and a 10 Gy boost to the surgical scar is administered. Adjuvant chemotherapy (six monthly cycles of cyclophosphamide, methotrexate and 5-fluorouracil) and/or hormonotherapy are administered from the start of radiotherapy according to different criteria such as pathological nodal stage, menopausal status and the presence of hormone receptors.

Response and toxicity criteria

Response and toxicity were evaluated following conventional criteria (Hayward et al, 1977; World Health Organization (WHO), 1979).

Statistical methods

Confidence intervals for response rates were calculated using standard techniques (Fleiss, 1981). Survival curves were estimated using the method of Kaplan and Meier (1958).

Results

From 1982 to 1989, 18 consecutive patients with inflammatory breast carcinoma were treated with neoadjuvant IA chemotherapy (Table I). Median age was 50.5 years (range 30–72 years). Ten patients were post-menopausal. Histologically there were 11 ductal infiltrating, six lobular infiltrating and one undifferentiated tumours. Tumour and nodal stages were as follows: 18 inflammatory, three N3, 11 N2, one N1 and three N0. None had either distant metastases or received previous therapy.

The total number of procedures was 49: one patient received four cycles, 12 patients three cycles, four patients two cycles and one patient one cycle. The internal mammary artery could not be selectively catheterized in 11 procedures and the drugs were infused at the origin of the subclavian artery and distal to the vertebral artery with a brachial compressive cuff (Table II).

Table II. Arteries used (49 procedures in 18 patients, one or two infused arteries in each procedure)

Artery	*n*
Internal mammary	22
Subclavian[a]	11
Axillary[a]	38
Lateral thoracic	6
Miscellaneous	2

[a]With a distal compressive cuff.

Response and follow-up (Table III)

Clinical response rate was 100% (81.4–100% at 95% confidence interval). Axillary nodes exhibited the same grade of clinical response as the primary tumour except in five patients, who presented a clinical complete response at the primary site and partial response in the regional nodes.

Histological study of the resected breast showed residual viable tumour cells at the primary site and regional nodes, with different grades of necrosis in all specimens but one, which presented complete pathological response.

IA chemotherapy was followed by radiotherapy in all patients: surgery in 17 patients (one patient who had achieved clinical complete response rejected mastectomy), chemotherapy in 12 and hormonotherapy in seven.

All patients with recurrence were treated with different protocols of chemotherapy that included several active agents. Chemotherapy was continued until progression or death.

Table III. Results and follow-up

Response	
Complete	8
Partial	10
Further treatment	
Radiotherapy	18
Surgery	17
Chemotherapy	12
Hormonotherapy	7
Follow-up	
NED	6
DWD	12
MDFS (months)	25
MOS (months)	33

NED: no evidence of disease; DWD: dead with disease; MDFS: median disease-free survival; MOS: median overall survival.

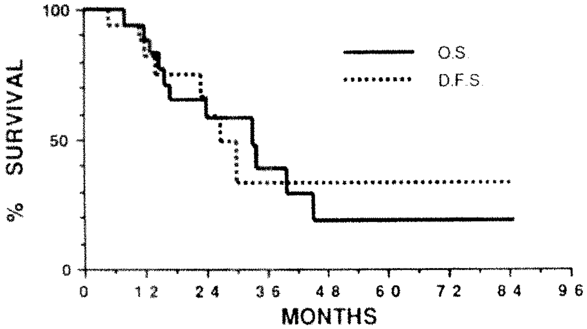

Figure 1. Actuarial median disease-free and overall survival according to Kaplan and Meier (1958).

Table IV. Toxicity

Local	
Hyperpigmentation	18
Reversible brachial nerve paralysis	1
Mammary pruritus	2
Cutaneous ulceration	1
Systemic	
Nausea/vomiting	18
Alopecia	18
Mucositis	1
Aplasia	1
Leukopenia	2
Nephrotoxicity	0

Figure 1 shows the actuarial disease-free and overall survival curves according to the Kaplan and Meier method. With a median follow-up of 21.5 months, six (33.3%) patients remain alive and free of disease at 18, 19, 24, 28, 68 and 85 months, respectively. The median actuarial overall survival is 33 months (range 8–85+ months) and the median disease-free actuarial survival 25 months (5–85+ months). 12 patients have died from distant metastases. No local recurrences have been observed.

Toxicity (Table IV)

Local. All patients presented with hyperpigmentation of the cutaneous area supplied by the internal mammary artery. One patient developed cutaneous ulceration so treatment was shifted to an intravenous route. Two patients developed significant mammary pruritus during the IA infusion time and one reversible brachial nerve paralysis. There have been no surgical complications attributable to IA therapy.

Systemic. All patients presented with some grade of nausea and/or vomiting and alopecia. Three patients presented with varying degrees of myelotoxicity (one patient Grade III and two Grade II).

Discussion

The principal aims in the treatment of locally advanced breast carcinoma with neoadjuvant chemotherapy are both to achieve the best response prior to local therapy (surgery and/or radiotherapy) and the systemic treatment of micrometastases that exist at diagnosis.

The response rate with neoadjuvant intravenous chemotherapy ranges from 70% to 80% and the 3-year survival rate has improved to 50% (Rouesse et al, 1986; Segel et al, 1988). Results with neoadjuvant IA chemotherapy have been reported by a number of groups in several countries. In all the experiences, response rates have been about 90% (Carter et al, 1988; de Dicker et al, 1988; Koyama et al, 1975; Noguchi et al, 1988). Noguchi et al (1988) have reported a 94% response rate in 27 patients with locally advanced breast carcinoma. The 5-year disease-free survival rates for patients with inflammatory and non-inflammatory carcinoma have been 20% and 56%, respectively (Stephens, 1990).

In the present series a 100% response rate has been observed. However, a histologically complete response has been seldom observed (only one out of 18 patients). The median actuarial disease-free and overall survivals have been 25 and 33 months, respectively. This compares unfavourably with previous reports and probably represents the need for a more aggressive adjuvant therapy; nevertheless, the local tumour control rate has been as high as 100%.

The internal mammary artery has to be catheterized for IA therapy; this vessel has been used for the treatment of other chest wall malignancies (Mattson et al, 1980), mesothelioma and lung carcinomas (Jonsson & Karlsson, 1985). The technique of cannulation of this vessel is well known and does not represent additional morbidity.

References

Barker, J. L., Nelson, A. J. & Montague, E. D., 1976. Inflammatory carcinoma of the breast. *Radiology, 121,* 173–176.

Carter, R. D., Fadis, D. M., Krementz, E. T., Salwen, W. A., Puyau, F. A. & Muchmore, J. H., 1988. Treatment of locally advanced breast cancer with regional intra-arterial chemotherapy. *Regional Cancer Treatment, 1,* 108–111.

de Dicker, R. P., Timmermann, J., Schumacher, T. & Schlinder, A. E., 1988. The influence of arterial regional chemotherapy on the local recurrence rate of advanced breast cancer. *Regional Cancer Treatment, 1,* 112–116.

Ellis, D. L. & Teistelbaum, S. L., 1974. Inflammatory carcinoma of the breast. A pathologic definition. *Cancer, 33,* 1045–1047.

Fleiss, S. L., 1981. *Statistical Methods for Rates and Proportions* (Wiley, New York).

Hayward, J. L., Carbone, P. P., Heuso, J. C., Kumaoka, S., Segaloff, A. & Rubens, R. D., 1977. Assessment of response to therapy in advanced breast cancer. *British Journal of Cancer, 13,* 89–94.

Hortobagyi, G. M. & Buzdar, A. V., 1986. Progress in inflammatory breast cancer: causes for a cautious optimism. *Journal of Clinical Oncology, 12,* 1727–1729 (Editorial).

Jonsson, K. & Karlsson, S., 1985. Angiography of the internal mammary artery. *Acta Radiologica, 26,* 113–120.

Kaplan, E. L. & Meier, P., 1958. Nonparametric estimation from incomplete observations. *Journal of the American Statistical Association, 53,* 457–481.

KOYAMA, H, WADA, T., NISHIZAWA, I. & TERASAWA, T., 1975. Intra-arterial infusion chemotherapy as a preoperative treatment of locally advanced breast cancer. *Cancer, 36,* 1603–1612.

MATTSON, W., MELLEKANT, C. & JONSSON, K., 1980. Intraarterial chemotherapy, (Letter to editor). *Lancet, 2,* 925.

NOGUCHI, S., MIYAUCHI, K., MISHIZAWA, Y., KOYAMA, H. & TERESAWA, T., 1988. Management of inflammatory carcinoma of the breast with combined modality therapy including intraarterial infusion chemotherapy as an induction therapy. Long-term follow-up results of 28 patients. *Cancer, 61,* 1483–1491.

ROUESSE, J., FRIEDMAN, S., SARRAZIN, D., MOURIESSE, H., LE CHEVALIER, T., ARRIAGADA, R., SPIELMANN, M., PAPACHARALAMBOUS, A. & MAY-LEVIN, F., 1986. Primary chemotherapy in the treatment of inflammatory breast carcinoma: a study of 230 cases from the Institut Gustave-Roussy. *Journal of Clinical Oncology, 12,* 1765–1771.

SEGEL, M. C., PAULUS, D. D. & HORTOBAGYI G. M., 1988. Advanced primary breast cancer: assessment with mammography of response to induction chemotherapy. *Radiology, 169,* 49–54.

SICHER, K. & WATERHOUSE, J. A., 1973. Evaluation of TNM classification of carcinoma of the breast. *British Journal of Cancer, 28,* 580–588.

STEPHENS, F. O. 1983. Clinical experience in the use of intra-arterial infusion chemotherapy in the treatment of cancers in the head and neck, the extremities, the breast and the stomach. *Recent Results in Cancer Research, 86,* 122–127.

STEPHENS, F. O., 1990. Intraarterial induction chemotherapy in locally advanced stage III breast cancer. *Cancer, 66,* 645–650.

WHO, 1979. *WHO Handbook for Reporting Results of Cancer Treatment.* (World Health Organization, Geneva, Switzerland).

1992, *The British Journal of Radiology*, 65, 252–257

The potential of ytterbium 169 in brachytherapy: a brief physical and radiobiological assessment

By *S. M. Loft, MSc, I. P. Coles, M.Sc, MInstP and R. G. Dale, PhD, FInstP, FIPSM

Riverside District Department of Medical Physics, Charing Cross Hospital, London W6 8RF, UK

(*Received 20 May 1991 and in revised form September 1991, accepted 3 October 1991*)

Keywords: Brachytherapy, Dosimetry, Radiobiology, Ytterbium 169

Abstract. Ytterbium 169 (half-life 32 days; mean gamma emission 93 keV, after excluding photons of energy < 10 keV) is a radionuclide with interesting potential for brachytherapy applications. Although not yet commercially available, its possible application as a clinical radionuclide is currently being considered by Amersham International. This article presents an assessment of some properties of the nuclide that may be clinically relevant. Use is made of some new ideas that allow quantification of the likely dose homogeneity that can be obtained in a brachytherapy distribution, and in this context ytterbium 169 is shown to be superior to some currently available brachytherapy nuclides. The assessment also uses recent extensions to the linear-quadratic model to consider the likely radiobiological implications associated with the use of the nuclide. From this it is suggested that the main potential for ytterbium 169 would be as a source that may be re-used for a number of short-term applications, rather than as a permanently implantable nuclide.

Only a limited number of radionuclides can be considered for brachytherapy applications. A review of available brachytherapy radionuclides has been given in *British Journal of Radiology* Supplement No. 21 (Trott, 1987), in which the important selection criteria relate to such aspects as half-life, emission characteristics, radiological protection considerations, ease of production, etc. These criteria, especially the last, severely limit the number of clinically useful nuclides. However, there are other considerations that could be added to the above list, including assessment of the intrinsic *clinical* usefulness of a nuclide, a property that has hitherto been difficult to quantify.

In recent years two new analytical tools (one physical and one radiobiological) have been developed. Each of these analytical techniques displays considerable potential, not only for assessing the outcome of individual brachytherapy treatments using "traditional" sources, but also in assessing the clinical usefulness of new brachytherapy nuclides.

After briefly discussing the production and properties of ytterbium 169 the main features of these analytical methods will be outlined, and then applied to an assessment of the clinical potential of the radionuclide.

Ytterbium 169: its production and principal physical properties

Ytterbium 169 has a half-life of 32 days and emits gamma radiations between 49 and 308 keV. The mean gamma energy is 93 keV (neglecting those energies below 10 keV, which have no dosimetric significance). The nuclide is produced by neutron activation of ytterbium oxide (Yb_2O_3). Very high-activity concentrations (comparable to those of iridium 192) may be produced, the only contaminant radionuclide present in any significant concentration being the short-lived ytterbium 175 (half-life 4.2 days). These properties suggest that both high-activity sources for high-dose-rate afterloading procedures, and permanently implantable interstitial sources, may readily be manufactured.

Assessment of dose uniformity in brachytherapy distributions by means of dose–volume histograms

The method of Anderson (1986) was introduced to provide a representative measure of dose (or dose-rate) uniformity in a brachytherapy distribution. Application of the technique to single- or multi-source distributions enables the development of a two-dimensional histogram, the area under which provides accurate representation of the volume of tissue receiving dose-rates within a specified range.

By assuming perfect inverse-square law obedience around point sources, Anderson has developed a function (dV/du) which, for a single source, is flat when plotted against a function [$u(D)$] of dose-rate, and which therefore suppresses the dominant inverse-square characteristic. The dose-rate transformation is given by:

$$u(D) = D_b^{-3/2} - D^{-3/2}$$

where D_b is the dose-rate at the centre of the lowest dose-rate interval considered.

The method has been further extended (Loft & Dale, 1990) in order to allow for deviations from true inverse-square behaviour; *i.e.* the effects of beam degradation, scatter and absorption have been allowed for. Such allowance is especially relevant for low-energy sources, but is of less significance for higher-energy gamma emitters. The modifications are achieved by incorporating specific tissue/nuclide radial dose functions (Dale, 1982, 1986) within the Anderson formulation, which lead to an expression for $\mathrm{d}V/\mathrm{d}u$ for single sources as follows:

---

*Present address: Department of Medical Physics and Bio-Engineering, Weston Park Hospital, Sheffield S10 2SJ, UK.

$$\frac{\mathrm{d}V}{\mathrm{d}u} = \frac{8\Pi(AC_s)^{3/2}[g(r)]^{5/2}}{3[rg'(r) - 2g(r)]} \tag{1}$$

where A is the source activity and C_s the specific dose constant, which defines tissue dose-rate at unit distance from an implanted point-source of unit activity. (This is the definition of C_s as originally used by Dale (1982). It should be noted that some recent articles by other authors define specific dose constant in terms of air kerma strength rather than source activity.)

The function $g(r)$ is of the general form:

$$g(r) = a_0 + a_1 r + a_2 r^2 + \tag{2}$$

where r is the distance from the source and a_0, a_1, etc., are constants specific to a particular tissue/nuclide combination. $g'(r)$ is the first differential of Equation (2). When the dose fall-off around a source perfectly obeys the inverse-square law, $a_0 = 1$, and $a_1 = a_2 = \ldots = 0$, and Equation (1) reduces to:

$$\frac{\mathrm{d}V}{\mathrm{d}u} = \frac{4\Pi S^{3/2}}{3} \tag{3}$$

where $S = AC_s$. Equation (3) is the standard Anderson equation for a perfect source for which, in contrast to the more general form given by Equation (1), the value of $\mathrm{d}V/\mathrm{d}U$ is constant and independent of r.

The histogram method is of clinical value in its application to multi-source implants, for which it allows quantitative assessment of unavoidable geometrical inhomogeneities. In such cases the area under the $\mathrm{d}V/\mathrm{d}u$ curve is a measure of the volume of tissue receiving dose-rates between specified dose-rate limits. However, for predicting the implantation properties of a nuclide, it is necessary only to consider the case of single sources.

Radiobiological assessment of brachytherapy treatments using the linear-quadratic model

The linear-quadratic (LQ) model, making use of fractionation factors in the form of α/β ratios, is well established in fractionated radiotherapy. The model has been further developed (*e.g.* Barendsen, 1982; Thames, 1985; Curtis, 1986) in order for it to be more generally applicable to other types of radiotherapy.

For temporary or permanent implants of decaying radionuclides, Dale (1985, 1989a) has developed LQ equations that allow calculation of the relative effectiveness of the treatment for a variety of radiobiological circumstances. One of the main results of such analyses is that it has been recognized that there is a likelihood that, with permanent implants of relatively long-lived nuclides, a considerable portion of the delivered dose may be "wasted" in combatting concurrent tumour repopulation. Although the amount of dose wastage will depend on the relative values of the critical radiobiological parameters (Ling, 1991), the main point is that higher total doses will need to be prescribed in cases where the wastage phenomenon is significant. This will cause adjacent normal tissues to receive higher total doses than if a nuclide with a shorter half-life were used.

The LQ equations associated with such assessments tend to be complex, but for what follows in this article it is necessary only to define the "effective life" of a decaying nuclide that has been permanently implanted into a tumour. This quantity may be expressed in terms of the radionuclide decay constant (λ) and the initial dose-rate (R_0) delivered by the nuclide to the tumour (Dale, 1989a), and is calculated from:

$$\text{Effective life} = -\frac{1}{\lambda}\ln\frac{K}{R_0} \tag{4}$$

where K is defined by:

$$K = 0.693/(\alpha\Phi)$$

α being the intrinsic radiosensitivity (Gy^{-1}) of the implanted tissue and Φ the clonogenic cell doubling time (days). In broad terms, a K value of around 2 Gy per day corresponds to a fast-growing and/or insensitive tumour, whilst K values of around 0.2 Gy per day or less correspond to sensitive and/or slow-growing tumours.

The essential feature of Equation (4) is that it indicates that effective treatment time is shorter in tumours that are relatively radioresistive (small α) and/or have a small doubling time (small Φ), and which are treated with relatively long-lived nuclides (small λ). Because a long-lived permanently implanted nuclide delivers dose over a long period, the initial dose-rate is always low. A high degree of radiation wastage is therefore predicted in unfavourable cases. It has previously been suggested (*e.g.* Marchese et al, 1984; Lee et al, 1988) that low initial dose-rates may be ineffective for eradicating tumours with fast growth kinetics.

The predicted characteristics of ytterbium 169 in various body tissues

Tissue-specific dosimetry

The dose-rate (D_r) at distance r from an unfiltered point-source of a given radionuclide in a given body tissue may be expressed in general terms as:

$$D_r = A \times C_s \times g(r)/r^2 \tag{5}$$

where A is the point-source activity (in becquerels), and C_s and $g(r)$ are, respectively, the specific dose constant (SDC) and radial dose function (RDF) computed by Monte-Carlo simulation for the specified tissue/nuclide combination (Dale, 1985; 1986). SDC has units of $\mathrm{Gy\,h^{-1}\,Bq^{-1}\,m^2}$, whilst RDF is a dimensionless polynomial function of the form given by Equation (2).

SDC and RDF may be derived from simulations that take account of the nuclide emission spectra, and that also allow for the attenuation characteristics of various body tissues and organs using the extensive compilations of White and Fitzgerald (1977).

By comparing SDCs for various body tissues, some intrinsic difficulties with low-energy emitters (such as

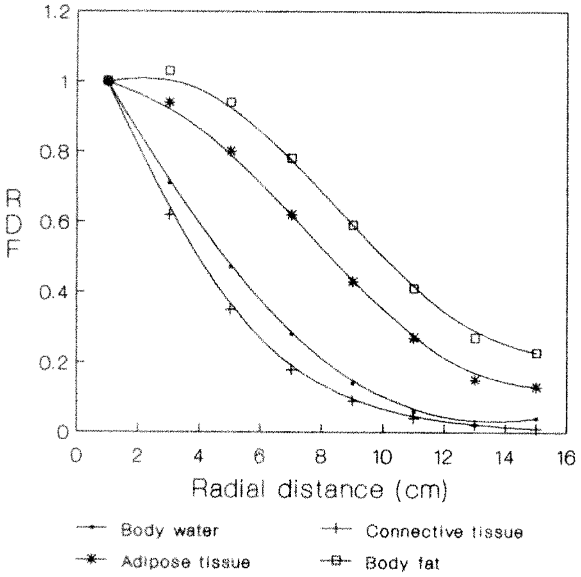

Figure 1. RDFs for unfiltered iodine 125 in four body tissues.

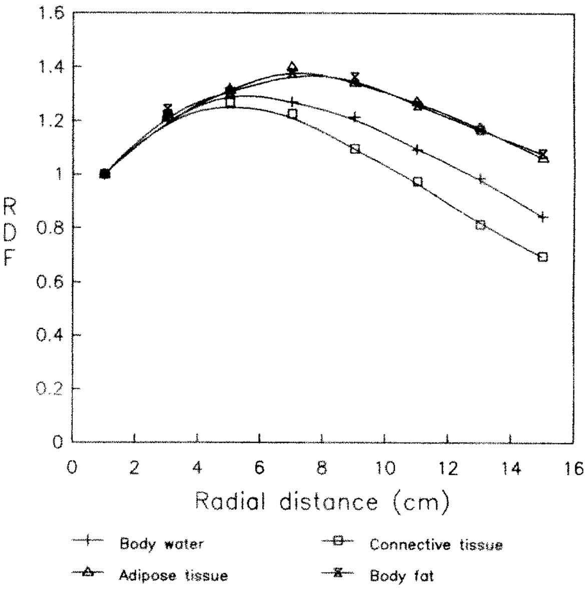

Figure 2. RDFs for unfiltered ytterbium 169 in four body tissues.

iodine 125) have previously been identified (Dale, 1982). Essentially these stem from the quite different photoelectric absorption characteristics that exist between tissues (due primarily to variations in carbon content). For fatty tissues in particular (e.g. adipose tissue and body fat), this can give rise to significant underdosage when low-energy emitters are used. The shapes of the $g(r)$ curves for low-energy emitters also vary significantly between tissues (Dale, 1986), as is demonstrated in Fig. 1.

In a recent paper (Loft & Dale, 1989) this effect has been further investigated, leading to the conclusion that emitters with an intermediate gamma energy (i.e. in the approximate range 60–200 keV) hold most promise because their photon energies are high enough to minimize the photoelectric interactions in soft tissue, but are low enough not to require excessive radiation shielding. The ideal nuclide will have principal emissions towards the lower end of this range, and it is in this context that ytterbium 169, with an emission spectrum including dominant lines at around 50 keV, appears to be particularly worthy of investigation.

The tissue-specific characteristics of ytterbium 169 (in terms of SDCs and RDFs) have been derived from Monte-Carlo simulation, and are summarized in Table I. The figures presented in the table are yet to be validated experimentally, but are in good agreement with the theoretical data of Mason et al (1991). Figure 2 shows the plotted $g(r)$ functions, from which it will be clear that the variability between tissues is of small significance with ytterbium 169, in contrast to the case where iodine 125 is used (Fig. 1).

Away from the transverse seed axis, the radial dose behaviour around commercially produced ytterbium sources displays a degree of anisotropy which is less than that associated with iodine-125 seeds. These

Table I. Theoretically derived coefficients of the radial dose function ($g(r)$), and specific dose constants for ytterbium 169 in four different body tissues.

Tissue	Coefficient				SDC[a]
	a_0	a_1	a_2	a_3	
Body water	0.8440	0.178	−0.020	0.00057	1.48
Connective tissue	0.8398	0.19	−0.025	0.00075	1.50
Adipose tissue	0.8457	0.166	−0.015	0.00035	1.29
Body fat	0.8501	0.17	−0.017	0.0004	1.20

[a] The units of SDC are Gy $m^2s^{-1}Bq^{-1}$ ($\times 10^{-17}$). To convert to cGy $cm^2h^{-1}mCi^{-1}$ the values in the column should be multiplied by 1.332.

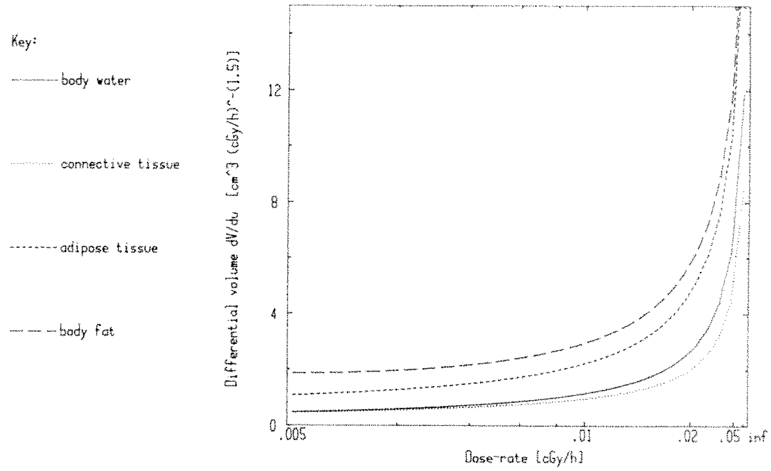

Figure 3. Modified Anderson histogram for a single source of iodine 125 in four body tissues.

aspects have been investigated in depth by Mason et al (1991).

Dose-homogeneity characteristics

In order to assess how the radial dose characteristics are likely to affect brachytherapy dose homogeneity, the modified Anderson histogram method, discussed earlier, has been used to derive plots of dV/du against $u(D)$ for point sources of both iodine 125 and ytterbium 169 in different body tissues (Figs 3 and 4, respectively).

In the case of iodine 125, the non-homogeneous behaviour of the nuclide is again clear, as is the lack of any discernible peak in any of the plots. The presence of a peak would be a useful indicator that enhanced dose uniformity might be achieved in a multi-source implant.

For ytterbium 169, the position is considerably improved. The dV/du plots demonstrate much less variation over a wide range of dose-rate (and hence distance from the source), and also exhibit definite peaks in the vicinity of the source. The existence of these peaks shows that the inverse square fall-off is being partially offset by build up of scatter close to the source, this being a key characteristic of emitters with photon energies in the range 60–200 keV.

Likely radiobiological characteristics

In order to make a meaningful assessment of the likely radiobiological properties of ytterbium 169, the characteristics of iodine 125 and gold 198 will first be compared. These nuclides are chosen on account of their very different half-lives (60 and 2.7 days, respectively). For these comparisons any differences in radiobiological effectiveness (RBE) are not taken into account.

We begin by considering the case of a gold grain implant designed to deliver a total dose of 70 Gy. The initial dose rate (R_0) is derived from the decay constant (λ, equal to 0.693/half-life) by:

$$R_0 = 70 \times 0.693/2.7 = 17.97 \text{ Gy day}^{-1}.$$

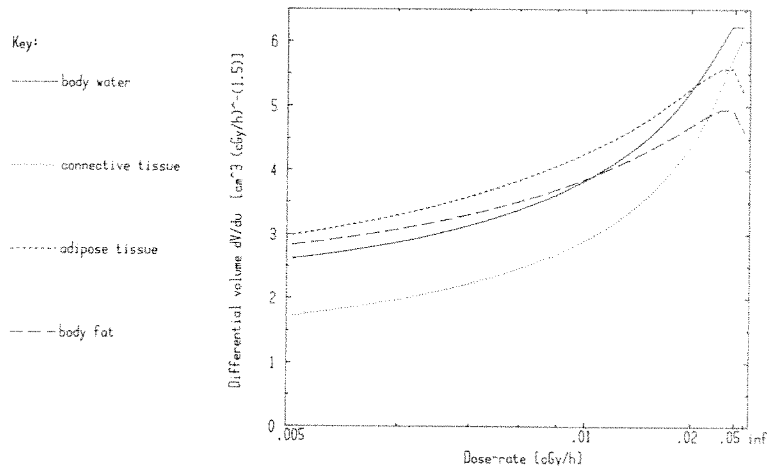

Figure 4. Modified Anderson histogram for a single source of ytterbium 169 in four body tissues.

For a tumour with a K value of 0.5 Gy day^{-1}, the effective treatment time is calculated from Equation (4) as being 14.3 days. At the end of this period, 97.2% of the prescribed total dose has been delivered, *i.e.* only 2.8% of the dose is "wasted".

For an iodine-125 implant designed to delivery the same total dose, the initial dose-rate would need to be 0.81 Gy day^{-1}. Repeating the above calculation, the effective treatment time for this nuclide is found to be 41.8 days, at which time only 38% of the total prescribed dose has been delivered, *i.e.* for iodine 62% of the prescribed dose of 70 Gy is "wasted". This "radiobiological inefficiency" may partly explain why much higher total doses are commonly prescribed with iodine seed implants (Ling, 1991), 160 Gy not being an uncommon figure. For ytterbium 169 (half-life 31 days), the initial dose-rate required for 70 Gy during complete decay is 1.56 Gy day^{-1}, and with a tumour K value of 0.5 Gy day^{-1} the effective treatment time is 50.8 days, at which time 68% of the dose has been delivered. Therefore, 32% of the prescribed 70 Gy remains wasted, even though the half-life of ytterbium is half that of iodine 125. It is therefore predicated that, for tumours with K values of this order, doses with permanent implants of ytterbium would have to be increased to be effective, but would probably be less than those routinely prescribed for iodine implants.

From this restricted radiobiological analysis it would appear that ytterbium may have limited value as a permanently implantable source. Its main strength would lie in its application in short-term removable implants, for which its half-life would allow re-use of a source stock several times over. (Early commercial production of ytterbium 169 has made the nuclide available in the form of seeds mounted in suturable ribbons. These are currently undergoing initial clinical evaluation for short-term implantation (Amersham International, private communication)).

Discussion

The degree of dose (or dose-rate) homogeneity attainable within any form of brachytherapy treatment (*e.g.* a seed implant, afterloaded gynaecological treatment, flexible wire application, etc.) will inevitably always fall well short of that available in a multi-field external-beam treatment. Equally, however, brachytherapy remains an important mode of cancer therapy, primarily because it offers better dose localization in the tumour and easier limitation of dose to normal tissues. Modern afterloading devices exploit these basic advantages and have allowed an expanding range of sophisticated treatments to be considered.

For non-afterloaded seed or wire applications it has long been held that delivery of radical doses over an uninterrupted period of 5–7 days offers the best chance of cure in rapidly dividing tumours (Fowler, 1988). Recent radiobiological assessments, both experimental and theoretical, support the view that low-dose-rate continuous radiotherapy offers many of the same advantages as accelerated hyperfractionation (Fowler, 1986, 1988; Steel, 1988; Dale, 1989b). It has been additionally suggested (Ling et al, 1985) that the use of low dose-rate may partially circumvent the problem of hypoxic cell radioresistance.

There thus remains a continuing requirement for brachytherapy as a treatment method in a significant number of clinical cases. Because of this, there is a commensurate need to continue to develop methods that can be used to provide useful quantitative measures of brachytherapy treatment quality. Until recently, the assessment of brachytherapy nuclides has been restricted to consideration of a limited number of basic physical properties. However, with the advent of Anderson's mathematical technique for examining the degree of dose homogeneity available within a brachytherapy implant, and with new ways of assessing radiobiological effectiveness, more advanced predictive techniques can now be employed.

Such techniques have been used here to demonstrate that ytterbium 169 possesses characteristics that make it a good contender as a brachytherapy nuclide. Whilst satisfying the majority of "established" selection criteria that are normally applied to brachytherapy sources, ytterbium offers essentially uniform radial-dose characteristics in a variety of soft tissues, regardless of their elemental composition. At the same time, using the modified Anderson method for homogeneity assessment, it has been shown that the expected homogeneity in any implant using ytterbium is likely to be superior to that obtainable with nuclides of either higher or lower energy.

Radiobiological predictions on the inherent efficacy of a decaying nuclide, although fundamentally important, are more controversial, and the methods of assessment described here remain essentially theoretical, not having been the subject of rigorous experimental investigation. However, clinical experience has shown the benefits of fixed-term low-dose-rate implants for aggressively growing tumours, and the extended LQ formulation supports that finding. Equally, for a given tumour response, permanent implants with a decaying source require substantially increased total doses if long half-life nuclides are employed, and this again is borne out by current radiobiological theory.

This correspondence of theory and clinical experience is not irrefutable proof of assumed underlying radiobiological mechanisms, but the case for considering ytterbium as a suitable nuclide for short-term (as opposed to permanent) implantation remains a strong one.

In summary:

1. Ytterbium 169 is capable of being produced in high specific activities.
2. The energy spectrum provides broadly similar dose fall-off characteristics in all implantable body tissues, especially in the range 0–5 cm.
3. When analysed according to the modified Anderson method, the nuclide behaviour in all tissues demonstrates a desirable peak in the plots of dV/du, indi-

cating a likelihood of better dose uniformity than for nuclides with higher or lower energies.

4. Although the half-life of ytterbium 169 is half that of iodine 125, ytterbium may not always be significantly better than iodine for permanent implants in tumours that are insensitive and/or rapidly dividing.
5. It is likely that ytterbium 169 could find potential as a re-usable brachytherapy source for short-term applications.

Acknowledgments

The authors gratefully acknowledge the technical help and support provided by Mr Keith Fletcher (Amersham International plc). Dr Arthur Porter and his colleagues (London Regional Cancer Center, Ontario, Canada) and Drs Lowell Anderson and Clifton Ling (Memorial Sloane-Kettering Hospital, New York) are also thanked for stimulating discussions and ideas.

References

Anderson, L. L., 1986. A "natural" volume–dose histogram for brachytherapy. *Medical Physics, 13*, 898–903.

Barendsen, G. W., 1982. Dose fractionation, dose-rate and iso-effect relationships for normal tissue response. *International Journal of Radiation Oncology, Biology, Physics, 8*, 1981–1997.

Curtis, S. B., 1986. Lethal and potentially lethal lesions induced by radiation — a unified repair model. *Radiation Research, 106*, 252–270.

Dale, R. G., 1982. A Monte-Carlo derivation of parameters for use in the tissue dosimetry of medium and low energy nuclides. *British Journal of Radiology, 55*, 748–757.

Dale, R. G., 1985. The application of the linear-quadratic dose–effect equation to fractionated and protracted radiotherapy. *British Journal of Radiology, 58*, 515–528.

Dale, R. G., 1986. Revisions to radial dose function data for ^{125}I and ^{131}Cs. *Medical Physics, 13*, 127–135.

Dale R. G., 1989a. Radiobiological assessment of permanent implants using tumour repopulation factors in the linear-quadratic model. *British Journal of Radiology, 62*, 241–244.

Dale, R. G., 1989b. Time-dependent tumour repopulation factors in linear-quadratic equations — implications for treatment strategies. *Radiotherapy and Oncology, 15*, 371–382.

Fowler, J. F., 1986. Potential for increasing the differential response between tumours and normal tissues: can proliferation rate be used? *International Journal of Radiation Oncology, Biology, Physics, 12*, 641–665.

Fowler, J. F., 1988. Dose–rate effects in normal tissues. In *Brachytherapy 2, Proceedings of the 5th International Selectron Users Meeting, The Hague*, ed. by R. F. Mould (Nucletron International B.V., Leersum, The Netherlands).

Lee, F., Torp-Pederson, S., Meiselman, L., Siders, D. B. & Littrup, P., 1988. Transrectal ultrasound in the diagnosis and staging of local disease after I-125 implantation for prostatic cancer. *International Journal of Radiation Oncology, Biology, Physics, 15*, 1453–1459.

Ling, C. C., 1991. Permanent implants using Au-198, Pd-103 and I-125: radiobiological considerations based on the α/β model. *International Journal of Radiation Oncology Physics* (in press).

Ling, C. C., Spiro, I. J. & Stickler, R., 1985. The variation of OER with dose-rate. *International Journal of Radiation Oncology, Biology, Physics, 11*, 1367–1373.

Loft, S. M. & Dale, R. G., 1990. The incorporation of specific tissue/nuclide attenuation data into the Anderson method for producing brachytherapy volume–dose histograms. *Physics in Medicine and Biology, 35*, 1519–1531.

Marchese, M. J., Hall, E. J. & Hilaris, B. S., 1984. Encapsulated ^{125}I in radiation oncology, I: Study of the relative biological effectiveness (RBE) using low dose-rate irradiation of mammalian cell cultures. *American Journal of Clinical Oncology, 7*, 607–611.

Mason, D. L. D., Battista, J. J., Barnett, R. & Porter, A. T., 1991. Ytterbium-169: calculated physical properties of a new radiation source for brachytherapy. *Medical Physics* (in press).

Steel, G. G., 1988. The radiobiological basis for low dose-rate radiotherapy. In *Brachytherapy 2, Proceedings of the 5th International Selectron Users Meeting, The Hague*, ed. by R. F. Mould (Nucletron International B.V., Leersum, The Netherlands)

Thames, H. D., 1985. An incomplete-repair model for survival after fractionated and continuous irradiation. *International Journal of Radiation Biology, 47*, 319–339.

Trott, N. G., (Ed.) 1987. *Radionuclides in Brachytherapy: Radium and After, BJR* Supplement 21. (British Institute of Radiology, London).

White, D. R. & Fitzgerald, M., 1977. A tabulation of 4th order polynomial coefficient calculated to fit the photon interaction data of 69 ICRP reference man tissues. *Health Physics, 33*, 628–633.

1992. *The British Journal of Radiology*, 65, 258–261

Technical notes

The application of microdosimetry to the metrology of low-energy X rays used in mammography

By *A. J. Waker, PhD and †M. Marco

Department of Medical Physics, University of Leeds, The General Infirmary, Leeds LS1 3EX, UK and
†Instituto de Estudios de la Energia, CIEMAT, Avenida Complutense 22, 28040 Madrid, Spain

(Received 18 March 1991 and in revised form 25 July 1991, accepted 4 September 1991)

Keywords: Microdosimetry, Dosimetry, X rays, Mammography

In a relatively recent contribution to this journal, Brenner and Amols (1989) published an article concerning the application of microdosimetry to the assessment of the radiological risk of mammography. The ultimate value of their work depends on whether the basic response function referred to in the paper and given in ICRU Report 40 (ICRU, 1986) truly reflects the relative efficiency of low-LET radiation for cancer induction. However, provided the particular response function employed can be expressed in terms of microdosimetric quantities the method itself is independent of the actual function and the paper of Brenner and Amols is a good illustration of the power of this type of analysis.

Microdosimetry is, however, more than just an interesting but somewhat esoteric branch of radiation physics. The objective of this communication is to show, using some preliminary mammographic data, how experimental microdosimetry as a measuring technique can be used to provide, in a direct manner, information concerning the quality of a radiation field and values of basic quantities such as absorbed dose and dose-rate.

Methods

The mammographic set used for the measurements was a Soredex Mamex dc, which is fitted with a molybdenum tube operated at a fixed current of 40 mA and applied potentials from 25 kV to a maximum of 31 kV. Total filtration is listed as 0.5 mm Al. The field size at the exit of the tube housing is 79 mm × 60 mm and the focus to cassette distance 65 cm. For the measurements described below the tissue-equivalent proportional counter (TEPC) used was a standard 0.5 in Rossi counter (Far West Technology, Goletha, California) placed in the centre of the beam directly below Perspex slabs of various thickness fixed to the tube housing. This set-up is by no means ideal but, based on the objective of the experiment and on materials easily to hand, was used out of expediency. Further studies obviously require the use of a more realistic phantom and measurement geometry. The Mamex dc was used with the maximum exposure time of 3.2 s and each measurement was made by summing the data recorded from three individual exposures. Figure 1 shows schematically the measuring arrangement.

The Rossi counter was filled with propane-based tissue-equivalent gas to a pressure of 8.7 kPa, which for this size of counter simulates a tissue site size of 2 μm. Tissue equivalence with respect to the TEPC refers to ICRU soft tissue and the mass energy absorption coefficients for the TEPC materials are for the photon range under consideration within 8% of breast tissue taken as 50% adipose and 50% glandular tissue. Signals from the TEPC are fed into two spectroscopy amplifiers set at two different gains a factor of 10 apart. In this way the whole range of pulse heights coming from the proportional counter could be covered and the complete spectrum constructed from the two overlapping sub-spectra. The output from each amplifier is recorded on a separate multichannel buffer card (EG&G Instruments Ltd). The proportional counter was calibrated by means of an internal alpha source (Waker, 1985) after which the voltage height of each pulse coming from the counter could be scaled in terms of the energy deposited. Each pulse arises from a single secondary electron produced by the primary photon field in the counter wall or cavity gas. Thus by carrying out pulse height

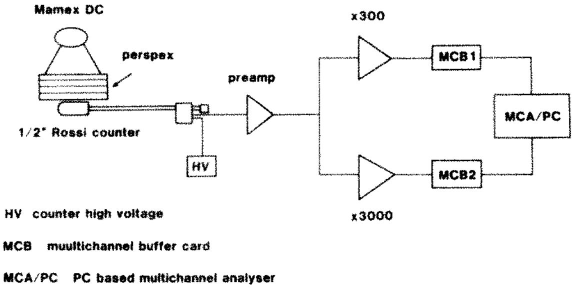

Figure 1. A schematic diagram of the experimental arrangement employed for microdosimetric measurements of an X-ray system used for mammography.

---

*Current address: AECL Research, Chalk River Laboratories, Chalk River, Ontario, Canada K0J 1J0.

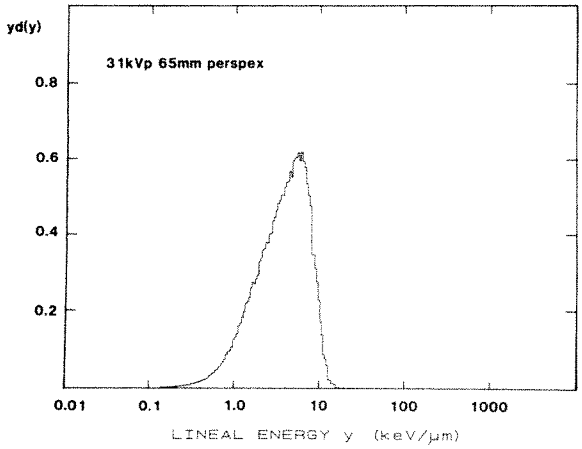

Figure 2. The microdosimetric event size spectrum for a 31 kVp beam and 65 mm of Perspex added filtration. The spectrum gives the fraction of the absorbed dose per logarithmic interval of linear energy and has been normalized such that equal areas under the curve represent equal fractions of the absorbed dose.

analysis the absorbed dose is determined on an event by event basis. The recorded pulse height spectrum itself contains information concerning the radiation field and it is usual to display microdosimetric spectra in terms of the fraction of the absorbed dose deposited as a function of the event size, where the event size is the imparted energy from a single event divided by the mean chord length of the sensitive volume which in this case is $2/3d$, where d is the simulated diameter of 2 μm.

Figure 2 shows an example of the recorded microdosimetric event size spectrum for 31 kV X rays and 65 mm Perspex. This spectrum has been normalized to unit dose and so the area under the curve between any two values of lineal energy gives the fraction of absorbed dose deposited by events of size between the two chosen values. It is these distributions of lineal energy that are used to fold into a given response function to obtain the total response and estimates of risk as demonstrated by Brenner and Amols. It is important to note, however, that the illustrated event size spectrum has been measured directly and that the elaborate calculations of Brenner and Amols to obtain such a distribution were carried out in lieu of making an experimental measurement as opposed to being the only way of obtaining such information.

The event size scale is divided into 50 equal logarithmic intervals per decade and before normalization the spectrum consists of the product of the event size y_i and the frequency with which it occurred during the measurement, $f(y_i)$, for each logarithmic interval i. The absorbed dose can then be calculated by summing over the six decades of event size and the dose-rate, $\dot{D}$, by dividing this summation by the measurement live-time, thus:

$$\dot{D} = \frac{1}{t} \cdot \frac{C}{m} \cdot \sum_{i=1}^{300} y_i f(y_i)$$

C is a factor that converts the accumulated event energy expressed in keV/μm into imparted energy in joules and depends on the simulated site size diameter, d, in μm thus:

$$C = (\tfrac{2}{3}d)[\mu\mathrm{m}] \cdot 1.6 \times 10^{-16}[\mathrm{J/keV}]$$

m is the mass of gas within the counter cavity (kg) and t the total live-time of the measurement(s). The calculation of the absorbed dose-rates and the evaluation of the event size spectra are carried out by a microcomputer operating directly on the measured pulse height spectrum. Multichannel analysers tend these days to be PC-based instruments and so data analysis can be carried out rapidly at the site of measurement.

Results and discussion

Table I, lists the calculated dose-rates, corrected for dead time, obtained by integration over the measured event size spectra for two tube high-voltage settings and various thicknesses of Perspex between tube and detector. For the purpose of this communication, which is to illustrate the use of experimental microdosimetric techniques in diagnostic X-ray dosimetry, the absorbed doses given in Table I are calculated from the counter

Table I. Dose-rates determined from microdosimetric spectra measured by summing three exposures of 3.2 s duration for each setting. Listed dose-rates are dead-time corrected. $\bar{y}_F$ and $\bar{y}_D$ are the frequency and dose averages derived from the measured spectra

kVp	Added filtration (mm Perspex)	Dose-rate (μGy/s)	Dead-time (%)	$\bar{y}_F$ (keV/μm)	$\bar{y}_D$ (keV/μm)
25	35	91.0	37	2.66	4.27
25	45	42.5	20	2.57	4.15
25	55	21.0	12	2.52	4.05
25	65	10.9	9	2.48	4.01
25	75	5.5	5	2.47	4.02
31	45	158.6	55	2.59	4.30
31	65	47.0	30	2.30	3.90
31	75	26.5	21	3.26	3.85

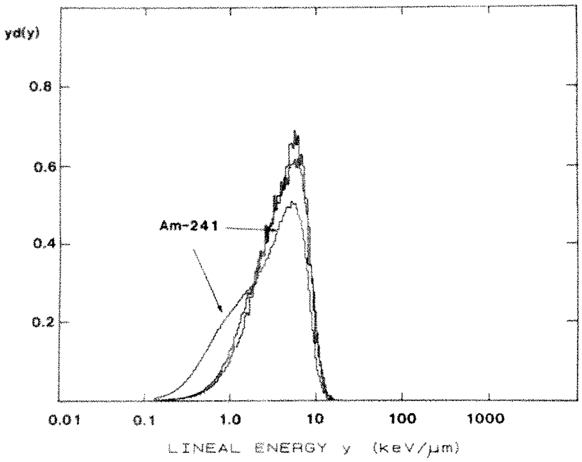

Figure 3. Microdosimetric event size spectra recorded for 31 kVp and 25 kVp beams with 65 mm Perspex and americium 241 60 keV photons.

readings with the assumption that the TEPC is operating as a Bragg–Gray cavity and that the absorbed dose to the A150 tissue-equivalent counter wall is the same as the absorbed dose to tissue. These assumptions are made for convenience and are not a limitation of the method. Cavity size corrections can be made and indeed experimental microdosimetry has been shown to be a good method for experimentally investigating cavity theory related to photon dosimetry (Dahmen et al, 1989; Waker & Eivazi, 1989). In a study of the response of tissue-equivalent proportional counters in low-energy standard ISO photon fields, it has been found that with a 2 μm simulated diameter the TEPC used in this work has a response of unity in terms of measuring the absorbed dose in water at a mean energy of 33 keV. As the response curve is already decreasing at this energy the absorbed dose recorded by the TEPC will underestimate the absorbed dose to tissue by an estimated 10% at 25 keV (Eivazi, 1990). Broad-beam linear attenuation coefficients can be derived from the data in Table I and give values of 0.0598 mm^{-1} and 0.0698 mm^{-1} for 31 kVp and 25 kVp beams, respectively, and first half-value layers (HVLs) of 11.6 mm and 9.9 mm in Perspex.

One of the most intractable problems with regard to the application of any counting technique with diagnostic X-ray equipment is that of the high count rates encountered. TEPC systems are no exception as indicated by the dead times given in Table I. Even at the highest count rate recorded in this work the dead time reflects more on the performance of the multichannel analyser as opposed to the TEPC itself. We estimate that at these count rates the probability of obtaining more than one event during the response time of the proportional counter is of the order of a few per cent. Thus the small increases in the microdosimetric frequency and dose mean values, given in Table I, which occur with decreasing filtration are probably the result of the increasing chance of pulse pile-up rather than a real change in radiation quality. Nevertheless, with current commercially available TEPCs the application of experimental microdosimetry will be restricted by count rate levels to measurements made in the centre of phantoms and exclude surface and shallow-depth dosimetry.

A method of reducing count rate problems that is in the control of the experimenter is to use a TEPC of smaller dimensions. Reducing the physical diameter of the counter by a factor of 10 will decrease the number of events per unit dose by a factor of 100. Building TEPCs of millimetre dimensions is difficult but not impossible (Rossi, 1984; Waker & Maynard, 1989) and would extend the range of application of the technique.

Figure 3 shows the measured event size spectra for the two tube potentials and for the same thickness of Perspex filtration. Shown also in the figure for comparison purposes is an event size spectrum for 60 keV photons from americium-241. The two spectra from the Mamex are almost identical showing a single peak at around 6 keV/μm and some 90% of the absorbed dose being delivered by events of size between 1 and 10 keV/μm. The spectra themselves are a result of the interaction of the secondary electrons produced by the primary photons and therefore reflect the nature of the secondary electron spectrum. The mean electron energies produced by the three photon fields are very similar, particularly for the Mamex fields, being between 11 and 15 keV from which event sizes of around 6 keV/μm would be expected. In the case of the 60 keV photons, however, almost 50% of the secondary electron energy is carried by the small number (10%) of photoelectrons produced. These electrons are of relatively high energy compared with the photoelectrons produced by the Mamex fields or the majority compton electrons produced by americium and it is these higher energy electrons that result in the shoulder at around 1 keV/μm in the americium-241 event size spectrum. As the fraction of energy carried by secondary electrons is dominated ($>90\%$) by photoelectrons below photon energies of 35 keV the mean electron energy and hence the shape of the event size spectrum will not change significantly over the range of tube potentials used in mammography.

The object of this communication has been to show that microdosimetry, apart from providing a means to estimate relative radiation risks, can be used as a direct experimental technique in dosimetry yielding values of absorbed dose and dose-rate in a manner that also facilitates some interpretation of the radiation field itself. Finally, it is of interest to compare the results of these experimental measurements with the conclusions of Amols and Brenner. This cannot be undertaken directly as the calculated event size spectrum in the paper of Brenner and Amols was not given. If, however, the reasonable assumption is made that the event size spectrum will not change significantly for the simulated diameter of 2 μm used in this work compared with that of the 1 μm used in the calculation, then the response function taken from ICRU Report 40 (1986) can be folded into the measured dose distribution for 25 kVp shown in Fig. 3 and compared with the relative risk factor reported by Brenner and Amols (1989) for 23 kVp. If this is done a value of 1.18 is obtained, which agrees within 10% with the figure of 1.29 quoted by Brenner and Amols (1989).

Acknowledgments

The assistance of Mr Stuart McArdle of the FAXIL group in the Department of Medical Physics in Leeds is gratefully acknowledged. This work has been supported by the British Council under the Acciones Integradas scheme.

References

Brenner, D. J. & Amols, H. I., 1989. Enhanced risk from low energy screen-film mammography X-rays. *British Journal of Radiology*, *62*, 910–914.

Dahmen, P., Menzel, H. G. & Grillmaier, R., 1989. Dosimetry of photons with low pressure proportional counters. *Radiation Protection Dosimetry*, *29*, 75–79.

Eivazi, M. T., 1990. Application of experimental microdosimetric techniques to the dosimetry of X-rays in the diagnostic energy range. PhD Thesis, University of Leeds.

ICRU, 1986. *The Quality Factor in Radiation Protection*, Report 40 (International Commission on Radiation Units and Measurements, Bethesda).

Rossi, H. H., 1984. Development of microdosimetric counters past present and future. *Radiation Protection Dosimetry*, *9*, 161–168.

Waker, A. J., 1985. Experimental uncertainties in microdosimetric measurements and an examination of the performance of three commercially produced proportional counters. *Nuclear Instruments and Methods in Physics Research*, *A234*, 354–360.

Waker, A. J. & Eivazi, M. T., 1989. The application of microdosimetric measurements to low energy X-rays. *Radiation Protection Dosimetry*, *29*, 81–85.

Waker, A. J. & Maynard, D. G., 1989. The effect of geometrical scaling on the gas gain of proportional counters intended for microdosimetric measurements. *Radiation Protection Dosimetry*, *29*, 37–40.

Accuracy of pelvimetry measurements on CT scanners

By J. P. Wade, BSc, MSc

East Anglian Regional Radiation Protection Service, Addenbrooke's Hospital, Hills Road, Cambridge

(Received 17 May 1991 and in revised form 25 July 1991, accepted 4 September 1991)

Keywords: Pelvimetry, Radiography digital, Pelvis measurement

There is an increasing awareness of radiation dose received by the patient and the use of low dose techniques is encouraged whenever possible. A low dose technique which is available is the use of the overview or scanogram facility on a computed tomography (CT) scanner to produce a digital radiograph for pelvimetry measurements instead of the conventional radiograph. Unfortunately ultrasound, which is the low dose technique, cannot be used for pelvimetry measurements because of the bone geometry. Several published papers discuss the dose reduction (of the order of 90%) which is received by the mother and the fetus by changing to CT pelvimetry examinations (Federle et al, 1982; Suramo et al, 1984; Dobson & Nelson, 1988), and the recent NRPB Report (1990) emphasized this dose reduction. As many district hospitals now have CT scanners, this technique is becoming more widely practised.

Whilst dose reduction is a major consideration when choosing a new technique, it is also important that the results obtained are as good or better than conventional techniques, since any inaccuracies may have serious repercussions and lead to complications during labour. For pelvimetries carried out on CT scanners, a lateral view or an antero-posterior (AP) scanogram, or both, is obtained of the pelvis and the required distances are measured on the viewing console using the distance measurement facilites provided in the software. A simple test is required to assess the accuracy of these measurements, which can be incorporated into the quality control surveys.

Technique

A uniform grid is an appropriate choice of object so that measurements both parallel and perpendicular to the direction of travel can be carried out. In the set of test objects produced by FAXIL (the Radiological Imaging Group, Department of Medical Physics, General Infirmary, Leeds), for the assessment of fluoroscopy equipment, there is a 26 cm diameter disc shaped object containing a regular grid of 2 cm pitch which is ideal for this purpose. The grid test object is placed in the scanning tunnel perpendicular to the direction the X-ray tube is pointing. When the X-ray tube is at the top as for an AP view then the test object should be lying horizontally, as shown in Fig. 1. The alignment lights are used to aid location of the plane where the axis of rotation occurs. A scanogram is performed with

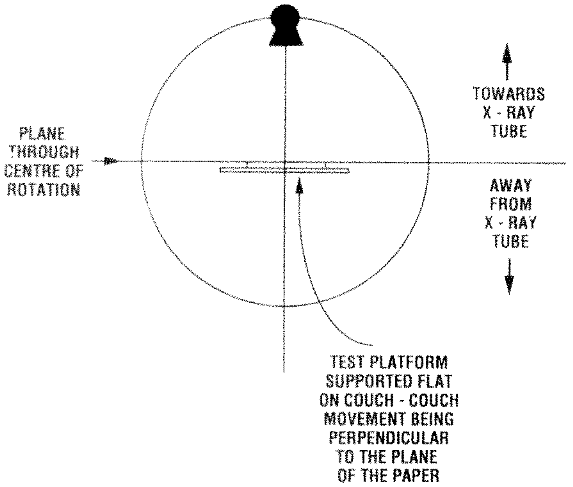
PLANE THROUGH CENTRE OF ROTATION
TOWARDS X-RAY TUBE
AWAY FROM X-RAY TUBE
TEST PLATFORM SUPPORTED FLAT ON COUCH - COUCH MOVEMENT BEING PERPENDICULAR TO THE PLANE OF THE PAPER

Figure 1. Diagram showing the set up of the grid phantom on the CT scanner.

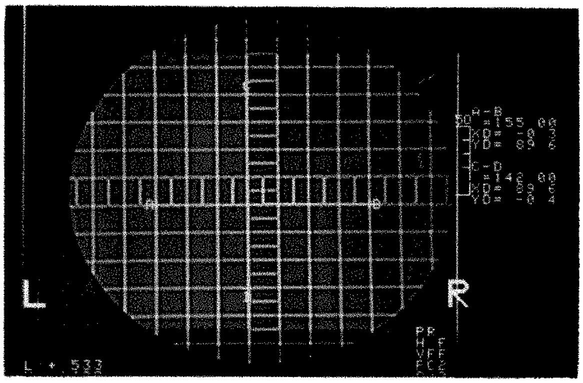

Figure 3. Scanogram of the test object moved 50 mm towards the X-ray tube.

the object lying in this plane, and further views can be carried out after moving the grid test object towards or away from the X-ray tube.

Distances can then be measured on the scanogram images, using the software facilities provided. If a number of scanograms are taken, at different focus–object distances, then the variation of magnification with distance from the midline can be obtained.

Results

This grid test object has now been used on five CT scanners (three different manufacturers). It was found that all measurements made on the image parallel to the direction of movement of the couch were accurate, but there were variations in the distances measured in the perpendicular direction. Images of the results from one scanner are shown in Figs 2, 3 and 4. For all three images the direction of movement is in the vertical direction of the image.

The first image (Fig. 2) is in the plane of rotation; the measurements in both directions are equal. The image shown in Fig. 3 shows the test object moved 5 cm towards the X-ray tube; measurements in the x direction have been magnified while those in the y direction are the same as in Fig. 1. The image shown in Fig. 4 shows the test object moved 5 cm away from the X-ray tube; measurements in the x direction are minified whilst those in the y direction are the same as in Fig. 1.

The results in Table I show how the measurement of a dimension on the phantom varies with the position of the phantom for several CT scanners. The images shown in Figs 2, 3 and 4 were obtained on scanner A; the results for three other scanners are also shown. With all the scanners, measurements taken on the centre plane were found to be within 5% of the expected value.

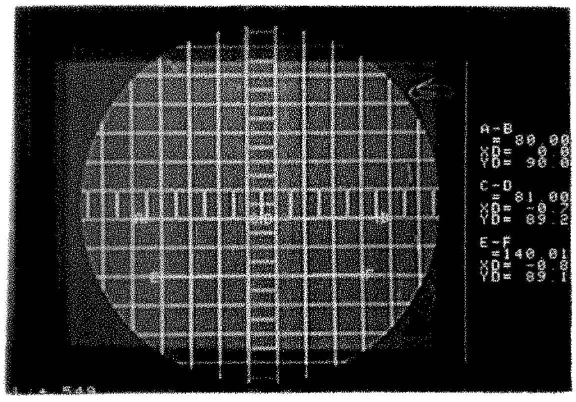

Figure 2. Scanogram of the test object positioned in the plane of the centre of rotation.

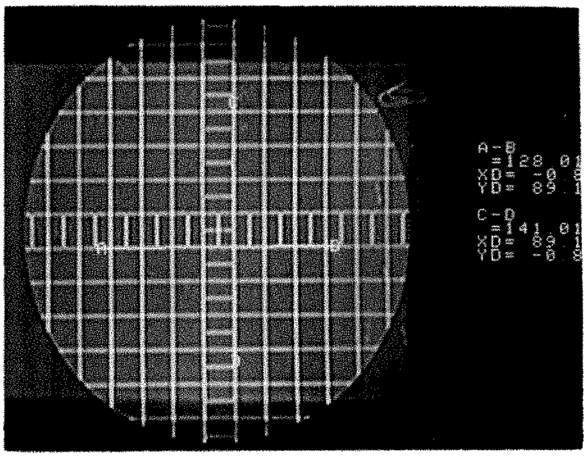

Figure 4. Scanogram of the test object moved 50 mm away from the X-ray tube.

Table I. Results of measurements taken with the test phantom at different distances from the plane of rotation

Distance from central plane (mm)	Measurement across 7 × 2 cm squares (mm) *i.e.* 140 mm	Reference to figures
Scanner A		
Towards Tube—85	169.60	
—80	167.28	
—75	165.71	
—50	155.00	Figure 3, A–B
—20	145.49	
Centre	140.01	Figure 2, E–F
Away from Tube—25	133.83	
—50	128.01	Figure 4, A–B
—75	122.17	
—100	116.73	
—115	113.62	
Scanner B		
Towards Tube—50	145.4	
Centre	134.31	
Away from Tube—50	127.8	
Scanner C		
Towards Tube—50	144.4	
Centre	136.5	
Away from Tube—50	127.8	
Scanner D		
Towards Tube—50	144.9	
Centre	135.2	
Away from Tube—50	125.4	

Discussion

As the use of scanograms is being encouraged for pelvimetry measurements, it is important for the user to know the measurements are accurate and the limitations of the scanner in use. With conventional radiographic techniques the pelvis measurements are normally quoted to the nearest 5 mm to the radiologist or obstetrician. For this accuracy to be achieved in CT pelvimetries without introducing an error caused by magnification, then the plane where measurements are required should be set to within 10 mm. In practice, it has been found that the pelvic inlet and pelvic outlet measurements taken on the lateral view are the most important dimensions and as these lie centrally in the body it is important to line up the patient carefully. On the anterior scout view, the transverse diameters of the pelvis are measured, but these will be at varying depths in the patient and so require different correction factors owing to the varying magnification. These measurements are not widely made because of the problems of defining the depth of these points in the patient (Lotz et al, 1987) and so using the right magnification.

It is important to verify the accuracy of distance measurements done on the scanogram where a CT scanner is used for pelvimetry as the accuracy appears to vary between models. There is very little information available from the manufacturer regarding the accuracy of measurements taken on the scanogram. This test has proved to be simple to perform and the results easy to evaluate and it should be incorporated into regular quality control procedures.

Acknowledgments

I would like to thank Mrs K. E. Goldstone for her encouragement and to the radiographers at the CT scanners, at various centres around East Anglia, for their help in doing these measurements.

References

Dobson, J. & Nelson, J., 1988. CT pelvimetry: replacing conventional with digital. *Radiography*, *54* (613), 18–19.

Federle, M. P., Cohen, H. A., Rosenwein, M. F., Braut-Zawadzki, M. N. & Cann, L. E., 1982. Pelvimetry by digital radiography: a low-dose examination. *Radiology*, *143*, 733–735.

Lotz, H., Ekelund, L., Hietala, S. O., Eriksson, L., Wicklund, D. E. & Wickman, G., 1987. Low dose pelvimetry with biplane digital radiography. *Acta Radiologica*, *28*, 577–580.

NRPB, 1990. *Patient Dose Reduction in Diagnostic Radiology*. Documents of the NRPB 1(3) (HMSO, London).

Suramo, I., Torniainen, P., Jouppila, P., Kirkinen, P. & Lahde, S., 1984. A low-dose CT-pelvimetry. *British Journal of Radiology*, *57*, 35–37.

1992, *The British Journal of Radiology*, 65, 264–265

A fine needle aspiration technique using high negative pressure

By *J. C. Rhymer, FRCS, D. W. McRobbie, BSc, MSc and J. E. Boultbee, FRCR

Department of Diagnostic Radiology, Charing Cross Hospital, Fulham Palace Road, London W6 8RF, UK

(*Received 24 May 1991, accepted 23 July 1991*)

Keywords: Aspiration

Ultrasound-guided aspiration for diagnostic or therapeutic purposes plays an important role in the management of thoracic, abdominal or pelvic fluid collections. The use of a fine needle is safe (Dewbury, 1990) having the advantages of minimal tissue trauma and minimal patient discomfort. The disadvantage of a small needle of 22 gauge is that its bore limits the rate of aspiration, which is significant in dealing with large or viscous collections. The use of a hand held syringe can be tiring for the operator and needle movement or displacement can occur during prolonged aspirations.

We describe a simple method of overcoming some of these disadvantages.

Method

The assembly consists of:

1. A 22 gauge spinal needle with a Quincke type point and a Luer Lok hub (Bector Dickinson & Co.).
2. A "Connecta" three way stopcock with a 10 cm extension tube and a Luer Lok fitting (Vigga-Spectramed).
3. A 50 cc or other suitably-sized syringe.

The fine needle is advanced into the collection using an aseptic technique after local anaesthesia. The placement of the needle is confirmed by aspirating fluid using a standard syringe, having withdrawn the stylet. The extension tube is used to connect the needle to the syringe. The three way tap at the syringe end of the tube is closed to the syringe, and the syringe plunger fully withdrawn and wedged in this position by inserting the plastic sheath, which protects the fine needle before use between the flange of the syringe plunger and the flange on the syringe barrel (Fig. 1). The three way tap is then opened and the collection aspirated.

Discussion

We have used this technique to aspirate serous and purulent collections. The use of the extension tube guards against needle displacement during movement of the syringe. It also allows intentional movement, repositioning the needle as the collection changes shape and size, whilst maintaining a continuous negative pressure. The three way tap allows the vacuum to be created in the syringe and is essential in the aspiration of pleural collections. The use of the plastic needle sheath means that no extra cost is incurred. The operator is not "tired" by continuous aspiration and is free to perform some other task whilst the syringe is filling. These factors, we believe, mitigate against needle tip displacement and increased tissue trauma.

Using "fish scales", we have calculated that some $96 \times 10^3\ \mathrm{Nn}^{-2}$ pressure is achieved in evacuating the tube, just less than 1 atm pressure. This pressure is compatible with values obtained using auto FNAC

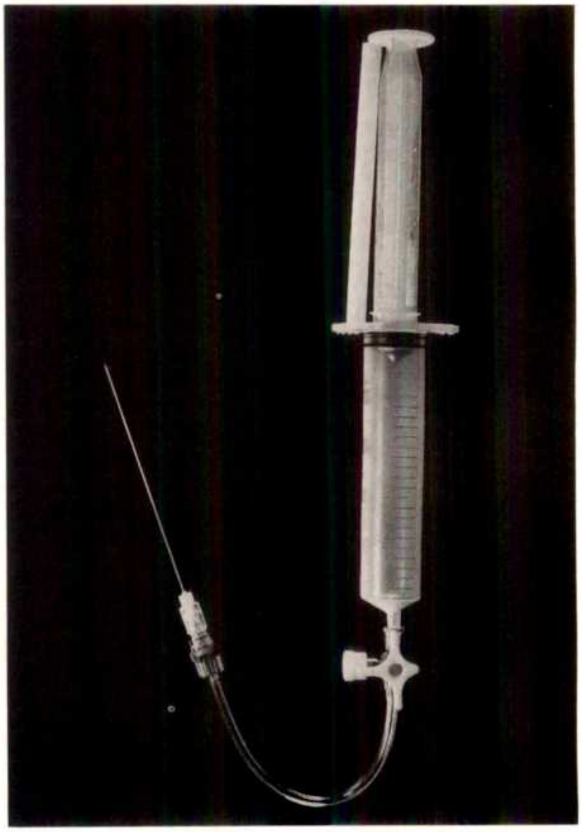

Figure 1.

---

*Present address: Department of Diagnostic Radiology, Queen Mary's Hospital, Roehampton, London SW15.

samplers as reported by Kreula (1990). For a non-viscous fluid such as water, a 20 ml syringe will fill in about 45 s using this assembly. The calculation does not take into account turbulence or friction, but agrees closely with experiments performed using the apparatus. The filling time is longer for viscous fluids such as pus.

References

DEWBURY, K. C., 1990. *Ultrasound in Techniques in Diagnostic Imaging*, ed. by G. H. Whitehouse & B. Worthington (Blackwell Scientific Publications, Oxford), p. 434.

KREULA, J., 1990. Suction and cell yield in fine needle aspiration biopsy. *Journal of Interventional Radiology*, *5*, 131–135.

1992, *The British Journal of Radiology*, *65*, 266–268

Case reports

Linear scleroderma and melorheostosis

By Alan Siegel, MD and *†Hadyn Williams, MD

Department of Radiology, Division of Nuclear Medicine, Hospital of the University of Pennsylvania, Philadelphia, Pennsylvania, USA and *Department of Nuclear Medicine, Veterans Administration Medical Center, Philadelphia, Pennsylvania, USA

(Received 5 March 1991 and in revised form 6 August 1991, accepted 4 September 1991)

Keywords: Melorheostosis, Scleroderma, Hyperostosis

Melorheostosis is an uncommon sclerosing bone dysplasia, which has been associated with other mesenchymal abnormalities. We present a patient with linear scleroderma who has radiographic and scintigraphic confirmation of melorheostosis. Bone scintigraphy in a patient with linear scleroderma and melorheostosis has not, to the best of our knowledge, been previously described.

Case report

A 65-year-old woman was admitted for treatment of bilateral plantar fasciitis.

Diagnosis of melorheostosis and linear scleroderma of the left leg was made in 1945 when the patient was 23 years of age. The disease process had reportedly been present since childhood. Owing to pain and limitation of movement in the left leg, she underwent a fasciotomy in the 1950s. Associated abnormalities include oesophageal dysmotility and Raynaud's phenomenon, for which she underwent a lumbar sympathectomy in 1953.

Examination of the left leg revealed skin thickening on the medial aspect from the knee to the lower leg. Multiple scars were present, secondary to previous surgery.

Radiographs revealed cortical hyperostosis of the medial femoral condyle, which apparently crossed the joint space, extended into the medial aspects of the proximal tibial plateau and continued down the entire length of the medial tibial diaphysis. There was narrowing of the medial compartment of the left knee (Fig. 1).

Bone scintigraphy, performed 4 h following intravenous administration of 925 MBq (25 mCi) of technetium-99m methylene diphosphonate, demonstrated increased activity in the medial left femoral condyle, crossing the joint space into the medial aspect of the tibial plateau. Non-continuous uptake was seen in the mid-left tibia medially. No abnormally increased uptake was seen elsewhere in the skeleton (Fig. 2).

Discussion

Melorheostosis, originally described in 1922 by Leri and Joanny, is a sclerosing dysplasia wherein the affected bone demonstrates a cortical or endosteal hyperostosis said to resemble dripping candle wax (Leri & Joanny, 1922). Although any bone may be involved, the appendicular skeleton is usually affected. The disease may be monostotic or, more frequently, polyostotic, but almost always involves a single limb. Characteristically, the involvement will be along one side of the involved bone, *i.e.* medial or lateral (Campbell et al, 1968).

Patients may be asymptomatic, or present with pain and/or limitation of motion (Campbell et al, 1968). The involved limb may be shortened, lengthened or bowed. There is no sex predilection and patients from birth to 71 years of age have presented with this disease (Fairbank 1948; Green et al, 1962; Wynne-Davies et al, 1985). Asymmetric contracture is the usual presenting complaint of infants and children (Younge et al, 1979). Heredity does not appear to be a factor and it is known that, at least in some cases, the skeletal changes are not present at birth. Melorheostosis tends to be slowly progressive (Campbell et al, 1968).

Melorheostosis has been associated with other abnormalities of mesodermal origin. These include glomus tumours, vascular naevi, haemangiomas, arteriovenous malformations, lymphangiectasia, lymphangiomas, neurofibromatosis, hypophosphataemic rickets and linear scleroderma (Morris et al, 1963; Campbell et al, 1968; Lee & Sanderson, 1989). Linear scleroderma represents a localized proliferation of connective tissue, which may overlie areas of melorheostosis (Wagers et al, 1972). It has been hypothesized that linear scleroderma and melorheostosis are manifestations of a congenital disorder of mesodermal development (Muller & Henderson, 1963; Wagers et al, 1972). The changes of scleroderma may present earlier than the melorheostosis (Campbell et al, 1968).

Melorheostosis has been discussed infrequently in the nuclear medicine literature, with only five previously reported cases involving radionuclide imaging, none with associated linear scleroderma (Janousek et al, 1976; Whyte et al, 1978; Resnick & Niwayama, 1981; Garver et al, 1982; Drane, 1987). Bone scintigraphy has shown mildly to moderately increased activity in all areas involved on radiographs and is said to be due to increased turnover of bone or increased bone mass in the affected area (Drane, 1987). In our case, the thin

---

Address reprint requests to: Alan Siegel, MD, Division of Nuclear Medicine, Department of Radiology, Hospital of the University of Pennsylvania, 3400 Spruce Street, Philadelphia, PA 19104, USA.

†Current address: Nuclear Medicine Department, Georgia Baptist Medical Center, Atlanta, Georgia, USA.

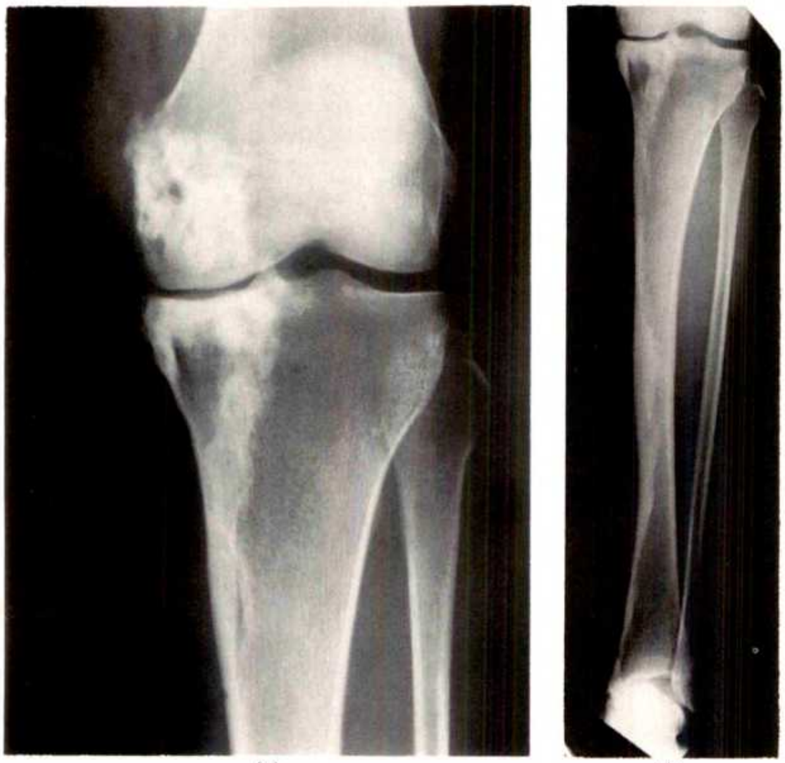

Figure 1. Anterior radiographs of the left knee (a) and the left lower leg (b). Cortical hyperostosis of the medial femoral condyle is present, crossing the joint space, and extending down the length of the medial tibial diaphysis.

regions of cortical hyperostosis in the proximal and distal tibia seen radiographically did not appear significantly abnormal on bone imaging. In view of the presumed constant state of metabolic activity of these osteosclerotic lesions, this is probably due to less abnormal bone mass in this region rather than less active osteoblastic activity. Nevertheless, radionuclide imaging produced results typical for melorheostosis:

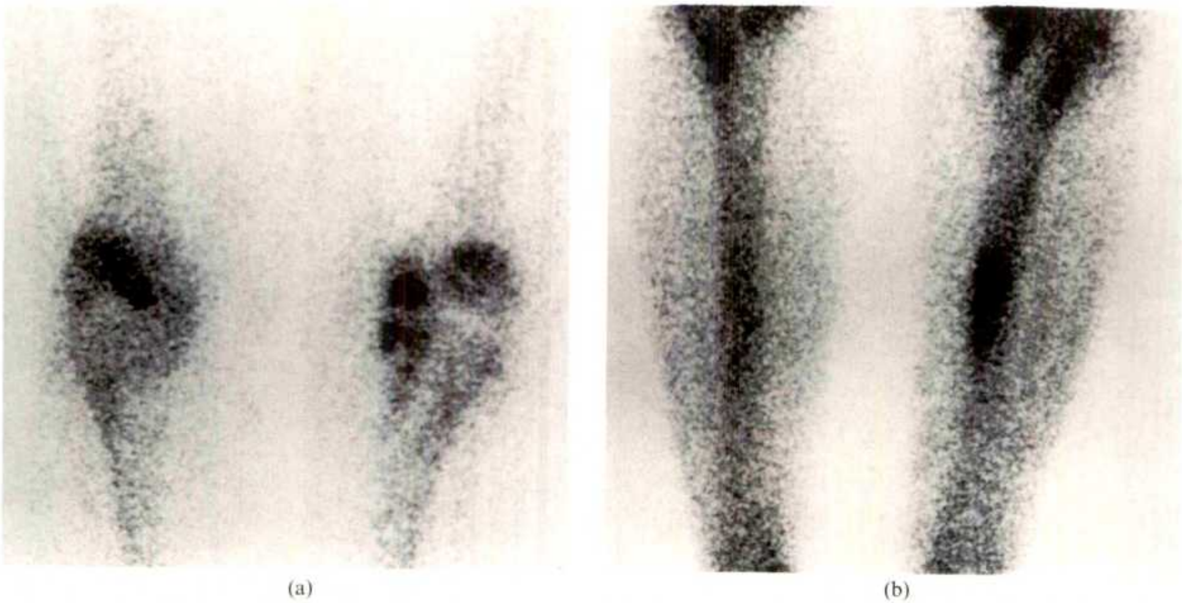

Figure 2. Anterior bone scan images of the knees (a) and the lower legs (b). There is increased uptake of bone tracer in regions of abnormal bone mass: the medial left femoral condyle, medial tibial plateau and the medial mid-left tibial diaphysis.

asymmetrical linear increased cortical uptake crossing a joint to involve a contiguous bone (Drane, 1987).

Linear scleroderma has rarely been associated with melorheostosis (17 previously reported cases) (Wagers et al, 1972; Soffa et al, 1975; Younge et al, 1979). Systemic findings of scleroderma have not been associated with melorheostosis (Soffa et al, 1975). However, our patient did have a history of oesophageal dysmotility and Raynaud's phenomenon, two entities that have been associated with the systemic disease (Gilliland, 1987).

Overall analysis of clinical presentation, radiographic findings and scintigraphic correlation are able to distinguish this rare entity from other causes of osteosclerosis.

References

Campbell, C. J., Papademetriou, T. & Bonfiglio, M., 1968. Melorheostosis: a report of the clinical, roentgenographic, and pathological findings in fourteen cases. *Journal of Bone and Joint Surgery*, *50A*, 1281–1304.

Drane, W. E., 1987. Detection of melorheostosis on bone scan. *Clinical Nuclear Medicine*, *12*, 548–551.

Fairbank, H. A. T., 1948. Melorheostosis. *Journal of Bone and Joint Surgery*, *30B*, 533–543.

Garver, P., Resnick, D., Haghighi, P. & Guerra, J., 1982. Melorheostosis of the axial skeleton with associated fibrolipomatous lesions. *Skeletal Radiology*, *9*, 41–44.

Gilliland, B. C., 1987. Progressive systemic sclerosis (diffuse scleroderma). In *Harrison's Principles of Internal Medicine*, ed. by E. Braunwald, K. J. Isselbacher, R. G. Petersdorf, J. D. Wilson, J. B. Martin & A. S. Fauci (McGraw-Hill, New York), pp. 1428–1432.

Green, A. E., Elswood, W. H. & Collins, J. R., 1962. Melorheostosis and osteopoikilosis with a review of the literature. *American Journal of Roentgenology*, *87*, 1096–1111.

Janousek, J. Preston, D. F., Martin, N. L. & Robinson, R. G., 1976. Bone scan in melorheostosis. *Journal of Nuclear Medicine*, *17*, 1106–1108.

Lee, S. H. & Sanderson, J., 1989. Case report: Hypophosphataemic rickets and melorheostosis. *Clinical Radiology*, *40*, 209–211.

Leri, A. & Joanny, J., 1922. Une affection non décrite des os: hyperostose "en coulée" sur toute la longueur d'un membre ou "melorhéostose." *Bulletins et Mémoires de la Société Médicale des Hôpitaux de Paris*, *46*, 1141–1145.

Morris, J. M., Samilson, R. L. & Corley, C. L., 1963. Melorheostosis: review of the literature and report of an interesting case with a nineteen year follow-up. *Journal of Bone and Joint Surgery*, *45*, 1191–1206.

Muller, S. A. & Henderson, E. D., 1963. Melorheostosis with linear scleroderma. *Archives of Dermatology*, *88*, 142–145.

Resnick, D. & Niwayama, G., 1981. Enostosis, hyperostosis, and periostitis. In *Diagnosis of Bone and Joint Disorders*, ed. by D. Resnick & G. Niwayama (Saunders, Philadelphia), pp. 2977–2983.

Soffa, D. J., Sire, D. J. & Dodson, J. H., 1975. Melorheostosis with linear sclerodermatous skin changes. *Radiology*, *114*, 577–578.

Wagers, L. T., Young, A. W. & Ryan, S. F., 1972. Linear melorheostotic scleroderma. *British Journal of Dermatology*, *86*, 297–301.

Whyte, M. P., Murphy, W. A. & Siegel, B. A., 1978. ^{99m}Tc-pyrophosphate bone imaging in osteopoikilosis, osteopathia striata, and melorheostosis. *Radiology*, *127*, 439–443.

Wynne-Davies, R., Hall, C. M. & Apley, A. G., 1985. Melorheostosis. In *Atlas of Skeletal Dysplasias* (Churchill Livingstone, New York), pp. 508–511.

Younge, D., Drummond, D., Herring, J. & Cruess, R. L., 1979. Melorheostosis in children. *Journal of Bone and Joint Surgery*, *61B*, 415–418.

Sonographic detection of neonatal hydrometrocolpos

By Arpan K. Banerjee, MB, BS, MRCP, O. Clarke, DCR(R), DMU and L. M. MacDonald, MB, BS, FRCR

Department of Diagnostic Radiology, St Thomas' Hospital, London SE1 7EH, UK

(Received 22 March 1991 and in final form 9 September 1991, accepted 20 September 1991)

Keywords: Sonography, Neonate, Hydrometrocolpos

Hydrometrocolpos is the result of an obstruction of the genital tract by an intact hymen, a midplane transverse septum, cloacal anomalies or vaginal atresia. This obstruction allows an accumulation of secretions from the infant cervical mucous glands in the vagina and uterus stimulated by maternal oestrogen (Wilson et al, 1978; Nyberg, 1990).

The incidence is reported to be between one in 16 000 births (Westerhout et al, 1964) and one in 30 000 births (Hill & Hirsch, 1985). Although several cases of hydrometrocolpos have been reported in the world literature (Mahoney & Chamberlain, 1940; Spencer & Levy, 1962; Reed & Griscom, 1973), there are very few reports of the ultrasonographic appearances of this condition (Sailer, 1979; Sawhney et al, 1990).

We present two cases of hydrometrocolpos which showed classical ultrasound features and review the literature on the subject.

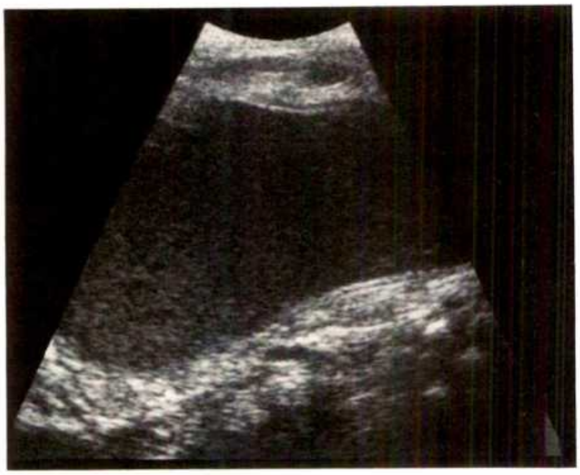

Figure 1. Ultrasound scan of pelvis (sagittal section) showing a large cystic mass with multiple internal echoes.

Case reports

Case 1

A 1-day-old white girl, the product of a normal pregnancy and delivery, presented with a fluctuating mass protruding from the vagina. Clinical examination revealed a palpable abdominal mass and a swollen labia. An ultrasound of the abdomen and pelvis was performed using a 5 MHz probe. A 6 cm × 4 cm cystic left adnexal mass was demonstrated with no posterior acoustic enhancement. The mass contained several internal echoes (Fig. 1). The bladder was not distended and therefore not seen, but both kidneys were normal. The vaginal membrane was incised and 150 ml of milky white fluid was expelled. A follow-up scan of the uterus showed a normal-sized uterus 2.5 cm × 2 cm with a prominent midline endometrial echo (Fig. 2). The patient remains well and symptom free.

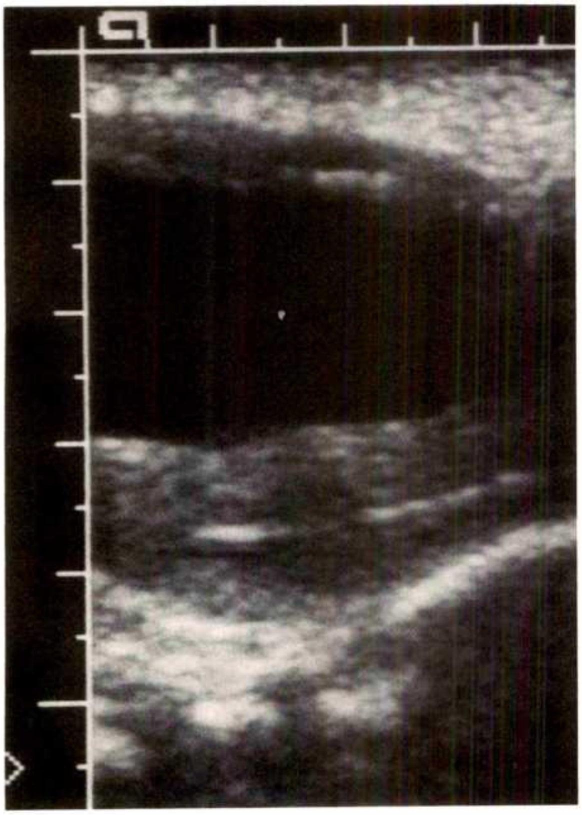

Figure 2. Long midline scan showing a normal uterus following incision of the vaginal membrane behind the full bladder.

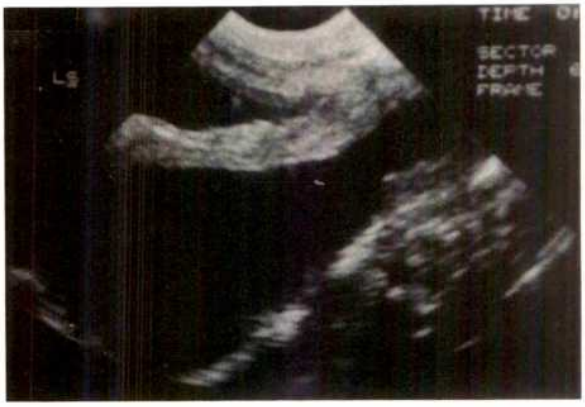

Figure 3. Ultrasound scan of pelvis (sagittal section) showing a large cystic mass posterior to the bladder. Initial ultrasound showed multiple echoes within the hydrometrocolpos.

Case 2

A baby girl, the product of a full-term normal delivery, presented at birth with a pelvic mass, having a prenatal diagnosis of a pelvic mass and bilateral hydronephroses. Post-natal ultrasound examination confirmed the bilateral hydronephroses and demonstrated that the pelvic mass was a hydrometrocolpos. Initially the dilated uterus and vagina contained fluid with echogenic material, but on subsequent scans the mucus was replaced by clear fluid (Fig. 3). Subsequent investigations revealed a common cloacal exit and the ureters inserted into the hydrometrocolpos (Fig. 4), resulting in bilateral hydronephroses. Division of the vaginal septum allowed drainage of both the bladder and uterus thus relieving the hydronephroses.

Corrective surgery was achieved on this child and normal ultrasound of the kidneys, bladder and uterus was performed at a recent appointment, aged 5 years.

Discussion

Hydrometrocolpos usually presents soon after birth with a lower abdominal mass and a bulging introitus. Although the condition is relatively rare, with only 79 reported cases as of 1965 (Ceballos & Hicks, 1970), it apparently represents 15% of abdominal masses in newborn girls.

The ultrasonographic features of the condition include a cystic adnexal pelvic mass with a sharp posterior surface but little posterior acoustic enhancement (Sawhney et al, 1990). Internal echoes within the cystic structure are seen as a result of reflections from the mucoid debris. Occasionally internal echoes may not be

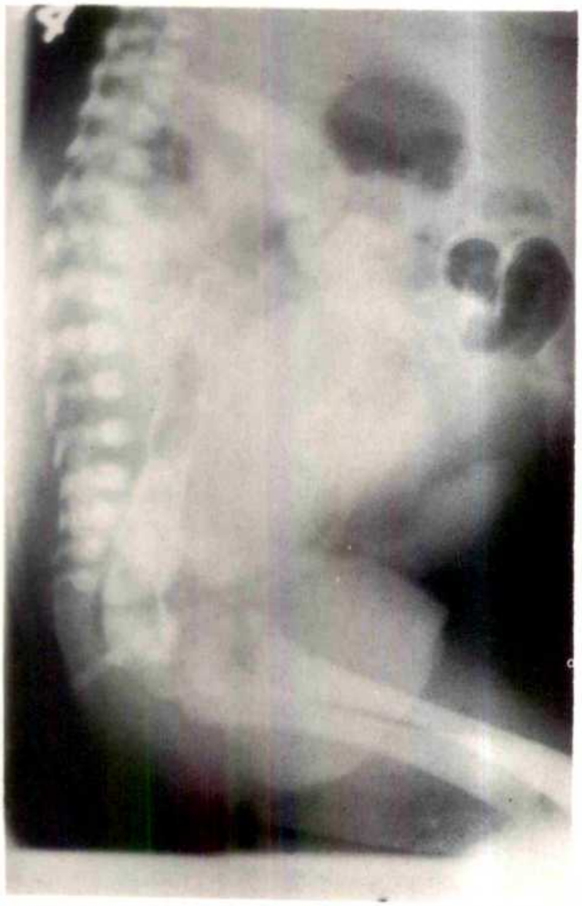

Figure 4. Lateral abdominal radiograph following intravenous and rectal contrast. A large soft-tissue pelvic mass with contrast enhancement (due to insertion of the ureters into the hydrometrocolpos) is seen between the colon and the bladder (the catheter is a feeding tube). A thick muscular uterine wall is seen on this figure and Fig. 3.

seen, especially if the diagnosis is made antenatally, when the echo-free pelvic mass may be seen lying between the bladder and spine. Cephalic extension into the fetal abdomen and caudal extension into the vagina may be seen (Davis et al, 1984).

The differential diagnosis of cystic abdominal masses arising from the pelvis in a female infant includes a distended bladder, pre-sacral teratoma, an anterior meningocoele, an ovarian cyst and a duplication cyst of the rectum. Ovarian cysts and duplication cysts may be unilocular or multilocular, and if multilocular this helps in differential diagnosis.

As the initial ultrasound examination of hydrometrocolpos frequently displays a non-cystic mass containing echogenic material, haemorrhage into an ovarian cyst or torsion of a cyst should be considered (Nussbaum et al, 1988). Ovarian tumours and possibly a distended rectum may also produce a similar appearance (Hill & Hirsch, 1985). A plain lumbar radiograph may help in the diagnosis, if a pre-sacral teratoma or meningocoele is considered a possibility.

Hydrometrocolpos may be accompanied by hydronephrosis, as demonstrated in Case 2, when the abnormality of the uterus and vagina is accompanied by a congenital renal abnormality. It may also be accompanied by a small bowel obstruction and plastic peritonitis (Ceballos & Hicks, 1970).

Other congenital anomalies associated with hydrometrocolpos include cardiac defects and polydactyly as part of the Kaufman–McKusick syndrome (Cartari et al, 1987). If the hydrometrocolpos is secondary to vaginal atresia and not just an imperforate hymen, there may be an associated imperforate anus or rectovaginal fistula. Other urinary abnormalities such as a persistent urogenital sinus, polycystic kidneys, renal hypoplasia and urethrovaginal fistula may also be found (Reed & Griscom, 1973; Janus & Godine, 1986).

The treatment of hydrometrocolpos consists of incision of the hymen and drainage of the fluid. Ultrasound is an appropriate method of monitoring progress. Plain abdominal radiography, intravenous urography and other contrast investigations may be necessary to identify fully the complicated hydrometrocolpos.

References

Cartari, A., Tacconi, M. L., Berincari, N., Picarazzi, A., Ceccoli, D. & Gaudino, S., 1987. Rare syndromes. The Kaufman–McKusick syndrome. A review of 44 cases reported in the literature. *Annales de Génétique*, *30*, 70–74.

Ceballos, R. & Hicks, G. M., 1970. Plastic peritonitis due to neonatal hydrometrocolpos. Radiologic and pathologic observations. *Journal of Paediatric Surgery*, *5*, 63–70.

Davis, G. H., Wapner, R., Kurtz, A. B., Chhibber, G., FitzSimmonds, J. & Blocklinger, A. J., 1984. Antenatal diagnosis of hydrometrocolpos by ultrasound examination. *Journal of Ultrasound in Medicine*, *3*, 371–374.

Hill, S. J. & Hirsch, J. H., 1985. Sonographic detection of foetal hydrometrocolpos. *Journal of Ultrasound in Medicine*, *4*, 323.

Janus, C. & Godine, L., 1986. Newborn with hydrometrocolpos and ambiguous genitalia. Clinical significance. *Journal of Clinical Ultrasound*, *14*, 739–741.

Mahoney, P. J., & Chamberlain, J. W., 1940. Hydrometrocolpos in infancy. Congenital atresia of the vagina with abnormally abundant cervical secretions. *Journal of Paediatrics*, *17*, 772–780.

Nussbaum, A. R., Sanders, R. C., Hartman, D. S., et al, 1988. Neonatal ovarian cysts: sonographic-pathologic correlation. *Radiology*, *168*, 817–821.

Nyberg, D. A. 1990. Intraabdominal anomalies. In *Diagnostic Ultrasound of Foetal Anomalies. Text and Atlas*, ed. by D. A. Nyberg, B. S. Mahoney & D. H. Pretorius (York Book Medical Publishers, Chicago), pp. 342–395.

Reed, M. H. & Griscom, N. T., 1973. Hydrometrocolpos in infancy. *American Journal of Roentgenology*, *118*, 1.

Sailer, J. F., 1979. Haematometra and haematocolpos. Ultrasound findings. *American Journal of Roentgenology*, *132*, 1010–1011.

Sawhney, S., Gupta, R., Brerry, M. & Bhatnagar, V., 1990. Hydrometrocolpos. Diagnosis and follow-up by ultrasound. A case report. *Australasian Radiology*, *34*, 93–94.

1992, *The British Journal of Radiology*, *65*, 271–273

Spencer, R. & Levy, D. M., 1962. Hydrometrocolpos: report of three cases and review of the literature. *Annals of Surgery*, *155*, 558–571.

Westerhout, F. C., Hodgman, J. E., Anderson, G. V. et al, 1964. Congenital hydrocolpos. *American Journal of Obstetrics & Gynecology*, *89*, 957–961.

Wilson, D. A., Stacy, T. M. & Smith, E. I., 1978. Ultrasound diagnosis of hydrocolpos and hydrometrocolpos. *Radiology*, *128*, 451–454.

An unusual osteochondral body in association with calcium pyrophosphate dihydrate crystal deposition disease

By A. C. Jones, BSc, MRCP, *B. J. Preston, FRCR and M. Doherty, MA, MD, MRCP

Rheumatology Unit, City Hospital, Nottingham NG5 1PB and *Department of Radiology, University Hospital, Nottingham, Clifton Boulevard, Nottingham NG7 2UH

(Received 19 June 1991, accepted 23 July 1991)

Keywords: Osteochondral body, Chondrocalcinosis, Knee, Pyrophosphate arthropathy

Chronic pyrophosphate arthropathy is a recognized subset of osteoarthritis (OA) characterized by deposition of calcium pyrophosphate dihydrate (CPPD) crystals (McCarty, 1976). Typically a disease of the elderly, there is symptomatic and radiographic involvement of characteristic sites, including the patellofemoral, radiocarpal and glenohumeral joints (McCarty & Haskin, 1963; Resnick & Resnick, 1983). CPPD deposition in cartilage (chondrocalcinosis) occurs particularly in the articular and the meniscal cartilages of the knee, the symphysis pubis and the triangular ligament of the wrist (McCarty & Haskin, 1963; Resnick & Resnick, 1983). It has been postulated that sporadic pyrophosphate arthropathy may represent a hypertrophic response to joint insult (Doherty et al, 1984), with CPPD crystal formation being a marker of high extracellular pyrophosphate production reflecting increased cellular biosynthetic activity (Caswell et al, 1983).

Osteochondral bodies, arising in synovium by enchondral ossification of islands of chondroid metaplasia, are a common accompaniment to OA and may be particularly florid in the subset of pyrophosphate arthropathy (McCarty & Haskin, 1963; Resnick & Resnick, 1983). Such bodies form by a process of layered growth (Milgram, 1977b), and possibly reflect a generalized hyperplastic response (*i.e.* attempted repair) by joint tissues. We present a patient with CPPD arthropathy who developed an osteochondral body that showed features both of ossification and chondrocalcinosis.

Case report

An 83-year-old man presented with a 3 year history of symptomatic knee arthropathy associated with multiple episodes of acute synovitis. CPPD crystals, identified by compensated polarized light microscopy, were repeatedly isolated from the knee synovial fluid. The patient had also experienced episodes of diuretic-induced gout affecting the olecranon bursa and the first metatarsophalangeal, ankle and knee joints (confirmed by identification of monosodium urate crystals). Diuretics had been given for episodes of ischaemic congestive cardiac failure; all symptoms of gout resolved when they were withdrawn. There was no family history of arthropathy.

On examination he was obese and had clinical signs of osteoarthritis of the knees with bony deformity and crepitus. Biochemically there was no evidence of predisposing metabolic

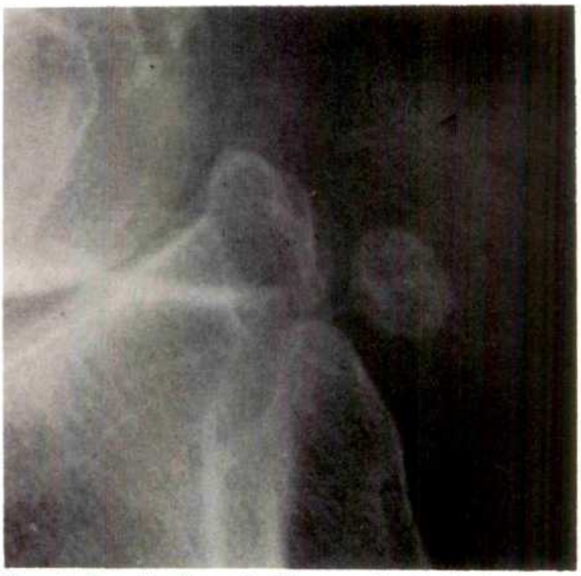

Figure 1. Lateral radiograph of the osteochondral body demonstrating the dense, possibly trabeculated core.

Address correspondence to A. C. Jones, Rheumatology Unit, City Hospital, Nottingham NG5 1PB.

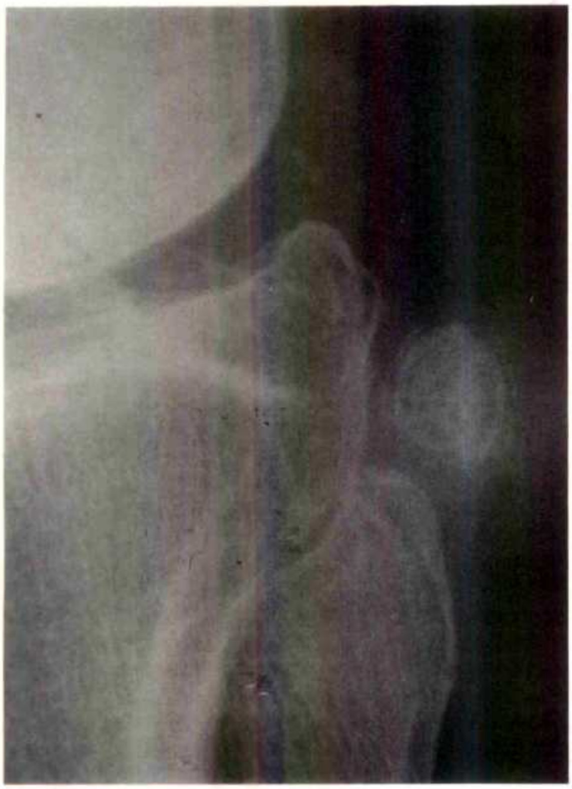

Figure 2. Repeat radiograph after 2 years demonstrating the development of a fine outer rim of calcification.

disease (Hamilton, 1976); the only abnormality was mild chronic renal failure (urea 16.3 mmol/l, creatinine 217 μmol/l).

Plain radiographs of his right knee demonstrated a well defined intracapsular body near the head of the fibula (Fig. 1). The densely calcified core appeared to contain trabeculae, and serial films (Fig. 2) demonstrated developing fine calcification of the outer rim, suggestive of chondrocalcinosis. In addition there was bilateral tricompartmental knee OA with faint chondrocalcinosis of the menisci and several other loose bodies. Radiographs of his lumbar spine showed large lateral osteophytes. There were minor OA changes of his first metatarsalphalangeal joints. There was no chondrocalcinosis at other sites.

Discussion

The radiographic appearance suggests ossification of the core of the chondrometaplastic island (osteochondral body) with calcification (*i.e.* chondrocalcinosis) of the superficial, newly formed fibrocartilage rim. Although confirmation of the crystal species responsible for the peripheral chondrocalcinosis would require tissue examination, it is tempting to speculate that it is CPPD, since this is the commonest cause for chondrocalcinosis of fibrocartilage and hyaline cartilage (McCarty et al, 1966). The patient had chondrocalcinosis elsewhere in the same joint and synovial fluid CPPD crystals were repeatedly identified. The principal feature of interest in this case is that chondrocalcinosis occurred in newly formed cartilage, in the setting of a compromised joint and in an individual predisposed to CPPD crystal formation. It is also of interest that this patient had coexisting urate gout; such predisposition to multiple crystal deposition is well recognized (Dieppe et al, 1988) and supports the importance of common factors that enhance crystal nucleation and growth (Stockman et al, 1980).

Although the appearance of this osteochondral body could arise from layered growth (Milgram, 1977b), possibly of a bony nidus (Milgram, 1977a), the central ossification appears too pronounced for such an explanation. Chondroid metaplasia with subsequent enchondral ossification seems a more likely explanation; this process reflecting an aspect of the hypertrophic repair process associated with pyrophosphate arthropathy (Doherty et al, 1984).

Although the patient is elderly the osteochondral body contains newly formed fibrocartilage. Chondrocalcinosis, even in those with familial or metabolic predisposition (Hamilton, 1976; McCarty, 1976), is strongly age-related. This observation suggests that fibrocartilage synthesized by chondrocytes within aged joints is qualitatively different from that synthesized in younger tissues. This could arise through age-related changes either in the synthetic cells themselves or in the perichondrocyte environment.

Acknowledgments

A. C. Jones is an Arthritis and Rheumatism Council junior clinical research fellow.

References

Caswell, A., Guilland-Cumming, D. F., Hearn, P. R., McGuire, M. K. B. & Russell, R. G. G., 1983. Pathogenesis of chondrocalcinosis and pseudogout. Metabolism of inorganic pyrophosphate and production of calcium pyrophosphate dihydrate crystals. *Annals of the Rheumatic Diseases*, *42*(S), 27–36.

Dieppe, P., Campion, G. & Doherty, M., 1988. Mixed crystal deposition. *Rheumatic Disease Clinics of North America*, *14*, 415–426.

Doherty, M., Dieppe, P. & Watt, I., 1984. Low incidence of calcium pyrosphosphate dihydrate crystal deposition in rheumatoid arthritis, with modification of radiographic features in coexistent disease. *Arthritis and Rheumatism*, *27*, 1002–1009.

Hamilton, E. B. D., 1976. Diseases associated with CPPD deposition disease. *Arthritis and Rheumatism*, *19*, 353–357.

McCarty, D. J., 1976. Calcium pyrophosphate dihydrate crystal deposition disease—1975. *Arthritis and Rheumatism*, *19*, 275–285.

McCarty, D. J. & Haskin, M. E., 1963. The roentgenographic aspects of pseudogout (articular chondrocalcinosis). *American Journal of Roentgenology, Radium Therapy and Nuclear Medicine*, *90*, 1248–1257.

McCarty, D. J., Hogan, J. M., Gatter, R. A. & Grossman, M., 1966. Studies on pathological calcifications in human cartilage. *Journal of Bone and Joint Surgery*, *48* (A), 309–324.

Milgram, J. W., 1977a. The classification of loose bodies in human joints. *Clinical Orthopaedics and Related Research*, *124*, 282–291.

1992, *The British Journal of Radiology*, *65*, 273–278

——1977b. The development of loose bodies in human joints. *Clinical Orthopaedics and Related Research*, *124*, 292–303.
Resnick, C. S. & Resnick, D., 1983. Crystal deposition disease. *Seminars in Arthritis and Rheumatism*, *12*, 390–403.
Stockman, A., Darlington, L. G. & Scott, J. T., 1980. Frequency of chondrocalinosis of the knees and avascular necrosis of the femoral head in gout: a controlled study. *Annals of the Rheumatic Diseases*, *39*, 7–11.

Three-dimensional imaging of dual isotope data-sets in a case of acute myocardial infarction

By Hugo P. Dilhuydy, BIng, *Daniel McNamara, MD, *Raymond J. Lemieux, MD, Yves Martel, BIng and Jacques A. de Guise, PhD

Institut de Génie Biomédical, Ecole Polytechnique de Montréal, Campus de l'Université de Montréal, Case Postale 6079, succursale "A", Montréal, Qué, H3C 3A7, Canada and *Service de Médecine Nucléaire, Hôpital du Sacré-Cœur de Montréal, 5400 boul. Gouin ouest, Montréal, Qué, H4J 1C5, Canada

(Received 6 December 1990 and in revised form 30 May 1991, accepted 4 September 1991)

Keywords: Myocardial infarction, Thallium 201, Indium 111-antimyosin, Dual isotope, Three-dimensional imaging

A patient with acute myocardial infarction was injected with indium 111 (^{111}In)-antimyosin Fab. He then underwent planar imaging before receiving an additional dose of thallium 201 (^{201}Tl) so as to perform a dual isotope single photon emission computed tomography (SPECT) acquisition. Planar images showed vague myocardial uptake of antimyosin antibody. With tomographic slices, a more defined area of antimyosin uptake was seen but still with a low ^{111}In signal-to-noise ratio. This area corresponded to a ^{201}Tl defect. Two three-dimensional (3D) rendering methods showed a well matched ^{201}Tl 3D defect and ^{111}In 3D hot spot and seemed to facilitate the localization of the infarct as well as the evaluation of its importance relative to the remaining viable tissue. This case study illustrates a situation where 3D imaging of dual isotope data-sets could be useful for direct visualization and localization of myocardial infarction.

Case report

A 61-year-old white male with a past history of occasional chest pain was admitted to the ICU for prolonged chest pain. He had multiple risk factors for coronary disease such as smoking (up to 40 cigarettes per day), essential hypertension, diabetes and a family history of coronary artery disease. Laboratory analysis showed elevated plasma enzyme levels of total creatine kinase (CK) (1289 U/l) and the electrocardiogram showed an infarct in the anterior wall and a possible old inferior wall infarction (see Fig. 1). Five days after his admission coronary angiography revealed severe three-vessel disease. The patient recovered well during hospitalization without recurrent chest pain at rest or heart failure. Because of the severe three-vessel disease, the patient was considered at risk and triple bypass surgery was carried out 20 days after his admission. During the procedure, the surgeon noticed an extensive antero-apical fibrosis. Four months later, the patient returned to work.

To evaluate further the location and extent of the infarct, ^{111}In-antimyosin (Amersham Canada Ltd, Oakville) scintigraphy was performed before surgery, 10 days after his admission. Acquisition of an antimyosin scan was obtained 36 h after intravenous administration of 80 MBq (2.2 mCi) of ^{111}In-DTPA-antimyosin. Chromatography revealed 93% binding. Both planar and tomographic studies were performed with a medium-energy high-resolution parallel-hole collimator on a SophyCamera (Sopha Medical Inc., Paris, France). Planar images were acquired during 10 min (approximately 500 000 counts) using both ^{111}In photopeaks (172 and 247 keV) with a 20% energy window and a 128 × 128 matrix. Three viewing angles were selected: anterior, left anterior oblique (LAO) 45° and LAO 70° (see Fig. 2). Before tomographic imaging, the patient was injected with 100 MBq (2.7 mCi) of ^{201}Tl. 10 min later, a dual isotope SPECT acquisition was performed with 32 projections for 40 s each (approximately 65 000 ^{201}Tl counts

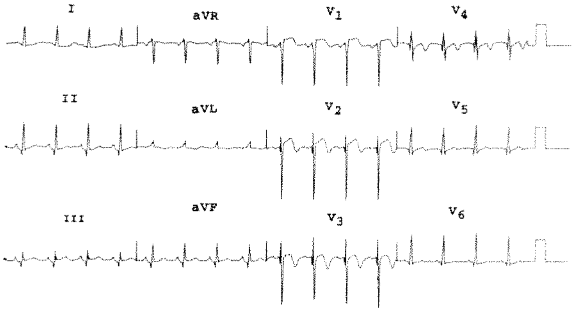

Figure 1. 12-lead electrocardiogram obtained on the first day of admission showing acute anterior and possible old inferior infarction.

---

*Address correspondence to R. J. Lemieux, MD, Service de Médecine Nucléaire, Hôpital du Sacré-Cœur de Montréal, 5400 Boul. Gouin ouest, Montréal, Qué. H4J 1C5, Canada.

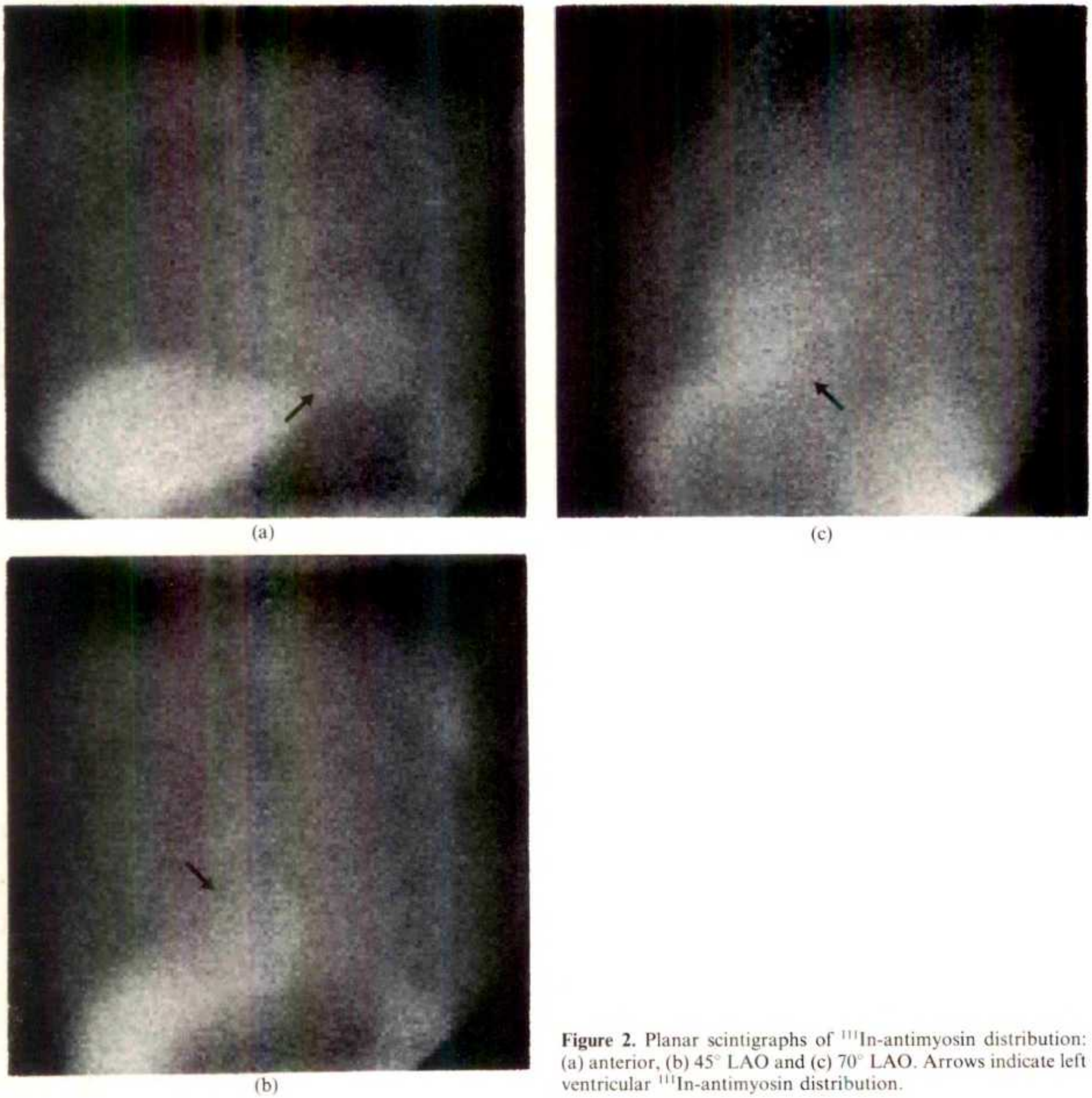

(a)

(c)

(b)

Figure 2. Planar scintigraphs of ^{111}In-antimyosin distribution: (a) anterior, (b) 45° LAO and (c) 70° LAO. Arrows indicate left ventricular ^{111}In-antimyosin distribution.

and 20 000 ^{111}In counts per projection) along a 180° adaptive body contour (from right anterior oblique (RAO) 45° to left posterior oblique (LPO) 45°). The low-energy ^{201}Tl photopeak (70 keV, 20% window) and the high-energy ^{111}In photopeak (247 keV, 20% window) were used with a 64×64 matrix and a 1.33 zoom factor. For each data-set, tomographic slices were obtained by filtered back-projection with the use of a Wiener filter. They were centred so that the left ventricle cavity (as seen on the ^{201}Tl slices) corresponds to the $64 \times 64 \times 64$ data-set centre. They were then zoomed by a factor of 2 using a trilinear interpolation method. Background subtraction was performed until most of the extracardiac activity was eliminated, which occurred at 20% of the ^{201}Tl maximum value and 35% of the ^{111}In maximum value. Finally, 3D oblique reorientation was carried out by rotating the data-sets until the left ventricle axes (horizontal long, vertical long, and short) were aligned with the transverse, sagittal and coronal cutting planes. All these manipulations were similarly performed on both ^{201}Tl and ^{111}In data-sets so as to conserve their spatial correspondence (see Fig. 3). The processed data-sets were then reviewed for diagnosis by scanning successively through serial ^{201}Tl and ^{111}In slices (Goris et al, 1986). Centred, zoomed and background subtracted but not reorientated slices were then transferred to a Personal Iris 4D/25GT workstation (Silicon Graphics Inc., Mountain View, USA) for 3D imaging purposes.

Two types of 3D rendering were performed: surface shading (Gibson, 1983: Webb et al, 1987) and volume rendering (Wallis et al, 1989; Wallis & Miller, 1990). The first implies thresholding of the tomographic slices and connecting the contours of the remaining voxels for each slice with a

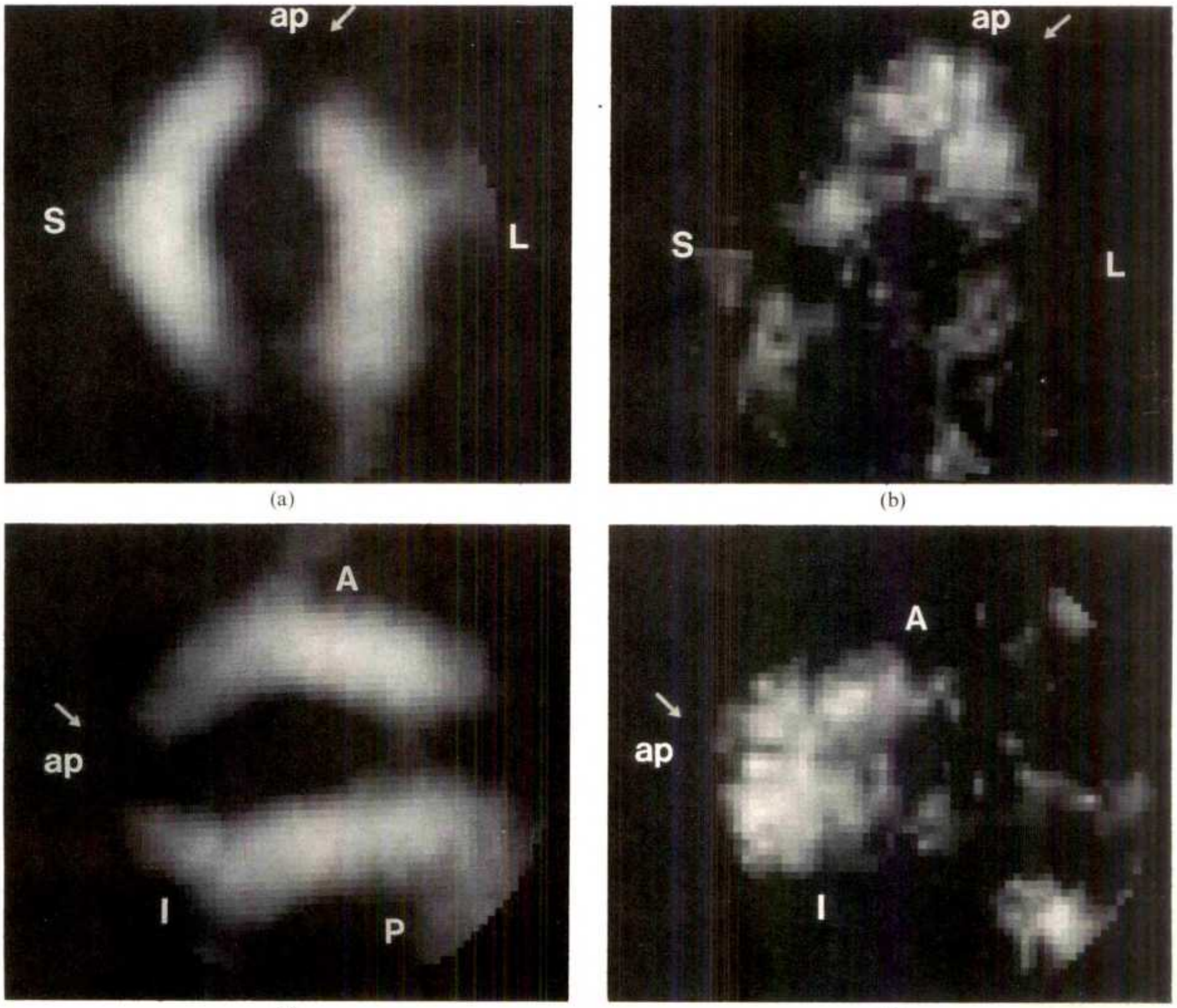

(a) (b)

(c) (d)

Figure 3. Horizontal long-axis slices: (a) ^{201}Tl and (b) ^{111}In. Vertical long-axis slices: (c) ^{201}Tl and (d) ^{111}In. Arrows indicate an apical ^{201}Tl defect and antimyosin uptake. A = anterior; I = inferior; L = lateral; P = posterior; S = septal; ap = apical.

"connecting cube" algorithm (de Guise & Martel, 1988). The second computes several "see-through" views of the tomographic 3D data-set as seen by an observer from different positions using attenuation for deeper voxels, transparency control and colormap coding. In both methods, the resulting ^{201}Tl and ^{111}In 3D models (surface shading) or reprojections (volume rendering) are merged only at the visualization stage. The surface rendering visualization is carried out with specially designed software that allows the operator real-time manipulations and volume measurements of the 3D reconstructed objects. The volume rendering method, on the other hand, requires a rotating cinematic animation of the different computed views with stop–motion capability.

Discussion

It is hoped that precise localization and quantification of infarcted myocardium could lead to a more appropriate therapy thus contributing to a better prognosis (Sobel et al, 1972; Holman et al, 1982; Rigo & De Landsheere, 1989). It has been demonstrated that antimyosin Fab antibody accumulates in acute infarcts. Theoretically this antibody localizes only in myocardial cells that have lost their membrane integrity, which signals irreversible damage (Khaw et al, 1976, 1987). ^{201}Tl is a well established agent, the uptake of which reflects myocardial perfusion and viability. Although ^{201}Tl is usually injected during treadmill exercise to evaluate coronary stenosis, it has also been used to localize and quantify infarct extent (Bailly et al, 1987; Prigent et al, 1987; Mahmarian et al, 1988). Simultaneous dual isotope imaging can improve myocardial infarct diagnosis in so far as the two tracers give independent information on the tissue viability or injury (Johnson et al, 1987, 1990; Hashimoto et al, 1988).

Amongst the three planar images of antimyosin distri-

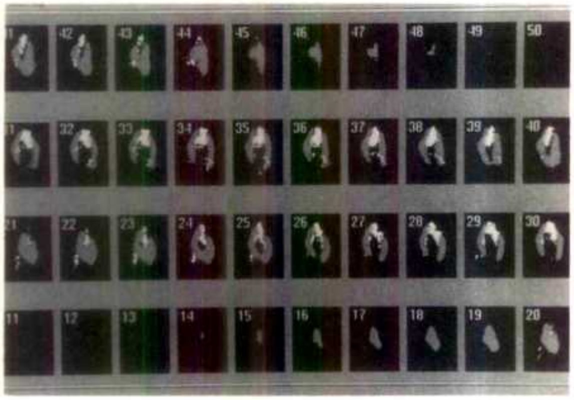

Figure 4. Bicolour superimposition of ^{201}Tl and ^{111}In-antimyosin horizontal long-axis slices after background subtraction and thresholding. ^{201}Tl activity is coded in dark grey, ^{111}In activity is coded in white and overlap is seen as light grey.

bution (Fig. 2), the anterior view was the most appropriate because of the absence of overlapping organs. This view shows intense liver uptake but a quite uniform heart uptake, which is essentially residual ^{111}In coming from the heart blood pool. The two other static views seem to show an apical uptake; however, superimposition of liver activity makes an accurate diagnosis very difficult.

The ^{201}Tl tomographic slices show a well identified antero-apical and infero-apical defect that is correlated with an antimyosin uptake on the ^{111}In slices (Fig. 3). However, the ^{111}In images show a low signal-to-noise ratio. This is mostly due to a low ^{111}In count rate and probably to residual blood pool, liver and spleen non-target activity overlapping the heart region on some of the projections. As mentioned earlier, these slices were obtained after a 3D oblique reorientation so that the clinician could more easily locate the ^{201}Tl defect and the ^{111}In hot spot with respect to the left heart anatomy. For perfusion slices (such as ^{201}Tl or technetium-99m-MIBI images), a "mental reconstruction" of the 3D tracer distribution using serial 2D slices is relatively easy to perform but for hot-spot slices (such as ^{99}Tc^{m}-pyrophosphate or ^{111}In-antimyosin images) the 3D necrosis localization and extent is less obvious. Even with the dual isotope data-sets, the 3D spatial correlation or mismatch is not directly available unless additional processing like bicolour superimposition is carried out (see Fig. 4).

With the 3D methods there is no need to make the left ventricle long axis perpendicular to the axis of rotation of the gamma camera. These methods seem to facilitate the visualization and localization of necrosis because a single image directly gives the 3D infarct extent. Spatial "reorientation" is easier and faster when manipulating 3D shaded or transparent objects because the whole ventricle tissue information (^{201}Tl + ^{111}In) can be seen moving in a 3D space, which is more intuitive. Appreciation of the infarction fraction is made easier by looking at the 3D antimyosin uptake in the 3D ^{201}Tl viable tissue. In this case, both methods revealed in a single image the antero-apical and infero-apical infarct (Figs 5, 6). An interesting feature of surface modelling is that volumes can be computed directly in 3D from reconstructed objects. An infarct volume can be estimated and compared with the viable tissue volume so as

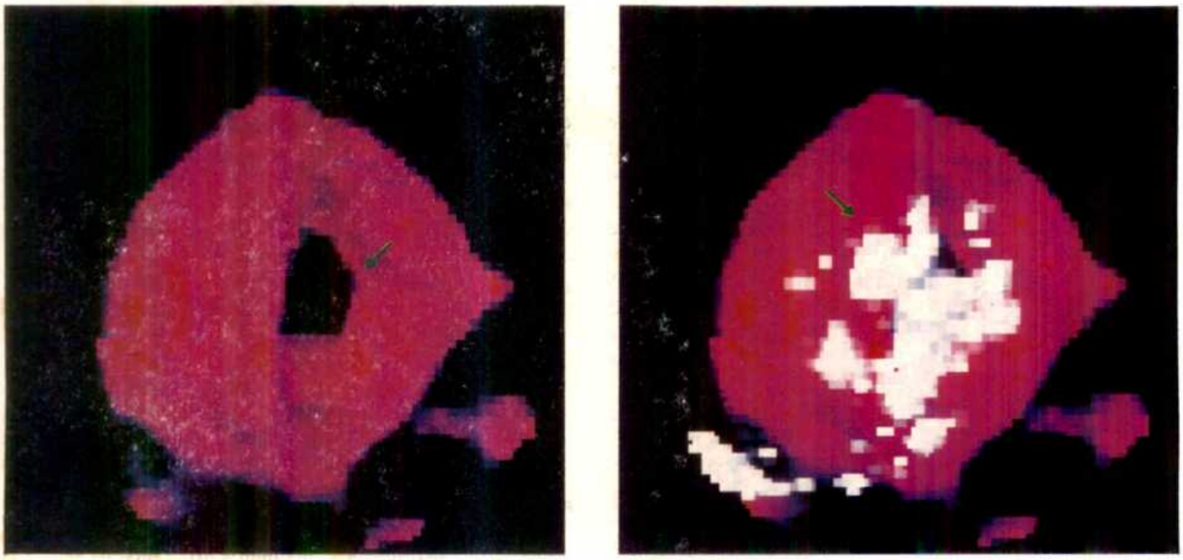

(a) (b)

Figure 5. 45° LAO 3D surface rendering view of: (a) ^{201}Tl only and (b) ^{201}Tl and ^{111}In-antimyosin superimposition. Arrows indicate an apical ^{201}Tl defect and antimyosin uptake.

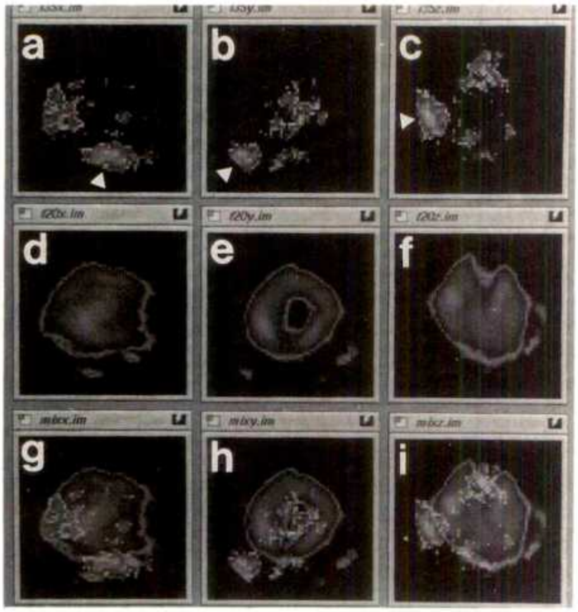

Figure 6. Volume rendering of ^{111}In-antimyosin uptake along (a) vertical long axis, (b) short axis and (c) horizontal long-axis; volume rendering of ^{201}Tl uptake along (d) vertical long axis, (e) short axis and (f) horizontal long axis. Composite superimposition of both agents' uptake along (g) vertical long axis, (h) short axis and (i) horizontal long axis. Arrows indicate antimyosin liver uptake.

to estimate the infarction fraction. Calibration can be undertaken with a heart phantom to select a proper activity threshold (Dilhuydy et al, 1990a,b). For this case, computed infarct volume was 15 cm^3 and computed viable tissue volume was 155 cm^3 (9% estimated infarction fraction) with 3D maximum activity thresholds of 38% for ^{201}Tl and 47% for ^{111}In. For this patient, blood CK samples were not drawn early enough and we could not perform an enzymatic estimate of the infarct volume. Such a correlation, with a sufficient number of patients, is essential to validate clinically the thresholds (Tamaki et al, 1982; Antunes et al, 1989).

Discrepancies between the original 2D slices and the 3D models may result from the thresholding operation. The reason is that a threshold transforms typical 255 grey-level images into binary (two levels) segmented images. ^{201}Tl and antimyosin match, overlap or mismatch may vary according to calibration and to the selected thresholds. In this case, the slight overlap of ^{201}Tl and antimyosin was preserved on the thresholded slices (Fig. 4). However, cutting planes through the 3D surfaces are needed to reveal the overlap information (which is hidden on the 45° LAO view of Fig. 5). The use of 3D surface imaging methods in terms of quantification are yet to be validated clinically, especially for the identification of patients at further ischaemic risk in which overlap or mismatch could be a prognosis index (Johnson et al, 1990). More complex approaches than simple thresholding may be used and down-scattering of indium photons into the thallium window may require additional correction (Crawley et al, 1988; Smith et al, 1990). Proper attenuation correction may also be required. Volume rendering is an interesting alternative because it does not depend so critically on a single threshhold value; the 3D reprojection of "depth weighted maximum activity" (Wallis & Miller, 1990) produces transparency and more gradual contours. However, cinematic display mode is absolutely necessary to offer a real 3D perception of both agents' uptake (Keyes et al, 1988). On the other hand, merging 3D reprojections of ^{201}Tl and antimyosin was more difficult than with the surface method because depth weighting and transparencies were calculated separately for each data-set. A simple colour superimposition was performed to produce the final composite images (see Figs 6g, 6h, 6i). Finally volume rendering does not allow for quantitative measurements because, even if the computation is based on 3D information, the result is still a series of 2D images.

There is a qualitative interest in looking at a single image that shows the necrosis, the viable tissue and their 3D spatial relation. In this particular case, the diagnostic capabilities, based on the 3D images, were similar to a slice-by-slice analysis. Nevertheless, the integration of both tracer distributions in a 3D scene facilitates the task as opposed to typically scanning a large number of slices for each data-set.

Conclusion

In conclusion, this case report suggests that with this particular patient ^{111}In-antimyosin planar imaging was not satisfactory for an accurate estimation of myocardial infarct extent. Dual isotope SPECT data-sets combining perfusion and infarct-avid agents confirmed without any doubt the presence of necrosis but there was still some difficulty in evaluating the 3D infarction fraction by a conventional dual isotope slice-by-slice analysis. 3D imaging of these data-sets showed an evident antero-apical and infero-apical infarct (correlating with ECG abnormalities and peroperative findings) with a clear visualization of the physiological infarction fraction. Further studies, both theoretical and clinical, are clearly needed in the area of 3D imaging and quantitative calibration so that these new tools may provide a potential advantage over conventional analysis and display of myocardial SPECT studies.

References

Antunes, M. L., Seldin, D. W., Wall, R. M. & Johnson, L. L., 1989. Measurement of acute Q-wave myocardial infarct size with single photon emission computed tomography imaging of indium-111 antimyosin. *American Journal of Cardiology*, *63*, 777–783.

Bailly, P., Peycelon, P., Lusson, J. R., Maublant, J., Veyre, A. & Cassagnes, J., 1987. La tomoscintigraphie du myocarde marqué au thallium 201. Intérêt dans la quantification et le pronostic de l'infarctus du myocarde. *Archives des Maladies du Cœur et des Vaisseaux*, *80*, 1625–1632.

CRAWLEY, J. C. W., SMITH, T., JAIN, D., RAVAL, U., ZANELLI, G. D. & LAHIRI, A., 1988. Problems and pitfalls in dual isotope imaging. In *Radioactive Isotopes in Clinical Medicine and Research*, edited by R. Hoefer & H. Bergmann. 18th International Symposium, Badgastein (Schattauer, Stuttgart), pp. 567–571.

DE GUISE, J. A. & MARTEL, Y., 1988. 3D-biomedical modelling: merging image processing and computer aided design. In *Proceedings of the Annual International Conference of the IEEE Engineering in Medicine and Biology Society*, New Orleans, Vol. 10 (IEEE, New York), pp. 426–427.

DILHUYDY, H., MARTEL, Y., LEMIEUX, R., MCNAMARA, D., CHOINIERE, P. & DE GUISE, J., 1990a. Three-dimensional (3-D) analysis and display of dual isotope myocardial SPECT studies: a phantom validation. *Proceedings of the 16th Canadian Medical and Biological Engineering Society Conference*, Winnipeg, pp. 47–48.

DILHUYDY, H., MARTEL, Y., LEMIEUX, R., MCNAMARA, D., CHOINIERE, P. & DE GUISE, J., 1990b. Three-dimensional (3-D) analysis and display of dual isotope myocardial SPECT studies. *European Journal of Nuclear Medicine, 16*, S184.

GIBSON, C. J., 1983. A new method for the three-dimensional display of tomographic images. *Physics in Medicine and Biology, 28*, 1153–1157.

GORIS, M. L., BOUDIER, S. & BRIANDET, P. A., 1986. Interrogation and display of single photon emission tomography data as inherently volume data. *American Journal of Physiologic Imaging, 1*, 168–180.

HASHIMOTO, T., KAMBARA, H., FUDO, T., TAMAKI, S., TAKATSU, Y., HATTORI, R., TOKUNAGA, S. & KAWAI, C., 1988. Significance of technetium-99m/thallium-201 overlap on simultaneous dual emission computed tomography in acute myocardial infarction. *American Journal of Cardiology, 61*, 1181–1186.

HOLMAN, B. L., GOLDHABER, S. Z., KIRSCH, C.-M., POLAK, J. F., FRIEDMAN, B. J., ENGLISH, R. J. & WYNNE, J., 1982. Measurement of infarct size using single photon emission computed tomography and technetium-99m-pyrophosphate: a description of the method and comparison with patient prognosis. *American Journal of Cardiology, 50*, 503–511.

JOHNSON, L. L., LERRICK, K. S., COROMILAS, J., SELDIN, D. W., ESSER, P. D., ZIMMERMAN, J. M., KELLER, A. M., ALDERSON, P. O., BIGGER, J. T. & CANNON, P. J., 1987. Measurement of infarct size and percentage myocardium infarcted in a dog preparation with single photon-emission computed tomography, thallium-201, and indium 111-monoclonal antimyosin Fab. *Circulation, 76*, 181–190.

JOHNSON, L. L., SELDIN, D. W., KELLER, A. M., WALL, R. M., BHATIA, K., BINGHAM, C. O. & TRESGALLO, M. E., 1990. Dual isotope thallium and indium antimyosin SPECT imaging to identify acute infarct patients at further ischemic risk. *Circulation, 81*, 37–45.

KEYES, J. W. JR., FAHEY, F. H., HARKNESS, B. A., EGGLI, D. F., BALSEIRO, J. & ZIESSMAN, H. A., 1988. Characterization of the rotating display. *Investigative Radiology, 23*, 692–694.

KHAW, B. A., BELLER, G. A., HABER, E. & SMITH, T. W., 1976. Localization of cardiac myosin-specific antibody in myocardial infarction. *Journal of Clinical Investigation, 58*, 439–446.

KHAW, B. A., STRAUSS, H. W., MOORE, R., FALLON, J. T., YASUDA, T., GOLD, H. K. & HABER, E., 1987. Myocardial damage delineated by indium-111 antimyosin Fab and technetium-99m pyrophosphate. *Journal of Nuclear Medicine, 28*, 76–82.

MAHMARIAN, J. J., PRATT, C. M., BORGES-NETO, S., CASHION, W. R., ROBERTS, R. & VERANI, M. S., 1988. Quantification of infarct size by Tl-201 single-photon emission computed tomography during acute myocardial infarction in humans. Comparison with enzymatic estimates. *Circulation, 78*, 831–839.

PRIGENT, F., MADDAHI, J., GARCIA, E. V., RESSER, K., LEW, A. S. & BERMAN, D. S., 1987. Comparative methods for quantifying myocardial infarct size by thallium-201 SPECT. *Journal of Nuclear Medicine, 28*, 325–333.

RIGO, P. & DE LANDSHEERE, C., 1989. Radionuclide imaging in the assessment of cardiac disease. *Current Opinion in Cardiology, 4*, 824–833.

SMITH, C., RUDDY, T. D., DAVIES, R. A. & GULENCHYN, K. Y., 1990. Need for scatter correction in dual isotope imaging is dependent upon radionuclide doses. *European Journal of Nuclear Medicine, 16*, S100.

SOBEL, B. E., BRESNAHAN, G. F., SHELL, W. E. & YODER, R. D., 1972. Estimation of infarct size in man and its relation to prognosis. *Circulation, 46*, 640–648.

TAMAKI, S., NAKAJIMA, H., MURAKAMI, T., YUI, Y., KAMBARA, H., KADOTA, K., YOSHIDA, A., KAWAI, C., TAMAKI, N., MUKAI, T., ISHII, Y. & TORIZUKA, K., 1982. Estimation of infarct size by myocardial emission computed tomography with thallium-201 and its relation to creatine kinase-MB release after myocardial infarction in man. *Circulation, 66*, 994–1001.

WALLIS, J. W. & MILLER, T. R., 1990. Volume rendering in three-dimensional display of SPECT images. *Journal of Nuclear Medicine, 31*, 1421–1430.

WALLIS, J. W., MILLER, T. R., LERNER, C. A. & KLEERUP, E. C., 1989. Three-dimensional display in nuclear medicine. *IEEE Transactions on Medical Imaging, 8*, 297–303.

WEBB, S., OTT, R. J., FLOWER, M. A., MCCREADY, V. R. & MELLER, S., 1987. Three-dimensional display of data obtained by single photon emission computed tomography. *British Journal of Radiology, 60*, 557–562.

1992, *The British Journal of Radiology*, 65, 279–280

Case of the month

Dysphagia paediatrica

By B. M. Stephenson, BSc, FRCS

Department of Surgery, University Hospital of Wales, Heath Park, Cardiff CF4 4XW, UK

(*Received 11 February 1991 and accepted 10 April 1991*)

A 3½-year-old girl presented with a 6 month history of recurrent chest infections and weight loss. Clinical examination was unremarkable. A barium swallow was performed as she suffered from intermittent vomiting and regurgitation of food (Fig. 1). What does this show and what is the differential diagnosis? What further investigations would be appropriate?

Address correspondence to Mr B. M. Stephenson, Surgical Registrar, Department of Surgery, Royal Gwent Hospital, Newport, Gwent NP9 2UB.

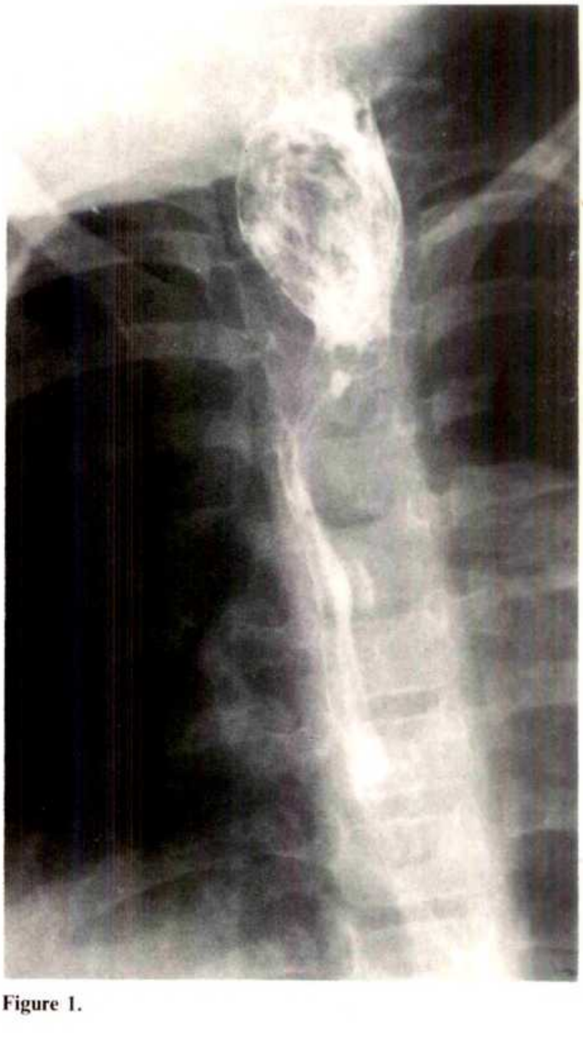

Figure 1.

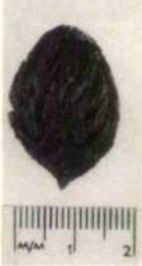

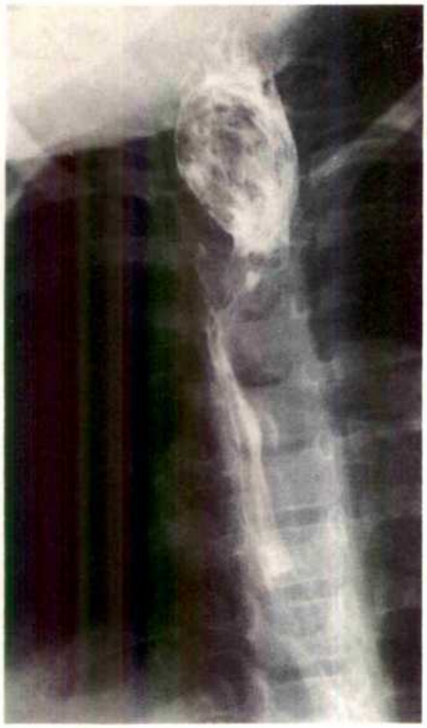

Figure 2. The removed peach stone.

The radiological report suggested food debris above a stricture or vascular ring. A flexible endoscopy was performed which revealed food debris overlying an inflamed and oedematous mucosa which was also pulsatile. She then underwent selective aortic arteriography which showed no evidence of a vascular abnormality. As her symptoms did not improve she underwent a rigid oesphagoscopy at which an impacted peach stone was removed (Fig. 2). A subsequent contrast study showed no sign of a stricture or web and there was no demonstration of gastro-oesophageal reflux.

Discussion

The differential diagnosis includes an impacted foreign body, a stricture from a foreign body or corrosive damage and a vascular ring.

The most common type of congenital anomaly of the aortic arch that produces a vascular ring is a right aortic arch with an anomalous left subclavian artery arising from the descending aorta and passing behind the oesophagus (dysphagia lusoria). This ring around the trachea and oesophagus leads to varying degrees of compression with affected patients presenting with stridor, cough and recurrent respiratory infections. However, symptoms can be mild and presentation may not occur until later life. Barium studies usually demonstrate indentation from right to left in the antero-posterior projection and a posterior indentation on lateral views. Although the barium swallow did not demonstrate these features, angiography was performed as the area was pulsatile on endoscopy.

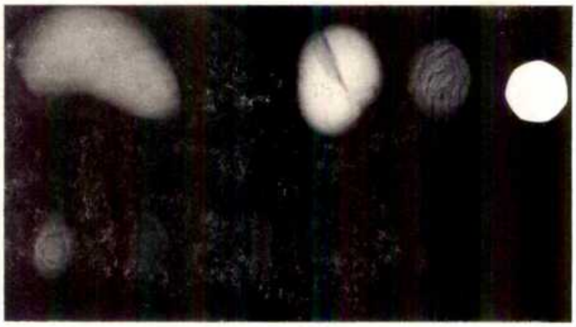

Figure 3. Radiograph of various fruit stones. Left to right, Top: mango, avocado, nectarine, 20 pence coin; Bottom: peach, plum, date, prune, orange, passion fruit.

Foreign bodies that become lodged in the oesophagus usually do so at one of three areas of physiological narrowing; just below the cricopharyngeal muscle, at the level of the aortic arch (as in this case), or just above the diaphragm. Rigid oesophagoscopy may be necessary to remove well embedded foreign bodies, as illustrated by this case. Despite the fact that there was no history suggestive of ingestion of the peach stone, the pattern on the barium swallow is recognizable. Furthermore, although plain radiography is usually considered unhelpful, unless a foreign body is metallic or sufficiently radio-opaque, other fruit seeds and stones have remarkably well defined patterns which are also easily recognizable (Fig. 3). It is of interest to note that of the 63 foodstuffs that Stephens (1966) found to be incriminated in causing either oesophageal or gastrointestinal obstruction, dried fruits and their seeds feature prominently. Although the avocado and mango stones are unlikely to be swallowed, large amounts of coconut have been reported to cause acute obstruction at both the proximal and distal ends of the small intestine (Latchmore, 1940).

Acknowledgments

The author thanks Mr J. Lari, Consultant Paediatric Surgeon, Cardiff for allowing him to report his patient.

References

LATCHMORE, A. J. C., 1940. Stomach-ache. *Lancet, i,* 1153–1155.

STEPHENS, F. O., 1966. Intestinal colic caused by food. *Gut, 7,* 581–582.

Keywords: Dysphagia

1992, *The British Journal of Radiology*, *65*, 281–282

Short communication

Percutaneous sclerotherapy for simple renal cysts in children

By I. Reiner, MD, S. Donnell, FRCS, M. Jones, FRCS, *H. L. M. Carty, FRCR and *A. M. K. Richwood, FRCS

Departments of Urology and *Radiology, Royal Liverpool Children's Hospital (Alder Hey), Eaton Road, Liverpool L12 2AP, UK

(*Received 5 June 1991, and in revised form 30 July 1991, accepted 16 August 1991*)

Keywords: Sclerotherapy, Renal cysts

Simple renal cysts are rare in children although numbers detected have increased of late owing to ultrasonography. Where the lesion is asymptomatic and the diagnosis is not in doubt, an expectant approach is appropriate, but other circumstances may call for active intervention. We describe their treatment by sclerotherapy.

Case reports

Between the years 1986 and 1990, 2880 renal ultrasound scans were performed on children referred to the Department of Urology. Sixteen renal cysts were identified in 16 patients, an incidence of 0.55%. In two cases symptoms were considered to be related to the cysts and in two further cases ultrasonography could not exclude other lesions.

Case 1

This female child presented at 4 years of age with episodic left hypochondrial pain. Intravenous urography (IVU) suggested a space-occupying lesion within the left upper renal pole, which ultrasonography confirmed as a simple, 4 cm × 4 cm cyst (Fig. 1a). Under ultrasound guidance, the lesion was punctured, aspirated and instilled with 150 mg tetracycline in 3 ml normal saline. The child has since been asymptomatic and at 18 months the cyst has not recurred (Fig. 1b).

Case 2

This female patient presented at 16 years of age with episodic right hypochondrial pain and ultrasonography demonstrated a 6 cm × 4.5 cm cyst within the right upper renal pole. Intervention was as in Case 1; 34 months post-treatment there has been no recurrence of symptoms or lesion.

Case 3

Right upper polar hydronephrosis had been detected by pre-natal ultrasonography in this male patient. Post-natally, ultrasonography and IVU indicated that the lesion was a simple, 3 cm × 3 cm cyst within the right upper renal pole although a duplication anomaly could not be excluded. The diagnosis was confirmed by cyst puncture with injection of contrast medium. Treatment was as in Case 1 and at 36 months the lesion has not recurred.

Case 4

This female child presented at 7 years of age with secondary diurnal enuresis. IVU and ultrasonography examinations were consistent with a large, 10 cm × 6 cm cyst within the right upper renal pole but a duplex system anomaly with ureteric ectopia (accounting for the enuresis), or even a large calyceal diverticulum, could not be excluded. Diagnosis was confirmed by cyst puncture with injection of contrast medium. Treatment was as in Case 1 and 6 months later the lesion has not recurred.

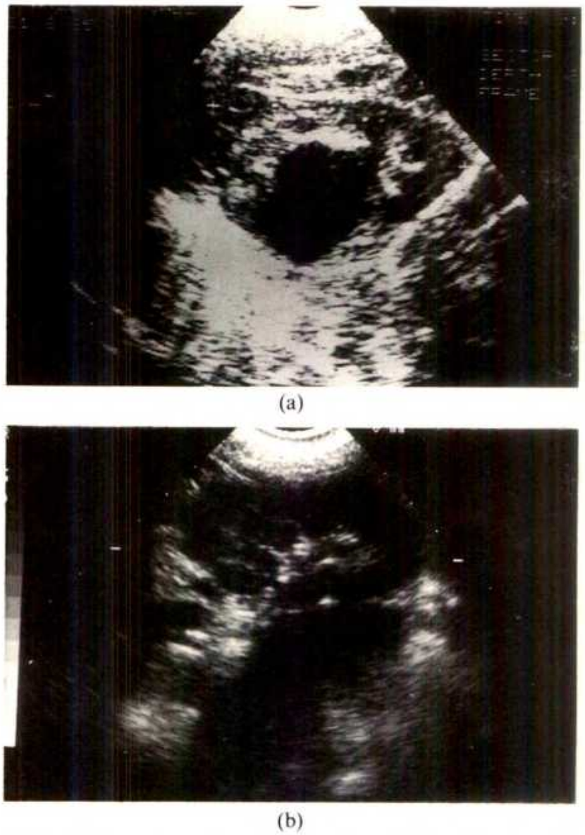
(a)

(b)

Figure 1. *Case 1.* (a) Ultrasonography: left renal cyst. (b) Ultrasonography 18 months after sclerotherapy. No cyst is seen.

Discussion

Simple renal cysts are found in 0.22% of abdominal ultrasonography examinations performed in children (McHugh

---

Address correspondence to Mr S. Donnell.

et al, 1991). In our selected series we found an incidence of 0.55%, so that although these lesions may be more prevalent than suspected clinically they are still rare in paediatric practice.

The simple renal cyst is defined as a sonographically rounded, anechoic lesion with distal acoustic enhancement (McHugh et al, 1991). Most are asymptomatic incidental findings (Bartholomew et al, 1980).

No further treatment is usually indicated but those presenting symptomatically clearly call for treatment. Cyst aspiration alone is almost always followed by recurrence (Bartholomew et al, 1980) while marsupialization, although effective (Kramer et al, 1982), requires open surgery. In our experience percutaneous sclerotherapy with tetracycline solution represents a simple, safe and effective remedy.

In children, solitary renal cysts may be confused with duplication anomalies, such as upper pole hydronephrosis secondary to an obstructing ureterocele or ectopic ureter, a more common and serious condition. Other possible differential diagnoses include calyceal diverticula or even renal tumour (Kramer et al, 1982; McHugh et al, 1991). Percutaneous puncture with injection of contrast medium may be necessary to confirm the diagnosis, and simultaneous sclerotherapy will also cure the lesion and allay any long-term parental anxiety.

References

BARTHOLOMEW, T. H., SLOVIS, T. L., KROOVAND, R. L. & CORBETT, D. P., 1980. The sonographic evaluation and management of simple renal cysts in children. *Journal of Urology, 123*, 732–736.

KRAMER, S. A., HOFFMAN, A. D., AYDIN, G. & KELALIS, P. P., 1982. Simple renal cysts in children. *Journal of Urology, 128*, 1259–1261.

MCHUGH, K., STRINGER, D. A., HERBERT, D. & BABIAK, C. A., 1991. Simple renal cysts in children: diagnosis and follow-up with US. *Radiology, 178*, 383–385.

1992, The British Journal of Radiology, 65, 283

Correspondence

(The Editors do not hold themselves responsible for opinions expressed by correspondents)

Anatomy of percutaneous femoral artery puncture

The Editor—Sir,

The paper by Grier and Hartnell (1990) discusses the use of the inguinal skin crease and the site of maximal pulsation in femoral artery puncture, but omits mention of the mid-inguinal point. Defined as being "midway between the anterior superior iliac spine and the symphysis pubis", this point is traditionally held by anatomists to be the most accurate landmark in locating the common femoral artery (Williams & Warwick, 1980).

The anatomical accuracy of the mid-inguinal point was tested by studying 10 adult cadavers, using one side only on each. A tape measure was placed accurately between the two points and the exact mid-point marked on skin. (As the symphysis pubis was impossible to palpate through embalmed skin it was located by a limited dissection.)

A point exactly 1 cm below the marking, and perpendicular to the line of the tape measure, was used for puncture. This was because initial attempts went through the inguinal ligament whereas the lower marker consistently punctured safely below it. Only punctures at the latter point are included in the results. A metal cannula was inserted vertically down to bone and, leaving the cannula *in situ*, a small distal skin flap was raised and the cannula's position visualized by dissection. No attempt was made to reproduce the 45° angle of insertion used clinically, as the sole purpose of this study was to confirm the reliability of the two bony landmarks in indicating the position of the vessel.

In 90% (9 out of 10) of the cadavers the cannula was through the artery. In 40% (4 out of 10) of the cadavers the artery was punctured as it lies over the pubic ramus. In 50% (5 out of 10) the artery was punctured at a site over the femoral head. In all cases the common femoral artery was punctured at least 1 cm above its bifurcation. In the single failed puncture, the cannula was observed lying 1 mm medial to the artery. The initial measurements in this case could not be faulted.

A total of 14 of Grier and Hartnell's original respondents stated that they did use "bony landmarks" and it would be interesting to know whether this involves use of the mid-inguinal point. Measured accurately, it would seem that the mid-inguinal point is at least as precise as the inguinal skin crease, as a guide to the position of the common femoral artery. It is also far less variable between patients.

Neither this study nor the original one by Grier and Hartnell attempts to quantify the variability in the depth of the common femoral artery below skin — this would be a useful subject for further study, and relevant to the angulated puncture normally employed for catheterization.

The clinical relevance of this study is untested, but a carefully marked out mid-inguinal point could be a useful visual clue in cases where the femoral pulse is impalpable. We would also suggest that in certain special cases the extra care in identifying the landmarks would be worthwhile, for example when fibrinolytic therapy is being used or contemplated, when stents are similarly used of contemplated (because these patients have to be obsessively anticoagulated) and for valvuloplasty in which relatively large shaft catheters are used. In all these situations inadvertent puncture of the wrong level would increase the risk of haemorrhage.

F. Stubbs
D. C. Cumberland

References

Grier, D. & Hartnell, G., 1990. Percutaneous femoral artery puncture: practice and anatomy. *British Journal of Radiology*, *63*, 602–604.

Williams & Warwick, 1980. *Gray's Anatomy*, 36th Edition (Churchill Livingstone, Edinburgh).

(Received 24 October 1991, accepted 6 December 1991)

Authors' reply

The Editor—Sir,

Thank you for giving us the opportunity to reply to the letter by Stubbs and Cumberland. We were certainly aware of the mid-inguinal point as a landmark for puncturing the femoral artery. In fact, this was the method which one of us was taught at the start of cardiology training over a decade ago. However, personal experience suggests that there are frequently practical problems when using this method for localizing femoral puncture sites.

In cadaver studies, it is easier to feel bone landmarks reliably as the subcutaneous tissues are fixed and therefore less mobile than in live patients. Certainly one would expect that in relatively thin patients the use of the bony landmarks described by Stubbs and Cumberland would probably represent a reliable marker for guiding femoral artery puncture. However, in the more obese patient, there is such a thickness of fat between the skin and the underlying bony structures that reliance on this method could produce marked errors. This will certainly be a frequent problem on the western side of the Atlantic Ocean. Undocumented and totally subjective personal experience suggests, however, that even in very obese patients, it is almost always possible to palpate the femoral pulse and that the maximum pulse is usually over the femoral head when checked with fluoroscopy. It is therefore our contention that although the mid-inguinal point may be a useful landmark for common femoral artery puncture, the point of maximum arterial pulsation remains the most reliable position for consistent safe puncture of the common femoral artery.

G. G. Hartnell
D. Grier

Department of Radiology,
New England Deaconess Hospital,
185 Pilgrim Road,
Boston, Massachusetts,
USA

(Received 13 November 1991, accepted 6 December 1991)

1992, *The British Journal of Radiology*, *65*, 284–286

Proceedings of the British Institute of Radiology

International particle therapy meeting

Abstracts presented at a meeting organized by the BIR Radiation Oncology and Radiobiology Committees, held at the British Institute of Radiology, 36 Portland Place, London W1N 4AT on Friday, 7 June 1991

Particle therapy facilities worldwide and the physical rationale for particle therapy, by D. K. Bewley
Biological rationale for particle radiotherapy, by M. C. Joiner
The National Cancer Institute fast neutron radiation therapy research programme, by T. W. Griffin and S. Zink
Discussion: have neutrons any part to play in the management of locally advanced cancers?
  S. J. Arnott. Abstract not received
  R. D. Errington. Abstract not received
  T. Bates
  S. M. Gore
The development of the Clatterbridge proton therapy facility, by D. E. Bonnett
Proton therapy for ocular malignant melanoma and the design of appropriate clinical trials, by J. H. Hungerford
The Havard Cyclotron Experience in treating Chordomas with 160 MeV protons, by D. Cole
The development of Loma Linda proton therapy facility: clinical rationale and overview of treatment protocols, by J. M. Slater
Rationalizing the current and future role of particle radiotherapy in Europe, by A. Wambersie

Particle therapy facilities worldwide and the physical rationale for particle therapy

D. K. Bewley
44 Addison Avenue, London W11

The conventional radiation beams used at the present time, X rays, gamma rays and electrons, leave much to be desired from the physical point of view. An ideal radiation would give a uniform dose (or whatever is desired) to the tumour and zero outside. Of the unconventional radiations now in use, fast neutron beams provide no advantage over X and gamma rays in this respect. Their advantage can only be biological and is under assessment in at least 17 centres around the world. On the other hand, boron capture therapy with epithermal neutrons does offer the possibility of better localization of the dose within the tumour, at any rate in brain tumours, and this method is under active consideration at several centres. Negative π mesons have been introduced at three centres, two of which are still operating, in an attempt to give a more concentrated dose distribution and to reproduce the radiation quality of neutrons within the tumour but not in more proximal tissues. The huge expense of this technique seems likely to prevent it from gaining wider acceptance. A more economical method is the use of stripped atomic nuclei, or light ions, in the range H to Si. These provide dose distributions close to the ideal and are under trial at 12 or more centres, with other facilities planned. Protons are the cheapest and provide a substantial physical advantage over X and gamma rays and electrons. Heavier ions in addition give a differential in radiation quality between the tumour at a depth and proximal normal tissues, but at considerably greater expense.

Biological rationale for particle radiotherapy

M. C. Joiner
Cancer Research Campaign Gray Laboratory, PO Box 100, Mount Vernon Hospital, Northwood, Middx HA6 2JR, UK

The use of light ions for radiotherapy can be justified alone because of the improved dose distributions that can be obtained. Protons have this physical advantage over conventional photon beams while still being of comparable linear energy transfer (LET), but light ions of greater mass also have the potential biological advantage of a higher LET. Neutrons have no physical dose-distribution advantages over photons, but are of higher LET so that the biological rationale for using high-LET particles can be assessed from the many studies done on both the radiobiological and the clinical properties of fast neutron beams. Initially, neutron therapy was based on the belief that the success of photon therapy was limited by the resistance of hypoxic tumour cells. High-LET radiations are relatively more effective against hypoxic cells than low-LET beams and so would give an effective radiosensitization of tumours, compared with normal tissues where the degree of hypoxia is small or non-existent. This rationale is still valid today, but it is now realized that many tumours self-sensitize through a course of clinical radiotherapy by the process of reoxygenation and, therefore, high-LET therapy will only give an advantage over photon therapy by this mechanism if tumours have large hypoxic fractions or reoxygenate poorly. Cells in late S phase tend to be maximally resistant to photon irradiation while cells in G_2 or Mitosis are most sensitive. These differences are reduced with high-LET radiations. Therefore, tumours which proliferate slowly or whose cells have long cycle times will acquire photon resistance as cells build up in resistant phases after several dose fractions, and these tumours might be better treated with high-LET beams to avoid this. Finally, studies on many human cell lines have shown that the spread of radiosensitivity is less after neutron rather than photon irradiation at the same median cell kill, and that the ranking of radiosensitivity to neutrons and photons of the cell lines may be different. Therefore, it is possible that some tumours which are radioresistant to photons compared with other tumours or normal tissues, may be relatively more radiosensitive and hence better treated, with high-LET beams. However, this highlights the need to select patients (using radiosensitivity measurements *in vitro*) whose tumours fall into this category since the cell line data indicate that less than 45% of tumours would benefit from high-LET therapy by this mechanism. Indeed, patient selection on the basis of hypoxia and cell kinetics should also be used to maximize the gain from high-LET particle therapy by these two other mechanisms and one is left with the conclusion that the use of high-LET radiation for cancer treatment should therefore be governed by the tumour radiobiology (radiosensitivity, hypoxia and cell kinetics) of each patient individually. Fortunately, these predictive assays are under development in a number of centres and should become a routine part of cancer management in the future.

The National Cancer Institute fast neutron radiation therapy research programme 1971–1991

Thomas W. Griffin MD and *Sandra Zink, PhD
*University of Washington, Seattle, Washington and *National Cancer Institute, Bethesda, Maryland, USA*

The National Cancer Institute (NCI) fast neutron radiation therapy research programme was initiated in the United States in 1971. Initially, physics laboratory based cyclotrons were modified for clinical use and later clinical trials were conducted using these machines between 1972 and 1984. Based on the results of these studies, the NCI sponsored the development of four hospital based neutron generators in 1979 (three cyclotrons and a DT generator). Patient treatments on these machines began in 1984. Three Phase III studies were designed to compare directly fast neutron with photon radiation therapy in patients with carcinomas of the head and neck, lung and prostate gland. 556 patients were randomized on these three studies, 178 with squamous cell head and neck cancers, 178 with adenocarcinomas of the prostate, and 200 with non-small cell lung cancers. As of March 1991, all NCI sponsored neutron studies have been completed. This 20 year, $70 million project involved the construction or modification of 10 separate neutron facilities and the treatment of several thousand patients. While it will be several years before the definitive results of this research effort can be reported, the initial data from the latest generation of neutron studies are now available for analysis.

Have neutrons a part to play in the management of locally advanced cancers?

Thelma Bates
South East Thames Radiotherapy Centre

On current evidence radiotherapists can safely accept a role for modern neutron therapy. Neutron therapy results for inoperable salivary gland tumours have been consistent, conclusive and as predicted by radiobiology. In a prospective trial neutrons achieved 67% locoregional control *vs.* 17% for photons ($p < 0.005$) with no difference in complication. Similar results have been observed in paranasal sinus tumours. Head and neck trials containing many different tumour types lack specificity and to date have shown no advantage for neutrons, but advantage has been seen repeatedly in patients presenting with positive neck nodes, a situation where hypoxia exists. Encouraging results are being observed in the RTOG trial in locally advanced prostatic adenocarcinoma (Stage C and D_1) comparing a mixed beam of neutrons and photons with photons alone. At 10 years, the mixed beam group has done statistically better than the photon group with survival rates of 42% *vs.* 27%. Neutrons may have a role in other radioresistant tumours. Supported by non-randomized data, several US centres use neutrons rather than photons in combination with chemotherapy and surgery for soft tissue, osteosarcomas and chondrosarcomas. Excessive morbidity has been reported mainly in the early, low energy neutron studies often caused by beam limitations and inadequate knowledge of dose scheduling. "Devastating" morbidity was generally related to very large tumours of those previously treated aggressively with surgery and radiotherapy. Recent US studies have established safe dose levels in relation to site, volume irradiated and neutron energy. The multileaf collimator now aids the precision of the modern high energy neutron beam.

Statistical overview of randomized trials of neutron therapy

Sheila M. Gore
MRC Biostatistics Unit, 5 Shaftesbury Road, Cambridge CB2 2BW

Integrity of randomization, analysis without exclusion of randomized patients and the reporting of a common endpoint (such as 1 year patient survival, read from a lifetable plot or, preferably, a table) are prerequisites for statistical overview without access to original data. *Pelvic cancer.* The above criteria are met by the randomized trials of low energy neutron *vs.* photon treatment for cancer of the bladder or rectum. Mantel-Haenszel overview showed that the observed number of low energy neutron survivors (99) at 1 year was 3.4 standard errors fewer than expected (115.3). The pooled relative risk (RR) of death within 1 year after randomization (photon *vs.* low energy neutrons) was 0.65 (95% confidence interval: 0.50–0.84) and for photons *vs.* high energy neutrons the adjusted relative risk, at termination of the Clatterbridge pelvis trial, was 0.66 (95% confidence interval: 0.40–1.10). The latter excluded (a) clinicians' median prior belief (elicited in March 1988) in RR of 1.14, and (b) high energy neutrons as practicable therapy for locally advanced pelvic cancer (March 1988 consensus set RR at 1.30 for neutrons as practicable therapy). *Head and neck cancer.* Some published low energy neutron trials and interim reports of high energy neutron *vs.* photon treatment for head and neck cancer fail the criterion of analysis without exclusion of randomized patients. Exclusions were 17% and 13% in published reports, and are 11% in an interim MRC/RTOG report. In February 1990, because randomization had ceased in the Clatterbridge pelvis trial and there was natural concern for head and neck cancer patients, statistical overview was made of the then available, albeit incomplete, data from head and neck cancer trials. Now (February 1991 update), as then, this overview of mortality at 1 year did not give grounds for randomization to cease; the observed number of neutron survivors at 1 year (156) accords with 159.2 expected (standard error 5.9).

The development of the Clatterbridge proton therapy facility

D. E. Bonnett MSc, PhD
MRC Cyclotron Unit, Clatterbridge Hospital, Merseyside, L63 4JY

The cyclotron at the Clatterbridge Hospital is capable of accelerating protons to 62 MeV. This beam has a maximum penetration of 33 mm in water which precludes the treatment of deep seated tumours. The properties of the protons, however, ideally suit them to the treatment of ocular melanoma. These properties include a well defined range, minimum scattering and the possibility of confining the high dose region to the target volume. In 1985, a series of feasibility studies were carried out to establish whether the Clatterbridge beam could be used for such treatments. These studies resulted in the design of a fixed horizontal beam line and treatment facility. Two beam configurations are used both incorporating a double flattening foil system with a central absorber. The first has a penetration of 31.9±0.2 mm in water and penumbra which vary from 2.3 to 3.6 mm, depending on the thickness of range limiting and beam modulation devices. The second has a penetration of 31.1±0.2 mm and a mean penumbra of 1.9±0.2 mm. The beam line incorporates irregular shaped collimators and it is found that the output varies by less than 2% over the range of field areas used. The facility became operational in June 1989 and to date (May 1991) a total of 157 patients have been treated.

The development of the Loma Linda proton therapy facility: clinical rationale and overview of treatment protocols

James M. Slater, MD, FACR
Department of Radiation Medicine, Loma Linda University Medical Center, Loma Linda, California, USA

Proton beams have unique advantages for radiation therapy. Their combination of mass, charge and radiobiologic behaviour enables radiation oncologists to position a tumouricidal dose precisely, and to spare normal tissues intimately adjacent to the designated treatment volume. The accelerator, the beam transport, delivery and control systems, and the personnel at the proton therapy center, are dedicated to applying these unique advantages for patient treatment. Presently, protocols have been developed for patients with certain ocular tumours, CNS malignancies, and cancers of the head and neck; all these patients are treated by a stationary proton beam. The first of three moveable beams begins operation shortly, enabling treatment of patients with localized disease below the neck. Protocols are being developed now for treating pelvic tumours; others soon will be developed systematically for patients with disease in other anatomic sites. Protocols are designed to compare and contrast proton with conventional irradiation; to identify disease presentations for which protons offer substantial therapeutic advantages; and to optimize radiation delivery by reducing overall treatment time wherever possible.

Rationalizing the current and future role of particle radiotherapy in Europe

André Wambersie
Université Catholique de Louvain, Cliniques Universitaires St-Luc, 1200—Brussels, Belgium

Proton beam therapy is used for the treatment of uveal melanoma (and/or superficial tumours) at PSI-Villigen, Uppsala, Clatterbridge, Louvain-la-Neuve (Orsay and Nice will start in the near future). "High-energy proton" therapy ($\geqslant$ 200 MeV) is in preparation in Orsay and PSI-Villigen. Other projects are contemplated, where the preference is given to well established technology (reliable and rather low cost, isochronous, non-supraconducting cyclotrons). Fast neutron therapy is currently applied in six centres in the European continent: Orléans, Louvain-la-Neuve, and four centres in Germany: Essen, Hamburg, Heidelberg, and Munster. Tumours of the salivary glands, antrum, some tumours of the head and neck (fixed lymph nodes), well differentiated soft tissue sarcomas and prostatic adenocarinomas are considered to be good indications for neutron therapy. A randomized trial for recurrent rectal carcinoma has been initiated. The experience of Louvain-la-Neuve indicates that the tolerance to mixed schedule irradiation (3 n + 2 ph, p(65) + Be neutrons) is similar to that after photon irradiation, also for pelvic tumours (*e.g.* prostate, bladder). Heavy ions combine the advantages of a high physical selectivity (similar to protons) and of the high linear energy transfer (for the treatment of some tumour types: slowly growing, well differentiated compared with fast neutron therapy). A feasibility study of a heavy ion accelerator, specifically designed for cancer therapy, and sponsored by the CEC, is nearly completed (the EULIMA project: four treatment rooms, about 3000 patients per year). However, as a first step, it is likely that heavy ion therapy will start in Europe using an existing machine (*e.g.* at the GSI in Darmstadt).

1992, *The British Journal of Radiology*, *65*, 287–288

Book reviews

Interventional Computed Tomography. By R. M. M. Seibel and D. H. W. Gronemeyer, pp. xvi + 355, 1990 (Blackwell Scientific Publications, Oxford), £95.00.

Truly a curious book. Has interventional computed tomography (CT) really expanded sufficiently to justify a complete and sizeable book? First glances at the list of contents raised high expectations; it includes not only the procedures usually practised under CT control but a wide range of techniques that will, I suspect, be new to some readers; in cancer care, pain relief and treatment of occlusive vascular disease. The authors are clearly prepared to place a needle absolutely anywhere in the body (but not the brain) under CT control and their ingenuity and wide experience are amply borne out by numerous case illustrations, which form the bulk of the book.

However be warned; this is a book to stimulate ideas, not a definitive manual. Much of the written text consists of the authors' experience reported in scientific paper style. There is minimal discussion of other workers' experience or alternative approaches and the reader looks in vain for the expected technical hints and detailed advice on practical difficulties. The case illustrations do not really bring out these considerations. In some places the text is so limited as to be almost bland and some chapters consist only of plates and legends, while others consist only of a single page of text.

This, and the fact that most of the 472 illustrations are half page, means that 355 pages pass by at a spanking rate; in half an evening to be precise. In a field which the authors have set so wide, this is superficial coverage, especially so in the case of complications, which are frequently dismissed in a sentence or two. Many of these techniques carry significant dangers and the fact that the authors had no complications in their series does not mean that they do not occur. The reader who is, understandably, inspired by this book to explore new horizons is well advised to look at the rest of the literature before leaping. In short, while respecting the authors' enterprise and skills, I feel that this book is basically anecdotal.

Nonetheless it should not be dismissed lightly. It does cover enormous ground and the case illustrations are all interesting. The images are all of high quality and they appear on most of the pages. The book also includes chapters on general background subjects, for example the autonomic nervous system, which do not often make an appearance in radiology. There is an interesting final section on the authors' work involving magnetic resonance imaging (MRI), ultra-fast CT and 3D combination of CT and fluoroscopy. Liberal use of cadaver sections and microscopy adds a touch of colour to the pages. Finally, important sections of text are highlighted in a bold yellow, a practice which would enliven some of our standard textbooks.

For all my reservations, I recommend this well produced, stimulating, (if, ultimately, somewhat frustrating) book to anyone who wants to enlarge their view of what is possible with a needle and a CT scanner. I have enjoyed reading it, though I feel it may belong more on the coffee table than on the library shelf.

STEPHEN GOLDING

Treatment of Radiation Injuries. Ed. by D. Browne, J. F. Weiss, T. J. MacVittie and M. V. Pillai, pp. x + 259, 1991 (Plenum Publishing, New York), $75.00.
ISBN 0–306–43729–5

This book reports on the proceedings of a meeting held in Washington DC in May 1989 that was seen as the first attempt to obtain a concensus in the treatment of radiation injuries. The conference was designed to address the important area of the potential treatment of haematopoietic injury, infectious complications and combined injuries, specifically those involving trauma. It does not attempt to cover the important problem of the treatment of beta-radiation skin burns, so important in the Chernobyl and Goiania accidents, radionuclide decontamination or iodine prophylaxis.

There are in total 21 contributors, of which the majority deal with different aspects of haematopoietic complications. The possible roles of bone marrow transplantation, colony stimulating factors, blood and bone marrow products are discussed. A particularly helpful aspect of the book was the attempt by the editors to summarize the discussion in a form related to specific important questions. These included the problem of what to do in cases of infectious complications and combined injuries, largely thermal burns and wounds, in addition to haematopoietic injury.

The book concludes with a consensus statement on a proposed treatment protocol. This protocol assumes a uniform total body dose, although it is conceded this may not be applicable to all accidents. In the majority of accidents the dose is non-uniform. Also it does not apply to a situation involving mass casualties. The value of such a protocol, where treatment is based on a series of yes or no answers to questions is difficult to judge. However, this does not detract from the general value of the book for those with an interest in radiobiology and likely possibilities for the treatment of radiation accident victims.

J. W. HOPEWELL

Digital Imaging In Diagnostic Radiology. Ed. by J. D. Newell and C. A. Kelsey, pp. ix + 163, 1990 (Churchill Livingstone, Edinburgh), £35.00.
ISBN 0–443–08634–6

The purpose of this book is to provide a basic introduction to both the clinical and technical aspects of digital imaging. It is intended to be read by anyone interested in the subject. The various chapters in the book have been written by a number of authors, all prominent in the field of digital imaging. The chapters are grouped together in two main sections, one dealing with clinical aspects and the other with the technical aspects of the subject.

Dr King from the University of New Mexico has written the first chapter describing the digital subtraction angiography using a mobile image intensifier television system linked to a digital image processor. The use of the technique is briefly described, as is its role in the clinical investigation of patients. There is also a section discussing the limitations of the technique, including the cost implications.

The editors of the book have collaborated on the second chapter on digital radiology of the thorax. The use of scanning equalization techniques are described, with particular emphasis on the development system of the University of Rochester and the Old Delft AMBER system. In addition, photostimulable phosphors, film digitization and image intensifier based digital imaging devices are also mentioned. The requirement for a 2048 × 2048 by 10 bit digital image display is of clinical importance.

Digital genitourinary, gastrointestinal and breast radiology are described by Hunter and Fajardo. The importance of digital imaging in the first two areas is illustrated by a series of interesting studies. As the authors point out, digital imaging has not been widely used in breast imaging due to the costs involved and the limited resolution of currently available equipment. A short chapter on teleradiology concludes the clinical section.

The section of the book on technical aspects commences with two excellent introductory chapters on digital radiography. I would recommend that radiology students read these chapters as part of their studies. Whilst there is some repetition in the two chapters, together they represent a sound introduction to the physics of the subject.

Some readers may find the subjects of the final two chapters to be an unusual choice, as they describe image compression and reconstruction and the economics of digital radiology, respectively. The short chapter on image compression will no doubt be considered by certain computer scientists as a superficial treatment of the subject, but it does cover the important points. The final chapter provides an insight into the economic arguments used in some hospitals to justify the investment in a new and expensive imaging modality.

In summary, I found this book to be informative and it is written in a clear and concise style. It is a good introduction to the subject of digital imaging. The book does not provide a comprehensive treatment of the subject, though to be fair to the authors this was never intended. I would recommend the purchase of this book to a teaching central library.

K. Faulkner

The Radiologic Clinics of North America. Ed. by H. J. Burhenne, pp. xiv + 1313, 1990 (Harcourt Brace Jovanovich, Kent).
ISBN 0033–8389

The pale blue cover of this slim-volume seems like an old friend, and its aquaintance does not disappoint. The 156 pages of text provide a lively update on interventional radiology of the biliary tract. There are contributions from seven countries, beginning with a vivid account of the final illness of the exiled Shah of Persia in 1979. Burhenne suggests that the radiologically controlled removal of a retained common duct stone in the Shah and its subsequent worldwide press coverage marked the start of biliary tract interventional radiology, and who would disagree?

Chapters cover interventional gallbladder procedures, intracoporeal and extracorporeal biliary lithotripsy, metallic *vs.* plastic stents, and combined radiological and endoscopic biliary interventions. The writing is lucid and the figures crisp and glossy. I was particularly impressed with the detailed technical information given to help those doing practical procedures—the occasional toe in the water (or bile) radiologist will find much guidance. Inevitably there is overlap of material, the two chapters on gallbladder drainage by Fache and von Sonnenberg giving similar information and images. I later learnt that PTFCS and BESWL were abbreviations for percutaneous fine calibre cholangioscopy and biliary extracorporeal short wave lithotripsy, whilst the penultimate chapter on experimental ablation of the cystic duct and gallbladder informed me that the electromagnetic technique is safe and effective for the human cystic duct.

I would recommend this update. It would have provided a balance to have a chapter recording the clinicians's view of these procedures, some of which are new challenges to their work, particularly as interventional radiologists tend to have an optimistic outlook on their own exciting studies. In this context, one whole-heartedly supports the editor's disappointment that, to date, randomized trials are largely lacking in assessing the results of techniques which have emerged with enormous haste over the past 10 years.

Robert Dick

1992, *The British Journal of Radiology*, *65*, 289–294

VOLUME 65 NUMBER 772

APRIL 1992

The British Journal of Radiology

Diagnosis of brain death: superiority of perfusion studies with $^{99}Tc^m$-HMPAO over conventional radionuclide cerebral angiography

By *A. de la Riva, F. M. González, J. M. Llamas-Elvira, J. M. Latre, A. Jimenez-Heffernan, †E. Vidal, Mª Martinez, M. Torres, ‡R. Guerrero, ‡F. Alvarez and A. Mateo

Departments of Nuclear Medicine, *Neurosurgery, †Internal Medicine and ‡Intensive Care, "Reina Sofia" Hospital, Avda. Menendez Pidal s/n, 14004 Cordoba, Spain

(*Received 20 June 1991 and in revised form 23 September 1991, accepted 8 October 1991*)

Keywords: $^{99}Tc^m$-HMPAO, Cerebral flow, Brain death

Abstract. The use of technetium-99m hexamethyl-propyleneamine oxime ($^{99}Tc^m$-HMPAO) in the diagnosis of brain death has been evaluated in 41 studies of 37 patients with severe brain injury, who were under the effect of drugs or when other diagnostic methods were equivocal. HMPAO studies were compared with conventional radionuclide angiography performed simultaneously by intravenous administration of HMPAO as a bolus. The ages of patients ranged from 4 months to 75 years. Dynamic flow images and 5-min static uptake images were acquired following bolus injection of 555 Mbq of $^{99}Tc^m$-HMPAO. All patients showing no brain uptake were confirmed as brain-dead by standard clinical criteria, with no contradictory cases in the static study. In addition, all patients who were not brain-dead showed HMPAO uptake at least in the brainstem. Dynamic flow images were equivocal in five patients, four of whom had no uptake on static images and clinically confirmed brain death. In addition, two other cases showed "mismatched" dynamic and static images: in one case no perfusion was observed on flow images but uptake restricted to the posterior fossa was seen on static images; the other case showed perfusion on the dynamic study and static imaging revealed hemispheric uptake with no posterior fossa uptake. Static perfusion $^{99}Tc^m$-HMPAO studies offer advantages over conventional brain scintigraphy, better results being due to adequate assessment of posterior fossa activity and avoiding equivocal studies.

Assessment of brain death has been increasing in importance since the advent of organ transplantation. Advances in life-support systems and the increasing demand for organ donors need diagnostic methods that identify irreversible loss of brain function accurately and promptly.

The diagnosis of brain death is difficult to establish in patients with artificial life-support systems, and is further hindered by the use of barbiturate-induced coma and hypothermia for suppression of brain metabolic activity. In these cases, electroencephalographic (EEG) activity may be absent or markedly reduced and the only reliable method of diagnosis is the absence of intracranial blood flow. This is especially important in patients with cranial trauma and serious facial lesions in whom neurological examination is difficult, as well as in children in whom EEG silence and clinical signs of loss of brain functions are often equivocal. In these conditions the assessment of brain blood flow may constitute a decisive diagnostic criterion (Black & Zervas, 1984; Pjura & Kim, 1987; Kaufman et al, 1989).

Contrast medium angiography of the brain is considered to be the "gold standard" for brain perfusion (Pjura & Kim, 1987), but is an expensive, invasive and technically complex procedure that requires transportation of the patient to an angiography facility and positioning on the table with the risk of clinical deterioration (Andrews et al, 1990).

Radionuclide cerebral angiography has been proposed as an alternative method for the evaluation of brain perfusion, showing a good correlation with four-vessel angiography (Kricheff et al, 1975; Korein et al, 1977). Scintigraphy has been widely accepted, although it has problems of interpretation in cases of poor bolus quality, severely reduced but not absent brain perfusion and in some patients with haematomas and trauma. The significance of venous sinus visualization has been recently clarified in two papers (Lee et al, 1987; Laurin et al, 1989). In addition, radionuclide perfusion scintigraphy only assesses hemispheric brain perfusion, with poor visualization of the posterior fossa and brainstem.

Technetium-99m hexamethyl-propyleneamine oxime ($^{99}Tc^m$-HMPAO) is a radiopharmaceutical that crosses the intact blood–brain barrier and is trapped by brain tissue in proportion to regional perfusion. Uptake on static images reflects brain perfusion (Sharp et al, 1986; Neirinckx et al, 1987).

Address correspondence to: Dr J. M. Llamas-Elvira, Servicio de Medicina Nuclear, Hospital "Reina Sofia", Avda. Menendez Pidal s/n, 14004 Cordoba, Spain.

Few reports exist about the usefulness of ^{99}Tc^{m}-HMPAO in the diagnosis of brain death (Roine et al, 1986; Galaske et al, 1988; Laurin et al, 1989; Reid et al, 1989). HMPAO brain uptake has been reported in patients thought to be brain-dead on clinical grounds and who subsequently recovered (Reid et al, 1989). We agree with George (1991) that further study is necessary to determine the role these studies may play in diagnostic protocols for establishing brain death, especially in relation to early diagnosis in organ donors in barbiturate-induced coma, children and trauma patients.

The purpose of this paper is two-fold. First, we review our experience with ^{99}Tc^{m}-HMPAO in the diagnosis of brain death, verifying its diagnostic usefulness and reliability in potential organ donors under the effects of drugs or when other diagnostic methods are equivocal. Secondly we compare these studies with conventional radionuclide angiography performed simultaneously through the intravenous administration of the radiopharmaceutical as a bolus with registration of sequential dynamic images of brain arterial perfusion.

Patients and methods

We performed 41 brain flow studies with ^{99}Tc^{m}-HMPAO (dynamic phase and perfusion static imaging) in 37 patients (24 men and 13 women) with acute and severe brain injury. Ages ranged from 4 months to 75 years (mean 28.8 years). Patients were admitted to the hospital with the following conditions: multitrauma with head injury (20), head trauma (4), brain haemorrhage (7), and sepsis, encephalitis, cerebral infarction, dehydration, myocardial infarction, and renal failure in one case each. Table I shows age, sex, reason for admission to hospital and other clinical details at the time of study.

Barbiturate coma was present at scintigraphy in 12 patients. Five other patients were studied 24–48 h following barbiturate withdrawal.

Scintigraphy was performed when brain death was clinically suspected. When the study disclosed brain uptake of HMPAO or brain activity on dynamic images in patients with a deteriorating clinical state, the study was repeated 24–48 h later. Standard clinical criteria for the diagnosis of brain death were applied in cases showing no brain uptake on scintigraphy except in the group of patients in barbiturate-induced coma. In the latter, a 48-h interval after barbiturate withdrawal was left before the evaluation of standard clinical criteria.

Radiopharmaceutical preparation

^{99}Tc^{m}-HMPAO was prepared by the addition of 2.5 ml of an eluate obtained from a recently eluated Mo/Tc generator (less than 6 h) with 1750 MBq activity to a Ceretec vial (code n109z, Amersham International plc) with vortex mixing for 3 min. Quality control ensued and individual doses were prepared: 555 MBq for adults and activity proportional to body surface in children with a minimum dose of 148 MBq.

Quality control was performed with column chromatography to determine the proportion of primary complex following the method validated by Mah et al (1989). Preparations with less than 85% of primary complex were rejected following the criteria of image quality reported by Ballinger et al (1990).

Doses were injected intravenously as a bolus using the most central venous line available. All doses were injected within 10 min of preparation.

Study acquisition

Scintigraphy was performed with the patient supine, including head and neck (or part of it) in the gamma camera's field of view. A stationary Siemens ZLC-37 gamma camera was used, and all patients were studied in the Nuclear Medicine facility. Rapid-sequence angiographic images with no scalp compression were acquired and registered on a 64 × 64 computer data matrix at 1 s images during 60 s. Simultaneously, 20 analogic images were obtained on radiographic film at 2 s per image. Five minutes later static brain images were obtained. Three planar static images (anterior and both laterals) were obtained on film at a minimum of 500 Kcounts and registered on a 128 × 128 matrix. Special care was taken to obtain good visualization of the posterior fossa on both lateral views.

Image evaluation

Angiographic images were carefully screened for activity in the principal cranial arteries. In cases of poor bolus quality, tracer extravasation or faint hemispheric activity, the study was interpreted as equivocal. Absence of HMPAO uptake in hemispheres and posterior fossa on static images was interpreted as consistent with brain death. Visualization of activity in saggital or transverse sinuses was not taken into account.

A nuclear medicine physician retrospectively re-evaluated all studies, and no changes in interpretation resulted.

Standard brain death criteria

Criteria for the diagnosis of brain death in this study were as follows.

1. Previous criteria: known aetiology of loss of brain function, central temperature higher than 33°C, systemic arterial blood pressure higher than 80/40 mmHg, no previous endogenous or exogenous intoxication, no previous administration of muscle relaxants.
2. Neurological criteria: profound coma and absence of response to painful stimuli, muscular hypotonia, non-reactive and dilated pupils, abolition of brainstem reflexes, unresponsiveness to the apnoea test despite hypoxaemia and hypercarbia, absent response of the heart rate to atropine.
3. EEG criteria: isoelectric EEG tracing for a period of 30 min despite stimulation.
4. Persistence criteria: persistence of all above criteria 6 h after the first examination in adults and 12 h in children.

Table I. Details of patients and findings

Case	Age	Sex	Previous condition	Additional data at time of study	Radionuclide angiography	Static imaging	Time interval between scan and clinical brain death diagnosis
1	4 mon	M	Head trauma		Equivocal (poor bolus)	Absent uptake	48 h
2	20	F	Head trauma	Pentobarbital withdrawn 48 h before	Equivocal	Absent uptake	24 h
3	45	F	Head trauma		Absent flow	Absent uptake	48 h
4	3	F	Fever convulsion	Pentobarbital	Absent flow	Absent uptake	48 h
5	21	M	Head trauma	Pentobarbital	Absent flow	Absent uptake	48 h
6	40	F	Polytrauma		Absent flow	Absent uptake	
7	22	M	Polytrauma	Pentobarbital	Absent flow	Absent uptake	48 h
8	28	M	Encephalitis		Absent flow	Absent uptake	
9	1	M	Polytrauma		Equivocal (poor bolus)	Absent uptake	
10	38	M	Brainstem haemorrhage		Absent flow	Absent uptake	
11	19	M	Polytrauma		Equivocal	Absent uptake	
12	46	M	Polytrauma	Pentobarbital	Absent flow	Absent uptake	48 h
13	8 mon	F	Dehydration	Pentobarbital withdrawn 24 h before	Absent flow	Absent uptake	24 h
14	16	M	Polytrauma	Pentobarbital withdrawn 48 h before	Absent flow	Absent uptake	48 h
15	16	M	Ventricular haemorrhage		Absent flow	Absent uptake	
16	37	F	Polytrauma		Absent flow	Absent uptake	
17	27	F	Polytrauma		Absent flow	Absent uptake	24 h
18	14	F	Subarachnoid haemorrhage		Absent flow	Absent uptake	
19	28	F	Polytrauma	Pentobarbital withdrawn 34 h before	Absent flow	Absent uptake	24 h
20	19	M	Polytrauma	Pentobarbital	Absent flow	Absent uptake	48 h
21	17	F	Polytrauma	Pentobarbital withdrawn 3 h before	Absent flow	Absent uptake	48 h
22	55	F	Polytrauma		Absent flow	Absent uptake	
23	20	F	Polytrauma	Pentobarbital	Absent flow	Absent uptake	48 h
24	44	M	Thalamic haemorrhage		Absent flow	Absent uptake	24 h
25	12	M	Ventricular haemorrhage		Absent flow	Absent uptake	
26	31	M	Polytrauma		Absent flow	Absent uptake	
27	23	M	Cardiac arrest		Absent flow	Absent uptake	
28	56	M	Polytrauma		Absent flow	Absent uptake	
29	42	M	Polytrauma	Pentobarbital	Absent flow	Absent hemispheric uptake, brainstem uptake	
29					Absent flow	Absent uptake	
30	19	M	Polytrauma	Pentobarbital	Absent flow	Absent uptake	48 h
31	11	M	Renal failure		Absent flow	Absent uptake	
32	49	M	Intracerebral haemorrhage		Absent flow	Absent uptake	
33	61	M	Cerebellar haemorrhage		Present flow	Hemispheric uptake, absent brainstem uptake	
33					Absent flow	Absent uptake	
34	75	M	Polytrauma	Anisocoria	Present flow	Uptake	
35	20	M	Polytrauma	Pentobarbital, fixed midriasis	Present flow	Uptake	
35				Pentobarbital,	Equivocal	Faint uptake	
36	30	M	Polytrauma	Pentobarbital, brainstem reflexes	Present flow	Uptake	
36				Pentobarbital withdrawn 48 h before	Absent flow	Absent uptake	
37	59	F	Cerebellar infarct	Coma, spontaneous breathing	Present flow	Hemispheric uptake, absent uptake in ipsilateral cerebellar hemisphere	

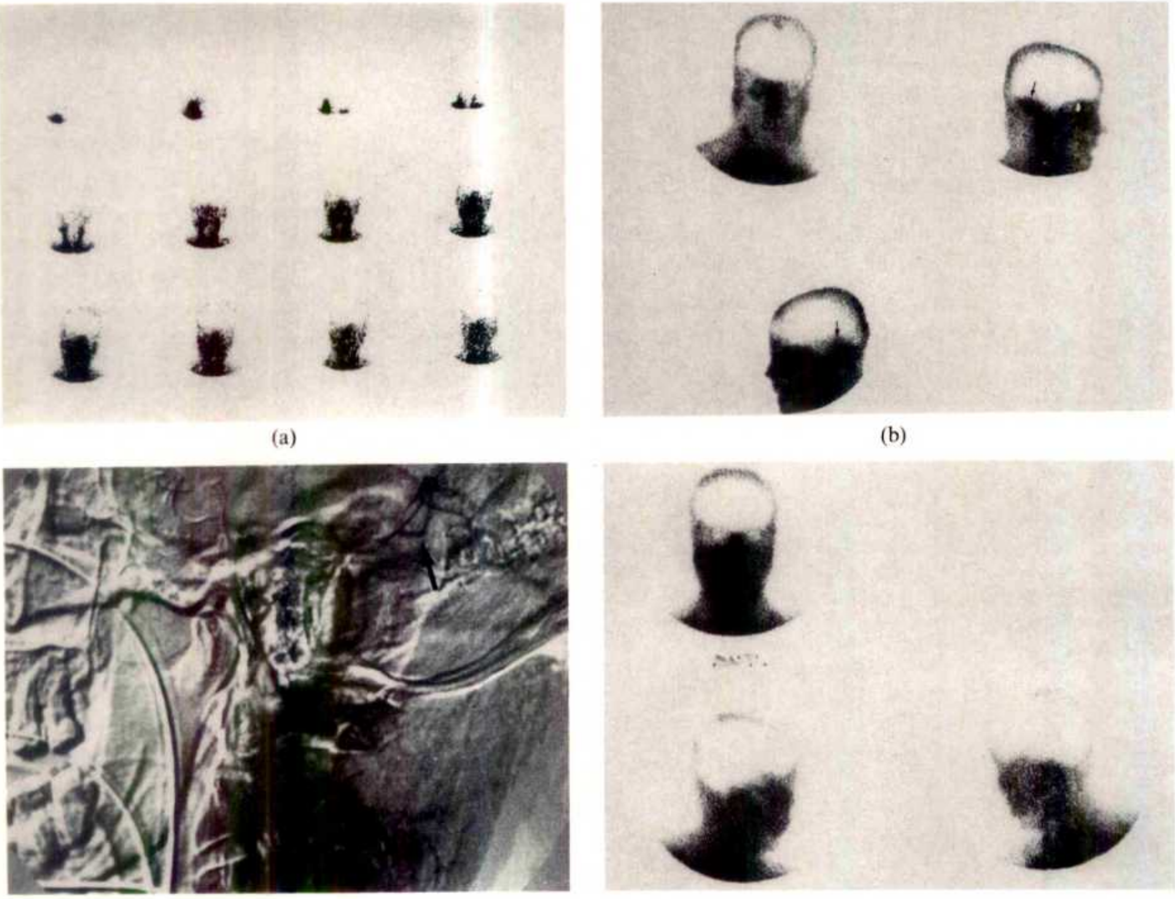

(a) (b) (c) (d)

Figure 1. *Case 29.* (a, b) Absent hemispheric activity in both phases; uptake in cerebellum and brainstem (arrows). (c) Faint flow (arrow) through vessel dependent of vertebral artery. (d) 48 h later: no uptake in cerebral hemispheres and posterior fossa.

Results

All cases showing no brain HMPAO uptake were confirmed by standard brain death criteria. In addition, in all patients who were not brain-dead, static images with HMPAO showed activity at least in the brainstem.

Equivocal dynamic flow images were seen in five cases, two of which were due to poor bolus quality (Cases 1 and 9). The other three were inconclusive studies (Cases 2, 11 and 35). On static images, four of these five patients (Cases 1, 2, 9 and 11) had absent brain uptake and were clinically confirmed as brain-dead; the fifth patient (Case 35) showed faint hemispheric uptake on static images, precluding an interpretation of a positive study for brain death, and died 24 h later.

In addition, another two cases showed "mismatched" dynamic flow and static images: one (Case 29) had absent perfusion on dynamic images with absent uptake in the cerebral hemispheres on static images but with evident uptake in the brainstem; the other case (Case 33) showed brain perfusion on dynamic images and no uptake in the posterior fossa on static images despite cerebral hemispheric uptake.

Five studies (Cases 33, 34, 35, 36 and 37) showed brain perfusion on dynamic images and brain uptake on static images. One patient (Case 34) recovered, one patient (Case 37) developed vegetative coma and three patients (Cases 33, 35 and 36) died; of these, two patients (Cases 33 and 36) had a second study performed before death showing no flow on dynamic images as well as no uptake on static images.

Table I shows the results of scintigraphy (dynamic and static phases) in all patients as well as the time interval that elapsed from scintigraphic diagnosis to diagnosis based on standard clinical criteria.

Discussion

Criteria for the diagnosis of brain death have evolved in response to advances in medical technology. Different criteria for brain death exist in different groups and countries. Several guidelines have been established and accepted including: deep coma; absent spontaneous

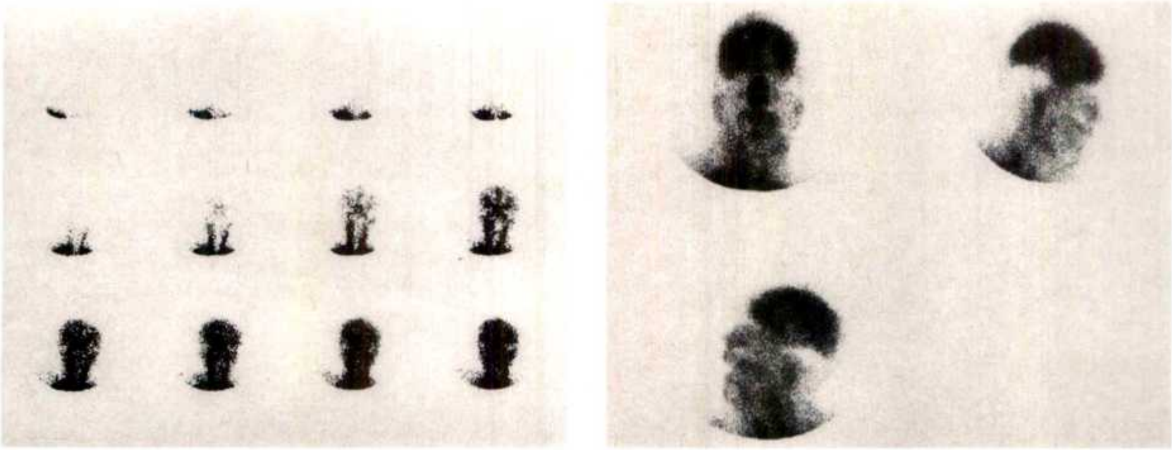

(a) (b)

Figure 2. *Case 33.* Cerebellar haemorrhage. (a) Radionuclide cerebral angiography showing hemispheric blood flow. (b) Static study showing cerebral hemisphere uptake and no posterior fossa.

breathing; absent cortical and brainstem reflexes; isoelectric electroencephalogram; persistence of the above for more than 6–24 h (with exclusion of reversible processes such as hypothermia and administration of certain drugs); and finally, absent intracranial circulation (Harvard Medical School, 1968; Collaborative Study, 1977; Molinari, 1978).

Persistence of these symptoms and signs for 24 h is required in most cases. An unequivocal early diagnosis of brain death is necessary in comatose patients who may be organ donors and this involves complicated moral, ethical, medical and legal considerations (Report of the Medical Consultants, 1981; Pinkus, 1984). Confirmatory tests are of great importance in cases of contradictory clinical criteria and other objective tests (Lee et al, 1987). In this context, demonstration of absent brain flow by angiography or other procedures is the best way of diagnosing brain death.

Radionuclide brain perfusion studies have advantages over conventional contrast angiography as they may be performed using portable gamma cameras at the bedside of patients with complicated life-support systems.

In brain-dead patients a clear cessation of carotid blood flow is seen as the arteries become intracranial in the rapid-sequence vascular phase images. The posterior fossa is not evaluated in the dynamic phase, and if activity on static images is observed at this site, criteria for brain death cannot be fulfilled even in the absence of cerebral hemispheric activity. ^{99}Tc^{m}-HMPAO studies provide a safe evaluation of posterior fossa perfusion in static images. Cases 29 and 33 illustrate this.

Case 29 was in deep coma with fixed bilateral dilated pupils, under the effects of pentobarbital. 12 h before pentobarbital withdrawal a first study with HMPAO was performed (Fig. 1a, b) showing absent cerebral hemispheric activity in both phases, with evident uptake in the cerebellum and brainstem. Following pentobarbital withdrawal the patient was responsive to apnoea with spontaneous breathing. Two hours later contrast angiography showed absent flow in both hemispheres and faint flow to the posterior fossa through the vertebral artery (Fig. 1c). A second HMPAO study was performed 48 h later showing absent hemispheric and posterior fossa uptake (Fig. 1d). At this time a positive apnoea test was obtained and all criteria for brain death were fulfilled, including two isoelectric EEGs. This case shows an excellent correlation between contrast angiography and static HMPAO images, which was not present with the dynamic phase images.

Case 33 was in deep coma owing to a large cerebellar haemorrhage, with bilateral fixed dilated pupils, hypotonia, absent respiratory movements, and activity on the EEG. A first HMPAO study demonstrated hemispheric activity on both phases with no uptake in the posterior fossa (Fig. 2a, b). A second study 24 h later revealed complete absence of hemispheric and posterior fossa uptake, as well as all other brain death criteria, including two isoelectric EEGs.

Our experience confirms the opinion of Laurin et al (1989) that ^{99}Tc^{m}-HMPAO studies appear safe and specific for brain death, and do not appear to be affected by the patient's metabolic status or by therapy. The latter is demonstrated by the fact that several patients in barbiturate-induced coma and metabolic situations similar to the other patients showed HMPAO brain uptake when not brain-dead. We have not observed any case of brain flow on dynamic images without cerebral hemispheric uptake on static images.

Our study, in conclusion, suggests a superiority of HMPAO studies over conventional radionuclide brain angiography, with less equivocal results. These studies are extremely useful when concomitant therapies complicate clinical evaluation of patients, especially in potential organ donors in whom an early diagnosis may be of vital importance.

References

Andrews, P. J. D., Piper, I. R., Dearden, N. M. & Miller, J. D., 1990. Secondary insults during intrahospital transport of head-injured patients. *Lancet, 335*, 327–330.

Ballinger, J. R., Gulenchyn, K. Y. & Reid, R. H., 1990. Radiopharmaceutical factors in the variable quality of ^{99}Tc^{m}-HMPAO images of the brain. *Journal of Nuclear Medicine, 31*, 118–122.

Black, P.Mc. L. & Zervas, N. T., 1984. Declaration of brain death in neurosurgical and neurological practice. *Neurosurgey, 15*, 170–174.

Collaborative Study, 1977. An appraisal of the criteria of cerebral death—a summary statement: a collaborative study. *Journal of the American Medical Association, 237*, 982–986.

Galaske, R. G., Schober, O. & Heyer, R., 1988. ^{99}Tc^{m}-HMPAO and ^{123}I-amphetamine cerebral scintigraphy: a new, non-invasive method in determination of brain death in children. *European Journal of Nuclear Medicine, 14*, 446–452.

George, M. S., 1991. Establishing brain death: the potential role of nuclear medicine in the search for a reliable confirmatory test. *European Journal of Nuclear Medicine, 18*, 75–77.

Harvard Medical School, 1968. Report of the ad hoc committee for the Harvard Medical School to examine the definition for brain death. *Journal of the American Medical Association, 205*, 337–340.

Kaufman, H. H., Geisler, F. H., Kopitnik, T., Higgins, W. & Stewart, D., 1989. Detection of brain death in barbiturate coma: the dilemma of an intracranial pulse. *Neurosurgery, 25*, 275–278.

Korein, J., Braunstein, P., George, A., Wichter, M., Kricheff, I., Lieberman, A. & Pearson, J., 1977. Brain death: I. Angiographic correlation with the radioisotopic bolus technique for the evaluation of critical deficit of cerebral blood flow. *Annals of Neurology, 2*, 195–205.

Kricheff, I. I., Braunstein, P., Korein, J., George, A. E. & Kumar, A. J., 1975. Isotopic and angiographic determination of cerebral blood flow. A correlation in patients with cerebral death. *Acta Radiologica (Suppl.), 347*, 119–129.

Laurin, N. R., Driedger, A. A., Hurwitz, G. A., Mattar, A. G., Powe, J. E., Chamberlain, M. J., Zabel, P. L. & Pavlosky, W. F., 1989. Cerebral perfusion imaging with technetium-99m HMPAO in brain death and severe central nervous system injury. *Journal of Nuclear Medicine, 30*, 1627–1635.

Lee, V. W., Hauck, R. M., Morrison, M. C., Deng, T. T., Fisher, E. & Carter, A., 1987. Scintigraphic evaluation of brain death; significance of sagittal sinus visualization. *Journal of Nuclear Medicine, 28*, 1279–1283.

Mah, G., Reilly, R. M., Wong, G. L. M. & Houle, S., 1989. A comparison of three methods to determine the radiochemical purity of ^{99}Tc^{m}-hexamethylpropylene amine oxime (^{99}Tc^{m}-HMPAO). *Nuclear Medicine Communications, 10*, 733–740.

Molinari, G. F., 1978. Review of clinical criteria of brain death. *Annals of the New York Academy of Sciences, 315*, 62–69.

Neirinckx, R. D., Canning, L. R., Piper, I. M., Nowotnik, D. P., Pickett, R. D., Holmes, R. A., Volkert, W. A., Forster, A. M., Weisner, P. S., Marriott, J. A. & Chaplin, S. B., 1987. Technetium-99m,*d,l*-HMPAO: a new radiopharmaceutical for SPECT imaging of regional cerebral blood perfusion. *Journal of Nuclear Medicine, 28*, 191–202.

Pinkus, R. L., 1984. Families, brain death, and traditional medical excellence. *Journal of Neurosurgery, 60*, 1192–1194.

Pjura, G. A. & Kim, E. E., 1987. Radionuclide evaluation of Brain death. In *Nuclear Medicine Annual 1987*, ed. by L. M. Freeman & H. S. Weissmann (Raven Press, New York), pp. 269–293.

Reid, R. H., Gulenchyn, K. Y. & Ballinger, J. R., 1989. Clinical use of technetium-99m HMPAO for determination of brain death. *Journal of Nuclear Medicine, 30*, 1621–1626.

Report of the Medical Consultants, 1981. Report on the diagnosis of death to the President's Commission for the study of ethical problems in medicine and biomedical and behavioral research: guidelines for the determination of death. *Journal of the American Medical Association, 246*, 2184–2186.

Roine, R. O., Launes, J., Lindroth, L. & Nikkinen, P., 1986. ^{99}Tc^{m}-Hexamethylpropyleneamine oxime scans to confirm brain death. *Lancet, ii*, 1223–1224.

Sharp, P. F., Smith, F. W., Gemmell, H. G., Lyall, D., Evans, N. T. S., Gvozdanovic, D., Davidson, J., Tyrrell, D. A., Pickett, R. D. & Neirinckx, R. D., 1986. Technetium-99m HMPAO stereoisomers as potential agents for imaging regional blood flow: human volunteer studies. *Journal of Nuclear Medicine, 27*, 171–177.

1992, *The British Journal of Radiology*, *65*, 295–297

Computed tomographic assessment of intraperitoneal fluid distribution prior to intraperitoneal chemotherapy for ovarian cancer

By †P. M. Hughes, MRCP, FRCR, I. Zammit-Maempel, MRCP, FRCR and *D. Murphy, MRCOG

Christie Hospital and Holt Radium Institute, Department of Radiology and *Department of Medical Oncology, Wilmslow Road, Withington, Manchester M20 9EX, UK

(*Received 13 May 1991 and in revised form 5 August 1991, accepted 12 September 1991*)

Keywords: Computed tomographic peritoneography, Ovarian carcinoma, Residual disease, Intraperitoneal chemotherapy

Abstract. Intraperitoneal chemotherapy (IPCT) is under evaluation in patients with ovarian cancer. Computed tomographic peritoneography (CTP) prior to IPCT establishes the distribution of the infusate, which if complete, demonstrates the patient's suitability for this method of treatment. We report our method of CTP and describe the intraperitoneal fluid distribution and complications encountered in 28 patients with advanced ovarian carcinoma being considered for IPCT.

In advanced ovarian cancer (Figo stage 2B-4), cytoreductive surgery and systemic chemotherapy have become a standard treatment in most centres (Richardson et al, 1985; Omura et al, 1986). But, although ovarian cancers represent one of the most chemotherapy sensitive solid tumours with response rates of up to 70–80%, most patients die of their disease (Neijt et al, 1987). Even with optimal initial surgery and appropriate chemotherapy as many as 30–50% of women with epithelial ovarian cancer will have residual disease identified at second-look laparotomy (Ozols & Young, 1984; Williams et al, 1985). In these patients local intracavity application of cytotoxic agents may offer a further therapeutic perspective (Howel et al, 1987). Effective intraperitoneal chemotherapy (IPCT) relies upon the infusate bathing the entire peritoneal cavity. Distribution may, however, be limited by both post-operative and malignant adhesions (Dunnick et al, 1979). Computed tomographic peritoneography (CTP) is necessary therefore to confirm adequate intraperitoneal fluid distribution prior to IPCT.

Patients and methods

CTP was performed on 28 patients (aged 31–67 years, mean age 53.1 years) with advanced ovarian carcinoma. All patients had minimal residual disease (< 2 cm) at second-look laparotomy. CTP was performed 2–4 weeks following laparotomy. Two types of intraperitoneal catheter were inserted, 18 patients had a temporary dialysis catheter (TDC) and 10 patients had a Tenchkoff catheter. The latter were inserted at second-look laparotomy, flushed with heparinized saline and left idle for 2–3 weeks to ensure healing of the laparotomy wound. The TDCs were inserted using local anaesthesia below the level of the umbilicus at a site free from operative scars and contrast immediately infused. The infusate consisted of 50 ml of urograffin 310 M diluted in 500 mls of N-saline, warmed to body temperature and run in over 15–20 mins. Patients were encouraged to remain ambulant for 30 mins after the infusion before scanning to promote distribution. Computed tomography (CT) scans were performed on either an EMI 7070 or GEC Pace scanner. A total of five 10 mm sections at equal intervals between the dome of the diaphragm and pubic symphysis were performed. Scans were assessed for adequacy of intraperitoneal fluid distribution and catheter malposition. Pain during infusion and other complications were also documented.

Results

There was complete or free intraperitoneal distribution of contrast in 22 patients (Fig. 1), and incomplete distribution (compartmentalization) in three patients.

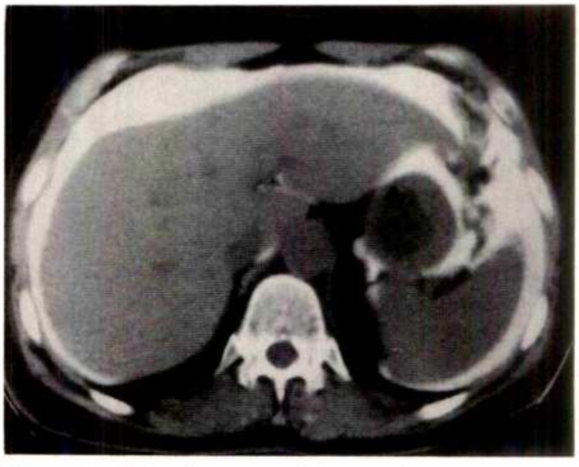

Figure 1. CT of upper abdomen demonstrates free intraperitoneal distribution of contrast.

---

†Author for correspondence.

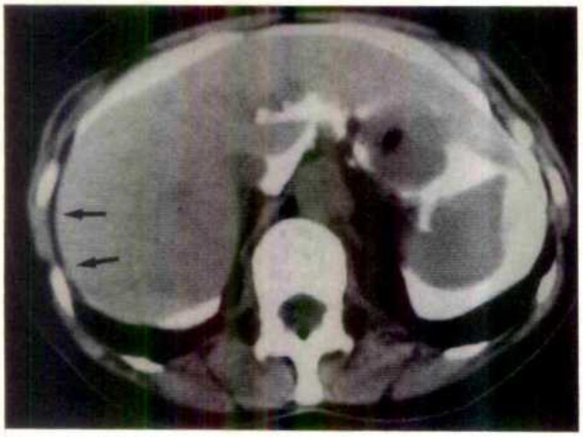

Figure 2. CT demonstrates incomplete contrast distribution over the lateral aspect of the right lobe of the liver (arrowed) (serosal metastases noted at laparotomy only).

Incomplete opacification over the liver surface was present in all three patients with restricted flow. Two had known hepatic surface (serosal) metastases (Fig. 2), while the other had loculated ascites (Fig. 3). The TDCs were malpositioned in three further patients, two were in the retroperitoneum (Fig. 4) and one in small bowel (Fig. 5). The former both experienced pain limiting infusion. The patients had all undergone multiple abdominal and pelvic operations; the TDCs being sited in the right flank. Incidental progressive disease was identified during CTP in three cases (hepatic metastases, serosal metastases and retroperitoneal adenopathy). No pain or discomfort was experienced by any patient with a correctly sited intraperitoneal catheter. All Tenchkoff catheters functioned satisfactorily. A wound infection was treated successfully with antibiotics in one patient, but no other complication or contrast reaction was recorded.

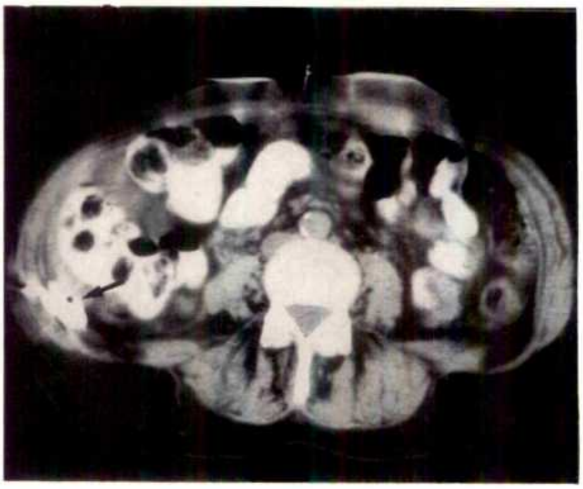

Figure 4. CT demonstrating retroperitoneal extravasation of contrast (arrowed) following malposition of a temporary dialysis catheter.

Discussion

Tumours of the colon, breast and ovary often metastasize extensively throughout the peritoneal cavity. Second-look laparotomy in patients with advanced ovarian carcinoma has identified minimal residual disease in up to 50% of patients following initial surgery and chemotherapy, these patients being suitable for IPCT. The "belly bath" technique for intraperitoneal administration of chemotherapeutic agents delivers a high local concentration of these drugs and is being used in an attempt to improve prognosis (Dunnick et al, 1979).

CTP has been shown to define accurately peritoneal fluid distribution (Dunnick et al, 1979; Giunta et al, 1990). Compartmentalization can result from post-operative adhesions or metastatic disease, both of which are

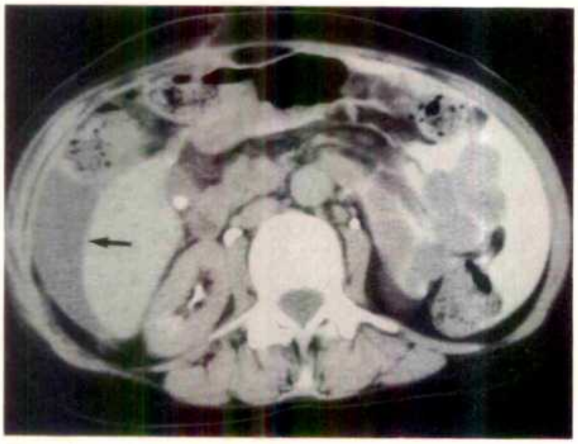

Figure 3. CT demonstrating compartmentalization of contrast due to loculation of ascites around the liver (arrowed).

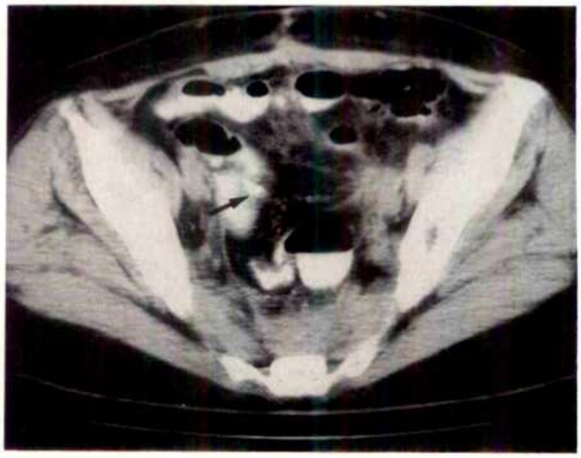

Figure 5. CT demonstrating small bowel opacification following catheter malposition (arrowed).

commonly found in patients with advanced ovarian cancer. Limited distribution of cytotoxic agents within the peritoneal cavity as evidenced by CTP is likely to indicate a suboptimal response to IPCT. Restriction of flow over the surface of the liver identified during the present study represented a significant finding since both of the patients had definite metastatic disease at this site. In our study no other sites of compartmentalization were observed within the peritoneal cavity but this has been reported (Giunta et al, 1990).

Limited rather than contiguous diagnostic sections were employed to assess fluid distribution, as patients had already undergone second-look laparotomy which remains superior to CT, CTP and ultrasound in assessing residual disease. The method of scanning and volume of infusate provided satisfactory diagnostic information regarding fluid distribution. Unlike other studies employing a larger volume infusate (Dunnick et al, 1979; Guinta et al, 1990), no patient in the present study experienced abdominal discomfort when the peritoneal catheter was correctly sited. A wound infection successfully treated represented the only complication other than the three cases of catheter malposition.

Two catheter types were employed, the Tenchkoff and TDC. The Tenchkoffs all functioned satisfactorily despite remaining idle for several weeks, whereas three of the 18 TDCs were incorrectly sited. CTP provided the only evidence of catheter malposition within the small bowel, whereas retroperitoneal extravasation was suspected by pain during infusion. If second-look laparotomy is practised as part of the evaluation of ovarian cancer we would therefore advise simultaneous Tenchkoff catheter insertion to avoid catheter malposition.

In conclusion, IPCT is a technique which, if of proven benefit, may be of use in advanced ovarian cancer. CTP is a quick reliable method of assessing peritoneal fluid distribution and catheter position. It is acceptable to the patient and pain-free when the catheter is correctly sited.

References

Dunnick, N. R., Jones, R. B., Doppman, J. L., Speyer, J. & Meyers, C. E., 1979. Intraperitoneal contrast infusion for assessment of intraperitoneal fluid dynamics. *American Journal of Roentgenology, 133,* 221–223.

Giunta, S., Tipaldi, L., Diotellevi, F., Squillaci, E., Cecconi, L., Nardis, P. F. & Squillaci, S., 1990. CT demonstration of peritoneal metastases after intraperitoneal injection of contrast media. *Clinical Imaging, 14,* 31–34.

Howel, S., Zimm, S., Markmann, M., Abramson, I. S., Cleary, S., Lucas, W. E. & Weiss, R. J., 1987. Long-term survival of advanced refractory ovarian carcinoma patients with small-volume residual disease treated with intraperitoneal chemotherapy. *Journal of Clinical Oncology, 5,* 1607–1612.

Neijt, J. P., TenBokkel Huinink, W. W., Van Der Burg, M. E. L., 1987. Randomized trial comparing two combination chemotherapy regimes (CHAP-5VCP) in advanced ovarian carcinoma. *Journal of Clinical Oncology, 5,* 1157–1168.

Omura, G., Blessing, J. A., Ehrlich, C. E., 1986. A randomized trial of cyclophosphamide and doxorucin with or without cisplatin in advanced ovarian cancer. *Cancer, 57,* 1725–1730.

Ozols, R. F. & Young, R. C., 1984. Chemotherapy of ovarian cancers. *Seminars in Oncology, 2,* 251–263.

Richardson, G. S., Scully, R. E., Nikrui, N., Nelson, J. H., 1985. Common epithelial cancer of the ovary. *New England Journal of Medicine, 312,* 474–483.

Williams, C., Mead, G., Macbeth, J., Thompson, J., Whitehouse, J. M. A., MacDonald, H., Harvey, V. J., Slevin, M. L., Lister, T. A., Shepherd, J. H. & Golding, P., 1985. Cisplatin combination chemotherapy *versus* chlorambucil in advanced ovarian carcinoma: mature results of a randomized trial. *Journal of Clinical Oncology, 3,* 1455–1462.

1992, *The British Journal of Radiology*, *65*, 298–301

How good is ultrasound in the detection and evaluation of anterior abdominal wall defects?

By S. A. Walkinshaw, BSc, MD, MRCOG, M. Renwick, G. Hebisch, MD, E. N. Hey, DM, FRCP
Northern Regional Fetal Abnormality Survey, Princess Mary Maternity Hospital, Newcastle upon Tyne, UK

(Received 3 June 1991 and in revised form 9 September 1991, accepted 3 October 1991)

Keywords: Anterior wall defects, Accuracy of ultrasound detection, Audit of obstetric ultrasound

Abstract. The ability of routine obstetric ultrasound to detect and accurately describe fetuses with anterior abdominal wall defects has been examined in an unselected population using data from a regional abnormality survey. Examination between 16 and 22 weeks gestation detected 60% of defects with a false positive rate of 5.3%. Fetuses with gastroschisis were incorrectly assigned as exomphalos in 14.7% of cases recognized before 22 weeks gestation. The diagnosis, including description of associated detectable anomalies, was completely accurate in 71.6% of cases. Some of the problems of diagnostic accuracy need to be considered when counselling couples with a fetal anomaly. Cross-referral between obstetric ultrasound units should be encouraged to improve diagnostic accuracy. These results form the basis for audit of obstetric ultrasound in the diagnosis of fetal abnormality within a geographically defined population.

The recent report from the Joint Study Group on Fetal Abnormalities (Members of the Joint Study Group on Fetal Abnormalities, 1989) reaffirms the recommendation that all pregnant women should be offered ultrasound examination between 18 and 20 weeks, this gestation being thought to maximize prenatal diagnosis of fetal anomaly.

Nevertheless, the precise impact of such screening remains unclear (Waldenstrom et al, 1988). Data on the ability of routine ultrasound to detect abnormality are scanty (Campbell & Pearce, 1983; Hill et al, 1985; Rosendahl & Kiniven, 1989), and its impact on obstetric care is not fully evaluated. The accuracy of prenatal diagnosis may also be less than optimal (Manchester et al, 1988).

One group of anomalies where it is agreed that accurate prenatal diagnosis may be of value to the infant and mother are anterior abdominal wall defects. Accuracy of diagnosis and identification of related defects are important since the prognosis of the two major types of anterior abdominal wall defects, gastroschisis and exomphalos, differ markedly (Kirk & Wah, 1983). Antenatal counselling and management therefore rely heavily on ultrasound guidance. There are, however, few data on the performance of ultrasound in the diagnosis of anterior wall defects.

Since 1984, the Northern Regional Fetal Abnormality Survey has collected data on both antenatally suspected and post-natally diagnosed fetal abnormalities. This has allowed us to examine the impact of routine ultrasound examination on the identification of these disorders within a large population and to determine the accuracy of diagnosis. This study is based on 115 cases of anterior abdominal wall defects reported between 1 January 1984 and 31 December 1988 from 202 488 live births and intra-uterine deaths beyond 22 weeks gestation.

Methods

Following permission from the Survey Steering Group, cases where either anterior abdominal wall defects were suspected antenatally, or a diagnosis of anterior abdominal wall defect was made following delivery, were identified from the survey register. The hospital of origin was identified and permission sought to study the antenatal case records. Neonatal case records, paediatric surgical case records and autopsy reports were studied where appropriate.

To ensure completeness, paediatric surgical operation records from 1984–1988 were examined to ensure that all living infants coming to surgery had been notified to the survey. The Northern Regional Perinatal Mortality Survey records for 1984–1988 were examined to ensure that all perinatal deaths in which an anterior wall defect was noted had been registered. In 1987 and 1988, pregnancies ending in intra-uterine death from 22–28 weeks were also notified to this survey. Each year Fetal Abnormality Survey returns are checked against the Office of Population Censuses and Surveys (OPCS) returns for termination in which clause 4, relating to termination on the grounds of fetal abnormality likely to result in major physical or mental handicap, is stated as an indication. Descriptions of infants or fetuses with autosomal trisomies referred to the regional cytogenetics units were examined. These additional searches resulted in the addition of four more cases to the survey, which were included in the study.

Dr Walkinshaw was in receipt of a subspecialty training fellowship in Fetal Medicine from the Royal College of Obstetricians and Gynaecologists.

Address reprint requests and correspondence to Dr S. A. Walkinshaw, Fetal Centre, Liverpool Maternity Hospital, Oxford Street, Liverpool L7 7BN, UK.

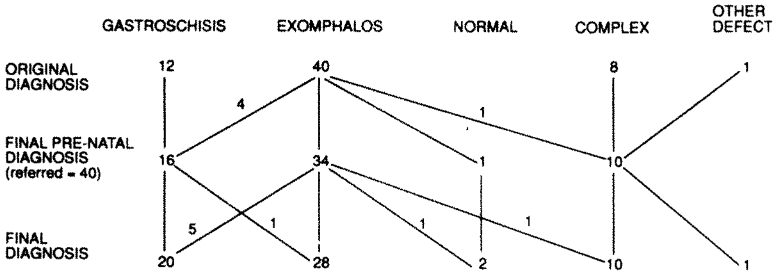

Figure 1. Accuracy of prenatal diagnosis at less than 22 weeks gestation.

Classification was based on ultrasound descriptions (presence or absence of sac, ability to delineate umbilical insertion separately), descriptions at birth, descriptions at autopsy and descriptions at surgery. In many of the complex cases photographs were available.

Gastroschisis was defined as a full thickness defect in the anterior abdominal wall arising lateral to the midline, usually to the right, through which herniation of the abdominal contents had occurred and where there was no evidence antenatally or post-natally of a covering membrane. The umbilical cord insertion was distinctly separate from the defect. Exomphalos was defined as a central defect resulting in herniation of intra-abdominal contents into the base of the umbilical cord. The presence of a sac noted at any time resulted in classification as exomphalos. If the umbilical cord insertion was not separate from the defect, in the absence of a sac, then the lesion was classified as exomphalos. An exomphalos was regarded as ruptured if a sac was identified at any time antenatally but not present at birth, if there was overt evidence of sac rupture at delivery, or if the defect was clearly central and involving the umbilicus. The third group consisted of complex anomalies. For the purpose of this study these were defined as multiple anomaly syndromes involving the anterior abdominal wall, but where the primary diagnosis was not necessarily one of anterior wall defect. These included body stalk malformations, cloacal extrophy, limb body wall disruption and early amnion rupture.

Results

Over a 5 year period, 115 cases of suspected or diagnosed anterior wall defects were reported to the survey. 75 of these were reported antenatally, four of which did not have an anterior wall defect at delivery. There was, therefore, a false positive diagnosis rate of 5.3%. The four cases consisted of two fetuses with other severe defects, one with Beckwith-Wiedemann syndrome without exomphalos, and one where no abnormality was detected at birth. In four other cases of anterior wall defects notified post-natally other fetal abnormality was suspected antenatally, but not an anterior wall defect.

Diagnostic ability of screening ultrasound

Of the 111 confirmed anterior abdominal wall defects, 97 had an ultrasound examination between 16 and 22 weeks gestation (median gestation 17.5 weeks). An anterior abdominal wall defect was correctly identified in 59 cases, a detection rate of 60.8% in those undergoing routine ultrasound assessment. There was a single false positive diagnosis.

A further six cases were identified in 15 women from this group, following repeat ultrasound for clinical indications (oligohydramnios, polyhydramnios and small for gestational age). There were three false positive diagnoses from these later scans. However, 32 cases were not identified. 16 of these had further ultrasound examination on clinical grounds (median gestation 31.5 weeks, range 27–36 weeks), which also failed to detect a defect. In four of these, other major anomaly was suspected, but anterior wall defects were not described. Eight women were scanned only on clinical grounds in the third trimester. In six cases a defect was identified. Six women had no ultrasound examination during pregnancy. Overall, 71 (64%) of defects were correctly suspected prenatally.

Accurate categorization of type of anomaly

Gastroschisis and exomphalos were accurately distinguished in 79.3% (46 of 58) of initial diagnoses and in 84.5% (48 of 58) of cases following referral for further assessment.

Figure 1 outlines in full the diagnostic errors in those defects suspected prior to 22 weeks. In six cases referral ultrasound confirmed, erroneously, the initial categorization. Of 21 cases not referred, the diagnostic category was correct in 18 cases. In all, the initial ultrasound categorization was correct in 45 out of 61 (73.8%) suspected cases. The final or working (referred and non-referred) antenatal diagnosis was correct in 52 (85.3%) cases.

Where the diagnosis was made in the third trimester, the primary diagnosis was gastroschisis in two cases, exomphalos in eight cases and complex anomaly in two cases. In two patients, gastroschisis was wrongly described as exomphalos and in one case referred for further examination, the diagnosis of exomphalos was incorrectly altered. The fetal diagnosis was therefore correct in nine of the 12 confirmed cases.

Identification of associated defects

42 cases (36 early, six late) were correctly described as isolated anterior wall defects (excluding minor genitourinary defects, malrotations and stenosis). In seven

cases, described as isolated, potentially diagnosable lesions were not detected: cardiac (1); facial clefting (2); arthrogryphosis (1); major skeletal (1); major urinary (1) and features of trisomy 13 (1).

In 22 cases (17 early, five late) additional anomalies were described. In 11 instances, ultrasound correctly identified all detectable anomalies. In the other 11 cases, although some additional defects were described, a number of potentially detectable anomalies were not identified (skeletal, cardiac, clefting, genito-urinary, features of trisomy). In five of these cases some of the defects described were not present, including suspected cardiac and neural tube defects.

Overall the ultrasound diagnosis of anterior wall defect with or without associated anomalies was accurate in 53 of the 71 cases (74.6%) diagnosed before birth.

Discussion

This study demonstrates that in an unselected population offered routine mid trimester ultrasound screening, only about two thirds of the fetuses with an anterior wall defect are currently being identified. This, rather than data based on tertiary referral data (Gilbert & Nicolaides, 1987), reflects more accurately the state of prenatal diagnosis using ultrasound in clinical practice. Unless initial ultrasound examination can detect the abnormality, then subsequent referral will not be generated. Diagnostic rates are a function of equipment, operator experience and time. The data presented here reinforce the argument for adequate facilities and time to perform detailed anatomical ultrasound examination.

The detection rate at routine screening should represent the minimum rate as the Northern Region has one of the lowest maternal serum α-fetoprotein (AFP) screening rates in the United Kingdom (currently less than 30%). Although there did not appear to be differences in detection rates between areas offering AFP screening and those not, in six cases an elevated maternal serum AFP result was available before ultrasound examination. In areas with higher application of screening, additional cases of anterior wall defects may be detectable (Mann et al, 1984).

Ability to detect abnormality only forms part of the function of diagnostic obstetric ultrasound. The other involves diagnostic accuracy. It is little appreciated that there is a false positive rate for anomaly screening, as demonstrated in this study. The rate for this study is comparable with the false positive rate of 4.9% for abnormal scans for all anomalies noted in the Belgian multicentre study (Levi et al, 1991). Such data need to be considered when counselling women with suspected fetal abnormality.

Obstetric management will rely heavily on ultrasound diagnosis, yet data on its accuracy are scanty. Scott and Renwick (1988), using data from the same survey, demonstrated that for renal tract anomalies the diagnosis in surviving infants was accurate in only 55% of cases. Even specialist centres dealing with particular groups of suspected defects would appear to have a rate of incorrect or incomplete diagnosis of approximately 20% (Davis et al, 1990). This study provides data on the accuracy of diagnosis for anterior wall defects. Unlike other studies, these data are derived from prospectively collected information on a geographically defined unselected low risk population.

It is clear that incorrect categorization is the major problem. In 16 (26.2%) cases, the primary diagnosis was incorrect, seven being altered correctly on referral. However, in six cases the referral diagnosis incorrectly confirmed the primary diagnosis. It would appear that there is overdiagnosis of exomphalos. From ultrasound reports it is not clear how this has arisen. In many cases, the comment "anterior abdominal wall defect—exomphalos" may be the only statement with no clear description of the anatomical findings. It may be that there is insufficient understanding of the relative obstetric implications of the two different diagnoses among ultrasonologists. In at least one case in our study termination of pregnancy was offered and accepted with an ultrasound diagnosis of exomphalos, the fetus having gastroschisis. There is therefore potential for improving this aspect of diagnosis. Colour Doppler imaging of the umbilical cord may be of use in difficult cases. Such lack of clarity in diagnosis causes difficulty with counselling regarding fetal karyotyping. Where the diagnosis is clearly gastroschisis, it is now felt inappropriate to offer prenatal cytogenetic testing. However, in two cases in this study, exomphalos was incorrectly diagnosed as gastroschisis. Such findings urge caution and where there is any uncertainty, prenatal testing may be appropriate.

The study emphasizes the need for liberal use of cross-referral between neighbouring units for confirmation of fetal malformation. In cases referred for such ultrasound, over half of the incorrect diagnoses were identified. The difficulties of even the most experienced ultrasonologists in categorizing correctly all defects emphasizes the need for caution where diagnosis is based on a single operator. The possible exception is complex anterior wall syndromes, which were well described on primary ultrasound. These are, in the main, lethal anomalies and it may be appropriate for these to be managed entirely within the initial hospital.

Many of the decisions on the management of these particular anomalies are based on the finding of associated defects. Gastroschisis appears to have little association with abnormality outside the gastrointestinal tract (Carpenter et al, 1984), whereas exomphalos is commonly associated with other major anomalies (Mann et al, 1984). To allow sensible prenatal counselling, the diagnosis of associated defects must also be accurate. Additional undiagnosed anomalies were present in 17% of lesions thought to be isolated and in some instances these were major defects. In two of these cases, it would have been appropriate to offer therapeutic termination of pregnancy. Even where additional defects were identified, the diagnosis was frequently incomplete; an offer of pregnancy termination would have been appropriate in one case had the complete diagnosis been achieved. Overdiagnosis carries similar risks of inappropriate action. Prenatal counselling must take cogniscence of the fallibility of obstetric ultrasound and repeated detailed examination of ongoing pregnancies should be standard practice.

Although in most instances additional features would not have altered the clinical outcome, it is clear that decisions, in particular to offer therapeutic termination, based on such uncertainties are unsatisfactory and this emphasizes the need to build up expertise in the diagnosis and management of fetal abnormality.

This study demonstrates that although obstetric ultrasound offers a service for fetal diagnosis, much work is required to fulfil the recommendations of the Joint Study Group. These data are based on experience between 1984 and 1988. During and since that time, both equipment and training have improved. Nevertheless, many anomalies are not being detected and the diagnosis is incomplete or erroneous in a significant proportion of cases. There is a further need to encourage cross-referral of prenatally diagnosed anomalies to ensure that obstetric decision making is based on the best data. Audit data must be collected to identify problems in diagnosis or management and fed back to those carrying out the ultrasound examinations.

Acknowledgments

We would like to thank colleagues in all specialities around the region who have enthusiastically supported the survey and who kindly allowed access to case records.

References

CAMPBELL, S. & PEARCE, J. M., 1983. The prenatal diagnosis of fetal structural anomalies by ultrasound. *Clinical Obstetrics and Gynecology, 10*, 475–506.

CARPENTER, M. W., CURCI, M. R., DIBBINS, A. W. & HADDOW, J. E., 1984. Perinatal management of ventral wall defects. *Obstetrics and Gynecology, 64*, 646–651.

DAVIS, G. K., FARQUHAR, C. M., ALLAN, L. D., CRAWFORD, D. C. & CHAPMAN, M. G., 1990. Structural cardiac abnormalities in the fetus: reliability of prenatal diagnosis and outcome. *British Journal of Obstetrics and Gynaecology, 97*, 27–31.

GILBERT, W. M. & NICOLAIDES, K. H., 1987. Fetal omphalocele: associated malformations and chromosomal defects. *Obstetrics and Gynecology, 70*, 633–635.

HILL, L. M., BRECKLE, R. & GEHRKING, W. C., 1985. Prenatal detection of congenital malformations by ultrasonography. *American Journal of Obstetrics and Gynecology, 151*, 44–50.

KIRK, E. O. & WAH, R. M., 1983. Obstetric management of the fetus with omphalocele or gastroschisis: a review and report of one hundred twelve cases. *American Journal of Obstetrics and Gynecology, 146*, 512–518.

LEVI, S., HYJAZI, Y., SCHAAPS, J. P., DEFOORT, P., COULON, R. & BUEKENS, P., 1991. Sensitivity and specificity of routine antenatal screening for congenital anomalies by ultrasound. *Ultrasound in Obstetrics and Gynecology, 1*, 102–110.

MANCHESTER, D. K., PRETORIUS, D. H., AVERY, C., MANCO-JOHNSON, M. L., WIGGINS, J., MEIER, P. R. & CLEWEL, W. H., 1988. Accuracy of ultrasound diagnoses in pregnancies complicated by suspected fetal anomalies. *Prenatal Diagnosis, 8*, 109–117.

MANN, L., FERGUSON-SMITH, M. A., DESAI, M., GIBSON, A. A. M. & RAINE, P. A. M., 1984. Prenatal assessment of anterior abdominal wall defects and their prognosis. *Prenatal Diagnosis, 4*, 427–435.

MEMBERS OF THE JOINT STUDY GROUP ON FETAL ABNORMALITIES, 1989. Recognition and management of fetal abnormalities. *Archives of Disease in Childhood, 64*, 971–976.

ROSENDAHL, H. & KINIVEN, S., 1989. Antenatal detection of congenital malformations by routine ultrasonography. *Obstetrics and Gynecology, 73*, 947–951.

SCOTT, J. E. S. & RENWICK, M., 1988. Antenatal diagnosis of congenital abnormalities of the urinary tract. Results from the Northern Regional Fetal Abnormality Survey. *British Journal of Urology, 62*, 295–300.

WALDENSTROM, U., AXELSSON, O., NILSSON S., EKLUND, G., FALL, O., LINDEBERG, S. & SJODIN, Y., 1988. Effects of routine one-stage ultrasound screening in pregnancy: a randomised controlled trial. *Lancet, ii*, 585–588.

1992, *The British Journal of Radiology*, *65*, 302–305

Detection and evaluation of fetal goitre by ultrasound

By E. Fred Avni, MD, *Frederic Rodesch, MD, Carine Vandemerckt, MD and
†Danièle Vermeylen, MD

Departments of Radiology, *Obstetrics and Gynecology, and †Neonatology, Erasme Hospital, University
Clinics of Brussels, 1070, Brussels, Belgium

(*Received 28 March 1991 and in revised form 14 June 1991, accepted 30 July 1991*)

Keywords: Fetus, Abnormalities, Goitre, Ultrasound

Abstract. Antenatal diagnosis of fetal goitre has been reported rarely. Once detected, however, it is important to evaluate fetal thyroid function so early treatment can be initiated if necessary. In reporting three new cases, the authors analyse the various methods of evaluation. The normal sequence of appearance of the various epiphyseal ossification centres is an indirect illustration of thyroid function and can be followed by ultrasound. Direct evaluation of hormone levels through cord blood sampling under sonographic guidance is a complementary method in doubtful cases. The mechanisms predisposing to the development of fetal goitres and the possible implications of these findings are also discussed.

Modern obstetric ultrasound (US) permits the detection of fetal goitre (Barone et al, 1985; Kourides et al, 1984; Leger et al, 1987; Weiner et al, 1982). Once detected, the evaluation of fetal thyroid function becomes necessary so early treatment can be initiated. Three new cases of fetal goitre are presented with an analysis of the various methods of evaluation, a hypothesis as to pathogenesis, and a discussion of the implications of such findings.

Case report

Case 1

An obstetric US scan was performed 28 weeks after the last menstrual period (LMP) of a 33-year-old gravida 2 para 1 woman. The pregnancy had been unremarkable up to that time.

At US, polyhydramnios was obvious and the fetal spine remained hyperextended (Fig. 1a). A 17 mm × 10 mm × 10 mm symmetrical bilobed solid mass was seen within the neck of the fetus (Fig. 1a,b). Because of the anterior location of the mass and its appearance, the diagnosis of goitre was suggested, although there was neither a previous history of thyroid pathology nor of any particular medication.

The fetus was otherwise normal; all measurements were a little above the 50th percentile for estimated gestational age. The fetal heart rate was normal. The calcaneal and talar ossification centres were present, implying no delay in bone maturation. It was decided to follow the mass and the ossification centres by sonography. At 32 weeks, the thyroid was still enlarged but its volume was unchanged. The distal femoral epiphyseal ossification centre (DFO) was present, confirming no delay in bone maturation. At 36 weeks, the thyroid volume remained the same; DFO centres measured 7 mm, proximal tibial ossification centres (PTO) were present and measured 5 mm (Fig. 2), and a faint proximal humeral ossification centre could be identified. The general growth of the fetus was normal.

Birth occurred uneventfully at 39 weeks. The healthy baby boy weighed 3300 g. The various thyroid hormone levels were normal both from the umbilical cord and in the blood. A goitre was neither palpated nor visualized by ultrasound. The baby was discharged at 7 days without any particular treatment.

Cases 2 and 3

Antenatal ultrasound was performed at 33 weeks of pregnancy in a woman known to have an euthyroid goitre. Her pregnancy was monochorial biamniotic. Sonography revealed bilobed solid masses within the anterior neck of each twin suggesting goitres. The masses measured approximately 27 mm × 20 mm × 15 mm in both fetuses (Fig. 3). There was no polyhydramnios. Femoral ossification centres were not present. Fetal heart rates were normal. Fetal measurements varied between the 10th and 30th percentile for the estimated gestational age.

To evaluate further the fetal thyroid function, cord blood sampling was performed *in utero*. The blood sample obtained from one twin (twin J) showed hormonal levels consistent with hypothyroidism. The second twin could not be evaluated. Premature labour occurred 1 week later before any treatment could be initiated and the twin boys were born vaginally shortly thereafter. Apgar scores at birth were 8.8 and 8.9 at 1 and 5 min, respectively. Births weights were 1980 g (10th percentile) and 2150 g (10–30th percentile).

Symmetrical goitres were clinically evident with hyperextended heads. The thyroid sizes were sonographically evaluated and each lobe measured about 30 mm × 20 mm × 20 mm in each baby. Both babies showed jaundice, hypotonia and delayed neurological performances (Finnström score was 31 weeks at Day 5). Bone maturation was estimated radiologically at 31 weeks. Hypothyroidism was confirmed by blood sampling and substitution therapy was initiated at Day 1, which was stopped at 1 month following the normalization of the clinical, radiological and biological findings.

Address correspondence to: E. F. Avni, Department of Radiology, Erasme Hospital, University Clinics of Brussels, Route de Lennik 808, 1070 Brussels, Belgium.

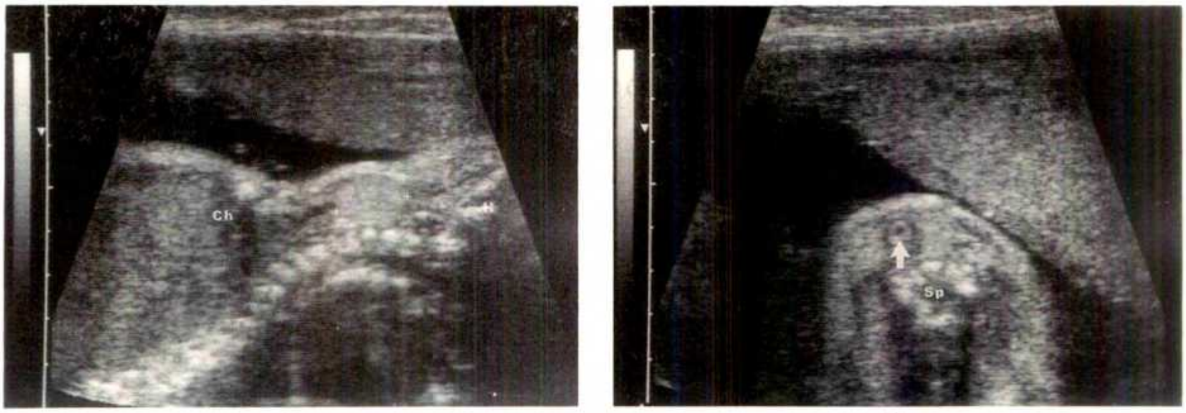

(a) (b)

Figure 1. *Case 1.* 28 weeks LMP. (a) Sagittal sonogram of the fetal neck. An ovoid solid mass (17 mm between crosses) is visible anterior to the spine. The spine and head remained hyperextended during the entire examination. Ch = fetal chest; H = fetal head. (b) Transverse sonogram of the fetal neck. The mass appears anterior, bilobed and symmetrical around the trachea (arrow). Sp = fetal spine.

Discussion

In utero diagnosis of fetal goitre has rarely been reported (Barone et al, 1985; Davidson et al, 1991; Kourides et al, 1984; Leger et al, 1987; Weiner et al, 1982). With the routine use of obstetric ultrasound, however, this diagnosis will be made more frequently. Our three cases were encountered within a 1-year period (in about 2500 births). *In utero*, the fetal thyroid is barely visible; thyroid enlargement is readily recognized especially when the size of the gland exceeds the normal thyroid size in newborns, as it was in our cases (Barone et al, 1985; Leger et al, 1987).

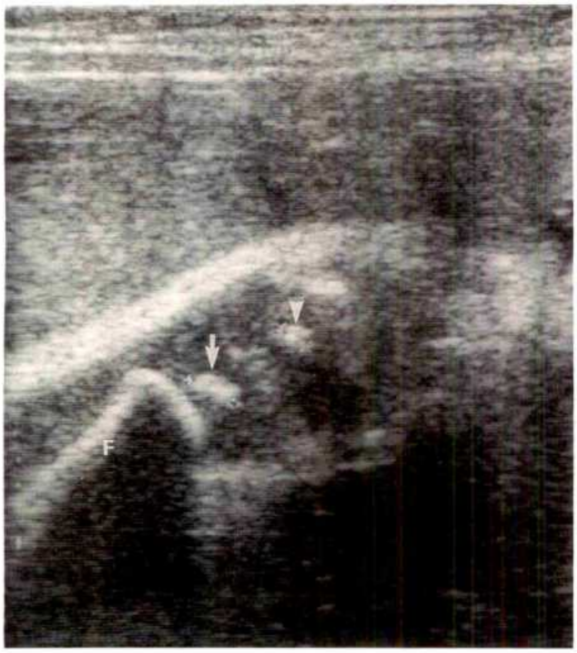

Figure 2. *Case 1.* 36 weeks LMP. Sagittal sonogram of the fetal knee. The distal femoral ossification centre (arrow) measures 7 mm whereas the proximal tibial ossification centre measures 5 mm (arrowhead). F = fetal femur.

A precise diagnosis of fetal goitre is usually easy. The differential diagnosis of anterior fetal neck masses should include thyroid cyst (reported in thyrotoxicosis), cystic hygroma, branchial cleft cyst, haemangioma, cervical neuroblastoma, teratoma and ectopic thymus (Barone et al, 1985; Kourides et al, 1984; Leger et al, 1987; Rypens et al, 1990; Weiner et al, 1982). The symmetrical solid appearance of the masses in our cases (Figs 1–3) facilitated the diagnosis. Polyhydramnios may be an associated finding related to oesophageal compression.

Once the mass is detected, the main problem is to evaluate thyroid function. Associated hyperthyroidism can be suspected if there is an accelerated heart rate and previous history of maternal thyrotoxicosis (Pekonen et al, 1984). This was not present in our cases. Differentiating euthyroidism from hypothyroidism *in utero* is less easy, but important in order to start treatment if necessary.

In utero, thyroid hormonal function can be evaluated by direct or indirect methods. Thyroid hormones participate in the development of the brain and in bone growth. While it is impossible to assess abnormal microscopic brain development *in utero*, it is easy to evaluate normal bone maturation by following the sequence of appearance of the various ossificiation centres (Chinn et al, 1983; Gentili et al, 1984). The calcaneus ossification centre appears at ±24 weeks, then the talus at ±28 weeks, the distal femoral ossification (DFO) centre at ±32 weeks, the proximal tibial ossification (PTO) centre at ±35 weeks and at about 36 weeks the proxi-

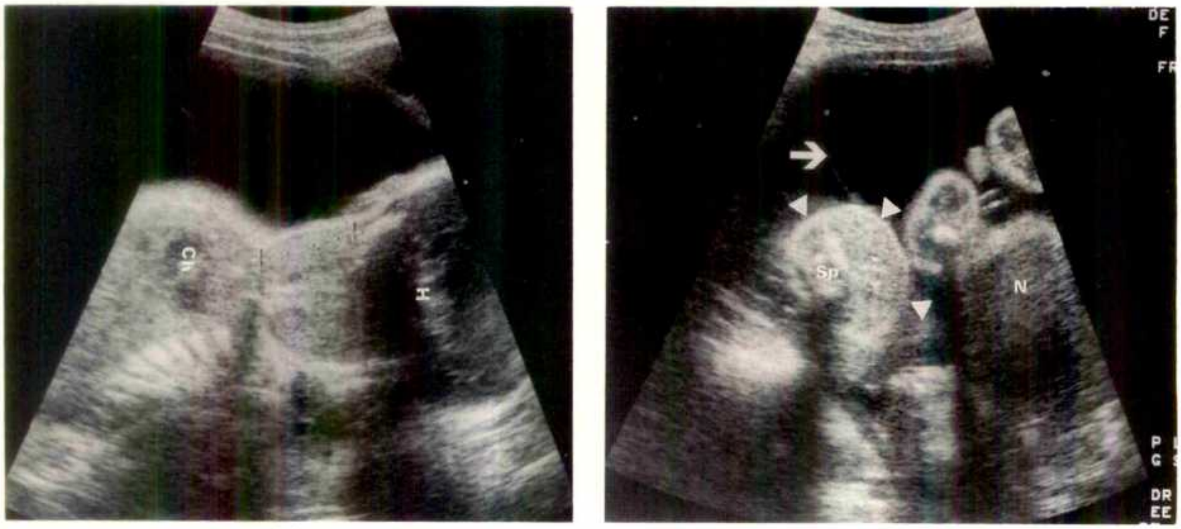

(a) (b)

Figure 3. *Cases 2 and 3.* 33 weeks LMP. (a) Frontal sonogram of the fetal neck (twin J) showing a symmetrical bilobed solid mass around the fetal trachea. Distance between the crosses is 27 mm. H = fetal head; Ch = fetal chest. (b) Transverse sonogram of fetal neck (twin J) showing a solid mass occupying the anterior part of the neck (arrowheads) in front of the spine (Sp). The arrow points to the amniotic membrane between the two fetuses. N = parts of the second twin.

mal humeral ossification (PHO) centre. The DFO and the PTO can also be measured and compared with normal values. When these ossification centres appear "on schedule" during successive examinations, one can reasonably postulate normal fetal bone development and, indirectly, normal thyroid function.

This was so in our first case (Fig. 2). The demonstration of normal bone maturation implied that the fetus was euthyroid and no further investigation such as amniotic fluid puncture was necessary. Conversely, any delay in appearance of bone ossification centres must be evaluated cautiously. First, because there is a normal variability in their appearance and secondly because the main cause for delayed ossification is intrauterine growth retardation (Chinn et al, 1983; Gentili et al, 1984; Zilanti et al, 1987), which is more frequent by far than hypothyroidism. Hypothyroidism should be suggested in cases of delayed bone maturation only in normal-sized fetuses. In our case of twins, neither had the DFO centres at 33 weeks. This could still be considered to be within normal limits; therefore, another method to evaluate hormonal status was needed, and it was decided to use fetal blood sampling.

Although raised thyroid-stimulating hormone (TSH) levels in the amniotic fluid have been shown to correlate with fetal hypothyroidism (Kourides et al, 1984), it seems that estimating the hormonal levels through fetal blood sampling provides a better and more direct evaluation of thyroid function in the fetus (Ponnero & Bloch, 1990; Thorpe-Beeston et al, 1991; Wenstrom et al, 1990). Normal values of thyroid function in the fetus have been recently published (Thorpe-Beeston et al, 1991). The values obtained in one of our twins through fetal cord sampling were consistent with hypothyroidism.

Although the type of hypothyroidism encountered in our cases was transitory (Delange et al, 1978), whatever the cause of the goitre, once hypothyroidism is diagnosed treatment must be considered in these patients to protect brain development. *In utero* treatment is possible and has been attempted successfully in a fetus with hypothyroidism by giving the mother, or by injecting into the amniotic fluid, 3,5 dimethyl-3′-isopropyl thyronine and thyroxine (Conute et al, 1978; Van Herle et al, 1975). Treatment could also be by direct injections into the umbilical cord under US guidance (Davidson et al, 1991).

Several questions remain unanswered in our cases. Why do these goitres occur and what explains their evolution? In Case 1, no real aetiology could be determined; yet, goitre was sonographically obvious based on thyroid size, hyperextended head and spine and polyhydramnios. The reason for the stabilization of the fetal thyroid volume around 32 weeks also remains unclear. Fetal thyroid intoxication could have been transitory (Cappoen, 1989; Rodesch et al, 1976) or there could have been a delayed maturation of the fetal pituitary gland or thyroid (Thorpe-Beeston et al, 1991). It is probable, yet not proven, that in the case of our twins, since the mother herself had a goitre, antibodies must have blocked the fetal thyroid function. The transplacental passage of antibodies causes hypothyroidism, which resolves with their progressive disappearance from the blood of the neonate after birth (Cappoen, 1989; Drexhage et al, 1981; Fort et al, 1988).

In conclusion, fetal goitre may be less rare than previously thought. It is best diagnosed by *in utero* ultrasound. Associated hyperthyroidism is suggested by maternal history and an accelerated fetal heart rate. Normal epiphyseal ossification centre development helps to exclude associated hypothyroidism. Determination of hormonal levels by amniotic fluid puncture or through direct fetal blood sampling is necessary in doubtful cases, so appropriate treatment can be started without delay.

Acknowledgment

The authors wish to thank W. Bank, MD, for editorial assistance.

References

BARONE, C. M., VAN NATTA, F. C., KOURIDES, I. A. & BERKOWITZ, R. L., 1985. Sonographic detection of fetal goiter: an unusual cause of hydramnios. *Journal of Ultrasound in Medicine*, *4*, 625–627.

CAPPOEN, J. P., 1989. Physiologie de la thyroïde pendant la grossesse. *Revue Française de Gynécologie et d'Obstétrique*, *84*, 893–897.

CHINN, D. H., BOLDING, D. B., CALLEN, P. W., GROSS, B. H. & FILLY, R. A., 1983. Ultrasonographic identification of fetal lower extremity epiphyseal ossification centers. *Radiology*, 147, 815–818.

CONUTE, F., BUNOW, G. N. & JORGENSEN, F. C., 1978. Thyroid hormone analogs and fetal goiter. *Endocrinology*, *102*, 1670–1674.

DAVIDSON, K. M., RICHARDS, D. S., SCHATZ, D. A. & FISCHER, D. A., 1991. Successful *in utero* treatment of fetal goiter and hypothyroidism. *New England Journal of Medicine*, *324*, 543–546.

DELANGE, F., DODION, J., WOLTER, R., BOURDOUX, P., DALHEM, A., GHNOER, D. & ERMANS, A. M., 1978. Transient hypothyroidism in the newborn infant. *Journal of Pediatrics*, *92*, 974–976.

DREXHAGE, H. A., BOTTAZO, G. F. & BITENZKY, L., 1981. Thyroid growth-blocking antibodies in primary myxoedema. *Nature*, *289*, 594.

FORT, P., LIPSCHITZ, F., PUGLIESE, M. & KLEIN, I., 1988. Neonatal thyroid disease: differential expression in three successive offsprings. *Journal of Clinical Endocrinology and Metabolism*, *66*, 645–647.

GENTILI, P., TRASINNETI, A. & GIORLANDINO, C., 1984. Fetal ossification centers as predictors of gestational age in normal and abnormal pregnancies. *Journal of Ultrasound in Medicine*, *3*, 193–197.

KOURIDES, I. A., BERKOWITZ, R. L., PANG, S. VAN NATTA, F. C., BARONE, C. M. & GINSBERG-FELLNER, F., 1984. Antepartum diagnosis of goitrous hypothyroidism by fetal US and amniotic fluid thyrotropin concentration. *Journal of Clinical Endocrinology and Metabolism*, *59*, 1016–1018.

LEGER, J., LE GUEN, H., PHOUHINEC, C., BRAUNER, R. & CZERNICHOUR, P., 1987. Antenatal diagnosis of fetal goiter by US. *Presse Médicale*, *16*, 1521–1524.

PEKONEN, F., TERAMOK MAKINEN, I., IKONEN, E., OSTERLUND, K. & LAMBERG, B. A., 1984. Prenatal diagnosis and treatment of fetal thyrotoxicosis. *American Journal of Obstetrics and Gynecology*, *150*, 893–894.

PONNERO, R. P. & BLOCH, C. A., 1990. Fetal blood sampling in the management of intrauterine thyrotoxicosis. *Obstetrics and Gynecology*, *76*, 509–512.

RODESCH, F., COURUS, M., ERMANS DODION, J. & DELANGE, F., 1976. Adverse effect of amniofetography on fetal thyroid function. *American Journal of Obstetrics and Gynecology*, *126*, 723–726.

RYPENS, F., AVNI, E. F., MULLER, F., BARAN, D. & STRUYVEN, J., 1990. Thymus ectopique cervical. *Journal de Radiologie*, *70*, 721–723.

THORPE-BEESTON, J. G., NICOLAIDES, K. H., FELTON, C. V., BUTTER, J. & MCGREGOR, A. M., 1991. Maturation of the secretion of thyroid hormone and thyroid-stimulating hormone in the fetus. *New England Journal of Medicine*, *324*, 532–536.

VAN HERLE, A. J., YOUNG, R. T., FISHER, D. A., ULLER, R. P. & BRINKMAN III, C. R., 1975. Intrauterine treatment of a hypothyroid fetus. *Journal of Clinical Endocrinology and Metabolism*, *40*, 474–475.

WEINER, S., SCHERF, J. I., BOLOGNESE, R. J. et al, 1982. Antenatal diagnosis and treatment of a fetal goiter. *Journal of Reproductive Medicine*, *24*, 39–42.

WENSTROM, K. D., WEINER, C. P., & GRANT, S. S., 1990. Prenatal diagnosis of fetal hyperthyroidism using funipuncture. *Obstetrics and Gynecology*, *76*, 513–517.

ZILANTI, M., FERNANDEZ, S., AZUAGA, A., JORGEZ, J., SEVERI, F. M. & COLOSI, E., 1987. US evaluation of the distal femoral epiphyseal ossification center as a screening test for intrauterine growth retardation. *Review of Obstetrics and Gynecology*, *70*, 361–364.

1992, *The British Journal of Radiology*, 65, 306–308

Impedance plethysmography and thrombo-embolic disease

By ‡D. Glew, FRCR, *T. Cooper, MD, A. E. Mitchelmore, FRCR, †D. Parsons, ‡P. R. Goddard, FRCR and *M. Hartog, FRCP

Departments of Radiology, *Medicine and †Medical Physics, Southmead Hospital, Southmead Road, Bristol BS10 5NB and ‡Department of Radiodiagnosis, Bristol Royal Infirmary, Marlborough Street, Bristol BS2 8HW, UK

(Received 7 May 1991 and in revised form 15 August 1991, accepted 18 October 1991)

Keywords: Impedance plethysmography, DVT, Pulmonary embolism

Abstract. This study compares the results of impedance plethysmography with lower limb venography in 68 patients referred for investigation of clinical deep vein thrombosis, and with the results of ventilation/perfusion isotope scans in 125 patients with suspected pulmonary embolism. Impedance plethysmography had a sensitivity of 100% and a specificity of 61% for the detection of thromboses involving popliteal or more proximal veins (30 patients), but a sensitivity of 90% and a specificity of 68% in the detection of thrombosis at any level, because of a low sensitivity in the detection of isolated calf vein thrombosis (60% in 10 patients). It is a non-invasive, portable and low-cost technique and, in centres where anticoagulation is only given to patients with popliteal or more proximal thrombosis, venography may only be necessary if impedance plethysmography is positive. It may also be of value in the assessment of patients with suspected pulmonary embolic disease and an indeterminate ventilation/perfusion lung scan.

Deep vein thrombosis (DVT) of the legs is common, and carries the risk of thromboembolism. The clinical signs of DVT are insensitive and non-specific (Salzman, 1986) and venography is often performed to establish the diagnosis. Although it is not usually a difficult procedure, lower limb venography may be unpleasant for the patient, is time-consuming and moderately expensive. Various non-invasive tests for DVT have been used, including Doppler and imaging ultrasound, thermography and photoplethysmography. Impedance plethysmography was chosen for this study because of its portability, rapid learning curve and well-established criteria for interpretation.

Impedance plethysmography for the diagnosis of DVT was first described in 1970 (Mullick et al, 1970) and there have been several subsequent reports (Wheeler et al, 1971, 1982; Hull et al, 1976, 1978; Huisman et al, 1986) but the technique has not been introduced into general clinical practice in the UK. The technique is based on measurement of the rate of change in impedance between two electrodes on the calf when a venous occlusion cuff is deflated. Free outflow of venous blood produces a rapid change in impedance whilst delay in outflow, in the presence of a DVT, leads to a more gradual change.

In the present study, the results of impedance plethysmography in two groups of patients are assessed. First, it has been compared with venography in a group of patients referred with a clinical diagnosis of DVT. Secondly, it has been performed in another group undergoing a ventilation/perfusion ($\dot{V}/Q$) scan for suspected pulmonary embolism.

Patients and methods

The first study group consisted of 68 patients referred for lower limb venography for possible DVT. The second study group consisted of 125 patients with suspected pulmonary embolism who were undergoing a $\dot{V}/Q$ scan.

No commercial supplier of impedance plethysmography equipment could be traced in the UK, so a portable impedance plethysmograph was designed and constructed by D.P. The device measures the change in potential difference between two "sensing" electrodes when a fixed 50 kHz alternating current is passed between two "driving" electrodes. Changes in the potential difference, and thus impedance, are recorded. The current is kept below the legal limit of 5 mA, and is impalpable.

In the venography group, impedance plethysmography was performed on the side of the suspected thrombosis, immediately before the venogram. In the lung scan group, it was performed bilaterally, a maximum of 4 days before the $\dot{V}/Q$ scan could be performed. For the procedure, the patient lies supine and the leg is elevated to approximately 25° and rotated externally. Four circumferential brass electrodes are coated with electrode gel and attached to the calf in two pairs separated by about 10 cm. The outer of each pair is the "driving" electrode, the inner the "sensing" electrode. These electrodes are attached to the plethysmograph, which displays the voltage difference on a voltmeter and on a chart recorder. A large blood pressure cuff is positioned at mid thigh.

The recording is made as follows. The cuff is inflated to 60 mmHg, chosen to be between venous and arterial diastolic pressures. Accumulation of blood within the calf leads to a change in the impedance between the

---

Address correspondence to Dr D. Glew.

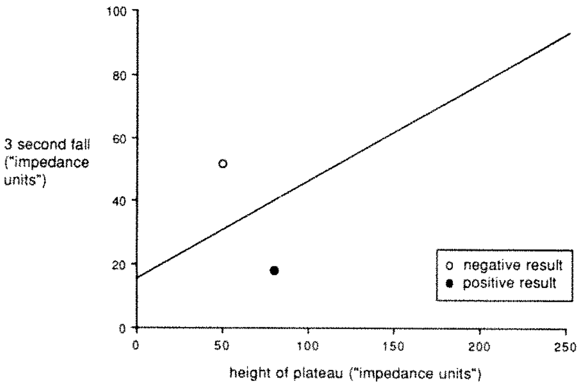

Figure 1. Impedance plethysmography: discriminant line.

Table I. Comparison of venography with impedance plethysmography

Venography	Impedance plethysmography	
	Positive	Negative
Thrombosis above knee	30	0
Thrombosis in calf only	6	4
No thrombosis	9	19

Table II. Comparison of $\dot{V}/Q$ scan with impedance plethysmography

$\dot{V}/Q$ scan group	Impedance plethysmography	
	Positive	Negative
Normal/low probability	15	54
Intermediate/indeterminate	18	10
High probability	25	3

pairs of electrodes. Two minutes of cuff inflation is usually adequate to produce a new steady plateau of impedance (Hull et al, 1978). A trace of the changing impedance is made as the cuff is deflated and a calibration trace is recorded which indicates a 0.4% change in impedance. The whole procedure is carried out three times.

The rate of change of impedance is calculated by measuring the fall in the impedance trace in the first 3 s after the release of cuff pressure and comparing it with the difference between zero and the plateau. These impedance changes are converted to "impedance units", equivalent to a 0.04% change in impedance, by comparison with the 0.4% impedance change produced by calibration. Of the three traces for each limb, the one with the most rapid initial fall is used. This is plotted in relation to the discriminant line described by Hull et al (1976), and read as a positive or negative result (Fig. 1).

In the venography patients, results of the venogram were classified as no thrombosis, thrombosis confined to the deep calf veins, or thrombosis involving the popliteal vein or above. In the group of patients referred for a lung scan, the $\dot{V}/Q$ scan was classified as normal/low probability, intermediate/indeterminate probability or high probability of pulmonary embolism according to the criteria originally described by Biello et al (1979) and modified by Alderson and Martin (1987). In this group the impedance plethysmography was performed as an addition to the clinical management, and venography was not carried out.

Results

Venography findings compared with impedance plethysmography are shown in Table I. These results can be analysed in several ways. If impedance plethysmography is to be used to predict the presence of proximal DVT, then only venograms showing thrombosis in the proximal veins can be considered positive. This gives impedance plethysmography a sensitivity of 100%, specificity of 61%, positive predictive value (PPV) of 67% and negative predictive value (NPV) of 100%. If impedance plethysmography is used to predict the presence of thrombosis at any level then the sensitivity is 90%, specificity 68%, PPV 80% and NPV 83%. Finally, Hull et al (1976) exclude patients with isolated calf DVT from their analysis, and, applied to these results, this would produce a sensitivity for proximal thrombosis of 100%, a specificity of 68%, a PPV of 77% and a NPV of 100%.

Table II compares the results of impedance plethysmography with $\dot{V}/Q$ scans in patients with suspected pulmonary embolism. Those with normal or low probability $\dot{V}/Q$ scans had a 22% positive impedance plethysmography rate (15 of 69). Those with an indeterminate or intermediate probability scan had a 64% positive rate (18 of 28) and those with a high probability scan had an 89% positive rate (25 of 28).

Discussion

The results of this comparison of impedance plethysmography with venography are similar to those reported from the USA and Holland (Hull et al, 1976; Wheeler et al, 1982, 1985; Huisman et al, 1986) and indicate that the technique is highly sensitive for thrombosis at the knee or above, but is less sensitive, and nonspecific, for thrombosis restricted to the calf veins. However, it has been argued that only proximal DVTs carry a risk of pulmonary thromboembolism (Kakkar et al, 1969; Moser & LeMoine, 1981), an assumption supported by trials that demonstrate the safety of DVT management without venography in the presence of normal impedance plethysmography (Wheeler et al, 1982; Huisman et al, 1986).

This study, in common with those mentioned above, has shown that impedance plethysmography may be falsely positive in patients in whom no thrombosis is shown by venography. This may be due to delay in the outflow of blood from the calf, from causes other than DVT, or to errors of technique. Delay, in the absence of DVT, could be due to external compression of the vein impairing venous outflow, or to inadequate venous filling as a result of peripheral vasoconstriction in conditions such as congestive cardiac failure, cold, pain or anxiety. This delay can be diminished by venous occlusion for 2 min before each recording (Wheeler, 1985). Sources of technical error include poor electrode contact with the skin, low battery power, saturation of the constant current drive and incomplete relaxation of the calf muscles. The specificity achieved in this study by impedance plethysmography in the detection of proximal DVT is lower than that quoted elsewhere (Wheeler, 1985). This may be partially due to the large majority of inpatients included, with multiple pathologies. However, it is also probable that some false positive results have been due to saturation of the constant current drive. This technical problem could be avoided by incorporating a warning device in the impedance plethysmograph to demonstrate when saturation occurs. The electrodes could then be moved closer together, overcoming the problem.

Assessment of the accuracy of impedance plethysmography by comparison with the results of the $\dot{V}/Q$ scan in patients with suspected pulmonary emboli depends on the assumption that a DVT is present in patients with a high probability $\dot{V}/Q$ scan and absent in patients with a normal or low probability scan, and that only proximal DVT, which is reliably detected by impedance plethysmography, leads to pulmonary emboli. Neither of these assumptions is entirely valid, but a previous comparison of impedance plethysmography with the presence of pulmonary emboli, confirmed by angiography, found that impedance plethysmography had positive and negative predictive values of 90% for the presence or absence of pulmonary embolism (Sasahara et al, 1979), although less impressive results were reported in another study (Hull et al, 1983). It may, however, be reasonably concluded that negative impedance plethysmography reduces the probability that a patient with an abnormal $\dot{V}/Q$ scan does have pulmonary emboli, whereas positive impedance plethysmography increases the probability. This is likely to be of particular value in the assessment of patients with an intermediate or indeterminate scan.

Impedance plethysmography has certain clear advantages over venography. It requires a single operator and the equipment is portable. It may be quicker than venography, is non-invasive and, in the USA, has been estimated to cost one-tenth as much (Wheeler et al, 1982). Ultrasound, either Doppler or imaging, shares some of these advantages but the equipment is more expensive and greater skill is required of the operator. However, if the equipment and expertise is available, then real-time imaging ultrasound has the further advantage of demonstrating other pathologies that may mimic the clinical presentation of DVT, such as popliteal cysts or muscle haematomata (Whitehouse, 1990).

In conclusion, we feel that impedance plethysmography is a useful investigation in centres where anticoagulation is only undertaken for popliteal or more proximal DVT. It can also be used serially to assess proximal extension of calf DVT (Huisman et al, 1986) and may have a role in the management of patients with an indeterminate $\dot{V}/Q$ scan.

References

Alderson, P. O. & Martin, E. C., 1987. Pulmonary embolism, diagnosis with multiple imaging modalities. *Radiology, 164,* 297–312.

Biello, D. R., Mattar, A. G., McKnight, R. C. & Siegel, B. A., 1979. Ventilation-perfusion studies in suspected pulmonary embolism. *American Journal of Roentgenology, 133,* 1033–1037.

Huisman, M. V., Biller, H. R., Ten Cate, J. W. & Vreeken, J., 1986. Impedance plethysmography for suspected deep vein thrombosis in outpatients. *New England Journal of Medicine, 314,* 823–828.

Hull, R. D., Hirsh, J., Carter, C. J., Jay, R. M., Dodd, P. E., Ockelford, P. A., Coates, G., Gill, G. J., Turpie, A. G., Doyle, D. J., Buller, H. R. & Raskob, G. E., 1983. Pulmonary angiography, ventilation lung scanning, and venography for clinically suspected pulmonary embolism with abnormal perfusion lung scan. *Annals of Internal Medicine, 98,* 891–899.

Hull, R., Taylor, W. D., Hirsh, J., Sackett, D. L., Powers, P., Turpie, A. G. G. & Walker, I., 1978. Impedance plethysmography. The relationship between venous filling and sensitivity and specificity for proximal vein thrombosis. *Circulation, 58,* 898–902.

Hull, R., Van Aken, W. G., Hirsh, J., Gallus, A. S., Hoicka, G., Turpie, A. G. G., Walker, I. & Gent, M., 1976. Impedance plethysmography using the occlusive cuff technique in the diagnosis of venous thrombosis. *Circulation, 53,* 696–700.

Kakkar, V. V., Howe, C. T., Flanc, C. & Clarke, M. B., 1969. Deep vein thrombosis of the leg, is there a "high risk" group? *American Journal of Surgery, 120,* 527–530.

Moser, K. M. & Lemoine, J. R., 1981. Is embolic risk conditioned by location of the deep venous thrombosis? *Annals of Internal Medicine, 94,* 439–444.

Mullick, S. C., Wheeler, H. B. & Songster, G. P., 1970. Diagnosis of deep vein thrombosis by measurement of electrical impedance. *American Journal of Surgery, 119,* 417–422.

Salzman, E. W., 1986. Venous thrombosis made easy. *New England Journal of Medicine, 314,* 847–848.

Sasahara, M. E., Sharma, G. V. R. K. & Parisi, A. F., 1979. New developments in the detection and prevention of venous thromboembolism. *American Journal of Medicine, 43,* 1214–1224.

Wheeler, H. B., 1985. Diagnosis of deep vein thrombosis, review of clinical evaluation and impedance plethysmography. *American Journal of Surgery, 150S,* 7–13.

Wheeler, H. B., Anderson, F. A., Cardullo, P. A., Patwardhan, N. A., Jian-Ming, L. & Cutler, B. S., 1982. Suspected deep vein thrombosis. Management by impedance plethysmography. *Archives of Surgery, 117,* 1206–1209.

Wheeler, H. B., Mullick, S. C., Anderson, J. N. & Pearson, D., 1971. Diagnosis of occult deep vein thrombosis by a non-invasive bedside technique. *Surgery, 70,* 20–28.

Whitehouse, G. H., 1990. Venous thrombosis and thromboembolism. *Clinical Radiology, 41,* 77–80.

1992, *The British Journal of Radiology*, *65*, 309–312

The role of $^{99}Tc^{m}$-HMPAO white cell imaging in suspected orthopaedic infection

By C. Copping, BSc, MSc, MIPSM, S. M. Dalgliesh, BSc, N. J. Dudley, BSc, MSc, MIPSM, P. A. Griffiths, BSc, PhD, FIPSM, M. Harrington, HNC, R. Potter, BSc, MSc, MIPSM and *B. D. Smith, FRCS

Departments of Medical Physics & Computing and *Orthopaedic Surgery, County Hospital, Lincoln LN2 5QY, UK

(*Received 14 March 1991 and in revised form 24 June 1991, accepted 3 October 1991*)

Keywords: Orthopaedic infection, White cell imaging

Abstract. Accurate diagnosis is essential for the effective management of suspected bone infection. Current imaging techniques have had limited success and further work is required. Although white cell labelling techniques have been available for many years the radiopharmaceuticals employed have disadvantages, particularly in their availability and suitability for imaging. These problems have been overcome by the use of $^{99}Tc^{m}$-HMPAO as an *in vitro* leukocyte labelling agent. The aims of this study were to assess retrospectively its role and accuracy in imaging orthopaedic infection and to compare the results with three-phase bone imaging. 30 patients with suspected bone infection underwent three-phase methylene diphosphonate (MDP) bone imaging and labelled leukocyte imaging on separate occasions. 16 bone scans were positive for infection, of which 14 were subsequently confirmed, and there were no false negatives. There were no false positive white cell studies and only one infection was not identified. $^{99}Tc^{m}$-HMPAO white cell imaging has been shown to be an accurate technique for the diagnosis of bone infection but should be performed only following a positive finding on three-phase bone scanning, since the latter is highly sensitive but significantly less expensive, making it a more appropriate screening procedure.

The management of bone infection forms a significant part of the work of the orthopaedic surgeon and the effectiveness of treatment depends heavily on early diagnosis (Froelich, 1985). A common problem is the differentiation between simple loosening and infection of joint replacements. Radiographs are of limited use since a positive diagnosis relies on the disease having produced significant changes to the bone morphology. The functional images produced by radionuclide imaging are of greater value, giving an earlier indication of pathology.

Nuclear medicine techniques are widely used in the investigation of painful joint prostheses and bone infection, traditional late bone imaging now being complemented by early (perfusion) images, gallium imaging (Williams et al, 1987) and indium-labelled leukocyte imaging (Mountford et al, 1986). Reviews of the techniques suggest that further work is required to clarify and standardize the approach in this field (Fogelman, 1990; Norris, 1986; Peters & Lavender, 1990).

Recently, a new radiopharmaceutical for leukocyte labelling has become available for routine use. $^{99}Tc^{m}$-HMPAO was originally developed by Amersham International plc as a cerebral blood flow imaging agent, but its uses in blood cell labelling have since been explored (Peters et al, 1986; Schumichen & Scholmerich, 1986). The advantages of HMPAO over indium 111 are that it can be kept in stock for use as and when required, the radiation doses to the cells and to the patient are lower, and $^{99}Tc^{m}$ is far more suitable for imaging owing to its lower gamma energy.

The aims of this study were to assess retrospectively the accuracy of $^{99}Tc^{m}$-HMPAO labelled leukocyte imaging in demonstrating orthopaedic infection and to compare the results with three-phase bone imaging.

Patients and methods

The patients included in the study were those referred from the Orthopaedic Unit for investigation of suspected bone infection. Methylene diphosphonate (MDP) and labelled leukocyte studies were performed on separate occasions.

Leukocyte labelling was performed using an established method as described by Roddie et al (1988), which was adapted slightly during the course of the study in an attempt to improve labelling efficiency. 102 ml of fresh venous blood was added to 18 ml of acid citrate dextrose (ACD). 20 ml of this mixture was centrifuged to yield plasma for cell suspension, with the remaining 100 ml being allowed to sediment for 60 min following the addition of 10 ml of 6% w/v solution of hydroxyethyl starch (Hespan). The leukocyte pellet was collected by removal of the supernatant and incubated for 10 min after addition of 1 ml of plasma and 4 ml of $^{99}Tc^{m}$-HMPAO at a concentration of 100 MBq/ml. The $^{99}Tc^{m}$-HMPAO was produced by reconstituting a vial of Ceretec (Amersham International plc) with 500 MBq of freshly eluted $^{99}Tc^{m}$ in 5 ml of isotonic saline. In the

---

Address correspondence to Mr N. J. Dudley, Department of Medical Physics & Computing, County Hospital, Lincoln LN2 5QY, UK.

latter part of the series 750 MBq in 2.5 ml were used, with 2 ml being added to the leukocyte pellet. During the incubation period the original supernatant was centrifuged to yield platelet-rich plasma for addition to the leukocyte pellet to terminate labelling at the end of the incubation. This solution was centrifuged, the supernatant removed, and the labelled cells resuspended in Hespan-free plasma for immediate reinjection into the patient.

The radiochemical purity of the $^{99}Tc^{m}$ was assessed using ascending chromatography and was in agreement with data provided by Amersham International plc. Cell viability was established using the neutrophil function test (Wardle, 1986).

Imaging was commenced immediately following intravenous injection of the labelled cells. 32 sequential images of 4 s duration were acquired, followed by a 150 s static image. Further images were acquired at 3–4 h, to a minimum of 100 000 counts, and at 24 h post-injection. Images were taken with the patient supine. The gamma camera was positioned to image the affected part and the contralateral site if possible for the first two phases. Positioning for the later images was similar, with additional images to include the affected part and contralateral site at the centre of the field of view. Images were reported from film, and those with excess accumulation of radioactivity in one or more locations in the area of interest were considered positive for infection.

Bone scans were performed following an intravenous injection of 400 MBq of $^{99}Tc^{m}$-MDP. Studies were commenced immediately after injection following the same protocol as for the white cell scans, with images of the perfusion phase, blood pool phase and bone phase (150 s per image) being acquired. Images were reported from film and were considered positive for infection where increased blood flow and/or pooling at the same location as increased bone uptake was shown. In cases involving joint prostheses, where increased bone uptake adjacent to the prosthesis was demonstrated without increased blood flow/pooling, the interpretation was loosening without infection.

The clinical diagnosis was confirmed by the outcome of surgery or aspiration, or the response to intensive antibiotic therapy or conservative management. Patients responding to antibiotics were assumed to have been infected and those who did not require further investigation or treatment following conservative management were assumed to have been free from infection.

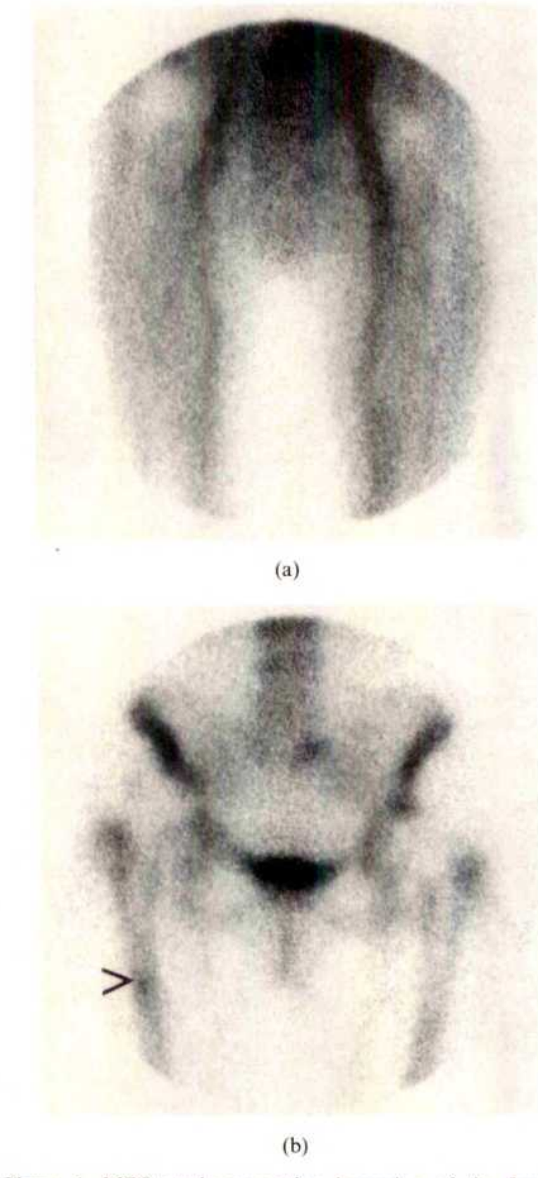
(a)

(b)

Figure 1. MDP study suggesting loosening of the femoral component of a right total hip replacement. (a) Blood pool image showing no abnormality. (b) Image at 3 h post-injection showing increased uptake at the tip of the femoral component (arrow).

Results

Amongst the 30 patients (aged 16–84 years, average age 59 years) undergoing investigation, 14 had total hip replacements, two had total knee replacements and one had a femoral nail and plate. The majority of these operative procedures had not been performed locally. The patients with prostheses initially presented with pain and were referred for nuclear medicine investigation following findings suggestive of infection, *e.g.* rarefaction on radiographs, discharging sinus. The remaining patients presented with unexplained pain, radiographic evidence of infection or rheumatological problems.

Labelling efficiencies were normally distributed ($p > 0.9$), ranging from 8% to 50% with a mean of 27%. The activity of reinjected cells ranged from 40 MBq to 322 MBq with a mean of 127 MBq. The mean labelling efficiency was significantly greater (37%) following the slight modification in technique ($p < 0.05$). 28 patients had white cell counts below the upper limit of normal

Table I. The detection of bone infection

	Infected	Not infected
HMPAO positive	13	0
HMPAO negative	1	16
MDP positive	14	2
MDP negative	0	14

Table II. Sensitivity, specificity, accuracy and predictive values of the two techniques for the detection of bone infection

	HMPAO	MDP
N	30	30
Sensitivity (%)	93	100
Specificity (%)	100	88
Accuracy (%)	97	93
Positive predictive value (%)	100	88
Negative predictive value (%)	94	100

(11×10^9/l) with only two having elevated white cell counts. A normal white cell count did not appear to adversely affect labelling efficiency; no significant difference between these groups was demonstrated ($p > 0.4$).

Figures 1 and 2 illustrate the criteria for differentiating infection from other symptomatic pathologies. Figure 1 shows MDP blood pool and delayed bone images for a loose total hip prosthesis that was not infected. Increased uptake at the tip of the femoral component is typical of loosening. No increased blood pooling is seen. Figure 2 shows MDP blood pool, delayed bone and delayed white cell images, respectively, for an infected total hip prosthesis. Increased blood pooling is seen with a similar distribution to the increased bone uptake around the femoral component. Patchy excess accumulation of white cells is present at the same sites.

Table I gives a summary of the number of patients correctly diagnosed by each technique. Table II shows the sensitivity, specificity, accuracy and predictive value of the techniques. Although white cell imaging was performed in three phases, none of the first-phase (dynamic) studies showed any clear evidence of infection and only a proportion of second-phase images showed increased blood flow. All "positive" second-phase studies were also positive for infection on delayed images.

The diagnosis was confirmed in 15 cases by swab and/or tissue culture. Three patients responded to antibiotic therapy and 12 patients were conservatively managed and required no further treatment. There were two false

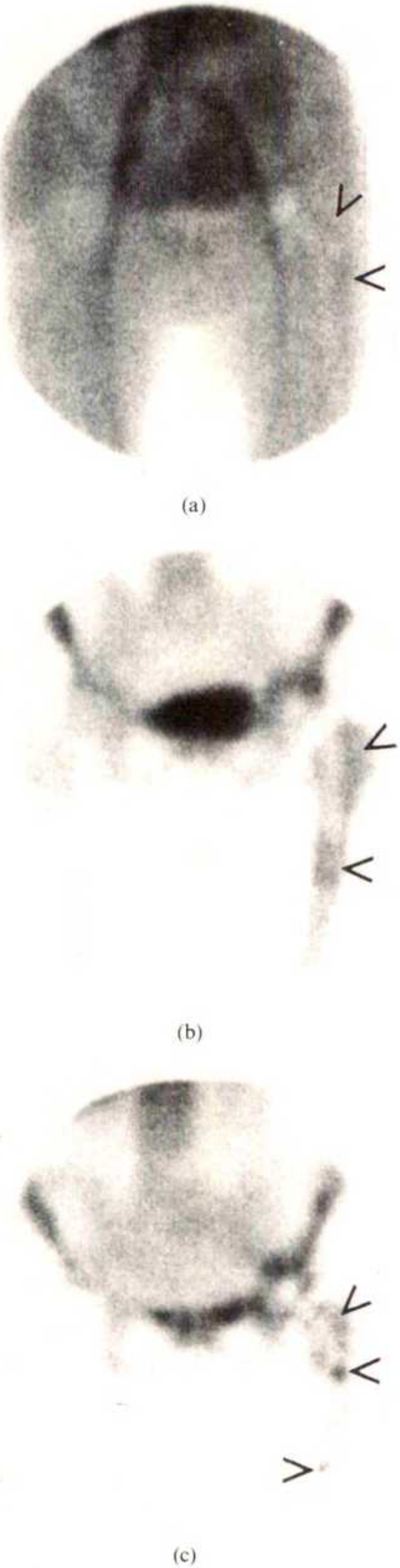
(a)

(b)

(c)

Figure 2. Infected total hip prosthesis. (a) MDP blood pool image. (b) MDP image at 3 h post-injection. (c) Labelled white cell image at 3 h post-injection. Arrows indicate the extent of areas of increased accumulation of radioisotope.

positive MDP results, both of which had true negative HMPAO scans. The single false negative HMPAO result was the only incorrect diagnosis using this technique.

Discussion

In many cases of this nature the symptoms are related to low-grade infection. This presents two problems when labelling and imaging white cells. Firstly the white cell count is often normal, which may result in a low labelling efficiency, and secondly the infection may be difficult to detect owing to a low white cell uptake in the infected area. Despite these potential problems the technique gave reasonably good labelling efficiencies, particularly after the slight modification, and positive diagnoses of infection were obtained even in those patients with white cell counts below 4×10^9/l. Images of diagnostic quality were obtained even in those cases where labelling efficiency was low, probably because of the selective labelling of granulocytes in a mixed leukocyte preparation (Roddie et al, 1988).

Review of the false negative HMPAO result revealed a white cell labelling efficiency of only 20% and clotting of the labelled sample. These factors limited both the amount of activity and the number of white cells available for patient administration, resulting in a low uptake in the infected area. The MDP scan had been positive for infection and there was also radiographic evidence for infection. Retrospectively, there was marginally increased white cell uptake seen in the femoral images. Infection was confirmed surgically.

HMPAO white cell labelling is clearly useful in the diagnosis of orthopaedic infection. The high sensitivity and specificity of 93% and 100%, respectively, indicate that virtually all infections may be detected and that patients with positive findings may be treated with confidence. Non-infected patients may also proceed without delay to further treatment if appropriate, *e.g.* revision of loose prosthesis. Although early phases were imaged, they did not add to the diagnostic accuracy of the technique.

Three-phase bone scanning alone, with 100% sensitivity but lower specificity, is of limited value. Despite this, any low-cost technique with 100% sensitivity must be useful as a screening tool. The pharmaceutical costs for white cell labelling are substantially higher than those for bone scanning. Our results suggest that three-phase bone scanning is useful for initial screening, with subsequent white cell scanning for all positive results. This protocol could reduce the need for white cell scanning for bone infection by up to 50%, with a significant cost saving and no reduction in sensitivity.

Although irregular distributions of bone marrow following hip replacement have not led to misdiagnosis in this study, other workers have suggested the use of a marrow imaging agent to differentiate between infection and normal marrow uptake of neutrophils (Peters & Lavender, 1990). The use of three-phase bone scanning for screening overcomes this problem. Labelled leukocyte accumulation coincident with increased activity on blood pool and delayed bone images is unlikely to be normal bone marrow. A prospective study of this problem is in progress.

References

FOGELMAN, I., 1990. 1, 2, 3 or 4 phase bone imaging—how many are necessary? *Nuclear Medicine Communications, 11,* 7–9.

FROELICH, J. W., 1985. Nuclear medicine in inflammatory diseases. *Nuclear Medicine Annual, 6,* 34–43.

MOUNTFORD, P. J., HALL, F. M., WELLS, C. P. & COAKLEY, A. J., 1986. ^{99}Tc^{m}-MDP, ^{67}Ga-citrate and ^{111}In-leucocytes for detecting prosthetic hip infection. *Nuclear Medicine Communications, 7,* 113–120.

NORRIS, S. H., 1986. Investigation of total joint replacement. *Seminars in Orthopaedics, 1,* 41–48.

PETERS, A. M., DANPURE, H. J., OSMAN, S., HAWKER, R. J., HENDERSON, B. L., HODGSON, H. J., KELLY, J. D., NEIRINCKX, R. D. & LAVENDER, J. P., 1986. Clinical experience with ^{99m}Tc-hexamethylpropyleneamineoxine for labelling leucocytes and imaging inflammation. *Lancet, ii,* 946–949.

PETERS, A. M. & LAVENDER, J. P., 1990. Diagnosis of bone infection. *Nuclear Medicine Communications, 11,* 463–467.

RODDIE, M. E., PETERS, A. M., DANPURE, H. J., OSMAN, S., HENDERSON, B. L., LAVENDER, J. P., CARROLL, M. J., NEIRINCKX, R. D. & KELLY, J. D., 1988. Inflammation: imaging with Tc-99m HMPAO-labelled leucocytes. *Radiology, 166,* 767–772.

SCHUMICHEN, C. & SCHOLMERICH, J., 1986. Tc-99m HMPAO labelling of leucocytes for detection of inflammatory bowel disease. *Compact News in Nuclear Medicine, 17,* 274–276.

WARDLE, E. N., 1986. Assessment of neutrophil function-1. *Postgraduate Medical Journal, 62,* 997–1000.

WILLIAMS, F., MCCALL, I., O'CONNOR, B. & MORRIS, V., 1987. Gallium-67 scanning in the painful total hip replacement. *Clinical Radiology, 32,* 431–439.

1992, *The British Journal of Radiology*, *65*, 313–316

Benign non-infected urachal cyst in an adult: review of the literature and a case report

By M. K. Al-Hindawi, FRCR, FFR, RCSI and *S. Aman, FRCS

Radiology Department, University Hospital, PO Box 13046, Amman, Jordan and *Surgery Department, Mubarak Hospital, Kuwait

(*Received 27 June 1990 and in revised form 21 August 1991, accepted 12 September 1991*)

Keywords: Urachal cyst, Complicated urachal cyst, US, CT

Abstract. Urachal cyst is rather a rare lesion with interesting and different ways of presentation. More urachal cysts are being shown by ultrasound and computed tomography, and their criteria for diagnosis are discussed.

Urachal cysts are retention cysts of the urachal remnants of varying size and containing mucus secretion (Blichert-Toft & Nielsen, 1971a). The lumen of the urachal cysts is closed towards the bladder as well as the umbilicus (Blichert-Toft & Nielsen, 1971b). The embryology, anatomy and pathology of urachal anomalies have been described in detail in the literature (Begg, 1930; Blichert-Toft & Nielsen, 1971a; Bauer & Retik, 1978; Nielsen, 1982). Urachal anomalies requiring clinical attention are rare and most occur in early childhood (Bauer & Retik, 1978; Buckspan, 1984). Urachal cysts typically remain clinically silent until size or infection complicates in adulthood (Blichert-Toft & Nielsen, 1971a,b; Bauer & Retik, 1978; Morin et al, 1979; Williams & Fisk, 1981). In all age groups, not more than 30 cases of non-infected cysts have been reported, and less than 15 have been recorded in adults. We have reviewed the literature for the incidence and complications of urachal cysts, and report the appearances of a benign non-infected urachal cyst in an adult.

Incidence

The incidence of urachal cyst has been reported as 1 in 5000 autopsies in children (Rubin, 1967; Elkin, 1980). During a 20-year period at the Children's Hospital of Buffalo, only six cases of infected urachal cysts were reported by Newman et al (1986). Blichert-Toft and Nielsen (1971a,b) reported two cases of infected urachal cysts out of five urachal anomalies in adults, collected from 40000 admissions to a surgical department between 1959 and 1970. In addition, they collected all reported cases of urachal anomalies from 1550 until 1970. The list included 24 non-infected urachal cysts in all age groups from 315 cases of urachal anomalies. There were only nine cases of non-infected urachal cysts in adults. Six more cases of benign non-infected urachal cysts in adults have been reported in the English literature, making a total of 15. They range from 20 to 60 years in age, and include nine cases reported by Begg (1930), two by Nielsen et al (1982), one by Spataro et al (1983), one by Bouvier et al (1984), one by Leyson (1984) and one by Nair (1987).

Complications

The reported complications of urachal cysts are as follows.

Infection

Infection is the most common complication and occurs most frequently in young adults (Sterling & Goldsmith, 1953; Blichert-Toft & Nielsen, 1971a). Infection can lead to the formation of abscesses and sinuses (Goldman et al, 1988), peritonitis by intraperitoneal rupture (Agatstein & Stabile, 1984; Newman et al, 1986; Nair, 1987) and urinary tract infection (Blichert-Toft & Nielsen, 1971a). Two reported cases of primary actinomycosis infection of urachal cysts have been collected by Gotoh et al (1988).

Intestinal obstruction

Amundsen (1959) found a loop of small intestine trapped in a perforated infected urachal cyst. Haupt and Keitel (1960) and Blichert-Toft and Nielsen (1971a) found the caecum and a loop of small intestine strangulated by the urachus forming a free intraperitoneal cord. Blichert-Toft and Axelsson (1977) reported a case of intraperitoneal rupture of an infected urachal cyst presenting as obstructed loops of small and large intestine.

Urinary tract lesions

In addition to infection, prostatism, obstructive uropathy and uraemia have been reported by Breschi (1969) and Standfield and Shearer (1981), calculi formation by Blichert-Toft and Nielsen (1971a,b), and Blichert-Toft and Axelsson (1977). An association with prune-belly syndrome was reported by Sanders et al (1974), and other genitourinary abnormalities by Newman et al (1986).

Haemorrhage

One case of spontaneous haemorrhage into the urachal cyst presenting as an acute abdomen has been reported (Davidson et al, 1987)

Complicating pregnancy

Nielsen et al (1982) reviewed the English literature from 1877 and found seven cases of urachal cysts, one case of urachal sinus and four cases of patent urachus complicating pregnancy. They reported one other case of patent urachus presenting during pregnancy. The symptoms and complications included retention, abdominal pain, antepartum and postpartum intraperitoneal perforation of infected urachal cyst and premature labour with neonatal death at the 26th week of gestation. They suggested that the increased bladder pressure and reduced capacity together with hormonal influences might be sufficient to open a functionally closed patent urachus. One other case of an infected urachal cyst in a pregnant woman was reported by Jaffa et al (1984).

Reiter's disease

Reiter's disease of the urachal remnant (Maxwell & Nicholson, 1987) has been reported in a single case. This interesting report suggests that urethritis may, like synovitis, be reactive rather than infective. The urachus is closely related embryologically to the urethra and has a similar uroepithelium, but in this case the urachal remnant had no patent connection with the urogenital tract. Thus, direct infection of the urachus would seem unlikely. The urachal inflammation would seem to have resulted from a reaction to the same factors that caused the relapse of the reactive arthritis (Hughes & Keat, 1988).

Malignancy

Cases of malignancy have been reported by Goodman et al (1980), Sheldon et al (1984), Thomas et al (1986), Brick et al (1988) and Narumi et al (1988). Urachal cancer is a rare tumour comprising about 0.01% of all cancers in adults. It accounts for less than 0.5% of all bladder cancers (Korobkin et al, 1988). About 84% of malignant lesions are adenocarcinoma and only 3% are transitional cell carcinoma (Sheldon et al, 1984). It is now generally accepted that the urachus is normally lined with transitional epithelium, which changes to a glandular epithelium in an orderly fashion through metaplasia (Mostofi et al, 1955; Sheldon et al, 1984; Brick et al, 1988).

Case report

A 42-year-old man was referred to the radiology department for transabdominal ultrasound (US) examination of the prostate. He complained of frequency of micturition and vague heaviness in the lower abdomen.

The prostate was normal but a round, well defined cystic mass containing scattered focal and linear echogenic areas was detected. It was 8 cm in diameter and closely related to the dome of bladder (Fig. 1). Computed tomography (CT) showed a smooth round cystic mass (27 Hu) associated with a faint punctate calcification at its base, which was inseparable from the bladder wall (Fig. 2). At surgery, the mass was excised *en bloc* together with the surrounding abdominal wall muscle and a cuff of the bladder wall.

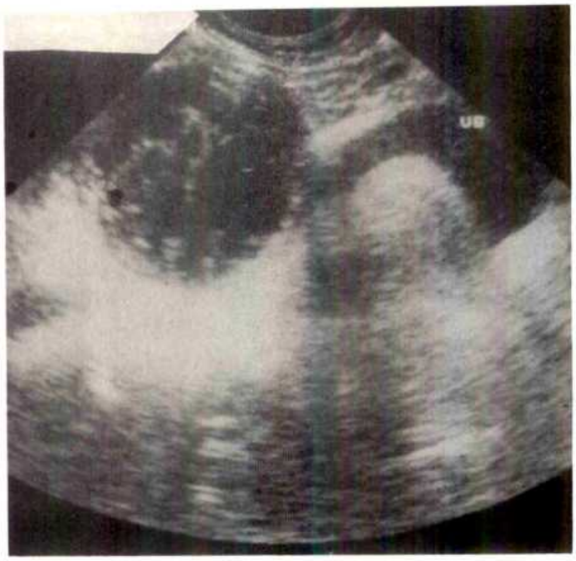

Figure 1. Ultrasound scan showing a round, mainly cystic mass with inhomogeneous internal echoes and anechoic areas. It has smooth and regular outlines and is closely related to the dome of the urinary bladder. Faint shadowing at its base is noted.

Histopathology showed a benign, non-infected unilocular urachal cyst, 8 cm in diameter with smooth partially calcified walls of 2–5 mm thickness. The cyst was filled with thick tenacious mucus. The lining in most areas was a single layer of columnar mucus-secreting epithelium, while other areas resembled colonic-type mucus-secreting glandular mucosa.

Discussion

Ultrasound

US is ideal for the diagnosis of urachal cysts because they are cystic, extraperitoneal and directly related to the bladder. The differential diagnosis includes abscess, vitelline cyst, haematoma (Amparo et al, 1982; Bouvier et al, 1984), echinococcus cyst (Constantian & Boldue, 1968) and mesenteric cyst (Goodman et al, 1980). Williams and Fisk (1981) reported the appearance of a giant multi-septated cyst, which was shown to be an infected urachal cyst. A simple, non-infected urachal cyst would appear as an echo-free midline mass above the bladder, often extending to the umbilicus (Sanders et al, 1974; Goodman et al, 1980). It is of interest that in our case the pathological examination revealed a unilocular cyst, but the US appearance was that of a complex and mixed echogenic cystic mass probably resulting from the thick and tenacious but acoustically inhomogeneous mucus content.

Computed tomography

CT scanning is of value in establishing the characteristics of the mass, its extent and its anatomical relationships (Berman et al, 1988). Furthermore, CT helps in

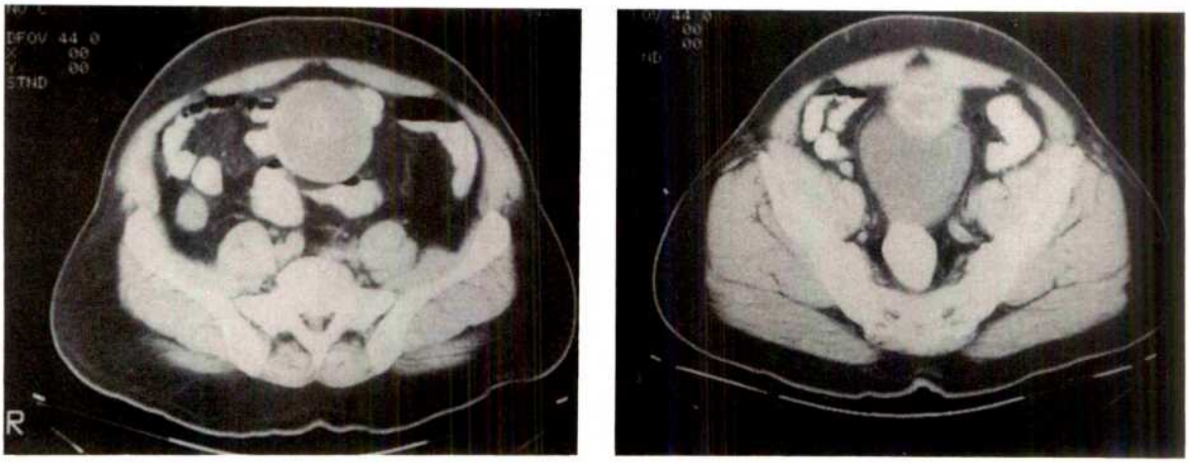

(a) (b)

Figure 2. (a) CT scan showing a well defined and regular urachal cyst. CT number of its contents is 27 HU. (b) Punctate calcification is noted in the lower part of the urachal cyst, close to the urinary bladder.

distinguishing between an infected thick-walled urachal cyst and carcinoma (Mekras et al, 1980; Kwok-Liu, 1980; Thomas et al, 1986), which may show direct invasion of surrounding structures (Korobkin et al, 1988), adjacent lymph node involvement (Mekras et al, 1980; Sarno et al, 1983) or secondary deposits (Fitzgerald & Pirani, 1985). CT readily identifies calcification thus enhancing the specificity of the diagnosis (Kwok-Liu, 1980). Narumi et al (1988) considered the calcification detected by CT to be pathognomonic of urachal adenocarcinoma. This is clearly not true in our calcified benign urachal cyst. Finally, CT and US may be used to direct fine-needle aspiration techniques (Spataro et al, 1983).

Magnetic resonance imaging (MRI)

MRI offered no additional information beyond that provided by CT, but MR may allow improved staging of carcinoma by its multiple imaging planes (Brick et al, 1988).

References

Agatstein, E. H. & Stabile, B. E., 1984. Peritonitis due to intraperitoneal performation of infected urachal cysts. *Archives of Surgery*, *119*, 1269–1273.

Amparo, E. G., Cohen, M. S. & Fagan, C. J., 1982. Benign urachal cyst in an adult. *Journal of Computer Assisted Tomography*, *6*, 1025–1027.

Amundsen, G., 1959. Urachus cyst som aarsak til ileus. *Nordisk Medicin*, *62*, 1484–1485.

Bauer, S. B. & Retik, A. B., 1978. Urachal anomalies and related umbilical disorders. *Urologic Clinics of North America*, *5*, 195–211.

Begg, R. C., 1930. The urachusitis anatomy, histology and development. *Journal of Anatomy*, *64*, 170–183.

Berman, S. M., Tolia, B. M., Laor, E., Reid, R. E., Schweizerhof, S. P. & Freed, S. Z., 1988. Urachal remnants in adults. *Urology*, *31*, 17–21.

Blichert-Toft, M. & Nielsen, O. V., 1971a. A congenital patent urachus and acquired variants. *Acta Chirurgica Scandinavica*, *137*, 807–814.

Blichert-Toft, M. & Nielsen, O. V., 1971b. Diseases of the urachus simulating the intra-abdominal disorders. *American Journal of Surgery*, *122*, 123–128.

Blichert-Toft, M. & Axelsson, C. K., 1977. Urachal lesion associated with calculus formation causing intestinal obstruction. *Scandinavian Journal of Urology and Nephrology*, *11*, 77–79.

Bouvier, J. F., Pascaud, E., Mailhes, F., Pascaud, J. L., Hummel, P. & Rousseau, J., 1984. Urachal cyst in the adult: ultrasound diagnosis. *Journal of Clinical Ultrasound*, *12*, 48–50.

Breschi, L. C., 1969. Prostatism and infected urachal cyst, a differential diagnosis. *American Surgeon*, *35*, 773–778.

Brick, S. H., Friedman, A. C., Pollak, H. M., Fishman, E. K., Radecki, P. D., Siegelbaum, M. H., Mitchell, D. G., Lev-Toaff, A. S. & Caroline, D. F., 1988. Urachal carcinoma: CT findings. *Radiology*, *169*, 377–381.

Buckspan, M. B., 1984. Patent urachus and infected urachal cyst in an adult: a case report. *Canadian Journal of Surgery*, *27*, 496–499.

Constantian, H. M. & Boldue, R. A., 1968. Echinococcus cysts simulating urachal cyst. *Journal of Urology*, *99*, 755.

Davidson, B. R., Brown, N. J. & Neoptolemos, J. P., 1987. Haemorrhage into a urachal cyst presenting as an acute abdomen. *Postgraduate Medical Journal*, *63*, 493–494.

Elkin, M., 1980. *Radiology of the Urinary System: Anomalies Related to the Development of the Bladder* (Little Brown, Boston), pp. 122–127.

Fitzgerald, E. J. & Pirani, M., 1985. Computed tomography and ultrasound of a urachal cancer. *British Journal of Radiology*, *58*, 88–90.

Goldman, I. L., Caldamone, A. A., Gauderer, M., Hampel, N., Wesselhoeft, C. W. & Elder, J. S., 1988. Infected urachal cysts: a review of 10 cases. *Journal of Urology*, *140*, 375–378.

Goodman, J. D., Schneider M. & Haller, J. O., 1980. Ultrasound demonstration of an infected urachal cyst. *Urologic Radiology*, *1*, 245–246.

Gotoh, S., Kura, N., Nagahama, K., Higashi, Y., Fukui, I., Takagi, K., Terada, T., Kao, T., Kamiyama, R. & Oshima, H., 1988. Actinomycosis of urachal remnants. *Journal of Urology, 140,* 1534–1535.

Haupf, G. J. & Keitel, H. K., 1960. Intestinal obstruction in a child with a peritonealized urachal remnant. *Journal of Pediatrics, 57,* 741–743.

Hughes, R. A. & Keat, A. C., 1988. Reiter's disease of a urachal remnant. *Journal of the Royal Society of Medicine, 81,* 491–492.

Jaffa, A. J., Noy, S. & Peyeser, M. R., 1984. Preoperative sonographic diagnosis of infected urachal cyst in a parous woman. *American Journal of Obstetrics & Gynecology, 148,* 220–221.

Korobkin, M., Cambier, L. & Drake, J., 1988. Computer tomography of urachal carcinoma. *Journal of Computer Assisted Tomography, 12,* 981–987.

Kwok-Liu, J. P., 1980. Carcinoma of the urachus: the role of computer tomography. *Radiology, 137,* 731–734.

Leyson, J. F. J., 1984. Calcified urachal cyst. *British Journal of Urology, 56,* 438.

Maxwell, H. & Nicholson, R., 1987. Reiter's disease of a urachal remnant. *Journal of the Royal Society of Medicine, 80,* 778–779.

Mekras, G. D., Block, N. L., Carrion, H. M. & Ishikoff, M., 1980. Urachal carcinoma: diagnosis by computed axial tomography. *Journal of Urology, 123,* 275–277.

Morin, M. E., Tan, A., Baker, D. A. & Sue, H. K., 1979. Urachal cyst in the adult: ultrasound diagnosis. *American Journal of Roentgenology, 132,* 831–832.

Mostofi, F. K., Thomson, R. V., Dean, A. Jr., 1955. Mucous adenocarcinoma of the urinary bladder. *Cancer, 8,* 741–758.

Nair, K. P. N., 1987. Mucous metaplasia and rupture of urachal cyst as a rare cause of acute abdomen. *British Journal of Urology, 59,* 281–282.

Narumi, Y., Sato, T., Fujita, K. K. M., Saiki, S., Miki, M. K. T. & Kotake, T., 1988. Vesical dome tumors: significance of extravesical extention on CT. *Radiology, 169,* 383–385.

Newman, B. M., Karp, M. P., Jewett, T. C. & Cooney, D. R., 1986. Advances in the management of infected urachal cyst. *Journal of Pediatric Surgery, 21,* 1050–1054.

Nielsen, T. P., Nelson, R. M., Lee-Green, B., Lowe, P. N. & Reese, L. A., 1982. Patent urachus complicating pregnancy: a review and report of a case. *American Journal of Obstetrics and Gynecology, 143,* 61–68.

Rubin, A., 1967. *Handbook of Congenital Malformations* (W. B. Saunders, Philadelphia), p. 334.

Sanders, R. C., Kook Sang, O. H. & Dorst, J. P., 1974. B-scan ultrasound: positive and negative contrast material evaluation of congenital urachal anomaly. *American Journal of Roentgenology, 120,* 448–452.

Sarno, R. C., Klauber, G. & Carter, B. L., 1983. Computer assisted tomography of urachal abnormalities. *Journal of Computer Assisted Tomography, 7,* 674–676.

Sheldon, C. A., Clayman, R. V., Gonzalez, R., Williams, R. D. & Fraley, E. E., 1984. Malignant urachal lesions. *Journal of Urology, 131,* 1–8.

Spataro, R. F., Davis, R. S., McLachlan, M. S. F., Linke, C. A., Barbaric, Z. L., 1983. Urachal abnormalities in the adult. *Radiology, 149,* 659–663.

Standfield, N. J. & Shearer, R. J., 1981. Prostatism obstructive uropathy and uraemia associated with a urachal cyst. *British Journal of Urology, 53,* 482.

Sterling, J. A. & Goldsmith, R., 1953. Lesions of the urachus which appear in the adult. *Annals of Surgery, 137,* 120–128.

Thomas, A. J., Pollack, M. S. & Libshitz, H. I., 1986. Urachal carcinoma: evaluation with computed tomography. *Urologic Radiology, 8,* 194–198.

Williams, B. D. & Fisk, J. D., 1981. Sonographic diagnosis of giant urachal cyst in the adult. *American Journal of Roentgenology, 136,* 417–418.

1992, *The British Journal of Radiology*, *65*, 317–320

Cranial stereotactic multiple arc radiotherapy; treatment planning using angiographic images

By *E. S. Thomson, PhD and P. Clegg

Radiation Physics Department, St Bartholomew's Hospital, London

(Received 22 May 1991 and in revised form 6 September 1991, accepted 3 October 1991)

Keywords: Stereotactic, Radiotherapy, Angiography

Abstract. Stereotactic multiple arc radiotherapy (SMART) is an irradiation technique developed to treat small intracranial lesions. Calculation of absorbed-dose patterns for this treatment has traditionally involved complex computer programs incorporating algorithms designed to reconstruct the shape of the patient's head from computerized tomography (CT) images. A large proportion of the patients treated with SMART, however, have arteriovenous malformations for which angiography provides a better idea of lesion size and position than CT. This paper describes a computer program developed at St Bartholomew's Hospital which enables calculation of absorbed dose for a SMART treatment directly from angiographic radiographs, avoiding the need for CT. The program is compared with the existing CT-based treatment planning program.

Stereotactic multiple arc radiotherapy (SMART) is a technique developed for the treatment of small intracranial lesions using a linear accelerator (Betti & Derichinski, 1983; Colombo et al, 1985; Hartmann et al, 1985; Lutz et al, 1988; Podgorsak et al, 1988; Thomson et al, 1990). Steep absorbed-dose gradients around the edge of the target volume are achieved by rotating the beam in a series of non-coplanar arcs around a central point. In order to achieve accurate localization of such small target volumes, a stereotactic frame is used but the new relocatable devices, such as that described by Gill (1987) and Thomson et al (1990), allow repeat fixation when required.

One of the most difficult problems to overcome when implementing a SMART technique is the development of software capable of calculating the resulting absorbed-dose patterns. Several centres have now developed such software (Hartmann et al, 1985; Lutz et al, 1988; Podgorsak et al, 1988; Thomson, 1990). Some systems are available commercially but these tend to be expensive, with strict requirements relating to accompanying hardware and often only being sold as part of a complete equipment package or as an extension to existing treatment planning software. The reason for the degree of sophistication encountered is the complex nature of the treatment process. The central axis of the treatment beam may approach the patient from any angle and a full, 3-dimensional description of the shape of the patient's head is required. In practice, this is usually obtained from computerized tomography (CT) images and some form of interface is required between the treatment planning computer and the CT scanner. In addition to this hardware restriction, the treatment planning software must be capable of rapid handling of data taken from the CT images, once these are transferred. There is a consequent necessity for rapid processing speeds and a fast, efficient algorithm.

A large proportion of the patients treated using SMART have arteriovenous malformations (AVMs). These lesions are best visualized using angiographic techniques and at St Bartholomew's Hospital stereotactic angiograms have been used as an aid to planning since 1990. Unfortunately, angiographic images consist of 2-dimensional projections of the patient's head and 3-dimensional information can only be obtained about points that are easily identifiable on orthogonal anteroposterior (AP) and lateral images. As a result, it has been necessary for all patients to undergo a CT scan in addition to their angiogram, to enable a full 3-dimensional reconstruction to take place.

The aim of this paper is to present a SMART treatment planning program, developed at St Bartholomew's Hospital, capable of calculating absorbed-dose distributions directly from angiographic images. This is achieved by representing the head of the patient as an ellipsoid volume orientated at any angle to, and positioned at any location within the stereotactic frame coordinate system. Using this technique, the need for CT is avoided. In contrast to previously developed software packages, the hardware requirements of this treatment planning program are minimal and it currently operates on an IBM-compatible personal computer. Absorbed-dose distributions are calculated in three orthogonal planes through the isocentre and the calculation time for a treatment using five arcs of 140° each is under 5 min. Although this program was developed primarily for use with angiograms, if required the data necessary for planning may be taken from CT. It is felt that the portability and versatility of this program make it ideal for use at any treatment centre and it may provide an alternative to the more sophisticated, CT-based packages currently available.

The dosimetric accuracy of the angiographic treatment planning algorithm has been verified using measurements made in a phantom and by comparison of calculated results with those obtained using the CT-based SMART treatment planning program also available at St Bartholomew's Hospital (Thomson,

---

*Present address and address for correspondence: Radiotherapy Physics Department, Norfolk and Norwich Hospital, Brunswick Road, Norwich, Norfolk NR1 3SR.

1990). A brief description of both software options is given in this paper, followed by the results of the dosimetric comparison. In conclusion, the suitability of the angiographic SMART treatment planning program for routine use is assessed.

Method

As described, two SMART treatment planning programs have been written at St Bartholomew's Hospital, one calculating absorbed dose from CT data, the other from angiographic images. In order to evaluate the accuracy of the angiographic SMART treatment planning program, the results of calculations performed with the two alternative systems have been compared. A brief description of each will therefore be given.

CT treatment planning system

The CT-based SMART treatment planning program has been in clinical use since 1989. The program operates on the computer system used for conventional radiotherapy treatment planning at St Bartholomew's Hospital, a Data General Eclipse, normally running International General Electric (IGE) Target software. Outline data from CT images are transferred from the Target system to the SMART treatment planning program. There is no software restriction on the number of CT image planes that can be considered and typically between 15 and 20 are used. The slice separation may be varied and is usually between 1 and 3 mm in the region of the target volume, increasing to 10 mm once outside the volume and continuing until clear of the patient's head. Within the program, the 3-dimensional shape of the head is represented by the stack of surface outlines, a smoothing algorithm being used before display. Beam data for each circular field used consists of a percentage depth dose curve and a single beam profile. Absorbed dose is calculated using simple equations to find the depth and distance from the central axis of each point in the calculation matrix, for each beam position in turn. This technique is similar to that described by Hartmann et al (1985). The small amount of beam divergence occurring is accounted for using a calculated modification to the beam profile. A full description of the absorbed-dose calculation technique is given in Thomson (1990) and examples of treatment plans can be seen in Thomson et al (1990).

Angiographic treatment planning system

The computer program developed for use in conjunction with angiographic images relies on the assumption that the shape of the head can be represented by an ellipsoid volume. This in itself is not a new idea and has, for some time, been the basis of both treatment planning programs available with the commercially produced cobalt-60 radiosurgery units (Ahnesjo, 1982; Walton et al, 1987) and Monte Carlo computer phantoms (Kramer et al, 1986). In the SMART treatment planning program, the head has been considered as an ellipsoid volume centred at any point within the stereotactic frame and orientated at any angle to the cardinal axes of the stereotactic coordinate system. The dimensions of the ellipsoid are specified by its three half-axis lengths. These are measured from angiographic radiographs (Figs 1 a & b) or, if required, from CT images. In order to obtain the optimum size and orientation of ellipse for a given patient, a selection of ellipse cross-sections have been accurately drawn onto transparent acetate sheets. These cross-sections are superimposed onto the images and the best combination of position and angulation chosen. Skull dimensions are measured directly from the radiographs although, when using

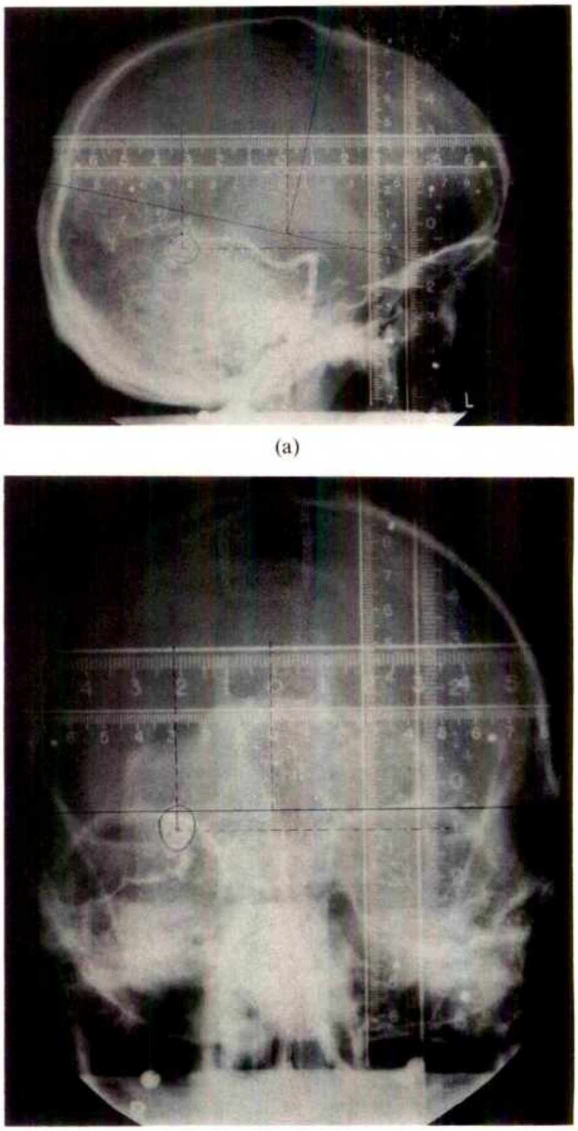
(a)

(b)

Figure 1. Angiographic radiographs showing the half axes of the skull ellipsoid used for planning (solid lines) together with the target volume and lines constructed for calculation of stereotactic coordinates (dotted lines). (a) Shows the lateral projection and (b) the anterior/posterior projection.

angiograms, superficial layers of skin and muscle are not normally visible. In order to compensate for this, 6 mm is routinely added to all ellipsoid dimensions measured in this way. In practice, it has been found that this technique approximates values close to those measured from comparable CT images. The only additional values required by the treatment planning program are the stereotactic coordinates of the centre of the target volume. All information may therefore be transferred to the computer via the keyboard.

The program is written in Fortran on an IBM-compatible 386SX personal computer and calculation times are typically around 5 min for calculation of the absorbed-dose pattern in all three planes. The dose calculation algorithm used is the same as that used with the CT-based system. Isodose curves are plotted on transparent acetate sheets and manually superimposed onto the required image (Figs 2 a & b). The magnification factor used corresponds to that in the central plane of the target volume.

Results

The accuracy of the CT-based system has been assessed using a series of measurements made with an ionization chamber and dosemeter combination (0.2 cm^3 Nuclear Enterprises 2515/3, ionization chamber and Farmer dosemeter) with the chamber inside a spherical phantom of water-substitute material. With the isocentre at various positions within the phantom, agreement between measured and calculated results, within the limits of uncertainty, was consistently found (mean difference 0.3% ± 2.1%). The quoted values of uncertainty are twice the standard deviation (SD) of the mean result, added in quadrature with the estimated uncertainty in the calibration chain. The calculated absorbed-dose pattern around the isocentre was also verified with measurements made inside the spherical phantom, this time using thermoluminescent dosimetry (TLD) detectors (Vinten, LiF-7, 99.5%). The detectors used were in the form of disc-shaped pellets, 4.5 mm in diameter and 0.9 mm thick. These were orientated such that their smallest dimension lay along the axis of the steep dose gradient. Agreement, within the limits of uncertainty of the measured results, was again found at all measurement sites (Fig. 3).

The accuracy of the angiographic SMART treatment planning system has been verified in two ways. Firstly, the calculated absorbed dose at the isocentre and the surrounding absorbed-dose pattern have been compared with the values measured inside the spherical phantom described above. As with the CT-based treatment planning program, agreement between measured and calculated values occurred, within the limits of uncertainty of the measured results, at all measurement sites. At the isocentre, the calculated absorbed dose was found to be within 1.0% ± 2.1% of the mean measured value. The calculated absorbed-dose pattern around the isocentre was verified with TLD. Figure 3 shows a comparison of the results computed with the two treatment planning programs, together with the results of measurements made with TLD detectors, at various distances from the isocentre. Again, there is agreement within the limits of uncertainty at all points. This analysis was repeated, with similar results, in other planes.

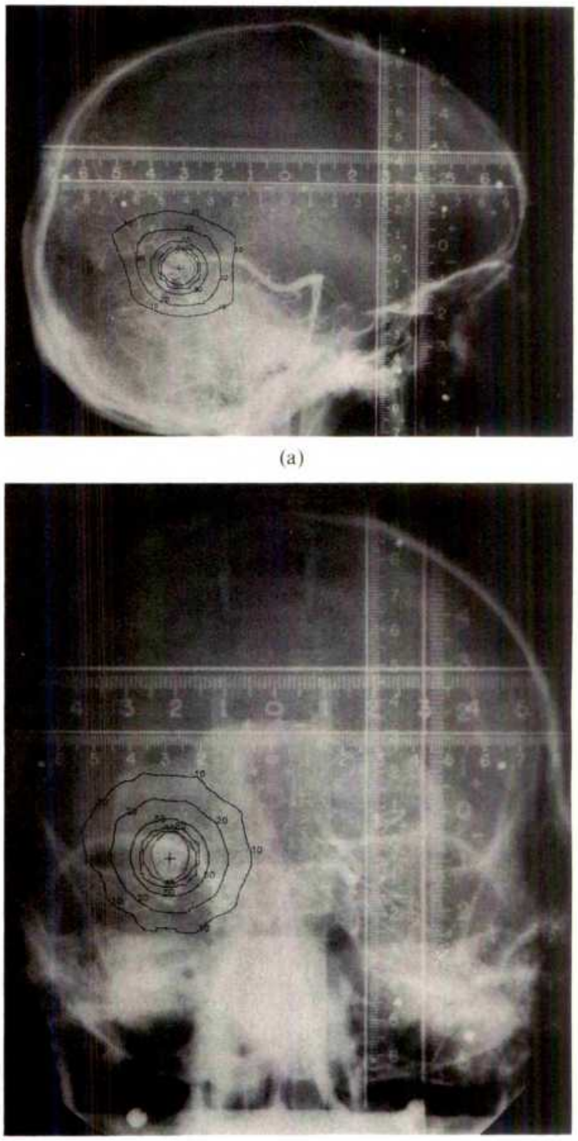
(a)

(b)

Figure 2. (a) Lateral and (b) anterior/posterior radiographs showing the position of the target volume with isodose curves superimposed.

The second method of assessment of the angiographic system involved a comparison of the calculated absorbed dose at the isocentre for a series of patients planned with both treatment planning techniques. This was carried out in order to determine whether the mathematical description of the head as an ellipsoid volume produces results as accurate as those resulting from a 3-dimensional reconstruction from CT data. The

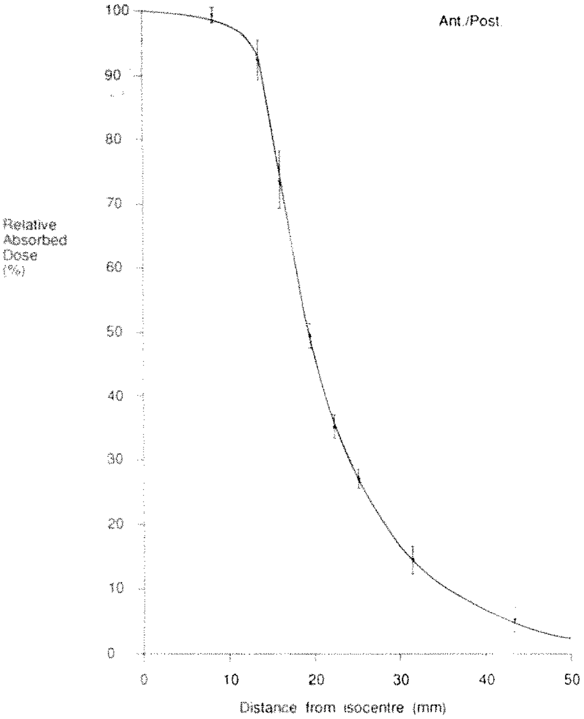

Figure 3. Graph to show the relationship between the absorbed dose distribution measured with TLD detectors (points), calculated using the CT based system (solid line) and calculated using the angiography based system (dotted line). Uncertainties in the measured values correspond to twice the SD of the mean result at each point.

assessment took the form of a retrospective analysis of 15 patients treated with SMART in 1990/1991. This group of patients had undergone both stereotactic CT and angiography before treatment. A variety of isocentre positions, head dimensions and orientations were encountered within this series. The mean difference between the two calculation techniques was found to be 1.4% ± 2.0% (uncertainty quoted is twice the SD of the mean), which was considered to be acceptable.

Conclusions

A SMART treatment planning program has been described which avoids the need for a planing CT scan where this is not useful for target localization. The accuracy of the calculation technique has been compared with that of a program that reconstructs the shape of the head from CT images. The results of the comparison show that there is no detectable loss of dosimetric accuracy.

Practically, it has been found that the subjective nature of the selection process for input parameters has little effect on the calculated result, so long as certain guidelines are followed. The use of accurately drawn templates, for example, is seen as helpful in the choice of the optimum size, orientation and position of the ellipse.

In summary, the application of a computational technique is described, which is capable of calculating the absorbed-dose patterns resulting from a SMART treatment. The hardware requirements are minimal, the program currently operating on an IBM-compatible personal computer. Computation times are approximately 5 min for calculation of the absorbed patterns in three orthogonal planes through the isocentre. The computer program is seen as a less sophisticated alternative to the currently available software packages and is felt to have particular advantages where CT images are not required. At St Bartholomew's Hospital, the treatment planning program is now in routine use for patients being treated with SMART for AVMs.

Acknowledgments

We are grateful to Mr D. Doughty of the Radiation Physics Department, St Bartholomew's Hospital, London for his valuable help and advice. In addition we would like to thank Dr P. N. Plowman of the Radiotherapy Department, St Bartholomew's Hospital for his continued clinical support of the project. Much of this work was funded by the Imperial Cancer Research Fund.

References

AHNESJO, A., 1982. *Programmer's Manual for the Dose Planning System KULA V3.1.* (Uppsala University Data Centre, Uppsala, Sweden).

BETTI, O., DERICHINSKI, V., 1983. Irradiation stéréotaxique multifaisceaux. *Neurochirurgia, 29,* 295–298.

COLOMBO, F., BENEDETTI, A., POZZA, F., ARANZO, R. C., CHIEREGO, G., MARCHETTI, C. & ZANARDO, A., 1985. A stereotactic external irradiation by linear accelerator. *Neurosurgery, 16,* 154–160.

GILL, S. S., 1987. United Kingdom patent application no. 8728150.

HARTMANN, G. H., SCHLEGAL, W., STURM, V., KOBER, B., PASTYR, O. & LORENZ, W. J., 1985. Cerebral radiation surgery using moving field irradiation at a linear accelerator facility. *International Journal of Radiation Oncology, Biology, Physics, 11,* 1185–1192.

KRAMER, R., ZANKL, M., WILLIAMS, G. & DREXLER, G., 1986. *The Calculation of Dose from External Photon Exposures Using Reference Human Phantoms and Monte Carlo Methods. Part I: The Male (Adam) and Female (Eva) Adult Mathematical Phantoms.* GSF-Bericht S-885 (Gesellschaft für Strahlen und Umweltforschung, Munich).

LUTZ, W., WINSTON, K. R. & MALEKI, N., 1988. A system for stereotactic radiosurgery with a linear accelerator. *International Journal of Radiation Oncology, Biology, Physics, 14,* 373–381.

PODGORSAK, E., OLIVIER, A., PLA, M., LEFEBVRE, P. Y. & HAZEL, J., 1988. Dynamic stereotactic radiosurgery. *International Journal of Radiation Oncology, Biology, Physics, 14,* 115–125.

THOMSON, E. S., 1990. *Stereotactic Brain Radiotherapy.* PhD Thesis (University of London, London).

THOMSON, E. S., GILL, S. S. & DOUGHTY, D., 1990. Stereotactic multiple arc radiotherapy. *British Journal of Radiology, 63,* 745–751.

WALTON, L., BOMFORD, C. K. & RAMSDEN, D., 1987. The Sheffield stereotactic radiosurgery unit: physical characteristics and principles of operation. *British Journal of Radiology, 60,* 897–906.

1992, *The British Journal of Radiology*, *65*, 321–326

Computer-assisted generation of multi-leaf collimator settings for conformation therapy

By A. R. Hounsell, MSc, P. J. Sharrock, C. J. Moore, PhD, A. J. Shaw, MSc, J. M. Wilkinson, MSc and P. C. Williams, PhD

North Western Medical Physics Department, Christie Hospital & Holt Radium Institute, Withington, Manchester M20 9BX, UK

(*Received 4 July 1991 and in revised form September 1991, accepted 30 October 1991*)

Keywords: Multi-leaf collimator, Conformation therapy, Computer methods

Abstract. Techniques for the automatic set up of the individual leaf positions of a Philips multi-leaf collimator system to cover a defined target volume are described. Tumour outline data for multi-field treatments may be obtained from one of two techniques, either from simulator images or from cross-sectional computed tomography (CT) slices. In the first technique, simulator images are digitized directly from image intensifier video signals or from conventional film radiographs using a CCD camera. Corrections for image distortion are carried out before reformatting the digitized images to a common data structure. Target outlines are subsequently traced interactively on the digital image to create an outline file. In the second technique, target volumes are defined on several individual CT slices and these are then used to obtain projected graphical views from any desired angle. In both techniques, a scaled graphical representation of leaf positions is then displayed and set relative to the outer edge of the target outline. Both techniques allow interactive repositioning of single leaves when required, or the operator can specify a margin around the projected target volume. Leaf prescription data files are created and are transferred via a Decnet–OSI–Opennet network link to an Intel microcomputer, which is used to drive the device itself. Examples of both techniques are given.

Megavoltage radiotherapy has been especially successful in the treatment of localized disease, where high tumour doses are achieved by multiple-field treatments. However, it has been recognized that, for some tumour sites, additional conformation of the treatment to target volumes can be achieved by complex beam shaping, so improving the tumour-to-treatment volume ratio (Tate et al, 1986; Tait et al, 1988). It is assumed that this will result in a lower normal-tissue morbidity, and that it may also permit a higher prescribed tumour dose with an associated increase in the local tumour control rate. The routine use of additional beam shaping has been restricted by the need to follow arduous and time-consuming treatment preparation and set-up procedures, although several methods for simple conformation therapy have been developed and implemented clinically. For example, most teletherapy units have the option of placing lead, or customized low-melting-point alloy blocks, on an accessory tray to shape the X-ray beam. Alternatively, some modern units have asymmetric collimators that can be used to abut variable off-set treatment fields. This technique has been combined with control of gantry motion and dose-rate variation to produce tailored dose distributions (Chin et al, 1983). Another approach to conformation therapy is the more complex and time-consuming technique requiring specialized hardware and software, in which the patient is tracked through a beam of changing cross-sectional area (Brace et al, 1981).

To combine conformal therapy with a high patient workload requires short treatment preparation and set-up times. The development of reliable multi-leaf collimators (MLC), where the irregular treatment volume is shaped by many independent collimator leaves, offers greater flexibility in treatment shape with minimal set-up time. Treatment preparation times can be reduced if the individual leaf positions are determined automatically. The combination of these two developments will enable conformation therapy to be fully investigated and used as a routine treatment for some types of malignancies.

An advanced multi-leaf collimator has been installed on a Philips SL25 dual-energy linear accelerator at this Institute since November 1989 (Jordan, 1991; Williams & Jordan, 1991) and comprises 40 pairs of tungsten leaves of 7 cm attenuating thickness, situated within the X-ray treatment head. The main collimation of the beam is performed by the leaves. Additional back-up collimators, designed to reduce radiation leakage, define the smallest regular field that subtends the target volume inside which the leaves produce the irregular shape. Each leaf has a projected width of 10 mm at the isocentre and a projected range of travel from 12 cm over the midline to a maximum opening of 20 cm. A maximum field size of 40 cm × 40 cm is possible. The mechanical positioning and verification of each leaf is controlled by a dedicated stand-alone microprocessor system based around an Intel 80386 processor. The individual leaf positions are retrieved from a stored MLC prescription file and the leaves are subsequently driven to match the required shape.

Software is supplied that creates prescription files for a series of predetermined geometrical shapes, defined by as many as eight parameters, but the choice of these parameters is difficult if the regular shapes are to be matched to irregular target areas. Simple examples of

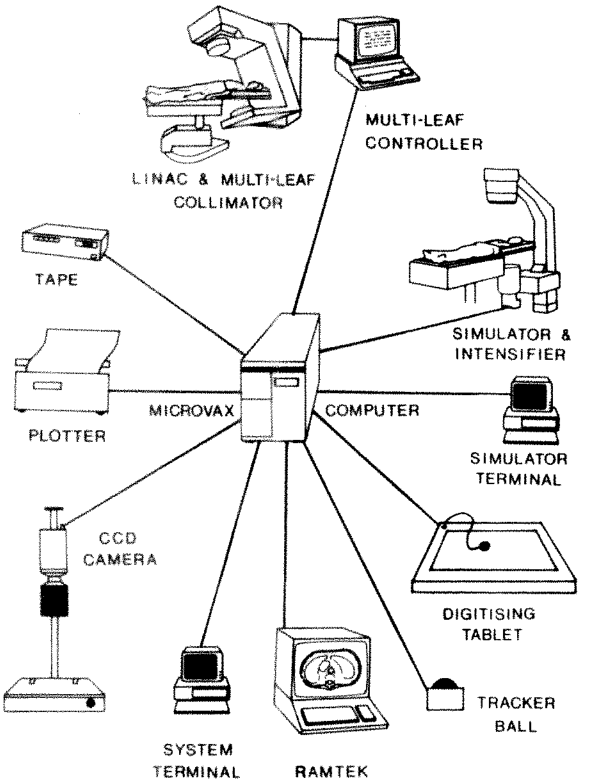

Figure 1. Schematic diagram of the computer system developed and used to generate MLC leaf positions from image data.

the available shapes include rectangles, circles and hexagons, or in more complex situations sections of the generic shapes can be combined. Better fits are possible by scaling and off-setting the shapes via the computer keyboard or using controls located on the accelerator treatment head. The use of the manufacturer's "shapes library", while reducing the normal-tissue irradiation and allowing for more accurate clinical margins to be used, does not fully exploit the true conformal potential of the MLC system in matching treatment and target volumes (Williams & Kane, 1991).

The best matches of treatment areas to target areas are achieved only when each leaf setting is optimized independently. In this paper we describe computer methods whereby the optimal settings are determined using tumour localization data, either from simulator images or CT cross-sections. This includes the creation of the MLC prescription files and their transfer to the treatment unit.

Equipment and methods

The system developed at this Institute to generate MLC prescription files is shown schematically in Fig. 1. The host computer is a Digital Equipment Corporation (DEC) Micro-VAX II running under the VMS operating system. CT cross-sectional images and radiotherapy simulator images are two modalities from which anatomical information can be extracted and used for prescription creation. Simulator images are digitized, using an image-processing card integrated into the host computer, either directly from the image-intensifier video signal or from film using a CCD camera. CT images are transferred to the host computer via an industry standard magnetic tape drive. In the future other sources of anatomical information may become readily available, *e.g.* magnetic resonance images. Transfer media such as magnetic tape and network facilities supported by the host computer will allow these sources to be accessed when required. The display and manipulation of the images is via a RAMTEK 4660 imaging system. The processing hardware and firmware is linked to a 1024 × 1280 pixel, high-resolution monitor capable of both image and graphical overlay displays. Graphical overlays are used both in the interaction procedures when the target volumes and other important structures are defined, and also to display the final field shapes obtained from the computed leaf positions. Visual inspection of the leaf settings prior to treatment can thus be performed. Manipulation of the image data is simplified by reformatting all images into an open structure as they are transferred to the host computer. Patient identification data are stored separately so that a directory of all images currently active within the system may be created subsequently. Screen management procedures have been developed and implemented in such a way that the system is operated easily by single key responses to a displayed menu of commands. The created MLC prescription file is passed to the INTEL microprocessor controlling the MLC via a Decnet/Opennet network link. A hard copy of the MLC settings scaled to the isocentric plane is produced, along with patient information and set-up factors. The hard copies are used to verify the field shape prior to treatment.

MLC definition using simulator images

Treatment simulation is used to obtain projected views of internal anatomy relative to a surface marker, and, from this, to determine the treatment settings. For regular fields, the collimator jaw settings are simply represented by the simulator field wires. For irregular target volumes, the automatic matching of the target volume by the MLC leaf positions requires the target outline information to be digitized. Whilst isolated target outlines may be easily obtained directly from a simulator film using a digitizing tablet, this does not allow the option of overlaying the final leaf positions on the anatomical image for visual inspection prior to treatment. Such inspection is regarded as an essential part of the quality assurance procedure for treatment planning. Digitization of the simulator image allowing this visual inspection of leaf position, along with the possibility of image enhancement and grey-scale windowing to aid the clinician in the definition of his target volume, has, therefore, been developed. In addition, comparison of digital portal images, taken during the treatment with the prescribed leaf positions over-

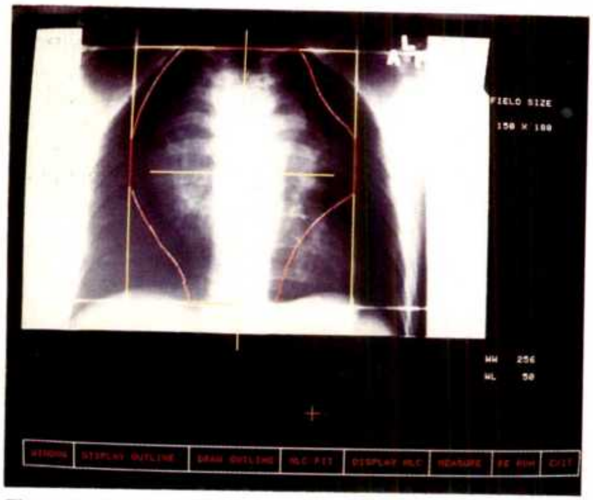

Figure 2. Digitized simulator radiograph displayed on the Ramtek imaging system after distortion correction.

layed on the simulator images is made possible if fully digitized simulator films are used.

The hardware and software required for image digitization can introduce distortions to the images, as, for example, an image captured using the digitizing card is elongated when displayed on the Ramtek 4660. This is due to the different aspect ratios of the pixels in each system. If the image is acquired directly from an image intensifier video signal, two other types of distortion can occur: pin-cushion distortion resulting from the convex input plane of the intensifier surface, and S-shape distortion resulting from interference between the geo-magnetic field and the electron optics of the intensifying system. Digitization from film using the CCD camera introduces a further aspect ratio elongation, attributed to the rectangular geometry of the CCD elements. Computer programs have been written to remove all sources of distortion from the digital images (Shaw & Moore, 1991). These processes are performed automatically and do not require any intervention from the user. A further problem inherent in the digitization of radiographs is the limited dynamic range of the camera. Large variations in film density that are greater than the contrast variation of the camera can occur, resulting in areas of the film appearing over- and underexposed when digitized. Selective use of neutral density filters, placed on the film prior to digitization, eliminates this problem without reducing the ability to distinguish the target area and field wire information necessary to position the leaves.

Once the simulator image has been captured, corrected for distortion and converted to a common image format, the process of positioning the leaves to the clinically defined target area can begin. The centre of the regular field is indicated on the digital image to reference the centre of the leaf bank to the centre of the treatment field and to a marker on the patient surface. The next requirement is to provide correct scaling for image computations by entering the distance between two of the field-defining wires that are visible on the simulator image. When this has been completed, the computer program automatically draws a graphical representation of the field-defining wires over the image, allowing immediate confirmation that the image distortion corrections have been correctly performed. The program has been written so that the clinician has minimal involvement during its operation. This is possible only if the target area has been indicated on the simulator film, whereas if the digital image is obtained directly from the image intensifier video signal, the clinician is required to draw the target area over the image using the trackerball, a slightly more time-consuming, but interactive process.

Figure 2 shows a display of an antero-posterior (AP) chest radiograph that has been digitized and corrected for differences in aspect ratios. The regular field size of 150 mm × 180 mm is overlayed on the simulator field wires, indicating the correct scaling and aspect ratio corrections have occurred. The target is shown outlined and in some areas can be seen to be well within the minimum rectangular field that is required to cover it.

The MLC leaf positions are calculated by searching for the target outline in the graphics overlay planes. The criteria applied are that each leaf projection should touch the target outline and that no part of the leaf should project onto the target volume. As the leaves project to a width of 10 mm at the target this results in a small additional volume of tissue being irradiated outside the target. The rational for this approach is that although irradiation of excess tissue is undesirable, the shielding of the target volume is unacceptable. In applications where shielding considerations are more important, the algorithm could be modified to set the leaves to the inner part of the outline. If the area delineated is unacceptable, the clinician has the option of moving individual leaves interactively using a trackerball. Currently a margin of 10 mm is automatically added to the leaf settings. This is in addition to the clinical margin and allows for penumbral effects, and thereby ensures that the whole of the target volume is contained within the treatment volume. Similar allowances are made in conventional treatment planning. The back-up collimator jaws are set to the maximum leaf positions in the direction normal to the leaves, and to the tumour edge plus margin in the direction parallel to the leaves.

Figure 3 shows the same radiograph with the MLC positions calculated and overlayed on the image. The scaling is such that not all the leaves are displayed, the remaining leaves being set to a closed position. Machine output factors for the treatments are calculated using the target depth obtained during simulation and the treatment area exposed by the leaf settings which is calculated by the computer program. Target area information is also calculated and can be compared with the treatment area and used as an index of how well conformation has been achieved.

Currently, standard treatment techniques are being

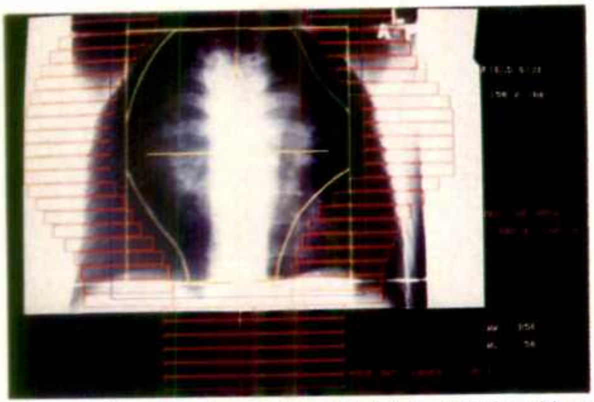

Figure 3. Simulator image after calculation of leaf positions and matching to the clinically determined target outline.

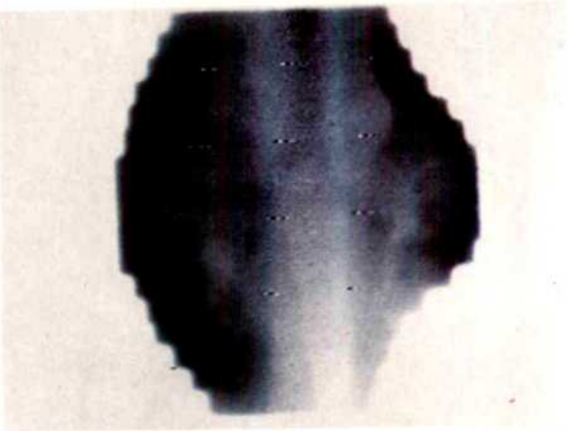

Figure 4. Digital megavoltage portal image of the treatment field using the MLC leaf positions created from the simulator radiograph.

used that include parallel opposed pairs and four-field treatments with anterior, posterior and parallel opposing lateral beams. To facilitate this, "mirror" MLC leaf settings are created to be used with treatment beams from opposing gantry angles. Finally, before transfer via the network to the treatment unit, the leaf settings are coded into the manufacturer's prescription format. Any patient information and machine settings required during treatment are printed and a paper template for the MLC leaves is produced for each gantry angle to be used for verification purposes during treatment. Further confirmation can be obtained during treatment using portal images. Figure 4 shows the portal image for this treatment, which completes the cycle from initial image, through planning, to treatment and verification, and should hence ensure that the treatments are accurately performed.

MLC definition using CT images

Simulator films provide a simple and effective method for determining the positions of the MLC leaves, but better methods of determining the precise location and shape of three-dimensional target volumes are available using cross-sectional images. If the extent of the target in each cross-section is known, a projected view of the target from any proposed treatment angle can be found, and the greater accuracy available in determining the target position allows the clinician to use multiple-field or dynamic arcing techniques to conform the treatment to the target volume. In principle, slices from any cross-sectional scanner can be used provided they show sufficient detail of both normal and diseased anatomy, although at present X-ray CT scanners are the main source of this information.

Image transfer from the CT scanners to the host computer can use several routes, including direct hardware links such as serial RS232 lines, more sophisticated network links, or via a transfer medium such as magnetic tape or floppy disk. RS232 links are limited by a very low data-transmission rate while faster network links require specialized commercial software to encode and decode the transmitted information. At present, very few CT scanners have networking capabilities and rely on optical disks and magnetic tape as their long-term archiving and transfer media. The system we have developed uses magnetic tape as the transfer media between the CT scanners and the MLC planning system.

Although loading the images onto magnetic tape is a straightforward task on all CT scanners, each manufacturer employs a different method for data reduction during the storage and transfer program. Decoding of the image data is possible if the format and compression structure used are known or relatively simple to determine. The program we have developed reformats the CT images at the data-transfer stage, a procedure that adds little to the several seconds already required to transfer physically each image from the tape to the computer memory, and ensures that all images on the host computer are in a common format.

The anatomical information can be found with sufficient accuracy using standard slice widths and separations of 10 mm, corresponding to the isocentric width of the leaves. If the tumour extends through a great many slices, with little variation between adjacent slices, then it may be advantageous to increase the slice separation and width or restrict the number of slices used. To provide a multiple display of images, the Ramtek is linked to a high-resolution monitor that allows up to four 512 × 512 full-resolution images to be displayed simultaneously. By magnifying the images and repeatedly changing the display off set, a movie loop of images is obtained that may aid the clinician in determining the position of the target volume.

Figure 5 shows four consecutive CT scans from an IGE Pace scanner displayed on the monitor at full resolution. Automatic patient outlining has been implemented using a routine described by Moore (1988), whereby a seed pixel is located and the outline followed by a "left-hand" search routine using multi-point gradient thresholding. The program automatically

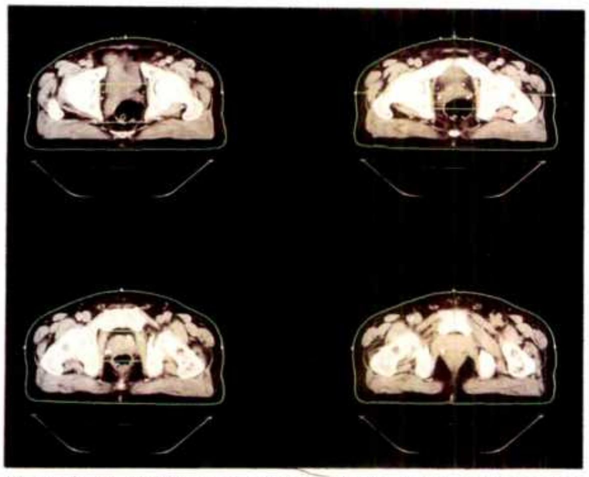

Figure 5. Four CT cross-sections of the lower pelvic region displayed simultaneously using the Ramtek imaging system. The external outline and target areas are represented by the graphical overlays.

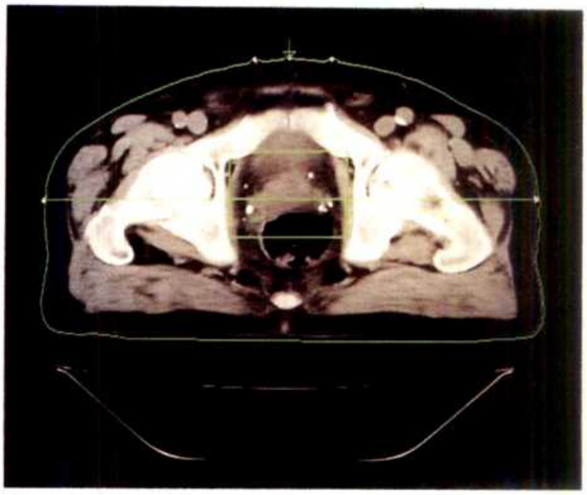

Figure 6. Magnified image of a reference slice with target volume represented by the rectangular box, and set-up markers by the arrow and lateral line.

outlines the images in this manner when they are first displayed and prior to clinical involvement. Once body outlining has been completed the clinician can page through the images and outline the target volume and any structures that need to be avoided, using the trackerball attached to the Ramtek. Four-field treatments, consisting of anterior, posterior and parallel opposed lateral fields, are used routinely to treat disease in the central pelvis, and with this arrangement it is convenient to delineate the cross-sectional treatment volume by a movable graphical box. The corners of the box can be repositioned by the clinician to enclose the target. Alternatively, the target can be defined continuously, but this is a more time-consuming process that does not provide any additional usable information when treating with the four-field technique. During this target volume determination stage, the images are magnified to fill the screen. While not increasing the information content, the clinician's ability to see smaller detail is improved, and grey-level windowing is available to improve the tumour to normal-tissue contrast.

Figure 6 shows a magnified image of the central slices. To be able to position the patient correctly during treatment an external marker is necessary, and this needs to be related to the internal structure. This is provided by a radio-opaque marker which is placed over a skin tattoo. This marker is visible on the CT images and can be identified using an arrow, as is shown in Fig. 6. The slice containing the marker is referred to as the reference slice, but this need not necessarily be at the centre of the tumour since the MLC leaves can be offset. Lateral body markers that are also used in ensuring accurate setting-up procedures are identified in Fig. 6 by the continuous lateral line.

After the target has been located in all relevant slices, projections of the target volume onto planes normal to the proposed beam direction are used to position the leaves. At the end slices, to allow for partial volume effects, the outlines are closed to a point that is half a slice width further up or down the body. The computerized search around the projected target volume outlines and the leaf positioning routines are similar to those described in the previous section.

Figure 7 shows the target projection outlines for four gantry angles (0°, 180°, 90°, 270°) together with the fitted leaf positions displayed simultaneously on the high-resolution monitor. The target is represented by the continuous outlines centred around the isocentric crosses. The lines to the left and right of each arrangement indicate the position of the external patient contour. The treatment gantry angle and the patient's anatomical position are indicated for each view. The

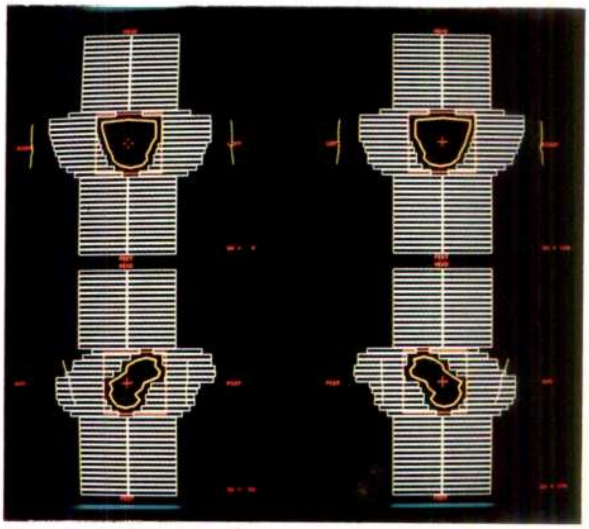

Figure 7. MLC leaf positions matched to the projected target volumes for anterior (top left), posterior (top right), left lateral (bottom left) and right lateral (bottom right) fields.

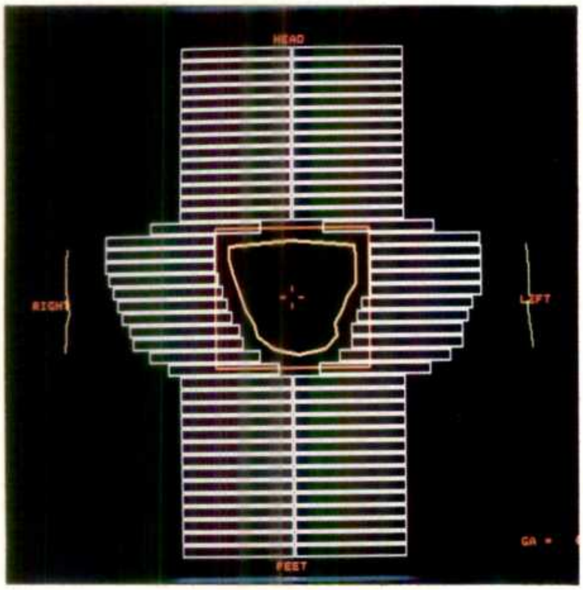

Figure 8. Magnified view of MLC leaf positions of the anterior field with the projected target volume (yellow), external outline (green) and back-up collimator positions (red) also shown.

margin can be varied independently in both the leaf opening direction and along the patient axis, if the treatment volume is deemed to impinge on a sensitive structure. Alternatively, individual leaves can be repositioned interactively using the trackerball, allowing fine tuning of the treatment to target volume. In Fig. 8 the MLC settings for the anterior field have been magnified prior to the repositioning of individual leaves. The treatment area is calculated for each field, along with the volume irradiated by all four fields. On acceptance of the treatment shapes, the MLC prescription files for each gantry angle are created prior to network transfer. The number of machine monitor units for a given dose is calculated using a dose model based around a scatter integration described by Hounsell and Wilkinson (1990). The monitor unit calculation along with patient information is printed and transferred to the treatment machine along with plotted MLC templates for each gantry angle being used.

Prescription transfer to treatment unit

The prescription files, whether created from the CT images or from the simulator images, are stored on the Winchester disk in the Micro-VAX computer. Transfer to the Intel computer that controls the MLC system is possible via an Opennet network link supported by both processors. The prescription files are defined using an ASCII format and have a header section containing the shape code, in this case the code for an irregular field, and values for each of the 80 leaves and four back-up collimators.

To prevent unauthorized communication or data transfer from the Micro-VAX, network access is initiated from the treatment unit and Intel alone. In this situation the clinical user logs onto the Micro-VAX from the Intel terminal via user-written software programs that initiate data transfer. After the MLC prescription files and patient data are transferred, the network link is closed.

Conclusions

Multi-leaf collimators can be used to produce irregularly shaped fields that allow good conformation of the treatment volume to the target volume. The positioning of the individual MLC leaves is most effectively performed automatically from simulator or CT images. The ease of use of the menu-driven programs allows patient treatments to be planned quickly and the subsequent leaf positions are easily transferred in the correct format to the computer that controls the MLC via a network link. Typical treatment preparation times of less than 30 min per patient from receipt of simulator film or CT images have enabled a rapid throughput of patients for conformation therapy. These programs are now in routine use at this Institute and the clinical significance of conformation therapy is being studied.

References

BRACE, J. A., DAVY T. J., SKEGGS, D. B. L. & WILLIAMS, H. S., 1981. Conformation therapy at the Royal Free Hospital. A progress report on the tracking cobalt project. *British Journal of Radiology*, *54*, 1068–1074.

CHIN, L. M., KIJEWSKI, P. K., SVENSSON, G. K. & BJARNGARD, B. E., 1983. Dose optimisation with computer-controlled gantry rotation, collimator motion and dose-rate variation. *International Journal of Radiation Oncology, Biology, Physics*, *9*, 723–729.

HOUNSELL, A. R. & WILKINSON, J. W., 1990. Tissue standard ratios for irregularly shaped radiotherapy fields. *British Journal of Radiology*, *63*, 629–634.

JORDAN, T. J., 1991. Commissioning of a multisegment collimator. Abstract Proceedings: dosimetry protocols, quality assurance and asymmetric collimators. *Physics in Medicine and Biology*, *36*, 669–670.

MOORE, C. J., 1988. Mathematical analysis and picture encoding methods applied to large stores of archived digital images. PhD thesis, University of Manchester, Ch. 4.

SHAW, A. J. & MOORE, C. J., 1991. Image processing supporting radiotherapy treatment. In *Healthcare Computing: Current Perspectives in Healthcare Computing* (British Journal of Healthcare Computing, Surrey), p. 30–39.

TAIT, D., NAHUM, A., SOUTHALL, C., CHOW, M. & YARNOLD, J. R., 1988. Benefits expected from simple conformal radiotherapy in the treatment of pelvic tumours. *Radiotherapy and Oncology*, *13*, 23–30.

TATE, T., BRACE, J. A., MORGAN, H. & SKEGGS, D. B. L., 1986. Conformation therapy: a method of improving the tumour treatment: volume ratio. *Clinical Radiology*, *37*, 267–271.

WILLIAMS, P. C. & JORDAN, T. J., 1991. Performance characteristics of the Philips multileaf collimator. *British Journal of Radiology*, *64*, (Congress Supplement), 83.

WILLIAMS, P. C. & KANE, B., 1991. Use of predefined shapes for producing irregular fields with a multileaf collimator. *British Journal of Radiology*, *64* (Congress Supplement), 82.

1992, *The British Journal of Radiology*, *65*, 327–333

An investigation of the dose equivalent to radiographers from a high-energy neutron therapy facility

By *J. Finch, BSc and †D. E. Bonnett, MSc, PhD

MRC Cyclotron Unit, Clatterbridge Hospital, Bebington, Merseyside L63 4JY, UK

(Received 2 July 1991 and in revised form 27 September 1991, accepted 23 October 1991)

Keywords: Radiographers, Neutrons, Dose equivalent, Radioactivity

Abstract. The external radiation hazard to radiographers from the use of high-energy neutrons in radiotherapy has been investigated. The contributions from neutron-induced activity in the therapy gantry, the treatment room, the patient and ancillary equipment have been analysed as has the whole-body dose equivalent to radiographers. It was found that there are significant levels of gamma radiation throughout the treatment room, which increase both in the vicinity of the walls in line with the beam axis and in close proximity to the neutron therapy gantry. The mean dose equivalent to radiographers per field treated was found to be 5.1 ± 1.8 μSv. The dose per field also varied considerably with the particular site being treated but it was found that the dose equivalent per field per minute of set-up time was approximately constant. It was also found that the dose per field increased with the number of patients treated per day commensurate with a build-up of induced activity. The studies also showed that the dose equivalent to radiography staff was comparable to that at other high-energy neutron facilities but significantly greater than that recorded at facilities with low-energy beams.

Randomized clinical trials using the Clatterbridge high-energy neutron therapy facility commenced in February 1986, the principal sites being in the head and neck and pelvic regions. The facility provides a neutron beam with physical parameters comparable to an 8 MV X-ray beam (Bonnett et al, 1988; Blake et al, 1988). There is, however, one major difference between the two treatment modalities and that is the additional external radiation hazard to staff, particularly radiographers, from the use of fast neutrons. This arises from neutron-induced radioactivity in both the radiotherapy equipment and the treatment room itself and has been the subject of continued monitoring and investigation since the facility first became operational. The radiography staff initially consisted of a superintendent radiographer and two others. The superintendent was based permanently at the facility, whilst the other two posts were rotational on a 4-monthly basis. In 1988 the number of rotational posts was increased to three.

The purpose of this paper is to report the radiation hazards encountered during neutron therapy, the whole-body dose equivalent received by radiographers, an analysis of the main contributions to these doses and the variation in dose equivalent with site treated. The dose equivalent to radiography staff is also compared with those reported from other high-energy facilities.

The Clatterbridge fast-neutron therapy facility

The facility consists of a fixed-particle, fixed-energy cyclotron (Scanditronix model MC60) that accelerates protons to 62 MeV and an isocentric treatment gantry. These have been described in detail previously (Bonnett et al, 1988). The neutron beam is generated by bombarding a beryllium target located in the treatment gantry with the proton beam. The target is surrounded by a composite shield of pure iron, boronated hydrogenous material and lead. Where possible the materials used in the construction of the treatment gantry were chosen to minimize the neutron-induced radioactivity. For example, the use of aluminium with its large thermal neutron captive cross-section was excluded (Bonnett et al, 1980) and pure iron was used as a shielding material in order to exclude the contribution to induced activity from the thermal neutron reaction in manganese (^{56}Mn (n,γ)^{56}Fe). Initial tests on possible shielding materials were carried out for the manufacturer at the cyclotron at Louvain-la-Neuve. Six materials were irradiated in a neutron beam produced by 65 MeV protons on beryllium. Each irradiation was 0.5 Gy given to tissue in 5 min and the decay of the dose-equivalent rate from the induced activity measured. From an analysis of the decay curves it was then possible to calculate the build-up of dose-equivalent rate for repeated irradiations of 1 Gy given to tissue in 5 min each followed by a 10 min decay period. The results of the calculations are shown in Fig. 1. It can be seen that of the iron and steel samples, pure iron is the material of choice. The tungsten sample used at Louvain was a tungsten alloy and subsequent

---

Present addresses: *Health Physics and Safety Department, British Nuclear Fuels PLC, Capenhurst Works, Chester CH1 6ER, UK; †Department of Medical Physics, Leicester Royal Infirmary, Leicester LE1 5WW, UK.

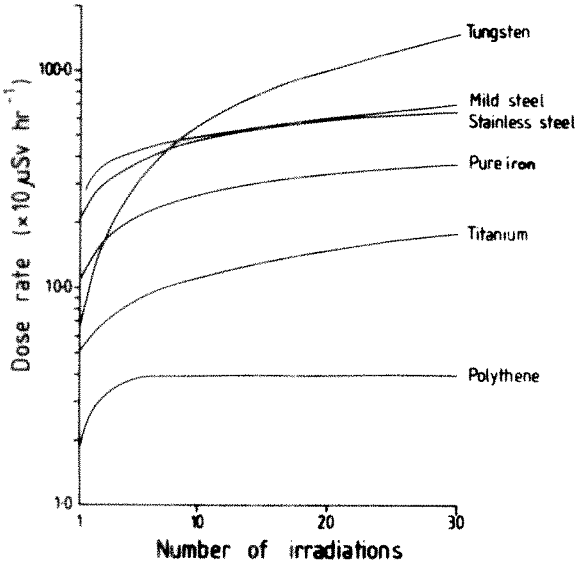

Figure 1. A comparison of the calculated build-up of dose equivalent rate to water resulting from induced activity in polythene, titanium, pure iron, mild steel, stainless steel and tungsten alloy.

Table I. The main activation products detected in the neutron therapy gantry, treatment room, ancillary equipment and the patient

Product	Half-life	Most significant reaction
Oxygen 15	2.03 min	$^{16}O(n,2n)^{15}O$
Aluminium 28	2.25 min	$^{28}Si(n,p)^{28}Al$ $^{27}Al(n,\gamma)^{28}Al$
Aluminium 29	6.50 min	$^{29}Si(n,p)^{29}Al$
Potassium 38	7.63 min	$^{39}K(n,2n)^{38}K$
Iron 53	8.50 min	$^{54}Fe(n,2n)^{53}Fe$
Magnesium 27	9.45 min	$^{30}Si(n,\gamma)^{27}Mg$
Nitrogen 13	9.97 min	$^{14}N(n,2n)^{13}N$
Tantalum 186	10.5 min	$^{186}W(n,p)^{186}Ta$
Carbon 11	20.3 min	$^{12}C(n,2n)^{11}C$
Potassium 44	22.0 min	$^{44}Ca(n,p)^{44}K$
Manganese 56	2.58 h	$^{56}Fe(n,p)^{56}Mn$
Tantalum 184	8.70 h	$^{184}W(n,p)^{184}Ta$
Tungsten 187	23.9 h	$^{186}W(n,\gamma)^{187}W$

measurements at Clatterbridge on pure tungsten have shown it to have less induced activity than pure iron but its use as a bulk shielding material would be excluded because of economic considerations. The design of the treatment gantry also incorporated a lead shutter to shield the induced radioactivity in the target at the end of an irradiation and a lead glass shutter at the end of the collimator, which reduces the dose-equivalent rate from activation γ rays in this region. The neutron and γ radiation penetrating both the labyrinth entrance and the earth shielding mound that covers the cyclotron vault and the treatment room has been shown to be "low and present no significant hazard to staff" (Bonnett et al, 1988). This result was confirmed by more recent measurements that included the use of a tissue-equivalent proportional counter (Bonnett et al, 1991). These measurements showed that for a typical neutron therapy beam the neutron dose rate outside the treatment room was 9×10^{-2} μGy h^{-1} and the quality factor derived from the results was 11.5 ± 4.0.

Measurement of neutron-induced radioactivity

Within the treatment room there are several sources of neutron-induced radioactivity that are potential radiation hazards. These include the treatment gantry, the treatment couch, the structural materials of the room itself, ancillary equipment that has been irradiated and the patients. Each of these was investigated in turn. Initially levels of activation γ rays and the associated decay were measured under standard conditions for each of these sources, with the exception of the patients, using survey dose-rate meters (36100, Keithley Ltd, PDM1, Nuclear Enterprises Ltd). Where possible, further information on the products formed was obtained from measurements of the γ-ray spectrum using a hyper-pure germanium spectrometer (Gamma-Gage, Ortec Ltd). Details of the main products detected in all of these investigations are given in Table I.

The measurements made under standard conditions were useful in assessing the relative magnitude of the various hazards. Subsequently, measurements were made in the treatment room during therapy sessions to monitor the levels that exist in practice, particularly at positions occupied most frequently by the radiographers.

Treatment gantry and couch

The activation of both the treatment gantry and the treatment couch have been reported earlier (Bonnett et al, 1988; Blake et al, 1988). To assess the build-up of induced activity 20 irradiations were given, each giving a tissue kerma of 1 Gy at the isocentre with an interval of 10 min between each. During this interval the decay of induced activity was measured at eight positions around the head. A section through the gantry showing these positions is shown in Fig. 2 and the result of the measurements is shown in Fig. 3. The main sources of induced activity were oxygen 15, aluminium 28, carbon 11 and manganese 56. Minor contributions are also evident from iron 53 and manganese 52. The dose equivalent rates measured around the treatment couch were found to be equivalent to those measured at positions 1 and 2 (Fig. 3) on the treatment head and were due to the production of oxygen 15 and carbon 11.

The treatment room

To assess the overall levels of induced activity in the room a water phantom measuring 40 cm × 40 cm × 40 cm was placed with its front face at the isocentre to

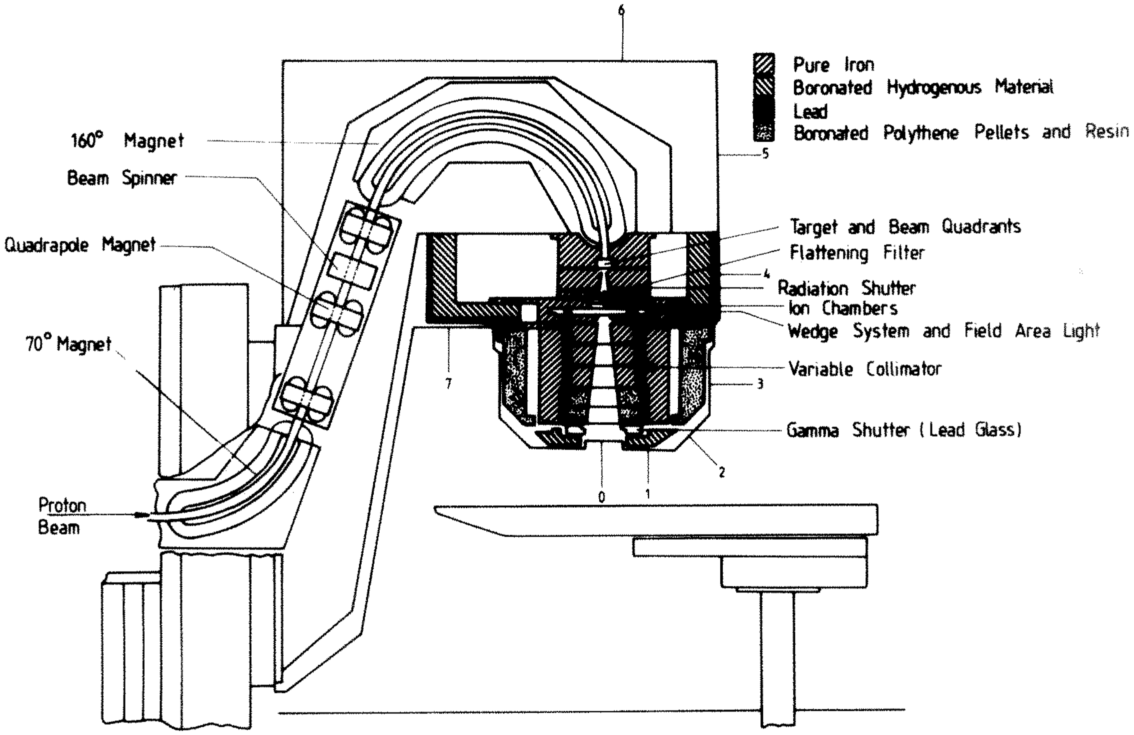
6
▨ Pure Iron
▨ Boronated Hydrogenous Material
■ Lead
▨ Boronated Polythene Pellets and Resin
160° Magnet
Beam Spinner
Quadrapole Magnet
70° Magnet
Proton Beam
5
Target and Beam Quadrants
Flattening Filter
4
Radiation Shutter
Ion Chambers
Wedge System and Field Area Light
Variable Collimator
3
Gamma Shutter (Lead Glass)
7
2
0
1

Figure 2. Cross-section of the isocentric treatment gantry showing the main features together with positions (0–7) of measurements of induced activity. (Reproduced from Bonnett et al, 1988, with the permission of the *British Journal of Radiology*.)

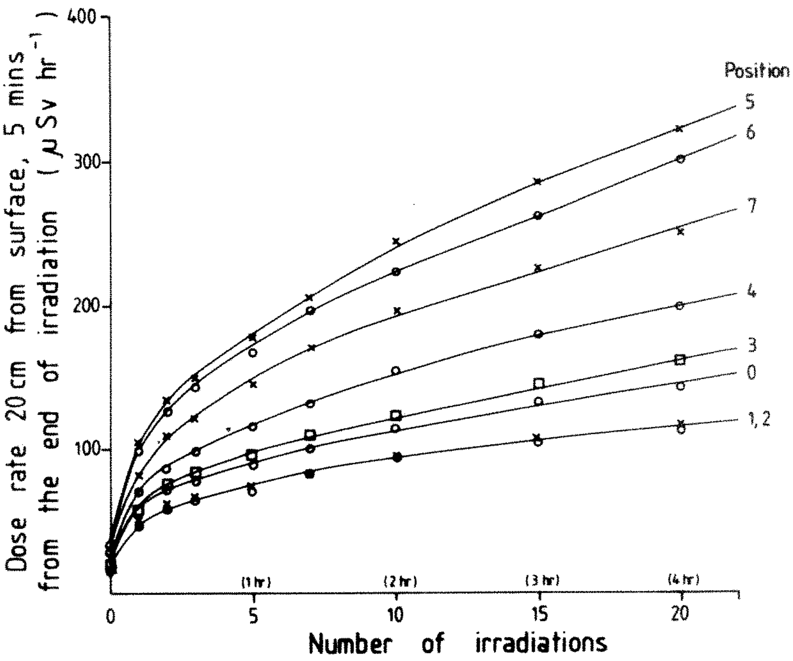

Figure 3. Measurements of the dose equivalent rate to water resulting from the build-up of induced activity around the isocentric gantry. (Reproduced from Bonnett et al, 1988, with the permission of the *British Journal of Radiology*.)

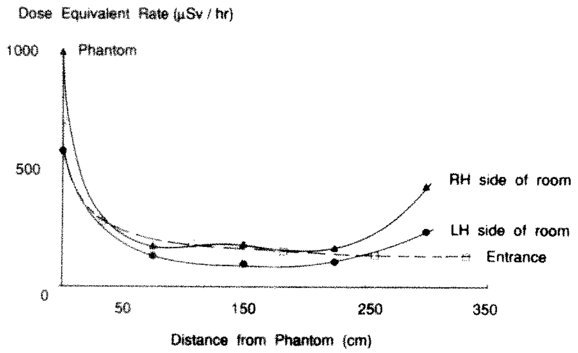

Figure 4. The variation in dose equivalent rate to water with distance from an irradiated water phantom 2 min from the end of irradiation of 2 Gy at the isocentre. (The neutron gantry was moved to the vertical position after irradiation.)

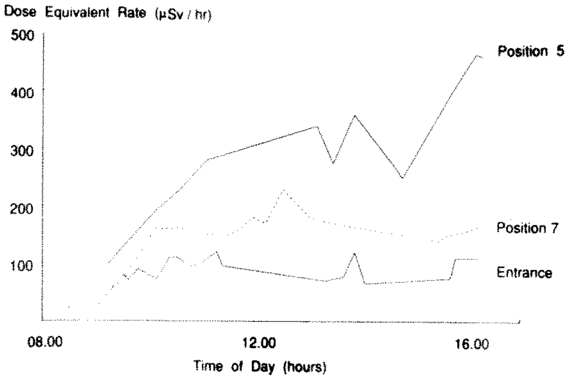

Figure 5. The variation in dose equivalent rate to water at three positions in the treatment room throughout a normal treatment day.

simulate neutron absorption and scattering by a patient. This was irradiated with a horizontal beam. An irradiation of 2 Gy to tissue in 6 min at the isocentre was given. The gantry was then moved to the vertical position (gantry angle 0°) and the dose equivalent rate from the induced activity measured. Three separate irradiations were made and the dose equivalent rate was measured at various distances in three directions in turn. These were from the front of the phantom to the left-hand wall of the treatment room, from the rear of the phantom to the right-hand wall and from the side of the phantom orthogonal to the beam axis towards the entrance to the treatment room. The measurements at each point were repeated over a period of 20 min and from the resulting decay curves values of the dose equivalent rate were obtained at 2 and 5 min from the end of irradiation. The values at 2 min from the end of irradiation are shown in Fig. 4. In general, values of the dose equivalent rate measured 5 min from the end of irradiation were a factor of 2 lower compared with those shown in Fig. 4. The induced activity in the walls of the treatment room was identified as aluminium 28, oxygen 15, potassium 38 and potassium 44. Measurements were also made with and without the water phantom present. It was found that at 2 min after the end of irradiation the phantom increased the dose equivalent rate measured at the phantom surface and 50 cm from the phantom surface by factors of 2.2 and 1.3, respectively. In a treatment situation the induced activity in the phantom would be replaced by that induced in the patient.

To assess accurately the radiation levels in the treatment room during the course of a treatment session, measurements of the dose equivalent rate from the induced activity were made during typical treatment sessions. Three positions were investigated, namely:

1. The entrance to the treatment room. This was chosen because the couch and gantry control pedestal is often operated there. It is the furthest possible distance from the gantry and had been identified previously as an area of minimum radiation (Fig. 4).
2. The region of position 7 (Fig. 2) on the surface of the gantry. Radiographers often stand in this position while setting up patients.
3. Position 5 (Fig. 2) on the surface of the gantry. This had been identified as the position with the highest levels of induced activity (Fig. 3).

Each position was investigated on a different day but with similar patient numbers. Following each irradiation the decay of the dose equivalent was measured and the dose equivalent rate 2 min from the end of each irradiation plotted against time from the start of therapy (Fig. 5). Before therapy there is a calibration period which will contribute to the induced activity in the room.

Measurements of the air extracted from the treatment room were also made and have shown levels of induced activity giving dose equivalent rates from annihilation gammas of 1–2 μSv h^{-1}. Oxygen 15 and nitrogen 13 were the predominant sources of activity. As these levels were quite minimal they were not investigated further but are subject to constant monitoring by a Geiger counter installed in the air extract system.

The patient

Measurements of activity induced in patients over the treated area have shown levels ranging from 105 to 165 μSv h^{-1} at the skin surface 2–4 min after treatment, decaying to around 40 μSv h^{-1} 10 min after treatment. From the analysis of the decay curves and gamma spectroscopy the two main components were identified as oxygen 15 and carbon 11.

Ancillary equipment

Ancillary equipment that might be in the beam for part or all of a treatment were the tungsten beam blocks used for patient shielding and the masks made of copolyester sheet used to immobilize the patient during the treatment of head and neck sites. Following a 1 Gy irradiation the dose equivalent rate level on the surface of the largest of the tungsten beam blocks (26 mm ×

Table II. The mean whole-body dose equivalent per 4-month period recorded by radiographers during the first 4 years of therapy

Year	Mean dose equivalent (mSv)	Range (mSv)
1986	3.5	1.5–4.2
1987	3.2	0.5–4.4
1988	4.1	3.8–4.5
1989	3.0	2.0–3.9

81 mm × 121 mm) was found to be 40 μSv h^{-1} at 2 min from the end of irradiation decaying to 20 μSv h^{-1} at 10 min. The main source of activity was tantalum 186. Two long-lived components, tantalum 184 and tungsten 187, were also identified, but these gave rise to very small contributions to the dose equivalent rate. The immobilization masks were examined after a therapy session. The main source of induced activity was carbon 11 and the maximum dose equivalent rate measured was of the order of 70 μSv h^{-1} 2 min from the end of the treatment.

Measurement of the whole-body dose equivalent to radiography staff

Monitoring of the whole-body doses to staff was carried out using β-γ and neutron film badges. Initially staff were also issued with extremity thermoluminescent dosemeters (TLD) for their fingers. These showed no significant difference in dose equivalent compared with the film badges and their issue was discontinued. Both badges and TLDs were supplied and processed by I.R.S. Ltd, Liverpool. In addition the radiographers were issued with Geiger type dosemeters with digital dose display (Pendix, Radiatron Components Ltd), which were read after each treatment session or when required in order to give further information on levels of dose equivalent to staff. The total weekly dose equivalent to, and the total number of fields treated by, each member of staff were recorded. Table II shows the mean dose equivalent per 4-month duty period received by radiographers during the first 4 years of therapy as measured by the β-γ film badges. The neutron film badges always gave results below the detectable threshold. The mean dose equivalents to radiographers per field treated calculated from the digital dosemeter results are given in Table III. These results give rise to a mean dose equivalent per field of 5.1 ± 1.8 μSv. The digital dosemeter results were also used to calculate the variation in dose equivalent per field treated with daily patient load and the variation in dose per field with treatment site; these are shown in Fig. 6 and Table IV, respectively. In addition the average times taken to set up a treatment for each particular site were measured and the results of the calculation of dose equivalent per unit time spent in the treatment room for each site are also given in Table IV.

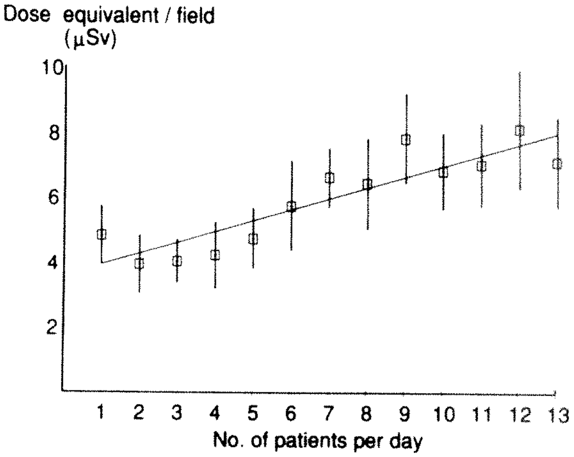

Figure 6. The variation in dose equivalent to radiographers per field treated with the total number of patients treated per day.

Discussion

The measurements shown in Fig. 4 illustrate much of the problem encountered in the use of fast neutrons in that there are significant levels of γ radiation throughout the treatment room, which increase both in the vicinity of the walls in line with the beam axis and in close proximity to the neutron therapy gantry. The induced activity in the walls only makes a significant contribution at distances less than 50 cm. The levels encountered in the room will vary with both the length of the irradiation and the number of previous irradiations. Measurements of the actual radiation levels recorded throughout a full day of patient treatment (Fig. 5) indi-

Table III. The mean dose equivalent to radiography staff per field treated

Year	No. of fields treated	Average no. of patients/day	Average no. of fields/patient	Dose to staff per field (μSv)
1986	977	2.6	2.9	5.52 ± 2.56
1987	1535	4.6	2.6	4.86 ± 1.41
1988	2586	5.8	2.7	5.46 ± 1.79
1989	2639	5.6	2.9	4.77 ± 1.49

Table IV. The variation in dose equivalent per field and dose equivalent per field per set-up time to radiography staff with site treated

Site	Mean dose/field (μSv)	Mean set-up time (min)	Dose/field/ set-up time (μSv/min)
Gynaecological	5.3 ± 2.1	6.4 ± 2.5	0.8 ± 0.5
Colo-rectal	4.8 ± 1.7	5.3 ± 2.7	0.9 ± 0.6
Parotid	9.9 ± 2.2	11.6 ± 2.1	0.9 ± 0.3
Antrum	8.8 ± 2.7	10.4 ± 3.8	0.9 ± 0.4
Misc. head and neck	7.7 ± 3.8	8.5 ± 5.0	0.9 ± 0.7

cate that following the calibration of the beam there is an immediate rapid rise, after which the levels at the entrance to the room and at the elbow of the gantry remained relatively constant. The levels at the position of maximum induced activity on the gantry increase slightly with time commensurate with the build-up of manganese 56 in the pure iron. At the other positions the levels are dominated by shorter-lived half-lives of oxygen 15 and carbon 11. Studies of radiation levels with and without a phantom also indicate a hazard to staff from activity induced in the patient. Tatcher and co-workers (1987) have suggested that the contribution to staff dose from induced activity in the patient is of the order of 7%; however, this may be larger if the radiographer spends a considerable time close to the patient. Measurements of the dose equivalent rate from induced activity in the patients indicate that the levels measured are equivalent to those recorded around the collimator area of the gantry. Investigations of the couch, the air in the treatment room and other ancillary equipment including beam blocks and patient restraining devices indicate that these are not major sources of hazard. The neutron activation of the air in a neutron therapy treatment room has also been studied by Ten Haken et al (1983), who concluded that the induced activity is of "only minimal reason for concern from a radiation protection viewpoint" provided that the room has adequate ventilation of six to eight changes per hour. These conditions are met by the treatment room at Clatterbridge.

The comparisons between the extremity and whole-body dose equivalents showed no significant difference indicating no extra dose to the hands from ancillary equipment. It should be noted that the magnitude of the whole-body dose equivalent per year for the radiography staff (Table II) was well below the current limits for designated radiation workers (50 mSv) and would also be below the revised limits of 20 mSv recently recommended by the International Commission on Radiological Protection (ICRP, 1991). The doses are, however, related to the numbers of patients treated and this, together with the time taken to treat a patient, will limit the number of patients that could be treated per day by any one group of radiographers. Figure 6 shows that there is an increase in dose equivalent field as the number of patients increases. There is also an indication that an approximate plateau of 7 μSv per field is reached but the relatively large uncertainties in the measurements mean that no definite conclusions can be drawn. Any such plateau would indicate there is no significant build-up of long-lived induced activity in the regions where the radiographers work during the treatment day, and therefore positions 1 and 2 of Fig. 2 are more typical of the behaviour of the levels of induced activity directly affecting staff than position 5. The particular site being treated will also affect the dose equivalent received by staff because of variations in the complexity of the set up. It can be seen from Table IV that the dose equivalent per field for head and neck treatments is higher than that for pelvic sites. The head and neck treatments involve more complicated treatment plans and often use tungsten blocks to shield critical organs such as eyes or spinal cord. There is also an increased use of treatment angles greater than 98° necessitating the use of the movable floor to move either couch or gantry to the correct position. The doses given to the patient are also higher in the head and neck cases: 20 Gy compared with 18 Gy for the pelvic region. Of the head and neck sites themselves the parotid cases seem to present the most hazard. The most significant factor affecting staff doses is, however, the time spent in the treatment room. It can be seen from Table IV that the dose equivalent per unit of time spent in the room is approximately constant over all sites indicating that the variation in dose per site treated is simply a function of time rather than due to the proximity of radiographer to either patient or other areas of higher induced activity.

Comparison of staff doses with other centres

The dose equivalent to staff involved in fast-neutron radiotherapy has been reviewed by Bonnett (1983) and Rosenberg et al (1984). These data refer mainly to low-energy neutron facilities. Data from facilities with energies comparable to Clatterbridge have been reported elsewhere in the literature (Eenmaa et al, 1987; Vynckier et al, 1989) as have preliminary results from Clatterbridge (Blake et al, 1988). A comparison of results is made difficult by the non-standard reporting of staff doses. Of the high-energy facilities, Fermilab, Chicago (p(66) + Be), reports a dose equivalent per fraction of 5 ± 1 μSv (Rosenberg et al, 1984) and the University of Washington, Seattle (p(48) + Be), reports a dose equivalent per field of 4 μSv (Eenmaa et al, 1987). In both cases this assumes a staff of two radiographers. These figures are comparable to the mean dose equivalent per field of 5.1 ± 1.8 μSv recorded at Clatterbridge. For the lower-energy facilities most staff doses have been reported in terms of 13- or 12-week periods. At the MRC Cyclotron at Edinburgh a dose equivalent of 1.2 mSv for a 12-week period was reported (Bonnett, 1983), which is similar to that at other low-energy facilities (Rosenberg et al, 1984). This compares with a mean of 3.5 mSv (range 1.5–4.5 mSv) for a 16-week period at Clatterbridge (from Table II) or 2.6 mSv (range 1.1–3.4 mSv) for a 12-week period. The average number of patients treated at the two centres was comparable, with seven per day at Edinburgh and five to six per day at Clatterbridge, thus the dose to staff is approximately two times greater with the higher-energy neutron machine. A comparison between the dose equivalent rates around the treatment gantry (Fig. 3) at Clatterbridge and Edinburgh (Bonnett et al, 1980) show that the levels at Clatterbridge are approximately twice those at Edinburgh for comparable positions around the collimator after similar irradiation times.

Conclusions

Four years of monitoring radiographers has shown that there are significant doses to staff involved in radiotherapy using high-energy neutrons and that this imposes restrictions on both the number of patients that can be treated in any one day and the length of time any radiographer may spend working in the Unit. It has been found that the dose equivalent per field treated varies with site but only as a consequence of time spent in the treatment room. The dose equivalent is also comparable to that recorded at other high-energy centres but is much higher than that for low-energy machines. At present the maximum permissible dose equivalent to designated workers is 50 mSv per year; however, the ICRP (1991) has recommended this be reduced to 20 mSv. This has implications for the maximum number of patients that could be treated using a high-energy therapy machine such as that at Clatterbridge. Further effort should be made to reduce the whole-body dose equivalent to staff in accordance with the ALARA principle. The materials used in the treatment gantry were selected to minimize the levels of induced activity, so that the only major improvement would be to increase further the thickness of external lead shielding, but this would incur unacceptable weight penalties. Reducing induced activity in the walls of the treatment room would not give a significant reduction in dose equivalent rates; therefore if there is a major role for neutrons in radiotherapy further effort needs to be made in reducing the time spent by radiography staff in the treatment room.

Acknowledgments

We wish to acknowledge the assistance of Mrs J. Neale, Superintendent Radiographer, at the Cyclotron Unit and the radiography staff whose co-operation and help made these studies possible. We would also like to thank Dr C. J. Parnell for his helpful comments and discussions of this work and Miss C. M. Hope for typing the manuscript.

References

BLAKE, S. W., FINCH, J., BONNETT, D. E. & SHAW, J. E., 1988. Patient dosimetry and staff protection at the Clatterbridge high energy neutron facility. *Radiation Protection Dosimetry*, *23*, 369–372.

BONNETT, D. E., 1983. Fast neutron therapy at Edinburgh: staff protection. *British Journal of Radiology*, *56*, 665–672.

BONNETT, D. E., BLAKE, S. W., SHAW, J. E. & BEWLEY, D. K., 1988. The Clatterbridge high-energy neutron therapy facility: specification and performance. *British Journal of Radiology*, *61*, 38–46.

BONNETT, D. E., WAKER, A. J., SHERWIN, A. J., MORE, B. R. & SOULIMAN, S. K., 1991. Radiation protection metrology at a high energy neutron therapy facility. *Radiation Protection Dosimetry*, *37*, 95–101.

BONNETT, D. E., WILLIAMS, J. R. & PARNELL, C. J., 1980. The isocentric fast neutron therapy facility at Edinburgh. *British Journal of Radiology*, *53*, 12–20.

EENMAA, J., WOOTTON, P. & RISLER, R., 1987. Technologists exposures and radiation protection aspects of the clinical neutron therapy facility in Seattle. *British Journal of Radiology*, *60*, 310.

ICRP, 1991. 1990 *Recommendations of the International Commission on Radiological Protection*, ICRP Publication 60 (Pergamon Press, Oxford).

ROSENBERG, I., AWSCHALOM, M., TEN HAKEN, R. K. & BENNETT, B. R., 1984. Analysis of personnel exposures in neutron therapy facilities. *Health Physics*, *46*, 407–412.

TATCHER, M., ROSENBERG, I. & COUCH, J. G., 1987. Dose to radiotherapy technologists from activation of patients at a fast neutron therapy facility. *Health Physics*, *53*, 311–312.

TEN HAKEN, R. K., AWSCHALOM, M. & ROSENBERG, I., 1983. Activation of the major constituents of tissue and air by a fast neutron radiation therapy beam. *Medical Physics*, *10*, 636–641.

VYNCKIER, S., PIHET, P. & WAMBERSIE, A., 1989. Results of 10 y of radiation protection dosimetry at the neutron therapy facility in Louvain-la-Neuve. *Health Physics*, *57*, 529–535.

1992, *The British Journal of Radiology*, 65, 334–338

The determination of total filtration on mammographic X-ray sets

By K. J. Robson, BSc, C. J. Kotre, BSc, MSc and K. Faulkner, BSc, MSc, PhD

Regional Medical Physics Department, Newcastle General Hospital, Newcastle upon Tyne NE4 6BE, UK

(*Received 10 January 1991 and in revised form 27 September 1991, accepted 18 October 1991*)

Keywords: Mammography, Radiation protection

Abstract. Data produced by a computer model are presented which allow the amount of molybdenum filtration on a molybdenum target mammographic X-ray set to be estimated from the measurement of the half value layer (HVL) in aluminium. Existing data refer either to tungsten target tubes or to molybdenum target tubes for a single anode angle and a constant potential waveform with the compression plate present. In addition to the tube voltage, the present data take account of the waveform of the tube potential and target angle. The results of an experimental verification of the model are presented and the effect of the geometry used in the experimental set-up discussed. Theoretical predictions of the molybdenum filter thickness made using the data from the model are in good agreement with the measured filter thickness, provided that attention is paid to the experimental geometry.

Since the tube filtration, in part, governs the output spectrum, and hence the dose to the subject, it is important that the total amount of filtration present on a mammography X-ray tube is known accurately. The International Commission on Radiological Protection (ICRP, 1982) recommend that for mammographic X-ray tubes, the total permanent filtration should be equivalent to at least 0.03 mm molybdenum or 0.5 mm aluminium.

As it is not normally possible to remove the filtration and measure its thickness, an indirect means of measurement is necessary. The technique most commonly employed is to measure the half value layer (HVL) at a specified kilovoltage and consult published data relating HVL to total filtration. For conventional diagnostic X-ray sets, the data of Cranley and Fogarty (1988) can be used. However, at present there is a lack of equivalent data relevant to mammographic X-ray tubes in respect of target material, target angle and voltage waveform. For example, the data presented in the Institute of Physical Sciences in Medicine Report 59 (IPSM, 1989), refer only to tungsten target tubes with aluminium filtration, whereas many machines now use molybdenum for both the target and filtration material. Indeed, it is recommended that the target material for mammographic X-ray tubes be molybdenum (DHSS, 1987). A recent publication (Cranley, 1991) presents data for a molybdenum target X-ray tube with a 15° target angle and a constant potential waveform, but includes the effect of the compression paddle. As the intention of this paper is to provide data for assessing the amount of filtration present on the tube, it is not appropriate to include the effect of the compression plate in the calculations.

By using a computer model to generate and filter X-ray spectra, the present work aims to provide data for determining the total filtration present on mammographic X-ray tubes from HVL measurements.

Method

The data presented in this work were calculated using a Pascal version of the algorithm of Birch and Marshall (1979). Mass attenuation coefficients required by the model were calculated for molybdenum and beryllium using the data of McMaster et al (1969). X-ray spectra for molybdenum targets were generated with values of constant tube potential in the range 27–32 kV at intervals of 1 kV for a target angle of 20°. The computer program allows spectra to be computed for different voltage waveforms. A photon spectrum, being an average of a series of constant potential waveforms, corresponding to different parts of the waveform, was used to calculate the HVL for time varying waveforms. Spectra were calculated for constant potential, three-phase six peak, and single-phase two peak waveforms. The three-phase waveform, a combination of three sinusoidal potentials, has a superimposed ripple of 13.4%. The single-phase waveform, corresponding to a full-wave rectification of a sinusoidal potential, is unsmoothed, *i.e.* it has 100% ripple. Various target angles in the range 10°–30° were also considered. Each spectrum was attenuated by 1 mm of beryllium to simulate the window of the X-ray tube. The molybdenum spectra were then further attenuated, corresponding to filtration with a series of molybdenum foils whose thickness varied from 10 μm to 60 μm in 5 μm intervals. In addition to the filtration described above, all the spectra were additionally attenuated by 500 mm of air.

Photon to kerma in air conversion factors from Birch et al (1979) were used to determine the output in μGy in air per mAs under scatter free conditions and the HVL calculated in millimetres of aluminium for each of the filtered spectra. Graphs of HVL against total filtration were produced in each case.

There are differences in the various sets of published mass attenuation coefficient data and photon to kerma in air conversion factors. The mass attenuation coeffi-

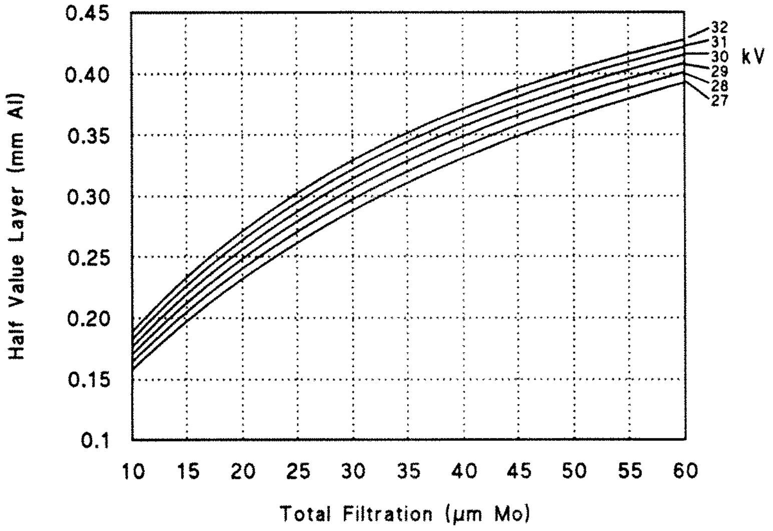

Figure 1. HVL as a function of filtration for a 20° effective target angle and a range of tube voltages. All the potentials have a constant potential waveform and all curves include 500 mm of air.

cient data of McMaster et al (1969) and the photon to kerma in air conversion data of Birch et al (1979) have been used to be consistent with the approach of Birch et al and to enable comparisons to be made between the two sets of theoretical calculations.

As the use of the correct target angle is important in the assessment of HVLs, data were calculated for target angles between 10° and 30°. It was felt that this range of target angles would allow the data to be used for most of the mammography sets commonly employed and a range of measurement geometries.

In order to maintain consistency with the established practice for measuring HVLs given in IPSM Report 59 (1989), emphasis is placed on data calculated at 30 kVp. In addition, the target/filter combination considered reflects that found most frequently on mammography sets.

Experimental verification

Experimental work was undertaken to verify that the computer model was satisfactory. The measurements were carried out on a Soredex Mamex DC mammography unit (Orion Corporation, Finland). The X-ray tube had a molybdenum target of angle 6° which was verified by radiographic means. The tube was modified in order to allow the fitted molybdenum filtration to be removed leaving only the beryllium window. The tube potential was produced by a medium frequency generator. In the model this potential was approximated to a constant potential waveform. The measurement of the HVL was performed using a mammographic ionization chamber and an MDH 2025 series dosemeter (Radcal Corporation, USA). A lead collimator was used to limit the beam size at the chamber to that of the chamber's sensitive area, thereby minimizing the effects of scattered radiation. The ionization chamber was positioned near to the central axis of the X-ray beam with a gap of at least 10 cm between it and the support table to minimize the backscatter from the table reaching the chamber.

High purity (99.99%) aluminium foils (Goodfellow Metals Ltd, Cambridge) placed midway between the tube focus and the ionization chamber were used to perform the HVL measurements. Molybdenum foils (99.9% purity) were placed as close as possible to the tube window in order to set the filtration, and the HVL measured for molybdenum thicknesses between 0 and 50 µm molybdenum. The readings were made at a nominal tube potential of 31 kV and 20 mAs. The actual tube potential was measured using an RMI 232 meter (Radiation Measurements Incorporated, Middleton, USA) calibrated using the method of Law et al (1989). The quoted accuracy of the meter is ±(1 kV + 2%). The HVL was calculated using the method of Wagner et al (1990).

The various factors contributing to the uncertainty of HVL measurements on mammographic equipment have been discussed by Wagner et al (1990). The estimated error on the HVL measurement has been calculated according to the method proposed by Wagner et al and was typically 1%. This estimated error is comparable with that given by Wagner et al. There is an additional uncertainty when using the molybdenum foils, arising from impurities in the material and variations in the foil thicknesses. The latter was deduced from measurements of foil mass and a knowledge of the density of molybdenum. The measurement accuracy of the kVp meter used results in typical uncertainties of 5% on the theoretical value.

Spectra were generated for the measured voltage and different thicknesses of filtration and the corresponding HVL calculated. The predicted HVLs were then compared with those found experimentally.

Results and discussion

The HVL data predicted by the model are shown in graphical form and, unless otherwise indicated, the data

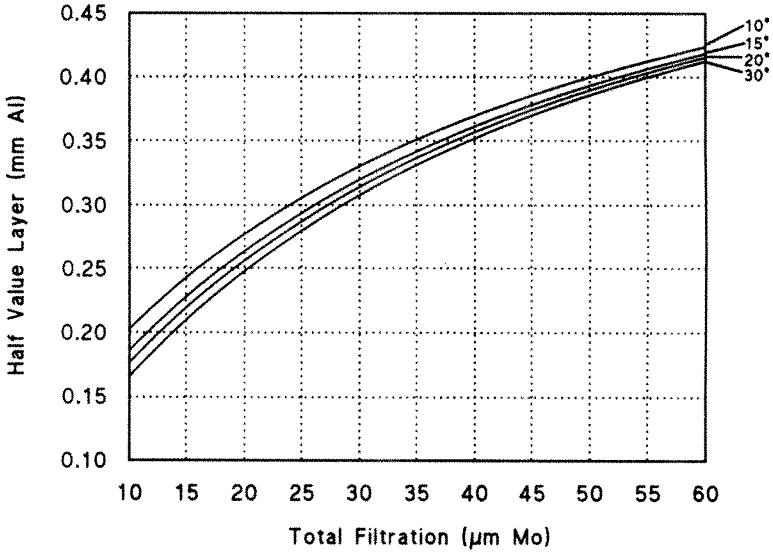

Figure 2. HVL as a function of filtration for a 30 kVp constant potential waveform over a range of effective target angles α. The additional attenuation caused by 500 mm of air is included.

refer to a constant tube potential of 30 kV and a 20° target angle. All the graphs take into account the additional filtration provided by 500 mm of air. The data shown are for tubes with molybdenum target and filtration. The calculated values of the HVL were compared with, and found to agree within 2% with, the published data of Birch et al (1979) over the limited range of tube potentials.

Although IPSM Report 59 (1989) recommends that the HVL be measured at a tube potential of 30 kVp, it may not be possible to perform the measurement at exactly this voltage. Fig. 1 shows data for various tube voltages in the range 27–32 kV, constant potential.

The effect of the target angle on the determination of filtration is shown in Fig. 2, while Fig. 3 demonstrates the influence of the waveform of the tube potential. Data for the following three voltage waveforms are included: (i) constant potential; (ii) three-phase, six peak, and (iii) single-phase, two peak.

The experimental verification required careful consideration of the geometry of the system. Fig. 4 shows the geometry of the experimental set-up. In the diagram, three angles are shown: α_T = the actual target angle, *i.e.* the angle between the target surface and the central axis of the X-ray beam; α_M = the measurement angle, with respect to the vertical, and α_C = the angle between the central axis of the X-ray beam and the vertical.

The effective target angle α is the angle between the

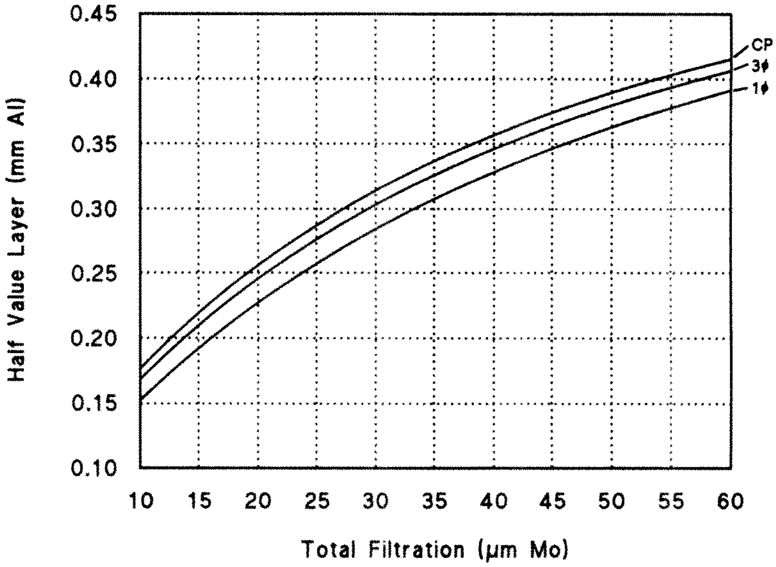

Figure 3. HVL for a 20° effective target angle and a tube potential of 30 kVp with the effect of 500 mm of air included. Data are shown for constant potential (CP), three-phase (3ϕ), and single-phase (1ϕ) waveforms.

face of the target and a line between the centre of the focal spot and the centre of the measurement chamber. From Fig. 4, it can be seen that in our experimental set-up, the effective target angle α is given by

$$\alpha = \alpha_T + \alpha_M - \alpha_C \qquad (1)$$

On the mammography unit used in this experiment, the central axis of the beam coincided with the edge of the support table. This made the measurement of the HVL along the central axis of the beam difficult, as only part of the chamber would be irradiated. In order to make a measurement here, the entire set-up would need to be rigidly fixed to avoid random fluctuations in the area of the chamber being irradiated. In practice, the measurement was made slightly away from the central axis of the beam so that the chamber was entirely within the X-ray field. From Fig. 4 it is evident that this results in an increase in the effective target angle as seen from the chamber. Tube tilt with respect to the horizontal also serves to alter the effective target angle (Birch & Marshall, 1979).

The change in effective target angle alters the X-ray spectrum at the chamber. In addition, because the filters and attenuators are both horizontal, the path lengths of the photons in both sets of foils are increased. A factor of $1/\cos(\alpha_M)$ should be applied to the measured HVL and a factor of $\cos(\alpha_M)/\cos(\alpha_C)$ applied to the calculated filtration. The latter correction is required since it is the filtration thickness along the central axis of the X-ray beam that is wanted, not the apparent thickness as seen from the chamber.

In the case of the experimental set-up used, the measurement angle α_M was 9.2°. Also, since in this case $\alpha_T = \alpha_C = 6°$, the effective target angle is equal to the measurement angle. The measured voltage was found to

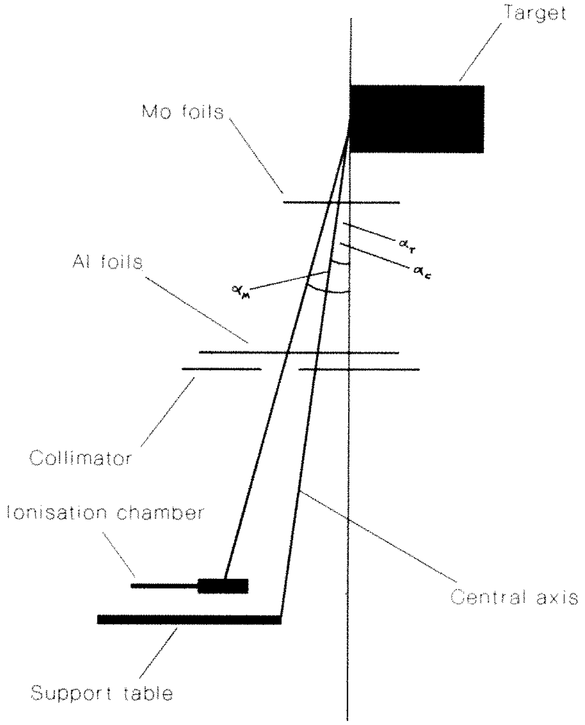

Figure 4. Diagram showing the experimental set-up used. Also shown are the definitions of the angles mentioned in the text. All the angles shown are exaggerated for clarity.

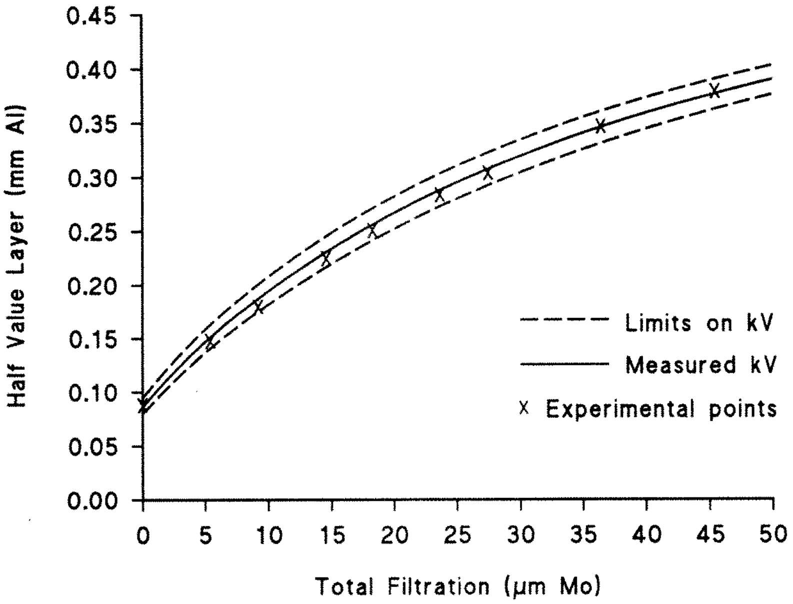

Figure 5. A comparison of the experimental data points with the values of HVL predicted by the model. The solid line represents the kV measured by the meter (28.5 kV), while the dashed lines give the upper and lower limits due to the uncertainty on the kV measurement. The theoretical curves include the attenuation due to 500 mm of air.

be 28.5 kV and this was used, together with the effective target angle of $\alpha = 9.2°$, to calculate the theoretical curve to fit the experimental points. Since the purpose of the experiment was to verify the model, all the required corrections were applied to the measured data points. The results of the experimental work are shown graphically in Fig. 5 and compared with the theoretical curve for the same conditions. The dashed lines show the theoretical curves for the upper and lower limits on the kV due to the accuracy of the kVp meter. In calculating the theoretical curves on Fig. 5, the attenuation due to air has been accounted for. This is particularly significant for the measurements with only a small amount of molybdenum filtration.

In practice, the two corrections required to account for the increased path length may be neglected, since they are both of the order of 1% and tend to cancel each other out. The change in the spectrum with increasing target angle however should not be ignored. This is particularly important for small effective target angles. The filtration can be calculated by interpolating between Figs 1 and 2 in order to take into account the effects of target angle and voltage, respectively. When using Fig. 2, the effective target angle rather than actual target angle should be used.

The geometry described above is specific to this particular X-ray set and measurement position. In general, to assess the amount of filtration present, a diagram of the tube showing the relationship of the target to the central axis and measurement position will be required and eqn 1 must be modified to give the appropriate value of effective target angle.

Conclusion

This work presents theoretical values of HVL calculated by a computer model. These data allow estimates of the total filtration in μm molybdenum to be made from HVL measurements in mm aluminium. Data are presented for different thicknesses of molybdenum filtration for molybdenum target tubes in the mammographic energy range. Results of experimental work to verify the model are also presented. The experimental data are compared graphically with the predicted results and the two sets of data found to be in good agreement. Owing to the design of most mammography sets, it is not normally practical to measure the HVL along the central axis of the X-ray beam. By considering a range of effective target angles, the present work allows a correction to be made for the measurement geometry through interpolation. For the accurate determination of filtration, it is vital that the geometry of the tube is known with regard to the effective target angle.

References

BIRCH, R. & MARSHALL, M., 1979. Computation of Bremsstrahlung X-ray spectra and comparison with spectra measured with a Ge(Li) detector. *Physics in Medicine and Biology*, *24*, 505–517.

BIRCH, R., MARSHALL, M. & ARDRAN, G. M., 1979. *Catalogue of Spectral Data for Diagnostic X-rays*. Scientific Report Series 30 (The Hospital Physicists' Association, London).

CRANLEY, K., 1991. Measuring the filtration of mammographic X-ray tubes with molybdenum targets. *British Journal of Radiology*, *64*, 842–845.

CRANLEY, K. & FOGARTY, G. W. A., 1988. The measurement of total filtration of diagnostic X-ray tubes. *British Journal of Radiology*, *61*, 388–392.

DHSS, 1987. *Guidance Notes for Health Authorities on Mammographic Equipment Requirements for Breast Cancer Screening*. Supplies Technology Division Report STD/87/34 (Department of Health, London).

ICRP, 1982. *Protection of the Patient in Diagnostic Radiology*, ICRP Publication 34 Annals of the ICRP 9 No 2/3 (Pergamon Press, Oxford).

IPSM, 1989. *The Commissioning and Routine Testing of Mammographic X-ray Systems*, IPSM Report No. 59 (Institute of Physical Sciences in Medicine, York).

LAW, J., FAULKNER, K. & SMITH, S., 1989. Measurement of X-ray tube potential in the mammographic region. *Physics in Medicine and Biology*, *34*, 717–725.

MCMASTER, W. H., KERR DEL GRANDE, N., MALLETT, J. H. & HUBBELL, J. H., 1969. *Compilation of X-ray Cross-sections*. UCRL Report 50174, Section II, Rev 1 (University of California, Livermore).

WAGNER, L. K., ARCHER, B. R. & CERRA, F., 1990. On the measurement of half-value layer in film-screen mammography. *Medical Physics*, *17*(6), 989–997.

1992, *The British Journal of Radiology*, *65*, 339–341

Technical note

A comparison of four mammographic image quality test objects

By M. Payne, BSc, MSc and C. P. Lawinski, BSc, MSc, MPhil

King's Centre for the Assessment of Radiological Equipment (KCARE) King's College Hospital, Denmark Hill, London SE5 9RS, UK

(Received 25 July 1991, accepted 16 August 1991)

Keywords: Mammography, Image quality, Test objects

The need for rigorous image quality assurance in mammography is well documented (Pritchard Report, 1989). However, there is still debate over the suitability of those image quality test objects commercially available. We have been able to compare three contemporary test objects with the "Barts" test object which has been in use since 1980 and has been used as a standard by many workers (Kirkpatrick & Law, 1987). The four mammographic test objects have been compared using six mammographic film-screen combinations. The following test objects were used.

The "Barts" mammographic image quality test object (White & Tucker, 1980). This object contains several series of opacities designed to mimic mammographic diagnostic features, some being fat equivalent, some water equivalent, some skin equivalent and some equivalent to calcifications, which are immersed in an epoxy-resin scattering medium. The object is designed to assess contrast and resolution combined in various ways.

The Dupont mammographic image quality test object (Ackermann, personal communication, 1988). This simulates microcalcifications, fibrous structures and small spherical objects. It also allows an assessment of minimal detail contrast, line resolution in two dimensions and point resolution. A selection of organic materials is included to simulate benign and malignant tumours, lymph nodes and tissues characteristic of a dense breast. It is designed to be used with a stack of attenuator plates to provide the appropriate absorption, scatter and geometrical unsharpness in test exposures.

The Leeds TOR [MAX] mammographic test object (Cowen et al, personal communication, 1988). This contains several different types of detail which provide information about unsharpness, low-contrast sensitivity, small detail visibility and noise in the test image. As with the Dupont test object it is designed to be used with a stack of attenuator plates.

The Leeds TOR [MAM] mammographic test object (Cowen et al, personal communication, 1990). This test object contains both organic and anthropomorphic test details to provide a radiographic review of image quality. It contains six groups of four filaments ranging in size from 0.2 mm to 0.45 mm, six groups of three low contrast details of 3.0 mm diameter and six groups of microcalcifications ranging in size from less than 100 μm to 350 μm. It also contains simulated breast tissue with "tumours" and microcalcifications. It is designed to be used in a similar manner to TOR [MAX].

Table I lists the six mammographic film-screen combinations that were selected following an assessment of 31 different film-screen combinations (KCARE report, 1991) to be representative of the extremes of sensitivity, contrast and resolution. This selection has allowed an assessment of the performance of the test objects over a wide range of the parameters which give an indication of "image quality".

Method

Each test object was imaged using a Soredex Mammex DC Mag mammography unit typical of those used in the National Health Service today. It has a molybdenum target and molybdenum added filtration. All images were produced at 28 kVp and were scored in line with the instructions supplied with the test objects. As the design philosophy and scoring system for each test object differs, the total possible score for each differs accordingly. Therefore, we did not consider the magnitude of the scores but concentrated on the response of the image score to the varying imaging conditions provided by the different film-screen combinations. Four images were made of each test object with each film-screen combination and scored by two observers.

Results and discussion

The image scores were correlated with measurements of film-screen sensitivity or speed and represented graphically (Fig. 1). The graph shows image score for

Table I. The film-score combinations used in this assessment

Film	Screen
3M FM	3M T2
Agfa MR3	Agfa detail S
Dupont micro vision	Dupont ortho M
Fuji MI-MA	Fuji HR fine
Kodak T-Mat M2	Kodak Min-R fast (pair)
Kodak Min-R	Kodak Kin-R

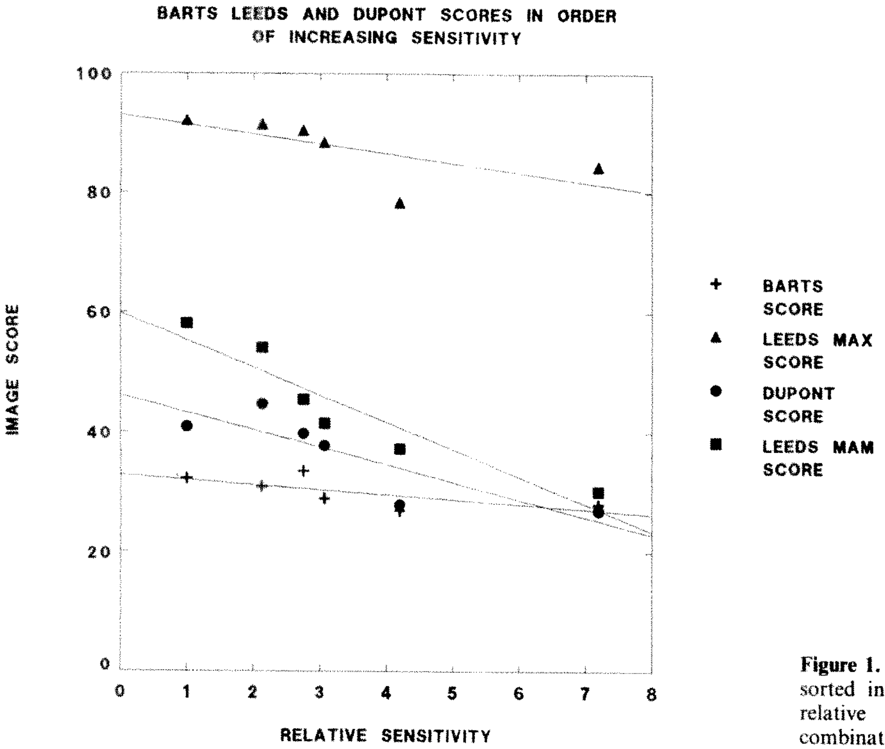

Figure 1. Image score for each test object sorted in order of increasing sensitivity relative to the Min-R Min-R combination.

each test object against sensitivity or speed relative to the Min-R Min-R combination. Linear fit curves are also displayed to demonstrate the trends more clearly. It is apparent that image score tends to decrease with increasing film-screen sensitivity.

While scoring images it was observed that a number of the sets of details on the Barts test object were of little value as all details in these sets could be seen on all film-screen combinations.

A noticeable decrease of image score was observed with the fifth film-screen combination which is a double sided film, twin screen system that is consequently subject to greater image unsharpness. This effect is particularly noticeable with the Leeds TOR [MAX] and the Dupont test objects which both incorporate limiting resolution test patterns.

Table II. The range of image score for each test object expressed as points scored, as the percentage decrease from maximum to minimum score for each test object and as the percentage decrease of score for each test object from the slowest to the fastest film-screen combination.

Test object	Range of score (points)	% Decrease of image score from maximum to minimum	% Decrease of image score from slowest to fastest film-screen system
Barts	6.5	19.4	13.2
Dupont	17.75	39.7	34.0
TOR [MAX]	13.58	14.8	8.2
TOR [MAM]	27.75	47.9	47.9

In Table II the range of image score for each test object is expressed as points scored, as the percentage decrease from maximum to minimum score for each test object and as the percentage decrease of score for each test object from the slowest to the fastest film-screen combination.

The results suggest that the Dupont and the Leeds TOR [MAM] test objects exhibit a greater change of image score than the other two test objects over the range of film-screen combinations used. The TOR [MAM] test object appears to be the most sensitive overall.

Acknowledgments

The authors wish to acknowledge the support of Mr Peter Oddy, Department of Health, project coordinator (KCARE). We would also like to thank Dupont (UK) Limited, the Medical Physics Department, St Bartholemews Hospital, London, and FAXIL, The General Infirmary, Leeds, for the loan of test objects and Medical X-ray Supplies Limited, London, for the loan of the Mammex mammography unit.

References

KCARE REPORT, 1991. *An assessment of commercially available film screen systems for mammography* (MDD/91/32).

KIRKPATRICK, A. E. & LAW, J., 1987. A comparative study of films and screens for mammography. *British Journal of Radiology, 60*, 73–78.

PRITCHARD, J., 1989. *Quality Assurance Guide-lines For Mammography*. Prepared by a sub-committee of the Radiological Advisory Committee of the Chief Medical Officer chaired by Dr John Pritchard (HMSO, London).

WHITE, D. R. & TUCKER, A. K., 1980. A test object for assessing image quality in mammography. *British Journal of Radiology, 53*, 331–335.

1992, *The British Journal of Radiology*, 65, 342–344

Case reports

Sonographic features in a case of Fitz-Hugh-Curtis syndrome masquerading as malignancy

By B. Banerjee, FRCS, FRCR, A. Rennison, BSc, DCRR and *B. E. Boyes, FRCP

Department of Diagnostic Radiology and *Medicine, Tameside General Hospital, Ashton Under Lyne, Lancashire OL6 9RW, UK

(Received 13 May 1991 and in revised form 6 September 1991, accepted 20 September 1991)

Keywords: *Chlamydia trachomatis*, Fitz-Hugh-Curtis syndrome, Ultrasound, Focal hepatic lesions

Pelvic inflammatory disease, associated with symptoms of pleuritic and upper abdominal pain, is characteristic of Fitz-Hugh-Curtis syndrome. The upper abdominal pain is due to perihepatitis. Gonococcal infection has previously been implicated almost exclusively as the cause of Fitz-Hugh-Curtis syndrome (Curtis, 1930; Fitz-Hugh, 1934). However, recent publications strongly indicate *Chlamydia trachomatis* as the causative organism in this syndrome. A case of Fitz-Hugh-Curtis syndrome is presented in which the sonographic demonstration of focal lesions in the liver, together with the presence of a pelvic mass led to an erroneous diagnosis of malignancy. Although Fitz-Hugh-Curtis syndrome was described over 50 years ago, it has not been widely publicized and to our knowledge the sonographic demonstration of focal hepatic lesions in Fitz-Hugh-Curtis syndrome has not previously been documented.

Case report

A 42-year-old divorced barmaid presented with anorexia, weight loss, upper abdominal pain, menorrhagia and pelvic discomfort. On examination the liver was palpated two fingers below the costal margin. There was tenderness over the right hypochondrium and epigastrium. Haematological investigations revealed a moderate hypochromic microcytic anaemia (haemoglobulin = 9 g/dl), elevated erythrocyte sedimentation rate (ESR) (36 mm/h) and abnormal liver function tests (alkaline phosphate = 184 i.u./l, gamma GT = 80 i.u./l).

Ultrasound examination of the abdomen and pelvis revealed multiple small abnormal foci within both lobes of a moderately enlarged liver. The focal lesions were both hypo- and hyperechoic in nature, but several target or "bull's eye" lesions were present (Fig. 1). There was irregular thickening of the liver capsule, particularly anteriorly (Fig. 2). The uterus appeared enlarged but with a relatively smooth contour. Some inhomogeneity of internal echo pattern was noted at the uterine fundus. There was a tubo-ovarian mass in the left adnexa but the right adnexa was obscured by overlying loops of bowel which appeared to be fixed to the adnexa (Fig. 3a). There was thickening of the endometrial lining with poor definition of its posterior margin, suspicious of an invasive endometrial lesion (Fig. 3b). No free fluid was demonstrated in the upper abdomen but there was a trace of fluid in the recto-vaginal pouch. Although the sonographic appearances were not conclusive, a diagnosis of pelvic malignancy with hepatic meta-

---

Address correspondence to Dr B. Banerjee.

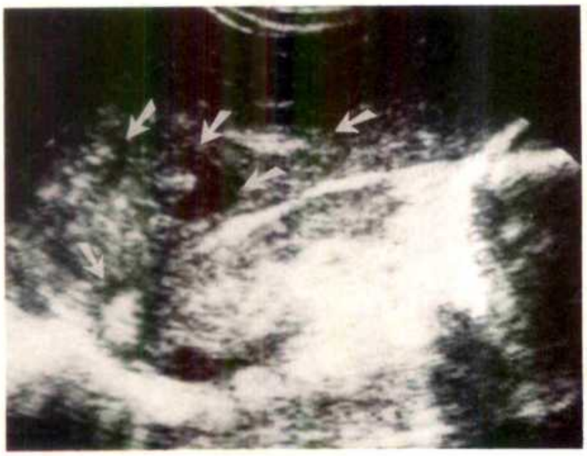

Figure 1. Sonogram of the liver showing several focal lesions, including target lesions (arrows).

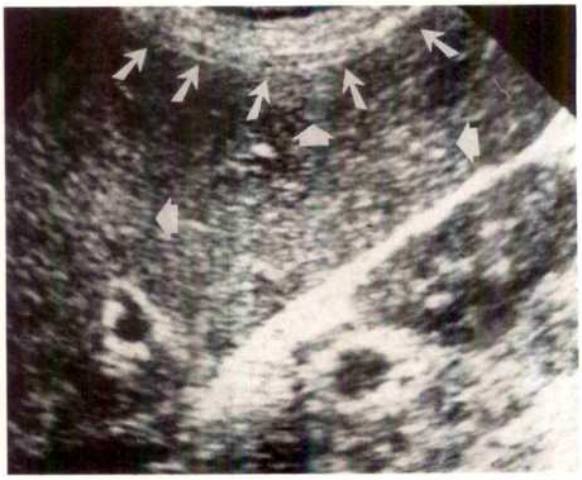

Figure 2. Longitudinal sonogram of the right lobe of the liver showing thickening of the anterior capsule of the liver (arrows). Several echogenic foci are also noted in the liver (arrowheads).

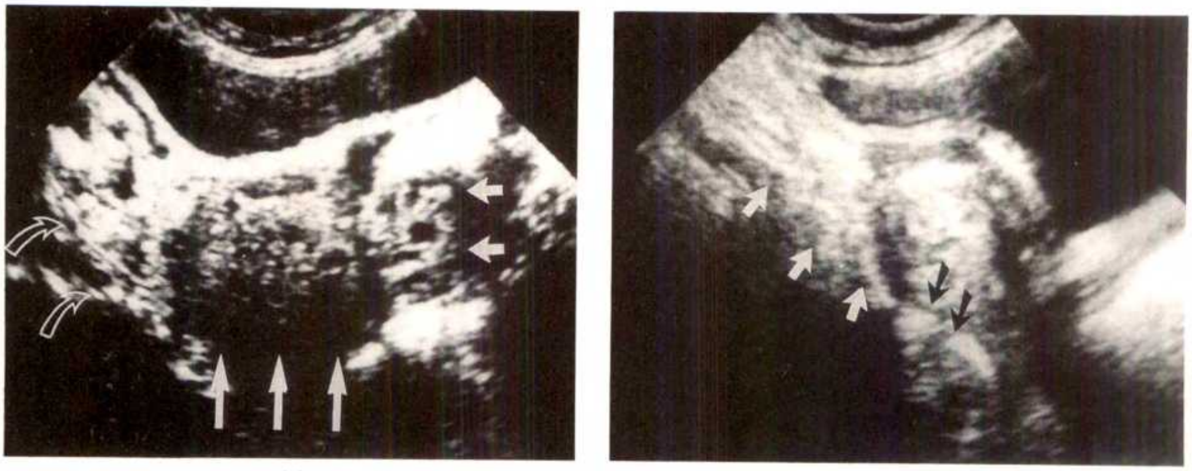
(a) (b)

Figure 3. (a) Transverse sonogram of the pelvis demonstrating uterine enlargement (long arrows) and a tubo-ovarian mass in the left adnexa (short arrows). Poor definition of the right adnexa is due to overlying bowel (curved arrows). (b) Longitudinal sonogram of the uterus demonstrating marked endometrial thickening and suggesting invasion in the posterior wall of the uterus (black arrows). Gas in bowel overlying the uterine fundus is causing distal shadowing (white arrows).

stases was suggested. Laparoscopy revealed evidence of subacute pelvic inflammation. The uterus was anteverted with filmy adhesions, and the Fallopian tubes were inflamed, thickened and convoluted owing to the presence of adhesions and the formation of tubo-ovarian masses. No macroscopic evidence of malignancy was seen. The liver surface was finely granular with white and yellow discolouration of the capsule. To avoid the risk of haemorrhage, laparoscopic liver biopsy was not performed. Laparoscopy was followed by endometrial curettage which showed no evidence of malignancy. A revised diagnosis of Fitz-Hugh-Curtis syndrome was made and the diagnosis was confirmed by demonstration of a high level of chlamydial antibodies (IgG chlamydial antibody titre of 1/640) in the patient's serum.

Treatment with tetracycline, the antibiotic of choice for *Chlamydia* infection, was commenced. Rapid symptomatic improvement was followed by gradual return of normal liver function and improvement of anaemia. Serial ultrasound examinations over several weeks showed gradual improvement and subsequent disappearance of the intrahepatic lesions, but some thickening of the liver capsule persisted (Fig. 4a). Although there was distinct improvement of inflammatory changes in the pelvic organs, some adnexal thickening and deformity remained (Fig. 4b).

Discussion

Chlamydia trachomatis is now recognized as a common cause of pelvic inflammatory disease (Mårdh et al, 1977). Although initially *Neisseria gonorrhoeae* was

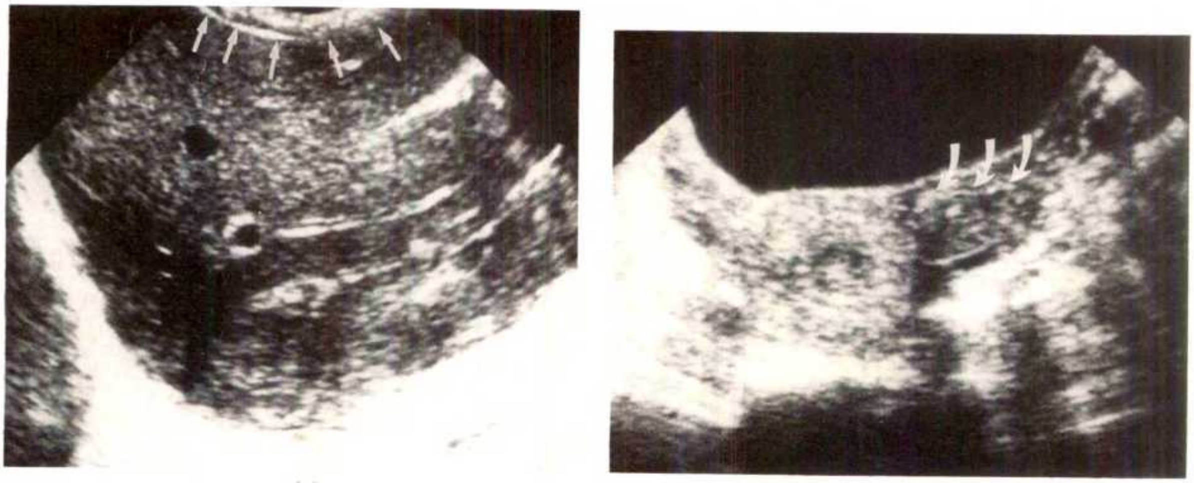
(a) (b)

Figure 4. (a) Longitudinal sonogram of the liver showing normal echo pattern. Complete resolution of focal hepatic lesions has taken place, but some capsular thickening of the liver is still present (arrows). (b) Transverse sonogram of the pelvis demonstrating improvement of pelvic inflammation, but some thickening and deformity of the left adnexa persists (arrows).

thought to be solely responsible for Fitz-Hugh-Curtis syndrome, a search for gonococcus in the majority of these cases has been negative. Moreover, recent studies are highly supportive of *Chlamydia trachomatis* as the causative organism in Fitz-Hugh-Curtis syndrome (Wang et al, 1980; Wølner-Hanssen et al, 1980).

Typical symptoms include abdominal pain, usually of sudden onset, in the right upper quadrant sometimes associated with pleuritic pain, in a female with pre-existing pelvic discomfort. Abdominal pain may overshadow the symptoms of pelvic inflammation. In the acute stage localized peritonitis involving the hepatic capsule may result in adhesions. In the majority of cases only the capsule of the liver is involved and the parenchyma remains unaffected. The liver enzymes therefore remain normal (Wølner-Hanssen et al, 1980). In our case, the liver enzymes were elevated suggesting parenchymal involvement and this was supported by the sonographic findings. Confirmation of Fitz-Hugh-Curtis syndrome is obtained by the isolation of *Chlamydia trachomatis* from the cervical smear or in fluid from the pouch of Douglas. The demonstration of significantly high levels of IgM and IgG Chlamydial antibodies in the patient's serum will also indicate the true diagnosis (Wang et al, 1980). A high level of IgG Chlamydial antibody may also be found in aspirated peritoneal fluid (Treharne et al, 1979).

In this case the hepatic lesions were presumably liver abscesses, as on ultrasound examination hepatic abscesses may appear both as hypo- and hyperechoic foci. Moreover, the disappearance of these foci after antibiotic treatment supports an infective aetiology.

Patients with Fitz-Hugh-Curtis syndrome may present with right upper quadrant pain and may easily be misdiagnosed as cholecystitis or pancreatitis. Further confusion may arise following biochemical investigations as in a few cases the serum amylase values may be elevated (Wølner-Hanssen et al, 1980). Our aim in this report is to increase awareness of this syndrome and to record the demonstration of focal hepatic lesions by ultrasound in Fitz-Hugh-Curtis syndrome, not previously documented.

References

Curtis, A., 1930. A cause of adhesions in the right upper quadrant. *Journal of the American Medical Associations*, *94*, 1221–1222.

Fitz-Hugh, T., 1934. Acute gonococcic peritonitis of the right upper quadrant in women. *Journal of the American Medical Association*, *102*, 2094–2096.

Mårdh, P. A., Ripa, K. T., Wang, S. P. & Westrom, L., 1977. *Chlamydia trachomatis* infection in patients with acute salpingitis. *New England Journal of Medicine*, *296*, 1377–1379.

Treharne, J. D., Ripa, K. T., Mårdh, P. A. & Sevensson, L., 1979. Antibodies of *Chlamydia trachomatis* in acute salpingitis. *British Journal of Venereal Diseases*, *55*, 26–29.

Wang, S. P., Eschenbach, D. A., Holmes, K. K., Wager, G. & Grayston, J. T., 1980. *Chlamydia trachomatis* infection in Fitz-Hugh-Curtis Syndrome. *American Journal of Obstetrics and Gynecology*, *138*, 1034–1038.

Wølner-Hanssen, P., Westrom, L. & Mårdh, P. A., 1980. Perihepatitis and Chlamydial salpingitis. *Lancet*, *i*, 901–903.

Peripheral neuropathy simulating lymphoma

By R. J. Swingler, MD, MRCP(UK), R. E. Cull, PhD, FRCP(E), *D. Kean, FRCR and *L. Turnbull, FRCR

Departments of Medical Neurology and *Radiology, Royal Infirmary of Edinburgh, Lauriston Place,
Edinburgh EH3 9YW, UK

(Received 4 June 1990 and in final form 29 May 1991, accepted 20 September 1991)

Keywords: Peripheral nerve hypertrophy, Hereditary motor and sensory neuropathy type I

Nerve hypertrophy occurs in some types of Charcot–Marie–Tooth syndrome (hereditary motor and sensory neuropathy (HMSN) type I), Dejerine–Sottas disease (HMSN type III), Refsum's disease (HMSN type IV), neurofibromatosis, amyloidosis, sarcoidosis, leprosy, diabetes mellitus, chronic relapsing neuropathies, acromegaly, hypothyroidism, isolated peripheral nerve lesions and, very rarely, multiple sclerosis (Dyck, 1984; Walton, 1985). We report a case of HMSN type I with marked intercostal, splanchnic and peripheral nerve hypertrophy producing radiological appearances of pleural lesions and mediastinal widening, which, together with systemic symptoms, simulated lymphoma.

Case report

An 18-year-old man (A.P., RIE 110264–1100) had ingrowing toe nails removed in 1982 and subsequently noticed numbness of the big toes, extending onto the dorsum of both feet, and a tendency to lift the feet high when walking.

On general examination he had mild pectus excavatum, bilateral pes cavus and paronychiae affecting both great toes.

Address correspondence to: Dr R. J. Swingler, Department of Neurology, Dundee Royal Infirmary, Dundee DD1 9ND, UK.

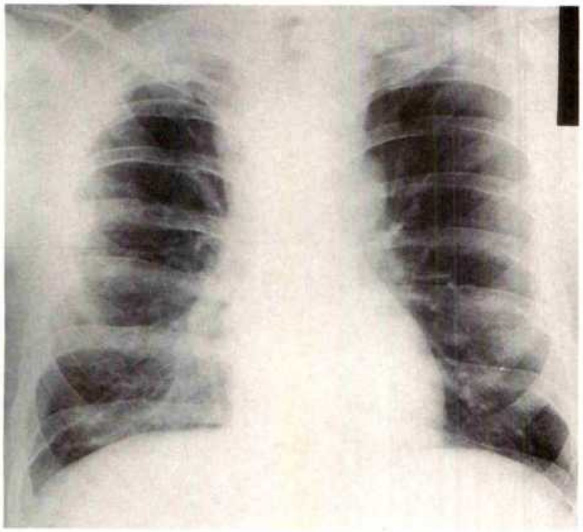

Figure 1. Postero-anterior chest radiograph showing widening of the mediastinum, particularly in its superior portion, and enlargement of the upper left hilum. There is also bilateral lobulated pleural thickening more prominent in the right hemithorax.

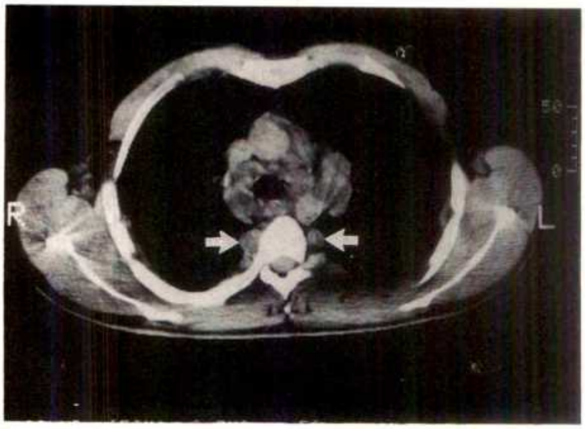

Figure 2. Upper mediastinal CT scan demonstrating extensive lobulated lesions (arrows) in both paravertebral areas and a low-density abnormality encircling the trachea and extending down into the left hilar region.

The peripheral nerves in the upper limbs and intercostal nerves over the chest wall were thickened with diameters of up to 2–3 cm. On neurological examination, tone was reduced in the hands and feet and there was distal wasting and weakness in all limbs with reduced sensation for all modalities in a stocking distribution to mid calf. Tendon reflexes were preserved in the upper limbs and knees but ankle reflexes and plantar responses were absent. Examination of the family revealed no neurological deficits.

On investigation the level of protein in the cerebrospinal fluid was elevated at 2.72 g/l but other indices were normal. Neurophysiological studies were performed using an MS91 Medelec system and, although normal responses were recorded from the upper limbs, no compound muscle action potential could be recorded from the left common peroneal nerve when the recording electrode was placed on the extensor digitorum brevis; a velocity of 31 m/s (normal > 44 m/s) was observed in tibialis anterior. Sensory nerve action potentials could not be detected in the sural nerves bilaterally.

Biopsy from the sural nerve demonstrated focal demyelination, with subendothelial deposition of myxoid material, swelling and separation of nerve fibres and focal Schwann cell hypertrophy. Although upper limb nerve conduction velocities were not grossly reduced, the clinical and histological findings were thought to be consistent with a diagnosis of HMSN type I. Zadek's operation was performed to remove the infected toe nails and the patient was fitted with foot splints.

In 1988 the patient returned with anorexia, intolerance of fatty foods and alcohol, occasional vomiting, floating stools, weight loss and progressive distal leg weakness and wasting. Re-examination revealed numerous subcutaneous swellings in the neck, axillae and groins of variable consistency, and while some were quite obviously following the course of nerves, others resembled enlarged lymph nodes. On examination of the upper and lower limbs there was evidence of progression of the distal weakness and wasting with sensory loss to the thighs. All tendon reflexes and plantar responses were absent.

On re-investigation, his chest radiograph revealed extensive superior mediastinal widening with pleural thickening suggestive of lymphadenopathy resulting from possible lymphoma (Fig. 1). However, serological studies, marrow aspiration and abdominal ultrasonography were normal and only a small hiatus hernia was detected on barium studies.

Computer tomographic (CT) scanning was performed on a GE 8800 scanner using a slice thickness of 10 mm and slice interval of 15 mm without contrast enhancement. Images of the chest, abdomen and pelvis (Figs 2–4) demonstrated soft-tissue lesions in the brachial plexus, intervertebral foraminae, mediastinum, abdomen, psoas, buttocks and pelvis, where the masses measured up to 5–7 cm in diameter. The density numbers of the lesions measured between 15 and 25 Hounsfield units (HU). These values are lower than those encountered in neurofibromata (45–60 HU) and enlarged lymph nodes (30–35 HU) but higher than those seen in fat (−120 HU). The appearances were thought to be consistent with marked hypertrophy of nerves.

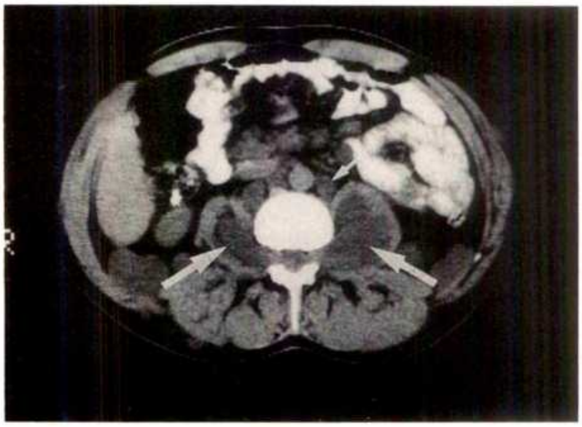

Figure 3. CT scan of the mid-abdomen showing large lobulated lesions (large arrows) extending out from the neural exit foraminae bilaterally causing considerable deformity and thinning of the adjacent psoas muscles. Smaller lesions are also seen in the left para-aortic areas (small arrow), aorto-caval sulcus and bilaterally lying adjacent to the psoas muscles.

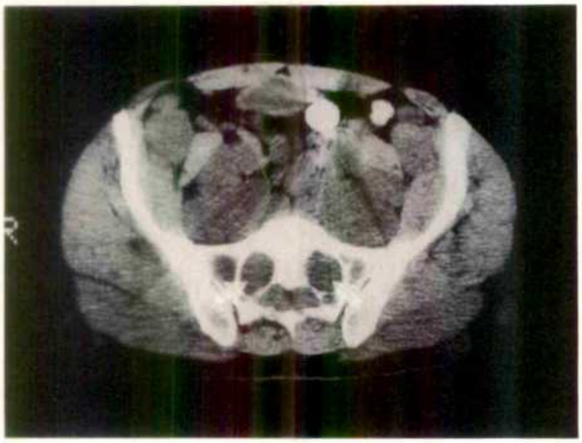

Figure 4. CT scan through the upper sacrum showing considerable widening of the sacral exit foraminae and bilateral elevation of the psoas muscles by large low-density mass lesions. Several low-density lesions are also seen subcutaneously in the buttocks.

Magnetic resonance (MR) imaging was performed on a 0.08 T resistive MR system, which has been described previously (Smith et al, 1984). An interleaved saturation–recovery inversion–recovery pulse sequence was employed with a time to repeat (TR) of 1 s and a time to inversion (TI) of 200 ms. Using this sequence, four images were available: (i) proton density; (ii) inversion–recovery; (iii) calculated T_1; and (iv) difference or "D" image. Areas of prolonged T_1 are seen as low signal intensity on the inversion–recovery image and high signal on the calculated T_1 image. The contrast in the difference image is dependent on the product of T_1 and T_2 prolongation (McRitchie et al, 1990) and, in general, long T_1 areas are seen as high signal regions. Images of the neck and abdomen confirmed the presence of lobulated lesions with a neural distribution (Figs 5–8). The "D" images showed the lesions to be of uniformly high signal and the calculated T_1 images demonstrated that the lesions had prolonged T_1 values of approximately 650 ms compared with typical values of 300 ms for fat, 280 ms for white matter and 350 ms for cortex.

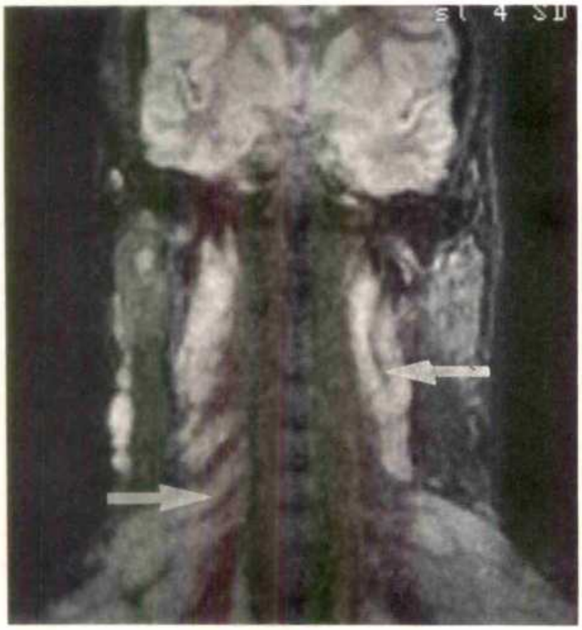

Figure 5. A coronal T_1-weighted "D" magnetic resonance image of the neck showing extensive abnormalities of high signal intensity (long T_1) extending out from all exit foraminae (arrows).

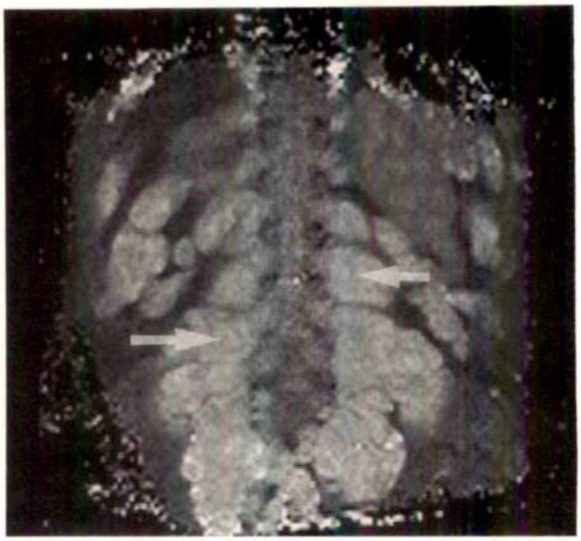

Figure 6. A coronal calculated T_1 image of the abdomen demonstrating multiple lobulated lesions (arrows) with moderate prolongation of T_1 extending bilaterally from all neural exit foraminae.

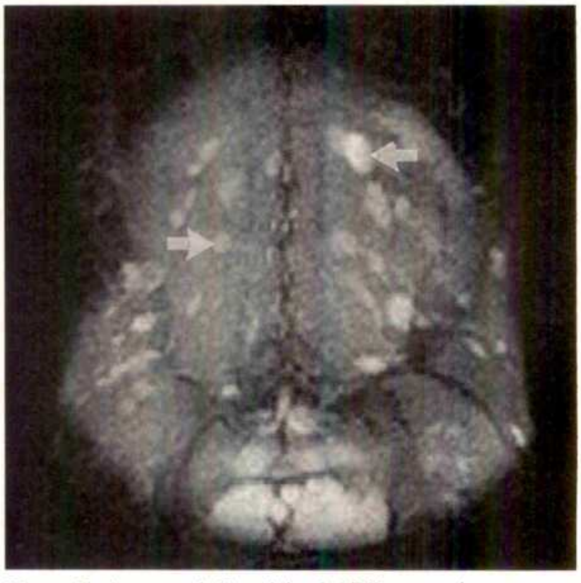

Figure 7. A coronal T_1-weighted "D" magnetic resonance image of the paraspinal area showing multiple lobulated high-signal lesions (arrows) in and adjacent to both psoas muscles.

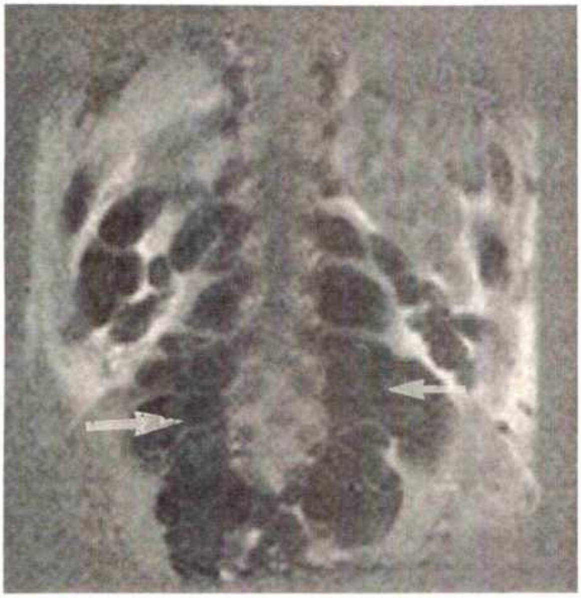

Figure 8. A coronal inversion–recovery magnetic-resonance image of the abdomen showing low-signal (long T_1) lobulated lesions extending bilaterally from the neural exit foraminae (arrows).

Surgical exploration of the neck demonstrated thickened nerves with no evidence of lymphadenopathy. Biopsy results were consistent with nerve hypertrophy and myxoid degeneration rather than lymphoma. After 18 months the patient remains well on review.

Discussion

This patient presented at the age of 18 years with a hypertrophic peripheral neuropathy and, in view of the mild onset, peroneal distribution of weakness, reduced nerve conduction velocities and histological appearances, a diagnosis of sporadic HMSN type I was made. It has been argued (Dyck & Lambert, 1968; Dyck, 1984) that isolated cases are usually due to dominant inheritance but close examination of his parents and siblings demonstrated no abnormalities and it was concluded that the patient was suffering from a sporadic or recessive form of the condition (Harding & Thomas, 1980).

When the patient returned with systemic symptoms and radiological evidence of pleural lesions and mediastinal widening, it was initially thought that he had developed a lymphoma. However, further investigations did not support this diagnosis, and the gastrointestinal symptoms (which subsided) were eventually attributed to a small hiatus hernia; 18 months later he remains well.

Several investigators have described the radiological appearances in patients with hypertrophic neuropathy. Plain radiographs of the spine may demonstrate scalloping of vertebral bodies, triangulation of pedicles and enlarged intervertebral foraminae (Bellon et al, 1972; Hammerschlag et al, 1977). The myelographic appearances have also been well documented and there have been cases of complete spinal canal block as a result of hypertrophied nerve roots in Dejerine–Sottas disease (HMSN type III) (Carlin et al, 1982). The tomographic appearances of hypertrophic neuropathy have recently been described by Morano and Russell (1986) who noted gross, symmetrical enlargement of nerve roots with dilatation of intervertebral foramina in a patient with Charot–Marie–Tooth syndrome. These features were also observed in our patient but we believe that this is the first report of intercostal and splanchnic nerve hypertrophy of such degree that it stimulated the appearance of pleural lesions and mediastinal widening. In this case, the characteristic neural distribution and density of these lesions were well demonstrated by CT and magnetic resonance imaging and we suggest that these non-invasive techniques should be performed before biopsy when there is any doubt about the diagnosis. Further classification and counselling of sporadic cases will continue to prove difficult until the underlying genetic defects have been elucidated.

References

Bellon, E. M., Kaufman, B. & Tucker, M. E., 1972. Hypertrophic neuropathy, plain film and myelographic changes. *Radiology*, *103*, 319–322.

Carlin, L., Biller, J., Challa, V. & Riela, A., 1982. Hypertrophic neuropathy with spinal cord compression. *Surgical Neurology*, *18*, 237–240.

Dyck, P. J., 1984. Inherited neuronal degeneration and atrophy affecting peripheral motor, sensory and autonomic neurons. In *Peripheral Neuropathy*, ed. by P. J. Dyck, P. K. Thomas, E. H. Lambert & R. Bunge (W. B. Saunders, Philadelphia), pp. 1600–1655.

Dyck, P. J. & Lambert, E. H., 1968. Lower motor and primary sensory neuron diseases with peroneal muscular atrophy: I. Neurologic, genetic, and electrophysiological findings in hereditary neuropathies; II. Neurologic, genetic, and electrophysiologic findings in various neuronal degenerations. *Archives of Neurology*, *18*, 603–619.

Hammerschlag, S. B., Adelman, L. S., Marcus, E. M. & Wolpert, S. M., 1977. Cervical myelographic changes in hypertrophic interstitial polyneuropathy. *Annals of Neurology*, *2*, 83–84.

Harding, A. E. & Thomas, P. K., 1980. Genetic aspects of hereditary motor and sensory neuropathy (types I and II) *Journal of Medical Genetics*, *17*, 329.

McRitchie, H. A., Ridgway, J. P., Turnbill, L. W. & Kean, D. M., 1990. An observation of increased contrast due to both T_1 and T_2 weighting in a synthetic image. *Magnetic Resonance Imaging*, *8*, 261–266.

Morano, J. U. & Russell, W. F., 1986. Nerve root enlargement in Charcot–Marie–Tooth disease: CT appearance. *Radiology*, *161*, 784.

Smith, M. A., Best, J. J. K., Douglas, R. H. B. & Kean, D. M., 1984. The installation of a commercial resistive NMR imager. *British Journal of Radiology*, *57*, 1145–1148.

Walton, J. N., 1985. *Brain's Diseases of the Nervous System*, 9th edn (Oxford University Press, Oxford), pp. 546–548.

1992, *The British Journal of Radiology*, *65*, 348–349

Dystrophic umbilical artery calcifications in an infant

By G. Beluffi, MD, P. Fiori, MD and *A. T. Pandiscia, MD

Section of Paediatric Radiology, Department of Radiodiagnosis, IRCCS Policlinico S. Matteo, Piazzale Golgi, 2, I-27100 Pavia PV, Italy

(*Received 11 March 1991 and in revised form 8 July 1991, accepted 12 September 1991*)

Keywords: Umbilical artery calcification, Dystrophic calcifications, HIP, Congenital dislocation

The radiological observation of calcification within an obliterated umbilical artery is a rare occurrence in children. Only a few papers in the literature deal with this subject (Currarino & Weinberg, 1985; Sirinelli et al, 1989); a total of 10 cases have been reported. The case described here is the only one observed in the last ten years in our Section of Paediatric Radiology. During this time 4200 infants underwent pelvic X-ray examination for suspected congenital dislocation of the hip (CDH) and 13 500 children of different ages underwent abdominal radiography for various reasons.

Case report

A 6-month-old girl was referred to the Section of Paediatric Radiology of the IRCCS Policlinico S. Matteo, for a pelvic radiograph to exclude CDH. There was no history of perinatal disease, infections or oedema of the lower limbs. The radiograph showed no sign of CDH, but revealed the presence of two pelvic calcifications near the lower border of the iliac bones in proximity to the inferior iliac notches (Fig. 1). The calcification on the right was dense and round with a diameter of 3 mm; the left had a round portion about 2 mm in diameter attached to a curvilinear tail about 5 mm long. Lateral films were not taken. A diagnosis of dystrophic calcifications in obliterated umbilical arteries was made and no further investigation was performed.

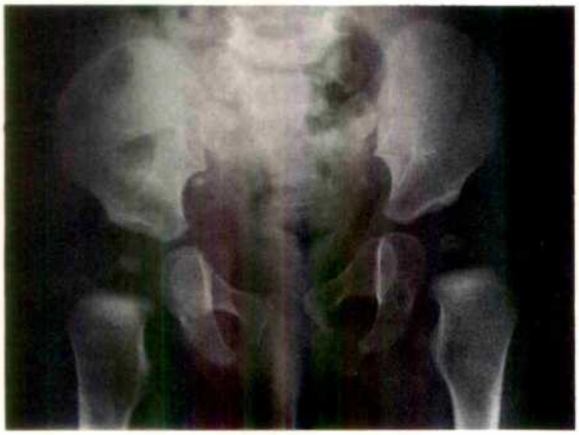

Figure 1. Presence of dystrophic calcifications within the obliterated umbilical arteries at 6 months of age.

Discussion

The occurrence of calcification within obliterated umbilical arteries is a rare finding in children. 10 other cases have been recorded (Currarino & Weinberg, 1985; Sirinelli et al, 1989). In all cases the calcifications have been an incidental finding in healthy children undergoing screening for CDH; in three cases they were bilateral and in seven cases unilateral. These calcifications were usually located near the iliac bones, at sites where umbilical arteries are found.

According to Currarino and Weinberg (1985), different vascular structures (ductus arteriosus, umbilical vein and arteries, ductus venosus) which are patent during fetal life undergo spontaneous obliteration soon after birth after passing through a fibrous phase during which they may become partially calcified.

Calcifications within obliterated umbilical arteries were observed in two of seven patients (age range 7 days–23 months) at autopsy. These were in the horizontal pelvic tracts of the umbilical arteries (Currarino & Weinberg, 1985). This finding suggests that calcifications can occur in any portion of the umbilical arteries.

Stretching of the ligaments during growth, which could cause disruption and fragmentation of the calcifications, may explain their disappearance on radiographs in older children (Sirinelli et al, 1989).

Dystrophic umbilical artery calcifications are to be differentiated from other pelvic calcifications such as phleboliths, distal ureteric stones and appendiceal faecaliths. Phleboliths are rare in children, located posteriorly in the pelvis and often have a radiolucent centre (Marquis, 1977). Ureteric stones are denser and more medially located, while appendiceal faecaliths are bigger, often only faintly calcified and can be moved by compression (Fiori et al, 1986).

Even though very rare, dystrophic calcifications in obliterated umbilical arteries must be considered in order to avoid unnecessary radiological exposure in those children in whom they present as a serendipitous finding.

References

CURRARINO, G. & WEINBERG, A., 1985. Dystrophic calcification in obliterated umbilical artery. *Pediatric Radiology*, *15*, 346–347.

Address correspondence to Dr G. Beluffi.
*Trainee in radiology.

1992, *The British Journal of Radiology*, 65, 349–350

FIORI, P., BELUFFI, G. & DALLOCCHIO, T., 1986. Coprolita appendicolare e anuria. *La Radiologia Medica*, *72*, 769–771.
MARQUIS, J. R., 1977. The incidence of pelvic phleboliths in pediatric patients. *Pediatric Radiology*, *5*, 211–212.
SIRINELLI, D., SILBERMAN, B., MONTAGNE, J. PH. & FAURE, C., 1989. Calcifications de l'artère ombilicale chez le petit nourrisson. *Journal de Radiologie*, *70*, 285–287.

Small bowel fistula secondary to endarteritis obliterans, complicating chemotherapy for small bowel lymphoma

By S. Knowles, H. E. Smart, *A. Al-Dawoud and D. J. Kerr

Beatson Oncology Centre, Belvidere Hospital, Glasgow and *Department of Pathology, Glasgow Royal Infirmary, Glasgow

(Received 17 May 1991 and in revised form 16 August 1991, accepted 3 October 1991)

Keywords: Lymphoma, Chemotherapy, Endarteritis obliterans

Endarteritis obliterans, pathological thickening of the intima associated with luminal stenosis of small and medium sized arteries, is a relatively common late tissue effect following radiotherapy, but it is not associated with cytotoxic drug administration. We report a patient treated with chemotherapy for recurrent lymphoma of the sigmoid colon, who developed a fistula between the large and small bowel which was associated with severe endarteritis obliterans.

Case report

A 66-year-old man presented to the surgeons with intermittent abdominal pain and diarrhoea. A barium enema demonstrated an annular narrowing in the sigmoid colon and the patient had a laparotomy which revealed a large tumour of the sigmoid colon invading the bladder and retroperitoneal structures. A palliative sigmoid colectomy was performed and a primary end to end anastomosis fashioned. Histological examination of the resected specimen of bowel revealed non-Hodgkin's lymphoma (diffuse centroblastic-centrocytic in type) and the patient was referred for further therapy. There was no evidence of arteritis in this specimen.

Clinical examination at this stage revealed a suprapubic mass, extending 10 cm above the pubic symphysis. Initial investigations were as follows: computed tomographic (CT) scan demonstrated a large soft tissue mass (10×7 cm) lying anteriorly in the left side of the lower pelvis; bone marrow trephine biopsy revealed normal, cellular marrow; normal full blood count; normal biochemical profile.

The patient was entered in the current, local Phase II trial of chemotherapy for non-Hodgkin's lymphoma. He received prednisolone 50 mg, daily orally throughout. Week 1—intravenous doxorubicin 35 mg/m^2 and cyclophosphamide 250 mg/m^2; Week 2—intravenous vincristine 1.4 mg/m^2 and bleomycin 10 mg/m^2; week 3—intravenous doxorubicin 35 mg/m^2 and oral etoposide, 100 mg/m^2 daily for 5 days.

By Week 4, the patient was severely myelosuppressed (total white cell count $= 0.8 \times 10^9$/l, platelets $= 67{,}000 \times 10^9$/l) and complained of frequent, watery diarrhoea, with 6–8 stools per day. On examination, the suprapubic mass had resolved, but there was generalized gaseous distension of the abdomen with normal bowel sounds. The appearance of the plain abdominal radiograph was consistent with distal subacute obstruction. Repeat abdominal CT showed that there had been complete resolution of the previously noted mass, although matted loops of bowel were noted above the bladder. Diarrhoea and gaseous abdominal distension persisted and a limited enema with Gastrografin demonstrated a fistulous connection between the small and large bowel.

Following recovery from myelosuppression, the patient had a further laparotomy and a perforated section of large bowel, and two perforated sections of small bowel were resected and a Hartman's procedure performed. Subsequent pathological examination of the material revealed ischaemic necrosis of the bowel wall associated with thickening of the intima and luminal stenosis of underlying small arteries, characteristic of endarteritis obliterans. Endarteritis was also noted in areas of the resected specimen not directly associated with ulceration.

Discussion

It would appear that this patient developed fistulae between the small and large bowel in association with

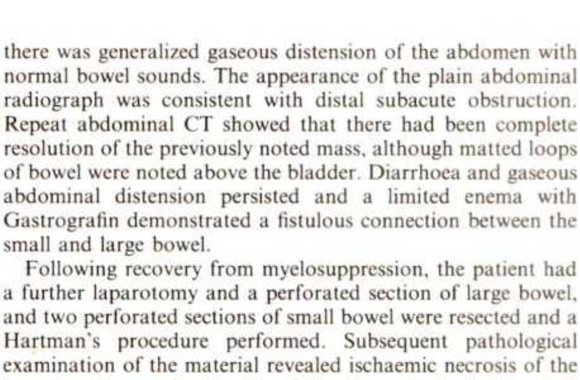

Figure 1. A medium size artery showing marked thickening of the intima and the media together with obliteration and recanalization of the lumen. (Haematoxylin and eosin ×29.)

Address reprint requests to Professor D. J. Kerr.

multifocal ischaemic necrosis secondary to severe endarteritis obliterans. This was contrary to our initial expectation as we thought it likely that he had perforated his bowel due to cytoreduction of his colonic lymphoma, in response to chemotherapy.

Obliterative endarteritis is found in chronic inflammatory conditions such as the base of chronic peptic ulcers, lesions of syphilis, silicosis and tuberculous meningitis and in small arteries exposed to radiotherapy (Marcial-Rojas & Castro, 1962; Silverberg, 1990). The changes of endarteritis obliterans were seen in areas not associated with ischaemic ulceration, which makes it more likely that the ulceration was secondary to the endarteritis rather than the obverse. As far as we are aware there are no reports linking non-Hodgkin's lymphoma with underlying endarteritis. There is some evidence to suggest that platinum based chemotherapy, especially in combination with vincistine and bleomycin, is vasculotoxic and is associated with Raynaud's phenomenon and cerebral and myocardial infarction (Doll et al, 1986). The pathophysiology of endarteritis obliterans is unclear in this case, but could relate to chemotherapy inclusive of vincristine and bleomycin.

Acknowledgments

The authors would like to thank Fiona Conway for typing the manuscript.

References

Doll, D. C., List, A. F., Greco, F. A., Smith, G. S. & Toit, L., 1986. Acute vascular ischaemic events after cisplatin-based combination chemotherapy for germ-cell tumours of the testis. *Annals of Internal Medicine, 105*, 48–52.

Marcial-Rojas, R. & Castro, J. R., 1962. Irradiation injury to elastic arteries in the course of treatment for neoplastic disease. *Annals of Otology, Rhinology and Laryngology, 71*, 945–958.

Silverberg, S. G., 1990. *Principle and Practice of Surgical Pathology*. 2nd Edn (Churchill Livingstone, Edinburgh), p. 87.

1992, *The British Journal of Radiology*, 65, 351–352

Case of the month

A case of malignant hypertension

By P. H. Williams, BM, BCh and A. P. Hemingway, FRCP, FRCR

Department of Radiology, Royal Hallamshire Hospital, Glossop Road, Sheffield S10 2PL, UK

(*Received 18 April 1991, accepted 16 May 1991*)

A 44-year-old woman presented with a 3 day history of central visual field impairment in the left eye, which had not changed since onset. The only past medical history of note was that during both pregnancies she had been hypertensive, for which she had required hospital admission. She had not been investigated post-partum and was on no anti-hypertensive medication.

On examination, she had a tachycardia of 112 per min with no radio-femoral delay, a blood pressure of 240/130 in both arms and a bruit audible over the left renal area. No abdominal mass was palpable. Fundoscopy showed a blot haemorrhage in the left retina, bilateral papilloedema with blurred disc margins and arterio-venous nipping. Urinalysis revealed proteinuria. The blood pressure remained elevated on atenolol, nifedipine and enalapril (180/95). A primary cause for her refractory hypertension was sought and in view of the bruit a renal arteriogram was performed (Fig. 1a, b & c).

What investigation is essential before proceeding with the arteriogram? What does the arteriogram show?

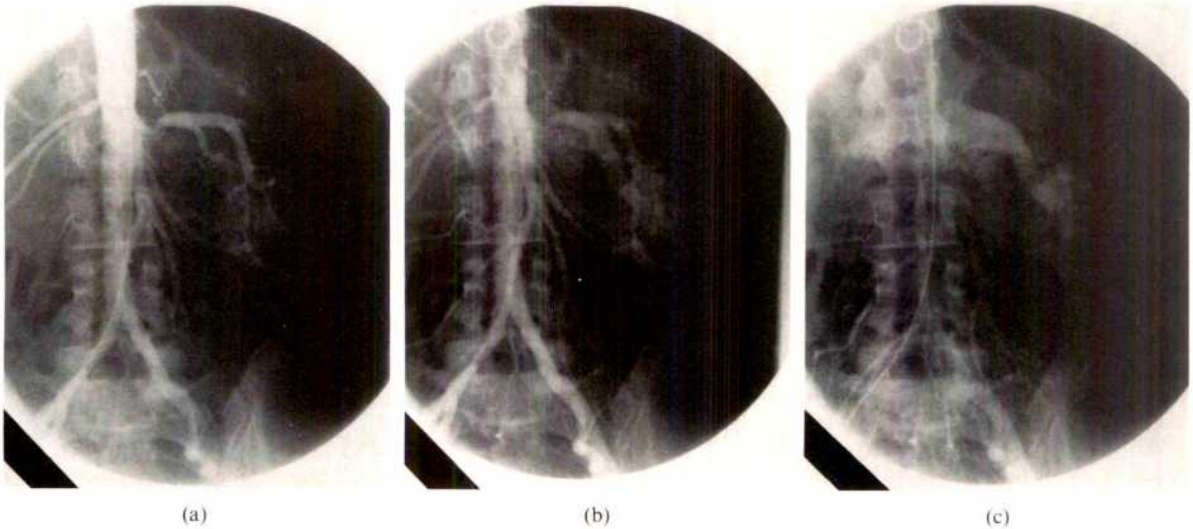

(a) (b) (c)

Figure 1a, b & c. Three right posterior oblique (RPO) views of the left kidney during a flush aortogram.

---

*Address correspondence to Dr P. H. Williams, Department of Radiology, Southampton General Hospital, Tremona Road, Southampton SO9 4XY.

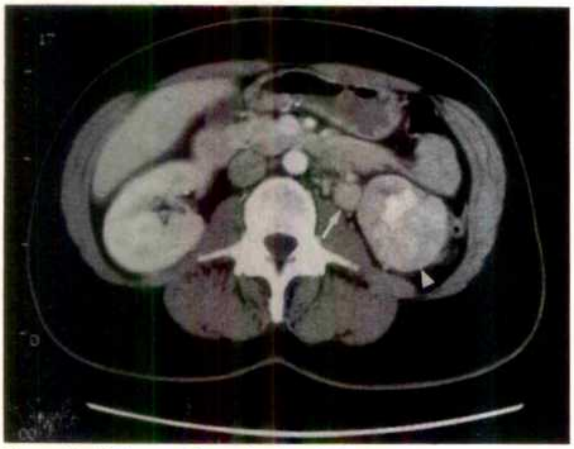

Figure 2. CT scan through the abdomen just below the left renal hilum showing the lower pole tumour (arrowhead) and involved lymph nodes lying medially (arrow).

Before undertaking arteriography in a patient such as this, the possibility of a phaeochromocytoma must be considered as injection of radiographic contrast material can provoke catecholamine secretion by the tumour and precipitate a dangerous or even fatal crisis if the patient is not adequately alpha- and beta-blocked beforehand. Biochemical evidence in the form of blood or urinary catecholamines must be sought before undertaking arteriography. Urinary vanillyl-mandelic acid (VMA) was normal in this patient.

The arteriogram showed a large tumour circulation in the lower pole of the left kidney (Fig. 1a). There was rapid arterio-venous shunting and early opacification of the renal vein (Fig. 1b & c). The renal artery was kinked (Fig. 1a) but not stenosed and the vein markedly dilated (Fig. 1b & c). There was evidence of increased vascularity in the para-aortic area suggestive of nodal involvement. The right kidney was normal.

A subsequent computed tomography (CT) scan confirmed the lower pole mass and identified 1 cm lymph nodes around the left hilum (Fig. 2). At operation, a renal cell carcinoma was removed together with lymph nodes containing metastatic deposits. Glands were seen around the renal pedicle but there was no compression of renal vessels. The patient was eventually discharged with a normal blood pressure on atenolol only.

Discussion

Hypertension, in 10–20% of cases, has a primary cause which it is important to seek, particularly in younger patients with grossly elevated blood pressures that are difficult to control. Renovascular hypertension is the commonest primary cause in such patients (Kaufman, 1979). The presence of a bruit over the upper abdomen is presumptive evidence of a renovascular lesion.

Table I. Causes of renal arterio-venous fistula

Congenital

Acquired
- Trauma iatrogenic
  - accidental
- Inflammatory diseases
- Rupture of aneurysm into vein
- Hypernephroma eroding vessels

The most likely cause of hypertension in this patient was fibromuscular hyperplasia, which accounts for 2% of cases of hypertension (Youngberg et al, 1977). The condition is more common in females than males and has a peak incidence in the third and fourth decades. It may produce a bruit over the renal artery.

Renal arterio-venous fistula is rare. Its causes are listed in Table I. Hypertension is the outstanding clinical feature, because normally functioning renal tissue is deprived of its blood supply which passes preferentially through the shunt. A bruit is typically present over the upper abdomen. Hypernephroma presenting with hypertension due to arterio-venous fistula, which resolves following removal of the tumour, is recognized but has been only rarely reported (Moran, 1990).

Extrinsic compression of the renal artery by a tumour mass has also been described as a reversible cause of hypertension (Savin et al, 1989). However, in this case, there was no evidence of compression of the renal pedicle either by the primary tumour or by involved lymph nodes.

In this patient, an aggressive hypernephroma had produced massive arterio-venous shunting in the left kidney with secondary hypertension. The blood pressure is now well controlled. Unfortunately, the prognosis for the primary condition is less favourable.

References

KAUFMAN, J., 1979. Renovascular hypertension: the UCLA experience. *Journal of Urology*, *121*, 139–144.

MORAN, A., 1990. Malignant hypertension due to renal carcinoma. *British Journal of Urology*, *65*, 299.

SAVIN, H., JUTRIN, I. & RAVID, M., 1989. Reversible hypertension due to renal hygroma. *Urology*, *33*, 317–319.

YOUNGBERG, S. P., SHEPS, S. G. & STRONG, C. G., 1977. Fibromuscular disease of the renal arteries. *Medical Clinics of North America*, *61*(3), 623–641.

Keywords: Kidney, Hypertension, Renal cell carcinoma

1992, *The British Journal of Radiology*, *65*, 353

Erratum

Improved image quality for dense breasts in mammography

J. Law

Please note that the films reproduced in parts (a) and (b) of Fig. 2 (p. 51) should be interchanged to correspond with the caption and the text.

Thus the lighter film was obtained with the normal exposure (28 kV, 63 mAs), and the darker film was obtained with the increased exposure (28 keV, 120 mAs).

The Publisher apologises to both the author and the readers for this error.

Reference

LAW, J., 1992. Improved image quality for dense breasts in mammography. British Journal of Radiology, 65, 50–55.

1992, *The British Journal of Radiology*, *65*, 354–355

Correspondence

(The Editors do not hold themselves responsible for opinions expressed by correspondents)

Ultrasonic findings in visceral *Pneumocystis carinii* infection in AIDS

THE EDITOR—SIR,

Pneumocystis carinii (*P. carinii*) pneumonia (PCP) is reported in approximately 75% of AIDS cases (Hughes, 1987). Extrapulmonary infection is considered rare but recently has been increasingly reported. Clinical features of extrapulmonary infection are non-specific but there are radiographic features which may be helpful in diagnosis. A case is described of biopsy-proven disseminated *P. carinii* infection with widespread visceral lesions demonstrated by ultrasonography.

A 35-year-old male homosexual in whom AIDS had been diagnosed 3 years earlier, was investigated for recent onset of weight loss and diarrhoea. An abdominal ultrasound revealed ascites but no other abnormality. He was hospitalized 5 weeks later in an advanced state of cachexia. Chest radiography showed no evidence of active PCP, but gastroscopy with mucosal biopsy revealed haemorrhagic areas of mucosa containing cyst forms of *P. carinii* without chronic inflammatory reaction. Abdominal ultrasound was repearted and now demonstrated multiple intensely echogenic lesions throughout the liver, kidneys (Fig. 1) and spleen. The lesions were mostly 1–2 mm in diameter but in the spleen and liver some of the lesions formed conglomerates of up to 2 cm in diameter. These larger lesions showed associated acoustic shadowing but this was not a feature of the majority of smaller lesions. A scan 7 days later, 1 day pre-mortem, showed multiplication and increase in size of the lesions. New lesions were also identified in the pancreas and the duodenal wall. A diagnosis of disseminated *P. carinii* infection was made but the patient died despite appropriate treatment.

A recent review of the world literature (Raviglione, 1990) included a total of 50 cases of extrapulmonary pneumocystosis. The commonest sites of extrapulmonary involvement were lymph nodes, spleen, liver and bone marrow. The diagnosis of extrapulmonary infection was most commonly made at postmortem and the presence of extrapulmonary multisystem involvement carried a particularly poor prognosis. Treatment was effective in some cases with a single extrapulmonary site of infection but, since the clinical features were so non-specific, such a diagnosis required a high degree of awareness of the condition.

Early reports of extrapulmonary *P. carinii* infection in the pre-AIDS literature (Awen & Baltzan, 1971; Rahimi, 1974) suggested dissemination of the organisms occurred by either the haematogenous, or more commonly, the lymphatic route. The "miliary" distribution of lesions, seen on ultrasound in the case described above, suggested blood-borne dissemination.

Rahimi (1974) described multiple miliary nodules in the spleen, kidneys and liver which, on microscopy, consisted of clumps of organisms with little inflammatory reaction. Such clumps were also seen in the wall of the stomach and small intestine. Histological examination in other cases demonstrated granulomas containing *P. carinii* organisms and dystrophic calcification (Feuerstein et al, 1990). The presence of granulomatous reaction and calcification is presumably related to the host's ability to mount an immune response and duration of infection.

The radiological findings in extrapulmonary *P. carinii* infection reflect the histological abnormalities. Radin et al (1990) described multiple punctate calcifications in the liver, spleen, kidneys and adrenals which were visible on computed tomography scanning and sometimes even on plain radiographs. Ultrasound of the liver, kidneys and spleen in two of these cases revealed innumerable echogenic dots without acoustic shadowing similar to those seen in our case. The demonstration of multiple visceral pinpoint or miliary lesions by ultrasound may be a relatively late feature of disseminated *P. carinii* infection, but the finding should suggest this diagnosis and allow biopsy and instigation of appropriate treatment.

Yours, etc.,

P. GRECH

Department of Radiology,
St Mary's Hospital,
Praed Street, London W2 1NY, UK

(*Received 22 November 1991, accepted 2 January 1992*)

References

AWEN, C. F. & BALTZAN, M. A., 1971. Systemic dissemination of *Pneumocystic carinii* pneumonia. *Canadian Medical Association Journal*, *104*, 809–812.

FEUERSTIEN, I. M., FRANCIS, P., RAFFELD, M. & PLUDA, J., 1990. Widespread visceral calcifications in disseminated *Pneumocystis carinii* infection: CT characteristics. *Journal of Computer Assisted Tomography*, *14*, 149–151.

HUGHES, W. T., 1987. *Pneumocystis carinii* pneumonitis. *New England Journal of Medicine*, *317*, 1021–1023.

RADIN, D. R., BAKER, E. L., KLATT, E. C., BALTHAZAR, E. J., JEFFREY, R. B., MEGIBROW, A. J. & RALLS, P. W., 1990. Visceral and nodal calcification in patients with AIDS-related *Pneumocystis carinii* infection. *American Journal of Roentgenology*, *154*, 27–31.

RAHIMI, S. A., 1974. Disseminated *Pneumocystis carinii* in thymic alymphoplasia. *Archives of Pathology*, *97*, 162–165.

RAVIGLIONE, M. C., 1990. Extrapulmonary pneumocystosis: the first 50 cases. *Reviews of Infectious Diseases*, *12*, 1127–1138.

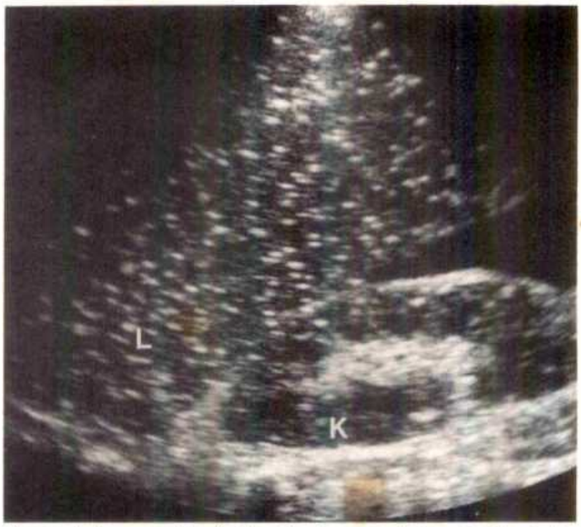

Figure 1. Innumerable "miliary" echogenic lesions in the right kidney (K) and liver (L). Similar lesions were seen in the spleen, pancreas, duodenal wall and left kidney (not shown).

Relapsing polychondritis

THE EDITOR—SIR,
Goddard et al (1991) have reported an unusual case of relapsing polychondritis which presented as acute encephalitis. I have treated a case of this condition with many of the other features described using radiotherapy with long term control. There was, however, no encephalitis.

A woman aged 43 presented in 1979 with malaise, anorexia and puffy inflammation of the pinnae, biopsy of one of which showed relapsing polychondritis. She was treated initially with prednisolone, azathioprine and chlorambucil, but her condition progressed to cough and stridor with collapse of the nose. She was treated with total nodal irradiation including the spleen to a dose of 2000 cGy in 10 daily treatments in two halves. There was a dramatic remission of all symptoms. Subsequently the inflammation of the pinnae relapsed. This responded to local radiotherapy in the same dose. She subsequently developed episcleritis which responded to local steroid therapy and later got stridor a second time. This responded to repetition of the total nodal irradiation. The pinnae relapsed again, but responded to re-irradiation in September 1990, and she has remained in remission to date.

Yours, etc.,
B. S. MANTELL

Department of Radiotherapy and Oncology,
The Royal London Hospital,
Whitechapel,
London E1 1BB, UK

(*Received 19 November 1991, accepted 14 January 1992*)

Reference

GODDARD, P., COOK, P., LASZLO, G. & GLOVER, S. C., 1991. Relapsing polychondritis: report of an unusual case and a review of the literature. *British Journal of Radiology*, *64*, 1064–1067.

Chest radiograph scoring system for use in pre-term infants

THE EDITOR—SIR,
Papers dealing with the chest radiograph in pre-term infants are sufficiently rare in the British radiological literature to merit enhanced attention. Yuksel et al (1991) are to be congratulated in helping to refine those features which have a bearing on the outcome of chronic lung disease in these infants.

Although not germane to the theme of the paper, I was struck by the fact that two patients had lobectomies because of expanding air cysts. I wonder whether the authors would still regard these operations as justified? The gross mediastinal displacements which these cysts can produce excites surgeons but most of them improve dramatically if the lung is "rested", either by balloon occlusion of the ipsilateral bronchus or by selectively passing the tracheal tube into the contralateral lung.

Yours, etc.,
I. HYDE

Timbers,
Chapel Lane, Lyndhurst,
Hants SO43 7FG, UK

(*Received 29 November 1991, accepted 30 January 1992*)

Reference

YUKSEL, B., GREENOUGH, A., KARANI, J. & PAGE, A., 1991. Chest radiograph scoring system for use in pre-term infants. *British Journal of Radiology*, *64*, 1015–1018.

Authors' reply

THE EDITOR—SIR,
We thank I. Hyde for his interest in our paper (Yuksel et al, 1991).

Two of our patients had undergone lobectomy for gross cystic degeneration following localized severe pulmonary interstitial emphysema. Both infants were ventilator-dependent at the time of lobectomy with deteriorating blood gases. As a consequence of this deterioration in respiratory status it was decided that they should undergo lobectomy following which their respiratory status improved and it was possible to extubate the infants.

These infants have been followed carefully since discharge from the neonatal unit and have no other respiratory problems. Lung function studies have been performed on both of these infants at 3 and 6 months following surgery and their functional residual capacity is within the normal range.

Although we agree that in certain infants it is possible to cause decompression of unilateral pulmonary interstitial emphysema by selective intubation of the contralateral bronchus, prolonged selective intubation may be poorly tolerated by critically ill infants and, unfortunately, does not result in decompression of interstitial emphysema in all cases and, indeed, was unsuccessful in the two patients we describe in the present report. We therefore do feel, in view of the excellent post-operative progress of these infants, that their operations were justified and we are pleased to emphasize that lobectomy is required in a relative minority of infants who have asymmetrical severe pulmonary interstitial emphysema.

Yours, etc.,
A. GREENOUGH
B. YUKSEL
J. KARANI
A. PAGE

King's College School of Medicine and Dentistry,
Bessemer Road,
London SE5 9PJ, UK

(*Received 2 January 1992, accepted 30 January 1992*)

Reference

YUKSEL, B., GREENOUGH, A., KARANI, J. & PAGE, A., 1991. Chest radiograph scoring system for use in pre-term infants. *British Journal of Radiology*, *64*, 1015–1018.

1992, *The British Institute of Radiology*, *65*, 356–359

Proceedings of the British Institute of Radiology

Hypoxic cell sensitizers: back in fashion?

Abstracts of papers presented at an all day meeting held at the BIR, 36 Portland Place, London W1N 4AT, on Friday 15 November 1991

Charimen: Dr J. M. Henk and Professor J. Denekamp

The clinical trial of hypoxic cell radiosensitizers, by S. Dische
New approaches to the use of bioreductive drugs in combination with radiation and other agents, by G. E. Adams, J. Bremner, E. M. Fielden, M. A. Naylor, I. J. Stratford and P. Wood
Oxygen and carbogen as radiosensitizers, by A. Rojas
The influence of carbogen breathing on hypoxic cells in human tumours, by S. J. Falk, R. Ward and N. M. Bleehen
Modifiers of haemoglobin/oxygen binding affinity as radiosensitizers, by D. G. Hirst and G. Calais
Alterations in tumour blood flow induced by chemical modifiers of radiation response: implications for therapy, by D. J. Chaplin
Hypoxic modification of tumours with special reference to the Danish head and neck study, by J. Overgaard. Abstract not received
Pentoxifylline—a modifier of blood cell deformability—as a radiosensitizer in a murine tumour, by D. J. Honess
Tumour oxygenation and radiosensitization by calcium antagonists, by P. J. Wood
Radiation chemical and *in vitro* studies on radiosensitization by DNA targeted compounds, by R. F. Anderson, W. A. Denny, P. B. Roberts and W. R. Wilson

The clinical trial of hypoxic cell radiosensitizers

S. Dische
Marie Curie Research Wing for Oncology, Mount Vernon Hospital, Northwood, Middx HA6 2RN

There has been a great effort in the clinic to apply laboratory knowledge concerning the oxygen effect to the benefit of patients receiving radiotherapy. A considerable number of randomized trials using hyperbaric oxygen have shown benefit but only a few of those using nitroimidazoles as hypoxic cell radiosensitizers. The results of studies using a second generation of chemical agents are now becoming available. In head and neck tumours nimorozole appears to give advantage but, so far, only a small non-significant margin has been shown with etanidazole. In carcinoma of the cervix, patients receiving pimonidazole did less well than those in a control group. The general lack of success with chemical agents probably lies in our failure to consider all the biological factors which may govern a response to radiotherapy. It is probable that tumours which show hypoxia are also those which have a capacity for rapid cellular proliferation so we may need to combine these approaches. Oxygen and the chemical agents may not lead to the same pattern of sensitization. There is promise that carbogen breathing with nicotinamide may prove a safer and more effective means of hypoxic cell radiosensitization than methods previously employed. Hypoxia is an important cause for radioresistance and is most probably a cause for radiation failure in at least some of the tumours which are treated clinically. There is sufficient in past experience to justify the present and future effort in the field.

New approaches to the use of bioreductive drugs in combination with radiation and other agents

G. E. Adams, J. Bremner, E. M. Fielden, M. A. Naylor, I. J. Stratford and P. Wood
MRC Radiobiology Unit, Chilton, Didcot, Oxon, OX11 0RD

It is well known that some bioreductive agents act as radiation sensitizers for hypoxic cells in tumours. One approach used in their development has been to seek compounds that are able to mimic oxygen in enhancing radiation action on mammalian cells by increasing the severity of radiation damage to intracellular DNA. There is much evidence that sensitizers such as misonidazole, etanidazole and related monofunctional nitroimidazoles act in this manner. More recently, emphasis has switched to the development of bioreductive drugs that are active as hypoxic cytotoxins. These agents are chemically reduced by intracellular enzyme reductases to form highly cytotoxic metabolites. Since many of these reductive processes are reversible by oxygen, the full expression of this toxic action is mainly evident in oxygen deficient tissues and this is the main rationale for their tumour selectivity. Classes of drugs include the dual function nitroimidazoles of which RB 6145, the lead compound, should shortly be available for trial, various fused ring quinones some of which are more hypoxia-specific analogues of mitomycin C, and some triazine di-N-oxides. In this paper, particular attention is given to a new series of fused pirazine mono-N-oxides of which RB 90740 is the lead compound. This agent is a potent hypoxic cytotoxin *in vitro* in a range of murine and human tumour cell lines with differential hypoxic/oxic cytotoxicity ratios up to about thirty. It is also highly active in experimental tumours *in vivo* when given post-irradiation. The compound is also vasoactive as shown by studies *in vivo* including magnetic resonance spectroscopy *in situ*.

Oxygen and carbogen as radiosensitizers

A. Rojas
Gray Laboratory of the Cancer Research Campaign, PO Box 100, Mount Vernon Hospital, Northwood, Middx HA6 2JR, UK

Since the early 1950s, normobaric oxygen and carbogen (95% O_2 + 5% CO_2) have been shown to be effective radiosensitizers in a variety of rodent tumours. Their use unfortunately was abandoned in favour of hyperbaric oxygen and chemical radiosensitizers. Recently, enhancement ratios (ER) of up to 1.45 were reported for oxygen with clinically relevant dose-fractionation regimes (30 fractions in 6 weeks and 36 fractions in 12 days). In fractionated schedules ERs in mouse tumours (1.3–1.6 for carbogen and 1.3–1.45 for oxygen) are greater than with chemical radiosensitizers, and allow for a significant therapeutic gain. Although rodent haemoglobin has a lower affinity for oxygen than human haemoglobin, polarographic measurements show a consistent and rapid increase of pO_2 in human tumours with both gases. The clinical and experimental evidence suggests that both carbogen and oxygen could be effective at overcoming hypoxic-cell radioresistance. More recently we have shown that the effectiveness of oxygen and carbogen can be further enhanced by nicotinamide, the amide derivative of vitamin B_3. Horsman et al showed large increases in tumour radiosensitivity with nicotinamide using single X-ray doses in air. In fractionated schedules in air we saw a small therapeutic benefit with nicotinamide, but the combination of carbogen or oxygen with nicotinamide gave a large and significant gain. Strikingly, an ER of ~2 in tumours was seen at 2 Gy per fraction for carbogen plus nicotinamide. Nicotinamide plasma concentrations of up to 1.1 $\mu mol\ ml^{-1}$ have been reported recently in humans, after an oral dose of 6 g. This is three- to five-fold lower than seen in mice with a dose of $0.4 g kg^{-1}$. However, combining carbogen with lower doses of nicotinamide than those used in our fractionated X-ray regimes should still give a considerable degree of radiosensitization. Single dose data show a similar ER for 0.5, 0.3 and 0.1 mg kg^{-1} of nicotinamide plus carbogen. The animal and human data obtained so far for carbogen alone or combined with nicotinamide and the very large therapeutic index of the vitamin indicate that carbogen with nicotinamide could be a potent radiosensitizer combination for use in radiotherapy and should be well tolerated in humans.

The influence of carbogen breathing on hypoxic cells in human tumours

S. J. Falk, R. Ward, N. M. Bleehen
University Department and MRC Unit of Clinical Oncology and Radiotherapeutics, Addenbrooke's Hospital, Hills Road, Cambridge, UK

The presence of hypoxic cells within human tumours is considered a major determinant of response to ionizing radiation. In mouse tumour models carbogen breathing (95% O_2, 5% CO_2) has been shown to increase radiosensitivity. We have used the novel polarographic microelectrode system (Eppendorf $p0_2$ histograph) to evaluate changes in tumour tissue oxygenation *in vivo* during carbogen breathing. In seven patients carbogen was inhaled through a closed system for periods of 15–30 min. A series of at least 200 tumour measurements in accessable tumours were taken before, and subsequently continuously from 2 min after the commencement of carbogen breathing, and presented in groups of 50 readings as oxygen partial pressure frequency histograms. In each patient there was an increase in mean tumour $p0_2$ during carbogen breathing, although there was a wide variation from 3–316%. There was a rapid increase in $p0_2$ during the first 5 min of carbogen breathing. This was maintained for 10–15 min, but then decreased throughout the subsequent treatment period. However, there was no consistent change in the proportion of hypoxic values (<10 mmHg). In a non-small cell lung cancer lymph node the proportion of hypoxic values fell from 48% to 18%, but in a primitive neuro-epithelioma there was a smaller reduction from 20% to 18%. Carbogen breathing can increase tumour $p0_2$ in man and may reduce the proportion of hypoxic cells. This occurs rapidly following the commencement of carbogen breathing and thus has implications for the planning of clinical trials utililizing radiotherapy with carbogen breathing.

Modifiers of haemoglobin/oxygen binding affinity as radiosensitizers

D. G. Hirst and G. Calais
CRC Gray Laboratory, PO Box 100, Mount Vernon Hospital, Northwood, Middx HA6 2JR, UK

The oxygenation of tumours, in common with all tissues is dependent on the properties of the circulating blood. Radiobiologists have been aware for some time that alterations in haemoglobin level, viscosity, pO_2 and oxygen binding affinity can influence the oxygenation of tumours and modify their radiosensitivity. Changes in Hb/O_2 binding affinity occur naturally as a powerful means of compensating for inadequacies in inspired pO_2 or haemoglobin level and are well documented in anaemic cancer patients. There is clear evidence from experimental studies in the laboratory that when the Hb/O_2 binding affinity is reduced by a variety of means, transplanted tumours can be sensitized to radiation. Our studies have focused on the use of drugs to modify haemoglobin. In some of our previous studies, several antilipidaemia drugs have been shown to reduce Hb/O_2 binding affinity *in vivo* and to sensitize tumours to radiation. The most effective agent, clofibrate, reduced the fraction of radiobiologically hypoxic cells in several rodent tumours by factors of 3–10 at doses of 0.3–4.1 mmole/kg. Large single doses of radiation were used. The purpose of the experiments described here was to determine the effectiveness of this approach using more clinically relevant radiation fractionation and to determine under these conditions how much clofibrate would have to be given to obtain significant radiosensitization. Clofibrate at several doses was administered p.o. before each of 10 fractions of radiation given in 5 days to intradermal NT carcinomas in the CBA mouse. Irradiation was carried out in 2.5–8.0 Gy fractions using a 250 kVp X-ray machine. The response to treatment was assayed using regrowth delay as the end point. The optimum pre-irradiation interval for clofibrate administration was found to be 2 h for single doses, confirming our previous experience with other tumours: when combined with the 10 fraction in 5 day regime intervals between 2 and 4 h were equally effective. Clofibrate dose-response curves were constructed from data obtained for high and low (clinically relevant) doses per fraction (10 F/5 day). An enhanced response to radiation was seen at a clofibrate dose of 0.5 mmole/kg, though the individual data sets were not significantly different from controls until 1.0 mmole/kg. Full radiation dose-response curves gave enhancement ratios of 1.21–1.28 (±0.04–0.06; 95% CL) over a range of total dose from 25–60 Gy. Clofibrate reduces the binding affinity of haemoglobin for oxygen so that, as well as promoting the release of oxygen to the tissues, it also reduces slightly its uptake from the lungs. We have therefore combined clofibrate (2 h before irradiation) radiosensitization with the breathing of carbogen (95% O_2, 5% CO_2) 5 min before and during irradiation, to establish if additional sensitization could be achieved. A slight additional effect was obtained though it did not reach the level of statistical significance. There is no doubt that clofibrate can oxygenate mouse tumours and sensitize them to radiation. The doses required are, however, higher (by factors of 4 to 8) than have been used clinically for the long term control of hyperlipidaemia. In this situation, however, clofibrate is given daily over many months and very little information is available for acute high dose toxicity in man. This information will be needed before any clinical usefulness as a radiosensitizer can be established.

(This work is supported by the Cancer Research Campaign.)

Alterations in tumour blood flow induced by chemical modifiers of radiation response: implications for therapy

D. J. Chaplin
Xenova Ltd, 240 Bath Road, Slough, UK

Temporal and spatial heterogeneity in tumour blood flow is known to occur in experimental murine tumours and human tumour xenografts. If it also occurs in primary tumours it could limit the efficacy of radiation and some chemotherapy treatment regimes. Thus drugs which prevent the transient microregional alterations in tumour blood flow could provide a class of agents with a defined use in cancer therapy. The most effective agent identified to date in reducing microregional alterations in blood flow is nicotinamide. This compound is known to improve the radiation response of tumours when used alone. One obvious way to improve the radiation response even further is to combine an agent which overcomes blood flow heterogeneity with a modality which improves the oxygen carrying capacity of the blood. Recent studies in murine tumour systems with nicotinamide combined with fluosol DA and carbogen have demonstrated that large enhancements of radiation response can be achieved. Knowledge of how microregional heterogeneity of blood flow can influence the outcome of radiation therapy raises the question of whether drugs administered prior to radiation treatment alter blood flow. Studies with the radiation sensitizer pimonidazole have shown that it can reduce tumour blood flow in experimental murine tumours when administered intravenously. Similar results have been obtained with the bioreductive drug RSU1069. In contrast results with cis platinum indicate that this can increase tumour blood flow. These results have potentially important consequences for therapeutic outcome and indicate that blood flow modifying effects of drugs used in combination with radiation therapy should be measured.

Pentoxifylline—a modifier of blood cell deformability—as a radiosensitizer in a murine tumour

D. J. Honess
MRC Clinical Oncology and Radiotherapeutics Unit, MRC Centre, Cambridge CB2 2QH, UK

Pentoxifylline is a methylxanthine known to increase the deformability of erythrocytes and leucocytes, thereby facilitating their passage through congested vasculature, and has previously been used clinically to treat the vascular disorder known as claudication. An agent which can decrease blood viscosity by this mechanism should be able to improve compromised tumour blood flow and hence increase tumour oxygenation and radiosensitivity. This hypothesis has been tested using the RIF-1 tumour system, grown subcutaneously in the lower back, and used at 400-800 mm^3. The pharmacokinetics of pentoxifylline were measured by HPLC for intraperitoneal doses of 100 mg/kg and 10 mg/kg. The kinetics were dose-dependent with half-lives (±2 s) of 7.6 (7.2–7.9) and 4.6 (4.2–5.1) min, respectively. Relative tissue perfusion was measured using the ^{86}Rb extraction technique, giving up pentoxifylline at a range of doses from 5 to 100 mg/kg 15 min before iv injection of ^{86}Rb, *i.e.* after 2–3 pentoxifylline half-lives. Increased perfusion, expressed as percent of control values ±2 s, was measured following doses of 10 mg/kg (130±26%; 137±19%), 20 mg/kg (157±29%; 124±14%), 50 mg/kg (170±22%) and 100 mg/kg (150±12%). Perfusion changes in skin, muscle, kidney, liver and lung were minimal, although spleen perfusion was elevated. Radiation survival was measured by clonogenic assay immediately after 25 Gy 250 kV irradiation; irradiation was started 15 min after drug administration. Mean surviving fraction ±2 s for radiation alone was 8.2 (6.8–10.0) x 10^{-4}, and 5.5 (3.4–9.0) x 10^{-4} for 5 mg/kg; 2.1 (1.4–3.3) x 10^{-4} for 10 mg/kg; 3.8 (2.1–6.8) x 10^{-4} for 20 mg/kg; 3.8 (2.9–5.1) x 10^{-4} for 50 mg/kg and 5.5 (3.2–9.4) x 10^{-4} for 100 mg/kg. This demonstrates that the measured increase in perfusion is associated with increased radiosensitivity. Unlike the radiosensitizer nicotinamide, pentoxifylline is effective as a tumour perfusion modifier and radiosensitizer at doses which neither reduce core temperature nor inhibit renal clearance. Pentoxifylline shows considerable promise as a radiosensitizer and warrants further evaluation.

Tumour oxygenation and radiosensitization by calcium antagonists

P. J. Wood
MRC Radiobiology Unit, Chilton, Didcot, Oxon OX11 0RD

The calcium antagonists prevent contraction of cardiac and vascular smooth muscle by blocking calcium uptake via the plasma membrane calcium channel, and may be subclassified by chemical structure and preferential target site within the cardiovascular system. Verapamil and diltiazem are primarily cardiac acting, while nifedipine targets major blood vessels, and flunarizine has peripheral activity. Studies with murine tumours show that these four agents at clinically acceptable doses (0.05–5 mg/kg) are radiosensitizers, all producing a 5–10 fold increase in cell kill. This radiosensitization is associated with an increase in tumour blood supply, as measured by ^{86}Rb extraction. In addition, a reduction in inorganic phosphate (Pi) is seen after flunarizine treatment, using ^{31}P MRS, the time course of which coincides with that for radiosensitization. These results indicate that the calcium antagonists are improving tumour oxygenation by increasing blood supply, irrespective of their target site within the host cardiovascular system. Since clinical data indicates that these agents have minimal effects on a normal cardiovascular system, the physiological state of the tumour itself may be responsible for the manifestation of calcium antagonist activity. Thus, increased tumour oxygenation by the calcium antagonists at clinically acceptable doses, with minimal effects on the host cardiovascular system, indicates their potential as clinical radiosensitizers.

Radiation chemical and *in vitro* studies on radiosensitization by DNA targeted compounds

R. F. Anderson, *W. A. Denny, +P. B. Roberts and W. R. Wilson
*The Gray Laboratory of the Cancer Research Campaign, PO Box 100, Mount Vernon Hospital, Northwood, Middlesex, HA6 2JR, *Cancer Research Laboratory and Pathology Department, University of Auckland School of Medicine, Auckland, New Zealand and +Institute of Nuclear Sciences, DSIR, PO Box 31 312, Lower Hutt, New Zealand*

The radiosensitizers etanidazole and pimonidazole represent attempts to develop sensitizers less toxic than misonidazole through the manipulation of pharmacokinetics. An alternative approach to improving therapeutic potential through increasing sensitizing potency relative to intrinsic cytotoxicity has received less attention. Targeting electron-affinic compounds to DNA and thereby, perhaps, increasing the interactions between the compounds and radical-damaged sites on DNA is of interest as an approach to try to improve radiosensitization potency. Also there is some evidence that such DNA targeting offers, at the same time, a decrease in availability of radiosensitizers to the bioreductive enzymes responsible for toxicity. The possible value of this approach can be assessed from combined radiation chemical and *in vitro* studies where the kinetics of the interaction between DNA radicals and compounds can be compared with radiosensitization. Our initial approach has been to use electron-affinic intercalators to see if positioning compounds between the DNA bases gives rise to increased interaction between the compounds and DNA radicals. The first series of compounds investigated, nitroacridines, show a correlation between the scavenging of migrating electrons (formed by attachment of e_{aq}^- to the DNA) and radiosensitization potency. However, their potency is much less than for non-intercalating nitroheterocycles of similar redox potential on an intracellular concentration basis. Tight binding and high cellular uptake severely limits intercellular diffusion and may also restrict interaction with target radicals. Nitroquinolines, which bind much more weakly to DNA than nitroacridines, show better penetration into spheroids but do not increase radiosensitization potency over that seen for nitroheterocyles. In all cases, toxicity appears to be increased to a greater extent than radiosensitization by DNA binding. While other electron-affinic compounds that are even weaker than DNA binders are being investigated, attention is turning to non-electron affinic compounds (and hence of low toxicity) which interact with DNA radicals to separate redox dependent cytotoxicity and radiosensitization.

A report of this meeting is given in the BIR Bulletin at the back of this issue of BJR (p. B31).

1992. *The British Journal of Radiology*, *65*, 360

Book reviews

MRI of the Extremities: An Anatomic Atlas. By H. S. Kang and D. Resnick, 1991 (W. B. Saunders Co., Eastbourne), £85.00. ISBN Not known

Reviewing this textbook was a relatively simple task as it only comprises of images of the joints.

The book is divided into seven sections, covering the shoulder, elbow, wrist and hand, fingers, hip, knee, ankle and foot. Multiple sections are displayed through each joint in coronal, axial and sagittal planes using a T_1-weighted sequence and displayed on the same page as an anatomical section in precisely the same plane in colour. The images were obtained at 1.5 Tesla using an extremity coil for the elbow, wrist and hand, finger, knee, ankle and foot with a head coil for the shoulder and hip. The pictures are well annotated with lines leading from the named structure outlined for clarity. The anatomical sections correspond very closely with the magnetic resonance (MR) sections. For the shoulder the coronal and sagittal images are orientated with respect to the gleno-humeral joint rather than the body. In some of the images the joint anatomy was enhanced by intra-articular injection of a solution of copper sulphate. The photographs are of high quality and the MR images are "state-of-the-art".

This atlas provides the answer for the observant student who indicates a small, round dark structure in the foot, will not be satisfied by being told it is a tendon and recourse to Gray's anatomy does not provide a section in exactly the right plane. It makes an ideal reference manual for all MR departments that perform musculo-skeletal imaging, but is unlikely to find its way into personal libraries.

J. B. Bingham

Atlas of Diagnostic Radiology of the Horse Part 3: Diseases of the Head, Neck and Thorax. By Kees Dik and Ilona Gunsser, pp. 171, 1990 (Wolfe Publishing, London). £65.00. ISBN 0-7234-1638-9

I can remember purchasing Part 1 in this series which covered the fore limb. I was a university veterinary radiologist with, as is often the case, more experience in small animal radiology. In most veterinary faculties, except in the USA and Utrecht, this would be a common occurrence as radiology departments in this country are not big enough to support specialists in both large or small animal radiology. To this end I hoped that such a collection of atlases would expose me to the collective experience of two well known large animal experts. I suppose I have not been disappointed.

The latest addition to the series covers radiology of the head and neck which is well within the scope of most equine practitioners, even with relatively low output portable X-ray sets. Chest radiology is, of course, only really practicable in larger institutions. A linear tomographic view of a cerebral abscess is included, which is probably a little far fetched and beyond the scope of the general practitioner. The aetiology of the abscess was iatrogenic and I would hope that this hardly represents a common condition!

The quality of the book and the radiographic reproductions is very high and the accompanying line diagrams, where appropriate, are mostly helpful. The only poor films are those of dental disease, where the area of interest includes the very radiodense tooth roots and the air lucency of the paranasal sinuses in close proximity. Such areas often need bright light illumination and are obviously impossible to reproduce in a textbook. The text is brief and is essentially comprised of brief clinical details and concise radiological reports, which accurately employ the nomenclature accepted and approved by the American College of Veterinary Radiology. The bilingual format (German/English) is a little irritating, but is understandable when such texts are likely to have a very limited circulation.

This format provides a reference atlas for the rusty large animal radiologist, a useful set of examples with good radiological description and syntax for the trainee radiologist and a reference book for equine practitioners and undergraduates. I am always wary of thoroughly recommending atlas texts to the latter two categories of reader, as there is always a temptation to make the clinical films "fit" a picture in the book. This is dangerous as this is an incomplete text and the examples shown may not necessarily be "classic cases".

The cost (£65.00) is likely to confine its circulation to libraries and radiologists and the very keen equine practitioner. I would still consider it good value for money.

J. V. Davies

1992, *The British Journal of Radiology*, *65*, 361–369

VOLUME 65 NUMBER 773 MAY 1992

The British Journal of Radiology

High-intensity zone: a diagnostic sign of painful lumbar disc on magnetic resonance imaging

By C. Aprill, MD and *N. Bogduk, MBBS, PhD

Diagnostic Conservative Management, 3715 Prytania Street, New Orleans, and *Faculty of Medicine, University of Newcastle, Newcastle 2308, Australia

(*Received 12 August 1991 and accepted 22 October 1991*)

Keywords: Lumbar spine, Back pain, MRI

Abstract. The prevalence, validity and reliability of high-intensity zones in the annulus fibrosus seen on T_2-weighted magnetic resonance images of patients with intractable low-back pain were determined. This sign was readily recognized by two independent observers. It occurred in 28% of 500 patients undergoing magnetic resonance imaging for back pain. The presence of a high-intensity zone correlated significantly with the presence of Grade 4 annular disruption and with reproduction of the patient's pain. Its sensitivity as a sign of either annular disruption or pain was modest but its specificity was high, and its positive predictive value for a severely disrupted, symptomatic disc was 86%. This sign is diagnostic of painful internal disc disruption.

Magnetic resonance imaging (MRI) provides high-quality images of the central nervous system and surrounding tissues. Understandably, therefore, when MRI has been employed in the study of lumbar disorders it has largely been in the pursuit of lesions affecting the lumbar nerve roots, such as disc herniations, lateral canal stenosis and post-operative root fibrosis (Breger et al, 1989; Bundschuh et al, 1988; Burnett & Levine, 1986; Chafetz et al, 1983; Crawshaw et al, 1984; Djukic et al, 1990; Edelman et al, 1985; Frocrain et al, 1989; Hochhauser et al, 1988; Hueftle et al, 1988; Hyman & Gorey, 1988; Kent & Larsen, 1988; Kricun et al, 1990; Lee et al, 1988; Maravilla et al, 1985; Masaryk et al, 1988; Modic & Weinstein, 1984; Modic et al, 1984, 1986a,b; Murayama et al, 1990; Ross et al, 1987, 1989a,b; Sotiropoulos et al, 1989; Weisz & Kitchener, 1987; Weisz et al, 1988). This emphasis, however, contrasts with the epidemiology of low-back disorders.

Clinical studies have shown that fewer than 30% and as few as 5% of low-back problems can be legitimately ascribed to nerve root compression (Friberg, 1954; Horal, 1969), and contemporary authorities place this figure perhaps as low as 1% (Mooney, 1987). The majority of low-back disorders present with back pain, with or without referred pain, but not with sciatica and objective neurological signs. Such presentations deny a neurogenic basis for the pain, and suggest a somatic origin within the musculoskeletal tissues of the lumbar spine.

Prominent amongst putative, somatic sources of back pain are intrinsic disorders of the lumbar intervertebral discs. One condition, described by Crock (1970, 1986), is that of internal disc disruption. This condition is characterized by disruption of the internal architecture of the disc, which becomes painful, but its external shape remains essentially normal, and nerve root compression is not involved. Consequently, myelograms and computed tomographic (CT) scans are normal (Crock, 1986).

The pathology of internal disc disruption involves disruption of the inner annulus fibrosus in the form of radial fissures. Its pathogenesis is believed to be an inflammatory, biochemical degradation of the disc matrix following compression injury of a vertebral end-plate (Bogduk & Twomey, 1991). The disc becomes painful as a result of chemical irritation of the nerve endings in the outer fibres of the annulus fibrosus, or as a result of excessive strains being incurred by these fibres in the course of normal activities of daily living (Antti-Poika et al, 1990; Bogduk, 1988; Bogduk & Twomey, 1991).

The studies of Vanharanta et al (1987, 1988) have shown that the morphological features of internal disc disruption can be demonstrated by CT-discography, and strong correlations occur between the extent of annular diusruption and the reproduction of the patient's pain by provocation discography. Fissures restricted to the inner third of the annulus fibrosus are rarely associated with pain, but over 70% of fissures reaching the outer third of the annulus are associated with pain reproduction, and, reciprocally, over 70% of painful discs exhibit third-degree fissures as defined by the Dallas discogram scale (Sachs et al, 1987;

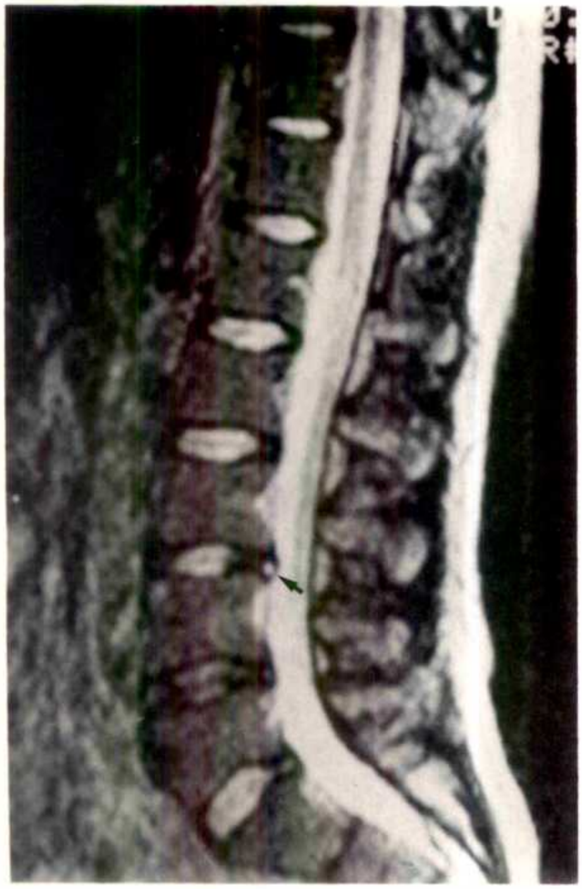

Figure 1. A T_2-weighted, mid-sagittal magnetic resonance image of a lumbar spine (TR2000, TE100) showing a high-intensity zone (arrow) in the annulus fibrosus of the L3–4 disc.

Vanharanta et al, 1987, 1988). In this context the results of provocation discography are highly specific. Provocation discography is not painful in normal volunteers (Walsh et al, 1990). Reproduction of pain by discography is therefore indicative of a clinically significant abnormality of that disc.

However, CT-discography is not an appealing means of diagnosing internal disc disruption, and is an invasive and complicated procedure. Also, it involves considerable radiation exposure to the patient (Nachemson, 1989). For these reasons some physicians have an aversion to the procedure, even though it is the only known way of objectively demonstrating internal disc disruption. A less invasive procedure is desirable to provide evidence of internal disc disruption and MRI provides this.

MRI demonstrates internal disc morphology not just contour. Good quality, spin-echo (SE), T_2-weighted images provide contrast between the nucleus pulposus and the outer annulus of normal discs. Signal intensity is proportional to the water content of the proteoglycan matrix of the disc (Gibson et al, 1986; Hickey et al, 1986; Hukins et al, 1988; Jenkins et al, 1985; Modic et al, 1984; Panagiotocopulos et al, 1987). By signal reduction, SE T_2-weighted images reveal degradation of the matrix in diseased discs. Thus some of the changes of symptomatic, internal disc disruption could possibly be revealed by MRI.

Initial studies indicate that there is a correlation between loss of signal intensity on MRI and abnormal morphology of the disc as seen on discography (Gibson et al, 1986; Schneiderman et al, 1987; Weisz et al, 1988). However, correlations have not been explored between MRI and pain reproduction by provocation discography or the internal structure of the disc as seen on CT-discography, the object of the present study.

In idiopathic low back pain, focal, high-intensity signal located in the posterior annulus fibrosus in one or more of the lumbar intervertebral discs as seen on SE T_2-weighted, sagittal images of the lumbar spine was noted. This sign seemed common and appeared to correlate with the affected disc being symptomatic on provocation discography. A formal study was therefore undertaken to determine the prevalence of this sign and its reliability and validity.

Method

Criteria were established to define what was to become known as the high-intensity zone (HIZ). These were a high-intensity signal (bright white) located in the substance of the posterior annulus fibrosus, clearly dissociated from the signal of the nucleus pulposus in that it is surrounded superiorly, inferiorly, posteriorly and anteriorly by the low-intensity (black) signal of the annulus fibrosus and is appreciably brighter than that of the nucleus pulposus (Fig. 1). This contrast can be best appreciated by viewing the image at arm's length against bright sunlight.

Provided the above criteria are satisfied, the HIZ can be considered to be present regardless of the state of the annulus fibrosus. It can occur centrally in an otherwise normal annulus or in a bulging annulus, or it may be located superiorly or inferiorly behind the edge of the vertebral body in a severely bulging annulus (Fig. 2). In the latter case the HIZ is distinguished from a disc prolapse by being discontinuous with the nucleus pulposus, and by the presence of an uninterrupted high-intensity signal of the annulus surrounding the HIZ and separating it from the epidural space.

To determine the reliability of these criteria, 67 T_2-weighted sagittal images of lumbar spines were viewed independently by each of two observers who scored the images for presence of absence of an HIZ.

The prevalence of HIZ was determined by scoring prospectively the images of 500 consecutive patients who were referred for, and underwent, MRI in a specialized, spinal, diagnostic radiology facility. All patients who underwent imaging in the period January 1989 to April 1990 entered the study; none was excluded.

The patients were aged between 20 and 60 years, with a male : female ratio of 5 : 2. They were drawn largely from the metropolitan area of New Orleans, but

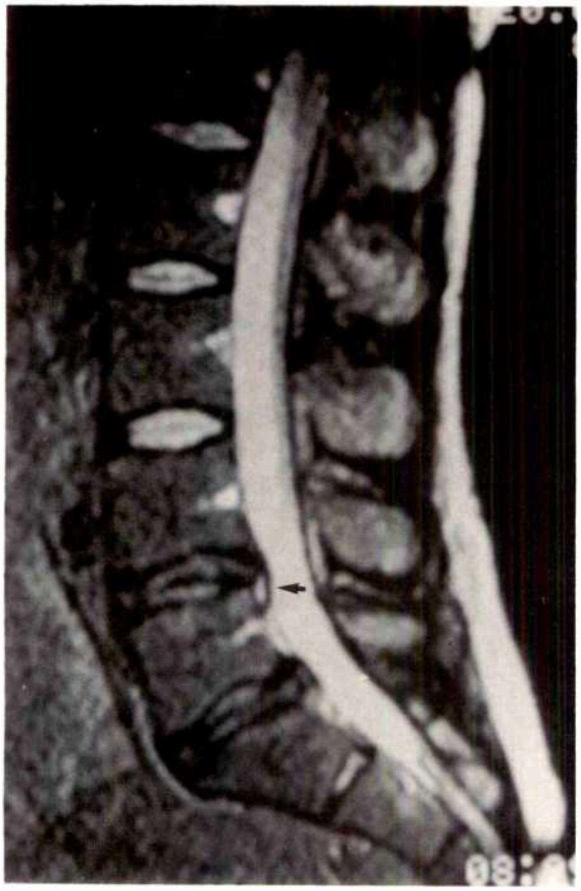

Figure 2. A T_2-weighted, sagittal magnetic resonance image of a lumbar spine (TR2000, TE100) showing a high-intensity zone (arrow) located inferiorly behind the L5 vertebral body but within the L4–5 annulus fibrosus.

included some interurban and interstate referrals. All had low back pain with or without referred pain or radicular pain in the lower limb, which had been present for at least 3 months. The pain was sufficiently disabling for them to have sought specialist attention from an orthopaedic surgeon, neurosurgeon or specialist in physical medicine. The referring physician had not been able to formulate a definitive diagnosis on the basis of conventional clinical examination, plain radiography or CT scan, and, consequently, referred the patient for MRI.

All MRI scans were acquired on a Technicare system (Technicare, Teslacon–Solon, Ohio, USA) operating at 0.6 T. A 7.5 in surface coil was employed. Each study included images in the coronal, axial and sagittal planes. Section thickness varied from 4.0 mm to 5.0 mm with 1.0 mm interspace gaps. SE and gradient pulse sequences were employed. T_2-weighted images were obtained with long repetition times (TR 1800–2200 ms) and long echo times (TE 80–120 ms). Additional parameters included two to four excitations and acquisition with 196 × 256 or 256 × 256 matrix, and display at 256 × 256. Occasionally cardiac gating was employed for motion suppression.

The morphology of the HIZ and its relationship to symptoms was studied in a subset of 41 patients in whom discography and post-discography CT scanning could be performed. These patients had been referred for both MRI and later discography as part of a staged, spinal investigation. The patients were aged 36 ± 8 years (mean ± SD); all had low back pain, but none had neurological signs or other features of nerve root compression. For ethical reasons, discography could not be performed in those patients who had been referred solely for MRI.

Discography was performed using a standard, postero-lateral, extrapedicular approach using a single 22 g or 25 g spinal needle at L4–5 and above, and a double needle technique (25 g/20 g) at the L5 level. At least two discs were studied in each patient, including the one exhibiting the HIZ. Under image intensifier guidance, the needle was directed towards the centre of the disc. Once accurate placement had been achieved, 1.5–3.0 ml of non-ionic contrast medium (Iohexol) was slowly instilled into the nucleus using a 3 ml syringe. Intermittent screening during injection verified nuclear opacification. Contrast medium installation was stopped if pain was induced or if firm resistance was encountered.

A disc was classified as symptomatic if, on injection, the patient's accustomed pain was reproduced, provided that injection of at least one adjacent disc did not reproduce symptoms. No positive diagnosis was entered unless one adjacent disc was found to be asymptomatic. A diagnosis of multiple symptomatic discs was entered if stimulation of more than one disc reproduced symptoms, but provided that at least one adjacent disc was discerned as asymptomatic.

CT scanning was performed between 1 and 3 h after discography. Scans were obtained using a TECH 2020 HR scanner. Cuts of 5 mm × 3 mm or continuous 2 mm cuts were obtained using windows and centre settings optimal for defining contrast medium and bone.

The morphology of the CT discograms was classified according to the Dallas discogram scale for annular disruption (Sachs et al, 1987), which recognizes four grades of annular disruption: "0" if the contrast medium is restricted to the annulus fibrosus; "1" if it extends radially along a fissure into the inner third of the annulus; "2" if it extends into the middle third; and "3" if it extends into the outer third (Fig. 3). For the present study, this scale was extended to record a Grade 3 disruption in which the contrast medium also spread circumferentially through the annulus fibrosus. This was defined as a Grade 4 disruption. A Grade 4 disruption was distinguished from Grade 3 if the contrast medium spread circumferentially within the substance of the annulus fibrosus and subtended an arc greater than 30° at the centre of the disc.

Once data has been collected on the presence of an

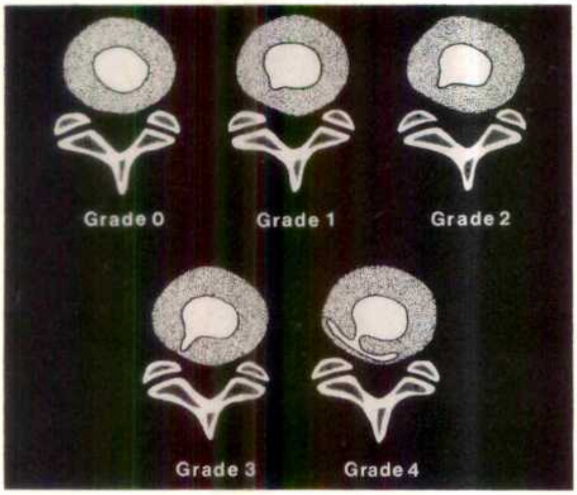

Figure 3. Diagrams of the grades of annulus disruption evident on CT-discography based on the Dallas discogram scale (Sachs et al, 1987).

HIZ, the response to discography and the appearance of the CT scan, contingency tables were constructed. Correlations were explored using a χ^2 test for significance.

Results

Of the 67 selected images, the two observers disagreed on the presence of an HIZ in only one instance (Table I). In that case, while both observers agreed on the presence of a rarefaction at a site appropriate for an HIZ, one observer felt that the criterion of brightness was not satisfied because of the poor quality of the film. Apart from this one case, the two observers were fully in agreement as to the presence or absence of an HIZ, a concordance in 66 out of 67 patients, or in 411 out of 412 discs (Table I).

Of the 500 patients studied, 143 exhibited an HIZ in at least one disc, a prevalence per patient of 28.6%. 16 patients exhibited HIZs at two segmental levels. HIZs occurred largely at L4–5 and L5–S1. They were infrequent at L3–4 and not encountered at either L2–3 or L1–2 (Fig. 4).

Table I. Concordance between two observers as to the presence of a high-intensity zone (HIZ) in a given patient and in a given disc

Observer 1	Observer 2	
	HIZ present	HIZ absent
Concordance by patient ($n = 67$)		
HIZ present	47	1
HIZ absent	0	19
Concordance by disc ($n = 412$)		
HIZ present	167	1
HIZ absent	0	244

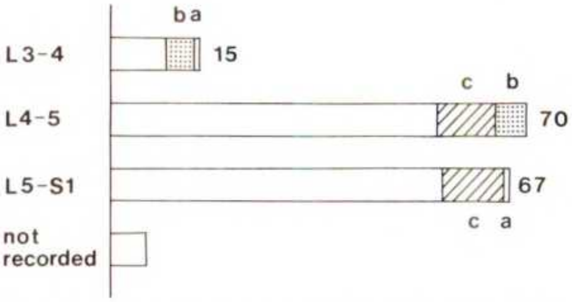

Figure 4. A frequency histogram showing the segmental location of high-intensity zones affecting 158 discs in 143 patients from a sample of 500 patients. (a) One patient with HIZs at both L3–4 and L5–S1. (b) Five patients with HIZs at both L3–4 and L4–5. (c) 10 patients with HIZs at both L4–5 and L5–S1.

In all patients who exhibited an HIZ, CT-discography of the affected disc revealed either a Grade 4 or a Grade 3 annular disruption (Fig. 5). No disc with an HIZ was normal on CT-discography (Table II). Grade 4 disruptions also occurred in discs without an HIZ, but many discs without HIZ were structurally normal on CT-discography. The contingency table shows that the correlation between the extent of annular disruption

Table II. Contingency table for the grade of annular disruption and presence or absence of a high-intensity zone (HIZ) in 106 lumbar discs in 41 patients

HIZ	Annular disruption grade				
	4	3	2	1	0
Present	37	4	0	0	0
Absent	31	3	6	3	22

$\chi^2 = 24.2$, d.f. $= 4$; $p < 0.01$.
For Grade 4 disruption, sensitivity = 37/68 (54%), specificity = 34/38 (89%), and positive predictive value = 37/41 (90%).

Table III. Pain response according to grade of annular disruption in 106 discs in 41 patients studied by CT-discography

Disruption grade	Pain reproduction		
	Exact	Similar	Nil
0	0	3	19
1	0	0	3
2	0	0	6
3	3	3	1
4	35	16	17

$\chi^2 = 47.9$, d.f. $= 8$, $p < 0.01$.

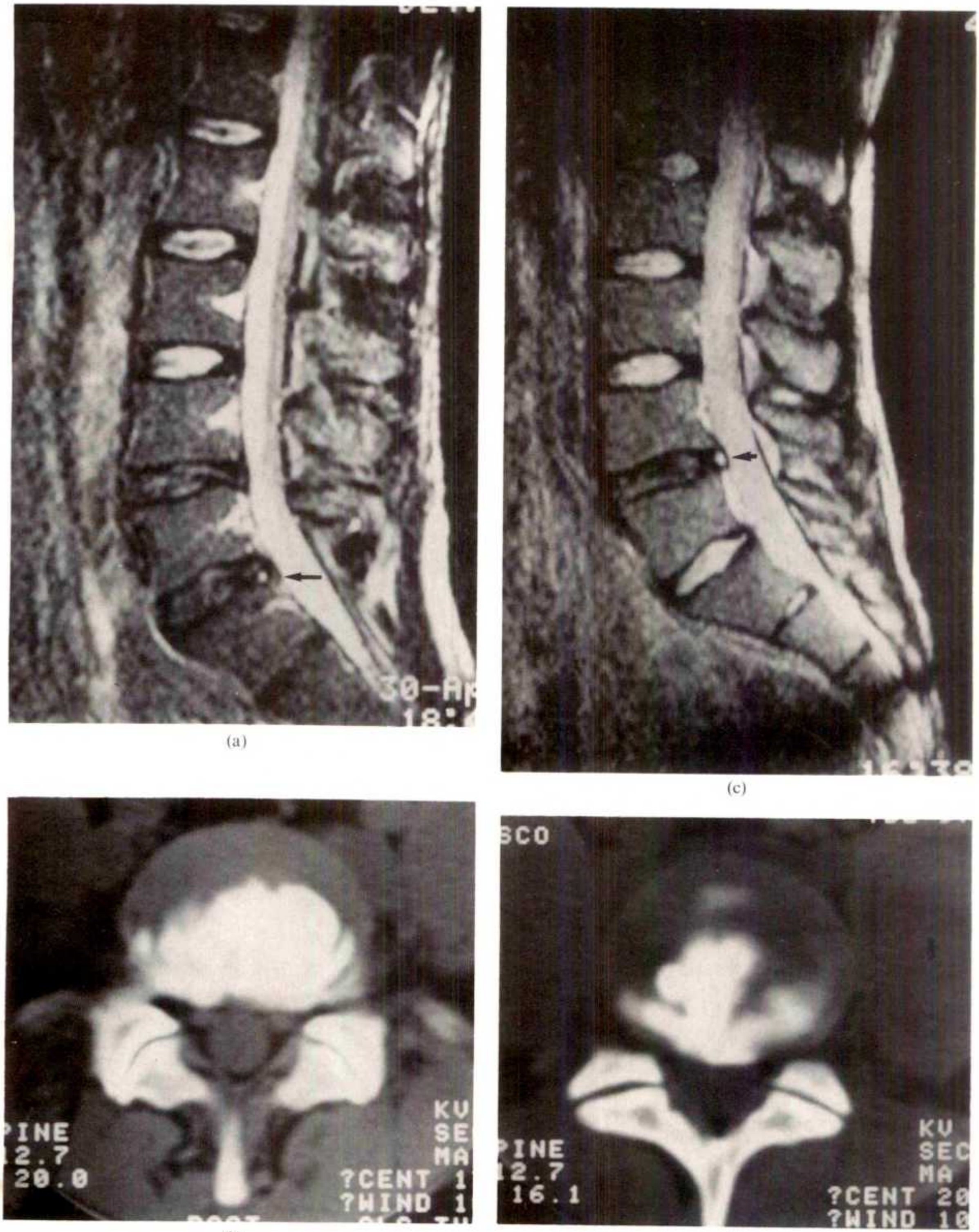

Figure 5. (a) A T_2-weighted magnetic resonance image (TR2000, TE100) showing an HIZ in the L5–S1 disc (arrow) and (b) the CT discogram of the same disc showing severe, Grade 4 annular disruption. (c) A T_2-weighted magnetic resonance image (TR2200, TE100) showing an HIZ in the L4–5 disc (arrow) and (d) the CT discogram of the same disc showing Grade 4 annular disruption.

Table IV. Contingency table for pain reproduction and the presence or absence of a high-intensity zone (HIZ) in 118 discs in 41 patients studied by provocation discography

HIZ	Pain reproduction		
	Exact	Similar	Nil
Present	31	7	2
Absent	7	15	56

$\chi^2 = 63$, d.f. $= 2$, $p < 0.01$.
For exact pain reproduction, sensitivity = 31/38 (82%) and specificity = 71/80 (89%).
For exact or similar pain reproduction, sensitivity = 38/60 (63%), specificity = 56/58 (97%), and positive predictive value = 38/40 (95%).

and the presence or absence of an HIZ is significant at $p < 0.01$ (Table II). The sensitivity of an HIZ in detecting a Grade 4 disruption was low (54%), but its specificity was high (89%), as was its positive predictive value (90%).

In the patients studied by CT-discography, most of the Grade 4 and Grade 3 disruptions were symptomatic (Table III). Reproduction of symptoms was significantly related to increasing grade of disruption ($p < 0.01$).

The presence of an HIZ was strongly related to reproduction of pain (Table IV). The sensitivity of an HIZ in detecting exact pain reproduction was 82%; its specificity was 89%. In detecting exact or similar pain reproduction its sensitivity was 63% but its specificity was 97%. The reduction in sensitivity results from the relatively greater number of discs without an HIZ that exhibited similar but not exact reproduction of pain. Strikingly, the positive predictive value of an HIZ for reproduction of exact or similar pain was 95% (Table IV).

For the composite condition of Grade 4 disruption together with exact or similar reproduction of pain, the HIZ exhibited a highly significant correlation (Table V). The sensitivity of an HIZ for a painful, Grade 4 disruption was 71%; its specificity was 89%, and its positive predictive value was 86% (Table V).

Table V. Contingency table correlating the presence or absence of a high-intensity zone (HIZ) against Grade 4 annular disruption with exact or similar pain reproduction and all other grades of disruption and pain responses in 105 discs in 41 patients studied by CT-discography and MRI

HIZ	Grade 4 disruption with exact or similar pain reproduction	Grade 4 disruption with no pain	All other grades with pain	All other grades with no pain
Present	36	1	4	1
Absent	15	16	4	28

$\chi^2 = 44.6$, d.f. $= 3$, $p < 0.01$.
For a painful Grade 4 disruption, sensitivity = 36/51 (71%), specificity = 48/54 (89%) and positive predictive value = 36/42 (86%).

Discussion

The present study found that an HIZ could be readily detected independently by two observers and that it occurs in 28% of patients with back pain attending a spinal radiology practice. To the question why this common sign has not been recognized previously, three answers are suggested.

First, the HIZ is evident only on good quality MRI scans. Patient motion artefacts or poorly photographed images render the sign indistinct, for recognition of the HIZ relies critically on the brightness of the signal (Fig. 6). Section thickness is of critical importance. Thicker sections render the small area of bright signal less conspicuous. Consequently, an HIZ is unlikely to be apparent in 6.0 mm, 8.0 mm and 10.0 mm sections, which are occasionally employed with SE T_2 imaging to reduce scanning time.

On truly T_2-weighted images, the nuclear region of normal discs is quite bright with an intensity approaching that of the almost white cerebrospinal fluid (CSF). On such images, an HIZ will approach the brightness of the adjacent CSF. HIZs are not detectable on SE T_1-weighted images.

Gradient echo sequences are becoming popular because they require less acquisition time. The spatial resolution of these images is good, and the resulting T_2* image contrast results in a myelogram effect, but the image contrast of the disc is not a measure of its true T_2 characteristics. Gradient echo sequences are not reliable in detecting the HIZs described in this study. True SE T_2-weighted images of no more than 5.0 mm thickness are required to study internal disc disruption adequately.

The second reason why the HIZ has been overlooked possibly relates to the inclination of neuroradiologists who use MRI to focus on disorders of the lumbar nerve roots rather than on the disc itself. The patients in the present study (in the MR/CT-discography comparison group) did not exhibit convincing evidence of nerve root compression, either clinically or on imaging. This might invite attribution of any abnormalities seen in the discs to non-specific degenerative changes. However, all the patients in the present study had back pain and most had a symptomatic, Grade 4 annular disruption. The HIZ, although readily overlooked as insignificant, was nonetheless strongly diagnostic of a disrupted and painful disc.

Thirdly, the HIZ is evident typically and essentially exclusively in mid-sagittal images. Its absence in other images and its absence in T_1-weighted images renders it more likely to be overlooked or dismissed as an incidental, insignificant finding. Yet, this is far from the case.

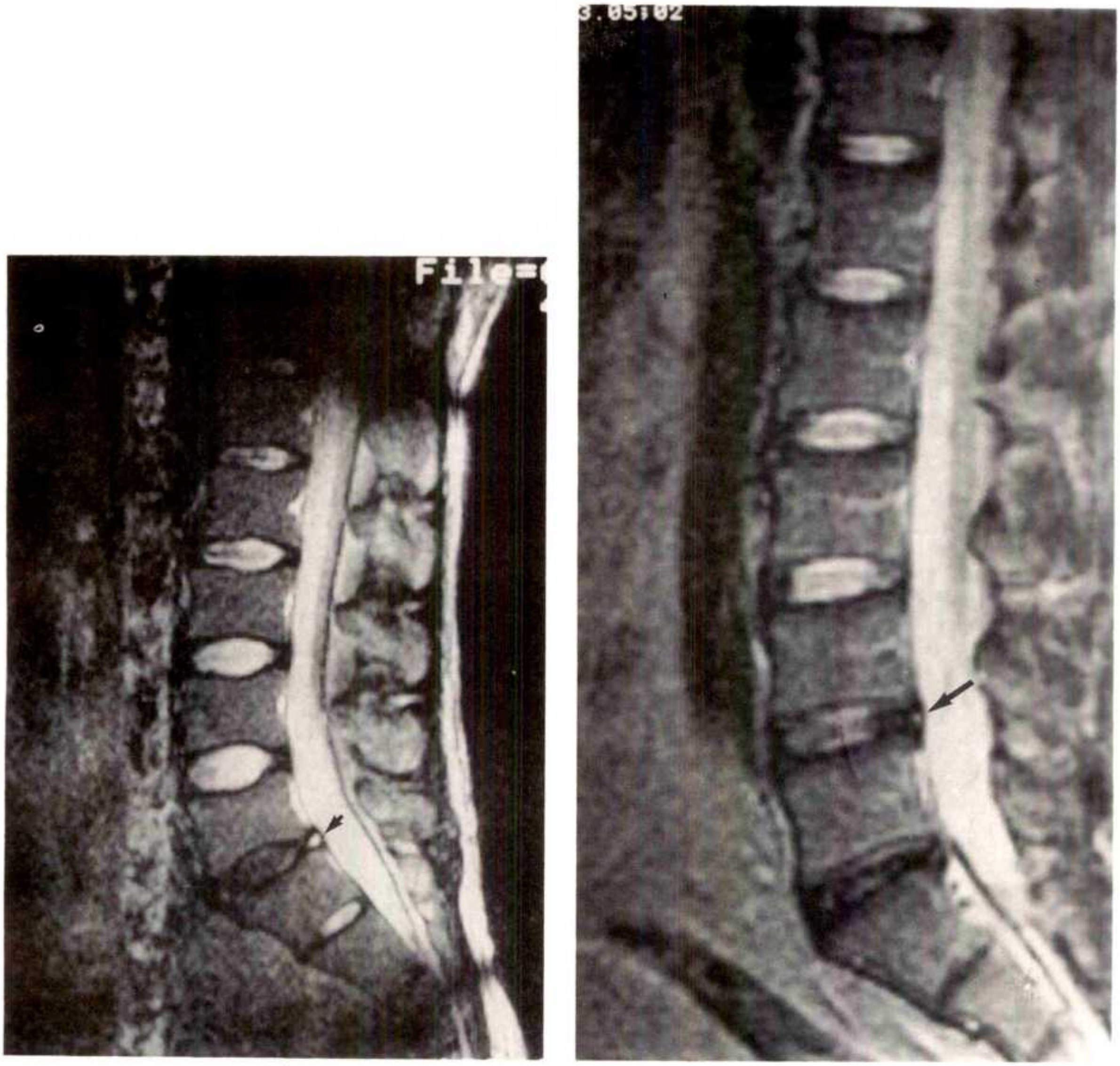

(a) (b)

Figure 6. Two magnetic resonance images of contrasting quality. (a) One in which a high-intensity zone (arrow) is clearly evident, and (b) one in which a possible HIZ (arrow) is masked by the overall lack of brightness in the scan.

Because of the inherent bias of the sample of patients studied, the observed prevalence of HIZ may not necessarily reflect its prevalence in patients with low-back pain at large. Rather, the prevalence more likely applies to those patients, like the present sample, who had back pain without radiculopathy serious enough to warrant orthopaedic consultation and expensive, radiological investigation.

The prevalence of HIZ in an asymptomatic population is not known. However, in those studies describing asymptomatic lumbar spines on MRI, no mention is made of an HIZ (Powell et al, 1986; Weinreb et al, 1989). Either this sign has been overlooked because of technical reasons like those mentioned above, or it does not occur in asymptomatic subjects. The latter would be concordant with the present study, in that HIZs were never encountered in structurally normal discs (Table II). Nevertheless, given the significance of the HIZ revealed in the present study, it is clearly critical that the prevalence of HIZs using contemporary technology capable of producing good quality SE T_2-weighted images should be established in normals.

The present study complements clinically the pathoanatomical studies initiated by Yu and associates (Yu et al, 1988). These investigators showed that various fissures evident in the annulus fibrosus of cadavers could be demonstrated on MRI. They identified three types of fissure. Type I were crescentic fissures unconnected with the nucleus pulposus. Type II fissures were radial fissures extending from a nucleus pulposus to the outer annulus. Type III fissures were transverse tears of the annulus near its attachment sites. Type I fissures were difficult to demonstrate on MRI, but Type II and Type III fissures were evident on MRIs of cadaveric lumbar spines (Yu et al, 1988).

The HIZ appears to be a sign of a severe form of Type II fissure: one in which a radial fissure extends circumferentially by more than 30° to become a Grade 4 fissure as defined in the present study. The HIZ is not the centre of a prolapse for the signal is contained wholly within the annulus fibrosus, and on MRI it exhibits no connection with the nucleus pulposus. CT-discography demonstrates that the circumferential fissure is contained within the annulus and is connected only circuitously to the nucleus pulposus through a radial fissure.

The results of the present study suggest that only Grade 4 fissures manifest themselves as an HIZ. However, because very few Grade 3 disruptions were encountered in the present study, it is not possible to exclude the possibility that in other patients, Grade 3 disruptions might also manifest as an HIZ.

The signal of an HIZ is similar to that of the nucleus pulposus. This, together with the CT data, suggest that the circumferential fissure contains fluid of nuclear origin. However, the HIZ is noticeably brighter than the nuclear signal, which suggests there is more to it. We postulate that the HIZ constitutes nuclear material trapped between the lamellae of the annulus fibrosus, which has become inflamed, and that this inflammation accounts for the brighter signal. We suggest that the HIZ is analogous to the Type II fissures described by Ross, Modic and Masaryk (Ross et al, 1989c), which enhanced on injection of gadolinium-DPTA, a behaviour taken to indicate inflammation, neovascularization or invasion by granulation tissue (Ross et al, 1989c), and which has been shown experimentally to correspond to granulation tissue in traumatized disc (Nguyen et al, 1989).

However, it was not the purpose of the present study to explore the histopathology of the HIZ. The study was designed only to explore the reliability and validity of this sign. It is quite clear from the clinical data obtained that the HIZ is a frequent sign on MRI of patients with back pain, and that it is highly specific and strongly predictive of a symptomatic disc with severe annular disruption. It is not necessarily the only sign of a symptomatic disc, and it is not present in all painful discs. However, it is a sign that is readily recognized and should draw attention away from the disc–nerve root interface and towards significant, and hitherto neglected, changes within the disc itself.

The data on sensitivity, specificity and positive predictive value of HIZ are sufficient to warrant that the HIZ, when present, is pathognomonic of an internally disrupted and symptomatic intervertebral disc. As such, the HIZ is the first sign evident on MRI that has been shown to be diagnostic for low-back pain.

References

Antti-Poika, I., Soini, J., Tallroth, K., Yrjonen, T. & Konntinen, Y. T., 1990. Clinical relevance of discography combined with CT scanning. *Journal of Bone & Joint Surgery, 72B*, 480–485.

Bogduk, N., 1988. The innervation of intervertebral discs. In *The Biology of the Intervertebral Disc, Vol. 1*, ed. by P. Ghosh (CRC Press, Boca, Raton), pp. 135–149.

Bogduk, N. & Twomey, L. T., 1991. *Clinical Anatomy of the Lumbar Spine*, 2nd edn (Churchill Livingstone, Melbourne), pp. 161–173.

Breger, R. K., Williams, A. L., Daniels, D. L., Czervionke, L. F., Mark, L. P., Haughton, V. M., Papke, R. A. & Coffer, M., 1989. Contrast enhancement in spinal MR imaging. *American Journal of Neuroradiology, 10*, 633–637.

Bundschuh, C. V., Modic, M. T., Ross, J. S., Masaryk, T. J. & Bohlman, H., 1988. Epidural fibrosis and recurrent disk herniation in the lumbar spine: MR imaging assessment. *American Journal of Roentgenology, 150*, 923–932.

Burnett, K. R. & Levine, J. B., 1986. MR of lumbar disk disease. *Applied Radiology, 15*, 133–141.

Chafetz, N. I., Genant, H. K., Moon, K. L., Helms, C. A. & Morris, J. M., 1983. Recognition of lumbar disk herniation with NMR. *American Journal of Roentgenology, 141*, 1153–1156.

Crawshaw, C., Kean, D. M., Mulholland, R. C., Worthington, B. S., Finlay, D., Hawkes, R. C., Gyngell, M. & Moore, W. S., 1984. The use of nuclear magnetic resonance in the diagnosis of lateral canal entrapment. *Journal of Bone & Joint Surgery, 66B*, 711–715.

Crock, H. V., 1970. A reappraisal of intervertebral disc lesions. *Medical Journal of Australia, 1*, 983–989.

Crock, H. V., 1986. Internal disc disruption: a challenge to disc prolapse 50 years on. *Spine, 11*, 650–653.

Djukic, S., Genant, H. K., Helms, C. A. & Holt, R. G., 1990. Magnetic resonance imaging of the postoperative lumbar spine. *Radiologic Clinics of North America, 28*, 341–360.

Edelman, R. R., Shoulimas, G. M., Stark, D. D., Davis, K. R., New, P. F. J., Saini, S., Rosenthal, D. I., Wismer, G. L. & Brady, T. J., 1985. High resolution surface coil imaging of lumbar disk disease. *American Journal of Roentgenology, 144*, 1123–1129.

Friberg, S., 1954. Lumbar disc herniation in the problem of lumbago sciatica. *Bulletin of the Hospital for Joint Diseases, 15*, 1–20.

Frocrain, L., Duvauferrier, R., Husson, J. L., Noel, J., Ramee, A. & Pawlotsky, Y., 1989. Recurrent postoperative sciatica: evaluation with MR imaging and enhanced CT. *Radiology, 170*, 531–533.

Gibson, M. J., Buckley, J., Mawhinney, R., Mulholland, R. C. & Worthington, B. S., 1986. Magnetic resonance imaging and discography in the diagnosis of disc degeneration. *Journal of Bone & Joint Surgery, 58B*, 369–373.

Hickey, D. S., Aspden, R. M., Hukins, D. W. L., Jenkins, J. P. R. & Isherwood, I., 1986. Analysis of magnetic resonance images from normal and degenerate lumbar intervertebral discs. *Spine, 11*, 702–708.

Hochhauser, L., Kieffer, S. A., Cacayorin, E. D., Petro, G. R. & Teller, W. F., 1988. Recurrent postdiskectomy low back pain: MR-surgical correlation. *American Journal of Roentgenology, 151*, 755–760.

Horal, J., 1969. The clinical appearance of low back disorders in the city of Gothenburg, Sweden. *Acta Orthopaedica Scandinavica, Supplementum 118*, 1–108.

Hueftle, M. G., Modic, M. T., Ross, J. S., Masaryk, T. J., Carter, J. R., Wilber, R. G., Bohlman, H. H., Steinberg, P. M. & Delmarter, R. B., 1988. Lumbar spine: post operative MR imaging with Gd-DTPA. *Radiology, 167*, 817–824.

Hukins, D. W. L., Aspden, R. M. & Hickey, D. S., 1988. Potential of magnetic resonance imaging for the investigation of disc pathology. In *The Biology of the Intervertebral Disc, Vol. 2*, ed. by P. Ghosh (CRC Press, Boca Raton), pp. 161–197.

Hyman, R. A. & Gorey, M. T., 1988. Imaging strategies for MR of the spine. *Radiologic Clinics of North America, 26*, 505–533.

Jenkins, J. P. R., Hickey, D. S., Zhu, X. P., Machin, M. & Isherwood, I., 1985. MR Imaging of the intervertebral disc: a quantitative study. *British Journal of Radiology, 58*, 705–709.

Kent, D. L. & Larsen, E. B., 1988. Magnetic resonance imaging of the brain and spine. *Annals of Internal Medicine, 108*, 402–424.

Kricun, R., Kricun, M. E. & Dalinka, M. K., 1990. Advances in spinal imaging. *Radiologic Clinics of North America, 28*, 321–339.

Lee, S. H., Coleman, P. E. & Hahn, F. J., 1988. Magnetic resonance imaging of degenerative disk disease of the spine. *Radiologic Clinics of North America, 26*, 949–964.

Maravilla, K. R., Lesh, P., Weinreb, J. C., Selby, D. K. & Mooney, V., 1985. Magnetic resonance imaging of the lumbar spine with CT correlation. *American Journal of Neuroradiology, 6*, 237–245.

Masaryk, T. J., Ross, J. S., Modic, M. T., Boumphrey, F., Bohlman, H. & Wilber, G., 1988. High resolution MR imaging of sequestered lumbar intervertebral disks. *American Journal of Neuroradiology, 9*, 351–358.

Modic, M. T., Masaryk, T. J., Boumphrey, F., Gourmastic, M. & Bell, G., 1986a. Lumbar herniated disc disease and canal stenosis. Prospective evaluation by surface coil MR, CT and myelography. *American Journal of Neuroradiology, 7*, 709–711.

Modic, M. T., Masaryk, T. J. & Paushter, D. M., 1986b. Magnetic resonance imaging of the spine. *Radiologic Clinics of North America, 24*, 229–245.

Modic, M. T., Pavlicek, W., Weinstein, M. A., Boumphrey, F., Ngo, F., Hardy, R. & Duchesneau, P. M., 1984. Magnetic resonance imaging of intervertebral disk disease. *Radiology, 152*, 103–111.

Modic, M. T. & Weinstein, M. A., 1984. Nuclear magnetic resonance of the spine. *British Medical Bulletin, 40*, 183–186.

Mooney, V., 1987. Where is the pain coming from? *Spine, 8*, 754–759.

Murayama, S., Numaguchi, Y. & Robinson, A. E., 1990. The diagnosis of herniated intervertebral disks with MR imaging: a comparison of gradient refocused-echo and spin-echo pulse sequences. *American Journal of Neuroradiology, 11*, 17–22.

Nachemson, A., 1989. Editorial comment. Lumbar discography—where are we today? *Spine, 14*, 555–557.

Nguyen, C. M., Ho, K-C., Yu, S., Haughton, V. M. & Strandt, J. A., 1989. An experimental model to study contrast enhancement in MR imaging of the intervertebral disk. *American Journal of Neuroradiology, 10*, 811–814.

Panagiotocopulos, N. D., Pope, M. H., Krag, M. K. & Block, R., 1987. Water content in human intervertebral discs part I: measurement by magnetic resonance imaging. *Spine, 12*, 912–917.

Powell, M. C., Wilson, M., Szypryt, P., Symonds, E. M. & Worthington, B. S., 1986. Prevalence of lumbar disc degeneration observed by magnetic resonance in symptomless women. *Lancet, ii*, 1366–1367.

Ross, J. S., Masaryk, T. J., Modic, M. T., Bohlman, H., Delamarter, R. & Wilber, G., 1987. Lumbar spine: postoperative assessment with surface coil MR imaging. *Radiology, 164*, 851–860.

Ross, J. S., Delamarter, R., Heuftle, M. G., Masaryk, T. J., Aikawa, M., Carter, J., Vandyke, C. & Modic, M. T., 1989a. Gadolinium-DPTA-enhanced MR imaging of postoperative lumbar spine: time course and mechanism of enhancement. *American Journal of Neuroradiology, 10*, 37–46.

Ross, J. S., Modic, M. T., Masaryk, T. J., Carter, J., Marcus, R. E. & Bohlman, H., 1989b. Assessment of extradural degenerative disease with Gd-DTPA-enhanced MR imaging: correlation with surgical and pathologic findings. *American Journal of Neuroradiology, 10*, 1243–1249.

Ross, J. S., Modic, M. T. & Masaryk, T. J., 1989c. Tears of the anulus fibrosus assessment with Gd-DTPA-enhanced MR imaging. *American Journal of Neuroradiology, 10*, 1251–1254.

Sachs, B. L., Vanharanta, H., Spivey, M. A., Guyer, R. D., Videman, T., Rashbaum, R. F., Johnson, R. G., Hochschuler, S. H. & Mooney, V., 1987. Dallas discogram description. A new classification of CT/discography in low-back disorders. *Spine, 12*, 287–294.

Schneiderman, G., Flannigan, B., Kingstons, S., Thomas, J., Dillin, W. H. & Watkins, R. G., 1987. Magnetic resonance imaging in the diagnosis of disc degeneration: correlation with discography. *Spine, 12*, 276–281.

Sotiropoulos, S., Chafetz, N. I., Lang, P., Winkler, M., Morris, J. M., Weinstein, P. R. & Genant, H. K., 1989. Differentiation between postoperative scar and recurrent disk herniation: prospective comparison of MR, CT and contrast-enhanced CT. *American Journal of Neuroradiology, 10*, 639–643.

Vanharanta, H., Guyer, R. D., Ohnmeiss, D. D., Stith, W. J., Sachs, B. L., Aprill, C., Spivey, M., Rashbaum, R. F., Hochschuler, S. H., Videman, T., Selby, D. K., Terry, A. & Mooney, V., 1988. Disc deterioration in low-back syndrome. A prospective, multi-center CT/discography study. *Spine, 13*, 1349–1351.

Vanharanta, H., Sachs, B. L., Spivey, M. A., Guyer, R. D., Hochschuler, S. H., Rashbaum, R. F., Johnson, R. G., Ohnmeiss, D. & Mooney, V., 1987. The relationship of pain provocation to lumbar disc deterioration as seen by CT/discography. *Spine, 12*, 295–298.

Walsh, T. R., Weinstein, J. N., Spratt, K. F., Lehmann, T. R., Aprill, C. & Sayre, N., 1990. Lumbar discography in normal subjects. *Journal of Bone and Joint Surgery, 72A*, 1081–1088.

Weinreb, J. C., Wolbarsht, L. B., Cohen, J. M., Brown, C. E. L. & Maravilla, K. R., 1989. Prevalence of lumbosacral intervertebral disk abnormalities on MR images in pregnant and asymptomatic nonpregnant women. *Radiology, 170*, 125–128.

Weisz, G. M. & Kitchener, P. N., 1987. The use of magnetic resonance imaging in the diagnosis of postoperative lumbar conditions. *Medical Journal of Australia, 146*, 99–101.

Weisz, G. M., Lamond, S. T. & Kitchener, P. N., 1988. Magnetic resonance imaging in spinal disorders. *International Orthopaedics, 12*, 331–334.

Yu, S., Sether, L. A., Ho, P. S. P., Wagner, M. & Haughton, V. M., 1988. Tears of the anulus fibrosus: correlations between MR and pathologic findings in cadavers. *American Journal of Neuroradiology, 9*, 367–370.

1992, *The British Journal of Radiology*, *65*, 370–374

The basal turn of the cochlea

By Peter D. Phelps, MD, FRCS, FRCR

Department of Radiology, Royal National Throat, Nose and Ear Hospital, Gray's Inn Road, London WC1X 8DA and Walsgrave Hospital, Clifford Bridge Road, Coventry CV2 2DX, UK

(*Received 9 July 1991 and in revised form 3 October 1991, accepted 22 October 1991*)

Keywords: Cochlea, Congenital abnormalities, Otosclerosis, Cochlear implant

Abstract. The coils of the cochlea are now readily demonstrated by thin-section high-resolution computed tomography (CT) in the axial plane. This assessment has become important in severely deaf patients who are candidates for cochlear implant surgery. The commonest abnormality shown in these cases is post-meningitic or tympanogenic labyrinthitis ossificans, which can obstruct the passage of the electrode. Severe otosclerosis can cause a similar problem. Congenital deformities of the labyrinth are rarely suitable for implantation, but the procedure may be indicated for the true Mondini deformity. Implantation is contraindicated for severe dysplasia of the cochlea and for the recently described variety of x-linked deafness with deficient bone at the fundus of the internal auditory meatus.

The cochlea is the anterior part of the labyrinth of the inner ear and consists of a hollow tube making two and a half turns around the squat cone-like modiolus. The base of the modiolus forms part of the lateral end of the internal auditory meatus (IAM) and contains the spiral ganglion of the cochlear nerve. The small size and spiral nature of the organ has always made imaging the cochlea difficult even with the two-dimensional thin sections of the latest high-resolution computed tomography (CT). However, the natural plane for CT, namely the axial or base projection, does give the best demonstration of the individual coils of the cochlea (Fig. 1a). Coronal sections formerly used with polytomography cut the coils obliquely and are not so satisfactory (Fig. 1b), although the central bony spiral is well shown as a small curl (Phelps & Lloyd, 1990a). The state of the membraneous cochlea or the cochlea endorgan cannot be assessed by imaging at present, although magnetic resonance can confirm that the cochlea is filled with fluid rather than fibrous tissue (Harnsberger et al, 1987). For practical purposes, therefore, the radiological assessment is confined to the state of the bony cochlea.

Imaging the cochlear coils has recently become more important since cochlear implants introduced into the round window niche, or, more effectively, into the

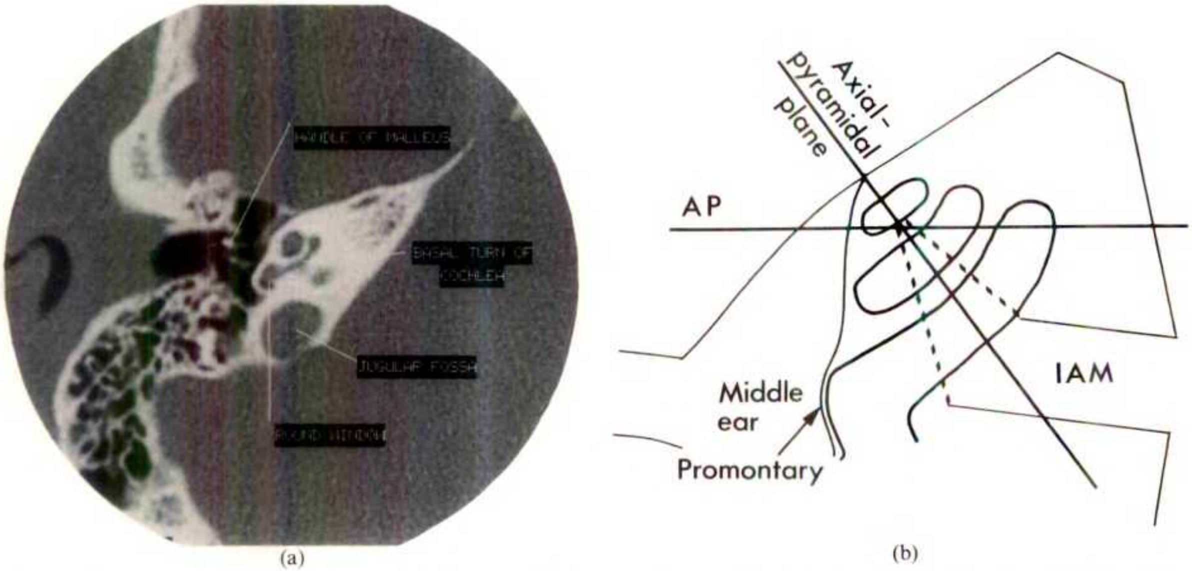

(a)

(b)

Figure 1. (a) Normal axial CT section through the basal turn of the cochlea. (b) Diagram of the cochlea in the axial or base plane showing the individual coils. Coronal sections (AP) transect the coils obliquely. The axial-pyramidal plane, used formerly with polytomography, also shows the individual coils, but is no longer required.

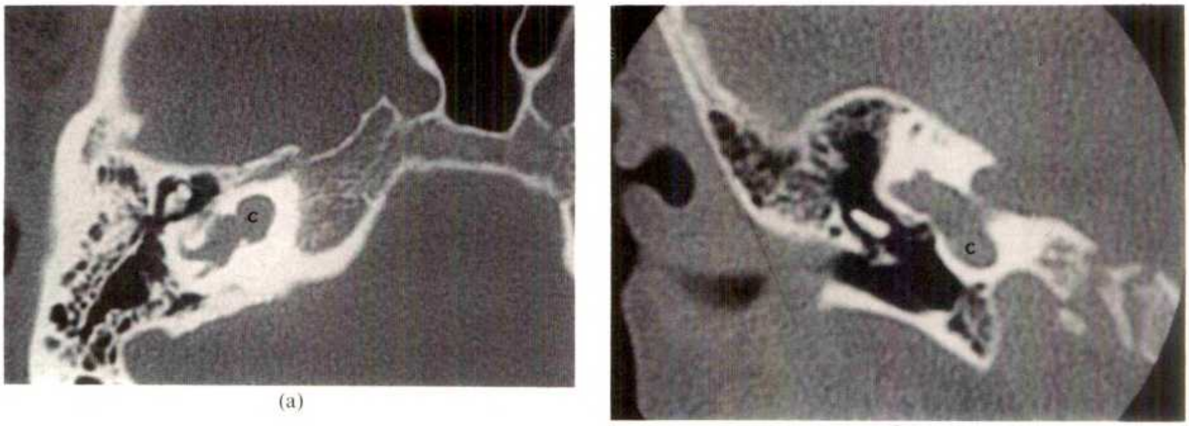

Figure 2. Severe dysplasia of the labyrinth in axial (a) and coronal (b) planes. The cochlea (c) is represented by an amorphous sac incompletely separated from the dilated vestibule. The patient presented with recurrent meningitis cured by packing the abnormal labyrinth with muscle via a tympanotomy.

lumen of the coils themselves, have become available. The pre-operative assessment to select suitable candidates for implantation now includes thin-section high-resolution CT of the cochlear coils. The most important lesions affecting the bony cochlea in severely deaf patients will be described.

High-resolution CT of the cochlea

Contiguous 1 mm thick sections are obtained in the axial plane, but at 30° to the baseline parallel to the roof of the orbit to reduce the radiation dose to the globe of the eye. The bone algorithm is used and the pictures viewed on a wide window setting. A supplementary examination is usually obtained using direct coronal sections.

Abnormalities of the basal cochlear turn occur in the following conditions.

Congenital

Arrest of development at various stages in fetal life leads to a wide range of malformations; the traditional classification and descriptions are inadequate. The following categories of congenital cochlear deformity are suggested.

Severe labyrinthine dysplasia. Arrest at 5 weeks of fetal life results in a severe type of cochlear dysplasia without a normal basal coil and a wide communication with a dilated vestibule (Fig. 2). This type of deformity is always associated with anacusis and a very real risk of a spontaneous cerebrospinal fluid (CSF) fistula or recurrent attacks of meningitis. The internal auditory meatus is often tapered (Phelps, 1986) but the most significant feature is the dilated basal turn of the cochlea. Comparison can be made with the normal side if, as in the great majority of cases, this lesion is unilateral. This deformity is *not* the one described by Mondini (Phelps, 1990).

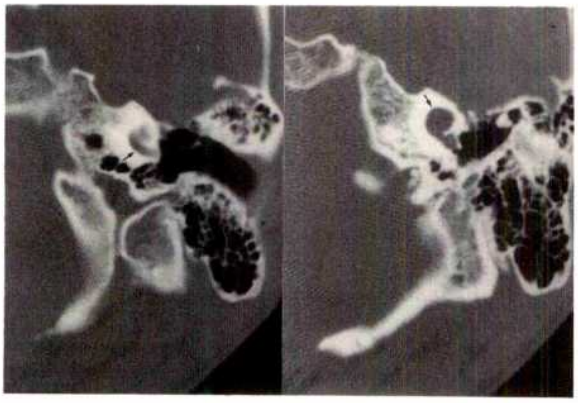

Figure 3. Mondini deformity. Two contiguous axial sections show normal basal turn and distal sac (arrows). Some hearing is present in this ear. (Courtesy of Sutton's *Textbook of Radiology*, in preparation.)

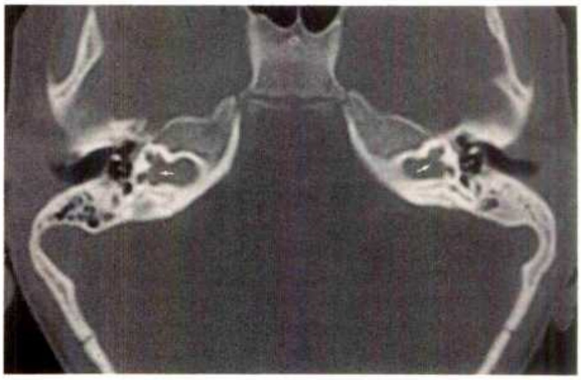

Figure 4. X-linked congenital deformity of the inner ear. This axial section shows incomplete bony lamina between the basal coil of the cochlea and the IAM (arrows).

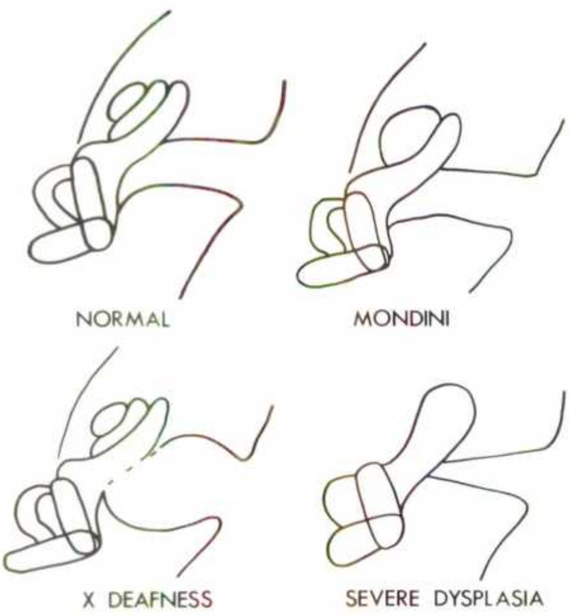

Figure 5. Line drawings showing various congenital deformities of the cochlea and IAM.

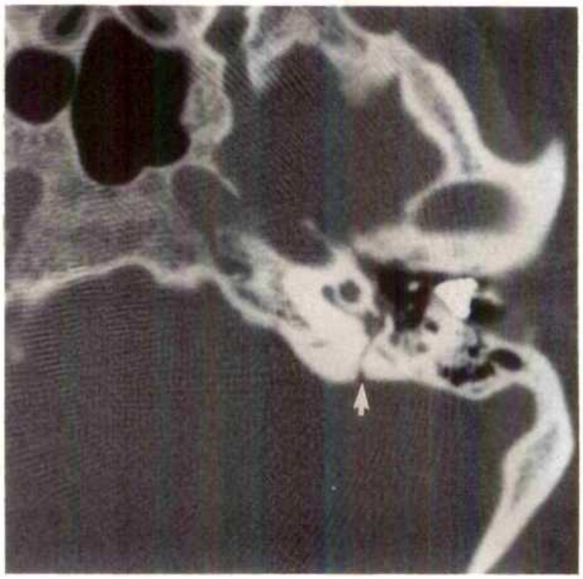

Figure 6. A transverse fracture through the petrous bone (arrow) passes through the basal turn of the cochlea and round window niche, which would make cochlear implantation difficult.

Mondini deformity. The original description of this lesion (Mondini, 1791) was of a cochlea having one and a half instead of two and a half turns of the spiral. The apical turn was missing and ended in a cavity which replaced the last spiral turn. The oval and round windows and the semicircular canals and their openings were stated to be normal, although the vestibule was enlarged. The IAM and cochlear aqueduct were not described but appear to be normal in the illustrations.

The presence of a normal basal turn in the Mondini deformity is important (Fig. 3) as some auditory function is therefore possible and we have seen several cases with confirmed hearing in the affected ear. Moreover, there is no risk of a spontaneous CSF fistula or of recurrent meningitis in these patients. There are two hereditary types of Mondini deformity, namely Pendred syndrome and branchio-oto-renal syndrome, although in the latter the lesion is not strictly a Mondini deformity but a smaller than normal cochlea with two instead of two and a half turns.

X-linked deformity. We have recently described a type of dysplasia of the cochlea and IAM occurring in one variety of x-linked deafness (Phelps et al, 1991). The characteristic feature of the deformity is not so much the bulbous IAM but deficient bone between the lateral end of the IAM and the basal turn of the cochlea (Fig. 4). There is, at least initially, often a conductive component to the deafness and so stapedectomy procedures have been attempted in 12 recorded cases from the world literature. A profuse flow of CSF resulted in each of these cases when the stapes were removed or a small exploratory hole was made in the footplate. This is known as a "stapes gusher". An abnormal communication between the subarachnoid space in the IAM and the perilymph in the basal cochlear coil probably causes a perilymphatic hydrops and results in the stapes gusher. The cochlear aqueduct appears to be normal. To our knowledge, no histological examination of the condition has been made. We have found this typical deformity of the inner ear in seven affected males from four pedigrees with x-linked deafness. The deformity appears to be always bilateral and constant in type, with only slight variations in severity. However, in some types of x-linked deafness the cochlea appears normal on imaging, suggesting an allelic variation or a second deafness locus. The differentiation between the severe type of dysplasia with anacusis and risk of spontaneous CSF fistula, the x-linked deformity with severe deafness and risk of a stapes gusher only if the stapes is disturbed, and a true Mondini deformity with the possibility of some hearing but in my opinion no risk of a CSF fistula is depicted in diagrammatic form in Fig. 5.

Trauma

Total or near total hearing loss following a fracture through the petrous temporal bone is very rare but the subject with remembered hearing is often a good candidate for a cochlear implant. The damage to the hearing organ will in most cases be from a transverse type of fracture to the petrous pyramid passing through the IAM or the labyrinth. The fracture line is often very fine and careful study by thin-section high-resolution CT is mandatory. A fracture passing through the basal turn of the cochlea may distort the anatomy and make insertion of a multichannel electrode difficult (Fig. 6).

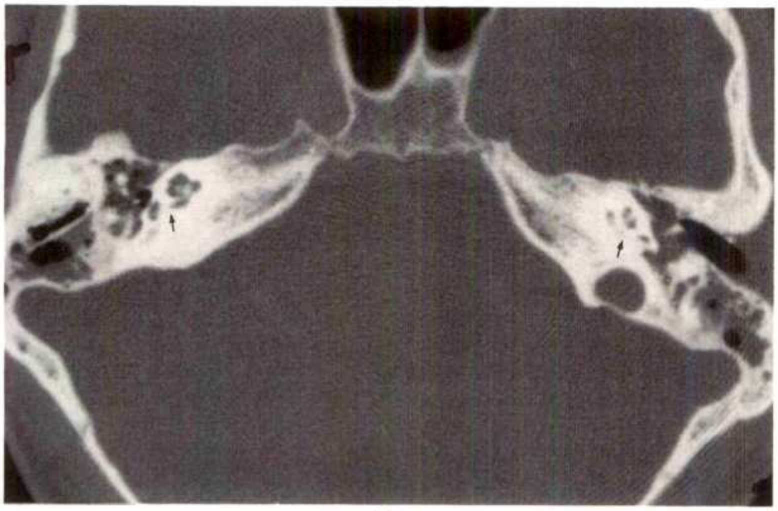

(a)

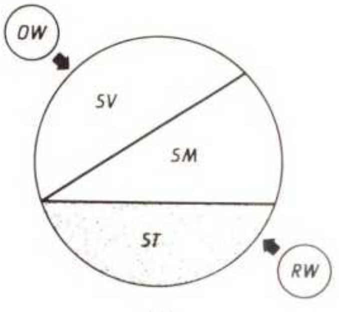

(c)

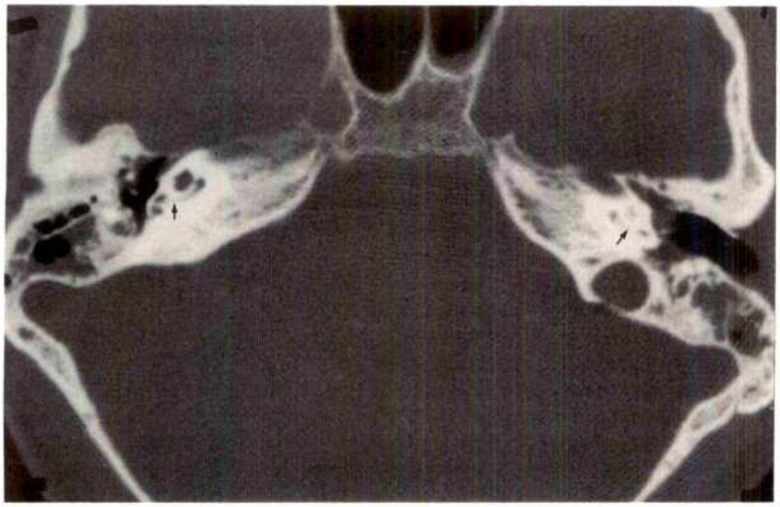

(b)

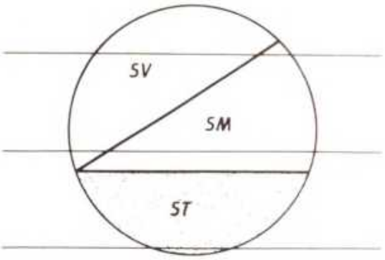

(d)

Figure 7. (a, b) Labyrinthitis ossificans with partial ossification of the lumen of the cochlea on both sides, especially at the basal turn (arrow). (c) Diagram depicting ossification of the scala tympani (ST) as a shaded segment. This is adjacent to the round window (RW). SM = scala media, SV = scala vestibuli, OW = oval window. (d) 1 mm axial sections may show a lumen that seems to be normal or alternatively appears obliterated on a section that crosses the scala tympani part of the coil.

Inflammatory disease

Extensive invasion of the labyrinth of the inner ear by a cholesteatoma usually results in a "dead ear", but there have now been several well documented cases of cholesteatoma eroding the cochlear capsule without associated hearing loss. We have seen such cases and have reviewed the other reports (Phelps & Lloyd, 1990b). A recent report and good review is by Canalis et al (1989), who describe two cases, one of which had almost total demineralization of the bony cochlea, but hearing function remained even after surgery.

An infective process, either of tympanogenic or meningitic origin, affecting the fluids of the inner ear destroys hearing. These patients are thus candidates for a cochlear implant, but unfortunately the end result of suppurative labyrinthitis is often a condition known as labyrinthitis ossificans or obliterans. Fibrous tissue or new bone formation occurs in the fluid-filled spaces of the inner ear. This may be a hindrance to successful implantation, especially of multichannel intracochlear electrodes. The obliteration is almost never total, but it has been shown in a recent histological report (Green et al, 1991) that the scala tympani of the basal turn of the cochlea is the most frequent area of ossification, regardless of the cause of the labyrinthitis ossificans (Fig. 7a). The ossification of the coils can usually be identified by 1 mm high-resolution CT in the axial plane (Fig. 7b) although fine partial obliteration and fibrous obliteration cannot always be predicted by this procedure (Wiet et al, 1990). The practical problems of interpreting partial obliteration on thin linear sections of a tubal structure are illustrated diagrammatically in Figs 7c and 7d. Nevertheless it is sometimes feasible to drill out the narrowed part of the basal coil and allow introduction of the electrode into the patent distal coils. Whether magnetic resonance imaging is indicated to predict

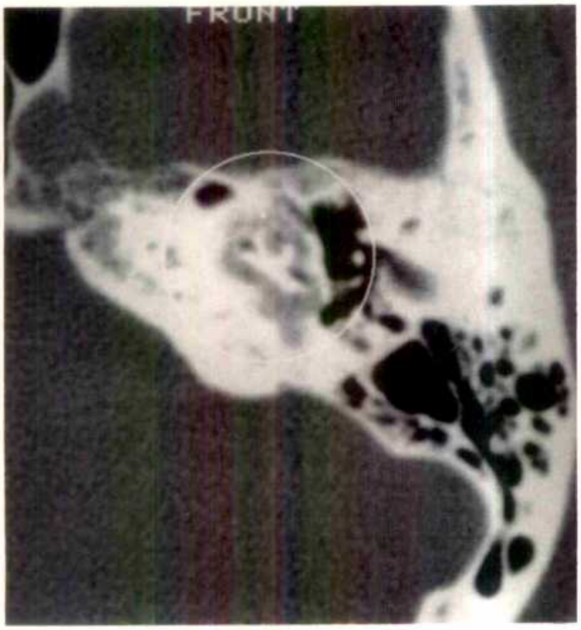

Figure 8. Severe mixed otosclerosis and otospongiosis with narrowing of the cochlear coil on this CT section. The densitometry reading at the white spot was 800 Hounsfield units: a severe degree of rarefaction.

fibrous obliteration by failing to demonstrate high signal from fluid in the labyrinth is not decided.

Otosclerosis/otospongiosis

The normal cochlear capsule is the densest bone in the body and cannot become more opaque but only thicker through apposition of otosclerotic bone. Thus the only way that imaging can demonstrate the sclerotic phase of the disease is by distortion of the normal outlines. On the other hand the more active spongiotic lesions are well shown by CT. Axial CT of a cochlea severely affected by otosclerosis and otospongiosis shows a mixture of rarefied bone and encroachment of bone of normal density into the lumen of the cochlea (Fig. 8). Neo-ossification of the basal turn associated with otosclerosis was limited to the proximal 6 mm of the scala tympani in all histological examinations described by Green et al (1991).

Discussion

The disease processes affecting the basal turn of the cochlea considered above and demonstrated by imaging nearly always indicate a profound or total loss of hearing. Formerly this information was of little more than academic interest, but has now attained considerable relevance for the pre-operative assessment of cochlear implants (Phelps et al, 1990).

Labyrinthitis ossificans and otosclerosis may obliterate the round window niche and part of the basal turn. This needs careful appraisal by the surgeon to decide whether an electrode can be introduced for the required distance with or without drilling to restore the lumen. Congenital deformities are uncommon in deaf patients being assessed for implants. A Mondini deformity would seem most suitable for an implant, but for patients with severe dysplasia or the x-linked malformation a cochlear implant would be contra-indicated. There is much confusion on this subject in the USA, where almost any congenital cochlear deformity is labelled "a Mondini defect" and the importance of differentiation between the severe dysplasia in which there is a risk of a CSF leak and the true Mondini deformity with no such risk and possibly some hearing is not appreciated. In this context, assessment of the width of the basal turn of the cochlea is most important.

References

Canalis, R. F., Abemayor, E. & McClean, P., 1989. Preservation of hearing in cholesteatomas with inner ear invasion. *Journal of Otolaryngology, 18*, 374–379.

Green, J. D., Jr, Marion, M. S. & Hinojosa, R., 1991. Labyrinthitis ossificans: histopathologic consideration for cochlear implantation. *Otolaryngology–Head and Neck Surgery, 104*, 320–325.

Harnsberger, H. R., Dart, D. J., Parkin, J. L., Smoker, W. R. K. & Osborn, A. G., 1987. Cochlear implant candidates: assessment with CT and MR imaging. *Radiology, 164*, 53–57.

Mondini, C., 1791. Anatomica surdi nati sectio. *Bononiensi scientiarum et artium instituto atque academia commentarii Bononiae, 7*, 419–428.

Phelps, P. D., 1986. Congenital cerebrospinal fluid fistulae of the petrous temporal bone. *Clinical Otolaryngology, 11*, 79–92.

Phelps, P. D., 1990. Editorial: Mondini and "Pseudo Mondini". *Clinical Otolaryngology, 15*, 99–101.

Phelps, P. D., Annis, J. A. D. & Robinson, P. J., 1990. Imaging for cochlear implants. *British Journal of Radiology, 63*, 512–516.

Phelps, P. D. & Lloyd, G. A. S., 1990a. Normal CT scanning of the temporal bone. In *Diagnostic Imaging of the Ear*, 2nd edn (Springer-Verlag, London, Berlin), pp. 13–15.

Phelps, P. D. & Lloyd, G. A. S., 1990b. Invasion of the labyrinth by cholesteatoma. In *Diagnostic Imaging of the Ear*, 2nd edn (Springer-Verlag, London, Berlin), pp. 124–126.

Phelps, P. D., Reardon, W., Pembrey, M. E., Bellman, S. & Luxon, L., 1991. X-linked deafness, stapes gushers and a distinctive defect of the inner ear. *Neuroradiology, 33*, 326–330.

Wiet, R. J., Pyle, G. M., O'Connor, C. A., Russell, E. & Schramm, D. R., 1990. Computed tomography: how accurate a predictor for cochlear implantation? *Laryngoscope, 100*, 687–691.

1992, *The British Journal of Radiology*, *65*, 375–383

Magnetic resonance imaging of extracranial head and neck tumours

By J. Kabala, MRCP, FRCR, P. Goddard, BSc, MD, FRCR and P. Cook, FRCR

Department of Clinical Radiology, Bristol Royal Infirmary, Marlborough Street, Bristol BS2 8HW, UK

(*Received 4 July 1991, accepted 4 September 1991*)

Keywords: MRI, Head neoplasms, Neck neoplasms

Abstract. The role of magnetic resonance imaging (MRI) in the investigation of head and neck tumours (excluding those primarily arising from the central nervous system or orbits) has been investigated. Follow-up data were obtained on 45 scans on 42 patients. MRI provided significant additional information compared with computed tomography (CT) in nine out of 17 (53%) scans performed for staging purposes. In the assessment of 19 patients with suspected tumour recurrence, MRI demonstrated a sensitivity of 100%, a specificity of 80% and an accuracy of 89%.

Direct inspection is the preferred method of examination for the superficial aspects of mucosal lesions of the head and neck. Computed tomography (CT) has developed into an accurate and powerful tool for the assessment of otherwise inaccessible lesions, although inaccuracies of tumour characterization and staging may be found in a significant proportion of cases (Som et al, 1988a; Werber & Lucente, 1989).

Magnetic resonance imaging (MRI) has become the modality of choice for the assessment of tumour spread (Byrne et al, 1989; Lloyd & Phelps, 1986; Mandelblatt et al, 1987; Schaefer et al, 1985; Vogl, 1990; Vogl et al, 1988) and offers a number of potential advantages compared with CT. There is generally good contrast between abnormal and normal tissues, including skeletal muscle (Curtin, 1989; Teresi et al, 1987a). Tumours of the head and neck should ideally be displayed in at least two planes and this is routinely achieved with MRI but is considerably more difficult to do with CT. Unlike CT there is an absence of artefact from sharp density steps, for example as caused by dental amalgam or cortical bone. Flowing blood produces a signal void enabling vessels to be clearly distinguished without using intravenous contrast medium (Cross et al, 1989a; Kassel et al, 1989a).

A study was undertaken to examine the current role being played by MRI in the investigation of head and neck tumours, excluding those primarily related to the central nervous system and orbits. In particular the accuracy of MRI detection of recurrent tumour and its usefulness in staging tumours compared with CT was examined.

Subjects and methods

61 scans on 56 patients examined for suspected or confirmed extracranial head and neck tumours (*i.e.* excluding those arising from the central nervous system and orbits) at the Bristol MRI Centre between June 1987 and June 1990 were reviewed. Follow-up data (clinical, pathological and/or operative) were obtained on as many of these patients as possible.

The scans were performed with a 0.5 T Picker Vista 2055HP MRI scanner with a surface coil. The following sequences were routinely performed:

1. Coronal T_1-weighted (T1W) spin–echo (time to repeat (TR) 500 ms, time to echo (TE) 26 ms).
2. Coronal short tau inversion–recovery (STIR) (TR 1500 ms, TE 30 ms, time to inversion (TI) 100 ms.
3. Transverse multi-echo-producing proton density (PD) and T_2-weighted (T2W) images (TR 1500 ms, TE 30 ms and 80 ms, respectively).

Results

Follow-up data were obtained for 45 scans on 42 patients. They can be categorized into four groups according to the clinical problem (Table I). The first two groups (28 scans) were for diagnostic purposes; the third and fourth groups (17 scans) were performed to stage a tumour known to be present.

The relevant information on the nine patients in the first group (suspected tumour of unknown nature) is displayed in Table II. In the three cases where neoplasms were not present (the inflammatory salivary

Table I. Clinical indication for MRI scans

Clinical problem	Number
Suspected tumour – ? nature	9
Previous tumour – ? recurrent	19
Staging tumour – primary	8
Staging tumour – recurrent	9
Total	45

Address correspondence to J. Kabala, Department of Clinical Radiology, Bristol Royal Infirmary, Marlborough Street, Bristol, UK.

Table II. Patients with a suspected tumour of unknown nature

Condition	Confirmation	Number
Neck lymph node mass (metastatic carcinoma)	Excision	3
Bilateral tortuous carotids	Ultrasound	1
Childhood developmental tumours	Excision	2
Inflammatory salivary gland mass	1-year clinical follow-up	2
Renal cell carcinoma metastasis to angle of mandible	Excision	1

Table III. Scans performed to determine if tumour has recurred

MRI negative	*n*
Nasopharyngeal	
Rhabdomyosarcoma	2
Lymphoma	1
Carcinoma	1
Lymphoma of the neck	3
Antral osteosarcoma	1
Total	8

gland masses and the tortuous carotids), MRI provided the diagnosis. In the remaining six cases in this group, MRI produced elegant images and demonstrated the extent of the lesions accurately but did not provide a specific tissue diagnosis.

Table IV. Scans performed to determine if tumour has recurred

MRI positive	*n*
Carcinoma of the laryngopharynx	3
Carcinoma of palate	2
Carcinoma of antrum	1
Chordoma	1
Carcinoma of submandibular gland	1
Carcinoma of floor of the mouth	1
Carcinoma of parotid	1
Nasopharyngeal carcinoma recurrent in neck lymph nodes	1
Total	11

19 scans (Group 2, Table I) were performed to determine if tumour had recurred following treatment. Eight scans showed no recurrence (Table III). There has been no evidence of tumour recurrence after 1–2.5 years follow-up in this group and all these patients have been regarded as true negatives. 11 scans demonstrated recurrent tumour (Table IV). Six of these had histological confirmation of recurrence and three others showed involution of a mass and remission of symptoms with radiotherapy. These nine have been regarded as true positives. The remaining two scans showed lesions that remained static on follow-up MRI examination 4 months later and clinically 8 months later. One patient had been treated for carcinoma of the larynx (Fig. 1), the other for a left submandibular carcinoma. Both patients had undergone surgery and radiotherapy more than 1 year before the first MRI scan. They have both

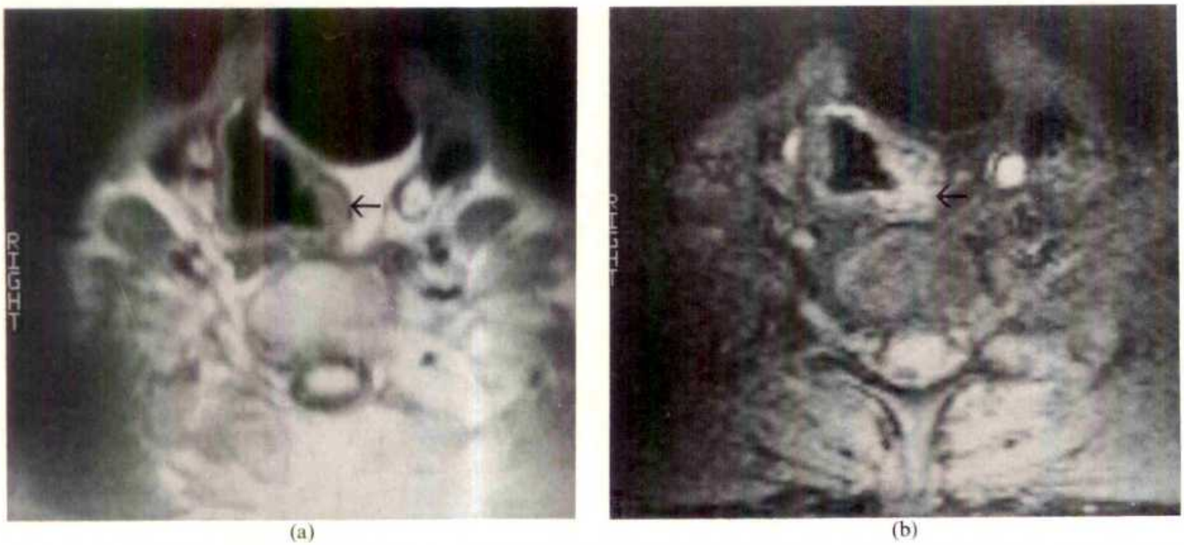

(a) (b)

Figure 1. (a) Transverse T1W scan (TR 600 ms, TE 26 ms) just below the level of the tracheostomy on a patient treated with surgery and radiotherapy 2 years before this scan. There is asymmetrical thickening of the left wall of the trachea (arrow). (b) The area of tracheal wall thickening (arrow) shows increased signal intensity on the STIR sequence (TR 1500 ms, TE 30 ms, TI 100 ms). A diagnosis of recurrent laryngeal carcinoma was made but appearances remained unchanged on repeat scanning 4 months later and there was no evidence of clinical recurrence 8 months after the initial scan.

been regarded as false positives. Thus, from these results on a heterogeneous group of 19 scans, the sensitivity of MRI for tumour recurrence was 100% (true positives divided by true positives plus false negatives) and specificity 80% (true negatives divided by true negatives plus false positives) with an overall accuracy of 89% (true positives plus true negatives divided by the total number). The prevalence of recurrence in this group was 47.4%.

17 scans were performed to stage tumours (Table V), nine being cases of recurrent tumour. In eight cases MRI and CT provided equivalent information. In nine cases MRI provided significant additional information, six being on patients with recurrent tumour. In two cases CT missed small lesions involving the maxillary nerve as it emerged from the foramen rotundum (Figs 2, 3), and in one case intracranial spread was indeterminate on CT but delineated on MRI (Fig. 4; the single case in which intravenous Gd-DTPA was employed). In one case the extent of lymph node involvement by a high-grade parotid carcinoma was underestimated by CT (Fig. 5) and in five cases the local extent of the tumour was clearly better seen on MRI than on CT (two parotid tumours, one sublingual carcinoma and two cases of recurrent carcinoma of the larynx; Figs 6, 7).

All tumours demonstrated medium signal intensity on the T1W sequence, slightly greater than skeletal muscle, except one case of recurrent sublingual carcinoma (isointense with muscle). On T2W sequences the tumours produced a high signal intensity, between skeletal muscle and fat, except in four cases (one nasopharyngeal plasmocytoma, one low-grade parotid carcinoma, one squamous cell carcinoma recurrent in the parotid and one nasopharyngeal rhabdomyosarcoma) where the tumour produced a very high signal intensity, similar to fat. The appearances of tumour on PD sequences were between that on T1W and T2W

Table V. Tumours staged with MRI

Primary tumours	
Nasopharyngeal	
Plasmocytoma	1
Lymphoma	1
Chordoma	1
Parotid carcimona (high grade)	2
Antro-ethmoid	
Carcinoma	1
Malignant melanoma	2
Recurrent tumours	
Nasopharyngeal	
Rhabdomyosarcoma	1
Carcinoma	1
Parotid	
Carcinoma	1
Lymphangiohaemangioma	1
Laryngopharyngeal carcinoma	2
Antral carcinoma	1
Carcinoma submandibular gland	1
Malignant melanoma recurrent in neck lymph nodes	1
Total	17

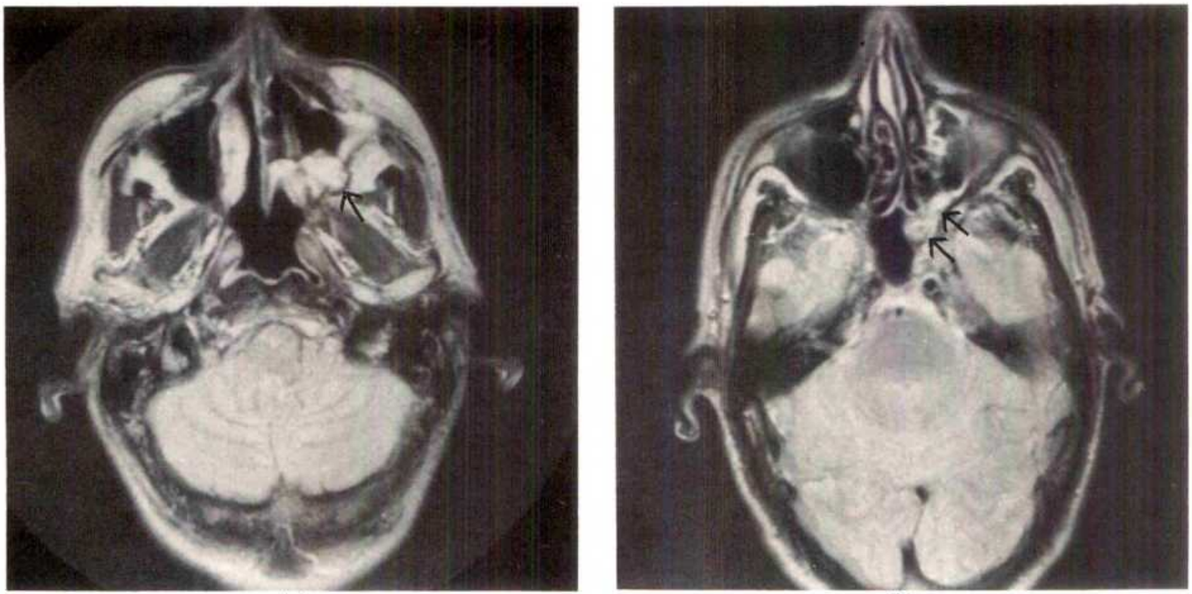
(a) (b)

Figure 2. (a) Transverse T2W scan (TR 1500 ms, TE 80 ms) showing recurrent carcinoma lying posteriorly in the left maxillary antrum and extending out of the antrum through the lateral wall (arrow). Note the prior removal of the medial wall of the antrum. (b) Transverse T2W scan (TR 1500 ms, TE 80 ms) showing a second, completely separate deposit along the course of the left maxillary nerve producing left facial pain (arrows). Symptoms remitted following radiotherapy.

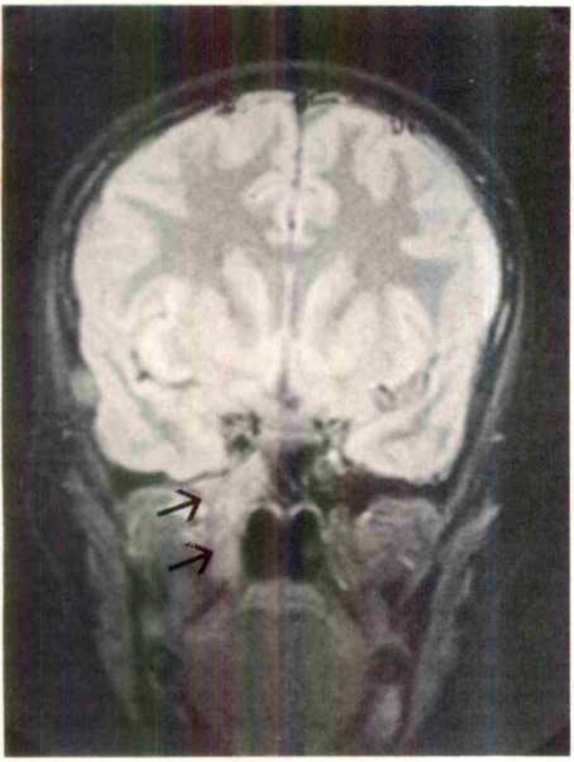

Figure 3. Coronal STIR scan (TR 1500 ms, TE 30 ms, TI 100 ms) showing high-signal-intensity tumour at the skull base and in the right pterygopalatine fossa (arrows). The patient was complaining of right facial pain in the distribution of the maxillary nerve. Radiotherapy produced remission of symptoms. The histological diagnosis was non-Hodgkin's lymphoma.

sequences, *i.e.* signal intensity greater than skeletal muscle but considerably less than that from fat. All tumours on the STIR sequence showed a high signal intensity, at least as bright as grey matter, with six tumours producing a very high signal, similar to that from normal nasal mucosa. These six tumours comprised two antral carcinomas, one case of malignant melanoma recurrent in neck lymph nodes and three parotid tumours (one haemangiolymphangioma and two carcinomas).

In four patients, tumour was seen at the primary site and in regional lymph nodes (one nasopharyngeal carcinoma, two high-grade parotid carcinomas and one squamous cell carcinoma recurrent in the parotid). The signal intensity from the lymph nodes was similar to that from the primary lesion. Not all patients underwent surgery and even those who were operated on did not necessarily have systematic lymph node excision, so it is not possible to comment on sensitivity and specificity of lymph node detection in this group of patients. There were, however, no known false positives or negatives in this series.

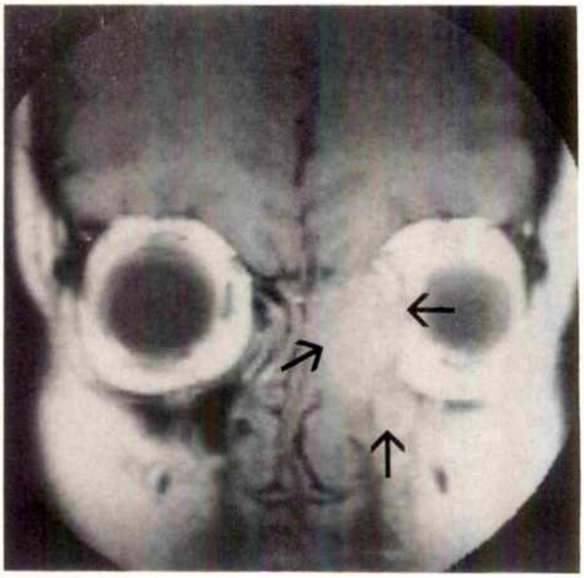

Figure 4. Coronal T1W scan (TR 500 ms, TE 26 ms) following gadolinium-DTPA. Heterogeneous-enhancing antro-ethmoid plasmocytoma (arrows) is seen invading through the cribriform plate on the left but without intracerebral invasion.

Eight patients had sinusitis of the maxillary antra. The signal intensity of the thickened mucosa on the T1W sequence was similar to, or slightly higher than, skeletal muscle (and therefore of virtually identical signal to tumour). On the T2W sequence, however, the signal intensity of inflamed antral mucosa was very high in all cases, similar to fat and nasal mucosa. The appearances on the PD sequence were mid-way between that on the T1W and T2W sequences, generally being of slightly higher signal intensity than tumour. On the STIR sequence, inflamed mucosa was of very high signal intensity, similar to the signal from normal nasal mucosa and again generally of slightly higher signal intensity than tumour.

The signal intensity of normal structures are well described in the literature on T1W, PD and T2W sequences (Crawford et al, 1989; Cross et al, 1989b) but not on the STIR sequence. Consequently the following observations relating to signal intensity on the STIR sequence have been made in this series to provide reference points for the discussion of tumour appearances. Nasal mucosa produced a very high signal intensity; grey matter, high signal; major salivary glands, medium to high; skeletal muscle, low; and fat, very low.

Discussion

Despite its considerable value as an imaging technique it is doubtful that MRI currently offers any advance over CT in achieving a histological diagnosis for head and neck tumours. Both modalities can make some prediction about the nature of mass lesions based on apparent organ of origin and frequency of occur-

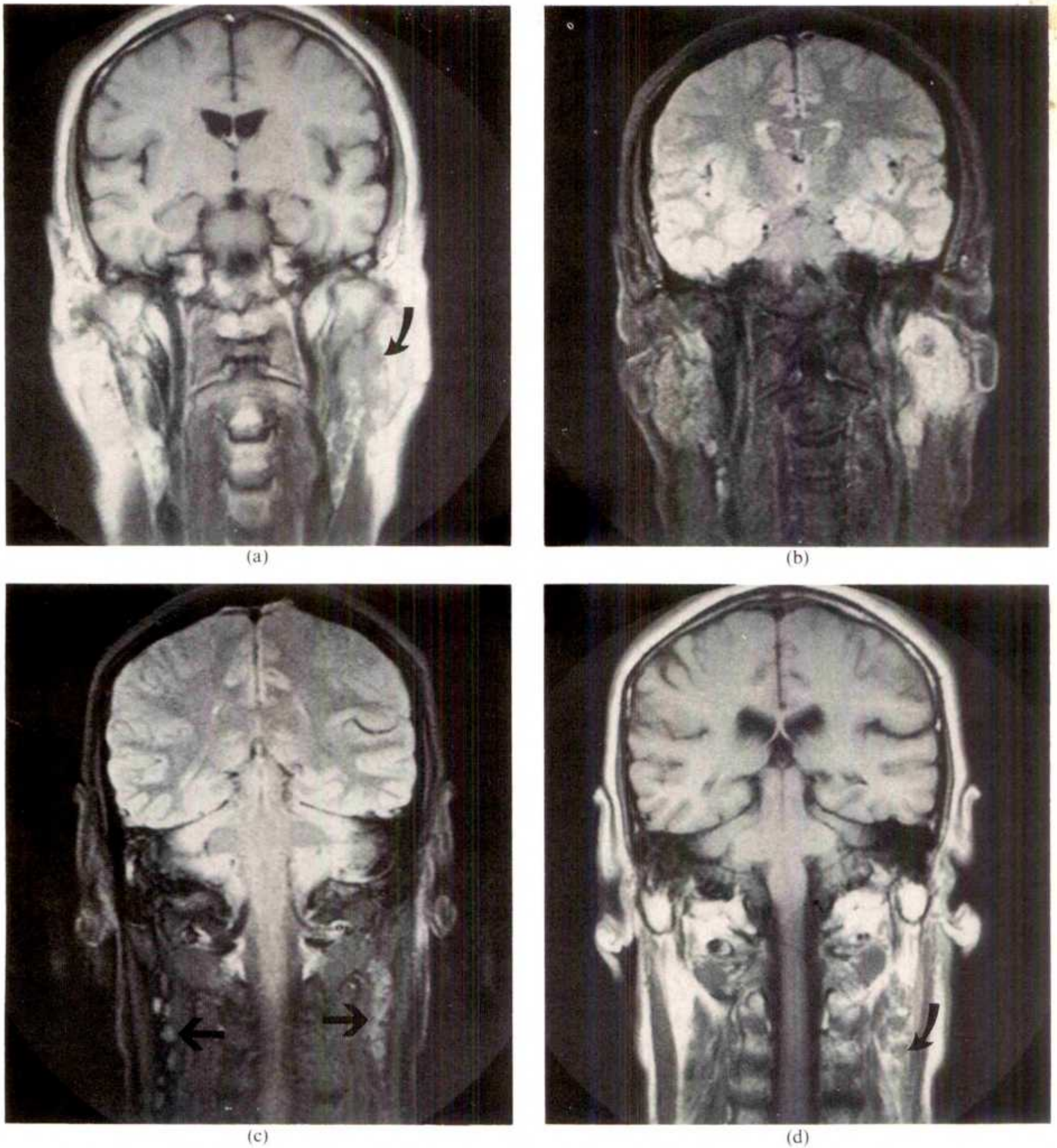

(a) (b) (c) (d)

Figure 5. (a) Coronal T1W (TR 500 ms, TE 26 ms) scan showing a heterogeneous, predominantly medium-signal-intensity carcinoma of the left parotid gland (curved arrow) (lower signal intensity than normal fatty parotid tissue but slightly higher signal intensity than skeletal muscle). Medium-signal-intensity cervical lymph nodes are seen bilaterally. These are more clearly visualized on the STIR sequence (TR 1500 ms, TE 30 ms, TI 100 ms) shown in (b) and (c) (slightly posterior scan). It is interesting to review the lymph node chains seen on the more posterior scan on the T1W sequence (d). The reduced contrast is clearly evident (the lymph node chain on the right is lost against the adjacent skeletal muscle) but the resolution is much improved (note particularly the chain of lymph nodes on the left hand side; curved arrow).

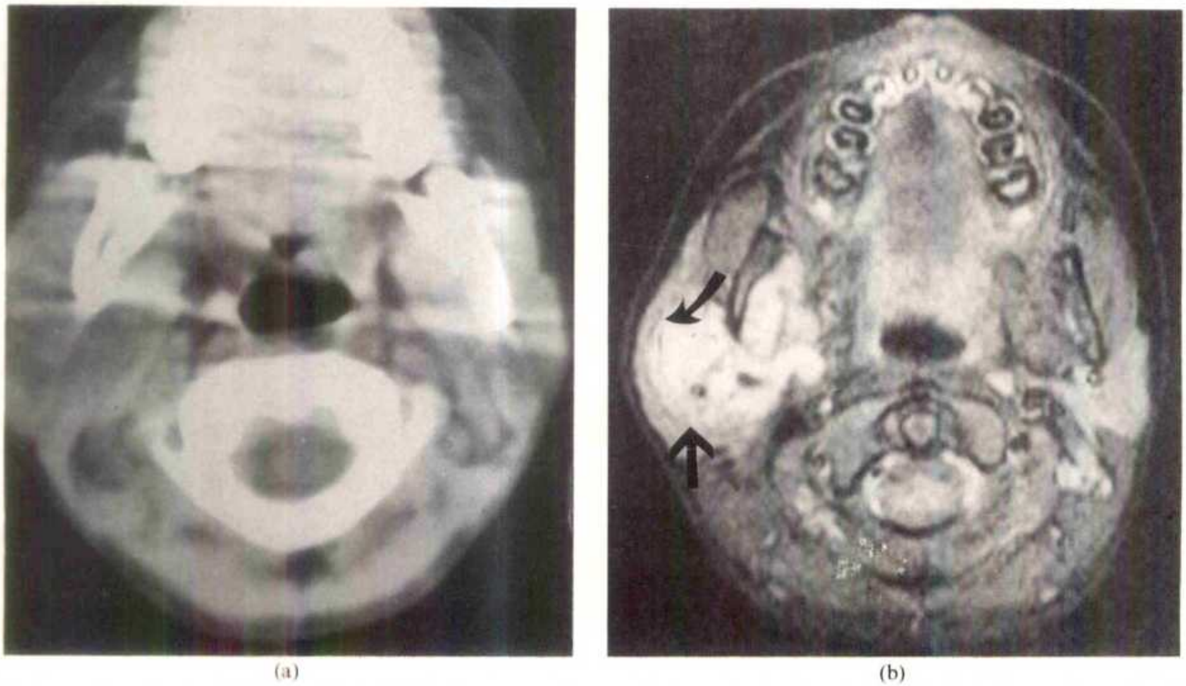

Figure 6. (a) CT scan showing a low-density right parotid tumour. The image is markedly degraded by artefact arising from the abrupt density step at cortical bone and at the pharynx. (b) Transverse STIR sequence (TR 1500 ms, TE 30 ms, TI 100 ms) showing high signal intensity from the parotid tumour (vertical straight arrow). Its extent is well defined. Note the strip of normal parotid compressed laterally by the tumour (curved arrow).

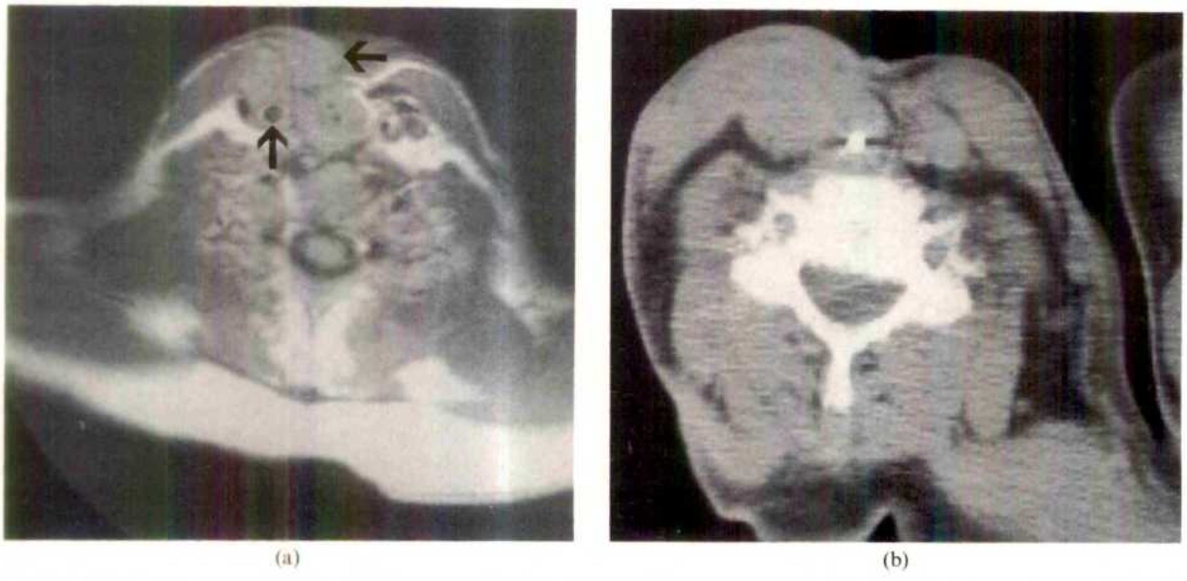

Figure 7. (a) Transverse T1W scan (TR 660 ms, TE 26 ms) showing medium- to high-signal-intensity recurrent laryngeal carcinoma (horizontal arrow) invading the muscles of the anterior neck, encasing the right common carotid artery (vertical arrow) and abutting the right internal jugular vein. (b) Contrast-enhanced CT scan of the same patient. The recurrent tumour is indistinguishable from normal muscle and, owing to poor timing of the intravenous contrast, the relationship of tumour to the local vasculature has not been determined.

rence of specific lesions (Som et al, 1988b; Whyte & Hourihan, 1989). The signal intensity of benign and malignant tumours show considerable overlap and on this criterion only tentative statements at best can be made regarding the aggressive capability of tumours (Byrne et al, 1989; Casselman & Mancuso, 1987; Som et al, 1989a; Teresi et al, 1987a).

The major role of MRI is in staging tumours for surgery and radiotherapy and the diagnosis of recurrent tumour (Tabor & Curtin, 1989; Teresi et al, 1989a). In this series MRI provided additional significant information over that provided by CT in nine patients undergoing tumour staging (Figs 2–7).

In staging tumours MRI has two advantages over CT: its ability to image in any two or three planes desired, and its superior tissue contrast (Curtin, 1989; Lufkin & Hanafee, 1987; Teresi et al, 1987a). The multiplanar ability of MRI allows complex anatomy and pathology to be well demonstrated. This has been especially noted in the region of the head and neck; for example, demonstration of perineural tumour extension into the skull basal foramina and fossae (Laine et al, 1990; Teresi et al, 1987b, c). This was seen in two patients in this current series (Figs 2, 3).

The superior tissue contrast of MRI allows tumour and involved lymph nodes to be differentiated from inflamed mucosa, retained secretions, fibrosis and normal structures, particularly skeletal muscle and blood vessels (Cross et al, 1989b; Kassel et al, 1989b). On CT the attenuation values of these show considerable overlap on unenhanced scans (Som et al, 1988a; Stutley et al, 1989).

Although there is some disagreement between reports, tumours in the region of the head and neck are generally described as having the following signal intensities: similar to or just less than skeletal muscle on T1W sequences, higher than skeletal muscle but less than fat (*i.e.* often similar to the fat-containing major salivary glands) on T2W sequences and somewhere between these on proton density sequences (Casselman & Mancuso, 1987; Som et al, 1987, 1988a, b, 1989a; Vogl et al, 1989).

The results in this series parallel those described elsewhere except for the appearances on T1W sequences, where with only one exception (the recurrent sublingual carcinoma isointense with skeletal muscle) the tumours showed a signal intensity slightly greater than skeletal muscle.

The STIR sequence used in this current series is not commonly described elsewhere in the American literature although reports of its usefulness for increasing the visibility of malignant lesions can be found (Cobby et al, 1990; Goddard et al, 1988; Shuman et al, 1988). The STIR sequence suppresses fat and is T_1 plus T_2 weighted. As a result structures containing water produce a high signal. This highlights both tumours and acute inflammatory lesions. In this series most tumours had a high signal on T2W and STIR sequences but only a minority had the very high signal intensity of inflammatory tissue and normal nasal mucosa.

For staging tumours the T1W sequence produces excellent demonstration of anatomy, including blood vessels, easily delineated by their signal void. On this sequence tumours are easily differentiated from fat and fatty structures such as the major salivary glands. The T2W and STIR sequences produce better differentiation of tumour from normal muscle, retained secretions and inflammatory lesions (Cross et al, 1989c).

The limited numbers with lymph node metastases in this series (four true positives, no *known* false positives or negatives) do not permit anything more than a tentative comment about the use of MRI for the detection of lymph nodes involved by tumour. Lymph nodes involved by tumour show similar signal intensities to the primary tumour and to inflammatory tumours (Kassel et al, 1989b; Teresi et al, 1989b; van den Brekel et al, 1990).

In the upper neck, lymph nodes are generally larger than in the lower neck, presumably because of recurrent inflammation associated with common oropharyngeal and dental ailments. The following criteria for involvement have been suggested: a maximum diameter greater than 1 cm in the lower neck (producing 80% true positives), greater than 1 cm in the upper neck (submandibular and jugulodiagastric regions of the internal jugular nodes) if spherical or in a high-risk group (*i.e.* known primary carcinoma) but above 1.5 cm in the upper neck if not in a high-risk group (Som, 1987). Any lymph node showing central necrosis (areas of increased signal intensity on a T2W sequence, areas failing to enhance with gadolinium or areas measuring 10–18 HU on CT) can be considered involved and it has been claimed that this is the single most specific feature of metastatic involvement (van den Brekel et al, 1990).

There is no doubt that both CT and MRI will miss lymph node micrometastases (Curtin, 1989) and it has been claimed that neither produces a significant increase in accuracy over clinical examination (Feinmesser et al, 1990; Som, 1987; Werber & Lucente, 1989). Van den Brekel et al (1990) have suggested that the accuracy of MRI can be up to 89% with gadolinium, compared with 77–78% for clinical examination. Whether or not a similar accuracy would be achievable using the STIR sequence without gadolinium is not known.

Gadolinium enhancement is not required routinely (Vogl et al, 1989) although it can be useful for assessing intracranial extension and meningeal involvement, and may improve differentiation from adjacent inflammatory lesions. Retained secretions will not enhance whereas tumour (and involved lymph nodes) and acutely inflamed tissue will enhance, the latter generally to a greater extent (Robinson et al, 1989; van den Brekel et al, 1990). Many of the centres describing the usefulness of gadolinium are not using the STIR sequence, which to a certain extent fulfills the same function without intravenous contrast, *i.e.* producing an increase in signal intensity and visibility of tumours and inflammatory tissue.

Considering the problem of recurrent tumour, on CT the appearances may be similar to post-radiotherapy or post-operative fibrosis. The immediate post-intervention appearances (within 4 months of radiotherapy or surgery) on MRI are similar to inflammation from other causes and to the appearances of inflamed mucosa in the eight patients in whom this was noted in this series (medium signal intensity on the T1W sequence and high on the T2W and STIR sequences). Six months or so after intervention, the signal intensity of fibrosis generally becomes low on the T1W sequence (a little below that of skeletal muscle) and low to intermediate on the T2W, proton density and STIR sequences (Kassel et al, 1989c; Som et al, 1988a, 1989a).

Inspissated secretions could potentially cause problems in delineating sinonasal tumours although, as mentioned above, secretions will not enhance with gadolinium (Dillon et al, 1990). However, even without gadolinium the signal intensity from tumours and sinonasal secretions is generally different. Acute secretions will have low signal intensity on T1W and high signal on T2W sequences owing to a 95% water content. With increasing chronicity the water content falls and the signal intensity becomes medium to high on T1W and high on T2W sequences. Occasionally the protein content exceeds 25% and all water present is bound, producing a very low signal intensity on both T1W and T2W sequences (Som et al, 1989b).

Criteria that may suggest tumour recurrence include increased signal intensity on the T2W sequence later than 6 months after intervention, bulky mass beyond the original primary site and obliteration of tissue planes (Kassel et al, 1989c). The last one clearly may also be seen simply as a sequence to the previous intervention. In this series, recurrent tumour always had a signal intensity just above skeletal muscle on the T1W sequence (except one case which was isointense) and a high signal intensity (sometimes very high) on the T2W and STIR sequences.

In this series tumour recurrence was diagnosed with a sensitivity of 100% and a specificity of 80%. Two false positives were encountered (Fig. 1). In both these patients the appearances of the suspicious tissue on the T1W sequence (isointense with skeletal muscle in one and less than skeletal muscle in the other) might suggest fibrosis but the increased signal intensity on the T2W and STIR sequences was highly likely to represent an active process, which more than 1 year after surgery or radiotherapy suggested tumour recurrence. It seems from these results that in order to maintain a high sensitivity one has to accept occasional false positives.

Conclusions

MRI is the modality of choice for staging the non-neurological tumours considered in this study. It displays high tissue contrast and excellent delineation of anatomy in multiple planes, an invaluable feature when dealing with the complex anatomy of the head and neck. MRI has a high sensitivity for the diagnosis of recurrent tumour, albeit at the cost of occasional false positives.

Acknowledgments

The authors wish gratefully to acknowledge the co-operation and encouragement of the trustees, Dr A. L. T. Beddoe, Dr P. Goddard, Dr C. Johnson and Dr J. L.G. Thomson, and the radiographers, Miss A. Case (Superintendent), Miss Joanne Waring (Deputy Superintendent) and Mrs M. Riley, of the Bristol MRI centre.

References

Byrne, M. N., Spector, J. G., Garvin, C. F. & Gado, M. H., 1989. Preoperative assessment of parotid masses: a comparative evaluation of radiologic techniques to histopathological diagnosis. *Laryngoscope, 99*, 284–292.

Casselman, J. W. & Mancuso, A. A., 1987. Major salivary gland masses: comparison of MR imaging and CT. *Radiology, 165*, 183–189.

Cobby, M., Browning, J., Jones, A., Whipp, E. & Goddard, P., 1990. Magnetic resonance imaging., computed tomography and endosonography in the local staging of carcinoma of the cervix. *British Journal of Radiology, 63*, 673–679.

Crawford, S. C., Harnsberger, H. R., Lufkin, R. B. & Hanafee, W. N., 1989. The role of gadolinium-DTPA in the evaluation of extracranial head and neck mass lesions. In *Radiologic Clinics of North America; MRI of the Head and Neck*, ed. by P. M. Som and M. P. Shapiro (W. B. Saunders, Philadelphia), 27 (2), pp. 222, 227.

Cross, R. R., Shapiro, M. D. & Som, P. M., 1989. MRI of the parapharyngeal space. In *Radiologic Clinics of North America; MRI of the Head and Neck*, ed. by P. M. Som and M. P. Shapiro (W. B. Saunders, Philadelphia), 27 (2), p. 353 (a); p. 363 (b); pp. 373–374 (c).

Curtin, H. D., 1989. Imaging of the larynx: current concepts. *Radiology, 173*, 1–11.

Dillon, W. P., Som, P. M. & Fullerton, G. D., 1990. Hypointense MR signal in chronically inspissated sinonasal secretions. *Radiology, 174*, 73–78.

Feinmesser, R., Freeman, J. L., Noyek, A. M., Birt, D., Gullane, P. & Mullen, J. B., 1990. MRI and neck metastases: a clinical, radiological, pathological correlative study. *Journal of Otolaryngology, 19*, 136–140.

Goddard, P., Waring, J., Case, A., Yeats, R., Bullimore, J. A., Whipp, E. & Barley, V., 1988. The STIR sequence in MRI of neoplastic lesions. *Bristol Medico-chirurgical Journal, 103(ii)*, 26.

Kassel, E. E., Keller, M. A. & Kucharezyk, W., 1989a. MRI of the floor of the mouth, tongue and oropharynx. *Radiologic Clinics of North America, 27(2)*, 337.

Kassel, E. E., Keller, M. A. & Kucharezyk, W., 1989b. MRI of the floor of the mouth, tongue and oropharynx. *Radiologic Clinics of North America, 27(2)*, 331.

Kassel, E. E., Keller, M. A. & Kucharezyk, W., 1989c. MRI of the floor of the mouth, tongue and oropharynx. *Radiologic Clinics of North America, 27 (2)*, 348.

Laine, F. J., Braun, I. F., Jensen, M. E., Nadel, L. & Som, P. M., 1990. Perineural tumour extension through the foramen ovale: evaluation with MR imaging. *Radiology, 174*, 65–71.

Lloyd, G. A. S. & Phelps, P. D., 1986. The demonstration of tumours of the parapharyngeal space by magnetic resonance imaging. *British Journal of Radiology, 59*, 675–683.

Lufkin, R. B. & Hanafee, W. N., 1987. Magnetic resonance imaging of the head and neck. *Investigative Radiology, 2*, 162–169.

Mandelblatt, S. M., Braun, I. F., Davis, P. C., Fry, S. M., Jacobs, L. H. & Hoffman, J. C., 1987. Parotid masses: MR imaging. *Radiology, 163,* 411–414.

Robinson, J. D., Crawford, S. C., Teresi, L. M., Schiller, V. L., Lufkin, R. B., Harnsberger, H. R., Dietrich, R. B., Crim, J. R., Duckwiler, G. R., Spickler, E. M. & Hanafee, W. N., 1989. Extracranial lesions of the head and neck: preliminary experience with Gd-DTPA enhanced MR imaging. *Radiology, 172,* 165–170.

Schaefer, S. D., Maravilla, K. R. & Suss, R. A., 1985. Magnetic resonance imaging versus computed tomography: comparison in imaging oral cavity and pharyngeal carcinomas. *Archives of Otolaryngology, 111,* 730–734.

Shuman, W. P., Baron, R. L., Peters, M. J. & Tazioli, P. K., 1988. Comparison of STIR and spin-echo MR imaging at 1.5 T in 90 lesions of the chest, liver and pelvis. *American Journal of Roentgenology, 152,* 853–859.

Som, P. M., 1987. Lymph nodes of the neck. *Radiology, 165,* 593–600.

Som, P. M., Braun, I. F., Shapiro, M. D., Reede, D. L., Curtin, H. D. & Zimmerman, R. A., 1987. Tumours of the parapharyngeal space and upper neck: MR imaging characteristics. *Radiology, 164,* 823–829.

Som, P. M., Shapiro, M. D., Biller, H. F., Sasaki, C. & Lawson, W., 1988a. Sinonasal tumours and inflammatory tissues: Differentiation with MR imaging. *Radiology, 167,* 803–808.

Som, P. M., Sacher, M., Stollman, A. L., Biller, H. F. & Lawson, W., 1988b. Common tumours of the parapharyngeal space: refined imaging diagnosis. *Radiology, 169,* 81–85.

Som, P. M. & Biller, H. F., 1989. High-grade malignancies of the parotid gland: Identification with MR imaging. *Radiology, 173,* 823–826.

Som, P. M., Dillon, W. P., Sze, G., Lidov, M., Biller, H. F. & Lawson, W., 1989a. Benign and malignant sinonasal lesions with intracranial extension: differentiation with MR imaging. *Radiology, 172,* 763–766.

Som, P. M., Dillon, W. P., Fullerton, G. D., Zimmerman, R. A., Rajagopalan, B. & Marom, Z., 1989b. Chronically obstructed sinonasal secretions: Observations on T1 and T2 shortening. *Radiology, 172,* 515–520.

Stutley, J., Crooke, J. & Parsons, C., 1989. Normal CT anatomy of the tongue, floor of the mouth and oropharynx. *Clinical Radiology, 40,* 248–253.

Tabor, E. K. & Curtin, H. D., 1989. MR of the salivary glands. In *Radiological Clinics of North America: MRI of the Head and Neck*. Ed. by P. M. Som and M. P. Shapiro (W. B. Saunders Co., Eastbourne), pp. 383–385.

Teresi, L. M., Lufkin, R. B., Wortham, D. G., Abemayor, E. & Hanafee, W. N., 1987a. Parotid masses: MR imaging. *Radiology, 163,* 405–409.

Teresi, L. M., Lufkin, R. B., Vinuela, F., Dietrich, R. B., Wilson, G. H., Bentson, J. R. & Hanafee, W. N., 1987b. MR imaging of the nasopharynx and floor of the middle cranial fossa part I. Normal anatomy. *Radiology, 164,* 811–816.

Teresi, L. M., Lufkin, R. B., Vinuela, F., Dietrich, R. B., Wilson, G. H., Bentson, J. R. & Hanafee, W. N., 1987c. MR imaging of the nasopharynx and floor of the middle cranial fossa part II. Malignant tumours. *Radiology, 164,* 817–821.

Teresi, L. M., Lufkin, R. B. & Hanafee, W. N., 1989a. MRI of the larynx. *Radiologic Clinics of North America, 27(2),* 393.

Teresi, L. M., Lufkin, R. B. & Hanafee, W. N., 1989b. MRI of the larynx. *Radiologic Clinics of North America, 27(2),* 402.

Van den Brekel, M. W. M., Castelijns, J. A., Stel, H. V., Valk, J., Croll, G. A., Golding, R. P., Luth, W. J., Meyer, C. J. L. M. & Snow, G. B., 1990. Detection and characterization of metastatic cervical adenopathy by MR imaging: comparison of different MR techniques. *Journal of Computer Assisted Tomography, 14(4),* 581–589.

Vogl, T. J., 1990. Head and neck: editoral overview. *Current Opinion in Radiology, 2,* 81–82.

Vogl, T. J., Bruning, R., Grevers, G., Mees, K., Bauer, M. & Lissner, J., 1988. MR imaging of the oropharynx and tongue: comparison of plain and Gd-DTPA studies. *Journal of Computed Tomography, 12(3),* 427–433.

Vogl, T. J., Dresel, S., Bilaniuk, L. T., Grevers, G., Kang, K. & Lissner, J., 1989. Tumours of the nasopharynx and adjacent areas: MR imaging with Gd-DTPA. *American Journal of Roentgenology, 154,* 585–592.

Werber, J. L. & Lucente, F. E., 1989. Computed tomography in patients with laryngeal carcinoma: a clinical perspective. *Annals of Otology, Rhinology and Laryngology, 98,* 55–58.

Whyte, A. M. & Hourihan, M. D., 1989. The diagnosis of tumours involving the parapharyngeal space by computed tomography. *British Journal of Radiology, 62,* 526–531.

1992, *The British Journal of Radiology*, 65, 384–389

The role of 3D CT in the assessment of acetabular fractures

By R. L. Guy, MRCP, FRCR, *P. A. Butler-Manuel, FRCS, P. Holder, FRCS and *R. N. Brueton, MD, FRCS

Department of Radiology and *Orthopaedic Academic Unit, St Thomas' Hospital, Lambeth Palace Road, London SE1 7EH, UK

(*Received 12 June 1991 and in revised form 8 October 1991, accepted 20 November 1991*)

Keywords: Acetabular fractures, Plain radiography, Computed tomography, Three dimensional reconstruction

Abstract. A total of 16 patients with acetabular fractures were evaluated by plain radiography, axial computed tomography (CT) and three dimensional (3D) CT. It was possible to classify the fracture type in each case from the plain radiographs alone. Axial CT gave additional detail in certain areas, notably the region of the teardrop, the obturator foramen and the acetabular roof. Intra-articular and impacted roof fragments and associated soft tissue injuries were also shown. 3D CT provided the best and most easily interpreted overall assessment of the fractures. In addition to projections equivalent to the plain radiographs, two other views were of particular clinical value in demonstrating surgically inaccessible areas, namely the view of the pelvis from above and the view of the inner aspect of the fractured hemipelvis. However, fracture lines demonstrated on plain radiographs and axial CT were not always apparent on the 3D CT scans. Although 3D CT is a valuable addition to the imaging of acetabular fractures, it is not a substitute for good quality plain radiography and analysis of the axial CT images.

Early open reduction and internal fixation of acetabular fractures offer the best chance of achieving a good long-term result (Pennal et al, 1980). Accurate pre-operative planning is vital and requires detailed knowledge of the complex relationship of the fracture fragments.

A classification of acetabular fractures based on a series of plain radiographs was devised by Judet et al (1964). Axial computed tomography (CT) is now also routinely used in the assessment of acetabular fractures (Harley et al, 1982; Rafii et al, 1983). More recently there have been enthusiastic reports about the value of three dimensional (3D) CT (Burk et al, 1985; Pozzi Mucelli et al, 1986) and some authors have claimed that it is a substitute for plain radiography (Scott et al, 1987).

The aim of this study was to assess the relative merits of plain radiography, axial CT and 3D CT in the diagnosis of acetabular fractures.

Materials and methods

A total of 16 patients with acetabular fractures were studied, 12 of whom subsequently underwent operative treatment. Each patient was investigated by plain radiography, axial CT and 3D CT.

Four standard plain radiographs were taken in each case: antero-posterior (AP) radiograph of the whole pelvis and AP, iliac oblique and obturator oblique radiographs of the affected hip (Letournel, 1980). The plain radiographs were studied in detail and the fracture lines were traced. In each patient an initial diagnosis was made on the basis of the plain radiographs according to the classification of Judet et al (1964).

The CT scans were performed on a Siemens Somatom DR H scanner with contiguous 4 mm cuts using a low mAs (Gholkar et al, 1988). Part of the sacro-iliac joint was included to aid in orientation.

The 3D reconstructions were made using a surface imaging technique utilizing the scanner's computer. In addition to reconstructing the whole pelvis, the affected hemipelvis was reconstructed alone giving greater detail and enabling the inner surface of the ilium to be viewed. The projections chosen were at 45° increments about the z (vertical) axis, at angles of 30°, 45° and 60° about the x (horizontal) axis and as if viewed from above and below. In two patients the head of the femur was removed to enable the articular surface of the acetabulum to be viewed.

Both the axial and 3D CT images were assessed to determine whether they altered the initial radiological diagnosis. The ability to demonstrate the fracture type and the relationship of the fragments was compared using the different techniques. Any additional information contributed by axial CT and 3D CT was also noted.

Results

It was possible to identify the fracture lines and to classify the type of acetabular fracture from the plain radiographs in all 16 patients (Table I), although bowel gas did partially obscure the fracture lines in one case (Fig. 1b).

The axial CT scans did not change the initial radiological diagnosis in any patient. The areas of the teardrop and apex of the obturator foramen were particularly well shown. In the two patients with

---

Present addresses: R. L. Guy, Department of Radiology, Royal Marsden Hospital, Sutton, Surrey and P. A. Butler-Manuel, Hastings Orthopaedic Centre, Royal East Sussex Hospital, Hastings, East Sussex.

Address correspondence to Dr R. L. Guy, Department of Radiology, Royal Marsden Hospital, Downs Road, Sutton, Surrey.

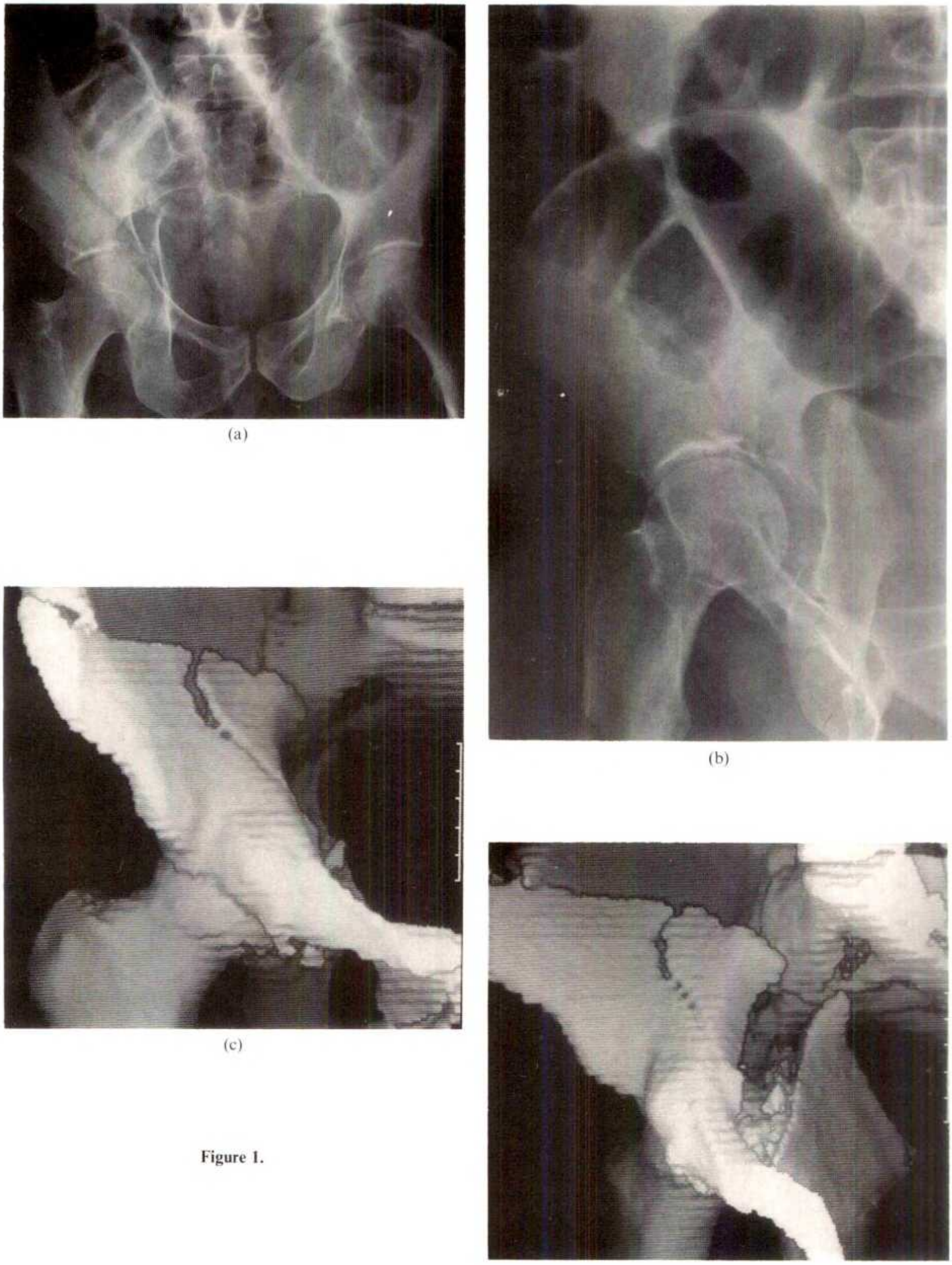

(a)

(b)

(c)

(d)

Figure 1.

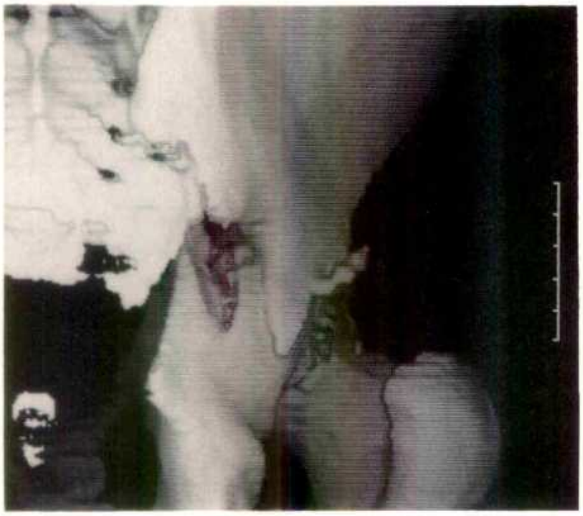

(e)

Figure 1. Right two-column acetabular fracture. (a) AP and (b) iliac oblique radiographs of the pelvis. (c) Frontal, (d) iliac oblique and (e) posterior 3D CT images. Although the fracture can be classified from the plain radiographs, the shape of the fracture line and the relationship of the major bony fragments are particularly well seen on the 3D CT images. The iliac oblique 3D projection also demonstrates the disrupted quadrilateral plate and intra-articular fragments. The posterior projection shows clearly how the posterior column should be reduced onto the stable fragment.

Table I. Diagnoses of the 16 acetabular fractures according to the classification of Judet et al (1964)

Two-column	4
Transverse plus posterior wall	3
Transverse	2
T-shaped	2
Anterior column plus posterior hemitransverse	2
Posterior wall	2
Anterior column	1

T-shaped fractures this enabled the vertical fracture or stem segment to be seen more clearly than on the obturator oblique plain radiograph, where there was overlap of the fragments.

The roof of the acetabulum was demonstrated as a distinct condensation that became increasingly apparent on successive cuts. An intra-articular bone fragment not seen on plain radiographs was detected in one patient and in another patient impacted roof fragments were demonstrated. The axial CT scans frequently demonstrated secondary fracture lines and additional small fragments that had not been recognized on the plain radiographs. In addition, two large pelvic haematomata requiring drainage were identified. Similarly, 3D CT did not alter the initial radiological diagnoses or the decision whether to operate, but it did provide the best and most easily interpretable overall assessment of the fractures. However, fracture lines demonstrated on plain radiographs and axial CT were not always apparent on the 3D CT scans. This occurred in one undisplaced transverse fracture and in one two-column fracture where a fracture of the posterior column was not seen.

Both the projections corresponding to the standard plain radiographs and other unique 3D CT projections were found to be useful, in particular the internal lateral and superior projections (Figs 1 & 2). When there was an associated dislocation or subluxation of the femoral head, it was best demonstrated on the inferior 3D projection (Fig. 3).

Discussion

The aim of surgical treatment is to achieve a perfect reduction of the fracture, thereby restoring the articular surface of the acetabulum. To achieve this the surgeon must understand the fracture sufficiently to be able to draw the fracture lines on a dry bone before surgery.

The acetabulum is supported within an inverted "Y" formed by two columns. The anterior column extends from the anterior part of the iliac crest to the pubic symphysis, and the posterior column extends from the inferior sacroiliac joint and sciatic notch to the ischial tuberosity.

Judet et al (1964) described five primary types of acetabular fracture: posterior column or anterior column fractures where each column is separated from the pelvis; anterior or posterior wall fractures where a fragment of the acetabular wall is detached and transverse fractures where the fracture line passes through the acetabulum crossing both columns. They also described five more complicated types of acetabular fracture which are combinations of these five basic types.

The pioneering work of Judet et al (1964) greatly improved our understanding of pelvic radiographs and it is a tribute to them that the advent of axial CT and 3D CT has not altered their original classification. In all cases we were able to make the correct diagnoses from the plain radiographs alone. No problems were encountered positioning patients for plain radiographs in the acute stages, as has been reported by Scott et al (1987), although bony detail may be obscured by overlying bowel gas.

Axial CT has been shown previously to demonstrate the extent of the fracture and the presence of intra-articular fragments, as well as associated injuries such as sacral fractures and pelvic haematomata (Harley et al, 1982; Rafii et al, 1983). In addition, we have found it to be of particular value in the assessment of fractures of the acetabular roof and the obturator foramen. The detection of secondary fracture lines and additional small fragments was found to be of little practical value.

Although not instrumental in altering the diagnosis, the axial and 3D CT images were useful in confirming the diagnosis. 3D CT presents the information in the most readily interpretable form, demonstrating the

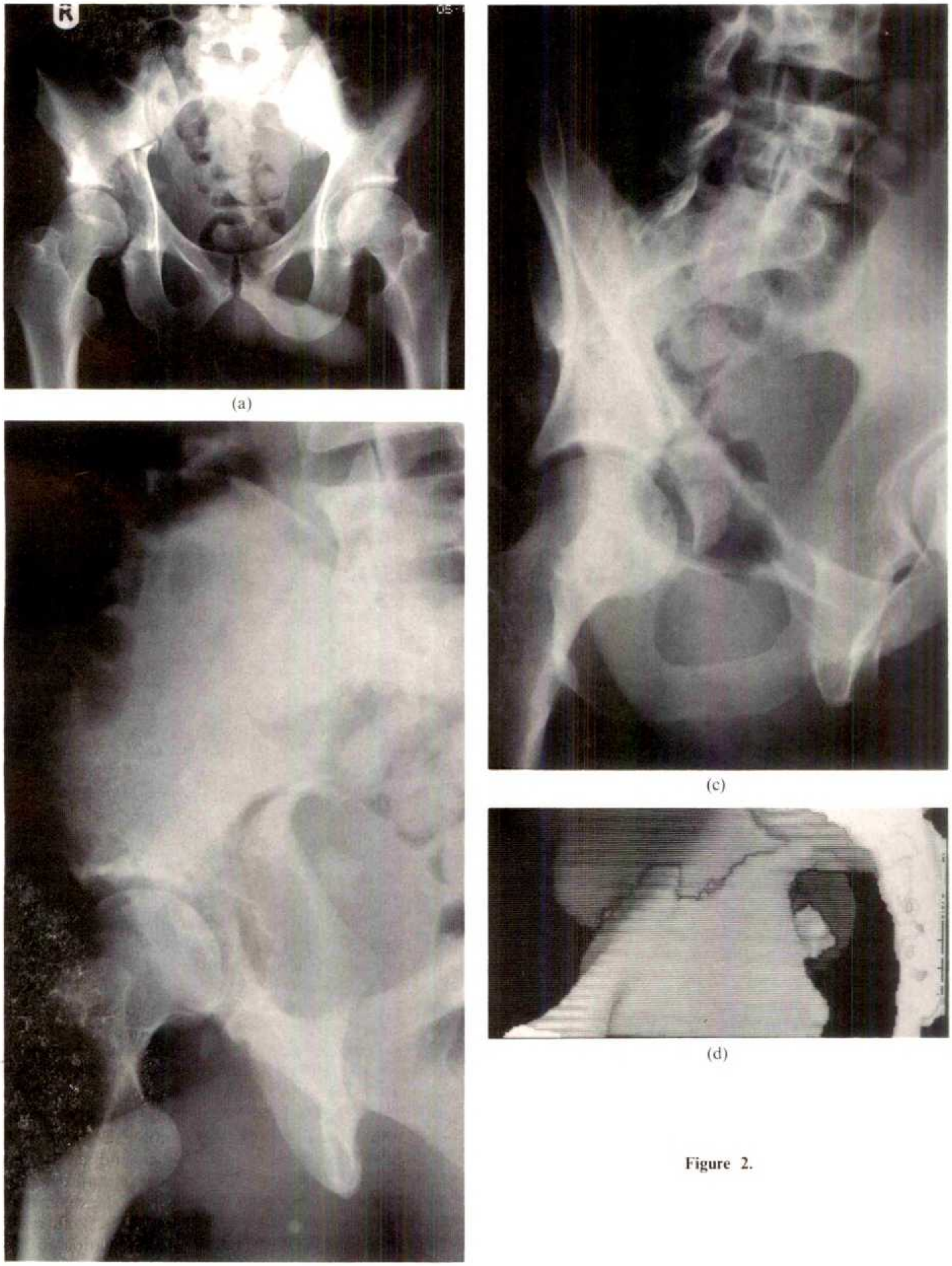

(a)

(b)

(c)

(d)

Figure 2.

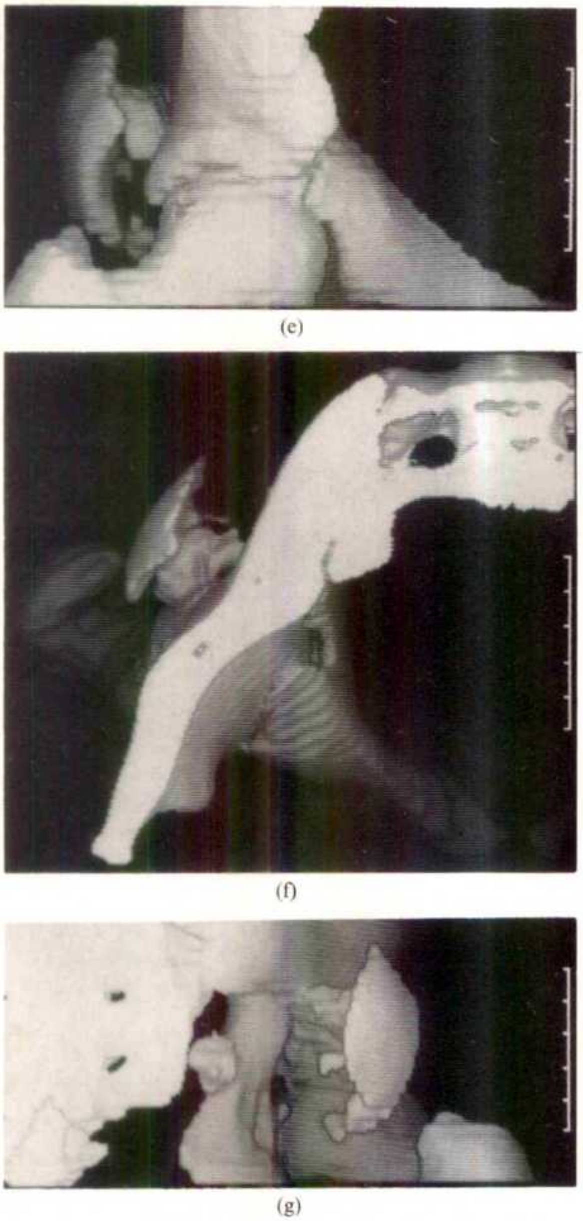

(e)

(f)

(g)

Figure 2. Right transverse acetabular fracture. (a) AP, (b) iliac oblique and (c) obturator oblique radiographs of the pelvis. (d) Internal lateral, (e) obturator oblique, (f) superior and (g) posterior 3D CT images. The fracture can be classified from the plain radiographs but the fracture line is particularly well shown on the superior and internal lateral 3D projections. Although visible on the plain radiographs, the position and size of the separate posterior fragment are best seen on the obturator oblique, superior and posterior 3D projections, where the uncovered head can also be seen.

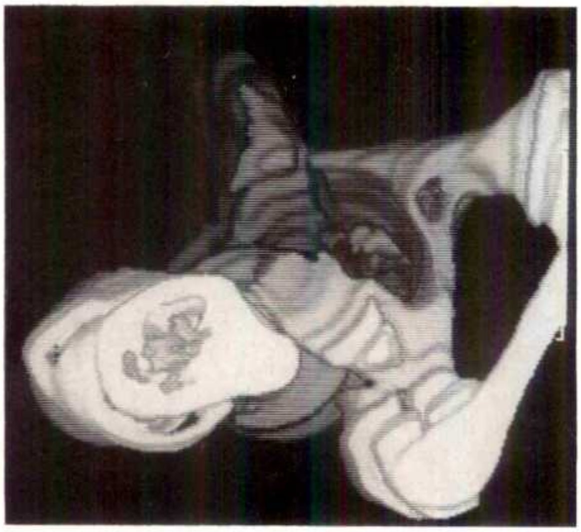

Figure 3. Right transverse plus posterior wall acetabular fracture. The inferior 3D CT projection clearly demonstrates the posterior subluxation of the femoral head.

complexity of the fracture lines. Two views were found to be of particular value giving information relating to the surgically least accessible parts of the pelvis. The view from above shows the surgeon what he can expect to find when he approaches a fracture from the ilio-inguinal approach. The view of the inner aspect of the hemipelvis demonstrates fracture lines crossing the quadrilateral plate, which even at surgery may be difficult to visualize and which may only be identified by palpation.

The 3D CT programme was less satisfactory for undisplaced fractures which may be averaged out unless very thin slices are used. Use of the software may be time-consuming although faster programs are now available. 3D CT is not suitable for post-operative follow-up as the internal fixation devices degrade the 3D CT images.

Editing out the femoral head from the 3D reconstructions was less helpful than expected. This is because the key to diagnosis is to understand the fracture lines of the innominate bone as a whole. When these are reduced accurately the articular surface of the acetabulum will also automatically be reduced.

The inexperienced observer is likely to find it more difficult to interpret the plain radiographs and axial CT scans and to relate the operative findings to these investigations. 3D CT is therefore of particular value in this situation and is also a useful teaching aid.

Although 3D CT is an excellent method of demonstrating the complex nature of the fracture, it should be regarded as being complementary to and not a substitute for good quality pre-operative plain radiographs and axial CT scans.

Acknowledgments

We would like to thank Mr F. W. Heatley, Dr A. B. Ayers, Dr K. A. Tonge and the Special Trustees of St Thomas' Hospital for their help in obtaining the 3D software.

References

Burk, D. Jr, Mears, D. C., Kennedy, W. H., Cooperstein, L. A. & Herbert, D. L., 1985. Three-dimensional computed tomography of acetabular fractures. *Radiology, 155,* 183–186.

Gholkar, A., Gillespie, J. E., Hart, C. W., Mott, D. & Isherwood, I., 1988. Dynamic low-dose three-dimensional computed tomography: a preliminary study. *British Journal of Radiology, 61,* 1095–1099.

Harley, J. D., Mack, L. A. & Winquist, R. A., 1982. CT of acetabular fractures: comparison with conventional radiography. *American Journal of Roentgenology, 138,* 413–417.

Judet, R., Judet, J. & Letournel, E., 1964. Fractures of the acetabulum: Classification and surgical approaches for open reduction. *Journal of Bone and Joint Surgery* (A), *46,* 1615–1646.

Letournel, E., 1980. Acetabulum fractures: classification and management. *Clinical Orthopaedics and Related Research, 151,* 81–106.

Pennal, G. F., Davidson, J., Garside, H. & Plewes, J., 1980. Results of treatment of acetabular fractures. *Clinical Orthopaedics and Related Research, 151,* 115–123.

Pozzi Mucelli, R. S., Muner, G., Pozzi Mucelli, F., Pozzi Mucelli, M., Marotti, F. & Dalla Palma, L., 1986. Three-dimensional computed tomography of the acetabulum. *European Journal of Radiology, 6,* 168–177.

Rafii, M., Firooznia, H., Golimbu, C., Waugh, T. Jr & Naidich, D., 1983. The impact of CT in clinical management of pelvic and acetabular fractures. *Clinical Orthopaedics and Related Research, 178,* 228–235.

Scott, W. W. Jr, Fishman, E. K. & Magid, D., 1987. Acetabular fractures: optimal imaging. *Radiology, 165,* 537–539.

1992, *The British Journal of Radiology*, 65, 390–392

Hydatid disease of the liver: evaluation of ultrasound and computed tomography

By M. I. El-Tahir, FRCR(UK), M. F. Omojola, FRCP(C), *T. Malatani, FRCS(C), *A. H. Al-Saigh, FRCS(I) and O. A. Ogunbiyi, FRCR(UK)

Departments of Radiology and *Surgery, College of Medicine, PO Box 641, Abha, Saudi Arabia

(Received 28 May 1991 and in revised form 8 October 1991, accepted 20 November 1991)

Keywords: Ultrasound, Computed tomography, Liver, Hydatid

Abstract. We have evaluated computed tomography (CT) and ultrasonography (US) in 41 patients with hepatic hydatid disease. CT was diagnostic in all patients, while US performed on 36 patients was diagnostic in 34. In the remaining two cases, heavy calcification in one and a large amount of intracavitary air in the other prevented accurate diagnosis. The US findings in the liver regarding cyst form (multilocular or unilocular), size and location were comparable to those of CT. CT detected associated extrahepatic cysts in the abdomen and pelvis in 11 patients while US performed on the same group of patients detected such cysts in seven patients. It is suggested that the entire abdomen and pelvis should be scanned in patients suspected of hydatid disease and when a hepatic lesion is suggestive of the disease.

Hydatid disease due to *Echinococcus granulosus* is endemic in sheep-raising countries such as Australia, New Zealand, Tasmania, parts of Africa and South America, particularly Argentina and Southern Brazil (Manson-Bahr & Apted, 1982), and is also prevalent in the Middle East, particularly in Iraq, Syria and Saudi Arabia (Ismael et al, 1980; Noah et al, 1986).

Cysts can occur anywhere in the body but the liver is the most common site (Choliz et al, 1982). Diagnosis is mainly radiological and serological. Several reports document the efficacy of computed tomography (CT) and ultrasonography (US) of the liver in hydatid disease. There is, however, little information in the literature comparing the efficacy of these two methods in the same patients.

Patients and methods

The hospital records of 41 patients with a diagnosis of hydatid liver disease seen at Asir Central Hospital between September 1987 and November 1989 were reviewed. There were 12 male and 29 female patients aged 18–85 years (average 52 years). The diagnosis was confirmed by serology and/or histology in all patients.

All 41 patients had a CT scan of the abdomen on a GE 9800 scanner and in four patients the scan included the pelvis. In 36 patients, contiguous 10 mm thick scans were obtained and in five patients scans were obtained at 15 mm intervals and 10 mm collimation. All except five patients received an intravenous bolus of 50 ml of sodium iothalamate (420 mg/ml). All patients received oral contrast media. Thirty-six patients had abdominal US and four of these also had pelvic US. A commercially available high-resolution real-time scanner (GE RT 3000) with 3.5 MHz transducer was used.

Plain radiographs of the abdomen and chest were obtained on all patients. All scans and plain radiographs were reviewed by consultant radiologists.

Results

Computed tomography

CT demonstrated hepatic cysts in all 41 cases. The cysts were smoothly marginated, thin-walled, spherical or oval masses of low attenuation (0–15±4 Hounsfield units (HU). Single cysts were found in 36 cases (88%). Two cysts were present in four cases (10%) and multiple cysts in one case (2%). Cysts were in the right lobe in 24 cases (58.5%), in the left lobe in 11 cases (26.8%) and in both lobes in six cases (14.6%). Daughter cysts were present in 22 cases (54%), while unilocular cysts were present in 19 cases (46%). Calcifications were noted in 14 cases (34%). The calcifications were mural and curvilinear in seven cases, ring-like in four cases and conglomerate intracystic in three cases.

Complications were recognized in three cases (7.3%). Intracystic infection with a thick ill-defined wall and an air–fluid level was noted in two cases and one case had ruptured through the right hemidiaphragm causing a right pleural effusion. Associated extrahepatic cysts were noted in the abdomen and pelvis in 11 cases (27%) (Table I). Three were in the mesentery, two were in each of the right kidney and spleen and one in each of the omentum, right ovary, uterus and the pancreas.

There was no evidence of enhancement in any of the 36 patients who received intravenous contrast media.

Ultrasound

Ultrasound was diagnostic in 34 out of 36 patients. In the remaining two cases, heavy calcification in one and a large amount of intracavitary air in the other prevented accurate diagnosis. Each of the positive patients showed

---

Address correspondence to Dr M. I. El-Tahir.

Table I. Distribution of extrahepatic hydatid in the abdomen and pelvis

	No. of cases detected by CT	No. of cases detected by US
Abdomen		
Mesentery	3	—
Spleen	2	2
Kidney	2	2
Pancreas	1	1
Omentum	1	—
Pelvis		
Ovary	1	1
Uterus	1	1
Total	11	7

one or more of the following ultrasonographic features of hydatid disease. A well-defined echo-poor cyst with distal enhancement was shown in 11 patients while a multilocular appearance as a result of daughter cysts was present in 22 cases. The split wall sign was shown in four cases. The ultrasonographic "water lily" sign was shown in two cases and a fluid level owing to "hydatid sand" was recognized in one patient.

Cyst calcification was detected in 12 patients compared with 14 patients detected by CT in the same group of patients. Of the 11 cases of associated extra-hepatic cysts detected by CT in the abdomen and pelvis, US detected such cysts in seven patients, though in two of them, the cysts were incorrectly localized. One of these was a huge splenic cyst thought to be in the left hepatic lobe and the other was a cyst in the upper pole of the right kidney, which was incorrectly thought to be part of a large posteriorly placed right hepatic cyst. The remaining four cases that were not detected by US were clinically unsuspected small abdominal cysts that were related to bowel. Three cases were in the mesentery and one was in the omentum (Table I).

CT did not show any extrahepatic cysts in the five patients who were not examined by US.

Plain abdominal radiograph calcifications were noted in seven cases (14%) and only two patients had pulmonary cysts (4.9%).

Discussion

The CT scan appearances of hydatid disease (Scherer et al, 1978; Choliz et al, 1982) include sharply marginated single or multiple round or oval cystic masses of fluid density (3–30 HU) and a thin dense rim, which does not enhance following intravenous contrast medium (Choliz et al, 1982). A multilocular appearance as a result of daughter cysts and cyst calcification are frequent findings.

US shows a well-defined echo-poor cyst with distal enhancement (Itzchak et al, 1980), which may be indistinguishable from a simple developmental cyst but this appearance must be highly suspect in endemic areas (Beggs, 1983). Multiple daughter cysts produce a multilocular appearance (Hadidi, 1982). The "split wall sign" is due to the separation of the laminated membrane from the pericyst (Gharbi et al, 1981). This is seen ultrasonographically as an echo-poor layer between the germinal layer and the pericyst. The "water lily sign" is due to detachment and collapse of the germinal layer, which is seen on US as an undulating linear collection of echoes either floating in the cyst fluid or lying in the most dependent part of the cyst (Niron & Ozer, 1981). A fluid level may be produced by hydatid sand (brood capsules and freed scolices), which sinks to the most dependent part of the cyst (Niron et al, 1981). This finding is, however, of limited diagnostic significance since debris within an abscess or necrotic tumour could also produce a similar US appearance.

Our findings indicate that CT is superior to US in the diagnosis of hepatic cysts and the detection of associated abdominal cysts, particularly small ones. However, the two techniques are equally accurate in detecting pelvic cysts. CT is also more accurate in the detection of calcification and infection, which may affect the typical US pattern of hydatid cyst (Niron et al, 1981). Of the two hepatic cases misdiagnosed by US in this series, one was a small heavily calcified cyst in which the calcification concealed the cystic nature of the mass and produced a strong acoustic shadow, which led to the wrong diagnosis of a granuloma. The other was an infected cyst with a large amount of intracystic air, which prevented accurate diagnosis.

Although CT is superior to US in the diagnosis of hepatic and associated abdominal hydatid cysts and their complications, US shares many of the advantages of CT but is safer, less expensive and more readily available. We therefore suggest that US should be the initial investigation and that CT be reserved for equivocal cases and for the pre-operative assessment of hepatic hydatid cysts. We recommed that the entire abdomen and pelvis be scanned when hydatid disease is suspected or when a hepatic lesion is suggestive of the disease. We also recommend that plain radiographs of the abdomen and chest be obtained to detect hepatic cyst calcification and pulmonary cysts, although only two patients in this series had associated pulmonary cysts.

Acknowledgments

We wish to thank Mrs Pushpama James and Mrs Shalimar Ledesma for their help in the preparation of the manuscript and Mr Rollie Go for secretarial assistance.

References

Beggs, I., 1983. The radiological appearances of hydatid disease of the liver. *Clinical Radiology*, *34*, 555–563.

Choliz, J. de D., Olaverri, F. J. L., Cascas, T. F. & Zubieta, S. O., 1982. Computed tomography in hepatic echinococcosis. *American Journal of Roentgenology*, *139*, 699–702.

Gharbi, H. A., Hassine, W., Brauner, M. W. & Dupich, K., 1981. Ultrasound examination of the hydatid liver. *Radiology*, *139*, 459–463.

Hadidi, A., 1982. Sonography of hepatic echinococcal cysts. *Gastrointestinal Radiology*, *7*, 349–354.

ISMAEL, M. A., AL-DABAH, M. A., AL-JANADI, T. A., AL-MOSLIH, M. I., AL-ANI, M. S., RASAM, S., FAWZI, A. H., SHAFIK, M. A. & AL-RAWAS, A. Y., 1980. The use of computerized axial tomography in the diagnosis of hydatid cysts. *Clinical Radiology, 31,* 278–290.

ITZCHAK, Y., RUBINSTEIN, Z., HEYMAN, Z. & GERZOF, S., 1980. Role of ultrasound in the diagnosis of abdominal hydatid disease. *Journal of Clinical Ultrasound, 8,* 341–345.

MANSON-BAHR, P. E. C. & APTED, P. I. C., 1982. *Mansons Tropical Diseases* (Baillière Tindall, London), pp. 245–247.

NIRON, E. & OZER, H., 1981. Ultrasound appearances of liver hydatid disease. *British Journal of Radiology, 45,* 335–338.

NOAH, M. S., LAAJAM, M. A., HAWASS, N. A. & ABDEL-HAFEZ, M. M. A., 1986. Hydatid liver disease: is it a diagnostic problem? Analysis of 42 consecutive cases in Saudi patients. *Annals of Tropical Medicine and Parasitology, 6,* 607–614.

SCHERER, U., WEINZIERL, M., STURM, R., SCHILDBERING, F. W., ZRENNER, M. & LISSNER, J., 1978. Computed tomography in hydatid disease of the liver: a report on 13 cases. *Journal of Computer Assisted Tomography, 2,* 612–617.

1992, *The British Journal of Radiology*, 65, 393–396

The spine deformity index in osteoporosis is not related to bone mineral and ultrasound measurements

By *Peter Bernecker, MD, †Peter Pietschmann, MD, ‡Friedrich Winkelbauer, MD, *Elisabeth Krexner, MD, *Heinrich Resch, MD and *§Robert Willvonseder, MD

*Department of Medicine, Krankenhaus der Barmherzigen Brüder, A-1020 Vienna, Austria; Departments of †Medicine II and ‡Radiodiagnostics, University of Vienna Medical School, A-1090 Vienna, Austria; §Ludwig Boltzmann Institute of Gerontology, A-1090 Vienna, Austria

(*Received 17 January 1991 and in final form 23 October 1991, accepted 20 November 1991*)

Keywords: Spine deformity index, Osteoporosis, QCT, SPA, Ultrasound attenuation

Abstract. In 34 female patients suffering from osteroporotic vertebral compression fractures, the spine deformity index (SDI_M) was determined, according to the method of Minne et al (1988), to reflect the radiological severity of established osteoporosis. Peripheral (single-photon absorptiometry (SPA) of the non-dominant distal forearm) and axial (quantitative computed tomography (QCT) of the lumbar spine) bone mineral measurements, as well as the broadband ultrasound attenuation of the os calcis, were performed in the osteoporotic patients and in a control group of 20 age-matched women. No correlation could be found between bone mineral measurements and radiological severity of osteoporosis, expressed as SDI_M. All three densitometry methods showed clearly reduced values in patients with vertebral crush fractures. Correlations established in the control group between peripheral and axial bone mass (SPA versus QCT) could no longer be found in the osteoporotic group, thus indicating changes in bone mineral density of the spine after the occurrence of osteoporotic fractures. Our data show that SDI_M is an additional parameter of osteoporotic change in the spine, independent from bone mass measurements. In the management of osteoporotic patients, quantitative radiological methods (*i.e.* SDI_M) in addition to densitometry might be of value for grading and monitoring the progress of disease.

Osteoporosis is a common disease in populations with high life expectancy, leading to increased morbidity and mortality in elderly people. Increased research in metabolic bone disease during the last years has been a consequence. Since the methods of bone mineral measurement have been improved, bone densitometry has become a valuable tool in the management of osteoporosis and in identifying those at risk (Hui et al, 1988; Ross et al, 1988). However, the role of densitometry in *manifest* osteoporosis has been controversial (Heaney et al. 1988; Ott et al, 1988; Melton et al, 1989).

Most studies of the therapy of established osteoporosis are based on densitometric methods, defining an increase in bone mineral density in longitudinal observations as a therapeutic success. Since spontaneous compression fractures of the vertebral bodies are the main clinical manifestation of osteoporosis (Hurxthal, 1968; Hedlund et al, 1989), a number of quantitative radiographic methods have been developed to estimate the severity of osteoporotic changes in the spine from lateral routine radiographs, with reduction in observer bias and interobserver errors (Barnett & Nordin, 1960; Jensen & Tougaard 1981; Kleerekoper et al, 1984). A newly developed "spine deformity index" (SDI_M), introduced by Minne et al (1988), may be clinically useful for comparing follow-up measurements in patients with osteoporotic vertebral fractures.

We have tried to clarify the possible relation between various densitometric methods and the radiological severity of manifest osteoporosis in post-menopausal women.

Subjects and methods

We examined 34 women aged 49 to 80 years (mean age 69.3 ± 1.2 years, mean time since menopause 19.4 ± 1.3 years) suffering from one or more atraumatic osteoporotic spinal fractures. Other metabolic bone disease was excluded by obtaining routine blood and urinary samples and determination of additional parameters of bone metabolism. None of the patients and controls had any history of diseases or drugs known to cause osteopenia. Patients with scoliosis were not included in this study.

As a control group, we studied 20 healthy and asymptomatic age-matched women (age range 51–81 years, mean age 67.9 ± 1.9 years) referred to our outpatient department for osteoporosis screening.

Lateral radiographs of the spine were taken. Target to film distance was 100 cm, the beam was centred for the thoracic and lumbar spine over T9 and L3, respectively. The radiographs of the osteoporotic group were analyzed by the method of Minne et al (1988). According to this method, the heights of the anterior and posterior edges and the centre of vertebrae T4–L5 were measured in millimetres using a transparent ruler. Analysis and calculation of the SDI_M were carried out using a MS-DOS compatible personal computer program kindly made available by the group of

---

Address correspondence to Peter Bernecker, MD, Department of Internal Medicine 3, Division of Rheumatology, University of Vienna, Waehringer Guertel 18–20, A-1090 Vienna, Austria.

Professor Minne (Heidelberg, Germany). The program calculated the intervertebral height relations (anterior, central and posterior) by defining the height of the fourth thoracic vertebra (which was unfractured in all osteoporotic patients) to be one individual unit and dividing the absolute height values of the other vertebrae below T4 by the absolute height of T4. This procedure eliminates the influence of individual body height. By comparing his original data with anatomical measurements carried out in 1876, 1895 and 1927, Minne et al found that in normals the increase of T4-related vertebral height values follows a constant mathematical relation, and that the relationship of the vertebral heights in the spine is not influenced by varying body heights of individuals (Minne et al, 1988), whereas the absolute vertebral heights are highly variable (Gallagher et al, 1988). The program then calculated the differences between the actual measured vertebral height ratios and the lower limit of the reference database of the computer program (containing the reference values Minne et al, determined in 110 normals, according to their original paper). The sum of these differences was called the "spine deformity index" (SDI_M). According to Minne et al, the intraobserver variance of the method is between 0.97% and 2.93%, whereas the interobserver variance is between 0.42% and 2.54% (coefficient of variation). In our study we determined the intraobserver variance to be 0.72% and the interobserver variance to be 0.51%.

Peripheral bone mineral content (BMC) of the non-dominant distal forearm was determined by single-photon absorptiometry (SPA) using a Novo Osteodensitometer GT 35 with a ^{125}I gamma radiation source. BMC was calculated as the mean of six scans and expressed in arbitrary units, *i.e.* mass of bone mineral per unit length of bone. The autolocated measuring site is that point where the distance between radius and ulna has increased to 8 mm. *In vitro* precision was established by repeated measurements of an aluminium standard every week. The coefficient of variation was 0.8% for consecutive tests during the same session and 1.2% over 1 year. We determined the reproducibility of the method to be 1.5% by repeated measurements of five normal subjects.

Bone mineral density of the lumbar spine was measured by quantitative computed tomography (QCT) with the single-energy technique (120 kV) using the Toshiba TCT 400 and the CIRS Lumbar Reference Simulator (Norfolk, Virginia). Volumes of 4 cm^3 of purely trabecular bone measured at the midplane of three non-fractured vertebral bodies from L1 to L5 were quantified and averaged. In two patients, only two uncrushed vertebrae could be found and measured. Using a lateral scout scan of the lumbar spine and cursor determined coordinates, midplanes of three vertebrae were identified and a single 1 cm thick section was obtained at each level. Analysis was performed using for the region of interest a rectangle, size 4 cm^2. Bone mineral density is expressed as milligrams of calcium hydroxyapatite/ml of bone. The reference phantom is surrounded by two fat equivalent rings, which can be fitted around it for simulating medium and large patients, and consists of reference vertebral inserts containing known amounts of calcium hydroxyapatite and fat in different parts to allow correction for the higher amount of fat in the vertebrae of elderly people. The coefficient of variation determined in repeated measurements of a single individual was 1.5% over 6 weeks and about 2.8% over 6 months.

Broadband ultrasound attenuation (BUA) of the os calcis based on the method developed by Langton et al (1984) was performed in a subgroup of 14 osteoporotic patients and in all the control group. We used a prototype of the Ultrasonic Bone Analyser 575 manufactured by Walker Sonix (Worcester, MA, USA). An emitting and a receiving unfocused transducer at both sides of the heel immersed in a water bath scan around the region of interest at various frequencies (0.2–0.6 MHz), with the os calcis functioning as a frequency-selective filter for the ultrasonic waves. This results in a spectrum of energy versus frequency, which is compared with a reference spectrum (without the heel in the water) to obtain the net attenuation spectrum and to allow corrections for the frequency response of the receiving transducer. Since higher frequencies are more readily attenuated than lower frequencies, the slope of the attenuation curve is computed by linear regression and represents the BUA value of the measurement, expressed in dB/MHz. By performing repeated measurements at a minimum interval of 3 days on one person, we determined the coefficient of variation to be 4.6%.

The Kruskal–Wallis test for comparison of two samples and the Kendall-τ rank correlation coefficient were used for statistical evaluation. The statistical tests are non-parametric methods, since data were not normally distributed. All data in the text are given as mean values ± SEM.

Results

The mean SDI_M value in the patients with osteoporotic spinal fractures was 3.43 ± 0.55 (range 0.111–12.550). SDI_M values were significantly correlated with the number of spinal fractures diagnosed by the radiologist ($\tau = 0.89$, $p < 0.001$). In the group of women with manifest osteoporosis, none of the densitometric methods showed a correlation with the radiological severity of osteoporotic changes in the spine, expressed as SDI_M (τ between -0.007 and -0.13, (NS) not significant). All three bone densitometry methods (SPA, QCT, BUA) showed markedly reduced values in the group of osteoporotic women compared with the values obtained in the control group (QCT: 64.16 ± 3.61 *vs.* 101.28 ± 5.58 mg/cm^3, $p < 0.0001$; SPA: 24.84 ± 0.9 *vs.* 30.26 ± 2.2 units, $p < 0.04$; BUA: 50.55 ± 2.17 *vs.* 61.69 ± 3.12 dB/MHz, $p < 0.03$).

Correlations between age and bone densitometry methods were found only in the group of controls, and there only between QCT and age ($\tau = -0.40$, $p < 0.001$). As expected, SDI_M did not show a correlation with age in the osteoporotic patients ($\tau = 0.20$, NS).

Additionally, we calculated correlations between the various densitometric methods in our study. A significant correlation could only be established between SPA and QCT in the control group ($\tau = 0.48$, $p < 0.03$). In the group of women with osteoporosis, not even a weak correlation between these methods could be found ($\tau = 0.15$, $p < 0.2$, NS), although QCT measurements were performed only in uncrushed vertebrae.

Discussion

In the early detection of post-menopausal bone loss and the identification of those at high risk of developing osteoporosis, the usefulness of bone densitometry has been proved by various studies (Hui et al, 1988; Gardsell et al, 1989).

The role of bone densitometry in the presence of osteoporotic spine fractures is still a matter of discussion. Ott et al (1988) found poor correlations between various bone densitometric methods and histomorphometric analyses of bone specimens in osteoporotic females, indicating a discrepancy between bone mass assessed by densitometry and the histological severity of established osteoporosis. On the other hand, Heuck et al (1989) found that QCT of the lumbar spine gave satisfactory discrimination between patients suffering from mild vertebral deformities and those with definite compression fractures, although there was a considerable overlap between the two groups.

It is widely agreed that bone strength is not only determined by bone mass but also by bone structure (Bell et al, 1987; Heaney, 1989). The only "densitometric" method more related to the structure of bone is BUA (Langton et al, 1984; Palmer & Langton, 1987, McKelvie et al, 1989). In our study, we confirmed previous observations that the bone mass of the axial and peripheral skeleton is reduced in patients with vertebral crush fractures (Genant & Cann, 1983; Nordin et al, 1988). BUA values of the os calcis were also reduced in patients with manifest osteoporosis, as described recently (Resch et al, 1990).

However, none of the densitometric procedures we used in our study showed any correlation with the radiological severity of spinal osteoporotic changes, quantified by Minne's spine deformity index (SDI_M). These findings confirm that SDI_M is an additional parameter of osteoporotic change in the axial skeleton, not related to bone mass measurements and providing information about the degree of wedging in osteoporotic patients. Since Minne et al used the lower limit instead of the standard deviation in their reference population for calculations of SDI_M, values below the normal range are believed to indicate pathological conditions, although in a few cases it might be difficult to discriminate between biological variance and early fractures (Minne et al, 1988). In addition, determination of SDI_M reduces the intra- as well as the interobserver bias, which is high in subjective grading of osteoporotic changes (Kovarik et al, 1981). Furthermore, variations in normal vertebral height owing to different body height are negligible when calculating the T4-related values of the SDI_M. Since SDI_M analyses of the radiographs can also be performed with a computer-assisted digitizing device, this method is also time-sparing, accurate and seems to be of good use for follow-up studies, assessing the osteoporotic vertebral column more exactly than densitometric methods.

Various authors have reported different correlations between bone mass of the axial and peripheral skeleton (Ott et al, 1984; Sambrook et al, 1985; Reinbold et al, 1986). The correlation we found between SPA of the non-dominant distal forearm and QCT of the lumbar spine in our control group is in accordance with data of Powell et al (1983) and Cann et al (1985). Interestingly, this correlation was not seen in patients with manifest osteoporosis, although it might be expected to be weaker owing to increased trabecular bone loss rather than cortical bone loss in the forearm.

These findings may substantiate the presumption that in patients with vertebral crush fractures, structural changes may occur in the vertebral bodies below the fracture site (such as microfractures or perhaps bone modelling processes resulting from changes in static load). Such changes in vertebral structure may cause a false positive effect on densitometric data, while morphometric data like SDI_M will remain unaffected. Thus, one possible cause for the absent correlation between SDI_M, which is based on vertebrae T4 to L4 and QCT of unfractured lumbar vertebrae, may be the incidence of microfractures in the cancellous part of vertebrae not already crushed. In studies of the therapy of manifest osteoporosis, such structural changes of the vertebrae resulting from increased static load could lead to misinterpretation of densitometric data, and, subsequently, may mislead the clinical investigator. In a recently published study by Riggs et al (1990), fluoride therapy in patients with osteoporotic spinal fractures increased bone mineral density in the lumbar spine but failed to prevent further vertebral fractures.

Since the principal clinical aim in manifest osteoporosis is the prevention of further fractures, quantitative radiological methods (such as SDI_M) performed in addition to densitometry may be of value in management, including grading and monitoring of the progress of the disease.

Acknowledgment

The author would like to thank Professor H. W. Minne and Dr G. Leidig from the Department of Internal Medicine I, Endocrinology and Metabolism, University of Heidelberg, Germany, for providing us with a copy of the SDI software they developed.

Note

We wish to inform the readers of *BJR* that the software used for calculation of SDI_M can be obtained by anyone who wishes to apply the system. Write to Dr G. Leidig, Department of Internal Medicine I, Endocrinology and Metabolism, University of Heidelberg, Bergheimerstrasse 58, D-6900 Heidelberg, Germany.

References

Barnett, E. & Nordin, B. E. C., 1960. The radiological diagnosis of osteoporosis. A new approach. *Clinical Radiology*, *2*, 166–174.

Bell, G. H., Dunbar, O., Beck, J. S. & Gibb, A., 1987. Variations in strength of vertebrae with age and their relation to osteoporosis. *Calcified Tissue Research*, *1*, 75–86.

Cann, C. E., Genant, H. K., Kolb, F. O. & Ettinger, B., 1985. Quantitative computed tomography for prediction of vertebral fracture risk. *Bone*, *6*, 1–7.

Gallagher, J. C., Hedlund, L. R., Stoner, S. & Meeger, C., 1988. Vertebral morphometry: normative data. *Bone & Mineral*, *4*, 189–196.

Gardsell, P., Johnell, O. & Nilsson, B. E., 1989. Predicting fractures in women by using forearm bone densitometry. *Calcified Tissue International*, *44*, 235–242.

Genant, H. K. & Cann, C. E., 1983. Clinical impact of quantitative computed tomography for vertebral mineral assessment. In *Diagnostic Radiology*, ed. by A. R. Margulis & C. A. Gooding (University of California Press, Berkeley, CA), pp. 445–448.

Heaney, R. P., 1989. Osteoporotic fracture space: a hypothesis. *Bone & Mineral*, *6*, 1–13.

Heaney, R. P., Avioli, L. V., Chestnut, C., Recker, R. R. & Gallagher, J. C., 1988. Is bone loss the cause of osteoporotic fractures or its consequence? *Journal of Bone and Mineral Research*, *3*, 88.

Hedlund, L. R., Gallagher, J. C., Meeger, C. & Stoner, S., 1989. Change in vertebral shape in osteoporosis. *Calcified Tissue International*, *44*, 168–172.

Heuck, A. F., Block, J., Glueer, C. C., Steiger, P. & Genant, H. K., 1989. Mild versus definite osteoporosis: comparison of bone densitometry techniques using different statistical models. *Journal of Bone and Mineral Research*, *4*, 891–900.

Hui, S. L., Slemenda, C. W. & Johnston, C. C., 1988. Age and bone mass as predictors of fractures in a prospective study. *Journal of Clinical Investigation*, *81*, 1804–1809.

Hurxthal, L. M., 1968. Measurement of anterior vertebral compressions and biconcave vertebrae. *American Journal of Roentgenology*, *103*, 635–644.

Jensen, K. K. & Tougaard, L., 1981. A simple X-ray method for monitoring progress of osteoporosis. *Lancet*, *ii*, 19–20.

Kleerekoper, M., Parfitt, A. M. & Ellis, J., 1984. Measurement of vertebral fracture rates in osteoporosis. In *Osteoporosis*, ed. by C. Christiansen, C. D. Arnaud, B. E. C. Nordin, A. M. Parfitt, W. A. Peck, B. L. Riggs (Aalborg Stiftsborgtrykkeri, Glostrup, Denmark), pp. 103–109.

Kovarik, J., Kuester, W., Seidl, G., Linkesch, W., Dorda, W., Willvonseder, R. & Kotscher, E., 1981. Clinical relevance of radiologic examination of the skeleton and bone density measurements in osteoporosis of old age. *Skeletal Radiology*, *7*, 37–41.

Langton, C. M., Palmer, S. B. & Porter, R. W., 1984. The measurement of broadband ultrasonic attenuation in cancellous bone. *Engineering in Medicine*, *13*, 89–91.

McKelvie, M. L., Fordham, J., Clifford, C. & Palmer, S. B., 1989. *In vitro* comparison of quantitative computed tomography and broadband ultrasonic attenuation of trabecular bone. *Bone*, *10*, 101–104.

Melton, L. J., Kan, S. H., Frye, M. A., Wahner, H. W., O'Fallon, W. M. & Riggs, B. L., 1989. Epidemiology of vertebral fractures in women. *American Journal of Epidemiology*, *129*, 1000–1011.

Minne, H. W., Leidig, G., Wüster, C., Siromachkostov, L., Baldauf, G., Bickel, R., Sauer, P., Lojen, M. & Ziegler, R., 1988. A newly developed spine deformity index (SDI) to quantitate vertebral crush fractures in patients with osteoporosis. *Bone & Mineral*, *3*, 335–349.

Nordin, B. E. C., Wishart, J. M., Horowitz, M., Need, A. C., Bridges, A. & Bellon, M., 1988. The relation between forearm and vertebral mineral density and fractures in postmenopausal women. *Bone & Mineral*, *5*, 21–33.

Ott, S. M., Chesnut, C., Hanson, J. A., Kilcoyne, R. F., Murano, R. & Lewellen, T. K., 1984. Comparison of bone mass measurements using different diagnostic techniques in patients with postmenopausal osteoporosis. In *Osteoporosis*, ed. by C. Christiansen, C. D. Arnaud, B. E. C. Nordin, A. M. Parfitt, W. A. Peck & B. L. Riggs (Aalborg Stiftsborgtrykkeri, Glostrup, Denmark), pp. 97–102.

Ott, S. M., Kilcoyne, R. F. & Chesnut, C., 1988. Comparisons among methods of measuring bone mass and relationship to severity of vertebral fractures in osteoporosis. *Journal of Clinical Endocrinology and Metabolism*, *66*, 501–507.

Palmer, S. B. & Langton, C. M., 1987. Ultrasonic studies of the os calcis. In *In Vivo Body Composition Studies*, ed. by K. J. Ellis, S. Yasumura & W. D. Morgan. IPSM 3 (Institute of Physical Science in Medicine, York, UK), pp. 452–460.

Powell, M. R., Kolb, F. O., Genant, H. K., Cann, C. E. & Stebler, B. G., 1983. Comparison of dual photon absorptiometry and quantitative computed tomography of the lumbar spine in the same subjects. In *Clinical Disorders of Bone and Mineral Metabolism*, ed. by B. Frame & J. T. Potts (Excerpta Medica, Amsterdam, Netherlands), pp. 58–61.

Reinbold, W. D., Genant, H. K., Reiser, U. J., Harris, S. T. & Ettinger, B., 1986. Bone mineral content in early-postmenopausal and postmenopausal osteoporotic women: comparison of measurement methods. *Radiology*, *160*, 469–478.

Resch, H., Pietschmann, P., Bernecker, P., Krexner, E. & Willvonseder, R., 1990. Broadband ultrasound attenuation: a new diagnostic method in osteoporosis. *American Journal of Roentgenology*, *155*, 825–828.

Riggs, B. L., Hodgson, S. F., O'Fallon, W. M., Chao, E. Y. S., Wahner, H. W., Muhs, J. H., Cedel, S. L. & Melton, L. J., 1990. Effect of fluoride treatment on the fracture rate in postmenopausal women with osteoporosis. *New England Journal of Medicine*, *322*, 802–809.

Ross, P. D., Wasnich, R. D. & Vogel, J. M., 1988. Detection of prefracture spinal osteoporosis using bone mineral absorptiometry. *Journal of Bone and Mineral Research*, *3*, 1–11.

Sambrook, P. N., Bartlett, C., Evans, R., Hesp, R., Katz, D. & Reeve, J., 1985. Measurement of lumbar spine bone mineral: a comparison of dual photon absorptiometry and computed tomography. *British Journal of Radiology*, *58*, 621–624.

1992, *The British Journal of Radiology*, 65, 397–402

Computed tomography in abdominal trauma: an audit of usage and image quality

By *Anwar R. Padhani, MB, BS, MRCP, FRCR, †Christopher J. E. Watson, MA, MB, FRCS, Leigh Clements, DCR, †Roy Y. Calne, MS, FRCS, FRS and Adrian K. Dixon, MD, FRCP, FRCR

Departments of Radiology and †Surgery, Addenbrooke's Hospital and the University of Cambridge, Hills Road, Cambridge CB2 2QQ, UK

(*Received 20 June 1991 and in revised form 13 November 1991, accepted 14 January 1992*)

Keywords: Abdomen, Audit, Computed tomography, Trauma

Abstract. The use and quality of computed tomography (CT) in the evaluation of blunt abdominal trauma has been assessed by a retrospective review of 122 patients referred in the first 8 years following the installation of CT of the body. The referral patterns were analysed, and the quality of the images was assessed, with particular reference to unsatisfactory (unacceptable or poor) images. Referrals increased over the 8 years following installation. A large proportion of these examinations were performed outside normal working hours (58/122, 48%). In 64 out of 122 (52%) of examinations the images were considered of unsatisfactory quality with inadequate use of intravenous contrast medium cited as the most common cause for unsatisfactory exminations. Image quality did not improve with time. Image quality was unsatisfactory in a larger proportion of those examinations performed outside normal working hours (35/58, 60%) than those during the routine working day (29/64, 45%), although this difference did not reach statistical significance ($0.1 > p > 0.05$). Fewer unsatisfactory examinations were produced by a system dedicated to body CT (31/74, 42%) than by a neuroradiological system (33/48, 69%) ($p < 0.01$). The proportion of unsatisfactory abdominal examinations was lower when the CT study concentrated on the abdomen (26/65, 40%) than when multiple regions (head, chest, abdomen, etc.) were examined (38/57, 67%) ($p < 0.01$). This audit revealed many unsatisfactory examinations. In order to complete the audit loop we have addressed many of the contributory factors. A new CT system now provides images of high quality and is used for all abdominal work. Guidelines, which describe an optimized technique, have been issued to radiographers and radiologists. In particular, we have emphasized that there is no place for a poorly supervised "quick look" at the abdomen following a cranial or thoracic study.

Computed tomography (CT) has long had widespread application in patients with suspected intracranial injury. However, its use in the evaluation of suspected intra-abdominal injury has not been so extensive in this country. The first comprehensive report on CT for abdominal trauma appeared in 1981 (Federle et al, 1981). Since then, its use as the initial test for haemodynamically stable patients including children (Brick et al, 1987; Federle, 1984) has grown in accordance with its ability to direct treatment and predict prognosis (Brick et al, 1987; Foley et al, 1987).

Recent studies have shown that CT, despite providing excellent anatomical information, is rather less sensitive than peritoneal lavage in detecting intra-abdominal injury (Meyer et al, 1989; Sorkey et al, 1989). However, some of the limitations of lavage were also revealed by these studies, which have emphasized the complementary role of the two techniques, especially in identifying those patients suitable for non-operative management. The lower sensitivity of CT in detecting solid organ injury raises several dilemmas; paramount amongst these is the technique of examination.

The techniques for optimal evaluation are now well established, particularly in the American literature (Federle, 1984; Walsh, 1989). Clinical and laboratory guidelines for the use of CT have been established and meticulous technique has been stressed, as some injuries are associated with subtle findings (Walsh, 1989). Some of the guidelines have provoked debate and have cost implications for UK practice. For exmple, should centres adopt the recommended abdominal trauma protocol of contiguous 8–10 mm thick slices from the diaphragm to below the kidneys (Walsh, 1989)? Should the pelvis be examined in all patients (Federle, 1984)? Will our anaesthetic colleagues allow us to give large volumes of intravenous and oral contrast medium to patients who may require urgent surgery (Federle, 1984)?

We have reviewed all CT scans for abdominal trauma performed in our hospital as a part of a general clinical audit on abdominal trauma. In particular, we were interested in assessing the overall quality of the images produced.

Materials and methods

We retrospectively reviewed all the CT examinations in patients who had been referred with abdominal trauma over a period of 8 years (January 1982 to December 1989). Only the first CT study was evaluated in patients with multiple examinations; follow-up examinations were excluded. We identified 122 such patients in whom the hard-copy images and adequate demographic details were available. Most were referred directly from the busy casualty unit at Addenbrooke's Hospital after discussion with the admitting surgical team. Some were examined at a slightly later stage after their injury, having been referred to this hospital, which is recognized for its hepatic surgical expertise (Calne et al, 1982). The CT scans were performed and interpreted either by the senior registrar or consultant radiologist responsible for body CT (during working hours) or by the senior registrar or consultant "on call" at the time of the study (outside working hours).

---

*Present address: Department of Radiology, Guy's Hospital, London, UK. This article is a full report of a presentation at "Radiology & Oncology, Brighton, 1991".

Address correspondence to Dr A. K. Dixon, University Department of Radiology, Addenbrooke's Hospital, Hills Road, Cambridge CB2 2QQ, UK.

All examinations were performed on one of two machines; a Siemens Somatom II (body machine) or a General Electric 9000 system (neuroradiological machine: 1984 onwards). In our department, "out of hours" radiographic cover (after 5 pm, before 9 am, all day Saturday and Sunday) is provided by a team of radiographers who usually have more experience of the neuroradiological machine. The latter system is primarily used for neuroradiological examinations, although it is capable of examining the whole body. Routine data acquisition time, slice thickness and increment were 5 s, 8 mm and 15 mm for the body machine and 10 s, 10 mm and 15 mm for the neuroradiological machine; incrementation was slightly wider (*e.g.* 20 mm) caudal to the liver and spleen. Neither machine is very modern. Indeed, the body CT machine (Somatom II) has recently been replaced. Accordingly, dynamic studies were relatively slow on both machines although technically simpler on the body machine than on the neuroradiological machine. The body machine comfortably provided 15 images at six images per minute during dynamic incrementaton. The neuroradiological system can only manage a total of six images at 250 mA during a 1-min dynamic run before thermal capacity is reached; furthermore the dynamic run has to be reviewed retrospectively. For these reasons a slightly slower technique is usually employed on the neuroradiological machine.

Table I. An analysis of the use of CT for abdominal trauma with time

Year	Neuroradiological machine: no. of patients (% of total)	Body CT machine: no. of patients	Total
1982	*—	6	6
1983	*—	6	6
1984	1 (10%)	10	11
1985	3 (21%)	11	14
1986	5 (50%)	5	10
1987	12 (52%)	11	23
1988	12 (46%)	14	26
1989	15 (58%)	11	26
Total	48 (39%)	74	122

*Suitable neuroradiological machine only installed in 1984.

The hard-copy images were retrospectively reviewed by a single consultant with a special interest in CT (A.K.D.). Aspects of technique and the subsequent image quality were scrutinized. These included the positioning of the patient, the anatomical areas examined, the incrementation of CT sections, the administration of oral and intravenous contrast medium (none given, given before, given during), the extent and origin of artefacts (movement, limb, respiration, etc.) and the photography of the images. Taking all these features into account, the overall quality of each examination was graded on a subjective scale (unacceptable, poor, satisfactory, good and excellent). The principal reasons for awarding the lower grades were noted. In particular, we attempted to assess those factors that led to unsatisfactory image quality.

The overall image quality was assessed in various subgroups (machine used "out of hours", associated injuries, etc.). The χ^2-squared test was used for statistical comparison.

Results

122 CT examinations were identified in patients who had sustained blunt abdominal trauma, either exclusively or in addition to other injury. 83 of the 122 patients were male. The age range was 5–86 years (mean 34 years). Table I illustrates the increasing use of CT for abdominal trauma with time.

58 (47%) studies were performed outside normal hours. Proportionately fewer examinations (14/58, 24%) were at weekends (*i.e.* Saturday and Sunday, day or night).

64 (52%) studies were considered of unsatisfactory quality: unacceptable (17), poor (47). 28 (23%) were considered of satisfactory quality; only 30 (25%) examinations were rated good (22) or excellent (8). The main reasons for unsatisfactory examinations are shown in Table II; leading causes were poor intravenous enhancement techniques (49 occasions) and artefacts (mainly movement, 44 occasions). Representative images are shown in Figs 1–5.

Contrast medium was administered intravenously in 90 out of 122 (74%) studies. In 36 patients intravenous contrast medium had been given before starting the series of images; in the other 54 patients intravenous contrast medium was given during the examination. Table III shows how there has been little change in the

Table II. The reasons cited for unsatisfactory studies

Inappropriate use of intravenous contrast medium	49
None given (32)	
Poor technique (17)	
Artefacts, usually related to movement	44
Poor anatomical coverage	4
Thin patient	4
Excessive increments	2
Others	5
Total	108

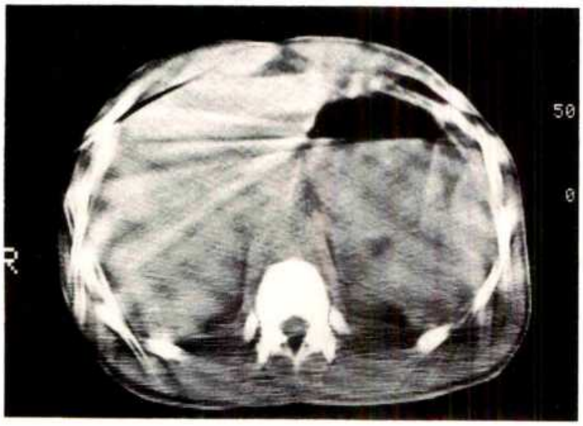

Figure 1. *Unacceptable* image quality in a 27-year-old man following a road traffic accident. The patient was in a lot of pain and extremely restless, hence the gross movement artefact. This study was performed on a Sunday afternoon. No intravenous enhancement was given during this examination, which was carried out on the neuroradiological machine. There was also a head injury that had been evaluated by CT. Sedation would be needed to improve these images, although better results would now be obtained on a faster machine. This was by far the worst example of an unsatisfactory image. Angiography revealed a rupture of the thoracic aorta, which was successfully treated.

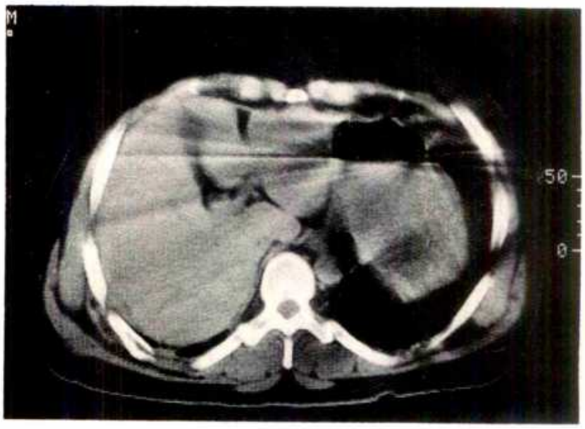

Figure 2. *Poor* quality image in a 42-year-old man examined out of hours on the neuroradiological CT machine following a road traffic accident. This abdominal study was performed subsequent to full cranial and thoracic CT; intravenous enhancement was not given during abdominal imaging. Severe streak artefacts from gastric air/fluid levels were noted. At surgery (24 h after CT) a tear of the diaphragm was repaired; there were no other abdominal injuries.

technique of enhancement with time. Oral contrast medium was given in 25 out of 122 (20%) patients.

The distribution of unsatisfactory examinations with time is summarized in Table IV. Table V analyses the proportion of unsatisfactory examinations according to the machine used; it also reveals the increased use of the neuroradiological machine outside working hours ($p < 0.001$). More unsatisfactory examinations emanated from the neuroradiological machine ($p < 0.01$).

Review of the 57 patients who had multiple anatomical regions examined with CT (head, chest, abdomen, etc.) revealed that the image quality of the abdominal studies was unsatisfactory in 38 (67%), compared with 26 unsatisfactory examinations in 65 patients (40%) in whom the CT study concentrated on the abdomen alone. The difference in image quality between these two subgroups is highly significant ($p < 0.01$).

Discussion

CT in the evaluation of haemodynamically stable patients with blunt abdominal trauma, used in association with subsequent peritoneal lavage, provides high diagnostic sensitivity and good anatomical representation of the injuries sustained. The contribution of CT in allowing non-surgical management of blunt hepatic and splenic trauma is now acknowledged in both adults (Mirvis et al, 1989a, b) and children (Brick et al, 1987). However, to obtain this information, three important principles of technique have been stressed (Federle, 1984):

Table III. The pattern of administration of intravenous contrast medium with time. Results expressed as a percentage of total examinations performed

Year	Number of studies	Intravenous contrast medium		
		None	Before	During
1982	6	66%	0	33%
1983	6	17%	17%	66%
1984	11	27%	55%	18%
1985	14	14%	43%	43%
1986	10	20%	30%	50%
1987	23	40%	30%	30%
1988	26	12%	38%	50%
1989	26	35%	12%	54%
Total	122	27%	30%	44%

Table IV. Unsatisfactory (unacceptable/poor) examinations by year. Percentages in parentheses

Year	Patients	Unsatisfactory
1982	6	5 (80)
1983	6	3 (50)
1984	11	6 (55)
1985	14	6 (43)
1986	9	6 (66)
1987	23	13 (57)
1988	26	12 (46)
1989	26	13 (50)
Total	122	64 (52)

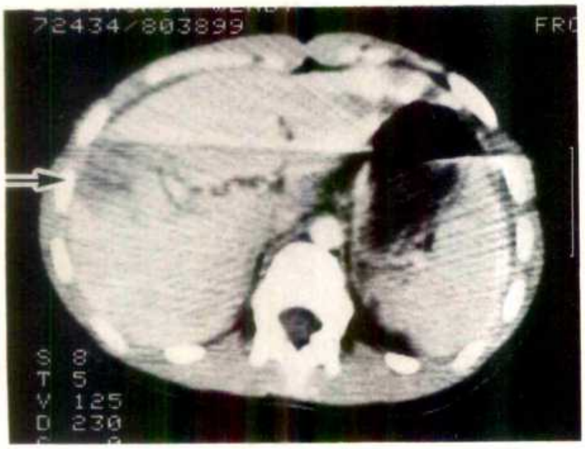

Figure 3. *Satisfactory* study in a 16-year-old girl who was examined during normal working hours on the body CT system following a kick from a horse. This enhanced examination was targeted to the upper abdomen alone. Despite a linear artefact from the gastric air/fluid level, extensive injury in the right lobe of the liver is well demonstrated (arrow). There is a trace of haemoperitoneum anterior to the liver. This patient had successful conservative treatment.

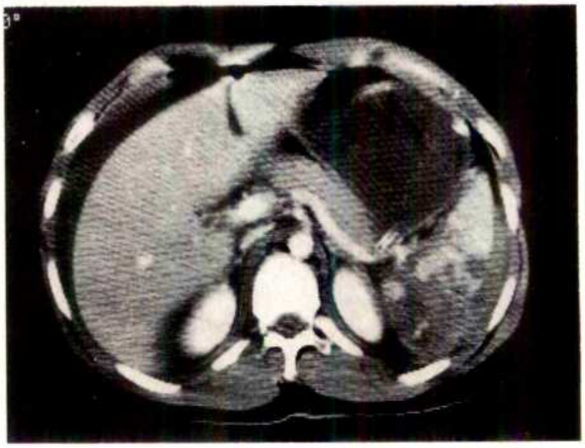

Figure 4. *Excellent* enhanced study obtained on a Saturday afternoon on the neuroradiological CT system. Splenic trauma was suspected in this 24-year-old woman who had been involved in a road traffic accident. CT of the head and dorsal spine was also performed but there was a clear request for upper abdominal evaluation. There is obvious evidence of a severely damaged spleen and haemoperitoneum anterior to the liver. She also had a major head injury with skull fractures and spinal injury. The splenic trauma was successfully managed conservatively.

1. The appropriate use of intravenous contrast medium.
2. The appropriate location and spacing of sections.
3. Adequate monitor viewing and subsequent photography of images.

Our results show a gradual increase in referrals of patients following abdominal trauma between 1982 and 1989 (Table I). Assuming that there had not been an increase in the amount of severe trauma in East Anglia during the study period, the increased referrals must be due to the numerous reports in the literature and to clinicians becoming more aware of the efficacy of CT.

Although 58 out of 122 (48%) studies were performed "out of hours", it is of interest that proportionately fewer examinations (14/58, 24%) were on Saturdays and Sundays. This may be due to the clinicians worrying about the potential delay of organizing a CT examination "out of hours" as opposed to the near-instant service possible during the working day. Alternatively, it may be due to a lower incidence of heavy motor vehicle and industrial accidents at weekends.

It is disappointing that the proportion of unsatisfactory examinations did not decrease as we gained increased experience in this evolving technique. After some initial improvement (1982–5, Table IV), around 50% of examinations were still unsatisfactory in 1987–9. One possible reason for this is the trend for the neuroradiological machine, which yielded poorer quality images in this study, to be used for a large proportion of "out of hours" referrals (Tables I, V). In the early years, the radiographers had no choice; there was only one system capable of performing body examinations. Furthermore, when any procedure becomes "routine", it is likely that there is some relaxation in the initial obsessional attention to technique.

It is now well recognized that one of the corner-stones of CT in trauma is the appropriate use of intravenous contrast medium (Federle, 1984); indeed, the failure to use contrast medium may result in missed diagnoses.

Table V. Analysis of unsatisfactory examinations in relation to the machine used

	Body CT machine	Neuroradiological CT machine	Significance of difference
All patients			
Number of studies	74	48	
Number unsatisfactory (%)	31 (42)	33 (69)	$p < 0.01$
Outside normal hours			
Number of studies	21	37	$p < 0.001$
Number unsatisfactory (%)	8 (38)	27 (73)	$p < 0.01$

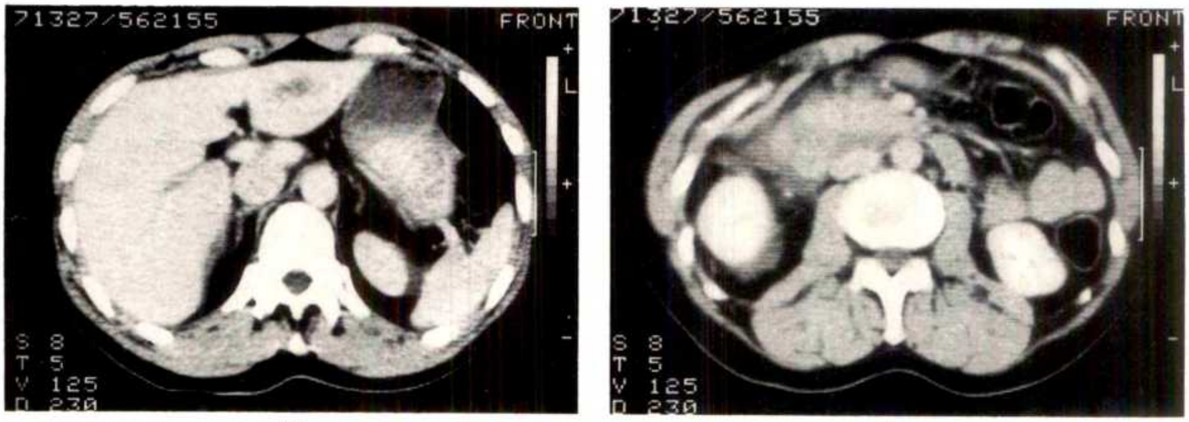

(a) (b)

Figure 5. *Excellent* enhanced images in a 52-year-old man who had been kicked by a horse. This examination, which concentrated on the abdomen, was performed on the body CT system during working hours. (a) There is a focal area of contusion in the lateral segment of the left lobe of liver. (b) There is indistinctness around the uncinate process of the pancreas and duodenum consistent with injury here. There is a small subcapsular collection around the posteromedial aspect of the right kidney. The patient made a good recovey with conservative management.

Improper administration also causes problems: slow administration increases the likelihood of encountering isodense haematomas; too rapid an injection may result in transient enhancement patterns (especially in the spleen) that may simulate abnormalities (Federle, 1984). In the early period of our study a bolus of 50 ml (325 mg iodine/ml) urographic contrast medium was usually given before the examination started, with the images obtained quickly thereafter (Table III). As techniques changed (Federle, 1984), it was recommended that the images should be obtained in a dynamic fashion during peak enhancement wherever possible. Larger volumes of contrast medium have also been recommended and were, on occasions, employed. Although the value of enhancement for abdominal trauma is well appreciated in this hospital, it is disappointing that intravenous enhancement was not consistently used during the examination. In the early years, the optimal method of enhancement had not been formally established, but it is surprising that there was no improvement during the latter years. This may, in part, be due to the fact that numerous referrals in the later years were for CT of the head and abdomen. Indeed, the cranial study may have been considered the more important of the two, with only a cursory examination of the abdomen. This accounted for several of the abdominal procedures that were performed without any intravenous enhancement—an unsatisfactory state of affairs (*e.g.* Fig. 1), which has been rectified.

Oral contrast medium via a nasogastric tube is now also recommended, especially when bowel injury is suspected (Walsh, 1989). Some authors recommend its use in all patients (Federle, 1984), arguing that duodenal and other injury may be missed without it. This aspect should be carefully discussed with local surgeons and anaesthetists and a local policy established. Advocates would argue that it is simple enough to aspirate the gastric residue via a nasogastric tube; this is particularly easy if one was passed to empty the stomach and administer the oral contrast medium in the first place. In practice, we now make every effort to give oral contrast medium when there has been an injury with a high likelihood of damage to bowel (lap/seat belt, handlebar, etc.) and this is discussed with the clinicians at the time of referral.

The analysis of examinations performed outside normal working hours showed increased use of the neuroradiological CT machine (37/48, 77%, $p < 0.001$); the majority (27/37, 73%) of these examinations were unsatisfactory ($p < 0.01$). These trends probably reflect the experience of the on-call radiographers of whom most are neuroradiographers, who are more confident with the neuroradiological machine. Although it is difficult to justify the use of the neuroradiological machine in the 14 patients who had no associated head injury, it is impractical and expensive to maintain a separate bank of on-call radiographers who have day-to-day experience of the body machine for body trauma. Nevertheless, this study indicated a deficiency in our training. All the on-call radiographers are now proficient on the new body CT machine, and have also been instructed that when the patient has suffered head and thoraco-abdominal injuries, the cranial CT examination should be performed first. The patient is then set up for the examination of other anatomical areas under the supervision of the radiologist. On the new body CT system with a 1 s data acquisition time, we have not had to consider sedation in these patients.

This audit revealed that many of our examinations between 1982 and 1989 were less than optimal. These poor examinations were due to various factors: the equipment that was available at the time of the study, the medical condition of the patients and poor attention to technique. Furthermore, what is now perceived as a "satisfactory" examination is likely to be very different from the state of affairs in the mid 1980s. There is, however, much room for improvement within the resources currently available and, as a profession, we must do our utmost to counter criticisms of our handling of traumatized patients (Prentice, 1991). We hope that our experience will serve as a guide to other radiologists and clinicians who rely on CT for abdominal trauma, especially those who will have to continue to use relatively old CT systems. Team work is vital.

As with any audit project, it is important to reflect on the findings and consider what changes should be implemented (*i.e.* how the audit loop is closed). We have done this, at a local level, by issuing new guidelines for radiographers and radiologists involved in CT of abdominal trauma. These stress the importance of using the most appropriate CT system for abdominal work (now the new body CT system, a Siemens Somatom Plus). The intravenous administration of contrast medium is mandatory and there are detailed instructions as to how this should be given for our machine. We have standardized the sequence of images for a "routine" CT referral for abdominal trauma, where the spleen and liver are usually under special scrutiny. This includes:

1. A scanogram of the lower chest and abdomen.
2. One CT image through the mid chest for pneumothorax).
3. A series of unenhanced CT images through the liver and spleen (to exclude isodense haematomas).
4. A series of enhanced CT images during peak parenchymal opacification through the liver, spleen and kidneys, continuing to the pubic symphysis. Delayed images may be necessary to assess pelvicalyceal and urinary bladder integrity.

Thus we have closed the loop of the audit cycle. We hope that this will lead to improved quality of CT images when reassessed at intervals in the future. However, it may prove difficult to separate improvement in technique from that inherent in the more modern CT system.

Acknowledgments

We are grateful to all the clinical, radiographic and radiological colleagues who helped with these patients. In particular, Mr H. Sherriff and Dr S. Mirvis provided valuable advice. The Addenbrooke's Hospital Cancer Scanner Appeal Fund funded the initial body CT system. Karin Frans prepared the manuscript.

References

BRICK, S. H., TAYLOR, G. A., POTTER, B. M. & EICHELBERGER, M. R., 1987. Hepatic and splenic injury in children: role of CT in the decision for laparotomy. *Radiology, 165,* 643–646.

CALNE, R. Y., WELLS, F. C. & FORTY, J., 1982. Twenty-six cases of liver trauma. *British Journal of Surgery, 69,* 365–368.

FEDERLE, M. P., 1984. CT of upper abdominal trauma. *Seminars in Roentgenology, 19,* 269–280.

FEDERLE, M. P., GOLDBERG, H. I., KAISER, J. A., MOSS, A. A., BROOKE JEFFREY, R. & MALL, J C., 1981. Evaluation of abdominal trauma by computed tomography. *Radiology, 138,* 637–644.

FOLEY, W. D., CATES, J. D., KELLMAN, G. M., LANGDON, T., APRAHAMIAN, C., LAWSEN, T. L. & MIDDLETON, W. D., 1987. Treatment of blunt hepatic injuries: role of CT. *Radiology, 164,* 635–638.

MEYER, D. M., ERWIN, R. T., WEIGELT, J. A. & REDMAN, H. C., 1989. Evaluation of computed tomography and diagnostic peritoneal lavage in blunt abdominal trauma. *Journal of Trauma, 29,* 1168–1172.

MIRVIS, S. E., WHITLEY, N. O. & GENS, D. R., 1989a. Blunt splenic trauma in adults: CT-based classification and correlation with prognosis and treatment. *Radiology, 171,* 33–39.

MIRVIS, S. E., WHITLEY, N. O., VAINWRIGHT, J. R. & GENS, D. R., 1989b. Blunt hepatic trauma in adults: CT-based classification and correlation with prognosis and treatment. *Radiology, 171,* 27–32.

PRENTICE, T., 1991. Road victims dying because hospitals fail, experts say. *The Times,* January 24, p. 9.

SORKEY, A. J., FARNELL, M. B., WILLIAMS, H. J., MUCHA, P. & ILSTRUP, D. M., 1989. The complementary roles of diagnostic peritoneal lavage and computed tomography in the evaluation of blunt abdominal trauma. *Surgery, 106,* 794–801.

WALSH, J. W., 1989. Blunt abdominal trauma. In *CT Review* ed. by J. E. S. Husband (Churchill Livingstone, London), pp. 165–177.

1992, *The British Journal of Radiology*, 65, 403–408

The incidence and severity of hypoxia associated with ^{99}Tc^{m} Technegas ventilation scintigraphy and ^{99}Tc^{m} MAA perfusion scintigraphy

By J. M. James, MB, ChB, MRCGP, J. J. Lloyd, BSc, MSc, *†B. C. Leahy, MB, ChB, MRCP, R. A. Shields, MSc, PhD, FIPSM, M. C. Prescott, MB, ChB, MD and H. J. Testa, PhD, FRCP, FRCR

Departments of Nuclear Medicine and Medical Physics and *Respiratory Medicine, Manchester Royal Infirmary, Oxford Road, Manchester M13 9WL, UK

(*Received 19 July 1991 and in revised form 1 November 1991, accepted 14 January 1992*)

Keywords: Hypoxia, ^{99}Tc^{m} Technegas, ^{99}Tc^{m} MAA, Scintigraphy

Abstract. Inhalation of the ventilatory radiopharmaceutical ^{99}Tc^{m} Technegas leads, in some patients, to symptoms that may be attributed to temporary lowering of oxygen saturation. In order to evaluate this, oxygen saturation was measured by pulse oximetry in a series of patients undergoing Technegas ventilation scintigraphy. A decrease in oxygen saturation was recorded in 87% of the patient group. The mean change, as a percentage of the initial value, was 8.3% (range 1–24%). Hypoxia arising in association with Technegas administration may be reduced by pre-oxygenation. In patients who were pre-oxygenated, oxygen saturation did not fall below 85% (PaO_2: 50 mmHg) but in 39% of those not pre-oxygenated the value fell below this level. Oxygen saturation was also monitored in a series of patients undergoing perfusion scintigraphy. In 17% of patients a decrease was recorded (range 2–11%). In view of the large number of perfusion scans performed annually in this department and elsewhere without untoward effect, such temporary decreases in oxygen saturation presumably present no hazard to the patient.

Technegas is a ventilatory radiopharmaceutical (Burch et al, 1986) which combines the optimum imaging properties of technetium 99m (^{99}Tc^{m}) with continuous availability. It is an ultrafine suspension of ^{99}Tc^{m}-labelled carbon particles, which produces images comparable to those obtained using other ventilatory radiopharmaceuticals (Sullivan et al, 1988; Peltier et al, 1990; James et al, 1991). We have found the optimum inhalation procedure to be a deep inspiration from functional residual capacity, followed by a 5 s breath-hold before returning to tidal breathing of room air. Some patients need to repeat this manoeuvre several times to achieve the desired level of lung deposition. The first inhalation of newly generated Technegas contains no oxygen. Second and subsequent inhalations contain proportionally more oxygen as air is drawn into the chamber to replace the Technegas removed. Following inhalation, some patients, particularly those with compromised respiratory function, feel unwell, reporting symptoms such as dizziness, light headedness and nausea. These symptoms are probably a consequence of temporary hypoxia induced by Technegas administration. The purpose of this study was to measure the degree of hypoxia produced, evaluate its significance and assess means of preventing it.

Materials and methods

Patients

Oxygen saturation was monitored in four patient groups.

Group A. 38 patients were studied during Technegas inhalation. There were 18 male and 20 female patients with an age range from 18 to 82 years (mean 50 years). 28 were referred for lung studies because of suspected pulmonary embolism (PE); of these, eight had known pre-existing respiratory disease and one had had previous pulmonary emboli. A further 10 patients known to have respiratory disease but in whom PE was not suspected were studied.

Group B. 25 patients were studied during Technegas inhalation following pre-oxygenation for 2 min with 67% oxygen. There were nine male and 16 female patients with an age range from 17 to 89 years (mean 49 years). All were referred for lung studies because of suspected PE; two had had previous emboli, four had known pre-existing respiratory disease and three had ischaemic heart disease.

Group C. 52 patients were studied before, during and for 5–10 min after an intravenous injection of ^{99}Tc^{m}-labelled macroaggregates of albumin (^{99}Tc^{m} MAA). There were 21 male and 31 female patients with an age range from 17 to 82 years (mean 52 years). All patients were referred for lung studies because of suspected PE; four had had previous emboli, 12 were known to have co-existent respiratory disease and a further six had ischaemic heart disease.

---

†Present address: Department of Medicine, Trafford General Hospital, Moorside Road, Urmston, Manchester M31 3SL, UK.

Address correspondence to Dr J. M. James, Department of Nuclear Medicine, Manchester Royal Infirmary, Oxford Road, Manchester M13 9WL, UK.

Group D. 40 patients were studied as controls for Group C to assess the effect on oxygen saturation of anxiety, pain or discomfort before, during and for 5 min after intravenous injection of radiopharmaceuticals other than ^{99}Tc^{m} MAA. There were 19 male and 21 female patients with an age range from 17 to 82 years (mean 49 years) who were attending the department for bone or renal studies. Full clinical details, including smoking history and the results of relevant investigations, were documented for each patient.

Equipment and procedure

Oxygen saturation was measured by means of a finger probe connected to an Ohmeda Biox 3700c pulse oximeter. This machine provides continuous oxygen saturation readings by measuring the absorption of selected wavelengths of light. Both oxygenated haemoglobin (HbO_2) and reduced haemoglobin (Hb) absorb light at known wavelengths. Arterial pulsation modulates light passed through the probe. The relative percentage of HbO_2 to total haemoglobin can be calculated and oxygen saturation derived. Oxygen saturation is calculated 25 times per second; a running average (weighted according to signal strength) is calculated over a 6 s period and the digital display updated every 0.75 s. The accuracy of the readings is 2%, the range 0–100% and the resolution 1% (Ohmeda, 1988). Nickerson et al (1988) have studied the reproducibility of oximeter measurements in normal volunteers and suggest that changes of 1% in the range of saturations above 90%, and 2% in the range below 90%, indicate that a clinical change has occurred. To define a normal range, oxygen saturation was measured in 20 volunteers: 10 male and 10 female, age range 18–55 years. Readings ranged from 95 to 98% (mean 96.6%). Seven of the vounteers were pre-oxygenated in the same manner as the Group B patients; all showed an increase in oxygen saturation to 100%.

The patient was attached to the oximeter and resting oxygen saturation recorded. Technegas was generated as previously described (James et al, 1991). All patients receiving Technegas (Groups A and B) underwent practice runs using the nose clip, Technegas mouth piece and delivery tubing. Group A patients then went on to inhale Technegas seated as for a posterior lung view in front of the gamma camera. They were instructed to take normal tidal breaths (of air) then a slow deep inspiration, at the start of which they were switched to Technegas. At, or near, total lung capacity they were instructed to hold their breath for 5 s and then to expire before returning to tidal breathing of room air. The number and type of inhalations required to achieve sufficient lung deposition for imaging were recorded, as was the length of breath-hold and the oximeter readings throughout and after inhalation. When a decrease in oxygen saturation occurred, second and subsequent inhalations were delayed until the oxygen saturation had recovered to the resting value. Eight patients within this group (Group A) required oxygen during the course of Technegas administration, either because they were initially hypoxic or experienced symptoms associated with a drop in oxygen saturation during inhalation. This was administered intermittently via a face mask in four cases, continuously via nasal cannulae in three cases and in one patient who would tolerate neither, a small piece of tubing carrying oxygen was taped to the cheek then placed inside the mouth adjacent to the Technegas mouthpiece.

Following the practice run, and before Technegas inhalation, the Group B patients were given oxygen via a face mask for 2–2.5 min. A flow rate of 10 litres/min was used with a mask designed to provide 67% oxygen at this rate. They then went on to inhale Technegas in the same manner as the Group A patients.

Oxygen saturation in the Group C patients was monitored before, during and after intravenous (IV) injection of ^{99}Tc^{m} MAA. 39 of these patients also received Technegas and 13 had ventilation studies performed with krypton-81m gas. Oxygen saturation in the Group D patients was monitored before, during and after IV injection of renal or bone imaging agents. Both Groups C and D were injected sitting.

Results

Oxygen saturation usually decreased after inhalation of Technegas and breath-holding, recovering to the initial value within 15–30 s. The lowest value (the minimum recording for the whole administration) usually occurred after the first or second inhalation and patients required between one and 11 inhalations to achieve sufficient deposition for imaging. The percentage decrease in oxygen saturation was calculated as (initial − lowest)/initial × 100. In no patient was a decrease in oxygen saturation recorded during the practice run, *i.e.* during breath-holding on air.

For the five patients in Group A who showed a large decrease with the first inhalation and were given oxygen, much smaller decreases (or none) were seen with subsequent Technegas inhalations.

Figures 1, 2 and 3 show the distribution of the initial and lowest values for Groups A, B and C. Figure 4 shows the distribution of the percentage decreases for all four groups. The means and ranges of these distributions are shown in Table I.

The distributions of initial values for all patient groups were similar with an overall mean of 94.6%. In only one patient (Group A) was initial oxygen saturation less than 85% (50 mmHg). Pre-oxygenation (Group B) increased the saturation so that in all patients it was 97% or more (mean 98.4%).

For Group A, lowest values ranged from 60 to 97% (mean 86%), the largest percentage change recorded being 24% (mean 8.3%). In 15 patients (39% of the group) saturation fell below 85% (50 mmHg). When compared with Group A, the lowest values for Group B patients (those pre-oxygenated) tended to be higher (range 85–99%, mean 90.2%) although the mean

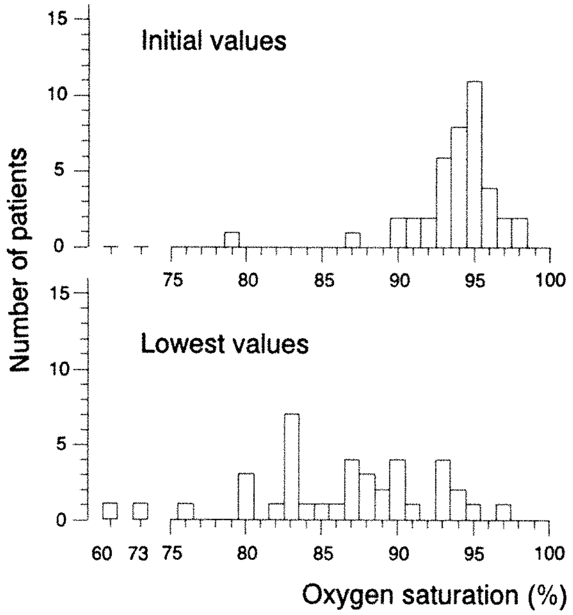

Figure 1. Histograms showing initial and lowest oxygen saturation readings for Group A patients (Technegas only).

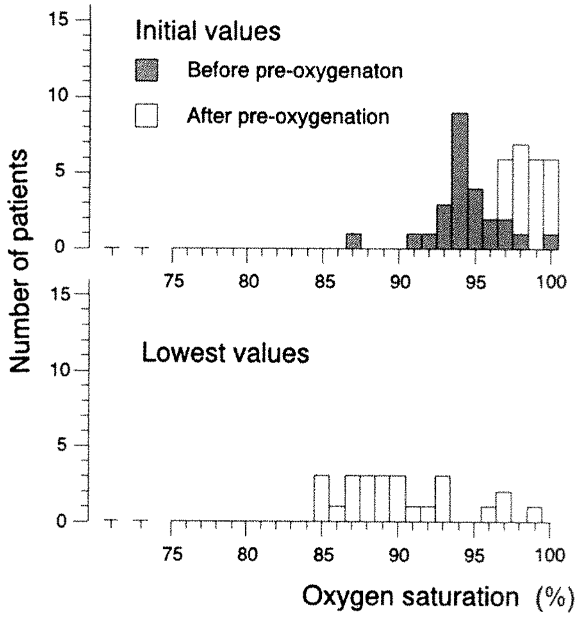

Figure 2. Distribution of initial and lowest oxygen saturation readings for Group B patients (Technegas following pre-oxygenation). The initial values are shown before and after pre-oxygenation as overlapped histograms.

percentage change (8.3%, range 1–15%) and number of inhalations required were very similar. In no patients within this group did oxygen saturation fall below 85%.

Some patients in Group C (who were monitored during ^{99}Tc^m MAA injection) also showed a decrease in oxygen saturation. This ranged from 2 to 11% and in five patients (10% of the group) was greater than 5%. In Group D (patients receiving intravenous injections of radiopharmaceuticals other than ^{99}Tc^m MAA) some small decreases (range 1–5%) in oxygen saturation were also observed but in only one patient (2.5% of the group) was a decrease of 5% seen. This was a 15-year-old patient who fainted following the injection. There was a small difference between the mean decreases in

Table I. The mean (and range) of the oxygen saturation distributions for the four patient groups. Figures for Group B show the values before and after pre-oxygenation

Patient group	No. of patients	No. of inhalations: mean (range)	Oxygen saturation: mean (range)		
			Initial (%)	Lowest (%)	Percentage decrease
A (Technegas only)	38	4.6 (1–11)	93.7 (79–98)	86.0 (60–97)	8.3 (0–24)
B (Technegas plus pre-oxygenation)	25	4.2 (1–10)	*Before* 94.4 (87–100) *After* 98.4 (97–100)	90.2 (85–99)	8.3 (1–15)
C (^{99}Tc^m MAA)	52	N/A	94.6 (88–98)	93.8 (81–98)	0.75 (0–11)
D (IV injection)	40	N/A	95.6 (81–99)	94.9 (80–99)	0.68 (0–5)

N/A = not applicable.

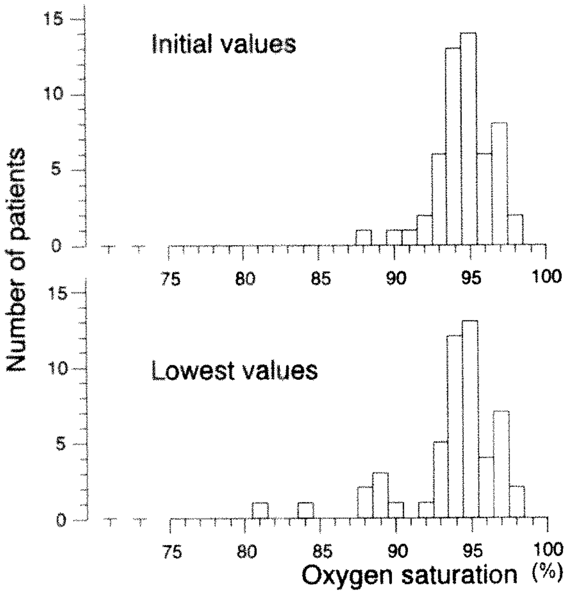

Figure 3. Histograms showing initial and lowest oxygen saturation readings for Group C patients ($^{99}Tc^{m}$ MAA).

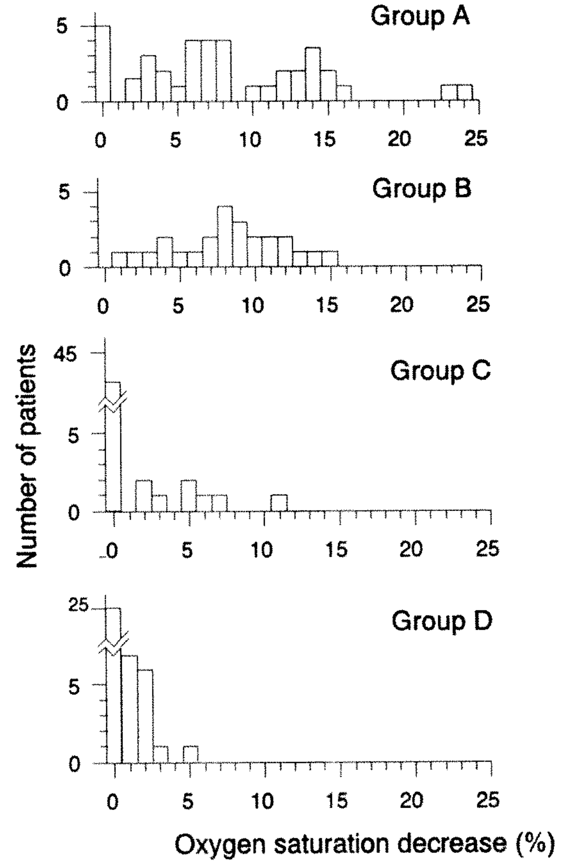

Figure 4. Histograms showing decreases in oxygen saturation (expressed as a percentage of the initial value) for Group A (Technegas only), Group B (Technegas plus pre-oxygenation), Group C ($^{99}Tc^{m}$ MAA) and Group D (IV injection of radiopharmaceutical other than $^{99}Tc^{m}$ MAA).

Groups C and D, which was significant at the 5% level (Wilcoxon's rank sum test, one-tailed).

The results for Groups A, B and C were further analysed by classifying the data according to the presence or absence of previous pulmonary disease, smoking history and the final scan report (normal, consistent with PE, or abnormal but not typical of PE). In no cases were differences between the means for each classification significant at the $p = 0.1$ level (two-tailed) using Wilcoxon's rank sum test and Krusall-Wallis one-way ANOVA by ranks. The correlation between the percentage decrease and the initial values for Groups A and B were analysed using linear regression. No significant association was found.

Discussion

Technegas is in use in several centres as a diagnostic agent in pulmonary ventilation studies. Several published series (Burch et al, 1986; Hilson et al, 1989) have documented its efficacy as a ventilatory radiopharmaceutical in the diagnosis of PE. When comparisons have been made with other ventilatory radiopharmaceuticals the images, in most instances, are found to be similar and to result in concordant diagnoses when PE is suspected (Sullivan et al, 1988; Peltier et al, 1990; James et al, 1991).

The design of the Technegas generator and the process by which Technegas is generated (Burch et al, 1986; James et al, 1991) result in the first inhalation containing Technegas particles and argon with the only oxygen being that contained in the tubing and the dead space of the patient's lungs. Isawa et al (1991) have estimated that if 0.5 litres of Technegas is inhaled in the first breath, the oxygen concentration in the chamber will become 1.6%, increasing to 4.2% if 1 litre of Technegas is inhaled in the second deep breath. The normal O_2 content of inspired air is around 21%. They concluded that for the first inhalation, mixing of Technegas with air was advisable as there is no oxygen in the newly generated radiopharmaceutical. No other study published to date has commented on this aspect of Technegas administration and none have reported adverse effects that could be attributable to Technegas-induced hypoxia.

Concurrent oxygen administration was undertaken in eight of the Group A patients via nasal cannulae, intermittent face mask or mouth tubing. None of the methods interfered with Technegas administration and all patients achieved sufficient lung deposition for imaging. In addition there was a lesser or no decrease in oxygen saturation seen with subsequent inhalations. When tolerated by the patient, nasal cannulae provide the most convenient means of concurrent oxygen administration. The Technegas mouthpiece can be used and the nose clip applied with the nasal cannulae in position, without patient discomfort. However, like Isawa et al (1991) we feel that the ability to add oxygen to the newly generated Technegas could usefully be incorporated into the generator should the manufacturers consider any revision.

In this study, lowering of oxygen saturation was recorded in 87% of patients receiving Technegas; in 58% the decrease was more than 5% and in 37% it was more than 10%. The amount by which oxygen saturation fell in individual patients bore no relationship to the initial value; in one patient a fall of 15% was recorded from an initial 98% whereas another fell by 4% from an initial 87%. All patients studied achieved the desired level of Technegas deposition for imaging (posterior count rate 1600 counts per second). The activity loaded for each patient was similar but a varying number of inhalations was required. Successful inhalation of Technegas depends to a large extent on patient cooperation, which is variable and influenced by the patient's clinical state, pre-existing disease and the way in which the inhalation technique is taught and practised. The number of inhalations is a reflection of all these variables but like the initial oxygen saturation this figure bore no relationship to the decrease recorded for individual patients. Similarly, neither the patient's previous history, smoking history nor the final scan diagnosis showed any correlation with the scale of decrease in oxygen saturation.

The physiological consequences of such temporary lowering of oxygen saturation are difficult to predict being dependent on many factors. The intial oxygen saturation is important, as is the duration and degree of hypoxia induced and the patient's ability to withstand changes in oxygen saturation. Patients with severely impaired coronary or cerebral circulations could theoretically suffer infarction in the presence of severe hypoxia; whether this is likely, however, with the temporary changes that occur following Technegas inhalation is uncertain. Such complications have not been reported to our knowledge.

The results of this study would suggest that if preventative action such as pre-oxygenation is undertaken, then this will be required by all patients. In those patients who were pre-oxygenated, saturation fell by more than 10% in 37% (as in the Technegas group) but because the initial oxygen saturation after pre-oxygenation was higher, in no patient did the level fall below 85%. The patients were pre-oxygenated for 2–2.5 min using a medium concentration face mask, which at a flow rate of 10 litres/min should deliver 67% oxygen. Use of 100% oxygen to achieve full oxygenation and nitrogen washout, although feasible, would be less comfortable for the patient. Our aim was to assess the practical usage of pre-oxygenation with the equipment currently available in the department and for this reason pre-oxygenation with 100% oxygen was not attempted. There are well known hazards associated with usage of 100% oxygen for long periods, particularly in patients with compromised respiratory function such as those commonly referred for ventilation–perfusion imaging; however, temporary 2 min usage of concentrations less than 100% are not hazardous. It is probably wise, therefore, to allow patients who are to undergo Technegas ventilation studies to inhale 40–67% oxygen via a face mask for 2 min prior to administration. Such usage is harmless and may well be beneficial in those patients who are likely to exhibit large decreases in oxygen saturation.

It is interesting to compare the decrease in oxygen saturation following Technegas with that occurring following ^{99}Tc^m MAA injection. A decrease of 5% or more was recorded in five patients (10% of the patient group). This was significantly different from the decrease noted with a control group receiving intravenous injections of other radiopharmaceuticals. The performance of the injection itself, therefore, would seem to be less important as a causative factor than the ^{99}Tc^m MAA. Renowden et al (1991) reported a decrease of 2–10% in 57% of a group of 63 patients receiving ^{99}Tc^m MAA before perfusion imaging. The decrease was short lived, persisting for up to 30 min, so was not thought to arise as a consequence of arteriolar blockade by the ^{99}Tc^m MAA particles, which is longer lasting (2–8 h). This group postulated that vasoconstriction resulting from a direct pharmacological effect of ^{99}Tc^m MAA on the blood vessels was the cause. In this department more than 1000 perfusion scans are performed annually without noticeable untoward effects; extrapolating from this series more than 170 patients per annum probably experience a fall in oxygen saturation as a result of ^{99}Tc^m MAA injection. The absence of symptoms or sequelae suggest that such temporary decreases are of little physiological consequence.

Conclusion

The majority of patients undergoing Technegas ventilation studies experience a decrease in oxygen saturation at some stage of the administrative procedure. In this study the decrease was greater than 10% in 37% of patients and it was not possible to predict which patients would exhibit the largest decreases. Decreases were also seen in some patients receiving ^{99}Tc^m MAA before perfusion imaging but overall these were of lesser magnitude. Decreases in oxygen saturation also occurred following pre-oxygenation; however, because of higher initial values, these were of less significance. Pre-oxygenation of all patients before Technegas administration should be considered. This is harmless, improves patient well-being and reduces the hypoxia induced by Technegas inhalation without significantly increasing the complexity of the procedure. When concurrent oxygen is required, nasal cannulae provide the most convenient means of administration and do not interfere in any way with Technegas inhalation.

Acknowledgments

The assistance of the North West Regional Health Authority in providing funds to cover purchase of the Technegas generator is gratefully acknowledged. We thank Dr R. Bowman (Consultant Anaesthetist, Manchester Royal Infirmary) for helpful discussion.

References

BURCH, W. M., SULLIVAN, P. J. & MCLAREN, C. J., 1986. Technegas—a new ventilation agent for lung scanning. *Nuclear Medicine Communications, 7*, 865–871.

HILSON, A. J. W., DIAMOND, P. D., PAVIA, D. & AGNEW, J. E., 1989. Lung ventilation scintigraphy with an ultra fine aerosol (Technegas): a comparison with ^{81}Kr^{m}. Seventeenth Annual Meeting of the British Nuclear Medicine Society: Abstracts. *Nuclear Medicine Communications, 10*, 257.

ISAWA, T., TESHIMA, T., ANAZAWA, Y., MIKI, M. & MOTOMIYA, M., 1991. Technegas for inhalation lung imaging. *Nuclear Medicine Communications, 12*, 47–55.

JAMES, J. M., HERMAN, K. J., LLOYD, J. J., SHIELDS, R. A., TESTA, H. J., CHURCH, S. & STRETTON, T. B., 1991. Evaluation of ^{99}Tc^{m} Technegas ventilation scintigraphy in the diagnosis of pulmonary embolism. *British Journal of Radiology, 64*, 711–719.

NICKERSON, B. G., SARKISIAN, C. & TREMPER, K. 1988. Bias and precision of pulse oximeters and arterial oximeters. *Chest, 93*, 515–517.

OHMEDA, 1988. Ohmeda Biox 3700e Pulse Oximeter Operation and Maintenance Manual Revision P (Ohmeda, Louisville, CO 80027, USA), pp. 1–6.

PELTIER, P., DE FAUCAL, P., CHETANNEAU, A. & CHATAL, J. F., 1990. Comparison of technetium-99m aerosol and krypton-81m in ventilation studies for the diagnosis of pulmonary embolism. *Nuclear Medicine Communications, 11*, 631–638.

RENOWDEN, S. A., DUNNE, J. A. & HAYWARD, M. W. J., 1991. Changes in arterial oxygen saturation during isotope perfusion scans using human macroaggregates of albumin. *Nuclear Medicine Communications, 12*, 959–963.

SULLIVAN, P. J., BURKE, W. M., BURCH, W. M. & LOMAS, F. E., 1988. A clinical comparison of Technegas and xenon-133 in 50 patients with suspected pulmonary embolus. *Chest, 44*, 300–304.

1992, *The British Journal of Radiology*, *65*, 409–416

Quality assurance of computer controlled radiotherapy treatments*

By †Helen M. Morgan MSc, MInstP, MIPSM

Department of Medical Physics and Computing, Royal Free Hospital, Hampstead, London NW3 2QG, UK

(*Received 22 February 1991 and in revised form 5 August 1991, accepted 3 October 1991*)

Keywords: Radiotherapy, Quality assurance, Conformation

Abstract. There is a need in conformal therapy, as in any radiation therapy, for adequate quality assurance of the treatment plan and the delivery of the treatment. This paper examines quality assurance of two methods of conformal treatment, on a cobalt treatment unit using computer control. Each of the two methods demonstrates a different aspect of computer controlled treatments. Following completion of each treatment plan, an additional "quality assurance plan" is prepared. This is used to assess the integrity of the treatment plan, and the precision with which the computer controls the treatment unit. A simple method, using solid state detectors in a Perspex phantom, is used to validate the dosimetry of the "quality assurance plan". Quality assurance of the computer control is performed daily prior to treatments. At each treatment, parameters identifying the start position and final position of the computer controlled couch movements and the exposure time are noted by the radiographers. Comparison of the recorded movement of the treatment couch and the exposure time with that intended during each course of treatment has demonstrated, inter alia, limitations on couch speed control at speeds of less than 10 mm per min.

Quality assurance in radiotherapy, for dosimetry and mechanical alignment of the treatment unit, has always been recognized as an important part of radiotherapy physics (Hospital Physicists' Association (HPA), 1971; Institute of Physical Sciences in Medicine (IPSM), 1988). With the advent of computer controlled treatment units there is need for even greater vigilance, since the treatment plan is more complicated than for conventional treatment.

In computer controlled conformation therapy, during which the computer is programmed to control many machine movements with the radiation on, any errors that do occur are likely to be more complicated to correct.

This paper describes the quality assurance for two types of treatment under computer control on a cobalt unit (Brace et al, 1981) at the Royal Free Hospital. The main difference between these two types of treatment is whether the couch is driven in position mode or in rate mode. In position mode the couch is driven to a specified position between exposures (*i.e.* with the radiation off). Rate mode is used to drive the couch when the radiation is on; in this mode the final position and the exposure time are specified.

Treatment planning

An example of using the couch in position mode is treatment of the pelvis and para-aortic nodes. Target volumes that include these sites are of the order of 350 mm long. The target is divided into short sections for treatment planning purposes (Fig. 1) and the couch is driven in position mode from one section to the next between exposures. The plan for each section is calculated on a commercial treatment planning computer using computed tomographic (CT) information. An arcing arrangement of radiation fields is used, as this is the most time efficient on a cobalt unit. Each section may have a different rotation centre. Owing to the complex shape of the target volumes, some sections may have up to three rotation centres to get the best fit of the isodose distribution to the target (Fig. 2).

Rate mode is used to drive the couch to treat long shallow target volumes such as those involving the spinal cord. The treatment planning of these volumes has been automated and details were reported by Shentall at a meeting "Computers for the control of radiotherapy treatment units", February 1988 in London. There are three phases to be planned: the opening and closing phases and the intermediate phase. In each phase the couch is driven in rate mode with the shutter open.

Both treatment techniques have been described (Davy, 1983). For both types of treatment, once the treatment plan details have been completed, a computer file is prepared.

Data preparation for computer control

To deliver a computer controlled treatment it is first necessary to determine a "start" position for the treatment couch. The start position is that required to set up to a reference point (tattoo) on the patient, which has been determined at their CT planning session. The patient location on the treatment couch will vary

---

*Presented at: "Computers for the control of radiotherapy treatment units", February 1988, London. †Current address: Wessex Regional Medical Physics Service, Royal United Hospital, Bath BA1 3NG, UK.

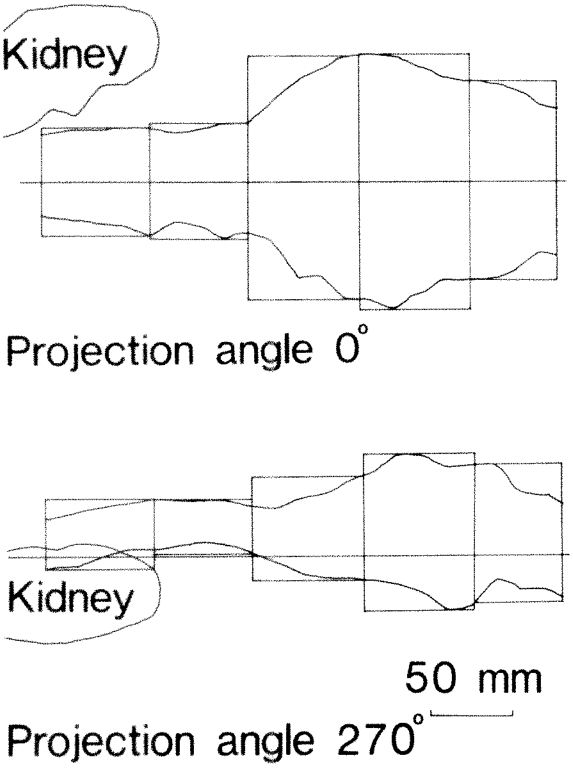

Figure 1. A typical pelvis and para-aortic node target volume displayed at orthogonal projection angles (AP and lateral views). The volume is divided into sections as shown, and a treatment plan calculated for each section.

slightly from day to day, and consequently the longitudinal, lateral (and vertical) coordinates of the treatment couch at the start position will vary similarly. All computer controlled movements are then relative to these start position coordinates.

For treatment to a pelvis and para-aortic nodes target, the couch is displaced from the start position to place the rotation centre of the first section at the treatment unit isocentre by driving the couch longitudinally, laterally and vertically in position mode. The radiation is delivered according to the treatment plan and then the couch is driven to position the rotation centre of the next section at the treatment unit isocentre. This continues until the last section of the target has been treated. If there is more than one rotation centre for a section, then the vertical and lateral couch drives are used to position the next rotation centre at the machine isocentre without operating the longitudinal drive. The complete set of treatment plans with the necessary couch displacements from the start position are translated into a set of computer instructions, which are identified by the patient's name. This is called the Patient File.

The spine treatment plans are carried out by driving the couch longitudinally in rate mode whilst the shutter is open. The gantry is usually held at 0° for the whole treatment. Again there may be couch vertical and lateral movements so that the centre of the target volume is driven through the machine isocentre along its whole course. A computer program has been developed to create a Patient File for these treatments (reported by Shentall at the meeting "Computers for the control of radiotherapy treatment units", February 1988).

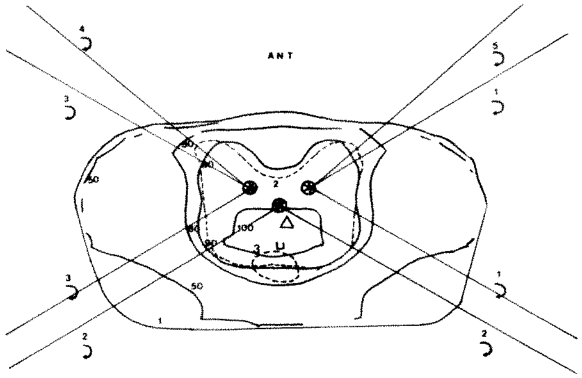

Figure 2. A treatment plan for a section of a pelvic target volume. There are three rotation centres (⊕) about which the gantry delivers an arcing field. Each of the two anterior rotation centres also has a static field. The target outline is represented by a dashed line and the projection of the start position onto this plane (△) is shown. The plan is normalized to 100% at the most posterior rotation centre.

For both treatment types a quality assurance (QA) file is also prepared on the computer. This QA file is used for quality assurance of dosimetry and to check reproducibility, and is identical to the Patient File except that when implemented (1) the gantry position is fixed at 0°, and (2) there are no couch lateral or vertical displacements from the start position. The field size, couch longitudinal displacement and exposure time vary identically to the Patient File. The lateral and vertical couch movements are excluded to simplify the measurement and calculation of the dose along the locus of the isocentre.

Quality assurance

Dosimetry

From the set of treatment plans or treatment phases for a particular target volume, the average depth of the isocentre within the patient for all treatment fields is determined. For an arcing field, the depth is determined at 15° intervals and the mean depth of each arc used to determine the overall average depth of the isocentre for the target volume. This depth is converted to an equivalent depth in Perspex and then rounded to the nearest integral 5 mm. This is called the QA depth. The tissue equivalent of the QA depth is used to calculate the dose along the locus of the isocentre, when the treatment unit is controlled by the QA file.

This dose profile is then measured with cylindrical solid state detectors (Therados SDS-C) in a Perspex phantom. The Perspex phantom consists of sheets of

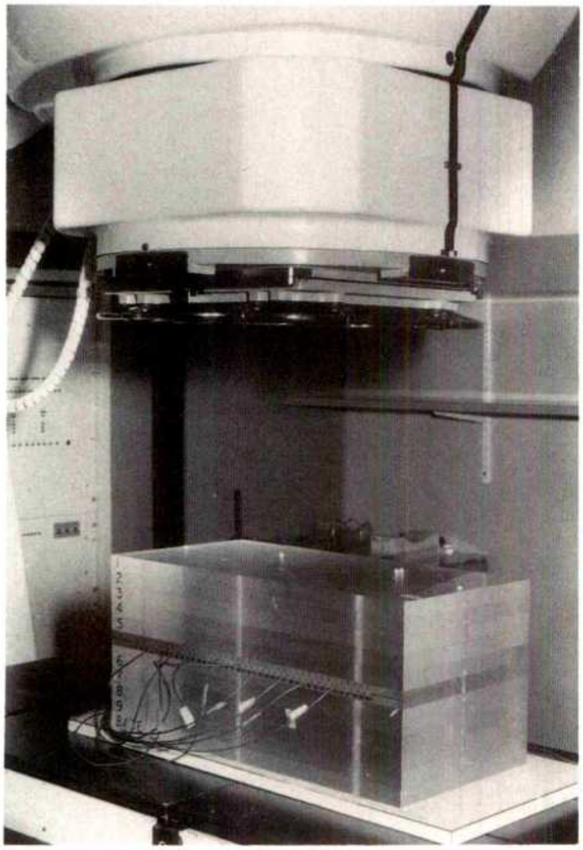

Figure 3. The Perspex phantom with solid state detectors in position. This is used to measure the dose delivered along the locus of the isocentre when the QA file is run (see text).

Perspex that interlock on top of each other. One 20 mm thick sheet is drilled to take the solid state detectors at 10 mm intervals along its midline (Fig. 3). The phantom is placed on the treatment couch, so that the solid state detectors lie along the rotation axis of the treatment unit. The start position of the treatment is set on the phantom and solid state detectors are inserted at positions to correspond with the planned superior and inferior borders of the target volume, the rotation centres and the borders between adjacent treatment regions to within 5 mm. Sheets of Perspex are placed over the detectors to achieve the QA depth, as calculated above.

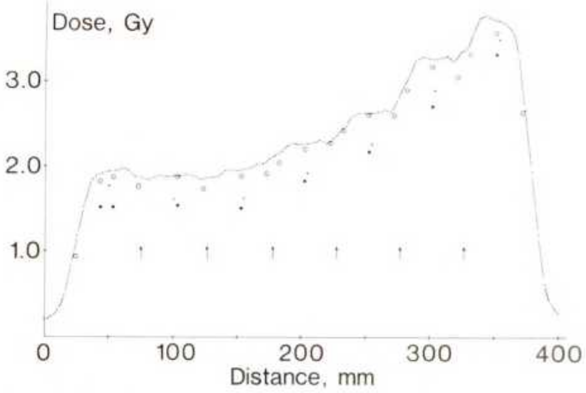

Figure 4. The calculated dose profile (—) in the Perspex phantom from a QA file for a pelvic treatment, together with the total doses measured from the solid state detectors (○), along the isocentre locus. The calculated direct dose to a single section (+) is shown for comparison with the direct dose measured by the solid state detectors (●). The junctions between adjacent treatment sections are marked (↑).

The measured doses are then compared with those calculated. This procedure is to confirm that the measured doses and overall treatment length are as predicted, to avoid gross discrepancies and to ensure that in the case of pelvic treatments there are no large dose discontinuities at the junction of adjacent treatment regions. For spinal treatments, which are planned in three phases, it is necessary to check that there are no large variations in dose between the three phases. Large discontinuities at field joins could be due to incorrect couch displacement, speed or field length. The criterion for acceptance is that the total doses measured with the solid state detectors should be within 5% of the calculated values (Fig. 4). Larger discrepancies require further investigation to search out errors in the computer file or treatment plan.

For a plan to treat the pelvis and para-aortic nodes, 5–20% of the total dose at a rotation centre is due to scatter from the treatment of adjacent sections. The amount of scatter depends on the position of the section within the target length: sections at each end of the target volume will receive a smaller proportion of scattered radiation than those sections at the centre.

Dose measurements from the solid state detectors are normally recorded when the QA file has finished running. However, the QA file may be interrupted at any time during its execution. By interrupting the running of the file between treatment regions (when the radiation is off), and recording dose measurements during the interruptions, the contribution of direct and scattered radiation to each section or phase from each region of the treatment can be measured. When this test is performed there are differences between the measured and calculated doses. The solid state detectors underestimate the direct dose by an average of 7%, overestimate the dose from scattered radiation by an average of 11%, and are field-size dependent.

Reproducibility of the QA file is checked by repeating the measurements with the solid state detectors without changing their positions in the phantom. This dosimetry check has demonstrated that the QA file is reproducible to within 1%. A significantly larger variation in reproducibility would require investigation.

To validate this method of dosimetry, this QA file has also been run with thermoluminescence dosemeters (TLD) (Harshaw TLD-100 chips), positioned along the

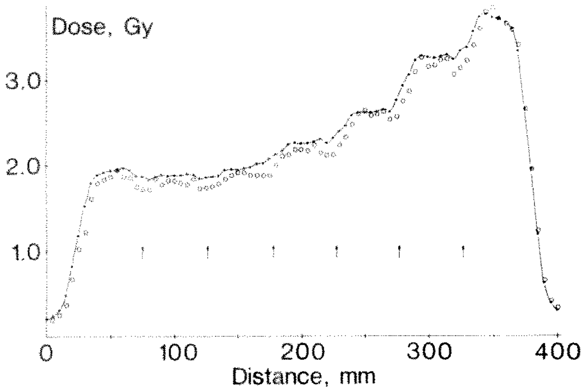

Figure 5. The calculated dose profile (—) in the Perspex phantom, for the same QA file as shown in Fig. 4, together with the total doses measured by TLD (○). The junctions between adjacent treatment sections are marked (↑).

locus of the isocentre in the same phantom (Fig. 5). Individually calibrated TLD were positioned at 5 mm intervals in a sheet of Perspex drilled to contain them. Where the solid state detectors and TLD were in the same position in the phantom, relative to the start position, the ratio of their readings was calculated. The mean of all the ratios was 0.999 with a coefficient of variation of 0.02.

At the start of each QA programme, the solid state detectors are individually calibrated in a water phantom in a 100 mm × 100 mm field at a depth of 50 mm on the cobalt treatment unit against a 0.6 cm^3 thimble ion chamber (N.E. Technology, model 2571) with an electrometer (N.E. Technology, Ionex Electrometer 2500/3). The thimble ion chamber and electrometer are calibrated in accordance with the current code of practice (HPA, 1983; IPSM, 1990). A consistency check is then carried out in the Perspex phantom, with all the solid state detectors within a large field size, on the cobalt unit. This consistency check is repeated each day before use of the solid state detectors with the QA file.

Despite the problems discussed above, the solid state detectors are a useful tool to guard against gross errors and large dose discontinuities, and also check the reproducibility of the QA file, *i.e.* control of field size and couch displacement. The method using TLDs is too time consuming to perform on a routine basis. Both methods measured total (direct plus scatter) doses lower than those calculated with a mean ratio of 0.973 for measured to calculated doses for both the solid state detectors and the TLD. The coefficient of variation was 0.017 for the solid state detectors and 0.013 for the TLD.

Control of couch position

In addition to checking the dosimetry with the QA file, the computer control of the couch movements in the Patient File are checked. The locus of the isocentre is determined from the treatment plan, and charts are drawn to show the required couch displacements in the vertical and horizontal plane. The vertical plane (Fig. 6) shows the required couch height and couch longitudinal displacements from the start position; the horizontal plane shows similarly the required lateral and longitudinal couch displacements.

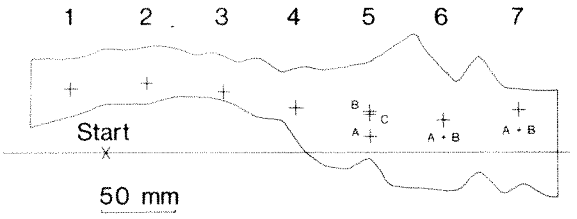

Figure 6. A chart used to demonstrate the required couch vertical and longitudinal displacements from the start position (×) to the positions of the rotation centres (+) for each treatment section of a pelvic target volume, in the vertical plane. A similar chart is used to demonstrate the required couch lateral and longitudinal displacements in the horizontal plane.

The charts are positioned on the treatment couch with a simple jig, ensuring that the laser positioning beams are centred on the start position (Fig. 7). The Patient File is then activated in the "test mode", which enables the shutter of the treatment unit to be locked in the closed position. A physicist remains in the treatment room whilst the file is running, and confirms that the required couch movements are being carried out correctly, by visual examination of the crosswires (projected by the field defining lamp in the treatment unit head) and the laser beams against the charts.

This check ensures that the treatment plans have been converted into computer instructions correctly and that the couch drives are not "hunting" excessively to reach the required positions. If excessive hunting occurs, adjustments to the servo systems must be made before patient treatments are carried out.

Daily check on treatment unit control

Each day, prior to computer controlled treatments, a special program (the run-up program) is executed to check that the computer can control the treatment unit correctly (Brace, 1982) (Table I). The first part of the sequence checks for noise on the various signals. The computer then drives the couch and treatment unit in position mode to specified positions in both positive and negative directions. Having checked the position mode, the rate mode is then checked. The couch and gantry are driven at specified speeds, again in both the positive and negative directions. The shutter open and close commands are also tested.

At the end of this series of tests the computer analyses how successfully the movements were carried out. If any tolerance is exceeded a "fail" message is given. The tolerances on the position drives for the couch and gantry are equivalent to 1 mm and 0.4°, respectively. On

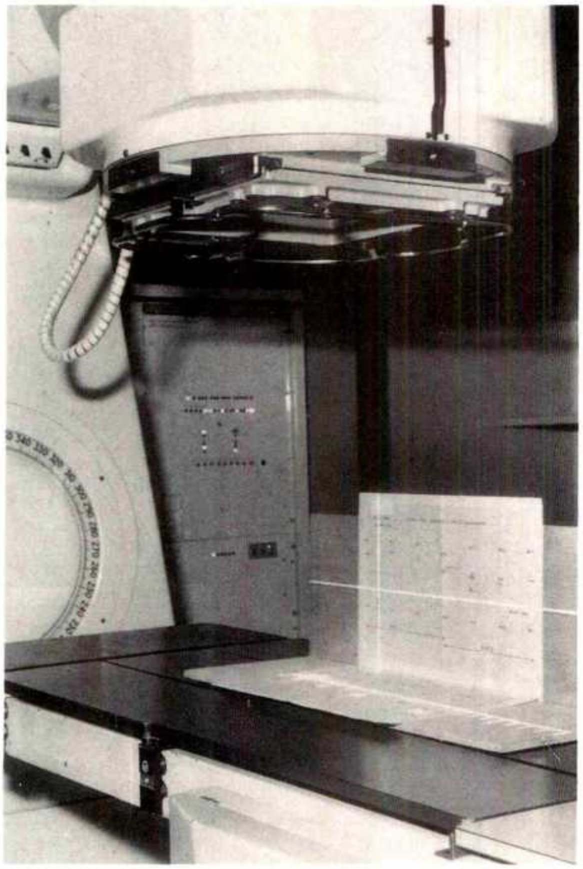

Figure 7. For each Patient File, the computer control of the required couch movements from the start position to each rotation centre is checked visually using the image of the crosswires and the alignment lasers.

the speed tests an error of 5% is allowed before the test is failed. In the event of a failure, further computer programs are available to the electronics engineer, computer scientist and physicist to pin-point the problem.

Table I. The run-up program used to check the computer control of the treatment unit on a daily basis. The tolerance for each test is given

Test	Tolerance
Noise	0 noisy readings
Move to start position	±1 mm, ±0.4°
Position test: +ve drive	±1 mm
Position test: −ve drive	±1 mm
Couch speed: $+50\ \mathrm{mm\ min^{-1}}$	±5%
Couch speed: $-50\ \mathrm{mm\ min^{-1}}$	±5%
Arm speed: $+360^\circ\ \mathrm{min^{-1}}$	±5%
Arm speed: $-360^\circ\ \mathrm{min^{-1}}$	±5%

When all sections of the run-up program are within tolerance, the unit may be used for computer controlled treatments. If the run-up program has failed, an error message will be given in order to prevent patient treatment.

Patient treatment

Whilst the patient is on treatment the following parameters are recorded manually by the radiographers at each attendance, independently of the computer: (1) the couch longitudinal start and end positions, and hence the total travel; and (2) the total exposure time recorded by the timer on the cobalt unit treatment console. These parameters may differ from those expected from the treatment file. Figure 8 shows the difference in mean recorded couch longitudinal travel compared with that demanded, for a series of 11 treatment courses, where the couch was driven in the position mode. The results are shown in date order of patient treatment course.

The difference between recorded and demanded total travel does not correlate with the number of demands for longitudinal movement. However, there is a slight trend up to treatment course number 6, for the travel to fall short of that demanded. Overhauling the couch movement mechanism resolved this problem.

If the total exposure time per treatment fraction exceeds the maximum time that can be set on the treatment unit timer (17.99 min), the instructions are split into two files. In normal circumstances the second file is run immediately after the first, without the radiographers entering the treatment room, but the exposure time of each file is recorded separately.

The treatment unit timer detects the shutter opening and closing at different positions during source transit from the computer. So although the recorded exposure time may be different from the demanded time, it should be reproducible for each treatment fraction. Figure 9

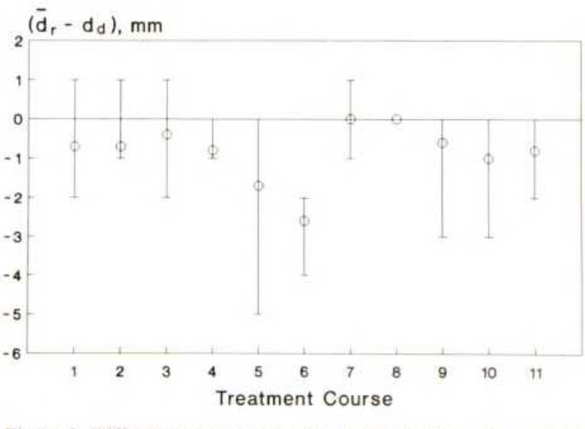

Figure 8. Difference between the mean recorded couch travel of all treatment fractions($\bar{d}_r$) and the demanded couch travel (d_d), when the couch is driven in position mode, for a series of 11 patients in order of treatment course. The range of the recorded couch travel for the treatment course is also shown.

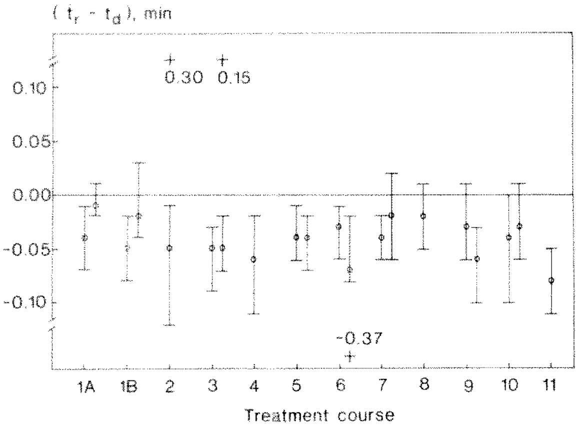

Figure 9. Difference between the mean recorded exposure time of all treatment fractions ($\bar{t}_r$) and the demanded exposure time (t_d), when the couch is driven in position mode, for a series of 11 patients in order of treatment course. Where the total exposure time exceeded the maximum that could be set on the cobalt unit treatment timer, two patient file details are shown. The range of the recorded exposure time for the treatment course is also shown. For the first treatment course, the daily dose was amended, hence the two sets of data. Three recorded exposure times (+) are outside the normal range (see text).

shows the difference between mean recorded and demanded exposure times for the 11 treatment courses delivered in position mode. Note that for the first treatment course in the series the Patient File was amended to reduce the daily dose, hence there are two sets of exposure times. Three values outside the normal ranges were noted. For two values the computer recorded an exposure time within the normal range. During the sixth treatment course in this series an exposure time of 0.37 min less than demanded was noted and the computer confirmed this deficit. No explanation was found for this and the deficit in time was not repeatable.

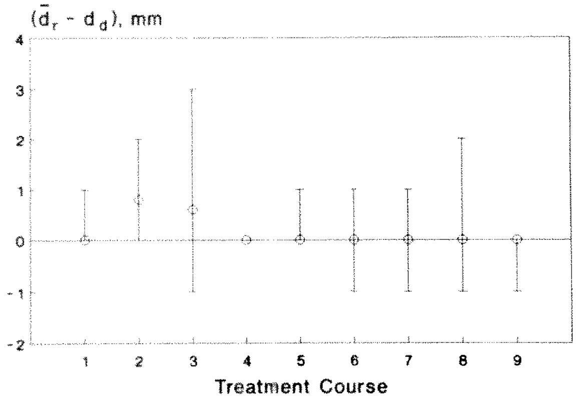

Figure 10. Difference between the mean recorded couch travel of all treatment fractions ($\bar{d}_r$) and the demanded couch travel (d_d), when the couch is driven in rate mode, for a series of nine patients in order of treatment course. The range of the recorded couch travel for the treatment course is also shown.

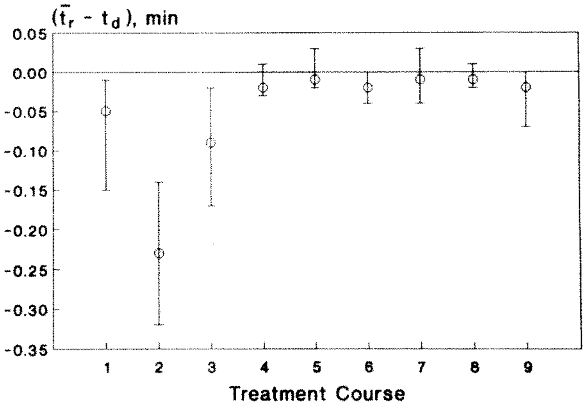

Figure 11. Difference between the mean recorded exposure time of all treatment fractions ($\bar{t}_r$) and the demanded exposure time (t_d), when the couch is driven in rate mode, for a series of nine patients in order of treatment course. The range of the recorded exposure time for the treatment course is also shown.

In the second series of nine patient treatment courses, the couch longitudinal movement was driven in rate mode. Figure 10 shows the difference between mean recorded and demanded couch longitudinal travel. It is clear that the couch position is achieved more accurately when driven in rate mode than position mode (see Fig. 8).

However, Fig. 11 shows the difference between mean recorded and demanded exposure time for this second series. It is evident that the improved positional accuracy achieved in rate mode can be at the expense of the accuracy of the exposure time. The first three cases show a greater difference between recorded and demanded exposure time than the other six. After investigation it was found that the first three treatment courses were delivered when the cobalt source was due for replacement. For these particular treatments of the spine, there is a phase at each end of the target volume where the couch longitudinal speed must be reduced to one-quarter that of the rest of the treatment. In these three particular cases the speed required was less than 10 mm per min, and the speed control at such low speeds was insufficient. The result was that the couch longitudinal drive tended to overshoot and the total exposure time was much less than demanded. For the six cases with the higher output cobalt source, the couch speed required was higher; consequently the difference between recorded and demanded exposure time is small.

In this type of treatment (rate mode), there are only three shutter open and close commands so the recorded exposure time is much closer to the demanded exposure time than for pelvis and para-aortic node treatments where there may be up to 18 shutter open and close commands.

Discussion

The QA programme for conformation treatment under computer control described above is in addition to the routine dosimetry and mechanical checks normally carried out on a radiotherapy treatment unit. The QA programme used at the Royal Free Hospital consists of two parts: (1) QA of the dosimetry and reproducibility of the planned course of treatment, and (2) daily QA of the computer control and treatment delivery during the course of treatment to the patient.

The use of the Perspex phantom and solid state detectors allows the integrity of the QA file to be checked. It also gives a guide to the dose delivered by running the QA file, and the reproducibility of the control of the treatment unit. Since the QA file is identical to the Patient File except for gantry position and couch lateral and vertical displacements, this procedure is also a valid test of the Patient File. The additional movements in the Patient File are checked by running this file in test mode. With the shutter locked in the closed position, a physicist remains in the treatment room to confirm that the gantry rotation and couch displacements are of the required amount and in the correct direction.

The run-up program used daily to check the operation of the treatment unit control has shown up faults that have developed in the system. These faults have then been corrected before delivering a computer controlled treatment. This cannot give a complete guarantee against a fault occurring during a treatment, but since the number of faults that have occurred during the run-up program has been small, this gives confidence that the likelihood of a fault occurring during treatment is also small. The QA checks carried out daily during each computer controlled treatment fraction have highlighted two main points:

1. It is imperative to ensure that the couch runs freely, with minimum friction.
2. Treatments delivered in rate mode cannot be given with optimum precision if the required couch longitudinal speed is 10 mm per min or less.

Couch movements becoming heavy or stiff are an inconvenience to the radiographers for conventional radiotherapy treatments, but will compromise a computer controlled treatment. Slow couch longitudinal speeds are necessary when the dose per treatment fraction is large or the radiation output is low.

The couch longitudinal speed can be varied between 0 and 200 mm per min in increments of 0.784 mm per min. When the couch is driven in position mode it is at maximum speed and can be controlled to within 0.784 mm per min, *i.e.* better than 0.5%. When the couch is driven in rate mode, the shutter is open and speeds of up to 50 mm per min are necessary to give the correct radiation dose. It can be seen that the accuracy of speed control in this region is much less. For this reason priority is given to position when the couch is driven in rate mode. This maintains the same degree of positional control in rate mode as in positional mode.

To improve the accuracy of speed control in rate mode following the initial studies, speeds around 10 mm per min or less are no longer used. In cases where these slow speeds would be required, two identical Patient Files are created, each one delivering half the required daily dose. This increases the required speed by a factor of 2. The two Patient Files are then used consecutively for each treatment fraction.

Conclusion

There is far more scope for error in a computer controlled treatment than a conventional treatment. All the normal quality assurance on the treatment plan and treatment unit must be performed, but in addition further quality assurance is necessary to check the computer control. A method using solid state detectors in a Perspex phantom has been used to check the integrity of the treatment plan and the reproducibility of the control system. Despite problems with the solid state detectors, good agreement with TLDs was obtained. The solid state detectors allow an instant measurement of the dose received and the method is less time consuming to use on a regular basis than that using TLDs.

By running the Patient File in test mode so that a physicist can remain in the treatment room, it can be confirmed that not only are the couch movements reproducible but that they are as intended.

Increased vigilance is needed on the part of the radiographer to confirm that each treatment fraction is delivered correctly. During each course of computer controlled treatment, two additional parameters are recorded for each treatment fraction: (1) the total couch longitudinal travel under computer control, and (2) the total exposure time. These two parameters demonstrate the necessity of ensuring that the couch drives are in good working order, and also that treatments delivered in rate mode should avoid slow couch speeds, since speed accuracy is lost. For computer controlled treatments the QA of a treatment plan does not end until the patient's treatment course is completed.

Acknowledgments

This work was carried out at the Royal Free Hospital, London. The author would like to thank Dr J. A. Brace, Dr T. J. Davy and Mr G. Shentall for their advice and assistance.

References

Brace, J. A., 1982. A computer controlled telecobalt unit. *International Journal of Radiation Oncology, Biology, Physics*, *8*, 2011–2013.

Brace, J. A., Davy, T. J. & Skeggs, D. B. L., 1981. Computer controlled cobalt unit for radiotherapy. *Medical and Biological Engineering and Computing*, *19*, 612–616.

Davy, T. J., 1983. Physical aspects of conformation therapy using computer controlled tracking units. In *Progress in Medical Radiation Physics*, Vol. 2, ed. by C. G. Orton (Plenum Press, New York) pp. 45–94.

HPA, 1971. *A Suggested Procedure for the Mechanical*

Alignment of Telegamma and Megavoltage X-ray Beam Units, Report Series No. 3 (Hospital Physicists' Association, London).

HPA, 1983. Revised code of practice for the dosimetry of 2 to 35 MV X-rays, and of Caesium-137 and Cobalt-60 gamma ray beams. *Physics in Medicine and Biology*, *28*, 1097–1104.

IPSM, 1988. *Commissioning and Quality Assurance of Linear Accelerators*, Report No. 54 (Institute of Physical Sciences in Medicine, York).

IPSM, 1990. Code of practice for high energy photon therapy dosimetry based on the N.P.L. absorbed dose calibration service. *Physics in Medicine and Biology*, *35*, 1355–1360.

1992, *The British Journal of Radiology*, *65*, 417–420

New evidence that tamoxifen does not induce osteoporosis: a nuclear activation analysis and absorptiometry study

By J. Kalef-Ezra, D. Glaros, *G. Klouvas, J. Hatzikonstantinou, †A. Karantanas, *K. C. Siamopoulos and *N. Pavlidis

Departments of Medical Physics, *Internal Medicine and †Radiology, Medical School, University of Ioannina, Ioannina 451 10, Greece

(*Received 26 June 1991, accepted 18 October 1991*)

Keywords: Tamoxifen, Breast cancer, Bone minerals, Neutron activation analysis, Bone phosphorus, Absorptiometry

Abstract. The possibility of increased risk for osteoporosis in breast cancer patients treated with tamoxifen was investigated. 26 patients aged 41–65 years without skeletal metastases were studied. All patients were treated with 20 mg/d tamoxifen for a mean time of 22 months. The data obtained by *in vivo* neutron activation analysis of the phosphorus content in hands, were supplemented with data obtained by single photon absorptiometry in the forearm and radiographic morphometry. Comparison of the data with that of age and sex matched normal controls showed that breast cancer patients treated with tamoxifen are not prone to osteoporosis.

Breast cancer is one of the most common malignant tumours in women. A significant proportion of these carcinomas are oestrogen dependent tumours, therapeutically managed by several hormonal manipulations (Wittliff, 1984). Tamoxifen, an anti-oestrogen compound, is commonly used either as an adjuvant therapy, or in the management of metastatic disease (Ingle, 1984). Recently, the role of tamoxifen as a potential promoter for osteoporosis became a subject of experimental and clinical investigations (Gotfredsen et al, 1984; Love et al, 1988; Fentiman et al, 1989; Turken et al, 1989). Primary osteoporosis is characterized by decreased bone mass and increased susceptibility to fractures in the absence of other recognizable causes of bone loss. Early menopause and the administration of certain drugs are accepted as pre-disposing risk factors (Riggs & Melton, 1986).

The goal of the present study was to determine whether the administration of tamoxifen in breast cancer patients was associated with significant alterations of the bone minerals. *In vivo* phosphorus measurements were applied in breast cancer patients by neutron activation analysis (NAA) for the first time in the literature. The data from this technique were supplemented with data obtained by two conventional techniques, single photon absorptiometry (SPA) and radiographic morphometry. NAA provided data on phosphorus, and SPA data indirectly on both calcium and phosphorus, with a preponderance of calcium.

Materials and methods

Patients and normal controls

A total of 26 female breast cancer patients with a mean age of 53 years (range 41–65) were studied. All patients underwent modified radical mastectomy and were ambulatory with good performance status. None of these patients had bone metastases. Three patients were pre-menopausal, 21 post-menopausal and two peri-menopausal (menopause duration less than 2 years). Mean duration of menopause was 80 months (range 15–215 months). Natural cessation of menses occurred in 17 patients, while early menopause had been induced either surgically or chemically in another six patients. All patients were receiving tamoxifen 20 mg daily for a mean time of 22 months (range 12–45 months). Tamoxifen was administered as an adjuvant therapy in 22 patients and as treatment for advanced disease in the remaining four women. Among the latter, one had both supraclavicular lymph node and lung metastases, one had mediastinal involvement, one had only parenchymal lung lesions, while the last patient had ipsilateral axillary metastases. Nine patients had previously received chemotherapy, mainly as an adjuvant treatment.

Blood samples were obtained from all patients for the determination of serum concentrations of calcium, phosphorus, proteins, alkaline and acid phosphatase by standard procedures.

A group of 50 healthy female volunteers matched to patients for age, bodily build and full-term pregnancies was used as a control (Table I). None of them had a history of clinical conditions related to bone disease or evidence of osteopenia and they were also not users of oral contraceptives or medications related to bone mineral alterations. Lateral radiographs of the spine were required for normal subjects older than 55 years in order to investigate radiological signs of osteopenia.

Techniques

Partial body neutron activation analysis (PBNAA). PBNAA was applied for measuring hand bone phosphorus (HBP). About 90% of the body's phosphorus is

---

Address correspondence to John Kalef-Ezra, PhD, Assistant Professor, Medical Physics Department, Medical School, University of Ioannina, 451 10 Ioannina, Greece.

Table I. Characteristics of patients and normal controls

Group	Patients	Controls	*p*
Number of subjects	26	50	
Age (years)	53.7 ± 7.2	53.0 ± 7.8	0.69
Mass (kg)	70.9 ± 10.3	69.4 ± 10.4	0.52
Height (cm)	153.6 ± 5.6	155.2 ± 6.8	0.31
Full-term pregnancies	1.8 ± 0.9	1.7 ± 0.9	0.60

Mean values ± standard deviation.

found in the skeleton. Body sections, such as the hands, can be selected to measure phosphorus, where the amount of soft tissue present is small compared with that of bone. The technique is based on the detection of the delayed γ-rays emitted from ^{28}Al, which is produced via the ^{31}P(n,α)^{28}Al fast neutron reaction. The 4 min irradiation of the hands with two ^{241}Am-Be neutron sources, is followed by a 4 min counting of the induced activity (Glaros et al, 1987). The 1.78 MeV photons emitted by ^{28}Al are counted with the hands sandwiched in contact with two cylindrical 20.3 cm × 10.2 cm NaI(Tl) detectors. The phosphorus content was expressed as the number of detected 1.78 MeV photons and no attempt was made to correlate quantitatively the ^{28}Al counts with the phosphorus mass because of the potential presence of large systematic errors. The short term *in vivo* precision (coefficient of variation) was found to be 2.9% for 50-year-old healthy women. This was found by measuring twice 30 normal volunteers within a period of a few days. The absorbed dose at any location of the skin palm ranges between 0.5 and 2.0 mGy. 80% of this dose is due to fast neutrons and the rest is due to photons. The dose equivalent does not exceed 0.2 mSv at any location in the trunk (Kalef-Ezra et al, 1990). The effective dose equivalent of the examination is about 100 μSv and the radiological risk factor of the examination is of lower magnitude than that of a typical lateral radiological examination of the lumbar spine.

Single photon absorptiometry (SPA). A modified version of the Cameron–Sorensen technique (Cameron & Sorensen, 1963) was applied for the measurement of bone mineral content (BMC) over the predominantly cortical distal third of the radius and the ulna with a prototype SPA system. The technique is based on the attenuation of a collimated γ-ray beam (59.5 keV from ^{241}Am) with the forearm submerged in water. The entrance skin dose was 40 μGy in a 6 cm^2 area.

Radiographic morphometry. Mammographic films were used for the postero-anterior radiographs of the hands. The Barnett-Nordin index (BNI) was determined at the midshaft of the right second metacarpal using a magnifier with a scale division of 0.1 mm. BNI values below 43 were assumed to be abnormal (Aloia et al, 1976). The entrance skin dose was 350 μGy in an area of about 120 cm^2.

Lateral radiographs of the patients' spines were obtained and read blindly. Vertebral compression, wedge-shape deformity, biconcavity and vertical trabeculation were investigated (Reinbold et al, 1986).

Data analysis

The normal control subjects were divided into five subgroups (41–45, 46–50, 51–55, 56–60 and 61–65 years) of 10 women each. The patients' data were expressed as the percentage of the mean normal values for the corresponding 5 year interval. Provided that the data were normally distributed, statistical analysis was performed using a *t*-test.

Results

No subject was classified as osteopenic in the spine according to conventional radiological criteria. Pathological BNI was found in the right second metacarpal in a 52-year-old patient who exhibited normal BNI in the left hand and early natural menopause at the age of 40 years. No case was found with a HBP value in the low 5% percentile of age matched controls (Table II). The age corrected HBP in the patient's group was 99.5% ± 9.6% (mean value ± 1 SD) and the *t*-test between the patients and the controls provided no evidence of difference in the mean values between the two populations ($p = 0.84$). The age corrected forearm BMC in the patient's group was 98.8% ± 12.5%, however, the *t*-test failed to provide evidence of the difference in the mean values between the two populations ($p = 0.65$).

The two groups reported similar dairy consumption, physical activity, full-term pregnancies, alcohol consumption and smoking habits, but differed in menopausal status. Measurements of serum, concentrations of calcium, phosphorus, proteins, alkaline and acid phosphatase were within normal limits in all patients.

We further investigated the influence of the following clinical parameters: duration of tamoxifen administration; prior chemotherapy; cause of menopause and presence of metastatic disease (Table III). Analysis of the data demonstrated that:

(a) the linear correlation of HBP and BMC values with the duration of tamoxifen administration ($r = 0.04$, $p > 0.1$ and $r = 0.24$, $p > 0.1$, respectively) indicated that the data failed to provide evidence of bone mineral loss.

(b) Comparison of the HBP and BMC values of those patients who had received chemotherapy with the

Table II. Age-adjusted data on the bone mineral status in the upper extremities by *in vivo* neutron activation analysis of phosphorus and single photon absorptiometry

Group	Controls	Patients	*p*
Hand bone phosphorus	100.0 ± 9.9	99.5 ± 9.6	0.84
Bone mineral content	100.0 ± 9.3	98.8 ± 12.5	0.65

Mean values ± standard deviation expressed as percent of matched controls.

Table III. Age-adjusted data on the bone mineral status in the upper extremities in subgroups of patients

Duration of treatment (months)	12–20	21–45	*p*
Number of patients	13	13	
Hand bone phosphorus	99.4 ± 8.5	99.8 ± 10.6	0.91
Bone mineral content	95.2 ± 14.0	102.4 ± 10.1	0.15
CMF chemotherapy	no	yes	*p*
Number of patients	17	9	
Hand bone phosphorus	99.0 ± 7.8	100.5 ± 12.9	0.73
Bone mineral content	100.3 ± 14.4	96.1 ± 7.8	0.44
Induced menopause	no	yes	*p*
Number of patients	20	6	
Hand bone phosphorus	100.4 ± 9.9	96.5 ± 8.5	0.40
Bone mineral content	100.5 ± 13.6	93.1 ± 9.6	0.21
Metastatic disease	no	yes	*p*
Number of patients	22	4	
Hand bone phosphorus	98.3 ± 8.7	106.8 ± 12.8	0.14
Bone mineral content	98.9 ± 13.1	98.4 ± 10.4	0.94

Mean values ± standard deviation expressed as percent of matched controls.

rest of the patients showed no statistically significant difference ($p = 0.7$ and $p = 0.4$, respectively).

(c) The patients with regular menses or natural menopause (age at menopause 49.3 ± 4.3 years) had mean HBP values similar ($p = 0.9$) to those of matched controls and to those six patients with iatrogenically induced menopause ($p = 0.4$). The BMC data on this group did not provide any evidence of difference from either the controls ($p = 0.8$) or the patients with induced menopause ($p = 0.2$). The HBP and BMC data in the small group of patients with iatrogenically induced menopause (age at menopause 44 ± 5 years) were in the normal limits.

(d) The HBP and BMC values of the patients free of metastatic disease showed no significant difference from the matched controls ($p = 0.5$ and $p = 0.7$, respectively). In addition, the HBP and BMC data in four patients with advanced disease were in the normal limits.

Discussion

The amount of calcium and phosporus in the skeleton plays a key role in the structural integrity of bone. It is still unknown whether bone mineral loss in aging and osteoporosis is solely related to reduction in bone mass, or if it is associated with changes in the elemental concentration in bone tissue (Baslé et al, 1990). Neutron activation analysis provided direct data on the amount of phosphorus, while SPA offered indirect data on both elements, with a preponderance of calcium. The data from the present study on the elemental composition of bone mineral refers to specific anatomic sites of the upper extremities and not to the entire skeleton, *i.e.* PBNAA on the amount of phosphorus in hands (about 5% of the total mineralized bone mass, ICRP, 1975), and SPA on the BMC in a few millimetres thick section of the radius and the ulna (about 0.05% of the total mineralized bone mass). Aloia et al (1987) reported that the BMC at the 8 cm site of the radius showed a higher correlation coefficient with total body calcium than the BMC in the lumbar spine assessed by dual photon absorptiometry (DPA) in both normal women and women with post-menopausal osteoporosis. Furthermore, data given by the same investigators indicate that total body calcium and radial BMC measurements showed the same reliability in the discrimination between normal and osteoporotic women of below 60 years (Aloia et al, 1987). With regard to skeletal phosphorus, there are no available data on the phosphorus in the different skeletal sites. Therefore, extrapolation of the HBP to other skeletal sites of clinical interest, as well as the correlation of HBP with other techniques, such as SPA and DPA, should be considered with caution and must be investigated further.

Controversial results have been reported on the influence of tamoxifen on bone minerals in animal models (Turner et al, 1987; Feldmann et al, 1989; Kalu et al, 1990). Various investigators applying absorptiometric techniques reported that tamoxifen does not lead to osteopenia in humans. Fentiman et al (1989) reported that administration of tamoxifen for up to 6 months does not exert any bone demineralization effect in the lumbar spine and in the femoral neck in pre-menopausal women with mastalgia. Gotfredsen et al (1984), in a longitudinal study, found no difference in radial BMC in breast cancer patients receiving either tamoxifen or placebo for 1 year. However, breast cancer patients in the latter study showed a significant bone loss, which could be attributed to metastatic disease in one fourth of them. In another study, Turken et al (1989) investigated post-menopausal women with breast cancer under tamoxifen treatment. They reported no statistically significant change in bone mineral density in the spine after 12 months of treatment. Wright et al (1990), applying quantitative computed tomography (CT), recently reported normal spinal trabecular density similar in 11 post-menopausal tamoxifen treated breast cancer patients. Love et al (1988) found no statistically significant difference in bone mineral density in the lumbar spine and the radius between women with breast cancer under tamoxifen treatment for at least 2 years, and patients without treatment. Moreover, they found no relationship between the duration of tamoxifen therapy and bone mineral density. The data given by Love et al (1988) and Turken et al (1989) were adjusted not only for age, weight and height, but also for time since menopause. However, one must be cautious in adjusting the data for time since menopause when trying to identify groups of patients with elevated risk for osteoporosis, because disorders such as breast cancer are frequently related to early menopause.

In the present study all patients had normal lateral radiographs of spine and normal BNI. Therefore, early bone mineral alterations could only be detected by precise and accurate non-traumatic techniques. Phosphorus measurements showed no evidence of osteopenia in the upper extremities in patients treated for at least 1 year with tamoxifen. This finding is in accordance with those obtained by SPA and radiographic morphometry. Other investigators applying absorptiometric techniques that provide indirect data on elemental composition reported similar findings. In addition, no evidence on the influence on the bone mineral status in the upper extremities was found for the duration of tamoxifen treatment, chemotherapy and the presence of non-skeletal metastases. In conclusion, the present study reconfirmed that breast cancer patients treated with tamoxifen are not prone to early osteoporosis.

Acknowledgments

We wish to thank Dr C. Seferiadis for the biochemistry work. This study was supported in part by the grant E 224 from the Ministry of Health, Welfare, and Social Security of Greece.

References

Aloia, J. F., Vaswani, A., Atkins, H., Zanzi, I., Ellis, K. & Cohn, S., 1976. Radiographic morphometry and osteopenia in spinal osteoporosis. *Journal of Nuclear Medicine, 18,* 425–431.

Aloia, J. F., Vaswani, A., Ellis, K. & Cohn, S., 1987. Bone mineral measurements and the pathogenesis of osteoporosis. In *In Vivo Body Composition Studies.* Ed. by K. J. Ellis, S. Yasumura, W. D. Morgan (The Institute of Physical Sciences, Oxford) pp. 250–260.

Basle, M. F., Mauras, Y., Audran, M., Clochon, P., Rebel, A. & Allain, P., 1990. Concentration of bone elements in osteoporosis. *Journal of Bone and Mineral Research, 5,* 41–47.

Cameron, J. & Sorensen, J., 1963. Measurement of bone mineral *in vivo:* an improved method. *Science, 142,* 230–232.

Feldmann, S., Minne, H. W., Pafvizi, S., Pfeifer, M., Lempert, U. G., Bauss, F. & Ziegler, R., 1989. Antiestrogen and antiandrogen administration reduce bone mass in the rat. *Bone and Mineral, 7,* 245–254.

Fentiman, I. S., Caleffi, M., Rodin, A., Murby, B. & Fogelman, I., 1989. Bone mineral content of women receiving tamoxifen for mastalgia. *British Journal of Cancer, 60,* 262–264.

Glaros, D., Xatzikonstantinou, J., Leodiou, J. & Kalef-Ezra, J., 1987. A partial-body activation analysis technique for the measurement of phosphorus in bone. In *In Vivo Body Composition Studies.* Ed. by K. J. Ellis, S. Yasumura, W. D. Morgan (The Institute of Physical Sciences, Oxford) pp. 294–299.

Gotfredsen, A., Christiansen, C. & Palshof, T., 1984. The effect of tamoxifen on bone mineral content in premenopausal women with breast cancer. *Cancer, 53,* 853–857.

ICRP, 1975. *Report of the task group on Reference Man.* ICRP Publication 23, (Pergamon Press, Oxford) p. 67.

Ingle, J. N., 1984. Additive hormonal therapy in women with advanced breast cancer. *Cancer, 53,* 766–777.

Kalef-Ezra, J., Siamopoulos, K., Karantanas, A., Xatzikonstantinou, J., Sferopoulos, G., Yasumura, S. & Glaros, D., 1990. Alterations of bone minerals in uremic patients and renal graft recipients. In *Advances in In Vivo Body Composition Analysis.* Ed. by S. Yasumura, J. Harrison, J. K. McNeill, A. Woodhead and A. Dilmanian (Plenum Press, New York) pp. 89–93.

Kalu, D. N., Salerno, E., Echon, R. M., Ray, M. & Holis, B. W., 1990. Effects of estrogen, progesterone and tamoxifen on bone: A comparative study in the ovariectomized rat model. *Journal of Bone and Mineral Research, 5,* S246 (abstract).

Love, R. R., Mazess, R. B., Tormey, D., Barden, H. S., Newcomb, P. A. & Jordan, V. C., 1988. Bone mineral density in women with breast cancer treated with adjuvant tamoxifen for at least two years. *Breast Cancer Research and Treatment, 12,* 297–301.

Reinbold, W. D., Genant, H. K., Reiser, U. J., Reiser, V., Harris, S. T. & Ettinger, B., 1986. Bone mineral content in early postmenopausal and postmenopausal osteoporotic women: comparison of measurement methods. *Radiology, 160,* 469–478.

Riggs, B. L. & Melton, L. J., 1986. Involutional osteoporosis. *New England Journal of Medicine, 314,* 1676–1686.

Turken, S., Siris, E., Seldin, D., Flaster, E., Hyman, G. & Lindsay, R., 1989. Effects of tamoxifen on spinal bone density in women with breast cancer. *Journal of the National Cancer Institute, 81,* 1086–1088.

Turner, R. T., Wakley, G. K., Hannon, K. S. & Bell, N., 1987. Tamoxifen prevents the skeletal effects of ovarian hormone deficiency in rats. *Journal of Bone and Mineral Research, 2,* 449–456.

Wittliff, J. L., 1984. Steroid-hormone receptors in breast cancer. *Cancer, 53,* 589–591.

Wright, C. D. P., Evans, W. D., Mansel, R. E. & Compston, J. E., 1990. Effects of long term tamoxifen therapy on bone mas. *Bone, 11,* 221 (abstract).

1992, *The British Journal of Radiology*, *65*, 421–424

Radical treatment of angiosarcoma of the scalp using megavoltage electron beam therapy

By *Stephen M. Sagar, BSc, MRCP, FRCR and Chandrakant M. Pujara, PhD
Newfoundland Cancer Clinic, Health Sciences Centre, St John's, Newfoundland, Canada

(*Received 17 July 1991 and in revised form 25 October 1991, accepted 14 January 1992*)

Keywords: Angiosarcoma, Scalp, Megavoltage electrons

Abstract Angiosarcoma of the scalp is a multifocal neoplasm that is often initially managed by wide excision and surgical reconstruction. Invariably, adjuvant radiotherapy is required to improve local control. Primary radical radiotherapy to the scalp is not well documented. The major limitation is the technical problem of treating homogeneously an extensive superficial curved volume. We describe a practical technique that can be administered with a standard linear accelerator capable of high-energy electron production. The technique uses a multiple abutted fixed field set-up at constant source to surface distance and the patient is immobilized in a custom wax helmet which also serves to optimize the electron absorbed dose in the treatment volume. Surgical excision and reconstruction is reserved for the salvage of local relapse.

Angiosarcoma of the scalp is a rare malignancy predominantly affecting elderly men. It is a multifocal skin disease that may invade the skull, involve the face and metastasize to the cervical lymph nodes and the lung. Clinical presentation includes bruise-like lesions and dusky red-purple plaques. Histological study reveals malignant vascular channnels arising within the dermis, forming clusters that may straddle collagen bundles and usually leave the overlying epidermis intact. The origin of the malignant cells from either vascular or lymphatic endothelium is unclear. Prognosis is generally poor with 50% of patients dying within 15 months of presentation and only 12% surviving 5 years or more (Wilson Jones, 1976; Holden et al, 1987).

Despite the overall poor prognosis, radical therapy to gain local control is essential in view of the distressing local progression of the lesions. Additionally, local control may contribute to survival, particularly if lesions are less than 10 cm in diameter (Holden et al, 1987). Previous reports of the efficacy of radiotherapy in the local control of disease have been disappointing. The literature includes reports of radioresistance (Morales et al, 1981), insufficient field margins (Knight et al, 1980) and complete local control but complicated by radionecrosis (Wilson Jones, 1976). Modern surgical management includes wide excision as determined by preoperative assessment of punch biopsies taken near the visible tumour margin (Barttelbort et al, 1989; Liu et al, 1990), but routine cervical lymphadenectomy (Hodgkinson et al, 1979) is controversial. Post-operative adjuvant radiotherapy to the reconstruction site and margin may reduce local recurrence (Hodgkinson et al, 1979; Barttelbort et al, 1989).

We considered that most reports of radiotherapy technique are insufficient, and case selection too biased towards more advanced cases, to conclude that primary radical radiotherapy is ineffective. On this basis, we managed the patient described in this report with carefully planned wide-field radiotherapy to the scalp using high-energy electrons and reserving wide surgical excision and reconstruction for local relapse. We aimed to deliver the most homogeneous dose possible to the target volume and to administer it with careful fractionation and a practical set-up technique to maintain patient immobilization and consistency of daily treatments.

Case report

A 53-year-old man presented 3 months after suffering head trauma, complaining of persistent bruising of his scalp. He gave a past medical history of chronic irritation of his scalp associated with seborrhoeic dermatitis. Examination revealed three dusky, purple-red plaques on his scalp (Fig. 1). Site 1 was on the anterior vertex of the scalp and measured 2 cm × 3 cm. Site 2 was on the superior left temporoparietal region and measured 3 cm × 3 cm. Site 3 was immediately adjacent to site 2 in the left anterior temporal region and measured 4 cm × 5 cm. Site 1 was biopsied and demonstrated infiltration of the dermis by spindle and round cells that formed a network of anastomosing vessels. These vessels were lined by cells exhibiting nuclear enlargement and pleomorphism, consistent with angiosarcoma. Further investigation revealed no cervical adenopathy and no radiological evidence of invasion of the calvarium or metastasis to the lung.

Method and materials

The patient's scalp was treated with a Varian Clinac 18 linear accelerator using multiple abutted 6 MeV electron beams at a source to surface distance (SSD) of

---

*Current address and correspondence to: Dr S. M. Sagar, Cancer Treatment and Research Foundation of Nova Scotia, Halifax Cancer Centre, 5820, University Avenue, Halifax, Nova Scotia, B3H 1V7, Canada.

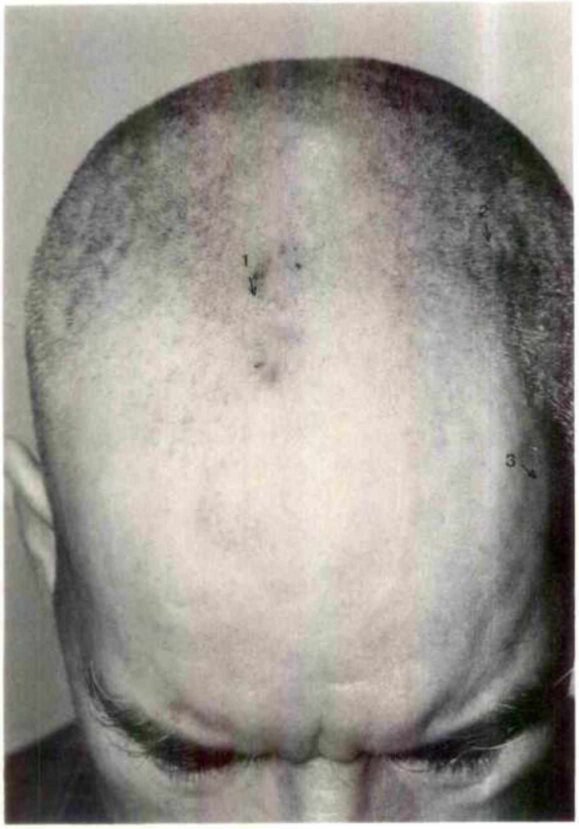

Figure 1. Angiosarcoma of the scalp presenting as three dusky, purple-red plaques on the scalp. Sites 1, 2 and 3 are described in the text.

100 cm, each directed through a common isocentre used as a reference point. The treatment volume extended from the tragus of the left ear over the left temporoparietal scalp to 10 cm beyond the midline at the vertex to include much of the right temporoparietal scalp. Anteriorly, the volume extended from the supraorbital ridges to the occipitoparietal junction posteriorly. The tumour margin was a minimum of 4 cm anteriorly, 9 cm posteriorly and 9 cm on the right side, but only 3 cm could be achieved inferior to the left temporal lesion because of the insertion of the pinna and proximity of the left eye. The target volume depth was assessed from skull radiographs and defined as the distance from the surface of the scalp to 5 mm below the surface of the calvarium, a total depth of 7.5 mm.

The scalp was shaved and the head positioned in the supine position. A 1 cm thick wax helmet was moulded over the patient's scalp to provide the necessary bolus, to position the patient and to enable set-up reference points to be marked. The margins of the volume were built up with thick wax to absorb the penumbra and scatter of the beams. The patients's shoulders and neck were supported by a custom cast of solidifying polyurethane foam (Voltafoam, Tiger Brand Products) and the wax helmet was slotted into the cast to provide rigid but comfortable immobilization (Fig. 2).

The aim of the isodose plan was to deliver the most homogeneous dose possible to the curved volume in the coronal plane with rapid fall-off in dose at depth to avoid radiation-induced meningitis and cerebral atrophy. The angle between adjacent beams was optimized using a Theraplan L electron dose distribution planning system to reduce dose inhomogeneity between abutted fields to a minimum (Fig. 3). The optimum plan consisted of six beams of dimensions 8 cm × 19 cm set up sequentially at 30° intervals. A 25 cm × 25 cm cone with a 1 cm thick cerrobend cut-out insert was used to produce a field size of 8 cm × 19 cm at the surface of the wax helmet. The SSD was kept constant at 100 cm to the surface of the wax and stand-off was 5 cm. Sequential beam entrance points 30° apart were marked on the wax mould. The position of the

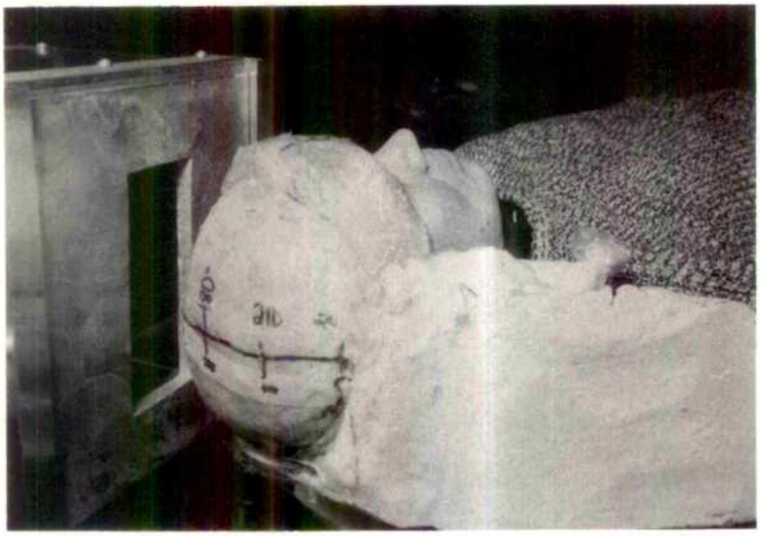

Figure 2. The patient set up in the wax helmet inserted into a polyurethane foam cast on the couch top. The gantry is at 90° to the couch and the electron cone with collimator is attached. The collimator stands off 5 cm from the surface of the wax and the SSD is constant at 100 cm. Adjustment of the couch position is used to direct each sequential beam and points of incidence are marked on the wax shell.

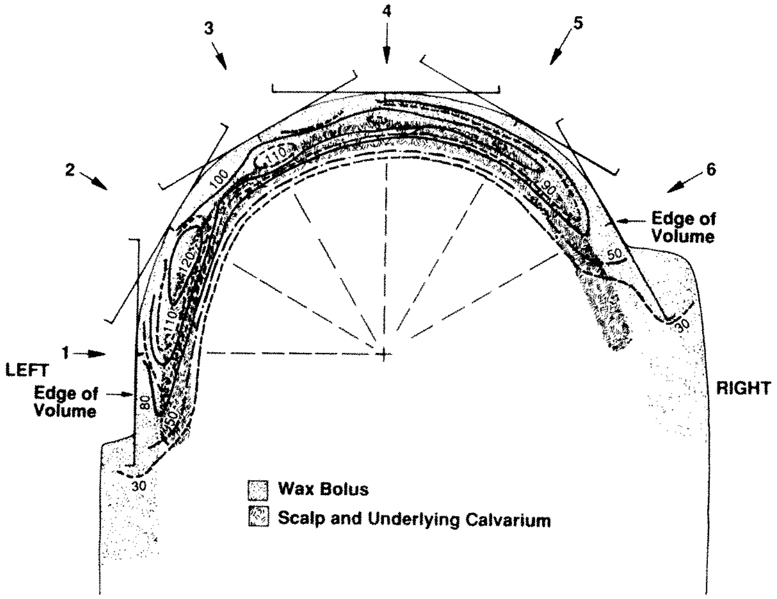

Figure 3. Isodose distribution for a six-field 6 MeV fixed electron beam technique. Thickness of the wax bolus is 1 cm except at the margin of the target volume, where it is 3 cm. Each beam is directed through a common reference point. The SSD is 100 cm; field size at the wax surface is 8 cm × 19 cm; and the angle between each beam is 30°. The weighting of each beam is 100% except beam number 1, which is 150%.

gantry was set horizontal at an angle of either 90° to treat one side of the scalp or 270° to treat the contralateral side. The treatment table was rotated between each field by 30° and the SSD maintained constant by subsequent longitudinal and lateral adjustment of the treatment table.

An additional matched anterior field was necessary to treat the forehead and to enable a minimum anterior margin of 4 cm.

The isodose distribution in the target volume was encompassed between 90% and 110% of the prescribed dose. A single hot spot of 120% lay within the involved skin at site 3. The dose at the surface of the brain was a maximum of 30% of the prescribed dose.

The dose administered to the 100% isodose curve was 50 Gy in 25 fractions over 5 weeks. Areas involved with angiosarcoma received a boost dose using a custom cut-out of cerrobend to encompass tumour with a 1 cm margin. The boost dose was administered with 6 MeV electrons set up to the wax helmet and 10 Gy in 5 fractions over 1 week was applied.

Results

Although the set-up procedure was practical and reproducible, it was time-consuming, taking at least 45 min. The patient developed erythema and dry desquamation of the scalp after 40 Gy but did not develop moist desquamation even in the boosted regions. Assessment at 2 months following completion of radiotherapy revealed complete resolution of disease apart from a persistent patch of purple discolouration in the left temporal region. This was biopsied and histologically demonstrated a chronic inflammatory infiltrate but no evidence of angiosarcoma. After 10 months of follow-up, there was scanty regrowth of hair but no clinical or histopathological evidence of local recurrence of disease and no evidence radiologically of lung metastases.

Discussion

Angiosarcoma of the scalp is a multifocal malignant neoplasm requiring generous treatment margins to reduce the risk of local recurrence. Surgical excision requires major reconstruction followed by adjuvant radiotherapy and the cosmetic result may not be satisfactory. The role of radiotherapy as a primary radical treatment of this rare tumour is poorly documented and the optimal dose is unknown. The therapeutic gain of radiotherapy may be aided by the excellent vascular supply to the scalp. Furthermore, a good vascular supply allows reconstructive surgery to be reserved for a salvage procedure. The therapeutic dilemma of initial management has been addressed by Morrison et al (1990). Their patients received either surgery and adjuvant radiotherapy or radiotherapy alone. A six-to-eight field technique that applied 6–9 MeV electrons was used. The whole scalp dose was 50 Gy at 2 Gy per fraction and involved regions were boosted to a median dose of 60 Gy. Despite most cases receiving radiotherapy with curative intent, the median freedom from relapse was only 7 months and survival 23 months.

The major limitation in the treatment of a large area of scalp has been the physical problem of treating homogeneously a superficial volume over a curved surface without a high exit dose through the cerebral cortex and without excess absorption into bone. Irradiation with high-energy electrons allows the treatment of a superficial volume with a rapid fall-off in exit dose and avoids the relatively high bone absorption displayed by orthovoltage photons. Multiple abutted electron beams may result in dose inhomogeneities at the field junctures. The achievement of a homogeneous dose over a curved surface may be facilitated by the technique of arcing electrons, in which the electron collimator stands off the treatment surface and the gantry rotates continuously through a defined angle and uses a computer-controlled dose delivery system (Leavitt et al, 1985). Not all linear accelerators have the capability of administering dynamic arcing electrons. An alternative pseudoarc technique uses multiple fixed fields and discards the electron collimator, resulting in increased scatter and blending of adjacent fields (Boyer et al, 1982). However, the resultant dosimetry to refine this techique is relatively complex. A further technique to reduce inhomogeneity at junctions of stationary fields uses a shift of the point of abutment after 50% of the prescribed dose has been delivered (Able et al, 1991).

The technique that we have described allows good immobilization, ease of patient set-up and may be carried out on most linear accelerators with electron capabilities. The "scalloped" dose distribution resulting from the junctions of multiple abutted electron cones is reduced by using the minimum number of beams (in this case, six fields) and optimizing the angle between the beams (in this case, 30°). The wax scalp shell inserted into the polyurethane mould on the couch top immobilizes the patient, provides a surface to mark the successive entry points of the electron cone, acts as bolus to treat to the appropriate depth and absorbs the superficial dose inhomogeneities produced at the site of abutment of adjacent beams. Collimation of the electron beam by the cone at the entry point of the beam along with thickening of the wax shell at the margins of the treatment area results in a well defined target volume.

The optimum treatment of angiosarcoma of the scalp remains a dilemma. There is no good evidence that surgical resection preceding radiotherapy increases the local control or survival. It would be reasonable to reserve surgery for a salvage procedure. Having established a reproducible technique for the administration of electron beam therapy to the scalp, which was well tolerated by the patient, escalation of the applied dose may be investigated to determine improvement in local control.

Acknowledgments

We wish to thank the therapy technologists for their expert facilitation of treatment, Dr David Jewer, specialist in reconstructive surgery, for joint management of this patient and the Department of Medical Illustration and Photography for the figures.

References

Able, C. M., Mills, M. D., McNeese, M. D. & Hogstrom, K. R., 1991. Evaluation of a total scalp electron irradiation technique. *International Journal of Radiation Oncology, Biology, Physics, 21*, 1063–1072.

Barttelbort, S. W., Stahl, R. & Ariyan, S., 1989. Cutaneous angiosarcoma of the face and scalp. *Plastic and Reconstructive Surgery, 84*, 55–59.

Boyer, A. L., Fullerton, G. D. & Mira, J. G., 1982. An electron beam pseudoarc technique for irradiation of large areas of chest wall and other curved surfaces. *International Journal of Radiation Oncology, Biology, Physics, 8*, 1969–1974.

Hodgkinson, D. J., Soule, E. H. & Woods, J. E., 1979. Cutaneous angiosarcoma of the head and neck. *Cancer, 44*, 1106–1113.

Holden, C. A., Spittle, M. F. & Wilson Jones, E., 1987. Angiosarcoma of the face and scalp, prognosis and treatment. *Cancer, 59*, 1046–1057.

Knight, T. E., Robinson, H. M. & Sina, B., 1980. Angiosarcoma (angioendothelioma) of the scalp. *Archives of Dermatology, 116*, 683–686.

Leavitt, D. D., Peacock, L. M., Gibbs, F. A. & Stewart, J. R., 1985. Electron arc therapy: physical measurement and treatment planning techniques. *International Journal of Radiation Oncology, Biology, Physics, 11*, 987–999.

Liu, A. C., Kapp, D. S., Egbert, B., Waters, L. & Rosen, J. M., 1990. Angiosarcoma of the face and scalp. *Annals of Plastic Surgery, 24*, 68–74.

Morales, P. H., Lindberg, R. D. & Barkley, H. T., 1981. Soft tissue angiosarcomas. *International Journal of Radiation Oncology, Biology, Physics, 7*, 1655–1659.

Morrison, W. H., Peters, L. J., Evans, H. L. & Byers, R. M., 1990. Angiosarcoma of the scalp and face: a therapeutic dilemma (abstract). In *Proceedings of the Seventy-Second Annual American Radium Society Meeting*, Scottsdale (The American Radium Society, Philadelphia), p. 3.

Wilson Jones, E., 1976. Malignant vascular tumours. *Clinical and Experimental Dermatology, 1*, 287–312.

1992, *The British Journal of Radiology*, *65*, 425–430

Quantitative analysis of CT brain images: a statistical model incorporating partial volume and beam hardening effects

By Raymond F. McLoughlin, MB, FRCSI, M. Veronica Ryan, DCR(R), DMU, Paula M. Heuston, DCR(R), Catherine T. McCoy, DCR(R) and James B. Masterson, FRCR

Department of Diagnostic Imaging, St Vincent's Hospital, Elm Park, Dublin 4, Ireland

(*Received 8 July 1991 and in revised form 2 October 1991, accepted 6 December 1991*)

Keywords: Brain, Atrophy, Head CT, Images, Processing

Abstract. The purpose of this study was to construct and evaluate a statistical model for the quantitative analysis of computed tomographic brain images. Data were derived from standard sections in 34 normal studies. A model representing the intracranial pure tissue and partial volume areas, with allowance for beam hardening, was developed. The average percentage error in estimation of areas, derived from phantom tests using the model, was 28.47%. We conclude that our model is not sufficiently accurate to be of clinical use, even though allowance was made for partial volume and beam hardening effects.

Computed tomography (CT) demonstrates the gross anatomy of the living brain. Quantification of cerebrospinal fluid (CSF), white matter, grey matter and dura mater areas on CT images would establish reference values for healthy subjects, and allow comparison between normal cases and those with neurological disorders, such as dementia.

Such quantitative analysis is difficult for two reasons. Firstly, some voxels include two tissues. The resultant pixel has an intermediate attenuation value, blurring the border between different tissues (partial volume effect). Secondly, the attenuation values for similar tissues may vary from case to case owing to beam hardening.

The purpose of this study is to construct and evaluate a statistical model for quantitative analysis of CT brain images that allows for the partial volume and beam hardening effects.

Materials and methods

The statistical model

In our model the statistics of the total population of pixels in a CT image are treated as the sum of those of the component regions into which the image is to be separated. The statistics of intracranial pixels are represented by a plot of area versus Hounsfield number (HN) for a region of interest (ROI) set on the cranium (Figs 1, 2). For the range of HN from -5 to 60, the area under this "area/HN" curve represents the total intracranial area. The component regions consist of pure tissue and partial volume pixel groups. We consider four intracranial pure tissues: CSF, white matter, grey matter and dura mater. By noting which pure tissues abut each other on Fig. 1, we expect partial volume pixels at the junction of CSF and white matter (C/W), CSF and grey matter (C/G), white matter and grey matter (W/G), grey matter and dura mater (G/D) and where CSF abuts a white/grey matter junction (C/CW/CG). Statistically, pure tissue and partial volume pixel populations are represented by a range of HN distributed about a mean value.

Our thesis is that the area/HN curve can be analysed into its pure and partial volume components (Fig. 3), allowing the areas of these components to be estimated.

CT scanner

Brain CT examinations were performed with the Somatom DR3 CT scanner (Siemens AG, Erlangen, Germany). Data were derived from a standard image through the basal ganglia in a plane parallel to the supraorbitomeatal line, just cephalad to the foramina of Monro (Fig. 1). Intravenous contrast medium was not used; 4 mm slice thickness, 125 kV and 1050 mAs were selected.

Statistical methods

Correlation between two variables was tested using simple linear regression analysis with the following models:

No constant in the model	$Y = X$
Constant in the model	$Y = \text{Constant} + X$

The coefficient of correlation (r) and statistical significance (p) were determined in each instance.

Subjects

The indication for a CT scan in 34 patients (21 women, 13 men, age range 20–91 years) was headache, facial pain or tic. All CT examinations were normal.

Area distribution curves

The average shape of each pure tissue area distribution curve was determined by summation of the distributions in appropriate ROI samples from each case. A

Address correspondence to R. F. McLoughlin, MB, FRCSI, Department of Diagnostic Imaging, St Vincent's Hospital, Elm Park, Dublin 4, Ireland.

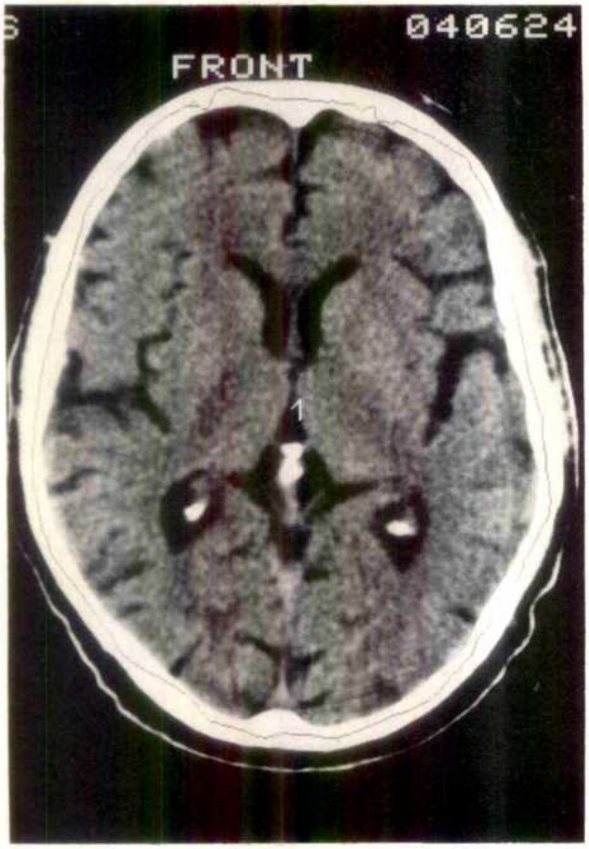

Figure 1. The "standard" CT brain section. The ROI set on the cranium and used to generate the area/HN curve (Fig. 2) is shown.

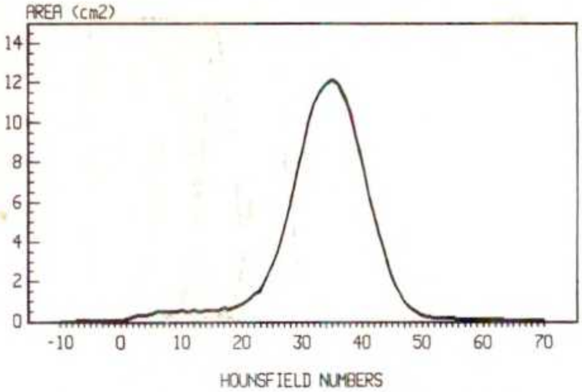

Figure 2. "Area/Hounsfield number" plot for an ROI set on the cranium of the standard CT brain section.

correction was made for differences in mean HN values between samples. In setting the ROI, tissue margins were avoided so as not to "contaminate" the samples with partial volume pixels. The CSF area distribution curve was derived from 32 samples; the white from 30; the grey from 32; and the dura mater from 20.

Partial volume area distribution curves were derived by combining the area distribution curves of the pure tissues involved. We have assumed that, on average, a partial volume pixel reflects a 50/50 contribution from adjoining pure tissues.

Allowance for beam hardening effect

Mean tissue HN values vary from case to case owing to beam hardening. We refer to the HN representing the greatest number of intracranial pixels on a CT brain image (*i.e.* the maximum point on the area/HN curve) as the "peak value". For images produced by the same CT scanner using a constant kV, beam hardening is the only mechanism that significantly changes HN of the area/HN curve as a whole or of its constituent parts. Therefore, we expect a correlation between peak and mean tissue HN values. This correlation will be used to derive the mean tissue HN values from the peak value for individual cases. Because the peak value reflects the amount of beam hardening, this derivation makes allowance for the beam hardening effect.

Pure tissue HN values were taken as the mean of 10 appropriate ROI samples in each subject. A mean HN value for CSF was determined in 32 subjects; for white matter in 30; for grey matter in 32; and for dura mater in 25. The peak value was determined from the area/HN curve in each case. Correlation between mean pure tissue HN values and peak values was tested using simple linear regression analysis.

Analysis of a CT image using the model

A CT image is analysed as follows.

An ROI set on the cranium allows construction of the area/HN curve, from which the peak value is derived. The average shapes of the pure tissue and partial volume area distribution curves have been determined and are assumed not to change from case to case. Mean HN values of the pure tissue area distribution curves are derived from the peak value. The mean HN values of partial volume area distribution curves lie halfway between the HN of the adjoining pure tissues (cf.

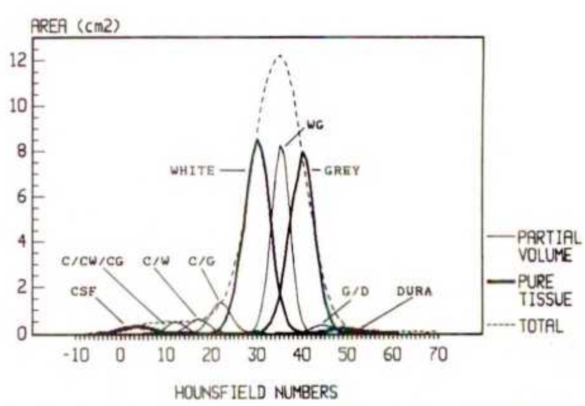

Figure 3. The pure tissue and partial volume area distribution curves, representing the area under the area/HN curve.

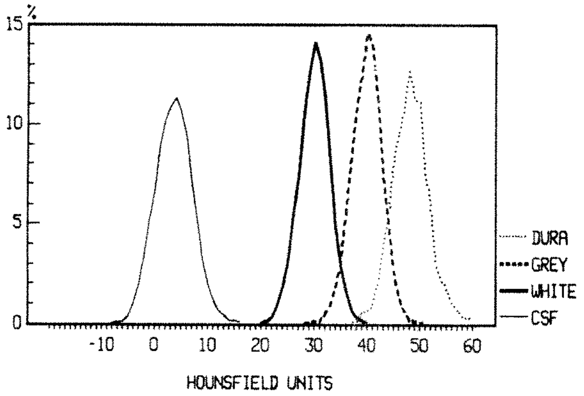

Figure 4. The pure tissue area distribution curves.

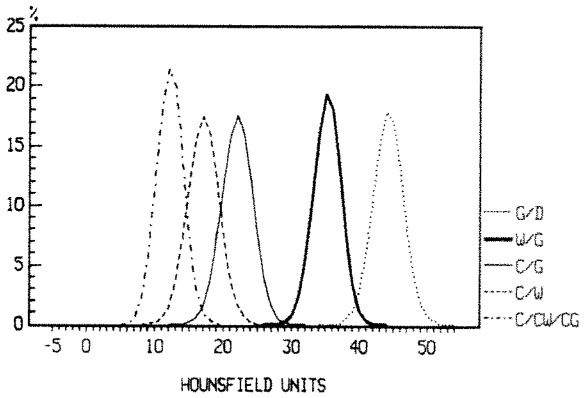

Figure 5. The partial volume area distribution curves (see text for abbreviations).

previous assumption that a partial volume pixel reflects, on average, a 50/50 contribution from these tissues).

Knowing the mean HN and shape of the various area distribution curves allows their areas to be calculated from the area/HN curve. This is achieved by solving simultaneous equations derived from data at the mean HN of the area distribution curve concerned. Where other distribution curves make a significant contribution to the total area at that point, data from those curves are included. Thus, equations with one, two or three variables are generated.

For example, consider a case where the mean HN of the CSF area distribution curve is at HN = 4. From the area distribution curve for CSF it is known that Y% of pixels have this Hounsfield value. No other distribution curves make a significant contribution to the total area at this point. Thus, Y% of the CSF area equals the area on the area/HN curve at HN = 4; *i.e.* $(Y/100)\times \mathrm{CSF} = \mathrm{H4}$. Then, CSF area $= (\mathrm{H4}\times 100)/Y$.

Finally, the true area of each tissue is calculated as the sum of the pure tissue area plus half the value of each partial volume area the tissue adjoined. Thus:

$$\begin{aligned}
\text{TRUE CSF} &= \mathrm{C}+0.5\mathrm{C/CW/CG} + 0.5\mathrm{C/W}+0.5\mathrm{C/G}\\
\text{TRUE WHITE} &= \mathrm{W}+0.25\mathrm{C/CW/CG} + 0.5\mathrm{C/W}+0.5\mathrm{W/G}\\
\text{TRUE GREY} &= \mathrm{G}+0.25\mathrm{C/CW/CG} + 0.5\mathrm{C/G}+0.5\mathrm{W/G}\\
\text{TRUE DURA} &= \mathrm{D}+0.5\mathrm{G/D}
\end{aligned}$$

To allow for difference in head sizes among individuals, results are expressed as a percentage of intracranial area.

Validation studies

Validation studies were performed using a phantom, consisting of four thin-walled plastic cubes, placed side by side, containing aqueous povidone iodine solutions with average HN values of 2, 27, 36 and 43. The cubes, with cross-sectional areas ranging from 9 to 19.26 cm^2, were altered from test to test. A model similar to that described above was constructed to analyse CT images of the phantom.

Reliability (the degree of agreement reached when a measurement was repeated under closely similar conditions) was assessed by comparing the areas calculated from 10 images of an identical section of one phantom, and expressed as a coefficient of variation (CV), such that:

$$\mathrm{CV} = \frac{\text{Standard deviation of measured areas}\times 100}{\text{Mean measured area}}\ \%$$

Accuracy (the extent to which a measurement agrees with the true value) was assessed by comparing the actual areas with those estimated from images of 10 different phantoms, with an average percentage error expressed as:

$$\frac{\text{Root mean square error}\times 100}{\text{Average actual area}}\ \%$$

where

"Root mean square error"

$$= \sqrt{\frac{\Sigma\,(\text{measured area}-\text{actual area})^2}{\text{number of areas sampled}}}$$

Results

Area distribution curves

The pure tissue and partial volume area distribution curves are shown in Figs 4 and 5.

Relationship between mean pure tissue HN and peak values

There was a strong correlation between mean pure tissue HN and the peak values (Fig. 6), because both are influenced by beam hardening, expressed as follows:

CSF = 0.116 Peak; $r = 0.954$; $p < 0.001$
WHITE = 0.851 Peak; $r = 0.999$; $p < 0.001$
GREY = 1.148 Peak; $r = 0.999$; $p < 0.001$
DURA = 1.376 Peak; $r = 0.999$; $p < 0.001$

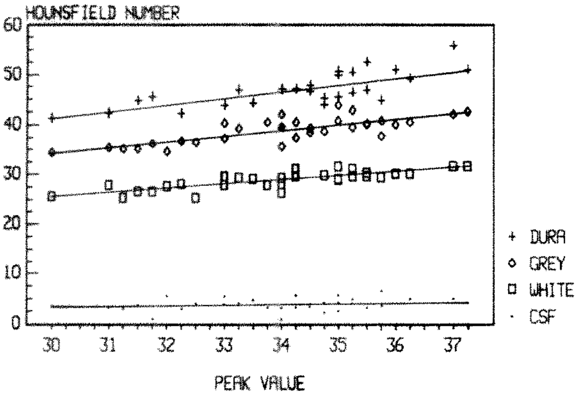

Figure 6. Correlation between the mean pure tissue HNs and the peak values.

Using these equations, mean pure tissue HN values can be calculated in each case from the peak value (see Methods).

Area equations

The equations derived from the area distribution curves for a case with a peak value of 35 HU are:

(a) CSF (C): $0.1131 \times C = H4$

(b) CSF/WHITE (C/W): $0.17448 \times C/W = H17$

(c) CSF/CSFWHITE/CSFGREY (C/CW/CG): $0.2145 \times C/CW/CG = H12$

(d) CSF/GREY (C/G): $0.17613 \times C/G = H22$

(e) WHITE (W): $0.14125 \times W = H30$

(f) WHITE/GREY (W/G):
$0.16104 \times W/G + 0.04960 \times W + 0.01684 \times G = H34$
$0.19392 \times W/G + 0.02900 \times W + 0.02861 \times G = H35$
$0.18162 \times W/G + 0.01698 \times W + 0.05438 \times G = H36$

(g) GREY (G):
$0.12439 \times G + 0.03465 \times W/G + 0.01067 \times G/D = H39$
$0.14570 \times G + 0.01219 \times W/G + 0.02724 \times G/D = H40$
$0.13738 \times G + 0.00340 \times W/G + 0.05838 \times G/D = H41$

(h) GREY/DURA (G/D):
$0.17923 \times G/D + 0.05114 \times G + 0.05338 \times D = H44$
$0.16938 \times G/D + 0.02618 \times G + 0.08116 \times D = H45$
$0.13202 \times G/D + 0.01339 \times G + 0.09477 \times D = H46$

(i) DURA (D):
$0.10730 \times D + 0.08217 \times G/D = H47$
$0.12800 \times D + 0.04300 \times G/D = H48$

where "HX" refers to the area in square centimetres at Hounsfield number "X" on the area/HN plot. Similar equations are generated for cases with different peak values. The solutions to these equations give the pure tissue and partial volume areas.

Analysis of 23 cases

The model was used to analyse the standard slice in 23 of our cases (15 females, 8 males, age range 22–91 years). The quantity of intracranial CSF increased with age; there was a complementary decrease in the amounts of white and grey matter, and little change in the dura mater (Fig. 7).

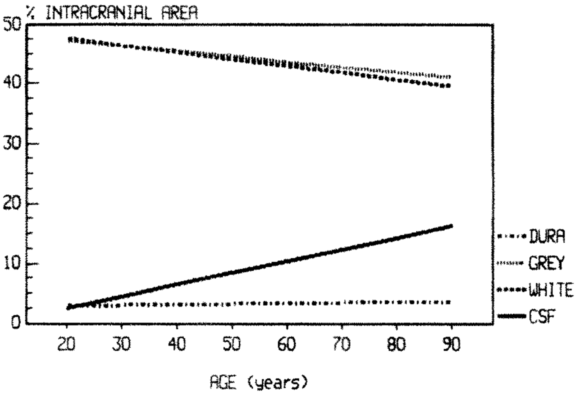

Figure 7. Plot of intracranial areas versus age, representing the following equations:

$\text{CSF} = -1.44 + 0.196 \times \text{age};\ r = 0.78;\ p < 0.001$
$\text{WHITE} = 49.74 - 0.114 \times \text{age};\ r = 0.55;\ p = 0.006$
$\text{GREY} = 48.98 - 0.090 \times \text{age};\ r = 0.53;\ p = 0.009$
$\text{DURA} = 2.70 + 0.009 \times \text{age};\ r = 0.10;\ p = 0.644$

Validation studies

The coefficient of variation ranged from 2.9 to 4.1%. Estimated areas tended to be less than the actual areas, with an average percentage error of 28.47% (Fig. 8).

Discussion

Since the development of cranial CT, researchers have attempted to devise methods of quantitating the information obtained. Initial efforts to estimate area involved planimetry (Barron et al, 1976; Johnstone et al, 1976). A difficulty with this method is that the CT representation of tissue interfaces is not a sharp line, but rather a "grey" zone representing partial volume averaging.

Other workers (Ito et al, 1981; Gado et al, 1982;

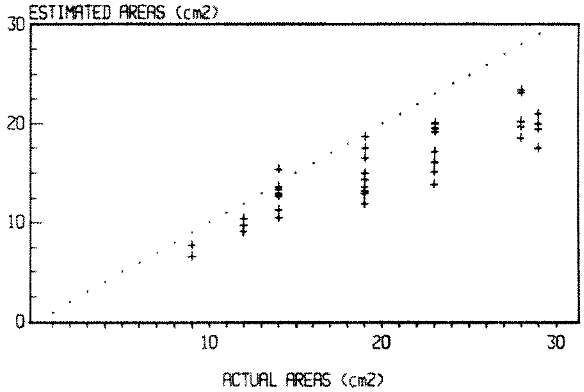

Figure 8. Estimated versus actual areas. The data represent estimations of seven different cross-sectional areas (9.0, 11.56, 14.44, 19.36, 22.56, 28.62 and 29.16 cm^2) from phantoms containing four of the areas at any one time. Estimated areas concurring with actual areas would lie close to the dotted line.

George et al, 1983) have characterized different tissues by arbitrary ranges of HN values. Tissue areas are then quantified by estimating the number of pixels within these ranges. However, no allowance is made for the variation in HN that may occur from case to case owing to beam hardening. For example, in our study the area distribution curve for white matter ranges from 16 to 36 HU in a case with a peak value of 31, but from 21 to 41 HU in a case with a peak value of 37. Secondly, the HN ranges representing certain tissues overlap. For example, in a case with a peak value of 35, a 35 HU pixel may represent white matter, grey matter or partial volume averaging at the junction of white and grey matter. Consequently, separation of brain into white and grey matter using such methods has not been possible.

There have been attempts to improve on the above methods by allowing for partial volume and beam hardening effects. Wasler and Ackerman (1979) addressed the problem of partial volume averaging, using an algorithm that estimated the proportional contribution of ventricle and brain to an ROI on the basis of the resultant CT number. This method required the designation of specific CT numbers characteristic of CSF and brain. The results obtained are therefore highly dependent on the user designation of CT numbers and only accurate for the volume measurement of homogeneous structures. Thaler et al (1978) describe a sophisticated statistical method for determining the proportions of grey matter, white matter and CSF on a CT section based on the assumption that the HN of pure tissue and partial volume voxels have Gaussian distributions. While this method is not dissimilar in principle from the one we describe, the problem of beam hardening is not considered, and the validity of the method was not assessed.

Jernigan et al (1979) followed Wasler and Ackerman, calculating the volume of CSF in a sample by using estimates of the characteristic HN of brain and CSF. Allowance from beam hardening was based on the assumption that attenuation values for brain tissue and CSF would be equally affected, and there would be a constant difference between the two. This allowed derivation of the CSF value from the brain tissue value, which was determined in each case. However, our results indicate that the attenuation values of different tissues are not equally affected by beam hardening. For example, at a peak value of 31, the mean CSF HN value is 3.6, that of grey matter is 31.98, and the difference is 28.38. At a peak value of 37, the corresponding figures are 4.3, 42.48 and 38.18 (Fig. 6).

In our method we have allowed for partial volume averaging by treating partial volume pixels as a distinct group. Derivation of tissue mean HN from the peak value in each case reflects the effect of beam hardening. It was hoped that these modifications over previous methods would give a model of sufficient accuracy to demonstrate subtle differences in tissue areas between normal and pathological brains. The average percentage error of 28.47% associated with our method indicates that this is not the case, and our model is not likely to be of clinical use.

There are two possible sources of inaccuracy in our method. First, we treat partial volume averaging as a 50/50 contribution from two tissues, whereas it may result from any combination of contributions from a number of tissues. The model becomes more complicated and does not work when a more comprehensive representation is introduced. Secondly, having generated area distribution curves that described the distribution of tissue areas over a range of HN, only part of these data was used to calculate the tissue areas. Perhaps use of the variances and means associated with the distribution curves to calculate the tissue areas, as outlined by Thaler et al (1978), would have made fuller use of the available data and given more accurate results.

The results of the analysis of 23 cases are of interest, but obviously must be viewed with caution. The similar rates of decrease in the white and grey matter areas as that of CSF increases, with no significant change in the amount of dura mater, are findings we would intuitively expect. While other workers (Barron et al, 1976; Ito et al, 1981) have documented similar changes in CSF volumes, we are not aware of any report documenting the changes in white and grey matter areas in the aging brain.

The most recent work on the analysis of brain and CSF volumes has been performed using magnetic resonance imaging (MRI). MRI eliminates the beam hardening effect and the partial volume effect has been minimized by the use of edge-detection algorithms (Ashtari et al, 1990), or of a quantitative analysis of two inversion–recovery sequences (Rusinek et al, 1991). Early reports indicate that intracranial tissue volume measurements using these methods are reliable and accurate (Ashtari et al, 1990; Kohn et al, 1991).

In conclusion, the method we describe is not accurate enough to be of likely clinical use, even though allowance was made for partial volume and beam hardening effects. Recent promising results indicate that the future of such quantitative analysis may lie in MRI studies.

Acknowledgment

We wish to thank Dr Adrian Dunne, Department of Statistics, University College, Dublin, for advice on the analysis of the validation study results.

References

Ashtari, M., Zito, J. L., Gold, B. I., Liberman, J. A., Borenstein, M. T. & Herman, P. G. 1990. Computerized volume measurement of brain structure. *Investigative Radiology*, *25*, 798–805.

Barron, S. A., Jacobs, L. & Kinkel, W. R., 1976. Changes in size of normal lateral ventricles during aging determined by computed tomography. *Neurology*, *26*, 1011–1013.

Gado, M., Hughes, C. P., Danziger, W., Chi, D., Jost, G. & Berg, L., 1982. Volumetric measurements of the cerebrospinal fluid spaces in demented subjects and controls. *Radiology*, *144*, 535–538.

George, A. E., de Leon, M. J., Rosenbloom, S., Ferris, S. H., GENTES, C., EMMERICH, M. & KRICHEFF, I. I., 1983. Ventricular volume and cognitive deficit: a computed tomographic study. *Radiology*, *149*, 493–498.

ITO, M., HATAZAWA, J., YAMAURA, H. & MATAUZAWA, T., 1981. Age-related brain atrophy and mental deterioration—a study with computed tomography. *British Journal of Radiology*, *54*, 384–390.

JERNIGAN, T. L., ZATZ, L. M. & NAESER, M. A., 1979. Semiautomated methods for quantitating CSF volume on cranial computed tomography. *Radiology*, *132*, 462–466.

JOHNSTONE, E. C., CROW, T. J., FIRTH, C. D., HUSBAND, J. & KREEL, L., 1976. Cerebral ventricular size and cognitive impairment in chronic schizophrenia. *Lancet*, *ii*, 924–926.

KOHN, M. I., TANNA, N. K., HERMAN, G. T., RESNICK, S. M., MOZLEY, P. D., GUR, R. E., ALAVI, A., ZIMMERMAN, R. A. & GUR, R. C., 1991. Analysis of brain and cerebrospinal fluid volumes with MR imaging. *Radiology*, *178*, 115–122.

RUSINEK, H., DE LEON, M. J., GEORGE, A. E., STYLOPOULOS, L. A., CHANDRA, R., SMITH, G., RAND, T., MOURINO, M. & KOWALSKI, H., 1991. Alzheimer disease: measuring loss of cerebral gray matter with MR imaging. *Radiology*, *178*, 109–114.

THALER, H. T., FERBER, P. W. & ROTTENBERG, D. A., 1978. A statistical method for determining the proportions of gray matter, white matter, and CSF using computed tomography. *Neuroradiology*, *16*, 133–135.

WASLER, R. L. & ACKERMAN, L. V., 1979. Determination of volume from computerized tomograms: finding the volume of fluid filled brain cavities. *Journal of Computer Assisted Tomography*, *1*, 117–130.

1992, *The British Journal of Radiology*, *65*, 431–437

The Reference Man in diagnostic radiology dosimetry

By Bengt A. Lindskoug, PhD

Regional Department of Radiation and Hospital Physics, S-301 85 Halmstad, Sweden

(*Received 14 June 1991 and in revised form 23 September 1991, accepted 25 November 1991*)

Keywords: Diagnostic radiology, Dosimetry, Reference Man, Detrimental effects

Abstract. Following the legislation for radiation protection in Europe, increasing interest has been given to patient dosimetry in diagnostic radiology. Dose comparisons between groups of patients have demonstrated considerable discrepancies. The equipment, as well as the procedures used, have been scrutinized in order to find the reasons for the variation and to reduce it. In this work, patient size and shape are considered in patient dose evaluations in diagnostic radiology. The size, shape and constitution of the patients are shown to relate exponentially to the energy imparted during examination of the trunk. The equivalent cylindrical diameter of the patient body is used as the independent variable. Exponential functions are created by linear regression. The ICRP Reference Man with an equivalent diameter of 22.9 cm is used as a body-size standard. A method is suggested by which coordinate transformations reduce data to a base line defined by the Reference Man. It is shown that the method reduces the range of energy imparted by between 30% and 60% for six common X-ray examinations of the trunk. Resulting data constitute a finer instrument for intercomparisons between hospitals for the same examination. Further, it is suggested that adipose tissues should not be included when detrimental effects of radiologic exposure are determined. The Reference Man, stripped of 10 kg subcutaneous adipose tissue, is used as the non-fat standard dimension corresponding to the equivalent cylindrical diameter 21.2 cm. The suggested method is used to estimate the fraction of energy imparted to vital organs only. The results show that the energy imparted is reduced by between 30% and 60% according to this model. Consequently, predicted deaths are reduced by the same amount.

For two decades, the overwhelming variability of absorbed dose given to patients in diagnostic radiology has worried the radiation protection authorities. Patients at different hospitals, having the same examination, receive very different doses. In the 1980s, considerable effort was expended all over Europe in checking equipment and training staff, in the belief that this would improve the situation. However, it became obvious that, whereas variation in output from an X-ray tube and generator as well as the overall uncertainty due to technique factors could be limited to less than 35% (Moores, 1989), the greatest sources of variation, the size and shape of the body, contribute more than two orders of magnitude to the range of absorbed dose. They probably also contribute considerably to the range of the image quality.

Materials

Five hospitals were visited and 17 laboratories were included in these measurements. 1020 patient examinations were registered (Table I). Special efforts were made to collect data concerning the shape and size of the patients. The weight (W) and the height (H) were measured for each individual. Parts of the sample (400 urography and colon patients also shown in Table I) were completely registered with film exposure, number of films, fluoroscopy exposure and fluoroscopy times separately. Table II shows the average, maximum and minimum values of films and fluoroscopy times used for all examinations.

Diamentor (PTW Freiburg) transmission ionization chambers were used during a time span of 3 years. The chambers were moved between laboratories at about 2 month intervals. They were calibrated on site at each X-ray tube in terms of area-air-kerma (Gy m^2) using a standard ionization chamber (30 cm^3) and applying air-kerma factors from the national dosimetry laboratory in Stockholm. The secondary standard ionization chamber was placed 10 cm above the table, *i.e.* close to the position of the target volume in the patient's body. In this positon three different, square field sizes were exposed; approximately 100 cm^2, 400 cm^2 and 900 cm^2. The actual field sizes were measured on X-ray films exposed at the calibration point with unchanged beam

Table I. Normal population energy imparted

Type of examination		Mean energy imparted	Number of patients
Heart & lung	mJ/film	3.8	112
Lung	mJ/film	4.5	204
Urography	mJ total	191	289
Lumbar spine	mJ/film	31	72
Colon	mJ total	423	316
Thorax spine	mJ/film	73	27
		Sum:	1020
Normalized			
Colon film	mJ/film	19	137
Colon fluoroscopy	mJ/min	53	138
Urography film	mJ/film	19	96
Urography fluoroscopy	mJ/min	32	29
		Sum:	400

Table II. Number of films and fluoroscopy time

Type of examination	Number of films			Fluoroscopy time (min)		
	max	average	min	max	average	min
Heart & lung	5	3	2	—	—	—
Lung	2	2	2	—	—	—
Urography	20	14	8	3.5	1.2	0.3
Lumbar spine	10	5	2	1.3	0.5	0.0
Colon	24	15	3	9.7	3.8	0.7
Thorax spine	6	4	2	6.0	3.3	0.8

parameters. The area-kerma product was computed from the average of the three measured values. The half-value layer (HVL) was measured in good geometry, free in-air, for the most commonly used kVp values using a small 1 cm^3 ionization chamber. The voltage (kVp) and the filtration were checked on all equipment using dedicated, commercial, computerized equipment (Digi-X, ORTIGO).

Method

The energy imparted was derived from the measured area-exposure using the Monte Carlo tables created by Alm Carlsson et al (1984). These tables contain the ratio between the total energy absorption and the free in-air area-exposure product *vs.* phantom thickness and HVL. The tabulated data were interpolated to the nearest centimetre and HVL 0.1 mm Al, which is acceptable since this ratio is a rather slow function of these parameters. In principle, the energy imparted (E_i, mJ) was computed from the formula

$$E_i = \text{factor}\ (D,\ \text{HVL},\ \text{kVp})\cdot X$$

where "factor()" is the tabulated factor as a function of the thickness D, HVL, and kVp. X is the measured area-exposure (Gy m^2) corrected for backscatter and body size.

The outer dimension of the trunk, measured skin-to-skin, is not particularly well correlated with the energy imparted to the body, as it does not include any information about the constitution of the body, such as the density. The body weight will take the average density into consideration but does not include the shape. The equivalent cylindrical diameter (D_e) includes both weight and height, thus takes the average density into consideration. Consequently, it carries some information about the trunk shape.

The concept of the equivalent cylinder is described mathematically by the following formula

$$D_e = 2\cdot\sqrt{[W/(H\cdot\pi\cdot 1000)]}$$

where W = weight (kg) and H = height (m).

The patient is approximated by a cylinder having the same height and weight as the body. Thus, the weight and the height of the patients were used to compute the equivalent cylindrical diameter and this parameter was used when computing the energy imparted according to

$$E_i = \text{factor}(D_e,\ \text{HVL},\ \text{kVp})\cdot X$$

Results

Figure 1 depicts the total energy imparted for complete urography examinations, film exposure and fluoroscopy combined. The vertical scale is natural logarithmic. Six different laboratories in four hospitals were involved in these urography examinations. On average, 14 films were used per examination, with a maximum of 20 films and a minimum of eight. The heavier and the shorter the patient, the larger the equivalent diameter and the larger the energy imparted. The

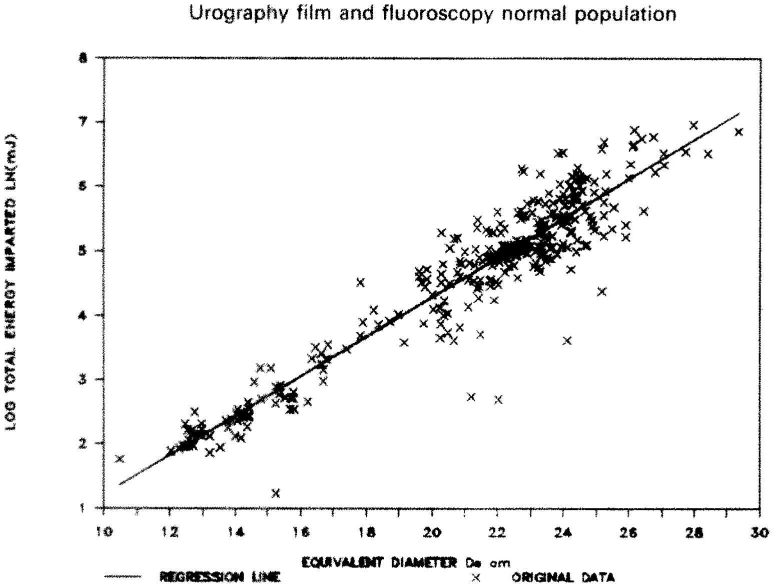

Figure 1. Total energy imparted for complete urography examinations, film exposure and fluoroscopy together, as a function of the equivalent cylindrical diameter of the patients. Regression line (RL) = 0.31 · D_e − 1.86. Regression coefficient (RC) = 0.94. SD of the RL, SD = 0.45. Number of patients (N) = 289.

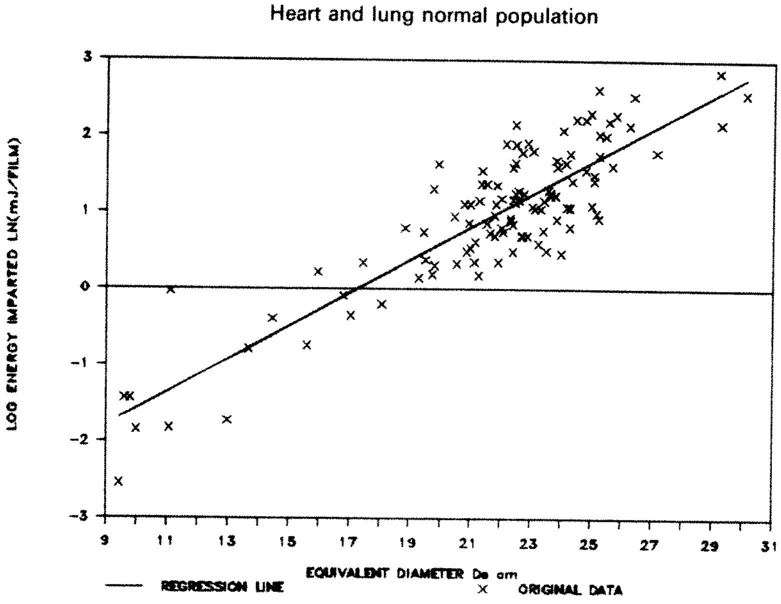

Figure 2. Logarithm of energy imparted to heart and lung patients, divided by the number of films used. Regression line (RL) = $0.216 \cdot D_e - 3.73$. Regression coefficient (RC) = 0.87. SD of the RL, SD = 0.47. Number of patients (N) = 112.

total energy imparted to the largest and to the smallest dimensions (D_e) differ by two orders of magnitude. Considering that all projections are included in the measurements, *i.e.* all films that have been taken, and the total fluoroscopy time used, the fit looks surprisingly close. One would expect that the differences in the number of films and the sensitivity of the imaging system, etc. would give a rather chaotic distribution. This is not the case. The influence of patient size and constitution are strong enough to dominate other sources of variability. Although the standard deviation (SD) of the mean is 100%, the SD of the regression line is only 50%.

To see the effect in the thorax region where few films (2–5) are being used, the energy imparted must be divided by the number of films. Then, dependency on the equivalent diameter is quite obvious (Fig. 2). The SD of the mean is 81%, whereas the SD of the regression line is only 47%.

The range of all patient examinations registered is presented in Table III. The table shows the SD of the mean energy imparted, the SD of the regression line, the maximum, the mininum and the ratio of maximum to minimum.

Analysis

Judging from the diagrams in Figs 1 and 2, it is obvious that it would not be adequate just to compute the average value and the SD and use these data for intercomparisons. The body size, shape and constitution, defined by D_e, play such a great part in the energy absorption that they must be taken into consideration. For instance, it should be possible to chose a level along the regression line as the standard of reference, perhaps using the ICRP Reference Man. The Reference Man concept was given by the ICRP (1975) as a "well defined reference individual for estimation of radiation dose in health physics". The expectation was that this individual "should be used by health physicists in comparing and checking their results without tedious enumeration of assumptions obscuring the basic agreement or disagreement of their results", which is precisely in accordance with the present purpose. Although the ICRP does not claim the Reference Man "to be predictive for any individual or randomly chosen population on this planet", they admit that the typical values selected often were average or median values of existing populations.

The equivalent cylindrical diameter of the Reference Man is 22.9 cm (70 kg, 170 cm), which is used here to establish a point of reference in the diagrams. The

Table III. Normal population various ranges

Type of examination	Standard deviation		Max	Min	Ratio max/min
	Mean	Regression line			
Heart & lung	3.1	1.8	17	0.1	220
Lung	3.1	2.2	19	0.4	42
Urography total	192	86	1061	3.4	310
Lumbar spine	16	10	75	4.3	17
Colon total	238	169	1906	72	27
Thorax spine	51	46	254	1.7	149
Normalized					
Colon film	11	7.7	97	3.9	25
Colon fluoroscopy	45	43	322	6.6	49
Urography film	14	6.4	81	1.0	80
Urography fluoroscopy	24	13	104	1.4	73

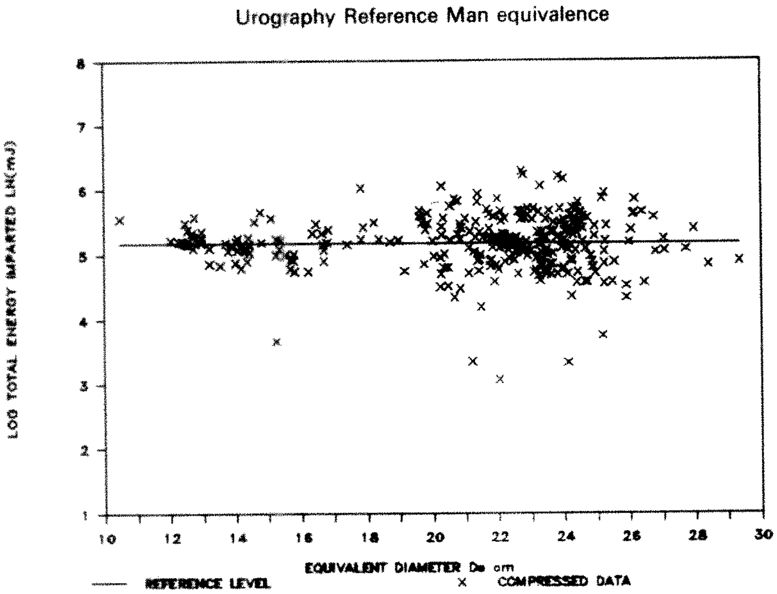
Urography Reference Man equivalence

Figure 3. Logarithm of total energy imparted from Fig. 1, compressed according to the Reference Man size ($D_e = 22.9$ cm). Reference level = 176 mJ.

corresponding values on the y axis are called the reference levels of energy imparted.

By rotating the regression lines in Figs 1 and 2 clockwise around the point of reference, until parallel with the abscissa, the data are brought to a "Reference Man level". In practice this is simply made by a coordinate transform using the following algorithm

$$x = x_m - x_r$$
$$y = y_m - y_r$$
$$x' = x\cos(\theta) + y\sin(\theta) + x_r$$
$$y' = -x\sin(\theta) + y\cos(\theta) + y_r$$

where (x_r, y_r) are the reference point coordinates, (x_m, y_m) are the coordinates for the measured data, θ is the angle of rotation and (x', y') are the new coordinates.

Figure 3 shows the data of Figure 1 compressed to the Reference Man size. The diagram could be interpreted as showing the energy imparted that the bodies should receive had they all been of the Reference Man size. The energy imparted to small bodies increases and the energy imparted to large bodies decreases. The range is substantially decreased in accordance with the logarithmic scale, which is also in accordance with the typically exponential attenuation of X-rays in tissue.

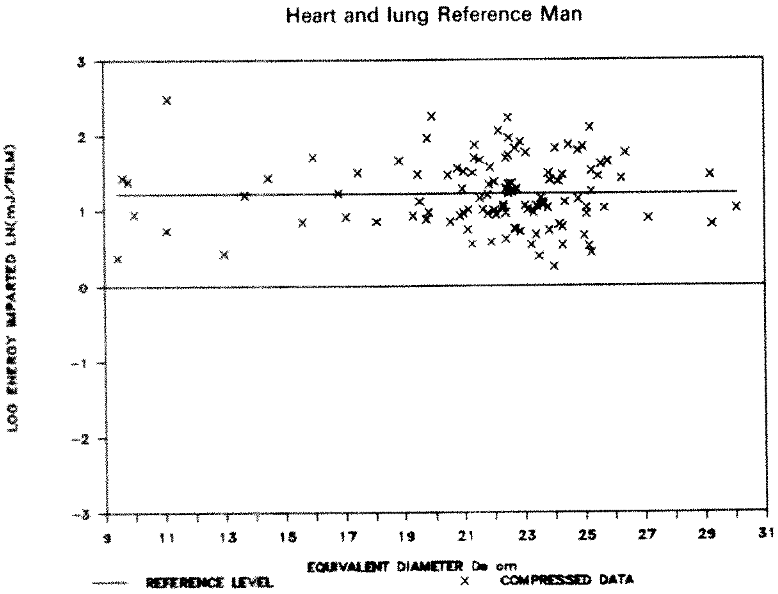
Heart and lung Reference Man

Figure 4. Logarithm of energy imparted per film from Fig. 2, compressed according to the Reference Man dimension. Reference level = 3.4 mJ/film.

The ratio between the highest and the lowest energy imparted is reduced by 92%, the SD is reduced by 59% and the reference level is 7% lower than the former average energy imparted.

Figure 4 shows the corresponding conversion to Reference Man size for the heart and lung examinations of Fig. 2. The ratio between the highest and the lowest energy imparted is reduced by 96%, the SD is reduced by 39% and finally, the reference level is 11% lower than the former average energy imparted. The result of the data compression applied to all patient examinations registered is shown in Table IV. The upper parts of the table show six typical examinations, mean energy imparted (mJ) and various ranges.

Table V summarizes the relative reduction of the various parameters. The remaining range may be due to circumstances other than the body size, shape and constitution. It is obvious that after this reduction, the data constitute a finer instrument for intercomparisons between hospitals for the same examinations.

How to correct for adipose tissue influence

ICRP[1] suggests that the body content of fat typically increases linearly with the total body weight. Different age groups have slightly different levels. The weight of fat, as a function of body weight, can be drawn in parallel lines for various ages, higher age at the top line. Thus, the body-fat mass constitutes a constant fraction of the total body weight. Further, ICRP claims that the non-essential adipose tissue covers the whole body, specifically in a subcutaneous layer and in between the abdominal organs. The Reference Man is defined to have 17 kg of adipose tissues of which 10.3 kg is subcutaneous. Consequently, when exposing the trunk, whatever projections used, one is bound to penetrate adipose tissue and, knowing the exponential characteristic of X-ray attenuation, it is obvious that much energy will be imparted to fatty tissue. A thin patient may have a diameter of 15 cm or less, whereas a thick patient may have a diameter of 30 cm or more. Estimates in a cylindrical model show that the subcutaneous adipose layer could reach an average thickness of 5 cm around a body with $D_e = 30$ cm. According to a typical depth dose curve for diagnostic radiology (60–80 kVp), the beam will lose between 40% and 50% of its energy after penetrating 5 cm of a fat tissue layer. The signal reaching the feed-back detector differs by one order of magnitude for thin and thick patients. Less than 1% of the intensity will reach the detector in the latter case. This should explain a considerable part of the variation of absorbed dose given to patients in diagnostic radiology.

Clearly, an essential fraction of the absorbed energy in bodies having D_e larger than 22.9 cm will be imparted to adipose tissue, which has very little bearing on the detriment of radiation and is not included among the organs suggested by ICRP in the calculation of the effective dose. The energy imparted to fat should therefore be excluded. Usually it is not, because whatever measured dose data is being used for the calculations, the fat attenuation will always be included. Whether one measures the skin entrance dose by thermoluminescent dosemeter (TLD), theoretically computes the average dose from known technique factors, or uses transmission or any other ionization chamber, the result will be similarly dependent on the body size, shape and constitution, *i.e.* in a first approximation dependent on the equivalent cylindrical diameter with subcutaneous fat included.

For instance, in the NRPB Monte Carlo calculated tables (NRPB, 1985), which are computed for the Reference Man size, the factors are normalized to unit entrance skin dose, which must be measured at the centre of the X-ray beam on the top of the body. Fat is not included in the tables, but it is included in the skin dose measurements because of the inherent feed-back mechanisms of the radiology procedures. Firstly, the automatic exposure control guides the exposure until the density of the target pattern on the film is sufficient. Secondly, the examination continues until the operators and the doctors are satisfied. The more adipose tissue the beam has to go through, the more energy is needed.

Table IV. Reference Man. Energy imparted

Type of examination		Reference energy	SD	Max	Min	Ratio max/min
Heart & lung	mJ/film	3.4	1.9	12	1.3	9
Lung	mJ/film	4.0	2.2	13	1.2	11
Urography	mJ/total	176	78	536	21	25
Lumbar spine	mJ/film	29	9.0	54	13	4.2
Colon	mJ/total	379	175	1257	108	12
Thorax spine	mJ/film	66	50	213	23	9
Normalized						
Colon film	mJ/film	17	6.6	40	5.5	7
Colon fluoroscopy	mJ/min	40	43	288	11	25
Urography film	mJ/film	15	5.3	37	7.2	5
Urography fluoroscopy	mJ/min	22	9.2	51	10	5

Table V. Reference Man. Relative reduction in

Type of examination	Energy imparted (%)	SD (%)	Max (%)	Ratio max/min (%)
Heart & lung	11	39	30	96
Lung	10	28	28	73
Urography	7.4	59	50	92
Lumbar spine	8.8	42	28	76
Colon	10	27	34	56
Thorax spine	9.2	1.1	16	96
Normalized				
Colon film exposure	6.6	32	59	71
Colon fluoroscopy	24	4.5	11	48
Urography film exposure	22	62	54	94
Urography fluoroscopy	33	62	51	93

Table VI. No adipose tissue. Energy imparted

Type of examination		Reference energy	SD	Max	Min	Ratio max/min
Heart/lung	mJ/film	2.4	1.3	8.3	0.89	9
Lung	mJ/film	2.7	1.5	9.0	0.80	11
Urography	mJ total	105	47	318	13	25
Lumbar spine	mJ/film	20	6.4	39	9.1	4
Colon	mJ total	272	125	902	78	12
Thorax spine	mJ/film	40	30	129	14	9
Normalized						
Colon film exposure	mJ/film	13	5.4	29	4.0	7
Colon fluoroscopy	mJ/min	33	34	232	9.2	25
Urography film exposure	mJ/film	9.1	3.2	23	4.3	5
Urography fluoroscopy	mJ/min	13	5.6	31	6.3	5

A method to correct for adiposity should be very useful. To a certain extent, the equivalent cylindrical diameter could be used in medicine as a measure of the total body fat mass. Thus, the parameter D_e could be accepted as the independent variable of choice in standardizing the dose data for the purpose of adipose tissue correction according to the method described above.

It can be argued that within every patient there is a Reference Man and that the reason why some bodies are heavier than the Reference Man is that they contain more adipose tissue. Individual deviations from these assumptions are of minor importance in the present discussion. 10 kg may be subtracted from the Reference Man weight in order to reduce the subcutaneous adipose tissue influence on the equivalent cylindrical diameter. This will move the reference points slightly to the left in the diagrams. What remain of the Reference Man are a mass of 60 kg and a diameter of 21.2 cm. Finally, the data reduction suggested above can be performed.

Table VII. No adipose tissue, relative reduction in

Type of examination	Energy imparted (%)	SD (%)	Max (%)	Ratio max/min (%)
Heart & lung	38	58	52	96
Lung	39	51	51	73
Urography	45	76	70	92
Lumbar spine	35	59	48	76
Colon	36	47	53	56
Thorax spine	45	40	49	94
Normalized				
Colon film	33	51	70	71
Colon fluoroscopy	39	23	28	48
Urography film	53	77	72	94
Urography fluorography	60	77	70	93

Table VI shows the energy imparted to the apparent Reference Man patients, almost totally stripped of the subcutaneous adipose tissues. The reference dose level is now between 30% and 60% less than the former average dose and the range is reduced by between 40% and 80% for the various types of examinations. Table VII summarizes the relative reduction of the various parameters.

The cylindrical diameter may be a gross simplification but it is quite useful in practice because anyone can handle it. You only need to register the patient weight and height at the time of examination. The alternative is to measure the absorbed dose directly in vital organs, which is considerably more intricate. However crude this measure may seem, it probably renders a more adequate anatomical realism in patient dose studies than just presenting the average dose, not reduced.

Reduction of detriment

Data reduction, however, is not the same as reduction of dose in real terms, therefore the question arises whether this transform has any realistic interpretation of any value. Obviously, statistical calculations based on the resulting reference energy level (Table VI) will render at least 30% less detrimental effects, *i.e.* in computing hypothetical cancer or genetic detrimental effects of diagnostic radiology, the outcome will be reduced by 30% to 60% compared with calculations based on the average energy imparted (Table I) not reduced accordingly. We are only dealing with hypothetical effects and real lives are not saved, but the number of predicted deaths are reduced.

According to an estimate by Bengtsson et al (1978), diagnostic X-rays induce about 110 malignant cancers or genetic injuries annually in Sweden. Using a risk factor of 1/100 per Sv, 2000 cancers/year have been estimated in the European Community (Moores, 1987). These estimates were based on average values of dose measurements not reduced to the Reference Man. If the same estimates were made after reducing the measured dose data to the non-adipose level, the results will be between 30% and 60% fewer. At the same time, the SD and the high/low ratio will be reduced by 40–80% and 50–96%, respectively, which serve to relieve the fear of diagnostic radiation.

Conclusions

By standardizing data in accordance with exponential functions using the equivalent diameter as the independent variable, provided that the height and the weight of the patients are measured at the time of examination, the estimated energy imparted to vital organs is reduced by between 30% and 60% and the range is reduced by between 40% and 80%.

Standardizing according to body shape and weight may be useful in the following circumstances.

1. When considering the causes of variations in patient dose between hospitals, or between different rooms in a single hospital. This is because variability of patient

size and constitution may be the greatest single contribution. Only when this variability has been removed along the lines suggested in this paper can we proceed to examine the technical factors which may account for the remaining variability in patient dose.

2. In setting limits for the purpose of dose reduction in radiology, which indeed is the task of workshops in Europe today (CEC, 1989 & 1991). It will either be necessary to separate the patients into weight classes or to state the dose limits in reference to a standard body. Guideline values of entrance surface dose for some common X-ray projections have already been suggested for the UK and Europe, relating to a standard 70 kg patient (Shrimpton et al, 1989; NRPB, 1990).
3. In the estimation of organ dose based on the Monte Carlo calculated tables valid for a standard body shape or a standard phantom. The patient data may be reduced to the same size as the tabulated body shape.
4. In the estimation of collective detrimental effects after diagnostic radiology.

Acknowledgments

The author is grateful to all radiographers, technicians, nurses and medical technologists in Halland, who contributed by participating in this work. This work was supported by the Swedish Institute of Radiation Protection.

References

Alm Carlsson, G., Carlsson, C. A. & Persliden, J., 1984. Energy imparted to the patient in diagnostic radiology: calculation of conversion factors for determining the energy imparted from measurements of the air collision kerma integrated over beam area. *Physics in Medicine and Biology, 29,* 1329–1341.

Bengtsson, G., Blomgren, P.-G., Bergman, K. & Åberg, L., 1978. Patient exposures and radiation risks in Swedish diagnostic radiology. *Acta Radiologica, Oncology, Radiation Physics, Biology, 17,* 81–105.

CEC, 1989. *Optimization of Image Quality and Patient Exposure in Diagnostic Radiology.* BIR Report 20. Ed. by B. M. Moores, B. F. Wall, H. Eriskat and H. Schibilla (British Institute of Radiology, London).

—— 1991. *Seminar on Dosimetry in Diagnostic Radiology,* Luxembourg. To be published.

ICRP, 1975. *Report of the Task Group on Reference Man.* Publication 23. (Pergamon Press, Oxford).

Moores, B. M., 1987. *Diagnostic Radiology Dosimetry—Physicists' Point of View.* Advanced Seminar on Diagnostic Radiology Dosimetry. (Commission of the European Communities, Joint Research Centre, Ispra, Italy).

—— 1989. Physical aspects of establishing tolerances and limiting values in diagnostic radiology. In: *Technical and Physical Parameters for Quality Assurance in Medical Diagnostic Radiology. Tolerances, Limiting Values and Appropriate Measuring Methods.* BIR Report 18. Ed. by B. M. Moores, F. E. Stieve, H. Eriskat and H. Schibilla (British Institute of Radiology, London), 81–84.

NRPB, 1985. *Organ Doses from Medical X-ray Examinations Calculated Using Monte Carlo Techniques. Report 186.* Ed. by D. G. Jones and B. F. Wall (NRPB Chilton, Didcot).

NRPB, 1990. CEC Study Group. *Patient Dose Reduction in Diagnostic Radiology.* Documents of the NRPB, Vol. 1, No. 3. (Appendix to BIR Report 20. Optimization of Image Quality and Patient Exposure in Diagnostic Radiology (British Institute of Radiology, London).

Shrimpton, P. C., Wall, B. F. & Hillier, M. C., 1989. *Proceedings 4th International Symposium of SRP, Malvern.* Ed. by E. P. Goldfinch (Bristol, IOPP).

1992, *The British Journal of Radiology*, *65*, 438–442

Technical notes

Calibration of a 0.08 Tesla magnetic resonance imager for *in vivo* T_1 and T_2 measurement

By S. F. Keevil, MA, MSc, MIPSM, G. Dolke, DCR(R), P. Armstrong, MB, BS, FRCR and *M. A. Smith, MSc, PhD, FIPSM

Academic Department of Radiology, St Bartholomew's Hospital, West Smithfield, London EC1A 7BE and *Department of Medical Physics, University of Leeds, Leeds General Infirmary, Great George Street, Leeds LS1 3EX, UK

(Received 28 November 1990 and in revised form 23 April 1991, accepted 6 August 1991)

Keywords: Magnetic resonance imaging, Relaxation times, Calibration

The magnetic resonance unit at St Bartholomew's Hospital is equipped with an upgraded MD800 resistive magnetic resonance imager (Imatec International Limited) operating at a field strength of 0.08 Tesla. *In vivo* spin-lattice relaxation times (T_1) can be measured using a saturation recovery/inversion recovery sequence (SRIR, $T_R = 1000$ ms, $T_I = 200$ ms) and spin–spin relaxation times (T_2) using a four echo Carr-Purcell-Meiboom-Gill sequence (CPMG, $T_R = 1000$ ms, $T_E = 32, 64, 96, 128$ ms). The SRIR sequence consists of selective 90° pulses every 1000 ms, alternate 90° pulses being preceded by 200 ms adiabatic fast passage (AFP) inversion pulses. It can be considered to be an interleaved saturation recovery and inversion recovery sequence with gradient echoes. In each case a relaxation time map is produced on a pixel-by-pixel basis without the need for elaborate off-line image processing.

The aim of the work described was to investigate the accuracy and reproducibility of T_1 and T_2 values measured using the imager, and to determine suitable calibration factors before commencing a programme of clinical research.

Methods and materials

The calibration was carried out using a relaxation time test object developed by the EEC Concerted Research Project *Identification and Characterisation of Biological Tissues by NMR* (EEC Concerted Research Project, 1988; Podo et al, 1988). This object consists of a Perspex disc with a series of holes into which glass tubes are inserted. Each tube contains a quantity of agarose gel doped with gadolinium (III) chloride to produce predictable relaxation properties (Walker et al, 1988, 1989). Calibration data and temperature correction factors for 0.08 T were available for the gels in the test object.

Our T_1 and T_2 measurements were investigated over a period of 3 months, but the accuracy of T_1 measurements can only be assessed over a shorter period following correction of an error in the commercial T_1 calculation software. T_1 measurements showed good reproducibility but poorer accuracy before this correction, as has been demonstrated by Richards et al (1987).

In the standard imaging protocol, the test object, together with a thermometer, was placed transversely in a head coil inside the bore of the magnet. After an interval of approximately 30 min to allow the temperature of the gels to stabilize, a single axial slice through the test object was imaged using the SRIR and CPMG sequences. A field of view of 256 mm was used, together with a slice thickness of 12 mm and a resolution of 128 × 128 pixels; two signal averages were collected in each case in order to improve signal to noise. These parameters are typical of those used for clinical imaging at our institution. The temperature in the magnet bore was checked before and after each sequence. Typical T_1 and T_2 maps of the test object are shown in Figs 1 and 2, respectively. The relaxation times of the gels were measured by positioning circular regions of interest as shown and were corrected to 20°C.

In addition, the standard protocol was modified in order to investigate the effects of imaging in the sagittal and coronal planes, varying the slice thickness, varying the number of signal averages, using a different imaging coil and varying the field of view. Up to four slices were imaged to guard against possible variation between slices in multislice imaging.

Results

Temperature corrected T_1 and T_2 measurements (mean ±1 standard deviation (SD)) made during the period of this study are plotted against the true relaxation times of the gels in Figs 3 and 4, respectively. In the case of T_1, only data obtained following the software correction have been included. Linear regression was used to produce the following fits and correlation coefficients.

Correspondence should be addressed to Stephen Keevil, Magnetic Resonance Unit, Academic Department of Radiology, St Bartholomew's Hospital, West Smithfield, London EC1A 7BE.

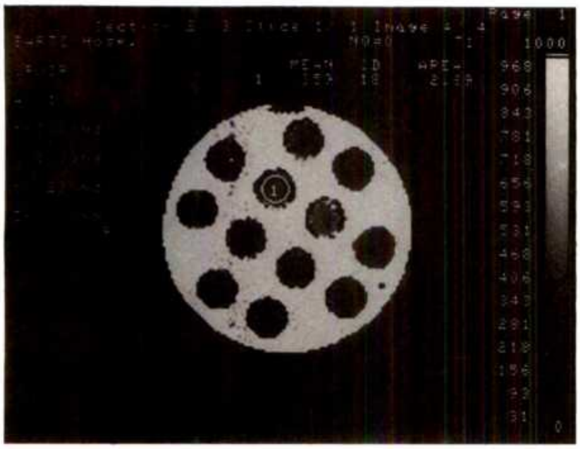

Figure 1. T_1 map of the EEC relaxation time test object showing region of interest.

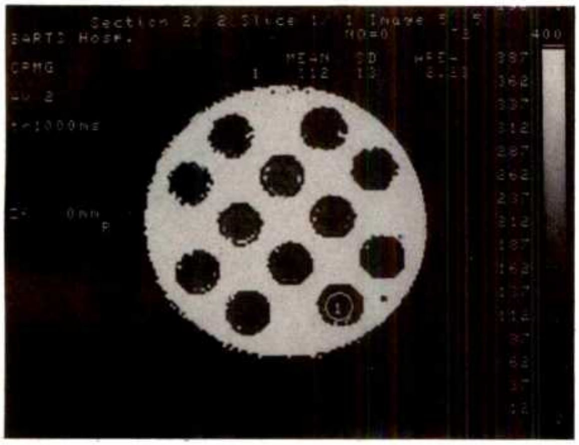

Figure 2. T_2 map of the EEC relaxation time test object showing region of interest.

$$T_1 = 9.17 + 1.03\ T_{1\text{meas}}\ (r = 0.997) \qquad (1)$$

$$T_2 = -3.04 + 1.08\ T_{2\text{meas}}\ (r = 0.996) \qquad (2)$$

where T_1 and T_2 are the true relaxation times of the gels and $T_{1\text{meas}}$ and $T_{2\text{meas}}$ the measured values. All relaxation times are in milliseconds.

The variation in the measured relaxation times of each of the gels over the course of the study is shown in Figs 5 and 6. Fig. 5 includes T_1 measurements obtained before the software correction referred to above, and discontinuities can be seen at the point in time at which this correction was introduced (Day 78). The discontinuity is worst in the case of gels with relatively long T_1 since one of the consequences of the error was to underestimate long T_1 significantly. The earlier results are valid as an indicator of reproducibility, but were neither taken into account when calculating accuracy nor when performing linear regression.

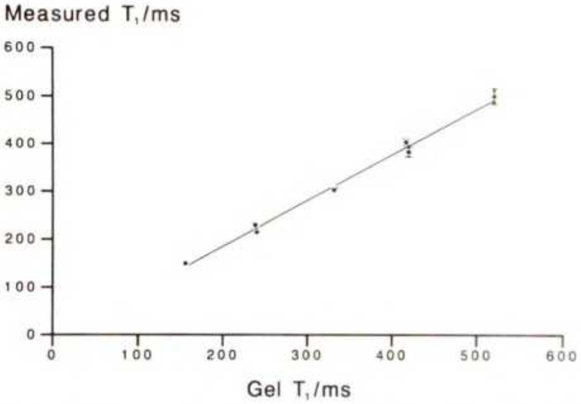

Figure 3. Measured T_1 values (mean ± 1 SD) plotted against the true T_1 of the EEC gels.

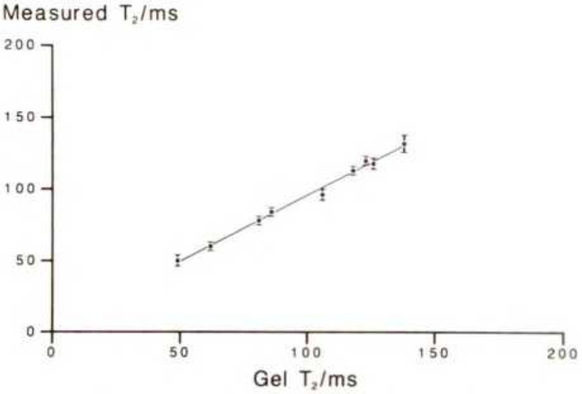

Figure 4. Measured T_2 values (mean ± 1 SD) plotted against the true T_2 of the EEC gels.

The accuracy of our measurements is indicated by the differences between the true and measured relaxation times of the gels. For T_1, the mean difference across the range of gel relaxation times following the software correction was -6.1% (range -10.4 to -2.9%), and for T_2 the mean difference was -3.8% (range -9.4 to 2.0%). The coefficient of variation of measurements made over the period of the study gives a measure of reproducibility. The mean coefficient of variation was 1.9% (range 1.1 to 3.2%) for T_1 and 4.2% (range 3.1 to 8.0%) for T_2. There were no trends in accuracy or reproducibility across the range of relaxation times covered by the gels. It is clear from Fig. 4 that the accuracy of the measured T_2 of one gel appears to be significantly worse than all the others. This is more likely to be caused by an error in the stated "true" T_2 than to a real discontinuity in the behaviour of the imaging system.

No variation was noted in the measurement of either relaxation time when the imaging protocol was modified in the ways described above. There was no variation

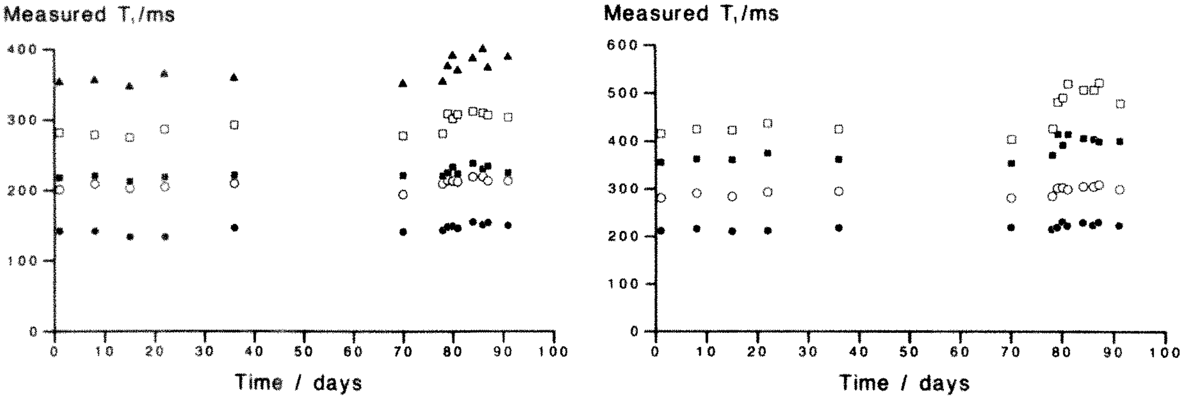

(a) (b)

Figure 5. Temporal variation in the measured T_1 of each of the EEC gels over the course of the study. The discontinuities mark the point at which the calculation software was corrected. The true relaxation times of the gels were as follows: (a) closed circles 156 ms, open circles 240 ms, closed squares 238 ms, open squares 333 ms, closed triangles 419 ms. (b) Closed circles 239 ms, open circles 331 ms, closed squares 416 ms, open squares 519 ms.

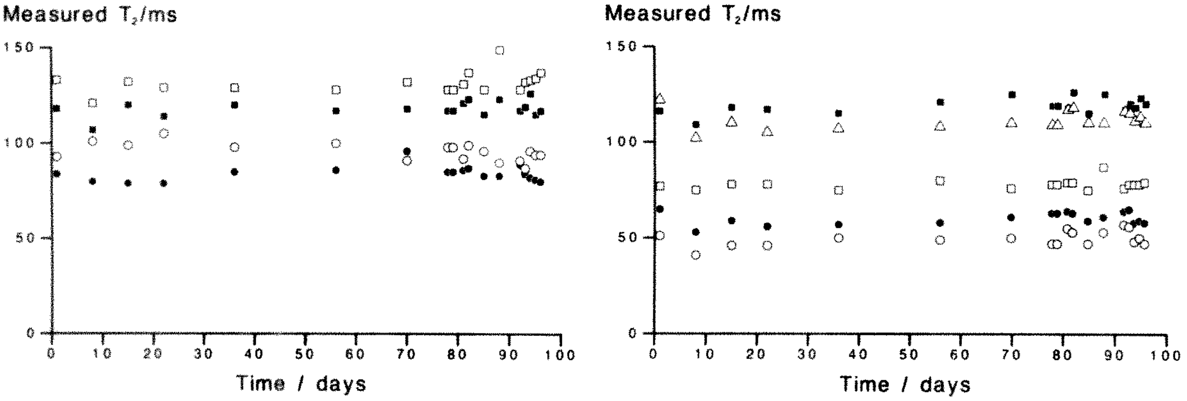

(a) (b)

Figure 6. Temporal variation in the measured T_2 of each of the EEC gels over the course of the study. The true relaxation times of the gels were as follows: (a) closed circles 86 ms, open circles 106 ms, closed squares 126 ms, open squares 138 ms. (b) Open circles 49 ms, closed circles 62 ms, open squares 81 ms, open triangles 118 ms, closed squares 123 ms.

between the relaxation times measured from different slices when multislice imaging was used. This is perhaps largely because the order in which slices are imaged by our system is such that contiguous slices are never excited consecutively.

Discussion

The widespread rejection of relaxometry as a clinical technique results from the belief that the wide range of *in vivo* T_1 and T_2 values to be found in the literature for a given tissue or pathology (Bottomley et al, 1984; 1987) reflects true biological variation. The alternative view (Smith & Taylor, 1986) is that these variations may be largely the result of inaccurate and imprecise measurement. Some of the factors which may give rise to measurement errors, such as physiological motion, cannot be overcome by calibration, but it is clearly important that as many sources of error as possible are eliminated in this way. Unfortunately, calibration and quality assurance have not been addressed in most published work on relaxometry, including the extensive reviews by Bottomley et al (1984, 1987).

The work of Richards et al (1987) demonstrated excellent reproducibility of T_1 measurements made with our imager using the SRIR sequence. There was slightly greater variability for T_1 values above about 490 ms, and this was ascribed to the use of a simplified algorithm for calculation of T_1, which assumes that T_1 is small compared with the repetition time (Redpath, 1982). An upgrade in 1988 introduced a more accurate algorithm which allows for partial saturation. The CPMG sequence for measurement of T_2 was implemented at the same time.

The work reported in this note demonstrates the improvement in T_1 reproducibility due to the new algorithm and also the reproducibility of T_2 measurements. Furthermore, the use of the European Community test object has enabled us to demonstrate the accuracy of our techniques relative to an internationally recognized standard. Our discovery and correction of an error in the T_1 calculation software demonstrates the importance of calibration and quality assurance of this kind to ensure accurate measurement of T_1 and T_2 using commercial imagers.

Since there is an approximately linear relationship between the measured and true T_1 and T_2 of the gels, simple calibration factors (eqns 1 & 2) can be used to bring *in vivo* measurement into agreement with the test object calibration. These calibration factors have been shown to remain valid when the standard imaging protocol is varied in the ways described above.

The accuracy of T_1 and T_2 measurements made using our system is in marked contrast to the poor results obtained from some other systems using the test object (Lerski et al, 1988). Some of the possible sources of error in relaxation time evaluation have been discussed by Johnson et al (1987) and, for T_2, by Crawley and Henkelman (1987). The SRIR sequence, the original "Aberdeen" imaging technique (Edelstein et al, 1980), is thought to be a particularly accurate way of measuring T_1 because the majority of T_1 information is incorporated into the signal by means of non-selective adiabatic fast passage, providing efficient inversion throughout the sample despite inhomogeneities in the radiofrequency field (Abragam, 1961).

The improved algorithm used to calculate T_1 from SRIR data is shown in eqn (3), $S1$ and $S2$ being the signals obtained following the saturation recovery and inversion recovery portions of the sequence, respectively. This normalized signal difference is compared with a "look-up" table in order to evaluate T_1.

$$\frac{S1-S2}{S1}=\frac{2\{\exp(-T_1/T_1)-\exp(-T_R/T_1)\}}{1-\exp(-T_R/T_1)} \tag{3}$$

The expression takes account of partial saturation, but it is assumed that inversion is 100% efficient and that the slice selective excitation pulse nutate spins through precisely 90° throughout the slice of interest. Errors due to slice profile effects can arise unless $T_R \gg T_1$. In fact, the slice profile generated by our system is satisfactory, since the radiofrequency pulse used for selective excitation is a three-cycle sync pulse apodized by a Hanning window function. It is therefore likely that incomplete inversion by the adiabatic fast passage (AFP) pulse is the dominant source of errors. The performance of the SRIR sequence for T_1 measurement, particularly with regard to the behaviour of the AFP pulse in the presence of B_0 and B_1 inhomogeneities, has been simulated and investigated experimentally by Hardy et al (1985). These authors demonstrate the dependence of the inversion produced by a linearly swept AFP on the sweep duration and derive a non-linear sweep function with superior performance. Our AFP pulses consist of a linear frequency sweep from −4 kHz to +4 kHz through resonance with a duration of 10 ms.

In the case of T_2 measurement, it is likely that the systematic error is largely due to imperfections in the excitation and refocusing pulses and approximations in the calculation algorithm.

Acknowledgments

This work was carried out within the context of the European Community Concerted Research Project *Tissue Characterisation by MRS and MRI* (COMAC-BME II.1.3). We are grateful to the project leader, Dr Franca Podo, and our other colleagues in this multinational collaboration for their support and encouragement. Dr J. P. Ridgway, Dr R. A. Lerski and Dr A. Lunt gave valuable advice on the use of the European Community test object. S. F. Keevil is supported by the Bunzl Gift Fund.

References

ABRAGAM, A., 1961. *The Principles of Nuclear Magnetism* (Clarendon Press, Oxford).

BOTTOMLEY, P. A., FOSTER, T. H., ARGERSINGER, R. E. & PFEIFER, L. M., 1984. A review of normal hydrogen NMR relaxation times and relaxation mechanisms from 1–100 MHz: dependence on tissue type, NMR frequency, temperature, species, excision, and age. *Medical Physics, 11*, 425–448.

BOTTOMLEY, P. A., HARDY, C. J., ARGERSINGER, R. E. & ALLEN-MOORE, G., 1987. A review of ^{1}H nuclear magnetic resonance relaxation in pathology: are T_1 and T_2 diagnostic? *Medical Physics, 14*, 1–37.

CRAWLEY, A. P. & HENKELMAN, R. M., 1987. Errors in T_2 estimation using multislice, multiple echo imaging. *Magnetic Resonance in Medicine, 4*, 34–47.

EEC CONCERTED RESEARCH PROJECT, 1988. Identification and characterisation of biological tissues by NMR. Concerted research project of the European Economic Community. IV. Protocols and test objects for the assessment of MRI equipment. *Magnetic Resonance Imaging, 6*, 195–199.

EDELSTEIN, W. A., HUTCHISON, J. M. S., JOHNSON, G. & REDPATH, T. W., 1980. Spin warp NMR imaging and applications to human whole body imaging. *Physics in Medicine and Biology, 25*, 751–756.

HARDY, C. J., EDELSTEIN, W. A., VATIS, D., HARMS, R. & ADAMS, W. J., 1985. Calculated T_1 images derived from a partial saturation-inversion recovery pulse sequence with adiabatic fast passage. *Magnetic Resonance Imaging, 3*, 107–116.

JOHNSON, G., ORMEROD, I. E. C., BARNES, D., TOFTS, P. S. & MACMANUS, D., 1987. Accuracy and precision in the measurement of relaxation times from nuclear magnetic resonance images. *British Journal of Radiology, 60*, 143–153.

LERSKI, R. A., MCROBBIE, D. W., STRAUGHAN, K., WALKER, P. M., DE CERTAINES, J. D. & BERNARD, A. M., 1988. Identification and characterisation of biological tissues by NMR. Concerted research project of the European Economic Community. V. Multi-centre trial with protocols and prototype test objects for the assessment of MRI equipment. *Magnetic Resonance Imaging, 6*, 201–214.

PODO, F., ORR, J. S., SCHMIDT, K. & BOVÉE, W. M. M. J., 1988. Identification and characterisation of biological tissues by NMR. Concerted research project of the European

1992, *The British Journal of Radiology*, *65*, 442–444

Economic Community. I. Introduction, objectives and activities. *Magnetic Resonance Imaging*, *6*, 175–178.

REDPATH, T. W., 1982. Calibration of the Aberdeen NMR imager for proton spin-lattice relaxation time measurements *in vivo*. *Physics in Medicine and Biology*, *27*, 1057–1065.

RICHARDS, M. A., GREGORY, W. M., WEBB, J. A. W., JEWELL, S. E. & REZNEK, R. H., 1987. Reproducibility of spin-lattice relaxation time (T_1) measurement using an 0.08 tesla MD800 magnetic resonance imager. *British Journal of Radiology*, *60*, 241–244.

SMITH, M. A. & TAYLOR, D. G., 1986. The absence of tissue specificity in MRI using *in vivo* T_1 or T_2 determination: true biological variation or technical artefact? *British Journal of Radiology*, *59*, 82–83.

WALKER, P. M., LERSKI, R. A., MATHUR-DE VRÉ, R., BINET, J. & YANE, F., 1988. Identification and characterisation of biological tissues by NMR. Concerted research project of the European Economic Community. VI. Preparation of agarose gels as reference materials for NMR relaxation time measurement. *Magnetic Resonance Imaging*, *6*, 215–222.

WALKER, P. M., BALMER, C., ABLETT, S. & LERSKI, R. A., 1989. A test material for tissue characterisation and system calibration in MRI. *Physics in Medicine and Biology*, *34*, 5–22.

The disappearing bladder—modifying imaging techniques after rectal excision

By W. C. G. Peh, FRCR, N. C. Chokshi, FRCR and *C. H. Young, FRCS

Departments of Diagnostic Radiology and *Urology, Selly Oak Hospital, Birmingham B29 6JD, UK

(Received 5 July 1991, accepted 3 October 1991)

Keywords: Bladder diseases, Pelvic surgery, Rectal surgery, Urinary outflow obstruction

Urological complications after abdomino-perineal excision of the rectum are well recognized. One complication is chronic urinary retention, which occurs in 14–50% of patients (Watson & Williams, 1952; Buckwalter et al, 1955; Eickenberg et al, 1976; Neal et al, 1982; Watters et al, 1983). The three main theories explaining causes of bladder dysfunction are direct nerve injury, loss of bladder support and pericystitis (Buckwalter et al, 1955; Eickenberg et al, 1976). Vesical neuropathy is now generally accepted as the main cause of urinary retention and this has been reflected in the emphasis on urodynamic studies, conducted mostly by urologists (Rankin, 1969; Fowler, 1973; Fowler et al, 1978; Neal et al, 1982; Chang & Fan, 1983; Lupton, 1986).

We present two male patients who developed posterior–inferior bladder prolapse subsequent to rectal excision and illustrate the modifications of standard imaging technique required to demonstrate the altered anatomy.

Case 1

A 65-year-old man presented with persistent discomfort and a feeling of fullness in the perineal region. He subsequently had difficulty in micturition and poor stream. Abdomino-perineal excision for rectal carcinoma had been done 9 years previously. Cystoscopy was normal. Computed tomography (CT) scan demonstrated a prolapsed bladder lying posteriorly against the sacrum. An intravenous urogram (IVU) examination was done and on the frontal projection, the bladder was noted to have an abnormal shape. The bladder also appeared to be in a low position (Fig. 1). A lateral projection done with the patient

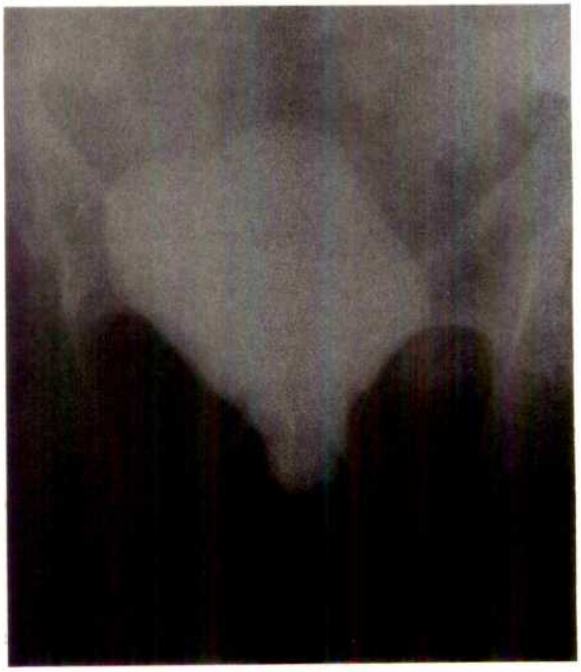

Figure 1. IVU—frontal view shows abnormal position of a misshapen bladder.

Address correspondence to Dr Wilfred C. G. Peh, Department of Diagnostic Radiology, University of Hong Kong, Queen Mary Hospital, Hong Kong.

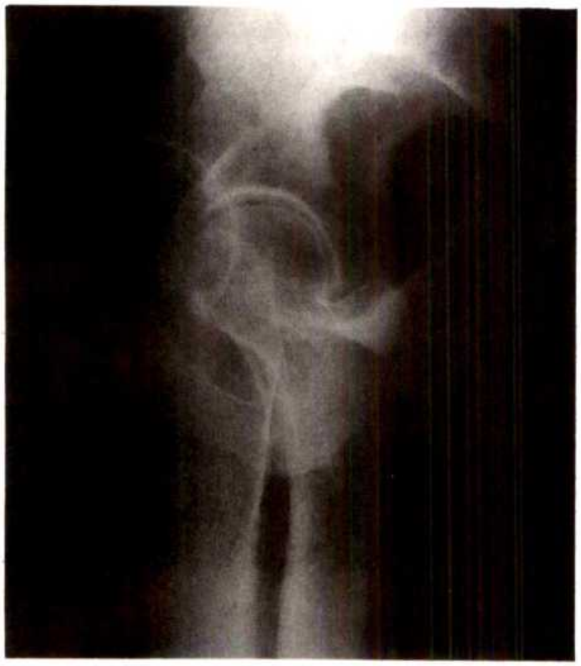

Figure 2. IVU—erect lateral view shows posterior and inferior bladder prolapse.

standing erect showed abnormal descent of the bladder inferiorly and posteriorly (Fig. 2). This finding was confirmed at operation where the bladder was found herniated through the pelvic floor. Reduction and repair were performed with improvement of urinary symptoms.

Case 2

A 68-year-old man presented with difficulty in micturition. He had intermittent poor stream and found that applying upwards pressure by hand to the perineum aided voiding. He had an abdomino-perineal excision for rectal carcinoma 3 years previously. Despite repeated attempts, the bladder could not be demonstrated by ultrasound with the transducer placed conventionally on the anterior abdominal wall. However, with the transducer placed perineally near the site of the former anal opening, the bladder was easily visualized (Fig. 3).

Discussion

In these two cases, inferior and posterior bladder prolapse is likely to have occurred owing to a combination of factors, such as severance of ligaments supporting the bladder, creation of a potential space by rectal excision and herniation of the bladder through a weakened or damaged pelvic floor.

Indeed, post-mortem specimens have shown posterior displacement of the whole bladder, including the bladder base and prostate after abdomino-perineal excision. Buckwalter et al (1955) postulated that these changes, accompanied by angulation of the bladder neck and urethra, resulted in mechanical interference with normal micturition. In women, however, bladder displacement is slight and the intact anterior vaginal wall is believed to provide support to the urethra (Watson & Williams, 1952).

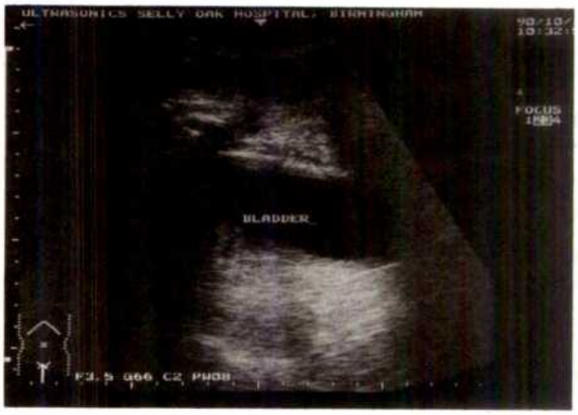

Figure 3. Ultrasound using the perineal approach demonstrates bladder prolapse.

An erect lateral film in the IVU series is both a simple and cheap way of demonstrating the bladder position. Similarly, using the perineal approach for ultrasound is not difficult and may demonstrate an otherwise elusive bladder.

Besides patients who have had abdomino-perineal excision of the rectum, other groups in which these modified techniques could be applied include those with major gynaecological exenterative surgery and panprotocolectomies. Demonstration of abnormal bladder prolapse as the cause of urinary problems, especially in males, would be helpful in planning corrective surgery.

References

BUCKWALTER, J. A., SHROPSHIRE, R. & JOINER, B. A., 1955. Morbidity of abdominoperineal resection. *Surgery, Obstetrics & Gynecology, 101*, 483–488.

CHANG, P. L. & FAN, H. A., 1983. Urodynamic studies before and/or after abdominoperineal resection of the rectum for carcinoma. *Journal of Urology, 130*, 948–951.

EICKENBERG, H., AMIN, M., KLOMPUS, W. & LICH, R., 1976. Urological complications following abdominoperineal resection. *Journal of Urology, 115*, 180–182.

FOWLER, J. W., 1973. Bladder function following abdominoperineal excision of the rectum for carcinoma. *British Journal of Surgery, 60*, 574–576.

FOWLER, J. W., BREMNER, D. N. & MOFFAT, L. E. F., 1978. The incidences and consequences of damage to the parasympathetic nerve supply to the bladder after abdominoperineal resection of the rectum for carcinoma. *British Journal of Urology, 50*, 95–98.

LUPTON, E. W., 1986. Management of urinary outflow obstruction after pelvic surgery: a review. *Journal of the Royal Society of Medicine, 79*, 734–737.

NEAL, D. E., PARKER, A. J., WILLIAMS, N. S. & JOHNSTON, D., 1982. The long term effects of proctectomy on bladder function in patients with inflammatory bowel disease. *British Journal of Surgery, 69*, 349–352.

RANKIN, J. T., 1969. Urological complications of rectal surgery. *British Journal of Urology, 41*, 655–659.

WATSON, P. C. & WILLIAMS, D. I., 1952. The urological complications of excision of the rectum. *British Journal of Surgery, 40*, 19–28.

WATTERS, G. R., BOKEY, E. L., CHAPUIS, P. H., MAHER, P. W. & PHEILS, M. T., 1983. Urological complications following abdominoperineal excision of the rectum for carcinoma. *Australasian & New Zealand Journal of Surgery, 53*, 445–447.

1992, *The British Journal of Radiology*, 65, 445–447

Case reports

Magnetic resonance imaging and treatment of an unusual seminoma metastasis occurring in the parasellar region

By R. L. Guy, MRCP, FRCR, *M. Mason, MRCP, FRCR and †L. Janse Van Rensburg, MFGP, MFamMed, MMed(Rad D)

Departments of Radiology and *Radiotherapy, Royal Marsden Hospital, Downs Road, Sutton, Surrey SM2 5PT, UK

(*Received 21 June 1991 and in revised form 26 September 1991, accepted 25 October 1991*)

Keywords: Magnetic resonance imaging, Seminoma, Parasellar

Seminoma of the testis is a relatively common tumour in young men and its typical pattern of spread is well documented. We describe an unusual case of a right parasellar seminoma metastasis presenting with partial fifth and sixth cranial nerve palsies. The appearances of the tumour on magnetic resonance imaging (MRI) and the current treatment for metastatic seminoma are discussed.

Case report

A 32-year-old man presented with a right testicular mass and underwent a right orchidectomy. Histology showed the testis to be replaced by a combined malignant teratoma undifferentiated and a classical seminoma. Staging investigations showed involvement of right iliac lymph nodes. The patient was treated with five courses of combination chemotherapy with vincristine, methotrexate, cisplatinum and bleomycin alternating with etoposide, actinomycin D and cyclophosphamide (POMB/ACE), following which he was in complete remission as judged by lymphography.

He remained disease free for 6 years until he developed a left testicular mass. He underwent a left orchidectomy and histology on this occasion showed a pure seminoma. Tumour markers were not elevated but computed tomography (CT) demonstrated left iliac and para-aortic node enlargement and this area was treated with radiotherapy to a "dogleg" field to 35 Gy in 25 fractions over 6 weeks. The response was satisfactory.

The patient re-presented 14 months later with a headache and numbness which had spread from the right temple to the right maxilla and tongue over a period of 4 weeks. He had a 2 week history of double vision. On examination he was found to have left supraclavicular lymphadenopathy, numbness both in the distribution of the maxillary division of the fifth cranial nerve and in the anterior two thirds of the tongue, but with no motor deficit, and diplopia on right lateral gaze. A diagnosis of right partial fifth and sixth cranial nerve palsies was made.

Axial T_1-weighted MR images were obtained pre- and post-gadolinium DTPA (Gd-DTPA) enhancement at 1.5 T and showed enhancing tumour in the parasellar region extending into the sphenoid sinus, predominantly on the right (Fig. 1). A coronal CT scan did not show any evidence of bony destruction. Biopsies were obtained from the left supraclavicular mass and from the mass in the right sphenoid sinus and histology of both showed involvement with pure seminoma.

He was treated with four courses of single agent carboplatin at a dose of 400 mg/m^2, as described previously (Horwich et al, 1989). However, the diplopia and facial paraesthesiae persisted and the MRI examination was repeated 4 months later. This demonstrated a reduction in tumour bulk, but there was some residual enhancing tissue present (Fig. 2). He was subsequently treated with radiotherapy to the parasellar and left supraclavicular regions, to 30 Gy in 15 fractions over 3 weeks, to consolidate his response to chemotherapy. His symptoms resolved and an MR scan 8 months later showed only a small residual soft tissue mass with minimal enhancement.

Discussion

Less than 15% of seminomas metastasize and when this does occur the most common sites for metastases are lymph nodes, bones and lung with brain being less common (Bredael et al, 1982). However, atypical sites for seminoma metastases have been described. A review of 221 cases of seminoma from this centre revealed metastases in kidney, muscle and stomach (Husband & Bellamy, 1985) and metastases to the orbit (Rush et al, 1981) and prostate (Sagalowsky et al, 1986) have also been described.

In this case the MR examination demonstrated the precise anatomical location of the tumour resulting in the cranial nerve palsies. The fifth nerve was involved at the level of the trigeminal ganglion in Meckel's cave and there was evidence of perineural tumour along the second and third divisions of the fifth nerve. The sixth nerve was involved within the cavernous sinus where it runs adjacent to the encased internal carotid artery. Other features on MRI which may suggest specific cranial nerve deficit include atrophy or fatty replacement in the involved muscles. The multiplanar capability of MRI and its excellent definition of soft

---

Address correspondence to Dr R. Guy, Department of Radiology, Royal Marsden Hospital, Downs Road, Sutton, Surrey SM2 5PT.

†Present address: L. Janse Van Rensburg, Department of Diagnostic Radiology, Tygerberg Hospital and University of Stellenbosch, 7505, Cape Province, Republic of South Africa.

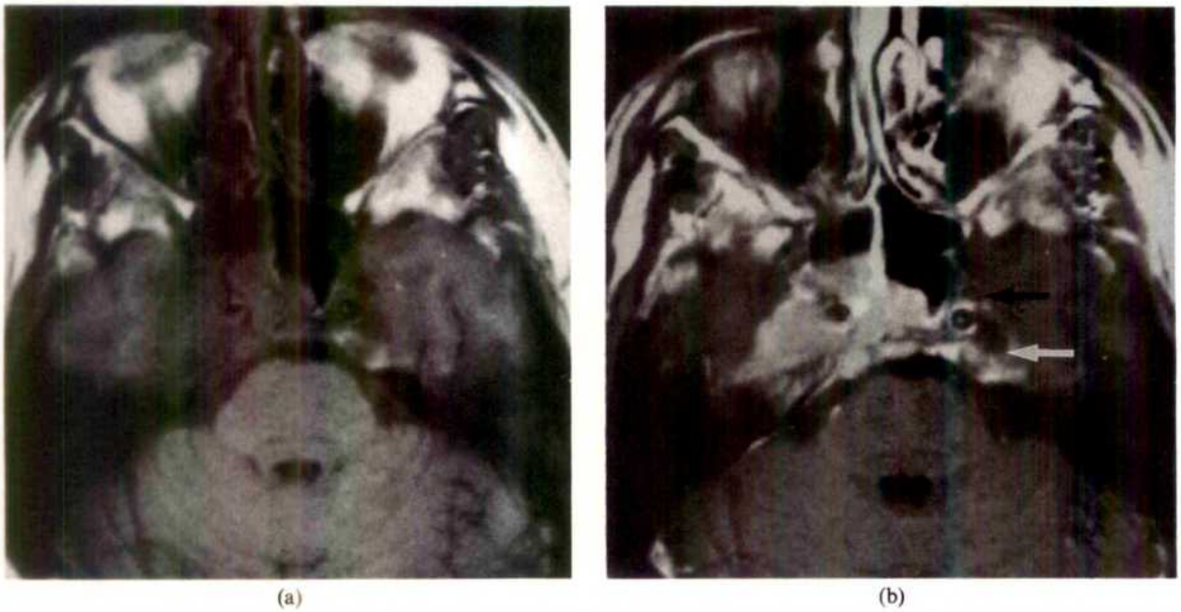
(a) (b)

Figure 1. Axial MRI (a) pre- and (b) post-Gd-DTPA enhancement. The enhancing seminoma metastasis in the right parasellar region involves Meckel's cave and extends into the sphenoid sinus, predominantly on the right. There is infiltration of the right cavernous sinus with encasement of the right carotid artery. The carotid artery (black arrow) and margins of Meckel's cave (white arrow) are indicated on the normal side of the enhanced scan.

tissues make it the ideal modality for visualizing the cranial nerves.

There is a wide differential diagnosis for the appearances of this tumour on MRI. In this case, the tumour in the sphenoid sinus with associated supraclavicular lymphadenopathy initially suggested the diagnosis of a nasopharyngeal carcinoma. The differential diagnosis would include other metastases, for example from a

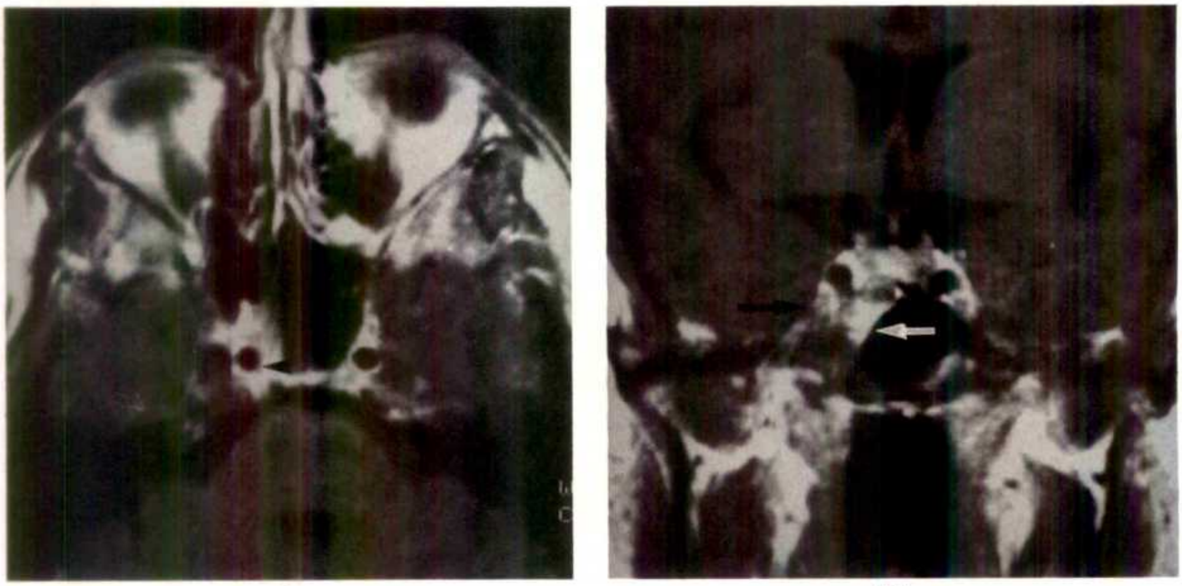
(a) (b)

Figure 2. (a) Axial and (b) coronal MR images following Gd-DTPA enhancement. Following chemotherapy there is a marked reduction in tumour bulk. However, there is still enhancing tissue present within the sphenoid sinus (white arrow) and encasing the carotid artery (black arrowhead). Perineural tumour enhancement is seen around the maxillary division of the right fifth nerve (black arrow).

1992, *The British Journal of Radiology*, *65*, 447–449

primary bronchogenic neoplasm, a primary nerve sheath tumour such as a malignant schwannoma or neurinoma, a parasellar meningioma and extension into the cavernous sinus from a pituitary adenoma. The histology of a seminoma metastasis at this site has been described previously and the similarity to that of a primary midline germinoma noted (Averback & Olivier, 1977).

The treatment of metastatic seminoma with carboplatin results in an overall disease free survival rate of 80% (Horwich et al, 1989), most of the remaining 20% of patients being salvaged by further intensive chemotherapy. This allows the majority of patients to be treated with a simple regime that can usually be given on an out-patient basis.

Most reports have suggested that T_2-weighted sequences have a high specificity for differentiating between fibrosis and tumour, but more recent work has cast some doubt on this (Lee & Glazer, 1990). Short T_1 inversion recovery sequences, emphasizing the effect of the prolonged T_1 and T_2 values characteristically found in tumour, have also been used to try to differentiate between active tumour and fibrosis (Dwyer et al, 1988).

In this case the persisting enhancement of the residual soft tissue mass 4 months after chemotherapy caused some difficulty in interpretation. It has been suggested that Gd-DTPA enhanced MRI may be of value in differentiating between tumour and fibrosis (Kassel et al, 1989). However, there have been reports of persistent enhancement in biopsy proven fibrosis at other sites even at 3 years (Werthmuller et al, 1989) and in the spine epidural fibrosis enhances following back surgery. Hence, persisting enhancement does not necessarily mean that there is active tumour present.

Acknowledgments

We would like to acknowledge the help of Dr J. E. Husband, Professor A. Horwich and Dr D. P. Dearnaley in preparing this manuscript.

References

AVERBACK, P. & OLIVIER, A., 1977. Metastatic intracranial seminoma. *Archives of Neurology*, *36*, 40.

BREDAEL, J. J., VUGRIN, D. & WHITMORE, W. F., 1982. Autopsy findings in 154 patients with germ cell tumours of the testis. *Cancer*, *50*, 548–551.

DWYER, A. J., FRANK, J. A., SANK, V. J., REINIG, J. W., HICKEY, A. M. & DOPPMAN, J. L., 1988. Short-T1 inversion-recovery pulse sequence: analysis and initial experience in cancer imaging. *Radiology*, *168*, 827–836.

HORWICH, A., DEARNALEY, D. P., DUCHESNE, G. M., WILLIAMS, M., BRADA, M. & PECKHAM, M. J., 1989. Simple non-toxic treatment of seminoma with carboplatin. *Journal of Clinical Oncology*, *7*, 1150–1156.

HUSBAND, J. E. & BELLAMY, E. A., 1985. Unusual thoracoabdominal sites of metastases in testicular tumours. *American Journal of Roentgenology*, *145*, 1165–1171.

KASSEL, E. A., KELLER, M. A. & KUCHARCZYK, W., 1989. MRI of the floor of the mouth, tongue and orohypopharynx. *Radiologic Clinics of North America*, *27*, 331–351.

LEE, K. T. & GLAZER, H. S., 1990. Controversy in the MR imaging appearance of fibrosis. *Radiology*, *177*, 21–22.

RUSH, J. A., OLDER, J. J. & RICHMAN, A. V., 1981. Testicular seminoma metastatic to the orbit. *American Journal of Ophthalmology*, *91*, 258–260.

SAGALOWSKY, A. I., MCCONNELL, J. D. & ADMIRE, R., 1986. Uncommon sites of recurrent seminoma and implications for therapy. *Cancer*, *57*, 1060–1065.

WERTHMULLER, W. C., SCHIEBLER, M. L., WHALEY, R. A., MAURO, M. A. & MCCARTNEY, W. H., 1989. Gadolinium-DTPA enhancement of lung radiation fibrosis. *Journal of Computer Assisted Tomography*, *13*, 946–948.

---

^{99}Tc^{m} HMPAO SPECT in progressive multifocal leucoencephalopathy

By Dr J. V. Bowler, BSc, MRCP, Dr P. T. G. Davies, MA, MRCP and Dr G. D. Perkin, FRCP
The Regional Neurosciences Centre, Charing Cross Hospital, Fulham Palace Road, London W6 8RF, UK

(Received 12 June 1991 and in revised form 19 September 1991, accepted 16 October 1991)

Keywords: SPECT, Progressive multifocal leucoencephalopathy

Progressive multifocal leucoencephalopathy (PML), a rare condition caused by the JC papovavirus, is characterized by multiple areas of demyelination within the central nervous system. It almost always occurs in the context of immunosuppression and as a result of AIDS the number of cases has increased (Levy et al, 1988; Lang et al, 1989). Both computed tomography (CT) scanning and magnetic resonance imaging (MRI) have been found to be of limited value in establishing the diagnosis of PML. An alternative technique that might support a clinical diagnosis of PML would therefore be valuable, particularly if it would avoid the need to proceed to biopsy. We report a case of biopsy proven PML investigated by single photon emission computerized tomography (SPECT) using ^{99}Tc^{m} hexamethylpropyleneamineoxime (^{99}Tc^{m} HMPAO). This is the first

---

Address correspondence to Dr J. V. Bowler.

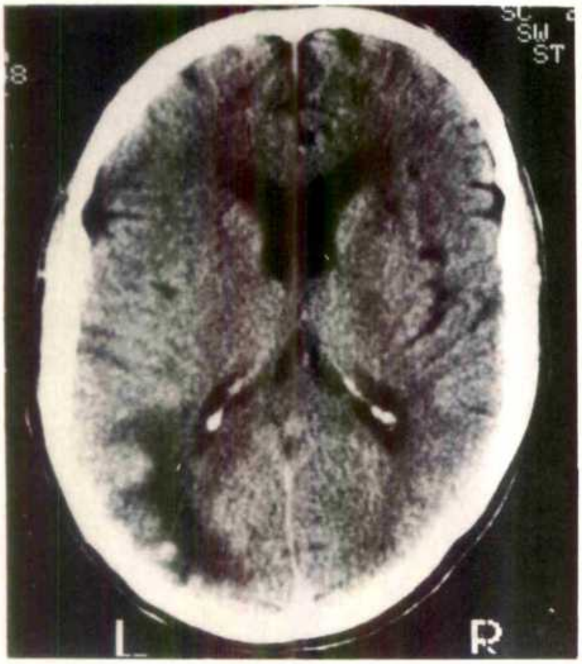

Figure 1. CT scan showing low density changes, later proven to be PML, confined to white matter.

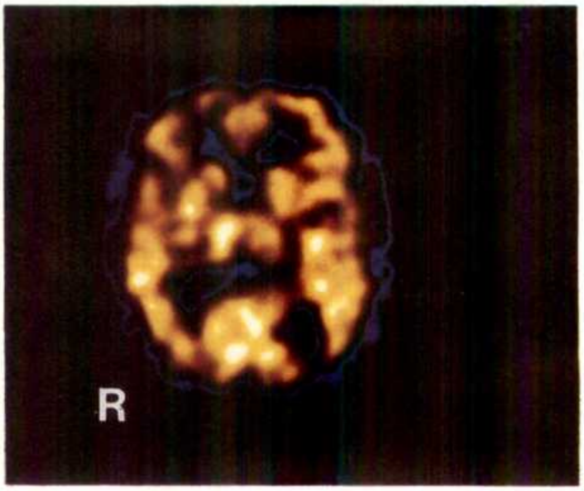

Figure 2. SPECT done 7 days after the first CT showing much more extensive changes including the overlying cortex and thalamus.

report of regional cerebral blood flow (rCBF) imaging in PML. We suggest that the appearances may be sufficiently characteristic to be of diagnostic use.

Case report

A 62-year-old man was diagnosed as having chronic lymphatic leukaemia in 1982 and was treated with chlorambucil from 1986. 8 years after diagnosis he started to misjudge distances while driving and was involved in a road traffic accident. Examination in casualty revealed an incomplete right homonymous hemianopia. Over the next 4 weeks he developed right sided clumsiness progressing to an inability to stand unaided. On admission to hospital his right homonymous hemianopia had become complete and he had a right hemiparesis. A CT brain scan performed soon after admission showed extensive diminished density in the left parietal, lateral occipital and posterior temporal regions, without enhancement. There was some mass effect but no midline shift (Fig. 1). Full haematological and biochemical investigations, electrocardiogram, echocardiogram and chest radiograph showed no relevant abnormality. Cerebrospinal fluid examination showed no malignant cells, no white cells, a glucose of 4 mmol/l and a protein of 0.37 g/l. SPECT showed an extensive area of white and grey matter perfusion deficits involving the left occipital cortex, lentiform nucleus and the anterior parietal lobe with its underlying white matter (Fig. 2). The uptake in these regions was compared with the contralateral side using standard regions of interest and was 1.08 for the cerebellum, 0.83 for the thalamus and 0.51 for the white matter of the occipital cortex, though in the heart of the lesion there was a substantial area with negligible uptake. Over the next 3 weeks there was a progressive neurological deterioration. He became apraxic, dyscalculic, dyslexic, hemiplegic and developed right/left and time and place disorientation. A repeat CT scan, 25 days after the first, showed no significant change. In view of his clinical deterioration he underwent an open brain biopsy which confirmed PML.

Discussion

The CT abnormalities in our case were insufficient to account for the neurological deficit. This discrepancy, which also applies to MRI, has been observed previously (Ledoux et al, 1989) and has been suggested as a diagnostic clue (Krupp et al, 1985). The only previous study of PML by functional imaging was a positron emission tomogram utilizing fluorodeoxyglucose (Kiyosawa et al, 1988), which revealed extensive metabolic changes remote from the lesion consistent with diaschisis. The modest decrease in HMPAO uptake seen in the contralateral cerebellum and ipsilateral thalamus would be consistent with diaschisis, though there were no clinical correlates of this. However, because PML is multifocal the possibility that these changes were caused by separate lesions and not by diaschisis cannot be dismissed. The changes seen in the occipital cortical grey matter are relatively severe for diaschisis, but this area of cortex is typically thin on SPECT (see the opposite side) and the decrease seen here may be in part partial volume and part diaschisis, though grey matter involvement cannot be excluded. The changes seen on ^{99}Tc^{m} HMPAO SPECT are much more consistent with the clinical picture than the CT findings. They suggest that rCBF changes secondary to demyelination and cystic change are more extensive than previously thought. Of particular interest are the grey matter changes. These are such rare and late features of PML imaged by CT scanning for their absence to be used diagnostically (Levy & Bredesen, 1988; Ledoux et al, 1989). Whether they can all be explained by diaschisis or whether there is some direct involvement of grey matter, perhaps of fibre tracts within predominantly grey matter, remains speculative.

1992, *The British Journal of Radiology*, *65*, 449–451

The pattern of the changes in HMPAO uptake demonstrated by SPECT were unique in this case. It is distinct in appearance from the changes of leukoariosis in that it is focal and relatively remote from the ventricles. It is distinguished from posterior cerebral artery lesions not only by its relative sparing of the medial occipital and inferior occipitotemporal cortex, but also by its prominent involvement of white matter and its extension forward into middle cerebral artery territory. Whilst the CT appearances might be mistaken for vasogenic oedema, the profound fall in HMPAO uptake demonstrates that it is not oedema alone. This, in combination with the close correlation with the clinical deficit, suggests that HMPAO SPECT may, in conjunction with CT or MRI, be of value in the diagnosis of PML. This observation may be of increasing importance as SPECT is readily available and the incidence of PML is expected to increase due to AIDS. Further examples in biopsy proven cases will be required.

References

KIYOSAWA, M., BOSLEY, T. M., ALAVI, A., GUPTA, N., RHODES, C. H., CHAWLUK, J., KUSHNER, M., SAVINO, P. J., SERGOTT, R. C., SCHATZ, N. J., REIVICH, M. & JAMIESON, D., 1988. Positron emission tomography in a patient with progressive multifocal leukoencephalopathy. *Neurology*, *38*, 1864–1867.

KRUPP, L. B., LIPTON, R. B., SWERDLOW, M. L., LEEDS, N. E. & LLENA, J., 1985. Progressive multifocal leukoencephalopathy: clinical and radiographic features. *Annals of Neurology*, *17*, 344–349.

LANG, W., MIKLOSSY, J., DERUAZ, J. P., PIZZOLATO, G. P., PROBST, A., SCHAFFNER, T., GESSAGA, E. & KLEIHUES, P., 1989. Neuropathology of the acquired immune deficiency syndrome (AIDS): a report of 135 consecutive autopsy cases from Switzerland. *Acta Neuropathologica (Berlin)*, *77*, 379–390.

LEDOUX, S., LIBMAN, I., ROBERT, F. & JUST, N., 1989. Progressive multifocal leukocephalopathy with gray matter involvement. *Canadian Journal of Neurological Sciences*, *16*, 200–202.

LEVY, R. M. & BREDESEN, D. E., 1988. Central nervous system dysfunction in acquired immunodeficiency syndrome. *Journal of Acquired Immune Deficiency Syndrome*, *1*, 41–64.

LEVY, R. M., JANSSEN, R. S., BUSH, T. J. & ROSENBLUM, M. L., 1988. Neuroepidemiology of acquired immunodeficiency syndrome. *Journal of Acquired Immune Deficiency Syndrome*, *1*, 31–40.

Increased attenuation value of a colloid cyst of the third ventricle following ventricular decompression

By N. G. Warnock, MRCP (UK), FRCR and T. Powell, FRCP, FRCR

Department of Diagnostic Radiology, Royal Hallamshire Hospital, Glossop Road, Sheffield S10 2JF, UK

(Received 8 August 1991, accepted 3 October 1991)

Keywords: Colloid cyst, Computed tomography

Case report

A 35-year-old woman presented with a 3 month history of postural unsteadiness. She complained of worsening headaches, with blurred vision for 1 week, accompanied by nausea and vomiting. On examination she was found to have bilateral papilloedema, with slight slowness of mentation but no other feature.

Axial computed tomography (CT) (Fig. 1) showed gross dilatation of the lateral ventricles, with a collapsed third ventricle, consistent with the presence of obstruction to cerebrospinal fluid (CSF) flow at the foramina of Munro. No mass was seen.

A ventriculo-peritoneal shunt was inserted into the right lateral ventricle, with relief of symptoms. A repeat CT at 4 days after shunting showed collapse of the right lateral ventricle, with a considerable reduction in the size of the left (Fig. 2). Cerebral angiography was performed and was normal.

When reviewed 6 weeks later, she had some recurrence of headaches and complained of pain in the right flank. Cranial CT (Fig. 3) showed that ventricles were unchanged, but that a rounded hyperdense mass had appeared in the anterior end of the third ventricle typical of a colloid cyst. Persisting flank pain was thought to be due to irritation by the shunt, which was therefore removed. A further scan 1 week later again showed the colloid cyst which appeared to have enlarged slightly (Fig. 4). The ventricles had increased in size and accordingly excision of the cyst was performed. The patient was discharged in good health after 1 week and remains well 1 year later.

Pathological examination of the specimen showed a typical colloid cyst containing amorphous eosinophilic material.

Discussion

The typical appearance of a colloid cyst of the third ventricle is a rounded hyperdense mass in the anterior end of the third ventricle in the plane of the foramina of Munro (Ganti et al, 1981). Infrequently isodense and hypodense cysts are encountered; they may be difficult to detect on CT. Contrast enhancement is reported (Zilkha, 1981; Hine & Chui, 1987), but in none of the reported cases are the measurement details sufficiently precise to judge the possible contribution of technical

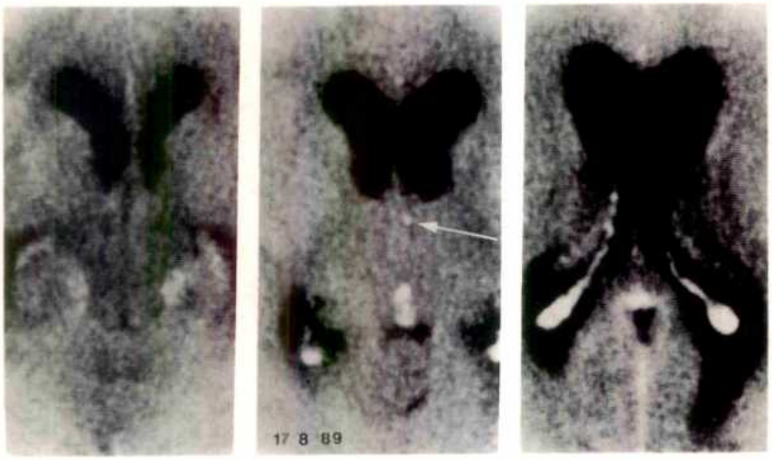

Figure 1. CT scan (unenhanced) at presentation. Dilatation of lateral ventricles with a collapsed third ventricle. Choroid plexus arrowed. (10 mm contiguous sections.)

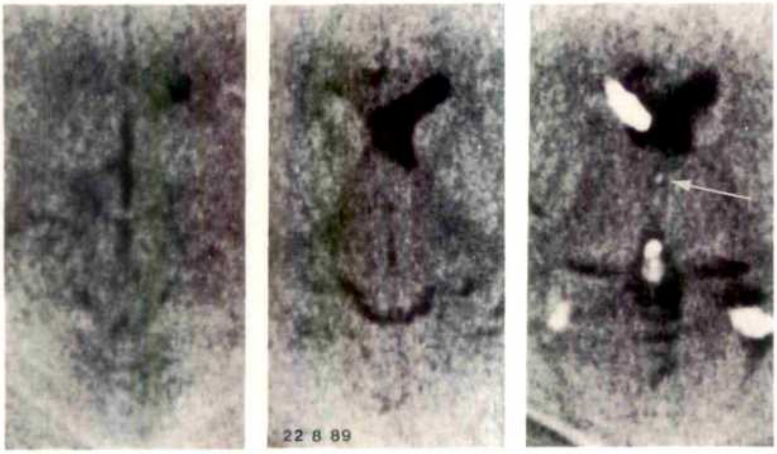

Figure 2. CT scan (unenhanced) after ventriculo-peritoneal shunting. Right lateral ventricle is collapsed, and left is reduced in size. Choroid plexus arrowed. (10 mm contiguous sections.)

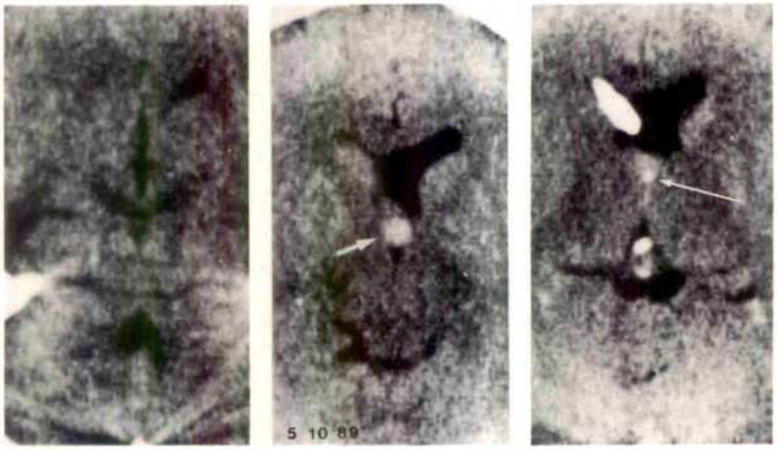

Figure 3. CT scan (unenhanced) 6 weeks later. Ventricles unchanged. A hyperdense mass 7 mm in diameter has appeared in the anterior end of the third ventricle, typical of a colloid cyst (short arrow). Choroid plexus (long arrow). (10 mm contiguous sections.)

factors to apparent changes in attenuation values. Partial volume averaging of adjacent enhanced vascular structures may also contribute to an apparent increase in cyst density. The histology of colloid cysts suggests that contrast enhancement may be rather implausible.

In the case described, an initially isodense cyst was not identified on CT studies before and shortly after shunting (Figs 1 & 2). The cyst had become markedly hyperdense 6 weeks later. It is suggested that this was a result of the lowered intraventricular pressure. At the

1992, *The British Journal of Radiology*, *65*, 451–452

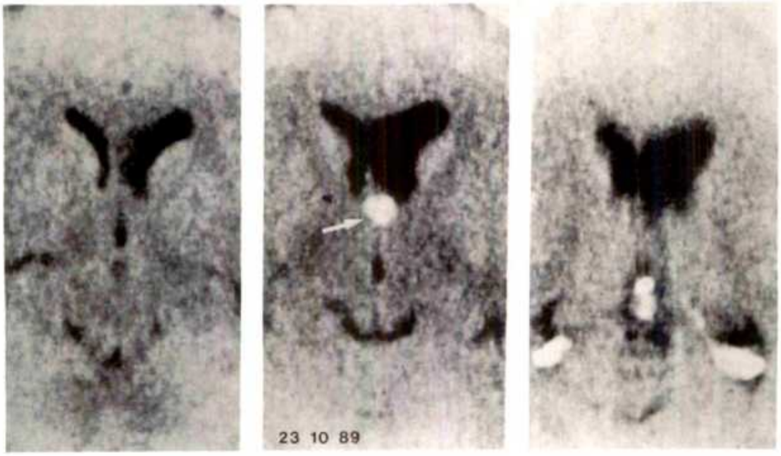

Figure 4. CT scan (unenhanced) 2½ weeks after removal of shunt, and immediately before surgery. Cyst unchanged, allowing for minimal difference in section planes, but ventricles increased in size. Choroid plexus (arrow). (10 mm contiguous sections.)

time of shunting the combined hydrostatic and osmotic pressure within the cyst would be balanced by the hydrostatic pressure in the ventricles. Lowered ventricular pressure would allow water to diffuse out of the cyst, concentrating its proteinaceous contents.

We have found a single reference to change in attenuation value of a colloid cyst; Ganti et al (1981) report a case of a cyst "initially isodense, but later turning haemorrhagic and hyperdense, and ultimately becoming partly calcified". The excised cyst in our case showed no pathological evidence of haemorrhage or calcification.

Colloid cysts are readily shown by magnetic resonance imaging (MRI) (Roosen et al, 1987; Alcock & Robertson, 1988), which is therefore indicated where the CT evidence suggests CSF flow obstruction in the region of the foramina of Munro, but where no mass is shown. Although MRI was not available in this case, its importance in such patients is nevertheless re-emphasized.

References

Alcock, M. K. & Robertson, A., 1988. Magnetic resonance imaging of a colloid cyst of the third ventricle. *Clinical Radiology*, *39*, 308–309.

Ganti, S. R., Antunes, J. L., Louis, K. M. & Hilal, S. K., 1981. Computed tomography in the diagnosis of colloid cysts of the third ventricle. *Radiology*, *138*, 385–391.

Hine, A. L. & Chui, M. S., 1987. Hypodense colloid cyst of the third ventricle. *Journal of the Canadian Association of Radiologists*, *38*, 288–291.

Roosen, N., Ghalen, D., Stork, W., Neuen, E., Wechsler, W., Schirmer, M., Lins, E. & Bock, W. J., 1987. Magnetic resonance imaging of colloid cysts of the third ventricle. *Neuroradiology*, *29*, 10–14.

Zilkha, A., 1981. Computed tomography of colloid cysts of the third ventricle. *Clinical Radiology*, *32*, 397–401.

Diagnosis and treatment of an oesophageal stricture due to lichen planus

By P. D. Holder, FRCS(Glasg.), W. L. Wong, MRCP, FRCR, J. Pemberton, MRCP, FFR, FRCR, †R. P. H. Thompson, DM, FRCP and *S. C. Parker, MA, MRCP

†Departments of Radiology and Gastroenterology and *St John's Dermatology Centre, St Thomas' Hospital, London SE1 7EH

(*Received 23 May 1991 and in revised form 15 July 1991, accepted 20 September 1991*)

Keywords: Oesophagus, Oesophageal stricture, Lichen planus

Involvement of the oral mucous membranes occurs commonly in lichen planus. Oesophageal involvement is less common and may result in pain, dysphagia and strictures. We present a case of an oesophageal stricture in a patient with lichen planus.

Case report

A 44-year-old woman with a 24 year history of oral lichen planus and a 9 year history of anogenital involvement gave a 2 year history of dysphagia. An endoscopy performed when she first noticed dysphagia showed oropharyngeal ulceration and the pharynx was narrowed with a friable mucosa. A further endoscopy in December 1990 showed an ulcerated nasopharynx but no abnormality in the oesophagus.

In January 1991 she presented with complete dysphagia.

Address correspondence to Dr P. D. Holder, Department of Radiology, St Thomas' Hospital, London SE1 7EH

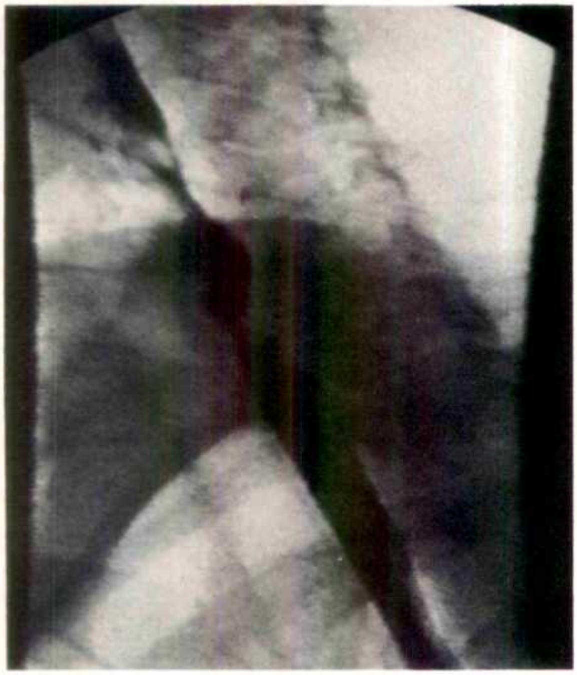

Figure 1. Barium swallow showing a tight stricture in the region of the cricopharyngeus.

Attempts to pass a fibreoptic endoscope under general anaesthesia were unsuccessful. A video barium swallow was performed (prone head down position), which showed a short narrow stricture in the region of the cricopharyngeus (Fig. 1). A rigid pharyngoscopy and balloon dilatation to 45 FG were performed and her symptoms improved. The histological appearances of biopsy specimens showed superficial stromal and deeper epidermal chronic inflammatory cell infiltrate and basal degeneration, consistent with lichen planus. A follow-up barium swallow confirmed that the stricture had improved (Fig. 2), and a fibreoptic endoscope was passed and the stricture further balloon dilated to 54 FG.

Discussion

Oral involvement in lichen planus occurs in 30–70% of patients. Oesophageal involvement is extremely rare, but a recent report (Dickens et al, 1990) found endoscopic evidence of oesophageal lesions in five of the 19 patients with lichen planus. Four had subtle papular lesions, but in one there were severe erosive changes throughout the oesophageal mucosa. Only a small number of cases of oesophageal stricture caused by lichen planus have been reported, and the barium findings in only a few (Al-Shibabi & Jackson, 1982; Lefer, 1982; Sheehan-Dare et al, 1986; Jobard-Drobacheff et al, 1988; Walton & Bennett, 1991). Lichen planus strictures are usually in the upper third of the oesophagus, but one (Jobard-Drobacheff et al, 1988) was in the lower third, perhaps as a result of unrelated acid reflux.

Histological examination of biopsy specimens shows submucosal lymphocytic infiltrates and, in patients with severe disease, a heavy infiltrate of plasma cells in the fibromuscular tissue of the oesophagus. There is a small incidence of malignant change in lichen planus. In one series there was only one case in 307 and this occurred in the tongue (Altman & Perry, 1961), but there are no reported cases of malignant change in oesophageal lichen planus.

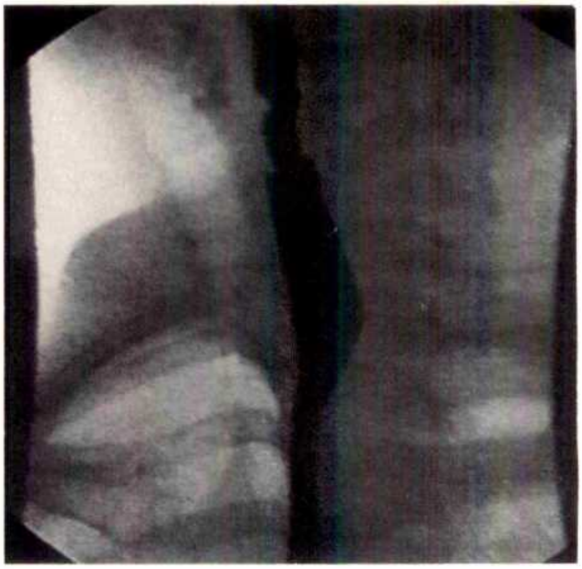

Figure 2. Barium swallow after dilatation showing improvement of the stricture.

The oesophageal lesions in lichen planus may improve with corticosteroid therapy but dilatation may be required, although endoscopic manipulation may exacerbate the oral lesions.

Acknowledgement

We are grateful to Professor M. W. Greaves, St John's Institute of Dermatology, for permission to report this case, and to Mr A. F. O'Connor for his help with pharyngoscopy.

References

AL-SHIHABI, B. M. S. & JACKSON, J. M., 1982. Dysphagia due to pharyngeal and oesophageal lichen planus. *Journal of Laryngology and Otology*, *96*, 567–571.

ALTMAN, J. & PERRY, H., 1961. The variations and course of lichen planus. *Archives of Dermatology*, *84*, 47–59.

DICKENS, C. M., HESELTINE, D., WALTON, S. & BENNETT, J. R., 1990. The oesophagus in lichen planus: an endoscopic study. *British Medical Journal*, *300*, 84.

JOBARD-DROBACHEFF, C., BLANC, D., QUENCEZ, E., ZULTAK, M., PARIS, B., OTTIGNON, Y. & AGACHE, P., 1988. Lichen planus of the oesophagus. *Clinical and Experimental Dermatology*, *13*, 38–41.

LEFER, L. G., 1982. Lichen planus of the Oesophagus. *American Journal of Dermatopathology*, *4*, 267–269.

SHEEHAN-DARE, R. A., COTTERILL, J. A. & SIMMONS, A. V., 1986. Oesophageal lichen planus. *British Journal of Dermatology*, *115*, 729–730.

WALTON, S. & BENNETT, J. R., 1991. Skin and gullet. *Gut*, *32*, 694–697.

1992, *The British Journal of Radiology*, 65, 453–454

Case of the month

An underdiagnosed abdominal mass?

By *R. D. Edwards, MRCP, FRCR and W. Kincaid, FRCR

Department of Radiology, Western Infirmary, Dumbarton Road, Glasgow G11 6NT, UK

(*Received 24 April 1991 and accepted 4 June 1991*)

A 49-year-old woman presented with a 6 h history of severe abdominal pain and a superficial, palpable mass in the right lower abdomen. She was obese and had noted a variable swelling in this area for 4 months. A right inguinal herniorrhaphy had been performed 3 months previously. Views from the initial ultrasound (US) of the anterior abdominal wall and subsequent barium follow-through (FT) are shown (Figs 1 & 2).

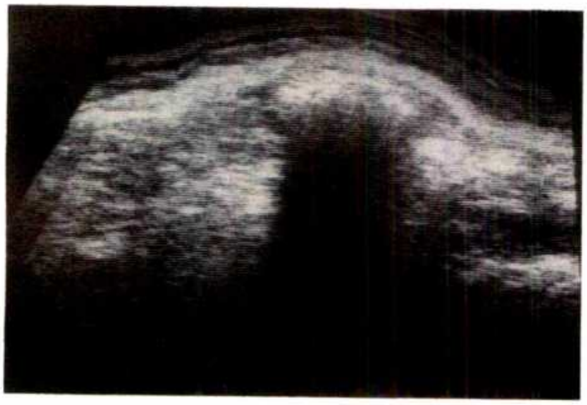

Figure 1. Longitudinal US scan of the anterior abdominal wall.

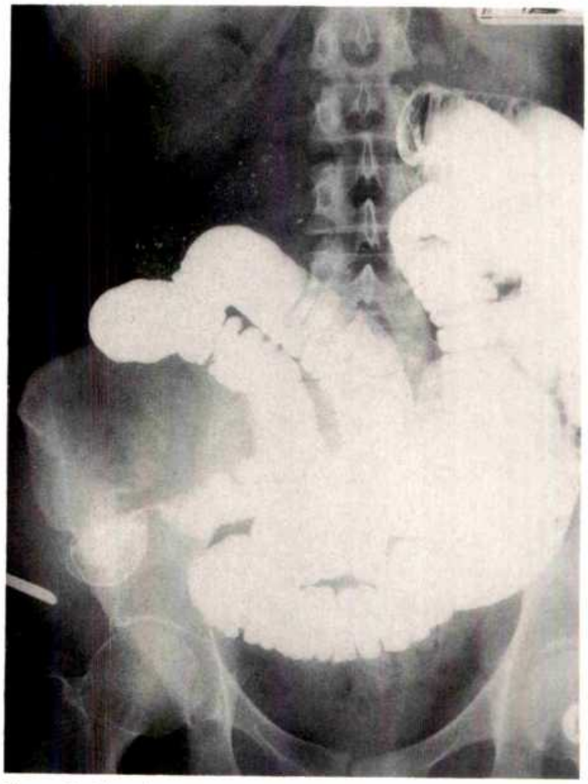

Figure 2. View from barium FT examination.

---

*Author for correspondence.

Keywords: Abdomen, Hernia, Spigelian hernia, Ultrasound

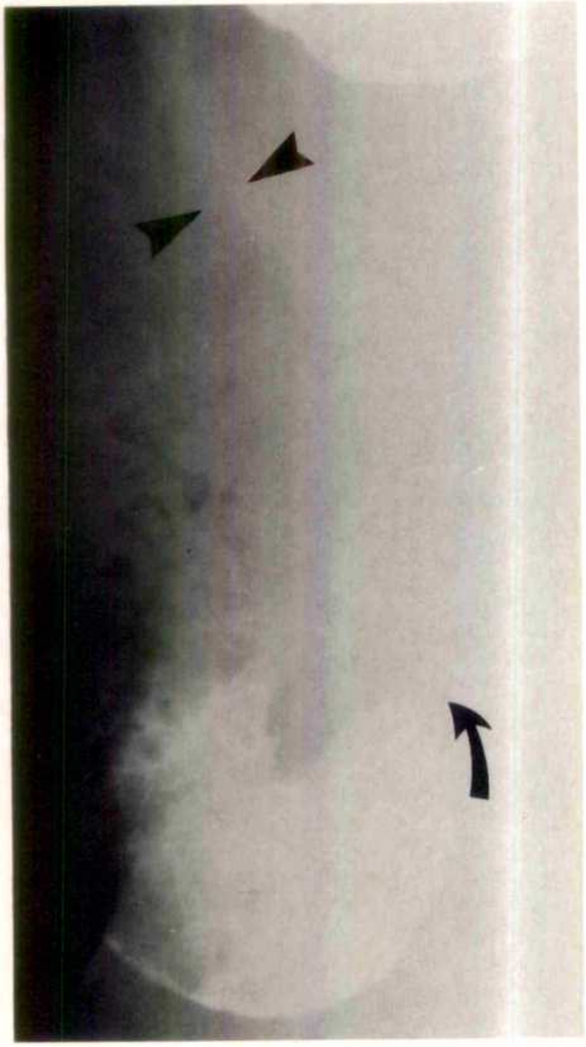

Figure 3. Oblique spot film of hernial sac.

The US shows an oval hypoechoic structure containing gas lying subcutaneously in the anterior abdominal wall. The barium FT shows a dilated proximal small bowel and a herniated loop of bowel in the right lower quadrant. An oblique spot film taken during the barium FT (Fig. 3) shows the neck of the hernial sac (curved arrow) and its relationship to the external oblique muscle (arrowheads).

Discussion

The patient has a Spigelian hernia (also known as a spontaneous lateral ventral hernia). This uncommon hernia consists of a defect in the aponeurosis of the transverse abdominal muscle between the semilunar (Spigelian) line and the lateral border of the rectus muscle. 90% occur between the level of the umbilicus and the anterior superior iliac spine. The hernial sac may dissect the layers of the transverse and internal oblique muscles and present clinically as a mass lateral to the semilunar line. In less than 5% of cases, the sac penetrates the external oblique muscle and lies subcutaneously, as was seen in this patient.

In a review of 744 patients with surgically confirmed Spigelian hernia (Spangen, 1984), the mean age was 50 years (range 6–94 years) with a slight female preponderance (male:female ratio = 1:1.4). The hernial orifice is usually less than 2 cm in diameter but may reach 8 cm. Incarceration is seen in 21% of cases treated surgically (Spangen, 1984). The hernial sac most often contains omental fat, small bowel or colon, but may consist solely of pre-peritoneal fat. Rarely, the sac may contain stomach, gallbladder, appendix, Meckel's diverticulum, ovary, uterine fibroid or testicle. An association with inguinal or femoral hernia is recognized.

The commonest symptom is pain, which is typically intermittent and is aggravated by prolonged standing or sustained physical effort. A lump, noticed by the patient in 54% of cases (Weiss et al, 1974), may be impalpable as it is normally covered by the external oblique aponeurosis. Localized tenderness may be the only physical sign and may lead to an unnecessary laparotomy.

In one series the correct pre-operative diagnosis was made in only 52% of cases, while the remainder were diagnosed as appendicitis, adhesions, tumours and intestinal obstruction (Weiss et al, 1974).

Ultrasound can identify the defect in the aponeurosis (Deitch & Engel, 1980), determine the contents of the hernial sac and distinguish it from other causes of an anterior abdominal wall mass (Fried & Meeker, 1979). Barium studies are of value only if the hernial sac contains bowel. Thin section computed tomography (CT) may demonstrate the hernial orifice (Pyatt et al, 1982).

Excision of the sac and repair of the defect is the standard surgical treatment. In this case necrotic omentum was found, but the herniated bowel had reduced spontaneously.

Awareness of the condition is probably the major factor in the diagnosis of Spigelian hernia. Ultrasound of the abdominal wall is the diagnostic method of choice and should be considered in a patient with relatively non-specific lower abdominal symptoms with or without a mass in the region of the Spigelian line.

References

DEITCH, E. A. & ENGEL, J. M., 1980. Spigelian hernia. An ultrasonic diagnosis. *Archives of Surgery, 115*, 93.

FRIED, A. M. & MEEKER, W. R., 1979. Incarcerated Spigelian hernia. Ultrasonic differential diagnosis. *American Journal of Roentgenology, 133*, 107–110.

PYATT, R. S., ALONA, B. R., DAYE, S., WENZEL, D. J., WOODS, E. & ALEXIEVA, B., 1982. Case report: Spigelian hernia. *Journal of Computer Assisted Tomography, 6*, 643–645.

SPANGEN, L., 1984. Spigelian hernia. *Surgical Clinics of North America, 64*, 351–366.

WEISS, Y., LERNAU, O. Z. & NISSAN, S., 1974. Spigelian hernia. *Annals of Surgery, 180*, 836–839.

1992, *The British Journal of Radiology*, *65*, 455–457

Short communication

The value of transvaginal scanning in the assessment of second trimester oligohydramnios

By P. Twining, FRCR

Department of Radiology, Queen's Medical Centre, Nottingham, UK

(*Received 26 March 1991 and in revised form 18 July 1991, accepted 4 September 1991*)

Keywords: Second trimester oligohydramnios, Potter's syndrome, Transvaginal scanning

Second trimester oligohydramnios is associated with a poor perinatal outcome (Barss et al, 1984), however, this is not a universal finding (Mercer & Brown, 1986). Therefore, it is important to establish an accurate diagnosis before a major management decision is made. The common causes of oligohydramnios are premature rupture of membranes, intrauterine growth retardation and Potter's syndrome. The most difficult problem is to differentiate severe intrauterine growth retardation from Potter's syndrome and transabdominal scanning often provides limited information due to the lack of liquor. The use of the transvaginal transducer, however, demonstrates fetal renal anatomy accurately even in the presence of oligohydramnios (Benacerraf, 1990). The present study describes four patients with severe oligohydramnios in whom transabdominal scanning provided equivocal findings. Subsequent transvaginal scanning demonstrated renal pathology in two patients, normal kidneys in the third and renal agenesis in the last.

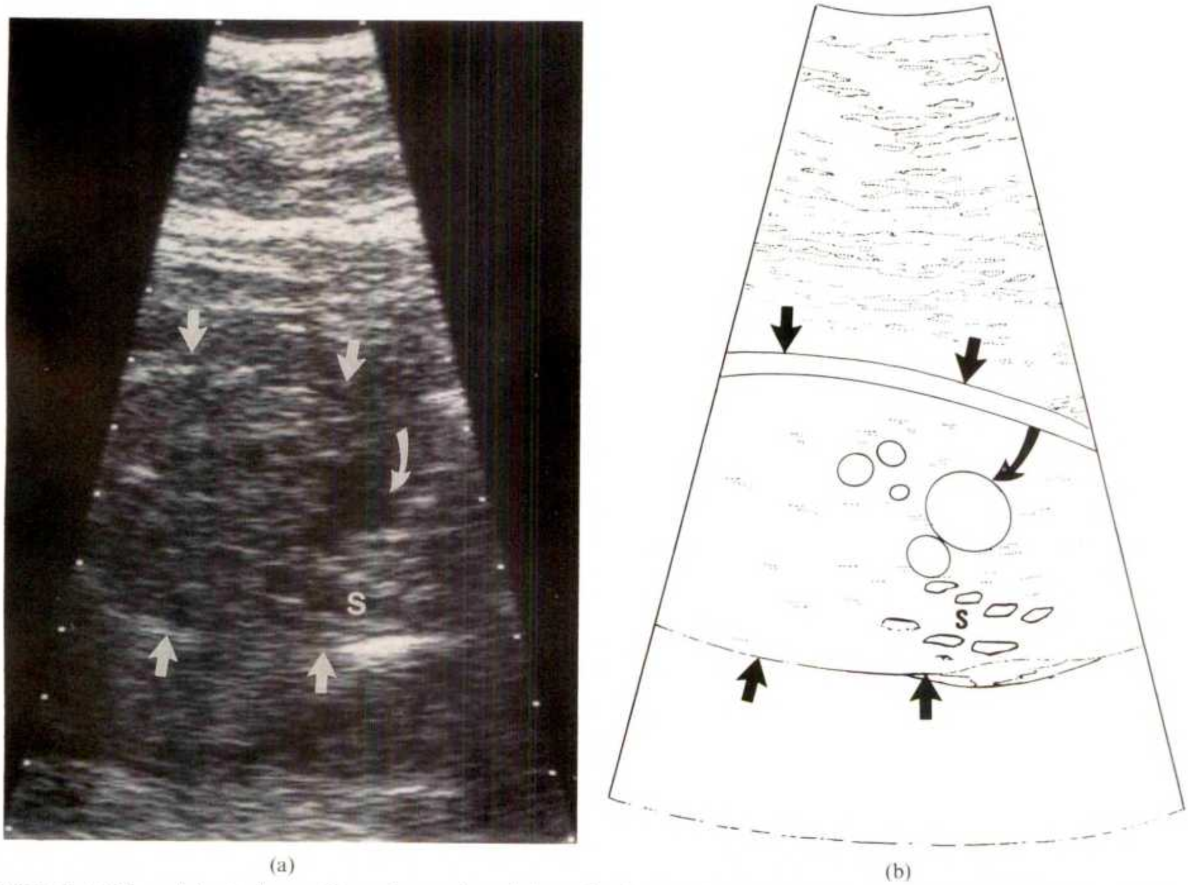

(a) (b)

Figure 1. (a) Transabdominal scan. Coronal scan through fetus showing possible cystic areas in the region of fetal kidneys. (Large arrows outline fetal body, curved arrow points to cystic areas, s = spine.) (b) Line diagram of Fig. 1(a) illustrating main points of interest. (Large arrows outline fetal body, curved arrow points to cystic areas, s = spine.)

Case reports

Case 1

A 21-year-old primigravid patient attended for routine ultrasound scan at 18 weeks gestation. Transabdominal scanning demonstrated possible cystic areas in the region of the kidneys (Fig. 1). Transvaginal scanning was carried out which revealed bilateral multicystic kidneys (Fig. 2). The patient opted for a termination of pregnancy and post-mortem examination confirmed the presence of bilateral multicystic kidneys.

Case 2

A 21-year-old primigravid patient who was 17 weeks pregnant was referred from another centre for a detailed scan. A previous ultrasound scan had shown oligohydramnios with no definite renal tissue visualized. The transvaginal scan demonstrated a unilateral multicystic kidney (Fig. 3) and also demonstrated a large ventricular-septal defect. The patient opted for a termination of pregnancy and post-mortem examination confirmed the ultrasound diagnoses.

Case 3

A 25-year-old patient attended for a routine ultrasound scan at 17 weeks gestation. She had previously had one normal pregnancy. At her initial scan there was oligohydramnios, a small fetal bladder was seen but no definite fetal kidneys. Transvaginal scanning revealed normal kidneys and bladder (Fig. 4). The pregnancy is continuing and liquor volume has subsequently improved.

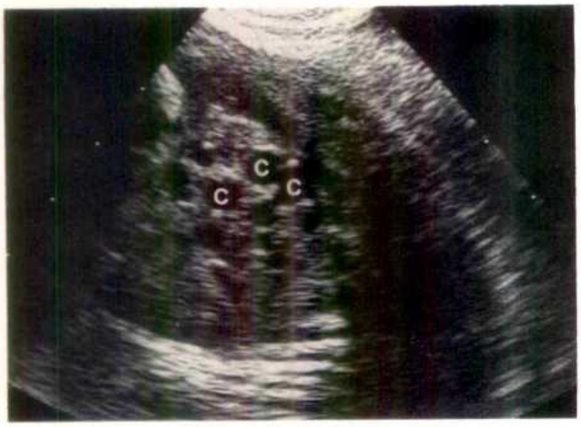

Figure 2. Transvaginal scan. Parasagittal section through the fetal kidneys showing multiple cysts (c = cyst).

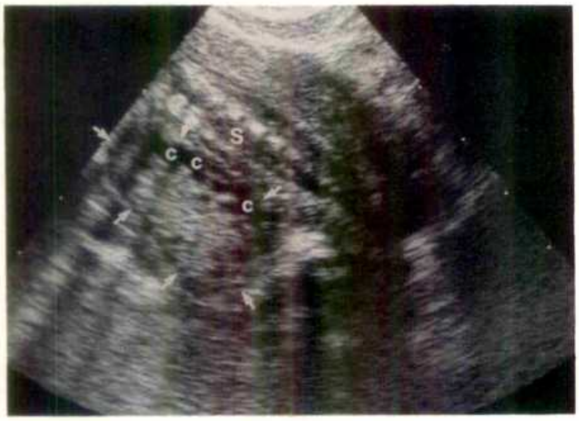

Figure 3. Transvaginal scan. Coronal section through fetus showing unilateral multicystic kidney. (Arrows outline kidney, c = cyst, s = spine.)

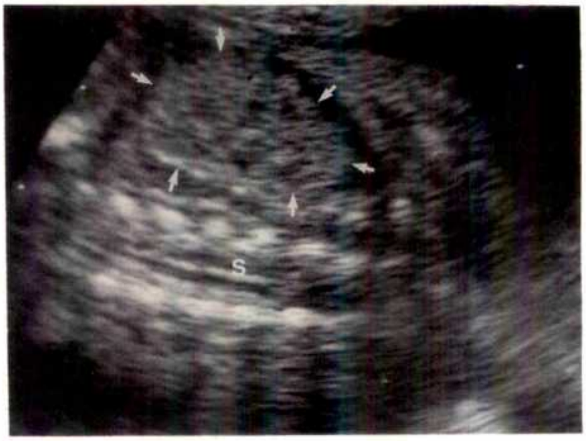

Figure 4. Transvaginal scan. Coronal scan through fetus showing a normal kidney (outlines by arrows, s = spine).

Case 4

A 19-year-old primigravid patient was referred from another centre for a detailed scan. The previous scan had shown a 17 week fetus with oligohydramnios and no definite renal tissue or bladder. The transvaginal scan demonstrated absent kidneys and bladder and a diagnosis of renal agenesis was made. The patient opted for a termination of pregnancy and the post-mortem examination confirmed the antenatal findings.

Discussion

The investigation of second trimester oligohydramnios is difficult as transabdominal scanning is often equivocal due to the lack of liquor and the fact that the fetus is often curled in an inaccessible position within the pelvis. This situation, however, is ideal for the use of a transvaginal probe, where higher frequency transducers and close proximity to the fetus compensate for the lack of liquor and difficult fetal position.

The normal fetal kidneys can be demonstrated as early as 12 weeks gestation using a transvaginal probe (Bronshtein et al, 1990) and multicystic kidneys diagnosed as early as 12 weeks and 4 days (Rottem & Bronshtein, 1990).

In severe oligohydramnios fetal anatomy can be demonstrated with greater clarity using a transvaginal probe, and the four cases described illustrate the superiority of transvaginal sonography over the transabdominal technique. Umbilical artery Doppler studies can be a helpful adjunct as abnormal Doppler waveforms are seen in severe intrauterine growth retardation but may also be observed when there are chromosomal abnormalities and multiple congenital anomalies (Hackett et al, 1987). All four cases described showed a normal umbilical artery waveform.

Investigations of oligohydramnios have previously included intra-amniotic infusion of fluid (Gembruch & Hansmann, 1988) and injection of fluid into the fetal peritoneum (Nicolini et al, 1989). These techniques, however, are associated with significant risk of chorioamnionitis and immediate rupture of membranes (Arulkumaran et al, 1990).

Transvaginal sonography is now a well established technique in the diagnosis of pelvic pathology. Transvaginal sonography clearly defines renal pathology and should be used routinely in the assessment of second trimester oligohydramnios to differentiate Potter's syndrome from severe intrauterine growth retardation.

Acknowledgments

I wish to thank all my clinical colleagues for referring patients for scanning. I also wish to thank Karen Dawkins for typing the manuscript and Linton Cochrane of Queen's Medical Centre, audiovisual department for preparing Fig. 1b.

References

ARULKUMARAN, S., NICOLINI, U., FISK, N. M. & RODECK, C. H., 1990. Fetal vesicorectal fistula causing oligohydramnios in the second trimester. Case report. *British Journal of Obstetrics and Gynaecology, 97*, 449–451.

BARSS, V. A., BENACERRAF, B. R. & FRIGOLETTO, F. D., 1984. Second trimester oligohydramnios, a predictor of poor fetal outcome. *Obstetrics and Gynaecology, 64*, 608–610.

BENACERRAF, B. R., 1990. Examination of the second trimester fetus with severe oligohydramnios using transvaginal scanning. *Obstetrics and Gynaecology, 75*, 491–493.

BRONSHTEIN, M., KUSHNIR, O., BEN-RAFAEL, Z., SHALEV, E., NEBEL, L., MASHIACH, S. & SHALEV, J., 1990. Transvaginal sonographic measurement of fetal kidneys in the first trimester of pregnancy. *Journal of Clinical Ultrasound, 18*, 299–301.

GEMBRUCH, U. & HANSMANN, M., 1988. Artificial instillation of amniotic fluid as a new technique for the diagnostic evaluation of cases in oligohydramnios. *Prenatal Diagnosis, 8*, 33–45.

HACKETT, G., NICOLAIDES, K. H. & CAMPBELL, S., 1987. Doppler ultrasound assessment of fetal and uteroplacental circulations in severe second trimester oligohydramnios. *British Journal of Obstetrics and Gynaecology, 94*, 1074–1077.

MERCER, L. J. & BROWN, L. G., 1986. Fetal outcome with oligohydramnios in the second trimester. *Obstetrics and Gynaecology, 67*, 840–842.

NICOLINI, U., SANTOLAYA, J., HUBINONT, C., FISK, N., MAXWELL, D. & RODECK, C., 1989. Visualisation of fetal intra-abdominal organs in second trimester severe oligohydramnios by intraperitoneal infusion. *Prenatal Diagnosis, 9*, 191–194.

ROTTEM, S. & BRONSHTEIN, M., 1990. Transvaginal sonographic diagnosis of congenital anomalies between 9 weeks and 16 weeks, menstrual age. *Journal of Clinical Ultrasound, 18*, 307–314.

1992, *The British Journal of Radiology*, 65, 458–462

Correspondence

(The Editors do not hold themselves responsible for opinions expressed by correspondents)

Biliary dilatation and pseudo-tumour of the liver

THE EDITOR—SIR,

The detection of intrahepatic biliary dilatation is central to the investigation of jaundice and the biochemical abnormalities associated with liver disease. While there may be difficulty distinguishing minimal biliary dilatation from the normal appearance, and biliary obstruction may occur with little biliary dilatation, it is generally agreed that ultrasonography is highly sensitive in the detection of moderately or markedly dilated intrahepatic ducts. A patient was recently encountered with markedly dilated ducts in which the ultrasonic appearances were atypical leading to an erroneous interpretation of the findings.

An asymptomatic 80-year-old male was found to have abnormal blood biochemistry suggestive of cholestasis. Initial assessment by ultrasonography and computed tomography (CT) of the liver was reported to be normal. Magnetic resonance imaging (MRI) of the liver 4 weeks later revealed a very small left lobe of the liver and dilated intrahepatic ducts in the right lobe. There was a region of increased T_2 signal in the left lobe thought to represent tumour. 6 weeks after initial presentation he became clinically jaundiced and was referred to this centre for further evaluation and management. A second ultrasound examination of the liver confirmed the presence of dilated right-sided intrahepatic ducts, the larger of which contained echogenic material. The common hepatic duct lumen was obliterated by echogenic material. The left lobe was small and hypoechoic with a diffusely abnormal texture (Fig. 1). No ducts were visible within the left lobe and the appearance was thought to represent replacement of liver tissue by tumour. Endoscopic retrograde cholangio-pancreatography (ERCP), later the same day, demonstrated an obstructing irregular hilar stricture (Fig. 2). There was dilatation of intrahepatic ducts in the right lobe and also, more markedly, in the left. The left ducts were crowded together suggesting atrophy of the lobe. No malignant cells were seen in cytological samples from the stricture but a presumptive diagnosis of malignant tumour was made on the basis of cholangiographic appearances.

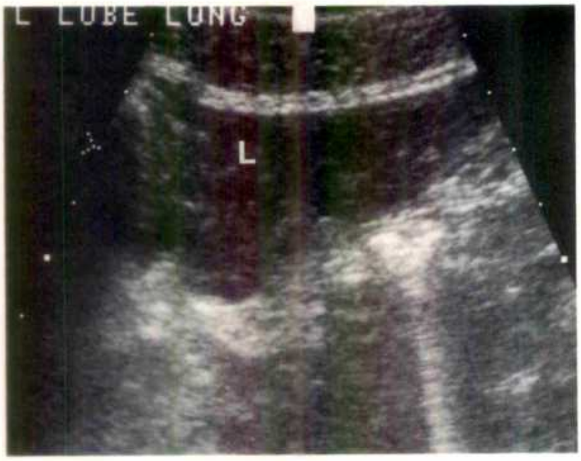

Figure 1. Longitudinal midline section. Left lobe of liver (L). There is a generalized abnormal echogenicity with no visualization of dilated intrahepatic ducts (Acuson™ 5 MHz curved linear array).

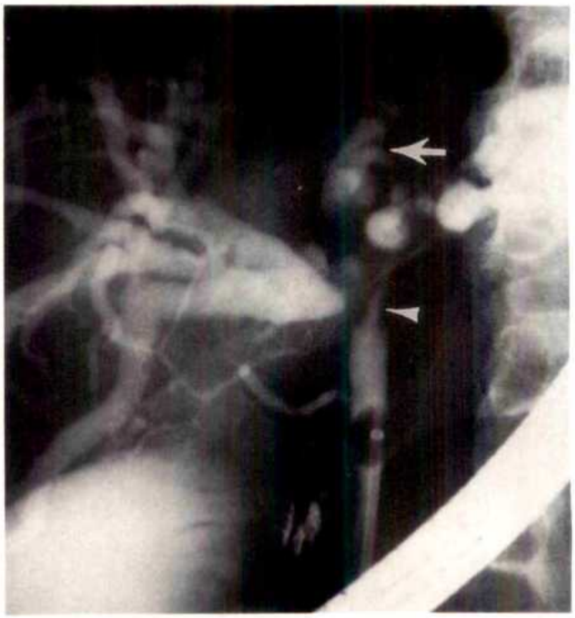

Figure 2. Cholangiogram showing irregular hilar stricture (arrowhead) with intrahepatic biliary dilatation, particularly in the left lobe (arrow).

In retrospect it is clear that the MRI appearance of high T_2 signal in the left lobe had been caused by bile in a dilated biliary system rather than by tumour. The region had not been adequately imaged by CT because of the small size of the left lobe and the region's susceptibility to respiratory and cardiac movement. Ultrasonography should have been the ideal imaging modality in this circumstance but the dilated ducts in the left lobe were not visible. The reason for this was the presence of echogenic bile ("biliary sludge") within the dilated biliary system. A small amount of such echogenic material was present in the right lobe ducts but the interface with the duct wall and liver parenchyma was preserved and there was no difficulty in detecting the presence of dilated ducts. In the left lobe obstruction was more complete and was presumably long-standing, resulting in complete filling of the biliary system with bile of similar echogenicity to the liver parenchyma. It was noticeable that the sonographic appearance of the left lobe was diffusely abnormal and, in retrospect, it could be seen that the ultrasound beam attenuation was, perhaps, less than would be expected for solid tumour but it was not appreciated that such an appearance could be a manifestation of biliary obstruction.

Gall bladder sludge occurs in the presence of biliary stasis and is thought to be due to crystalline calcium bilirubinate, cholesterol and mucus. It is seen relatively frequently but its significance remains uncertain (Ohara, 1990). Echogenic bile is also seen above obstructing bile duct lesions where blood, pus and cellular debris may also play a role in the abnormal appearance, but there is very little published information regarding this ultrasonic finding. Whatever the clinical significance, the presence of sludge in the bile ducts may obscure the signs of biliary dilatation. This condition should be considered when there are clinical or biochemical features of cholestasis and dilated intrahepatic bile ducts are not visible, especially if the sonographic liver texture is abnormal.

Yours etc.,

P. Grech

Department of Radiology,
Duke University Medical Center,
PO Box 3808,
Durham,
North Carolina 27710,
USA

(*Received 2 January 1992, accepted 30 January 1992*)

Reference

Ohara, N. & Schaefer, J., 1990. Clinical significance of biliary sludge. *Journal of Clinical Gastroenterology*, *12*, 291–294.

The use of theophylline, an adenosine antagonist in the prevention of contrast media induced nephrotoxicity

The Editor—Sir,

Impaired renal perfusion has been implicated in the pathogenesis of contrast media (CM) induced nephrotoxicity (El-Sayed et al, 1991). Animal and, more recently, clinical studies have suggested that endogenous adenosine may mediate the renal haemodynamic response to intravascular CM (Arend et al, 1987; Katholi et al, 1991). We have recently attempted to evaluate the protective effect of an adenosine antagonist, theophylline against CM-induced nephrotoxicity. 21 patients (14 males, 7 females; mean age 54 [±9.0] years) undergoing coronary angiography were randomly selected to receive either theophylline 125 mg tds or placebo. Treatment commenced a day before angiography and continued for 48 h afterwards. Iopramide 300 or Ioxaglate 320 was used for the examination. Creatinine clearances were measured before and 72 h after the examination. No significant change in the creatinine clearance was demonstrated following angiography in either group. In the placebo group (n=8) the mean dose of CM was 131.9 (±34.3) mls, the creatinine clearance before the examination was 86.9 (±25.4) mls, the mean creatinine clearance before the examination was 89.7 (±16.0) ml/min and 83 (±40.1) ml/min 3 days after. The mean serum theophylline concentration immediately before angiography was 5.8 (±3.1) mg/l. Three patients (mean age 52.7 [±5.3] years) in this study developed significant renal impairment with marked falls in creatinine clearance from 78 (±29) ml/min to 24.7 (±7.4) ml/min post-examination. Two of these patients were on theophylline. Two of the patients had received Ioxaglate 320 and one had received Iopramide 300. The mean CM dose was 133.3 (±2.4) mls. None of these patients were taking nephrotoxic drugs.

In this small series a protective effect of theophylline, with these doses, was not evident. However, the incidence of nephrotoxicity was 14% which is comparable with that reported in the literature (Burns, 1989). Larger studies using bigger doses of theophylline are required to reach a firm conclusion on the role of adenosine antagonists in preventing CM induced nephrotoxicity.

Yours etc.,

M. R. Gandhi
P. Brown
C. A. J. Romanowski
S. K. Morcos
*S. Campbell
§A. M. El Nahas
#T. A. Gray

Departments of Radiodiagnosis,
*Cardiology, §Renal Medicine
and #Chemical Pathology,
Northern General Hospital,
Herries Road,
Sheffield
S5 4LH, UK

(*Received 22 January 1992, accepted 30 January 1992*)

References

Arend, L. J., Bakris, G. L., Burnett, J. C., Megerian, C. & Spielman, W. S., 1987. Role for intrarenal adenosine in the haemodynamic response to contrast media. *Journal of Laboratory and Clinical Medicine*, *110*, 406–411.

Burns, A. S., 1989. Nephrotoxicity of contrast media. *Kidney International*, *36*, 730–740.

El-Sayed, A., Haylor, J. L., El-Nahas, A. L., Falzano, S. & Morcos, S. K., 1991. Haemodynamic effect of water soluble contrast media on the isolated perfused rat kidney. *British Journal of Radiology*, *64*, 435–439.

Katholi, R. E., Taylor, G. J., McCann, W. P., Woods, W. T., Womack, K. A. & MiKell, F. L., 1991. Contrast medium nephrotoxicity in humans is mediated by intrarenal adenosine and related to osmotic load. *Radiology* (suppl), *181*, 285.

A sense of déja vu

The Editor—Sir,

I have been stimulated to add to the correspondence on *A sense of déja vu* in your October issue (Hartnell, 1991; Hinwood & Manhire, 1991; Renny, 1991) following a similar feeling on reading a paper in your September issue on the use of the Vygon tube for small bowel enemas (Ashleigh et al, 1991) from North Manchester, UK.

Dr Hartnell makes the point that authors in non-European journals fail to acknowledge previous reports in European journals. This is true but factors of time as well as geography result in the "failure" of literature searches. Midline searches seem to go in 5, 10 or 15 year lengths (with 5 being the cheapest).

I published a paper describing the use of a nasojejunal tube made by Vygon Ltd. (trade names were banned then) for small bowel enemas in children in Booth Hall Children's Hospital, North Manchester (Ratcliffe, 1983), to which no reference is made by Ashleigh et al. My paper was written in the same city of the same country as the paper by Ashleigh et al, and it appeared in *Clinical Radiology* which is published in the same city, country and continent as the *British Journal of Radiology*, but more than 5 years ago.

Out of time is out of mind and apparently out of conscious memory too, because it would have been I who left several years' supply of the lurid green Vygon tubes in the store cupboard at Booth Hall. It may well be that my successor at Booth hall considered these tubes to belong to that category of apparatus which everyone's antecedent seems to have over-ordered and for which one can think of no rational and decent use.

As a point of historical accuracy and to get the attribution right it was Dr Victor Miller, gastroenterologist at Booth Hall Hospital who suggested that I should use the Vygon tube when I was discussing with him the difficulty of getting the standard Nolan tube around the duodenum which has a tighter curve in children than in adults.

Having used Vygon tubes for 10 years I endorse everything that Ashleigh et al say about them. I have tried several other types of tube but I still think the Vygon is the best tube for SBEs in children and have them imported specially to Australia. I am glad that they have been found and proved suitable for use in adults. It is worth making the point that if you want to know the nicest as well as the most effective way of doing something — ask a paediatric radiologist. We have usually got round to doing it years before the adult radiologists have thought of it.

Yours etc.,

J. Ratcliffe

X-ray Department,
Royal Children's Hospital,
Brisbane,
Australia

(*Received 6 January 1992, accepted 30 January 1992*)

References

Ashleigh, R. J., Spinks, B. C. & Bisset, R., 1991. The use of a disposable nasoduodenal feeding tube for the small bowel enema examination. *British Journal of Radiology, 64*, 869–870.

Hartnell, G. G., 1991. A sense of deja vu. *British Journal of Radiology, 64*, 976.

Hinwood, D. & Manhire, A. R., 1991. Percutaneous nephrostomy to relieve renal tract obstruction in pregnancy. *British Journal of Radiology, 64*, 976.

Ratcliffe, J. F., 1983. The small bowel enema in children. A description of a technique. *Clinical Radiology, 34*, 287–289.

Renny, F. H., 1991. Percutaneous nephrostomy to relieve renal tract obstruction in pregnancy. *British Journal of Radiology, 64*, 976.

Altered radiotherapy fractionation in medulloblastoma

The Editor—Sir,

Plowman and Doughty have recently described a partial transmission block technique for the treatment of children with medulloblastoma or similar tumours, who require total neuraxis radiotherapy (Plowman & Doughty, 1991). In this technique, the neuraxis radiotherapy is given in a larger number of smaller fractions, and it is proposed that this will reduce the neurological morbidity associated with the treatment without reducing tumour control rates. While we agree that late side effects are likely to be less severe, we do not accept that tumour control will be unchanged; indeed we expect that it will be significantly impaired.

Using the linear-quadratic model, a prediction of the biological effect of a fractionated course of radiotherapy can be obtained by rearranging the expression:

$$S_{F(n)} = e^{-n(\alpha d + \beta d^2)}$$

where $S_{F(n)}$ is the fraction of cells surviving after n radiation doses, each of d Gy. The biologically effective dose (BED) (Fowler, 1989) is given by:

$$\mathrm{BED} = nd\left(1 + \frac{d}{\alpha/\beta}\right)$$

In Table I we have used this equation to compare possible neuraxis treatments for the child with high-risk disease described by Plowman and Doughty. Normally, 35 Gy in 20 fractions over 4 weeks would be given, and this is shown as Regimen A. The proposed new treatment, Regimen B, is 35 Gy in 35 fractions over 7 weeks. Regimen C also gives 35 fractions over 7 weeks, but the total dose is calculated to give the same predicted late nervous system toxicity as the standard, shorter course.

The BED is shown for three values of alpha/beta. 3 Gy represents normal neural tissue, while 20 Gy and 50 Gy have been chosen as approximations of the medulloblastoma response. It is difficult to give precise values for the tumour alpha/beta ratio as there is little published data. Neuroblastoma is probably not analagous to medulloblastoma as its radiobiological behaviour is different (Deacon et al, 1984). The alpha/beta ratios for two medulloblastoma cell lines have been measured at 51 Gy and 82 Gy (Fertil & Malaise, 1981), but these values may be artefactually elevated (Williams et al, 1985), as sublethal damage is probably less effectively repaired

Table I. The biologically effective dose of various treatment regimens at different alpha/beta ratios.

Regimen	Total dose (Gy)	Biologically effective dose by alpha/beta ratio (Gy)		
		3 Gy	20 Gy	50 Gy
A. 20 x 1.75 Gy	35.0	55.4	38.1	36.2
B. 35 x 1.0 Gy	35.0	46.7	36.8	35.7
C. 35 x 1.145 Gy	40.1	55.4	42.4	41.0

in vitro than *in vivo*.

Table I shows that Regimen B, as proposed by Plowman and Doughty, gives a lower BED than Regimen A for all values of alpha/beta. The difference is small when alpha/beta is high, but becomes significant at lower levels of alpha/beta. It is quite possible that the true alpha/beta ratio of medulloblastoma is low enough for Regimen B to represent an important reduction in BED.

Regimen C illustrates the predicted reduction in neural toxicity obtained by using an increased number of fractions. Theoretically, 40.1 Gy could be given over 35 fractions with no more late nervous tissue damage than 35 Gy in 20 fractions. In practice, however, nervous tissue tolerance may not increase as predicted with reduced fraction size at these low fraction doses (Ang et al, 1985).

A further effect of the new regimen is to extend overall treatment time by 21 days. This is unlikely to result in any sparing of neural tissue injury (Van der Kogel, 1986), but would permit tumour proliferation. There is evidence that squamous cell head and neck malignancies enter a phase of rapid proliferation 3 or 4 weeks after starting radiotherapy (Withers et al, 1988). It is certainly possible that proliferation may accelerate even earlier (Fowler, 1989). The proposed new treatment duration would not only allow more proliferation at pre-treatment rates, but would extend into the period in which accelerated proliferation may be expected.

For both these reasons, the new regime proposed by Plowman and Doughty represents a reduction in the effective dose to the tumour, and we would expect this to worsen control rates. In the absence of cell kinetic data on medulloblastoma it is not possible to predict the increase in dose required to counteract proliferation. In view of this we would advocate caution before changing from a clinically tested treatment.

Yours etc.,

N. P. Bates
M. V. Williams

Department of Clinical Oncology,
Addenbrooke's Hospital,
Hills Road,
Cambridge
CB2 2QQ, UK

(Received 1 November 1991, accepted 12 February 1992)

References

Ang, K. K., Van der Kogel, A. J. & Van der Schueren, E., 1985. Lack of evidence for increased tolerance of rat spinal cord with decreasing fraction doses below 2 Gy. *International Journal of Radiation Oncology, Biology and Physics, 11*, 105–110.

Deacon, J., Peckham, M. J. & Steel, G. G., 1984. The radioresponsiveness of human tumours and the initial slope of the cell survival curve. *Radiotherapy and Oncology, 2*, 317–323.

Fertil, B. & Malaise, E.-P., 1981. Inherent cellular radiosensitivity as a basic concept for human tumor radiotherapy. International *Journal of Radiation Oncology, Biology and Physics, 7*, 621–629.

Fowler, J. F., 1989. The linear-quadratic formula and progress in fractionated radiotherapy. *British Journal of Radiology, 62*, 679–694.

Plowman, P. N. & Doughty, D., 1991. An innovative method for neuraxis radiotherapy using partial transmission block technique. *British Journal of Radiology, 64*, 603–607.

Van der Kogel, A. J., 1986. Radiation-induced damage in the central nervous system: an interpretation of target cell responses. *British Journal of Cancer, 53* (Suppl. VII), 207–217.

Williams, M. V., Denekamp, J. & Fowler, J. F., 1985. A review of alpha/beta ratios for experimental tumours: implications for clinical studies of altered fractionation. *International Journal of Radiation Oncology, Biology and Physics, 11*, 87–96.

Withers, H. R., Taylor, J. M. G. & Maciejewski, B., 1988. The hazard of accelerated tumor clonogen repopulation during radiotherapy. *Acta Oncologica, 27*, 131–146.

Authors' reply

The Editor—Sir,

The major morbidity of neuraxis radiotherapy in young children is late neuropsychological retardation, which may be severe (reviewed by Gamis et al, 1991). Two recent studies suggest that the total radiation dose to the neuraxis may not be lowered safely in (? any) group of these children (Deutsch et al, 1991, SIOP medulloblastoma second trial unpublished results), and this prevents the most certain method of reducing this morbidity. An alternative method of reducing this morbidity must be desirable, but carefully weighed against a possible loss of tumour control.

Like a bumble-bee's flight capability necessitating modification of the laws of aerodynamics, so the clinical observation of paediatric tumour (including primary brain tumour) responses to low daily fraction sizes may indicate the need for caution in accepting "biologically effective dose models" that reach conclusions contrary to such clinical observations. Until the α/β ratios for human tumours *in vivo* and the relevant proliferation factors are known, such models must be regarded critically.

Contrary to the statement by Bates and Williams, our partial transmission block method does not extend overall treatment (by 21 days) and we would point out that the conventional dose per fraction is maintained to the posterior fossa (highest risk site) throughout.

In his 1985 Leukaemia Research Fund Annual Guest Lecture, and in a radiobiological context, Professor Lazlo Lajtha stated "It is very dangerous to fall in love with models". We would suggest a Bart's amendment: "one may later regret...".

We believe that the late neuropsychological damage in children surviving neuraxis irradiation by conventional shrinking field technique may be severe and that this justifies careful exploration of our published partial transmission block technique, for which we maintain the rationale remains intact (Plowman & Doughty, 1991). In an upcoming paper, we apply the α/β concept to our application of the partial transmission block technique to pineal tumour therapy (Sebag-Montefiore et al, 1992).

Yours etc.,

P. N. Plowman
D. Doughty
D. Sebag-Montefiore

Department of Radiotherapy,
St Bartholomew's Hospital,
London
EC1A 7BE, UK

(Received 2 January 1992, accepted 12 February 1992)

References

Gamis, A. S., Neglia, J. P. & Robison, L. L., 1991. Neuropsychological sequelae of radiotherapy. In *Complications of Cancer Management*, Ed. by P. N. Plowman, T. J. McElwain and A. Meadows (Butterworth-Heineman, Guildford), pp. 348–360.

Deutsch, M., Thomas, P., Boyett, J., Krischer, J. P., Finlay, J., Kun, L., Hammond, D. & Vietti, T., 1991. Low stage medulloblastoma: a children's cancer study group (CCSG) and pediatric oncology group (POG) randomised study of standard versus reduced neuraxis irradiation. *Proceedings of the American Society of Clinical Oncology, 10*, 124.

Plowman, P. N. & Doughty, D., 1991. An innovative method for neuraxis radiotherapy using partial transmission block technique. *British Journal of Radiology, 64*, 603–607.

Sebag-Montefiore, D., Doughty, D. & Plowman, P. N., 1992. Intracranial germ cell tumours II: the application of a partial transmission block radiotherapy technique to reduce late morbidity. *Clinical Oncology*, in press.

1992, *The British Journal of Radiology*, *65*, 463–466

Proceedings of the British Institute of Radiology

Cerebral blood flow—practical measurement and clinical relevance, a multimodality approach

Abstracts presented at a meeting organized by the BIR Nuclear Medicine Committee, held at the British Institute of Radiology, 36 Portland Place, London W1N 4AT on Tuesday 12 February 1991

Chairman: Dr D. A. Cunningham

Cerebral blood flow, practical measurement and clinical relevance, by J. D. Pickard
Measurement of cerebral blood flow and perfusion by MRI, by M. A. Smith
MR angiography of the cerebral circulation, by T. S. Padayachee, M. Tarnawski, M. J. Graves, M. G. Taylor and P. Graves
Ultrasound and the assessment of cerebral blood flow in the infant, by M. Levene. Abstract not received.
A transcranial Doppler ultrasound: a non-invasive, atraumatic solution, by D. E. Dorrance
X-ray measurement of cerebral blood flow, by P. Butler. Abstract not received.
Measurement of blood flow in vessels using DSA video recordings, by J. N. H. Brunt, G. H. du Boulay, A. Wallis and D. A. G. Wicks
Radionuclide tracers in the management of cerebral blood flow and perfusion, by K. E. Britton, C. C. Nimmon and H. Huneidi
Radiolabelled ligands in the assessment of cerebral blood flow and perfusion, P. J. Ell
A split dose technique for measuring changes in cerebral blood flow patterns, by D. J. Wyper and J. Patterson
Prevalence of cerebral vascular reserve impairment in patients with symptomatic carotid artery disease, by A. R. Naylor, M. V. Merrick and C. V. Ruckley
PET and cerebral blood flow measurement, by A. A. Lammertsma
Radiological and clinical correlations—the relevance of cerebral blood flow, by I. F. Moseley. Abstract not received.

Cerebral blood flow, practical measurement and clinical relevance

J. D. Pickard
University Department of Neurosurgery, Addenbrooke's Hospital, Hills Road, Cambridge CB2 2QQ

Studies of human cerebral blood flow (CBF), however interesting, have often been criticized for their failure to provide information of immediate clinical utility. If careful attention is paid to matching the methodology to the question, then studies of the cerebral circulation and of cerebral metabolism in general, and of cerebrovascular reactivity in particular, do have a valuable place in clinical management. Many useful questions may be addressed using inexpensive, non-invasive and mobile techniques. Measurements of "big tube" flow (transcranial and cervical Doppler flow velocity; magnetic resonance angiography), global/hemisphere CBF (^{133}Xenon intravenous or inhalation), and regional CBF (quantitative: positron emission tomography; semi-quantitative: single photon emission computed tomography (SPECT)) are complementary in their study of pathophysiology, clinical decision making and definition of end points for therapeutic trials. Cerebrovascular reactivity is particularly useful. If populations of patients are compared with differing degrees of severity of pathology, for example, cerebral arterial narrowing ("vasospasm") after haemorrhage into the subarachnoid space, mean resting CBF may show subtle differences but with such variability that the results cannot be used to predict what will happen to an individual patient. The great value of cerebrovascular reactivity is that it is a much more robust discriminant between patients than is baseline or resting CBF alone: it can be used to predict what will happen to the individual, not just to a population. This concept has proven very helpful when assessing patients for cerebral aneurysm surgery, carotid endarterectomy and extracranial-intracranial bypass, and carotid ligation. Similarly, Doppler flow velocity and SPECT maps of cerebral perfusion may prove to have their everyday clinical applications.

Measurement of cerebral blood flow and perfusion by MRI

M. A. Smith
Department of Medical Physics, University of Leeds, Leeds General Infirmary, Leeds

In conventional magnetic resonance imaging (MRI) the signal intensity is influenced by motion. Flowing blood or cerebrospinal fluid (CSF) can produce an increase or a decrease in signal intensity, depending on a number of factors; in most MR images a signal void is produced by flowing blood enabling the structure of vessels to be identified. Techniques of magnetic resonance have been developed, however, which give specific information about flow within blood vessels. When we consider the motion of blood in MRI we must consider the size of the voxel in relation to the size of the vessel. One category of MR flow techniques give a quantitative measurement of velocity or flow in blood vessels that are larger than the size of the voxel. Velocity phase maps can be acquired in which the pixel value determined by the phase of the nuclear magnetic resonance (NMR) signal which is linearly related to the velocity at that point within a vessel. Such techniques can be used to obtain measurements of flow and velocity profiles within the great vessels at various points in the cardiac cycle. In addition, when certain constraints are applied to the pulse sequence, the pixel phase value is related to the time averaged volume flow. Errors owing to partial volume effect and vessel angulation to the slice can be effectively eliminated and flow in smaller vessels such as the middle cerebral arteries can be measured. When the vessels are smaller than the voxel we move towards the measurement of perfusion. In spin echo sequences the signal intensity of a voxel decreases owing to spin dephasing as a result of T2 or motion. In liquids the latter can be in the form of diffusion. The measurement of perfusion involves the study of flow in the capillary bed; in such a case the vessel size is very much smaller than the voxel volume. Within the voxel there is no preferred direction and the effect on spin dephasing is analogous to diffusion. In fact, for the purposes of some MR techniques, perfusion can be considered as "macrodiffusion". The study of perfusion in a single image using this principle is known as intra voxel incoherent motion (IVIM). Perfusion can also be studied following an injection of a paramagnetic substance such as Gd-DTPA. Multiple images are acquired allowing regional blood volume to be calculated.

MR angiography of the cerebral circulation

T. S. Padayachee, M. Tarnawski, M. J. Graves, M. G. Taylor and P. Graves
MR Flow Group, Division of Radiological Sciences, UMDS, Guy's Campus, London

The use of inflow magnetic resonance (MR) angiography to image the cerebral circulation is described. In the cerebral circulation, vessel dimensions, tortuosity and blood flow velocity vary considerably depending upon whether the vessels are intracranial or extracranial and if they are from the arterial or venous circulations. These variables must be considered when optimizing the choice of sequence parameters to image different vascular systems. Imaging of the extracranial cerebral arteries is optimally achieved using a 2D multiple single slice (MSS), axial acquisition, whilst for the intracranial cerebral artery circulation an axial, 3D volume acquisition is necessary to achieve sufficient signal-to-noise to image the smaller diameter cerebral arteries. The dural sinuses in comparison are of larger diameter and carry slower velocity blood flow and are imaged best with a 2D MSS, in-plane (axial or sagittal) acquisition. Although good images are achieved routinely in normal volunteers, patient studies suffer from additional constraints which require further modification of sequence parameters. For example, stenosis of the carotid arteries is associated with turbulent, high velocity blood flow which results in signal loss so that stenosis size and length may not be faithfully represented. Therefore, at present, extracranial cerebral angiograms can only provide a low resolution image which does not compare favourably with ultrasound colour flow mapping, since the latter provides both morphological and haemodynamic information non-invasively and in real-time. Intracranially, pathologies such as arterio-venous malformations (AVM's) can be demonstrated, but to be clinically useful additional dynamic information is required to define the source of feeding and draining vessels. Furthermore, although large cerebral aneurysms can be identified, small and even medium sized aneurysms can not be confidently resolved at present. The forte of this technique in the intracranial circulation lies in its ability to non-invasively monitor the response to therapy and to aid in planning neurosurgical procedures. With regard to the venous circulation the dural sinuses can be clearly imaged and reduced or absent flow demonstrated in pathology. Combination with conventional MR imaging make this technique the method of choice for investigating dural sinus thrombosis. In summary magnetic resonance angiography (MRA) shows potential for providing clinically useful angiograms and in some instances provides improved information over conventional imaging techniques. However, since current technological developments are still improving flow image quality, it is too early to judge the full clinical impact of MRA. Ultimately, the combination of quantitative flow data with qualitative images (angiograms) will make MRA an attractive alternative to conventional imaging modalities.

A transcranial Doppler ultrasound: a non-invasive, atraumatic solution

D. E. Dorrance
South East Thames Regional Neurosurgical Unit, Brook General Hospital, London SE18 4LW

Transcranial Doppler ultrasound (TCD) permits the measurement of blood flow velocities, but not absolute flow, in the major intracranial vessels in humans and animals. It has proved to be a versatile tool both clinically and in research. A 2 MHz microprocessor controlled, directional, range-gated Doppler transducer is placed on the skin surface at one of three "windows" (transtemporal, transorbital or basilar via foramen magnum). The signal obtained is spectrally analysed by fast Fourier transfer. The three commonest parameters calculated from the resultant sonagram are: (i) peak systolic velocity, Vpksys; (ii) time-averaged mean velocity, TAV and (iii) pulsatility index, PI ([peak systolic − end diastolic velocities]/mean velocity). During monitoring the middle cerebral artery is usually insonated for anatomical reasons and as it supplies upto 80% of the hemisphere flow. The main disadvantages of TCD are that absolute flow may not be calculated and reliable results are dependent on the knowledge, experience and skill of the operator. Some investigators believe that as interpretation of results may be subjective, TCD should be used in conjunction with other techniques. The main advantages of TCD are that it gives repeatable or continuous dynamic measurements of intracranial haemodynamics with excellent patient/volunteer acceptability. It is non-invasive with no recognized risks and may be used in conjunction with other techniques. The transducer requires a small area of access, places few constraints on the patient/volunteer, does not interfere with other equipment and permits other activities to continue. The equipment is truly portable. The fields in which TCD is used are varied. Diagnostically it is used to delineate areas of vessel absence, obstruction or narrowing, *i.e.* stenoses or vasospasm where lumen reduction is greater than 50%; in identifying feeder and feeder collateral vessels in arteriovenous malformations; in subcalvian steal syndrome. Extracranial compression tests may aid in the diagnoses. Although brain death is characterized by a waveform containing both forward and reverse flow monitoring the development of this waveform gives more confidence. Clinically, areas where TCD is used in monitoring include: (i) the time course of vasospasm or the effect of angioplasty in subarachnoid haemorrhage; (ii) cerebrovascular flow velocities during carotid surgery, cardiac bypass surgery and cardiopulmonary resuscitation and (iii) the effect of changes in carotid flow on cerebral flow velocities, *i.e.* after carotid ligation or spontaneous carotid dissection with possible subsequent recanalization. As a research monitoring tool TCD has proved successful. It is of particular use where the haemodynamic response is very sudden and/or short lived, *i.e.* during cigarette smoking, where there is a limited measurement time available; during nitrous oxide inhalation or where longer term monitoring is required; during sleep apnea. TCD measurements have not been confined to human studies; using a 8 MHz transducer changes in animal cerebral blood velocities have been monitored.

Measurement of blood flow in vessels using DSA video recordings

*John N. H. Brunt, George H. du Boulay, Adrienne Wallis and David A. G. Wicks
**Medical Biophysics Dept., Manchester University, Oxford Road, Manchester M13 9PT and Institute of Neurology, Queen Square, London WC1N 3BG*

We describe a video-recorded digital subtraction angiography (DSA) volume blood flow measurement technique for carotid and cerebral arteries. For validation, we recorded flows (100–1500 ml.min^{-1}) through 3D calibrated tortuous tubes of 2–7 mm diameter. A calibrated electromagnetic flowmeter measured the flows during contrast medium (CM) injections. Video sequences of 64 images (2.6 s) are played back, and are computer-processed as follows. A sampling area is positioned along a vessel of interest and values from perpendicular density profiles (corresponding to CM mass per unit vessel length) form a "vector". Each vector, corresponding to a single video frame, is drawn into a "parametric image" representing CM mass or concentration as a function of distance along the vessel and of time. Volume flow is obtained by incorporating calibre measurements and deriving instantaneous, local flow velocity from the inclination of the isoconcentration contour at any point in the image using various image processing algorithms. In the validation experiments the angiographic flow measurements agreed with electromagnetic flows to within 5% in the larger tubes. We have analysed carotid DSA recordings from five patients. The additional time required during a clinical angiogram to produce the video recordings is approximately 4 min. We conclude that accurate flow measurements can be made from carotid DSA video recordings. We expect the technique to have sufficient sensitivity to measure flow in the anterior and middle cerebral arteries, though precision may be less good.

Radionuclide tracers in the management of cerebral blood flow and perfusion

K. E. Britton, C. C. Nimmon and H. Huneidi
St Bartholomew's Hospital, West Smithfield, London EC1A 7BE

There are three major classes of tracers for cerebral blood flow (CBF) measurement. Diffusible indicators such as Xenon-133 measaure CBF/unit weight, called cerebral perfusion, based on a compartmental model whose assumptions concerning volume of distribution, partition coefficient and exchange rates may not be met in cerebral pathology. Non-diffusible indicators such as ^{99}Tc^{m} human serum albumin measure CBF, based on a linear system model giving regional blood volumes and using deconvolution to give the regional mean transit times so that regional flows are obtained in ml/min. Since autoregulation may be impaired in cerebrovascular disorders, independent measures of both volume and time are required. Total CBF under 600 ml/min indicates danger in operating on patients with subarachnoid haemorrhage. Single photon emission computed tomography (SPECT) is helpful in evaluating arterio venous malformation. Thirdly, single pass uptake tracers such as ^{99}Tc^{m} HMPAO and ^{99}Tc^{m} ECD, while primarily for SPECT qualitative regional distribution, may also be evaluated using the linear system approach to give global and hemispheric flows. This combination is useful in the evaluation of patients with head injuries during their rehabilitation.

Radiolabelled ligands in the assessment of cerebral blood flow and perfusion

Peter Josef Ell
Institute of Nuclear Medicine, Middlesex Hospital, Mortimer Street, London W1N 8AA

The investigation of regional cerebral blood flow (CBF) is now carried out in many hospitals in the UK and worldwide. The maturity reached by single photon emission tomography (SPET) and the availability of an increasing range of tracers has permitted regional cerebral blood flow (rCBF)/SPET studies to be carried out not only in the university, or university affiliated medical institutions, but also in the district general hospitals of the country. The discovery of ^{99}Tc^{m} HMPAO (Ceretec, Amersham International plc) was a major step in this field. Since this development, the ^{99}Tc^{m} based tracers have also been described. In this presentation we will review the present knowledge concerning these tracers. The areas of clinical applications continues to grow, particularly in the study of the psychiatric patient. A number of these applications will be demonstrated and also discussed in the light of other ligands, such as those imaging specific receptor functions (*e.g.* the Dopamine D2 receptor and its study via I-123 IBZM).

A split dose technique for measuring changes in cerebral blood flow patterns

D. J. Wyper and J. Patterson
Institute of Neurological Sciences, Southern General Hospital, Glasgow G51 4TF

Although positron emission tomography (PET) scanning is commonly regarded as the imaging technique of choice when measuring cerebral blood flow (CBF), the expense and complexity limits it's clinical value. The development of HMPAO (Certec Amersham International plc) has enabled CBF patterns to be obtained at a more reasonable cost. It has a number of attractive features for clinical use: ^{99}Tc^{m} is readily available and has good gamma emission characteristics; the trapping mechanism means that injection can be given during transient physiological states, and the scanning undertaken at some convenient time point within an hour or two of this; scans can be repeated if necessary. There are, however, two major drawbacks: (1) HMPAO does not enable absolute CBF to be measured with acceptable accuracy; (2) on account of the low washout rate, and 6 h half life of ^{99}Tc^{m} HMPAO it is difficult to measure changes in the pattern of perfusion. We have developed a split dose paradigm which enables regional differences in perfusion pattern to be measured. Approximately 160 MBq of ^{99}Tc^{m} HMPAO is administered for the first set of scans and the remaining 340 MBq for the second set. The scan time has to be increased for the initial scans but the technique enables two measurements to be made without increasing the radiation dose to the patient. The precision of the technique depends on the skill of the single photon emission computed tomography (SPECT) technician, on the clinical category of the patient and on the size and location of the region of interest chosen for comparison. Precision was measured in a control group of 10 patients of mixed brain pathology who had split dose HMPAO scans with no challenge between scans. The results were compared with precision measured on a phantom (test A), on patients who lay still on the couch and had repeat scans done with no movement between scans (test B), on patients who were repostioned on the couch between repeat scans (with a single injection of HMPAO) (test C), and on patients who had repeat CBF measurements 1 week apart (test

Table I. Precision measurements of SPECT scanning in five different test conditions. The precision is measured as 2 × standard deviation of the difference between measurements expressed as percentage. The values are averaged over the two hemispheres

Regions of interest	Typical area of ROI (cm^2)	Test A phantom	Test B patient with no movement	Test C patient with re-alignment	Test D patient rescanned after 1 week	Test E patient imaged using split dose
High frontal	—	—	—	—	9.7	3.6
Parietal	—	—	—	—	11.7	8.3
Frontal	10	2.7	4.6	6.9	11.1	5.7
Temporal	10	3.3	5.3	5.5	16.0	12.2
Posterior temporal	10	4.2	5.7	5.1	10.7	8.3
Occipital	7	3.5	7.0	10.8	12.7	8.1
Basal ganglia	3	9.3	9.2	11.5	14.3	15.9
n	—	6	8	8	10	9

D). The results (Table I) show: (1) that precision is best in the frontal regions of the brain which are least effected by positional errors, and poorest in the small regions, such as basal ganglia where partial voluming is significant; (2) that a patient who appears to lie still in the scanner during the 20 min scanning period does move more than a phantom; (3) that re-alignment significantly increases the error of the measurement; (4) and that the precision of the split dose technique was better than that of the test/retest.

Prevalence of cerebral vascular reserve impairment in patients with symptomatic carotid artery disease

A. R. Naylor, *M. V. Merrick and C. V. Ruckley
*Edinburgh Royal Infirmary, Lauriston Place, Edinburgh EH3 9YW and * Western General Hospital, Crewe Road, Edinburgh EH4 2XU*

There is increasing interest in the concept of cerebral vascular reserve (CVR) impairment in patients with cerebrovascular disease, particularly with regard to the potential long term risk of suffering a stroke. Preliminary work from this centre has suggested that patients with cerebral infarction in association with impaired CVR may be at higher risk of suffering an intra-operative neurological deficit during carotid endarterectomy. Although the prevalence of CVR impairment increases with the severity of extracranial disease, there is relatively little information on the potential contribution of other factors, *e.g.* intracranial vascular pathology. We have employed an isotopic method of quantifying regional mean cerebral transit time in order to evaluate the prevalence and factors associated with CVR impairment in a prospective study of 82 patients with symptomatic carotid artery disease. 22 patients (27%) had evidence of impaired CVR. Patients presenting with a stroke had a higher prevalence of impaired CVR (37%) than patients with TIA (26%) or amaurosis fugax (14%). This trend does not however reach statistical significance. Patients with computed tomography (CT) scan evidence of infarction were significantly more likely to have CVR impairment (48%) than patients undergoing a normal CT scan (17%, $p = 0.005$). As expected, the prevalence of CVR impairment increased with the degree of stenosis in the symptomatic carotid artery; $< 60\% = 6\%$, $> 60\% = 35\%$, $> 75\% = 41\%$, $> 90\% = 55\%$. Our data suggest that while the extent of extracranial vascular disease is a useful predictor of haemodynamic impairment, one should also remain aware of the potential importance of intracranial vascular pathology in the overall assessment of CVR impairment.

PET and cerebral blood flow measurement

A. A. Lammertsma
MRC Cyclotron Unit, Hammersmith Hospital, London W12

The measurement of regional cerebral blood flow (rCBF) with positron emission tomography (PET) is used in two different areas of research: (i) in combination with metabolic or receptor studies and (ii) for activation studies. In the first application, rCBF is measured to characterize delivery of a subsequent metabolic tracer or ligand. Here the rCBF measurement is important, since it provides further information on the ligand signal. For example, it is possible to assess if a reduction in tissue signal is due to a reduced extraction or to a reduced delivery (rCBF). In activation studies, repeat measurements are performed at baseline conditions and during a specific motor, visual, verbal, cognitive or pharmacological activation. These studies are important, firstly, in identifying which brain areas are involved in a certain task and, secondly, in determining the functional interconnectivity of different brain structures. It should be noted that for both types of rCBF measurements a short radioactive half life of the flow tracer is required in order to reduce overall study duration. Given its half life of 2 min the choice of oxygen-15 as a radionuclide is obvious. Although oxygen-15 labelled butanol has some theoretical advances, to date, most rCBF data has been obtained with oxygen-15 labelled water. In the present paper different methods to measure rCBF with oxygen-15 labelled water and PET will be discussed. It will be demonstrated that the two applications listed above have different methodological requirements and, consequently, have used different implementations.

1992, *The British Journal of Radiology*, *65*, 467–468

Book reviews

Textbook of Radiopharmacy: Theory and Practice. Ed. by Charles B. Sampson, pp. xvi + 388, 1990 (Gordon & Breach, New York), $40.00.
ISBN 2-88124-773-3

Radiopharmacy is a new field of work which has appeared in hospitals within the last 20 years. When ^{99}Tc^{m} first came into use in the mid 1960s, the "brews" made up in beakers on the laboratory bench were usually referred to as radioisotopically labelled compounds or something similar. However, the 1970s saw increasing concern with the conditions under which the preparation of these compounds took place and the subsequent introduction of much more elaborate facilities for preparation of what were then becoming known as radiopharmaceuticals. More recently there has been substantial progress in the development of new radiopharmaceuticals, and publications on research in this field are plentiful. This textbook however, goes to the basis of the subject and brings all its various aspects together in a teaching text. Experts in their field have written each of the 19 chapters which deal with the subject from basic nuclear physics through radionuclide generator systems, technetium chemistry, working procedures and quality control, to factors affecting the biodistribution of radiopharmaceuticals and adverse human reactions to them. There is also a chapter which I found particularly interesting on paediatric usage, which includes practical advice on doses and procedures. Clinical applications in nuclear medicine are also described and illustrated, thus providing a more complete textbook for the student.

"Radiopharmaceuticals are amongst the most highly regulated of materials administered to patients because they are controlled both as medicinal products and as radioactive substances"—thus starts a chapter on regulatory requirements for the dispensing and supply of radiopharmaceuticals which describes the situation in the UK. This is continually shifting ground, so the position described is that at the time of writing in 1990; in 1991 we now have the Medicines Control Agency, with probably a new set of rules about to appear!

Overall this is a fairly comprehensive basic textbook on the subject which describes clearly a well balanced and practical approach to the subject relevant to hospital radiopharmaceutical preparation. The general emphasis is on the essentials of the subject, so the editor and contributors have probably wisely steered clear of both novel and contentious issues. Procedures and the underlying principles are chiefly considered rather than details of equipment which are generally easily accessible in other books. An otherwise excellent book is unfortunately marred in places by rather more proof reading lapses than are usually expected.

E. D. WILLIAMS

Renal Cystic Disease AFIP Atlas of Radiologic-Pathologic Correlation Fascicle I. By David S. Hartman, pp. xxxii + 160, 1989 (W. B. Saunders, Philadelphia), £34.00.
ISBN 0-7216-2343-3

This is the first in a series of books on radiological and pathological correlations from the Armed Forces Institute of Pathology in the United States. Many radiologists appreciate the Atlases of Tumor Pathology well established since the 1940s.

This first fascicle in the series is a comprehensively illustrated treatise encompassing all aspects of renal cystic disease. The illustrations are generally of good quality and encompass the various available imaging techniques from plain radiographs to magnetic resonance imaging (MRI). Colour illustrations of gross pathological and microscopic sections are of high quality and aggregated together.

This can be recommended as an informative, easily read and well illustrated comprehensive guide to renal cystic disease. If the forthcoming volumes which are said to include cartilaginous lesions of the skeleton, mediastinal masses, polyposis syndromes, malignant hepatic tumours and gliomas maintain this high quality I am sure the series will be a highly successful and useful one.

D. G. SHAW

Textbook of Uroradiology. By N. Reed, R. W. McCallum and C. M. Sandler, pp. xii + 505, 1990 (Williams & Wilkins, London), £106.00.
ISBN 0-683-02696-8

This is a single volume, comprehensive, manageable textbook written for radiologists by radiologists. There are 22 chapters of easily readable, well illustrated text, complemented by a sympathetic index and generous bibliography section at the end of each chapter. The authors, an American/Canadian team of practising uroradiologists, have more than adequately achieved their aim of providing a standard textbook on the speciality. Interventional techniques are dealt with in a specific chapter and there is a logical chapter layout dealing with cystic disease, tumours, inflammatory disease, hypertension, nephrocalcinosis and nephrolithiasis, neurogenic bladder, renal failure and transplantation. There are no obvious gaps in this textbook, which also deals with the prostate gland, urethra, scrotum and adrenal glands. The depth of description is adequate for those radiologists and urologists particularly interested in the subject, and yet not too detailed for consultants in district general hospitals wishing to use the textbook as a reference. The relevant clinical aspects are particularly well described, especially in the chapters on hypertension and renal failure.

A minor criticism that might be made of the authors is the lack of relevant lists in the text that might be useful for candidates studying for the FRCR Part II examination. Three pages of text with seven illustrations are provided on the subject of penile prostheses.

I found this textbook extremely readable and valuable as a reference document to consult on everyday problems in the speciality. I commend the book to candidates preparing for the FRCR examination, consultants specifically interested in the subject and also those with more general interests. Urologists will also find the book useful for reference purposes. The cost and size of the book should not be prohibitive to either our business managers or the libraries of imaging departments. I can also recommend this textbook to general medical libraries.

M. C. COLLINS

Essentials of Neuroimaging. By J. Robert Kirkwood, pp. 497, 1990 (Churchill Livingstone, Edinburgh), £65.00.
ISBN Not known.

This is a well presented quality hardback edition of 497 pages. There are copious illustrations, the majority of which are of a high standard together with many useful lists and tables; these features together with the lucid text make this an interesting and enjoyable book.

In the preface the author states his intention to provide an in-depth discussion of the basic principles of neurodiagnosis. As the number and complexity of the available imaging techniques has so rapidly increased over the past few years this is an increasingly difficult task to undertake, especially in less than 500 pages. Overall the author has been successful in achieving his goal, though there are deficiences of content and balance. These are probably best illustrated in the first two chapters. In the first chapter on techniques and anatomy there is insufficient detail on the anatomy of the skull, the meninges and the brain and too much attention to the angiographic localization of intracranial mass lesions. The vascular anatomy is adequately described, but there is minimal correlation with its relationship to the brain. Little attention is given to normal anatomical variants. The section on magnetic resonance (MR) needs to be more comprehensive. The quality of the angiogram and MR illustrations is, on the whole, excellent, but those for computed tomography (CT) are too dark. The second chapter covers cerebrovascular disease and is well balanced. There is a helpful diagram defining the cerebral vascular territories, though a similar diagram for the posterior fossa could usefully have been included.

The chapters dealing with intracranial aneurysm and subarachnoid haemorrhage, arteriovenous malformations, cranial tumours in adults, children and adolescents, head trauma, infections, atrophy aging and dementia, hydrocephalus and congenital abnormalities of the brain are generally well constructed and more balanced accounts. It is perhaps a comment on current clinical imaging practice that the section dealing with skull fractures comes at the end of the chapter on head trauma. In view of the improved definition of white matter disease now afforded by MR, this topic could have been discussed in greater detail and I feel that the section on dysmyelinating disease would be more appropriate in the chapter on white matter disease rather than in that on congenital abnormalities of the brain. There is no reference to the MR changes seen in infancy during the normal evolution of myelination.

The final two chapters deal with the spine and spinal trauma. Whilst it is not possible to cover this subject thoroughly in only 120 pages, the author has almost succeeded. The major deficiency relates to normal anatomy and unlike the first chapter there is no mention of the vascular anatomy. The sections covering the investigation of post-operative spinal disease and arachnoiditis could be expanded, especially in relation to the contribution made by MR.

Despite the limitations referred to this book deserves to be a success. It will be of use to radiologists in training and to general radiologists looking for a concise text on neuroimaging for day to day use.

I. R. Colquhoun

The professional difference

The CadPlan 400

Take software:
Written by leading physicists in Europe, the planning software takes into account specific European needs.

Take hardware:
Hewlett Packard's reputation for excellency is fully manifested in the 9000 series of graphics workstations, ideally suited for treatment planning.

Take performance:
The modularity of the software and the wide range of hardware available allow the matching of performance to the needs of each user.

Varian International AG
Medical Equipment
Kollerstrasse 38, CH-6300 Zug, Switzerland
Phone (042) 44 88 44

Varian – the Predictable Future

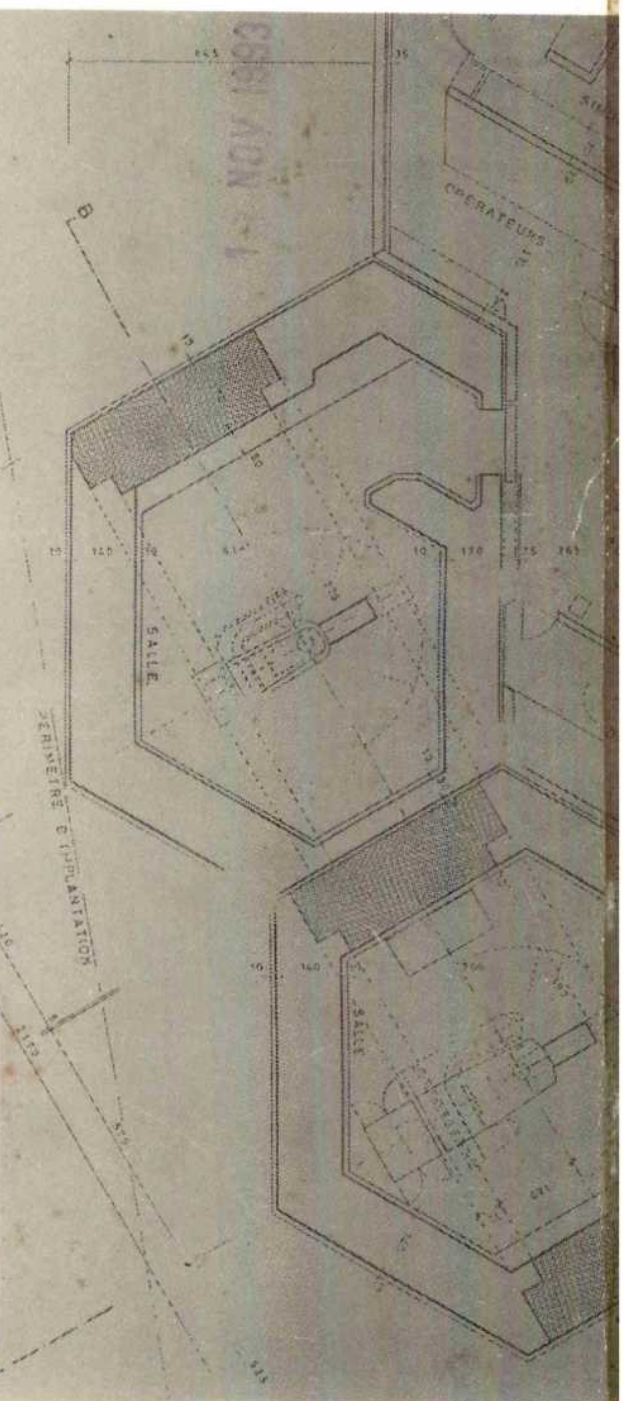

1 NOV 1993

varian